

AD _____

Award Number: DAMD17-98-1-8156

TITLE: Energy-and Intensity-Modulated Electron Beam for Breast
Cancer Treatment

PRINCIPAL INVESTIGATOR: Arthur L. Boyer, Ph.D.

CONTRACTING ORGANIZATION: Stanford University
Stanford, CA 94305-5401

REPORT DATE: October 2003

TYPE OF REPORT: Final Addendum

PREPARED FOR: U.S. Army Medical Research and Materiel Command
Fort Detrick, Maryland 21702-5012

DISTRIBUTION STATEMENT: Approved for Public Release;
Distribution Unlimited

The views, opinions and/or findings contained in this report are those of the author(s) and should not be construed as an official Department of the Army position, policy or decision unless so designated by other documentation.

20040324 030

REPORT DOCUMENTATION PAGEForm Approved
OMB No. 074-0188

Public reporting burden for this collection of information is estimated to average 1 hour per response, including the time for reviewing instructions, searching existing data sources, gathering and maintaining the data needed, and completing and reviewing this collection of information. Send comments regarding this burden estimate or any other aspect of this collection of information, including suggestions for reducing this burden to Washington Headquarters Services, Directorate for Information Operations and Reports, 1215 Jefferson Davis Highway, Suite 1204, Arlington, VA 22202-4302, and to the Office of Management and Budget, Paperwork Reduction Project (0704-0188), Washington, DC 20503

1. AGENCY USE ONLY (Leave blank)		2. REPORT DATE October 2003	3. REPORT TYPE AND DATES COVERED Final Addendum(1 Oct 2001 - 30 Sep 2003)	
4. TITLE AND SUBTITLE Energy-and Intensity-Modulated Electron Beam for Breast Cancer Treatment			5. FUNDING NUMBERS DAMD17-98-1-8156	
6. AUTHOR(S) Arthur L. Boyer, Ph.D.				
7. PERFORMING ORGANIZATION NAME(S) AND ADDRESS(ES) Stanford University Stanford, CA 94305-5401 E-Mail: boyer@reyes.stanford.edu			8. PERFORMING ORGANIZATION REPORT NUMBER	
9. SPONSORING / MONITORING AGENCY NAME(S) AND ADDRESS(ES) U.S. Army Medical Research and Materiel Command Fort Detrick, Maryland 21702-5012			10. SPONSORING / MONITORING AGENCY REPORT NUMBER	
11. SUPPLEMENTARY NOTES				
12a. DISTRIBUTION / AVAILABILITY STATEMENT Approved for Public Release; Distribution Unlimited				12b. DISTRIBUTION CODE
13. ABSTRACT (Maximum 200 Words) In order to deliver MERT plans efficiently, we have designed and manufactured a prototype EMLC based on the results of Monte Carlo simulations and a Varian 25 x 25 cm ² electron applicator. The performance of the EMLC was experimentally evaluated and the results were compared with those of Monte Carlo simulations and a PMLC. We have also developed a complete system of Monte Carlo-based inverse treatment planning system for MERT plans. The system incorporates the Monte Carlo simulated electron pencil beams into the inverse planning process. Additionally, we have characterized the EMLC using a multiple-source beam model for fast Monte Carlo simulation, incorporated the EMLC into the EGS/BEAM simulations as an MLC component module, and created MERT plans for breast cancers. We have also studied the effect of beam delivery on optimized modulated electron radiation therapy plans in the final dose calculation. Furthermore, we have developed aperture-based MERT techniques for fast delivery of MERT plans. We believe that MERT provides a viable alternative modality to conventional opposed tangential fields approach and photon IMRT.				
14. SUBJECT TERMS Modulated Electron Radiation Therapy (MERT), Multileaf Collimator (MLC), Electron Multileaf Collimator (EMLC)				15. NUMBER OF PAGES 349
				16. PRICE CODE
17. SECURITY CLASSIFICATION OF REPORT Unclassified	18. SECURITY CLASSIFICATION OF THIS PAGE Unclassified	19. SECURITY CLASSIFICATION OF ABSTRACT Unclassified		20. LIMITATION OF ABSTRACT Unlimited

NSN 7540-01-280-5500

Standard Form 298 (Rev. 2-89)
Prescribed by ANSI Std. Z39-18
298-102

Addendum to Final Report

Table of Contents

Cover	1
SF 298	2
Table of Contents	3
Introduction	4
Body	6
Key Research Accomplishments	23
Reportable Outcomes	25
Conclusions	33
References	33
Appendices	34

1. INTRODUCTION

Breast cancer is the leading incident cancer in the United States, affecting one in nine women over their lifetimes and accounting for 32% of all newly diagnosed cancers in women. Radiation therapy offers effective treatment of all stages of localized breast cancer. Especially for early stage (T1 – T2) patients, breast conservation with lumpectomy followed by irradiation has been very successful. Radiotherapy also plays an important role in the multi-modality management of locally advanced or inflammatory breast cancer as well as in the treatment for women with medial lesions and positive axillary nodes and those patients undergoing adjuvant bone marrow transplantation. It is expected that further development in radiotherapy will ensure improved local control with reduced complications, which will lead to increased cure rate for breast cancer.

Adequate targeting and delivery of desired radiation dose distribution to the primary tumor is essential to achieving local tumor control. The advantage of a photon beam is its high penetrating power and narrow beam penumbra. These features have been used in conventional treatment with tangential photon fields to reduce the dose to the normal structure adjacent the target. At present time, the most widely used radiotherapy technique for treating breast cancer consists of two opposed tangential photon fields. However, this technique has three major limitations. First of all, part of the lung and heart (in the case of the left breast treatment) may be exposed to a high radiation dose due to tumor location, patient size or in the case of chest-wall treatment. Secondly, because of lack of electron build-up in a photon beam, the skin surface receives a low dose. Thirdly, the contralateral breast may receive a significant amount of scatter dose. Consequently, irradiation-related complications such as arm edema, myocardial infarction, severe breast fibrosis, and secondary breast cancer may occur in the patients who have undergone conventional photon beam treatment. The state of the art computer-controlled medical linear accelerators and multi-leaf collimators (MLC) have become widely available now. These, combined with newly developed intensity modulated radiation therapy (IMRT)

treatment planning systems (TPS), provide significant improvement in the delivery and control of external beam radiation through beam-intensity modulation. Although the photon beam IMRT is a powerful tool for treating the tumors that extend deeply into tissue below the skin surface, it is not suitable for treating very shallow targets like breast cancers due to the low surface doses and large depth of photon beam penetration. For photon beam IMRT, the slow attenuation of photon beams can still deliver a significant dose to the critical structures that are far from the target.

A promising alternative approach is modulated electron radiation therapy (MERT) (1, 2). The rapid dose falloff of electron beams makes electron therapy an attractive treatment modality for some shallow targets like breast cancers. In addition, compared to photon beams, electron beams have negligible scatter radiation. Furthermore, because MERT mainly uses normal incident electron beams, it is less affected by patient's respiration as compared with tangential photon beams. Conceptually, each MERT plan consists of multiple ports (gantry angles) with different electron energies (energy modulation) and optimized beam intensity (intensity modulation). Dose conformity in the depth direction may be achieved by electron energy modulation, which is unique to MERT. Dose conformity and uniformity in the lateral direction may be achieved by intensity modulation using an electron-specific MLC (EMLC). Through both intensity and energy modulations, MERT is capable of delivering highly conformal doses to targets with complex shapes and of sparing surrounding normal tissue, particularly, the distal critical structures. However, difficulties associated with electron beam treatment are increased beam penumbra at depth and higher uncertainties in the dose calculation in the regions around the interface between soft tissue and bone or lung.

The objective of this project was to exploit MERT for breast cancer treatment. The rapid development in computer-controlled MLC technology and fast Monte Carlo simulation technique has made MERT possible. For the first time, Monte Carlo treatment planning has been implemented in clinical radiotherapy, which has been demonstrated to

reduce the uncertainty of the accelerator output for small irregular field electron beams from up to 10% to about 3%. In this study, we have used the Monte Carlo method to study the characteristics of the energy- and intensity-modulated electron beams. Based on the real beam data, we have developed a complete system of Monte Carlo-based inverse treatment planning system for modulated electron radiation therapy. The system starts with the prescribed dose distribution and derives a set of optimized beam intensities with variable energy, beam width and incident angles. The system incorporates the Monte Carlo simulated electron pencil beams into the inverse planning process. We have also modified an exiting photon beam leaf sequence algorithm to make it suitable for MERT plan delivery. Additionally, we have characterized the EMLC using a multiple-source beam model for fast Monte Carlo simulation. Furthermore, we have also compared the optimized MERT plans with the conventional treatment plans and those created using a commercial photon IMRT treatment planning system.

The original PI, Dr. C-M Charlie Ma, who left Stanford in October 2001, has successfully completed the project. The final report was accepted as written. In this addendum, I will summarize the extra research work that we have done since Dr. Ma left. This research work was not proposed in the original Statement of Work, but I feel that it is important to include these results in our final report in the form of an addendum. The research work can be divided into two major parts: 1) manufacturing an electron specific MLC (ELMC) and 2) developing a new algorithm for the use of EMLC and the delivery of MERT plans.

2. BODY

1. Manufacturing an EMLC using the Monte Carlo simulation

An essential requirement for MERT is to deliver, both accurately and efficiently, small-field electron beams (beamlets) of different energies and intensities. Traditionally, electron beams are shaped using a cutout and different energies at treatment depths may be achieved using variable incident energies. However, it would be very time consuming

to make cutouts for MERT beam delivery and the treatment time would become unacceptably long for routine clinical applications. Bolus can be used for missing tissue compensation and/or limited depth modulation. However, 3D bolus requires sophisticated techniques to build and it does not provide intensity modulation. As to the existing photon MLC (PMLC), although electron beam collimation can be achieved in some helium-filled scanned beam systems (3-6), there are some key limitations on accurate beam delivery with commonly accessible clinical accelerators. It has been found that a source to surface distance (SSD) of 70 cm is necessary to provide a clinically acceptable field using the PMLC in a Varian CLINAC 2100C linear accelerator. Beams collimated by a PMLC were found to be inferior to applicator fields in penumbra and uniformity. Monte Carlo simulations showed that the beam penumbra can be reduced significantly by either replacing the treatment head air with helium, together with a helium filled balloon between the accelerator and the patient skin or moving the MLC at least 11 cm towards the patient, or both (6). According to accelerator engineers, however, it is extremely difficult (if not impossible) to replace the air in an accelerator head with helium without major changes in the accelerator design. Therefore, an electron specific MLC has been proposed, which is located at the same level as a Cerrobend cutout, about 40 cm closer to the patient than the PMLC (7). An EMLC will be as accurate as a cutout in field shaping and as efficient as a PMLC for intensity modulation. It is generally believed that one of the reasons for the low use of electron beams in small cancer clinics is the extra manpower required to make customized cutouts for every patient. If so, the development of an EMLC will not only meet the needs for MERT, but also provide an efficient and effective device for beam shaping for conventional electron therapy.

We have performed extensive Monte Carlo simulations of electron fields collimated by 1.0 cm wide leaves to study the effect of material type and leaf thickness. Monte Carlo simulations were carried out on a cluster of 22 Pentium Pro CPUs (200 MHz) and 10 Pentium III CPUs (450 MHz), all running EGS4/BEAM, MCDOSE, and their utilities under the Linux operating system. Based on our Monte Carlo simulation

results (7, 8), we designed a manually-driven EMLC for the delivery of MERT plans. These parameters were determined based on our investigation results. We have chosen a 0.5 cm leaf width because thinner leaves will not provide effective beamlet collimation, especially for energies below 12 MeV, while wider leaves will deteriorate spatial resolution in the y direction (across the leaves). The EMLC leaf length was chosen to keep the overall dimension and weight low. The leaves will be installed on a movable carriage to compensate the limited leaf travel in the x direction. The 1.5 cm thickness is considered to be optimal for tungsten leaves in terms of leaf leakage (about 1.5% for 20 MeV electrons) and end scatter. Thicker leaves will further reduce leaf leakage, but will degrade beamlet penumbra. Straight leaf ends will ensure minimum interleaf leakage when a leaf pair is closed. Focused leaf sides will give slightly better beamlet penumbra in the y direction than unfocused leaf sides. For equal leaf width projected at 100 cm SSD, the actual leaf width will vary depending on the off-axis position. For easy construction (therefore low cost), the actual leaf width can be made the same for a nominal 0.5 cm leaf width. The effective leaf positions in the y direction will be determined experimentally and used in the beamlet dose calculation and treatment optimization.

Based on the above-described design, we have made a prototype manually-driven EMLC to test the Monte Carlo simulations. The EMLC consists of 30 steel leaf pairs, which were made using conventional steel bars for convenience and cost-effectiveness (Tungsten leaves are difficult to machine and cost too much to built it for this project). Leaf ends and sides are parallel to the beam axis, i.e., unfocused. Each leaf is 0.476 cm wide (about 0.5 cm wide projected at 100 cm SSD), 20 cm long, and 2.54 cm thick. The leaves were mounted on a steel frame attached to the bottom scraper of a 25 cm x 25 cm electron applicator on a Varian CLINAC 2100C (Varian Medical Systems, Palo Alto, CA). This was the best possible configuration that could be achieved without modifying the electron applicator itself. The leaves can slide in the steel frame and the leaf positions can be easily set using a pre-cut cardboard for a beam segment. The field shape is

maintained by tightening screws from the side. The largest radiation field available using the electron MLC was 15.7 cm x 15.7 cm projected at 100 cm SSD.

The geometry of this prototype EMLC was simulated using the BEAM system. The simulations began with the upper phase space file and proceeded through the remainder of the accelerator and prototype EMLC geometry. At the isocenter plane, particles were collected into a phase space file, which was then used for dose calculation on a homogeneous water phantom composed of $3 \times 3 \times 2 \text{ mm}^3$ voxels. The goal was to verify the accuracy of the Monte Carlo simulations, so extensive measurements were performed. The prototype EMLC was installed onto the treatment head of a Varian CLINAC 2100C and film (Kodak X-omat V, Eastman Kodak Company, Rochester, NY) measurements were performed in solid water. Measurements were taken for all three energies under study at an SSD of 100 cm (the upper surface of the solid water phantom coincided with the isocenter plane). The film was scanned using a Vidar scanner system. The RIT 315 software package was used to generate isodose distribution for comparison with the simulated dose results. An appropriate film calibration curve was created to convert the optimal density (OD) of the film to the delivered dose. In addition, a final BEAM simulation and dose calculation were also performed with the photon MLC as the final electron collimation system. These simulations were performed in a helium atmosphere, and the resulting dose distributions compared with the electron MLC simulation results.

Ideally, the EMLC leaves should be placed in such a position that the bottom of the leaves is as close to the patient skin as possible in order to produce a clinically acceptable field. However, because of the existing electronic circuitry used to detect the insertion of the electron cutout at the last scraper of a standard Varian $25 \times 25 \text{ cm}^2$ electron applicator, it was impossible to place the EMLC leaves at that position without changing the existing electron applicator design significantly. Thus, initially, the steel

frame of the EMLC leaves was temporarily inserted into the electron cutout mount and the leaves were placed about 1 cm above the last scraper. This configuration resulted in a 10 cm air gap between the bottom of the EMLC leaves and the patient skin for a nominal 100 cm source-surface distance (SSD). To further lower the EMLC leaves and, thus, reduce in-air electron scattering and the penumbra, we have now removed the entire last scraper of the electron applicator and its electronic accessories. The EMLC frame was placed at the bottom of the modified electron applicator and stabilized with eight screws. This modification reduced the air gap to 5.0 cm between the bottom of the EMLC leaves and the patient skin. Since the electronic circuitry for detecting the electron cutout was completely removed, we were able to avoid activating interlocks associated with electron beam accessory malfunction while inserting the EMLC assembly into the linac treatment head. Thus, even if the linac was in the electron mode, the gantry could still be rotated, making the delivery of MERT plans with multiple beam angles possible. Figure 1 shows a photo of the modified EMLC inserted on the treatment head of a Varian CLINAC 2100C linear accelerator.

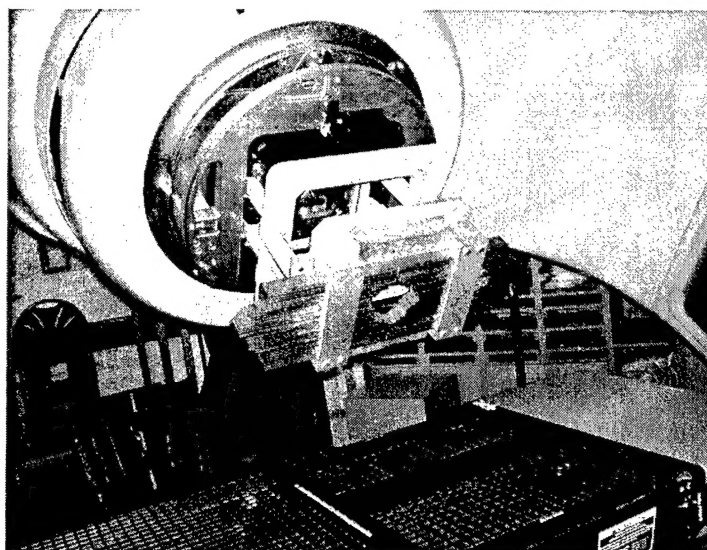


Figure 1 A photo of newly modified EMLC.

2. Developing special software required for the use of EMLC and MERT

Based on manufacturer's specifications of the beam production system and the electron applicator design, the electron beams produced by a Varian CLINAC 2100C linear accelerator and collimated by the EMLC were simulated using the EGS4/BEAM code. All simulation parameters, such as the electron and photon energy cutoffs (ECUT and PCUT), the maximum fractional energy loss per electron step (ESTEPE), and the number of initial electron histories, were specified in the EGS4/BEAM input file. In this study, we used ECUT = 700 KeV and PCUT = 10 KeV, below which all remaining energy was assumed to deposit on the spot. ESTEPE was set to 0.04. The EMLC was included in the EGS4/BEAM simulations as an MLC component module. The number of initial electron histories ranged from 2-30 million, depending on the electron energy. Phase space data were scored at a plane of 100 cm SSD after the particles had transported through the linac treatment head, the EMLC, and the air gap beneath it. The 1σ statistical uncertainty in the dose was, in general, less than 2% of the D_{\max} value. Based on this simulated electron beam, the MERT plans were then created using our modified EGS4/MCDOSE and other related codes.

To facilitate the description of the MERT treatment planning process, we will use the term *field* to specify each beam angle/electron energy combination and reserve the term *port* to indicate a single beam orientation (gantry angle). Thus, a plan in which five electron energies are delivered at a single gantry angle may be said to have one port and a total of five fields. Like the photon beam IMRT, the first step in creating a MERT plan was to select a set of suitable beam orientations, i.e., gantry angles, to fully cover the target volume while sparing the adjacent critical structures as much as possible. Each port was then divided into $1.0 \times 1.0 \text{ cm}^2$ beamlets, i.e., the smallest beam elements for dose calculation. All beamlets smaller than $1.0 \text{ cm} \times 1.0 \text{ cm}$ at the edge of the field were rounded to $1.0 \text{ cm} \times 1.0 \text{ cm}$. This means that beam intensity within a $1.0 \times 1.0 \text{ cm}^2$ beamlet would not be further differentiated. The beamlet size was defined at the isocenter plane. The goal of this step was to determine how many beamlets were required to

simulate for each port. The user specified the isocenter, gantry, collimator, and couch angles, the desired beamlet size, and the dimension of the search space. A program calculated which beamlets intersected the target and created a text file containing these beamlets and their coordinates. This file was used by MCDOSE to pre-calculate the beamlet dose kernels. The total number of beamlets was the sum of the beamlets over all ports. A beamlet could be turned off, i.e., assigned a weight of zero, but continued to remain active throughout optimization. After the selection of a proper set of beam angles, we needed to decide which electron energies to use for each beam angle. To do so, we computed a tumor depth map for each beam angle, whose pixel size was the same as that of a beamlet, i.e., $1.0 \times 1.0 \text{ cm}^2$. Based on the tumor depth distribution and assuming that the electrons lost energy at about 2 MeV/cm in tissue, we were able to determine a suitable set of electron energies for each beam angle. Since, in most of the cases, the target was not spherical in shape, different beam angles could have different sets of electron energies. The obvious advantage of this approach was the removal of those electron energies that contributed less to the target dose and, thus, the reduction in the number of fields used and delivery time.

The next step was to calculate beamlet dose kernels using MCDOSE. The beamlet dose kernel was the Monte Carlo calculated dose array for all structures due to a single beamlet. Each element of the dose kernel represented the dose delivered to a dose calculation point or voxel assuming a unit beamlet weight. These values were also referred to as dose deposition coefficients. Thus, the purpose of this step was, given a set of unit beamlet weights, to calculate the dose distribution in every structure that we were interested in. To optimize beamlet weights or intensity maps, a quadratic objective function augmented with dose-volume constraints was constructed. This was based on the assumption that there existed a quadratic relationship between the delivered dose and the biological effect. The overall objective function contained a linear component for each structure. Within each structure, each of the individual constraints contributed linearly to the objective function. Following the construction of the objective function, the

optimization of beamlet weights was initiated. The core of the optimization procedure was the well-known conjugate gradient search algorithm. The major advantage of the gradient search technique was its fast convergence speed, as compared to stochastic optimization techniques, such as simulated annealing. We believe that the gradient search algorithm was a good choice for future routine clinical implementation of MERT. During the optimization, care was exercised to avoid negative weights. These non-physical results were eliminated by scaling step sizes to avoid stepping over the boundary of the acceptable solution space and by projecting gradients onto the boundaries.

Following the beamlet weight optimization, the resulting optimized continuous intensity maps were stratified into five discrete intensity levels in preparation for leaf sequencing. We believe that five intensity levels provided a reasonably good approximation to the original intensity maps. The discrete intensity maps were then converted to step-and-shoot leaf sequences (9) based on the technique proposed by Bortfeld et al. (10). Since the dose distribution delivered by the ideal beamlets could be different from that delivered by the leaf sequences, a second Monte Carlo dose calculation was performed again based on the discrete intensity maps reconstructed from the corresponding leaf sequences. With these new dose kernels, the leaf sequence segment weights were re-optimized. This second optimization differed from the first one in two aspects. The first optimization was entirely based on idealized beamlets, without considering the EMLC geometry nor the leaf scatter effect, while the second optimization took into account not only the EMLC geometry, but also leaf end transmission bremsstrahlung leakage. Thus, the first optimization produced the best dose distribution possible, while the second one gave the actual delivered dose.

In the proposed planning scheme, the first optimization generates an approximate or preliminary plan. By applying a leaf-sequencing algorithm to the beamlet weights, the leaf positions are determined. This can be thought of as deciding in which general areas different energies are needed, and also grouping certain sections of the fields as being

“similar” in intensity requirements. The second round of optimization leaves the leaf positions fixed and adjusts the intensities of each segment. This optimization can, in part, compensate for bremsstrahlung leakage. Additionally, it can improve on the results of stratification into equal levels. After second round simulations and optimization, all leaf effects have been included. Thus, the resulting doses can be taken to be an accurate representation of the doses that would actually be delivered, at least insofar as the Monte Carlo transport physics can be considered accurate. The resulting dose distributions are a significant improvement over the single optimization plans, with leakage effects at least partially ameliorated.

3. Developing aperture-based algorithms for the use of EMLC and MERT

Currently, the most popular inverse treatment planning techniques fall into two major distinct categories: 1) beamlet-based inverse treatment planning and 2) aperture-based inverse planning. In the last section of this report, we briefly discussed the beamlet-based MERT technique without touching on the detailed mathematics. Basically, in beamlet-based inverse treatment planning, each field (a gantry angle/energy combination) is divided into a matrix of beamlets whose weights are optimized independently. The optimization therefore yields an intensity map that is then converted into a leaf sequence before being delivered. There are several problems associated with the beamlet-based inverse treatment planning. First of all, optimized intensity maps are often converted into a series of discrete levels in an attempt to make the sequencing easier. However this step also introduces some quantization errors and therefore results in loss of treatment plan quality. Secondly, leaf sequencing is constrained by hardware-related factors and therefore often requires a large number of complex field shapes to deliver a given intensity map, thereby decreasing the overall delivery efficiency. Thirdly, since the leaf-sequencing step is excluded from the intensity-map optimization process, therefore, all the delivery-related effects such as leakage, the tongue-and-groove design, and head scatter are not taken into account when choosing an intensity map. Efforts to include these effects into the optimization process have also introduced significant additional

complexity.

Aperture-based optimization is designed to reduce the complexity of IMRT and especially MERT treatment plans and is flexible-enough to easily include delivery-related effects into the optimization process. In particular, aperture optimization requires no leaf sequencing and apertures are guaranteed to satisfy delivery constraints. It is therefore a promising alternative to beamlet-based IMRT and MERT. In this study, we consider a method of contour-based treatment planning in which, unlike in Direct Aperture Optimization (DAO), the aperture shapes are initially chosen to be the Beam's Eye View (BEV) of the target and the critical structures, and therefore are given as constants in the optimization process. The obvious advantage of this approach as compared to DAO is that the only parameters that need to be optimized are the fields' weights, and the plan is not optimized over all the possible aperture shapes. Our hope is naturally that optimal aperture shapes are somewhat close to the BEV and that making this choice will save a significant amount of computation time.

Methods:

The goal of the following optimization scheme is to find the optimal beamlet weights that will deliver a dose distribution as close to the target dose as possible. A natural way to do so is to use an iterative approach: an initial plan is evaluated, adjustments are made, the plan is re-evaluated, further adjustments are made, and so on until some convergence criterion is met. In order to evaluate a treatment plan, we need to be able to assess 'how far' the current dose is from the target dose. This evaluation can be made by condensing the quality of a plan into a single value. This value is referred to as the objective function and naturally depends on the choice of criteria that was made to compute it. The objective function is therefore a mathematical function that takes as its input the dose distribution of both the evaluated plan and the prescription. Once we have determined the criteria that define the objective function, we can easily compare two possible treatment plans by comparing the values of their respective objective functions.

Notations for Plan Parameters:

We begin with a CT dataset containing structures of interest that are manually contoured. There are A structures (organs). Index $a = 0$ refers to the target structures while other structures are indexed from 1 to $A-1$. Each structure contains N_a dose calculation points, for $a=0,\dots,A-1$. It is also assumed that organs do not overlap, which means that every dose calculation point belongs to one and only one structure. As mentioned earlier, beam geometries and energies are specified before the optimization. Each beam angle/energy combination is called a field; a port refers to a single beam angle. Just like in beamlet-based optimization, each field is divided into beamlets, and we denote B as the total number of beamlets. All the beamlets belong to a total number of G fields (every beamlet only belongs to one single field). b_g is the number of beamlets in field g , and we thus have $B = \sum_{g=1}^G b_g$. For each beamlet b (where $b \in [1; B]$) and each structure a , we define the dose kernel $d_b^{(a)}$ as the array of doses received by each dose calculation point n in structure a when only beamlet b is given weight 1 and all the other beamlets are given zero weights. Since structure a contains N_a dose calculation points, we have $d_b^{(a)} = \{d_{b,1}^{(a)}, \dots, d_{b,N_a}^{(a)}\}$. Using accurate values for the beamlet kernels is critical to the final treatment plan quality, and this is why dose kernels are computed via Monte-Carlo simulation in this work. The weight given to beamlet b is denoted w_b , and we are trying to determine the set of weights that best matches the prescription. Once the dose kernels are computed (and they are only computed once prior to the optimization), the doses received at each point in each structure at any time depend only on the beamlet weights at that time. The vector $w = \{w_1, \dots, w_B\}$ that contains all the beamlet weights is referred to as the state-vector. Indeed, knowing the dose kernels and the state vector, we can easily compute the accumulated dose at every dose calculation point (or voxel). We denote $D_n^{(a)}$ as the total accumulated dose at point n in organ a . In particular, we have that $D_n^{(a)} = \sum_{b=1}^B w_b d_{b,n}^{(a)}$, which is the sum of the doses delivered by each individual beamlet.

We now need to specify our conventions regarding prescription doses, which are defined as follows. A prescribed dose is specified for the target, and then dose-volume constraints are defined for both the target and critical structures. We denote $\hat{D}_0^{(0)}$ as the prescribed dose for the target. Besides this prescribed dose, there are two additional dose-volume constraints that apply to the target. The upper dose-volume constraint is of the form: “no more than $v_1^{(0)}\%$ of organ 0 (i.e. the target) should receive a dose greater than $D_1^{(0)}$ ”, whereas the lower dose-volume constraint is of the form “no more than $v_1^{(0)}\%$ of organ 0 should receive a dose less than $D_1^{(0)}$ ”. For each other structure a , there are C_a dose-volume constraints, each one of them of the form “no more than $v_c^{(a)}\%$ of organ a should receive a dose greater than $D_c^{(a)}$ ”. Eventually each constraint c that apply to organ a (including the target) is given a relative weight factor $\alpha_c^{(a)}$.

Objective Function and Gradient for Beamlet-Based MERT

Under these conditions, the objective function is the sum of term that represents the target prescription dose, plus other terms that represent violations to all the constraints that apply:

$$F = F_0^{(0)} + \sum_{a=0}^{A-1} \sum_{c=1}^{C_a} (F_c^{(a)})$$

The term for the target prescription dose has the following quadratic form:

$$F_0^{(0)} = \frac{\alpha_0}{N_0} \sum_{n=1}^{N_0} [\hat{D}_0^{(0)} - D_0^{(0)}(\bar{w})]^2.$$

The terms that account for dose-volume constraints are more complicated since their computation requires some reordering of the delivered doses in order to count the number of points that are in violation of the constraints. In order to avoid technical details, we just give the overall objective function:

$$\begin{aligned}
F = & \frac{\alpha_0^{(0)}}{N_0} \sum_{n=1}^{N_0} \left[\hat{D}_0^{(0)} - D_0^{(0)}(\vec{w}) \right]^2 + \frac{\alpha_1^{(0)}}{N_0} \sum_{n=\bar{n}_{1,(0)}}^{N_1} \left[\hat{D}_1^{(0)} - D_{\bar{x}_n^{(0)}}^{(0)}(\vec{w}) \right]^2 \\
& + \frac{\alpha_2^{(0)}}{N_0} \sum_{n=\bar{n}_{1,(0)}}^{N_1} \left[\hat{D}_2^{(0)} - D_{\bar{x}_n^{(0)}}^{(0)}(\vec{w}) \right]^2 + \sum_{a=1}^{A-1} \sum_{c=1}^{C_a} \left(\frac{\alpha_c^{(a)}}{N_a} \sum_{n=\bar{n}_{c,(a)}}^{N_a} \left[\hat{D}_c^{(a)} - D_{\bar{x}_n^{(a)}}^{(a)}(\vec{w}) \right]^2 \right)
\end{aligned} \tag{1}$$

where

- 1) $\bar{n}_{1,(0)}$ is the point index from which we have to penalize for organ 0 for a low dose-volume constraint (all violating points are reordered by decreasing order).
- 2) $\bar{n}_{c,(a)}$ is the point index from which we have to penalize for organ a for a high dose-volume constraint.
- 3) $\bar{x}_n^{(a)}$ are the original indices of points, when n are the indices of the points that are sorted in decreasing order. Similarly, $\check{x}_n^{(a)}$ represent the original indices of points, when n are the indices of the points that are sorted in increasing order.

It can be shown that the objective function can be further simplified into:

$$F = \sum_{a=1}^{A-1} \frac{1}{N_a} \sum_{c,a} \sum_{n=1}^{N_a} \left[\zeta_{c,n}^{(a)} \alpha_c^{(a)} \left(\hat{D}_c^{(a)} - D_n^{(a)}(\vec{w}) \right) \right]^2 \tag{2}$$

$$F = \sum_{a=1}^{A-1} \frac{1}{N_a} \sum_{c,a} \sum_{n=1}^{N_a} \left[\zeta_{c,n}^{(a)} \alpha_c^{(a)} \left(\hat{D}_c^{(a)} - \sum_{b=1}^B w_b d_{w_b, x_n}^{(a)} \right) \right]^2 \tag{3}$$

where $\sum_{c,a}$ is the sum over all constraints of organ a, including the target prescription dose constraint and all dose-volume constraints. Moreover, $\zeta_{c,n}^{(a)}$ is either 0 or 1, depending on whether the point n in structure a should be incorporated in constraint c. Mathematically, $\zeta_{c,n}^{(a)}$ is defined as:

$$\zeta_{c,n}^{(a)} = \begin{cases} 1 & \text{if } a = 0, \text{ and } c = 0 \\ \sum_{m=\tilde{n}_{1,(0)}}^{N_0} \delta_{\tilde{x}_m^{(0)}} & \text{if } a = 0, \text{ and } c = 1 \\ \sum_{m=\tilde{n}_{1,(0)}}^{N_0} \delta_{\tilde{x}_m^{(0)}} & \text{otherwise} \end{cases}$$

where $\delta_{i,j} = \begin{cases} 1 & \text{if } i = j \\ 0 & \text{if } i \neq j \end{cases}$

From equation (3), the original gradient formula is obtained by differentiating with respect to each single beamlet weight.

$$F = F_c^{(0)} + \sum_{a=0}^{A-1} \sum_{c=1}^{C_a} (F_c^{(a)}),$$

Thus,

$$\nabla F = \nabla F_c^{(0)} + \sum_{a=0}^{A-1} \sum_{c=1}^{C_a} (\nabla F_c^{(a)})$$

It can be shown that the gradient of the objective function has the following form:

$$\frac{\partial F}{\partial w_b} = -2 \cdot \sum_{a=1}^{A-1} \frac{1}{N_a} \sum_{n=1}^{N_a} d_{w_b,n}^{(a)} \sum_{c,a} [\zeta_{c,n}^{(a)} \alpha_c^{(a)} (\hat{D}_c^{(a)} - D_n^{(a)}(\vec{w}))] \quad (4)$$

Once we have computed a gradient, we can move along its direction (departing from the initial state) and find a step size that minimizes the objective function. This step is referred to as the line-minimization, and comes down to finding step size t such that $F(w + t \nabla F)$ is minimal.

Objective Function and Gradient for Aperture-Based MERT

In aperture-based optimization, we want to express this function in terms of the weights of each field. In other words, we want to set the weights of all the beamlets, within each field, equal. We must also make sure that this simplification remains

throughout the optimization process. Thus, the gradient direction along which we evolve imposes the same changes in weights for all the beamlets that belong to the same field.

In order to achieve this, we need to modify the gradient computation. We can consider a modification of equation (3) by incorporating the fact that all beamlets from the same field must have the same weights. This yields the following objective function:

$$F = \sum_{a=1}^{A-1} \frac{1}{N_a} \sum_{c,a} \sum_{n=1}^{N_a} \left[\zeta_{c,n}^{(a)} \alpha_c^{(a)} \left(\hat{D}_c^{(a)} - \sum_{g=1}^G w_g \sum_{b'=1}^{B_g} d_{w_b',x_n}^{(a)} \right) \right]^2 \quad (5)$$

where G is the number of ports, B_g is the number of beamlets in port g .

If we repeat the proof through which we derived equation (4) from equation (3), we get a modified version of expression (4) that incorporates the fact that the objective function must only be differentiated with respect to all the beamlet weights that belong to the same field. This dramatically reduces the number of differentiations, thus limiting the dimension of the space over which we have to optimize. The new gradient expression is now:

$$\frac{\partial F}{\partial w_g} = -2 \cdot \sum_{a=1}^{A-1} \frac{1}{N_a} \sum_{n=1}^{N_a} \left(\sum_{b'=1}^{B_g} d_{w_b',x_n}^{(a)} \right) \sum_{c,a} \left[\zeta_{c,n}^{(a)} \alpha_c^{(a)} \left(\hat{D}_c^{(a)} - D_n^{(a)}(\vec{w}) \right) \right]$$

We must now take into account the effect of the non-negativity constraints, which already existed, in the original beamlet-based approach. These constraints simply account for the fact that beamlet weights must remain non-negative since a negative weight has no physical meaning, even though we can conceptually imagine that ‘removing’ dose from the patient would reduce the objective function.

Negative coefficients can occur for instance if we depart from a valid initial state, *i.e.* such that $w_b \geq 0$, for all b , and then perform a line minimization along the gradient direction, which yields a step size of t . If there is a b such that $th_b < -w_b$, then the new weight for beamlet b will become negative. In order to avoid such aberration, we must find a t that is $th_b \geq -w_b$ for all beamlets. This can be done by performing a loop through all the beamlets and scaling t down to $-w_b/h_b$ whenever $th_b < -w_b$. By scaling the initial t down to the t' , we are actually guaranteed (under technical yet general conditions) that the new step will result in some reduction of the objective function since we are still moving in the direction of the minimum. This loop is made clear in the following pseudo-code:

```

t' = t;
for b = 1 to B,
    w'_b = w_b + th_b;
    if w'_b < 0 then
        t' = - w_b / h_b
    end if
end for

```

However, several problems may arise from such scaling. If there is a beamlet b for which $w_b = 0$ and $th_b < 0$, then t will be scaled down to zero. One way to solve this problem is to modify the search direction before looping through beamlets, and in particular to set to zero the negative h_b that correspond to zero-weighted beamlets since we know that these beamlets will scale the step size down to zero if nothing is done preventively. However, by doing this we modify the search and we therefore have no other guaranty that the step size will be negative. We therefore need to come up with two search directions (one for positive steps t , one for negative steps t) along which the step size can be scaled down. This method is detailed in the following pseudo-code:

```

for b = 1 to B,
    if (wb = 0 and hb > 0) then
        hb- = 0
        hb- = hb
    else if (wb = 0 and hb < 0)
        hb- = hb
        hb+ = 0
    else
        hb- = hb
        hb+ = hb
    end if
end for

```

Eventually, once we have the two search directions, we just need to find t that minimizes the following function:

$$G(t) = \begin{cases} F(t + h^-) & \text{if } t \leq 0 \\ F(t + h^+) & \text{if } t > 0 \end{cases},$$

We believe that compared to beamlet-based MERT, aperture-based MERT is a more practical technique and should be further investigated.

3. KEY RESEARCH ACCOMPLISHMENTS

- Established clinical criteria for MERT beam delivery: The clinical requirements for MERT beam delivery are accuracy, efficiency, and cost-effectiveness.
- Performed Monte Carlo simulations to investigate EMLC parameters: We have investigated different materials and geometric configurations for the prototype EMLC and compared the results with those of a photon MLC and electron cutouts.
- Evaluated EMLC parameters based on the clinical criteria: We have evaluated the Monte Carlo results based on the clinical criteria. We conclude that the EMLC is superior to the PMLC and electron cutouts. The EMLC is more accurate (smaller beam penumbra) than the PMLC and more efficient, and cost-effective than electron cutouts.
- Finalized the EMLC design parameters: We have finalized the EMLC design parameters based on the optimal leaf material and geometric configuration.
- Manufactured a prototype EMLC for experimental MERT beam delivery study: We have manufactured a prototype EMLC based on the project budget and our current linear accelerator.
- Developed software for the use of EMLC: We have incorporated the Monte Carlo simulated electron pencil beams in the inverse treatment planning process. We have also modified a photon beam leaf-sequencing algorithm for MERT beam delivery. We have investigated the characteristics of the EMLC using a multiple-source model for fast Monte Carlo simulations.

- Included the effects of the EMLC in the final dose calculation: We have incorporated the EMLC into the EGS/BEAM simulations as an MLC component module and created MERT plans for breast cancers.
- Evaluated the functionalities of the prototype EMLC: We have performed film and BIS dosimetry to experimentally evaluate the quality of the EMLC in terms of dose distribution, flatness, and symmetry, and the extent of the beam penumbra. We have also measured the corresponding data for a PMLC.
- Developed new techniques for aperture-based MERT. We have developed new algorithms for aperture-based MERT in order to improve the MERT delivery efficiency.

4. REPORTABLE OUTCOMES

----PUBLICATIONS:

Manuscript

1. **C.M. Ma**, E. Mok, A. Kapur, T. Pawlicki, D. Findley, S. Brain, K. Forster and **A.L. Boyer**, "Clinical implementation of a Monte Carlo treatment planning system", *Med. Phys.* **26**: 2133-43, 1999.
2. **C.M. Ma** and S.B. Jiang, "Topical review: Monte Carlo modeling of electron beams from medical accelerators", *Phys. Med. Biol.*, **44**:R167-212, 1999.
3. A. Kapur and **C.M. Ma**, "Stopping-powers for clinical electron beams for a scatter-foil linear accelerator", *Phys. Med. Biol.*, **45**:2321-41, 1999.
4. **C.M. Ma**, T. Pawlicki, M.C. Lee, S.B. Jiang, J.S. Li, J. Deng, E. Mok, B. Yi, G. Luxton and **A.L. Boyer**, "Energy- and intensity-modulated electron beams for radiotherapy", *Phys. Med. Biol.*, **45**: 2293-2311, 2000.
5. J.S. Li, T. Pawlicki, J. Deng, S.B. Jiang, E. Mok and **C.M. Ma**, "Validation of a Monte Carlo dose calculation tool for radiotherapy treatment planning", *Phys. Med. Biol.* **45**: 2969-85, 2000.
6. Y. Chen, **A.L. Boyer** and **C.M. Ma**, "Calculation of x-ray transmission through multileaf collimator", *Med. Phys.*, **27**:1717-26, 2000.
7. S.B.Jiang, A. Kapur and **C.M. Ma**, "Electron beam modeling and commissioning for Monte Carlo treatment planning", *Med. Phys.*, **27**:180-191, 2000.

8. **C.M. Ma**, T. Pawlicki, S.B. Jiang, E.Mok, A. Kapur, L. Xing, L. Ma and **A.L. Boyer**, "Monte Carlo verification of IMRT dose distributions from a commercial treatment planning optimization system", *Phys. Med. Biol.*, **45**:2483-2495, 2000.
9. M. C. Lee and **C.M. Ma**, "Monte Carlo characterization of clinical electron beams in transverse magnetic fields", *Phys. Med. Biol.* **45**:2947-2967, 2000.
10. M.C. Lee, J. Deng, J.S. Li, S. Jiang and **C.M. Ma**, "Monte Carlo based treatment planning for modulated electron beam radiation therapy", *Phys. Med. Biol.* **46**:2177-2199, 2001.
11. M. Miften, M. Wiesmeyer, A. Kapur and **C.M. Ma**, "Comparison of RTP dose distributions in heterogeneous phantoms with the BEAM Monte Carlo simulation system", *J. Applied Clinical Med. Phys.*, **2**:21-31, 2001.
12. J. Deng, T. Pawlicki, Y. Chen, J. Li, S. B. Jiang and **C.M. Ma**, "The MLC tongue-and-groove effect on IMRT dose distributions", *Phys. Med. Biol.*, **46**:1039-1060, 2001.
13. S.B.Jiang, J. Deng, **A. L. Boyer** and **C.M. Ma**, "An extrafocal source model for photon beam dose calculation", *Med. Phys.* **28**:55-66, 2001.
14. T. Pawlicki and **C.M. Ma**, "Monte Carlo dose modeling for MLC-based IMRT", *Med. Dosimetry.* **26**:157-168, 2001.
15. J. Deng, S.B. Jiang, T. Pawlicki, J. Li and **C.M. Ma**, "Derive the electron and photon energy spectra from the electron beam central axis depth dose curves", *Phys. Med. Biol.* **46**:1429-49, 2001.
16. Y. Song, **A. L. Boyer**, T. Pawlicki, L. Xing, S. Jiang, Y. Yan, **C-M Ma**, and M. C.

Lee, "Modulated Electron Radiation Therapy (MERT): A Novel Treatment Modality for Parotid Cancers", *Technology in Cancer Research and Treatment* (Submitted), 2003.

Abstracts

1. **C.M. Ma**, T. Pawlicki, S.B. Jiang, E.Mok, A. Kapur, L. Xing, L. Ma and **A.L. Boyer**, "Verification of IMRT dose distributions using Monte Carlo simulations", ASTRO Annual Meeting, Phoenix, AZ, 1998.
2. S.B.Jiang, A. Kapur and **C.M. Ma**, "Electron beam modeling and commissioning for Monte Carlo treatment planning", AAPM Annual Meeting, Nashville, TN, 1999.
3. S.B.Jiang, J. Deng, **A. L. Boyer** and **C.M. Ma**, "An extra-focal source model for photon beam dose calculation", AAPM Annual Meeting, Nashville, TN, 1999.
4. J. Deng, S.B.Jiang, J.S. Li, T. Pawlicki and **C.M. Ma**, "Photon beam characterization and modeling for Monte Carlo treatment planning", AAPM Annual Meeting, Nashville, TN, 1999.
5. **C.M. Ma**, S.B. Jiang, T. Pawlicki, S.B. Jiang, J.S. Li, J. Deng, E.Mok, A. Kapur, G. Luxton and **A.L. Boyer**, "MCDOSE: a Monte Carlo dose calculation tool for radiotherapy treatment planning", AAPM Annual Meeting, Nashville, TN, 1999.
6. **C.M. Ma**, S.B. Jiang, T. Pawlicki, S.B. Jiang, J.S. Li, J. Deng, E.Mok, A. Kapur, M. Lee, G. Luxton and **A.L. Boyer**, "Energy- and intensity-modulated electron beams for treatment breast cancer", ASTRO Annual Meeting, San Antonio, TX, 1999.
7. **C.M. Ma**, "Monte Carlo as a QA tool for radiotherapy treatment planning", ESTRO Biannual Physics Meeting Symposium on treatment planning QA, Gottingen, Germany, 1999.

8. **C.M. Ma**, "Monte Carlo treatment planning for electron beam radiotherapy", AAPM Annual Meeting Symposium on Monte Carlo treatment planning, Nashville, TX, 1999.
9. **C.M. Ma**, JS Li, T Pawlicki, SB Jiang and J Deng, "MCDOSE - a Monte Carlo dose calculation tool for radiation therapy treatment planning", Proc. of the XIII International Conference on the Use of Computer in Radiation Therapy (ICCR), Eds: W Schlegel and T Bortfeld (Springer-Verlag, Heidelberg, 123-125, 2000.
10. **C.M. Ma**, T Pawlicki, MC Lee, SB Jiang, JS Li, J Deng, E Mok and **AL Boyer**, "Modulated electron beams for treatment of breast cancer", Oral presentation at the XIII International Conference on the Use of Computer in Radiation Therapy (ICCR), Heidelberg, Germany, May 22 - 25, 2000.
11. **C.M. Ma**, "Monte Carlo methods in electron beams treatment planning", invited talk at the 41st Annual Meeting of the American Association of Physicists in Medicine, Nashville, TN, July, 24-29, 1999, *Med. Phys.*, 26, 1999.
12. J. Deng, S.B. Jiang, T. Pawlicki, J. Li and **C.M. Ma**, "Electron beam commissioning for Monte Carlo dose calculation", ICCR Heidelberg, Germany, May 22 - 25, 2000.
13. **C.M. Ma**, T Pawlicki, SB Jiang, JS Li, Deng, D Findley, E Mok and **AL Boyer**, "Implementation of a Monte Carlo dose calculation module in the FOCUS treatment planning system", CMS' FOCUS 2000 User's Symposium, St. Louis, MO, April 10-11, 2000.
14. J. S. Li, T. Pawlicki, J. Deng, S.B. Jiang, A. Kapur, E. Mok and **C.M. Ma**, "Clinical validation of a Monte Carlo dose calculation code for radiotherapy treatment planning", *Med. Phys*, 26, 1083, 1999.

15. S.B. Jiang, T. Pawlicki, J. Deng, J. Li, and **C.M. Ma**, "Modulated electron radiation therapy: a new treatment modality", 42nd Annual Meeting of the American Society for Therapeutic Radiology and Oncology, Boston, MA, October 22-26, 2000.
16. M.C. Lee, S.B. Jiang and **C.M. Ma**, "Characteristics of clinical electron beams in transverse magnetic fields", 42nd Annual Meeting of the American Society for Therapeutic Radiology and Oncology, Boston, MA, October, 22-26, 2000.
17. T. Pawlicki, S.B. Jiang, J. Deng, J. Li, and **C.M. Ma**, "Compensating setup uncertainty and organ motion in IMRT treatment optimization", 42nd Annual Meeting of the American Society for Therapeutic Radiology and Oncology, Boston, MA, October 22-26, 2000.
18. J. Deng, S.B. Jiang, T. Pawlicki, J. Li, and **C.M. Ma**, "Beam delivery for modulated electron radiation therapy", 42nd Annual Meeting of the American Society for Therapeutic Radiology and Oncology, Boston, MA, October, 22-26, 2000.
19. **C.M. Ma**, SB Jiang, T Pawlicki, Y Chen, JS Li, J Deng, MC Lee, E Mok and **AL Boyer**, "A QA phantom for IMRT dose verification", Chicago 2000 World Congress on Medical Physics and Biomedical Engineering, Chicago, Illinois, July 23-28, 2000.
20. J. Deng, T. Pawlicki, Y. Chen, J. Li, S. B. Jiang and **C.M. Ma**, "The MLC tongue-and-groove effect on IMRT dose distributions, Chicago 2000 World Congress on Medical Physics and Biomedical Engineering, Chicago, Illinois, July 23-28, 2000.
21. J.S. Li, J. Li, L. Ma, **A.L. Boyer**, and **C.M. Ma**, "A water beam imaging system for IMRT dose verification", Chicago 2000 World Congress on Medical Physics and Biomedical Engineering, Chicago, Illinois, July 23-28, 2000.

22. T. Pawlicki, S.B. Jiang, J.S.LI, J. Deng, and **C.M. Ma**, "Compensating setup uncertainty in IMRT treatment optimization", Chicago 2000 World Congress on Medical Physics and Biomedical Engineering, Chicago, Illinois, July 23-28, 2000.
23. S. B. Jiang, T. Pawlicki, and **C.M. Ma**, "An aperture-based inverse planning algorithm for modulated electron radiation therapy", Chicago 2000 World Congress on Medical Physics and Biomedical Engineering, Chicago, Illinois, July 23-28, 2000.
24. Y. Song, S. B. Jiang, M. C. Lee, **C-M Ma**, and **A. L. Boyer**, "A multileaf collimator for modulated electron radiation therapy (MERT) for breast cancer", Presented at the Era of Hope 2002 DoD Breast Cancer Research Program Meeting, Orlando, Florida, USA, September 25-28, 2002.
25. L. Xing, J. G. Li, Y. Song, D. Y. Yang, D. Goffinet, and **A. L. Boyer**, "Combining electron with intensity modulated photon beams for breast cancer", Presented at the Era of Hope 2002 DoD Breast Cancer Research Program Meeting, Orlando, Florida, USA, September 25-28, 2002.
26. Y. Song, S. B. Jiang, M. C. Lee, **C-M Ma**, and **A. L. Boyer**, "A multileaf collimator for modulated electron radiation therapy (MERT) for breast cancer", Presented at the Era of Hope 2002 DoD Breast Cancer Research Program Meeting, Orlando, Florida, USA, September 25-28, 2002.
27. **A. L. Boyer**, Y. Song, Y. Yang, and L. Xing, "Sweeping window arc therapy", Presented at the 44th Annual Meeting of the American Association of Physicists in Medicine, Montreal, Canada, July 18-21, 2002.
28. Gary Luxton, Y. Song, Jenny Hai, and **A. L. Boyer**, "TLD measurement system for comprehensive dosimetric quality assurance in IMRT", Presented at the 44th Annual

Meeting of the American Association of Physicists in Medicine, Montreal, Canada, July 18-21, 2002.

29. Y. Song, M. C. Lee, and **A. L. Boyer**, “Energy and intensity modulated electron radiotherapy: A comparative dosimetric study of MERT and IMRT for head & neck cancer”, Presented at the 44th Annual Meeting of the American Association of Physicists in Medicine, Montreal, Canada, July 18-21, 2002.

30. T. Pawlicki, Y. Song, G. Zhang, T. Guerrero, K. Prado, N. B. Tolani, J. A. Both, and **A. L. Boyer**, “Automated Monte Carlo Commissioning for Photons Using the NXEGS Software”, Presented at AAPM 2003 Annual Meeting, San Diego, CA, USA, August 10-14, 2003.

31. **A. L. Boyer**, T. Pawlicki, C. Cardenas, and Y. Song, “IMRT Using Audio and Optical Respiration Gating”, Presented at AAPM 2003 Annual Meeting, San Diego, CA, USA, August 10-14, 2003.

32. L. Xing, Z. Shou, J. Li, Y. Song, T. Pawlicki, **A. L. Boyer**, and Quynh-Thu Le “Dose Matching of Two IMRT Plans or an IMRT and a 3D Conformal Treatment Plan”, To be presented at ASTRO 2003 Annual Meeting, Salt Lake City, Utah, USA, October 19-23, 2003.

33. A. Lo, Y. Song, **A. L. Boyer**, T. Pawlicki, and L. Xing “Combining IMRT and MERT for Breast-Conserving Radiation Therapy”, To be presented at RSNA 2003, Chicago, USA, November 30-December 5, 2003.

34. Y. Song, P. Peng, **A. L. Boyer**, and L. Xing “Concurrent Boost Using Forward Multiple-Segment Planning and Step-and-Shoot Delivery: A Novel Technique of

Breast-Conserving Radiation Therapy”, To be presented at ASTRO 2003 Annual Meeting, Salt Lake City, Utah, USA, October 19-23, 2003.

----FUNDING APPLIED FOR BASED ON WORK RESULTING FROM OR SUPPORTED IN PART BY THIS GRANT:

1. US Army Breast Cancer Research Program: Postdoctoral Training Grant, (PI: S.B. Jiang; Mentor: C. M. Ma): “Investigation of an electron MLC for energy and intensity modulated electron beam radiotherapy of breast cancer, awarded in 2000.
2. US Army Breast Cancer Research Program: Postdoctoral Training Grant, (PI: T. Pawlicky; Mentor: C. M. Ma): “Effect of organ motion and patient setup uncertainty on the treatment of breast cancer with energy and intensity modulated electron beam radiotherapy”, awarded in 2000.
3. US Army Breast Cancer Research Program: Predoctoral Training Grant, (PI: Michael C. Lee; Mentor: C. M. Ma): “Beam verification for modulated electron radiation therapy treatment of breast cancer”, awarded in 2001.
4. NIH: R01 “Modulated Electron Radiation Therapy”, PI, C. M. Ma, awarded in April, 2001.

----EMPLOYMENT RECEIVED ON TRAINING SUPPORTED BY THIS POST-DOCTORAL TRAINEESHIP:

1. C. M. Ma, Ph. D., Director of Radiation Physics Division, the Department of Radiation Oncology, Fox Chase Cancer Center, Philadelphia, PA.
2. Todd Pawlicki, Ph. D, Assistant professor, the Department of Radiation Oncology, Stanford University School of Medicine, Stanford, CA.

3. Steve B. Jiang, Ph.D., Assistant professor, the Department of Radiation Oncology, Massachusetts General Hospital, Harvard Medical School, Boston, MA.

4. Yulin Song, Ph.D., Assistant professor, the Department of Medical Physics, Memorial Sloan-Kettering Cancer Center, New York, NY

5. CONCLUSIONS

Based on the results of this study, we conclude that EMLC is able to provide sufficient beam collimation for MERT and Monte Carlo simulation provides an accurate technique for computing dose distributions from such a beam collimation system. In addition, we believe that aperture-based MERT offers a practical and viable alternative to beamlet-based MERT.

6. REFERENCES

1. Lee, M. C., Deng, J., Li, J., Jiang, S. B., and Ma, C-M, "Monte Carlo Based Treatment Planning for Modulated Electron Radiation Therapy", *Phys Med Biol*, **46**:2177-2199, 2001.
2. Ma, C-M, Pawlicki, T., Lee, M. C., Jiang, S. B., Li, J., Deng, J., Yi, B, Mok, E., and Boyer, A. L., "Energy-and Intensity-Modulated Electron Beams for Radiotherapy", *Phys Med Biol*, **45**:2293-2311, 2000.
3. Hyodynmaa, S., Gastafsson, A., and Brame, A., "Optimization of conformal electron beam therapy using energy- and fluence-modulated beams", *Med. Phys.*, **23**:659-666, 1996.

4. Lief, E. F., Larsson, A., and Humm, J. L., "Electron dose profile shaping by modulation of a scanning elementary beam", *Med. Phys.*, **23**:33-44, 1996.
5. Zackrisson, B., and Karlsson, M., "Matching of electron beams for conformal therapy of target volumes at moderate depths", *Radiotherapy and Oncology*, **39**:261-270, 1996.
6. Karlsson, M. G., Karlsson, M., Ma, C. M., and Satherberg, A., "MLC-collimated electron beams – a Monte Carlo based optimization", *World Congress on Med. Phys.* (Nice, France), 1997.
7. Ma, C. M., Pawlicki, T., Lee, M. C., Jiang, S. B., Li, J. S., Deng, J., Mok, E., Yi, B., Luxton, G., and Boyer, A. L., "Energy- and intensity-modulated electron beams for radiotherapy, *Phys. Med. Biol.* **45**:2293-2311, 2000.
8. Lee, M. C., Jiang, S. B., and Ma, C. M., "Monte Carlo and Experimental Investigations of Multileaf Collimated Electron Beams for Modulated Electron Radiotherapy", *Med. Phys.* **27**:2708-18, 2000.
9. Boyer, A. L., and Yu, C. X., "Intensity Modulated Radiation Therapy with Dynamic Multileaf Collimators", *Semin Radiat Oncol*, **9**:48-59, 1999.
10. Bortfeld, T., Kahler, D. L., Waldron, T. J., and Boyer, A. L., "X-ray Field Compensation with Multileaf Collimators", *Int J Radiat Oncol Biol Phy*, **28**:723-730, 1994.

7. APPENDICES

Copies of selected manuscripts and abstracts

Clinical implementation of a Monte Carlo treatment planning system

C.-M. Ma,^{a)} E. Mok, A. Kapur, T. Pawlicki, D. Findley, S. Brain, K. Forster,
and A. L. Boyer

Radiation Oncology Department, Stanford University School of Medicine, Stanford, California 94305

(Received 16 July 1998; accepted for publication 9 July 1999)

The purpose of this study was to implement the Monte Carlo method for clinical radiotherapy dose calculations. We used the EGS4/BEAM code to obtain the phase-space data for 6–20 MeV electron beams and 4, 6, and 15 MV photon beams for Varian Clinac 1800, 2100C, and 2300CD accelerators. A multiple-source model was used to reconstruct the phase-space data for both electron and photon beams, which retained the accuracy of the Monte Carlo beam data. The multiple-source model reduced the phase-space data storage requirement by a factor of 1000 and the accelerator simulation time by a factor of 10 or more. Agreement within 2% was achieved between the Monte Carlo calculations and measurements of the dose distributions in homogeneous and heterogeneous phantoms for various field sizes, source–surface distances, and beam modulations. The Monte Carlo calculated electron output factors were within 2% of the measured values for various treatment fields while the heterogeneity correction factors for various lung and bone phantoms were within 1% for photon beams and within 2% for electron beams. The EGS4/DOSXYZ Monte Carlo code was used for phantom and patient dose calculations. The results were compared to the dose distributions produced by a conventional treatment planning system and an intensity-modulated radiotherapy inverse-planning system. Significant differences ($>5\%$ in dose and >5 mm shift in isodose lines) were found between Monte Carlo calculations and the analytical calculations implemented in the commercial systems. Treatment sites showing the largest dose differences were for head and neck, lung, and breast cases. © 1999 American Association of Physicists in Medicine. [S0094-2405(99)00710-5]

Key words: radiotherapy treatment planning, dose calculation, Monte Carlo simulation, Monte Carlo treatment planning, EGS4 Monte Carlo

I. INTRODUCTION

Accurate dose calculations are essential to radiotherapy treatment planning (RTP). Radiotherapy treatments utilize the information provided by the treatment planning systems (TPS) and the clinical outcome can be improved if accuracy in the dose calculation is further improved.¹ Considerable efforts have been made to improve the dose calculation algorithms used in TPS to accurately reproduce all beam geometries and beam modification devices and to account for the effects of heterogeneities in the full three-dimensional (3D) patient geometry. Traditionally, patient dose calculations in radiotherapy have been based on correcting measured dose distributions. Newer dose calculation algorithms have been developed to predict the patient dose distribution from “first principles” using radiation transport models.² Comparisons of the traditional algorithms and the newer ones have been reviewed by Wong and Purdy,³ Cunningham and Battista,⁴ Mackie *et al.*,^{2,5} Jette,⁶ and Hogstrom and Steadham.⁷

Monte Carlo methods which use detailed phase-space information for the particles in the beam (including the energy, charge, angular, and spatial distributions)^{8–11} have been shown to be the most accurate method for radiotherapy dose calculations.^{1,8,12–22} The Monte Carlo technique is the only one that considers all aspects of photon and electron transport within a heterogeneous phantom. This accuracy is accompanied by an increase in the amount of time required to produce a statistically meaningful dose distribution. How-

ever, the rapid decrease in the price-to-performance ratio of general purpose computers has made RTP using Monte Carlo simulations a possibility. This trend is expected to continue for the foreseeable future when parallel and/or networked computer systems become readily available as dose computing engines for commercial TPS.²³

In this work, we investigate the clinical implementation of the Ottawa Madison electron gamma algorithm (OMEGA)²⁴ BEAM²⁵ and DOSXYZ²⁶ Monte Carlo codes for routine RTP dose calculations. We have commissioned the Monte Carlo simulated beam phase-space data by comparisons with the measured beam data. The beam phase-space data were analyzed and modeled using a multiple-source model. Software has been developed to build the 3D patient phantom from the computed tomography (CT) data and to convert the Monte Carlo calculated 3D dose data for display on a commercial RTP system. In this article, we report the implementation procedures, details of the Monte Carlo simulations, and comparisons of the dose distributions calculated using conventional algorithms that were implemented in a commercial TPS with those produced by our Monte Carlo simulations.

II. MATERIALS AND METHOD

A. Monte Carlo codes

The Monte Carlo codes used for the accelerator head simulation and dose calculation in the patient were

BEAM^{8,25} and DOSXYZ,^{8,26} respectively. Both codes were electron gamma shower version 4 (EGS4²⁷) user codes, running under the UNIX operating system, developed through the OMEGA project for Monte Carlo treatment planning dose calculations. Detailed descriptions of the software can be found in Ref. 8. For completeness, we briefly describe the two Monte Carlo codes used in this work.

The EGS4/BEAM code system was designed to simulate the radiation beams from any radiotherapy source, including low-energy x rays, Co-60 units, and photon and electron beams from clinical accelerators. The BEAM code produces a phase-space output of the beam (i.e., the energy, charge, position, direction, and a tag called LATCH to record the particle history) at any specified plane in a simulation geometry. The simulation geometry may consist of a series of individual component modules (CMs) positioned perpendicularly to the beam axis. The CMs used in this work to simulate the clinical linear accelerators included SLABS and CONESTAK for electron scattering foils, CONESTAK for photon target and primary collimators, and shielding rings, FLATFILT for photon flattening filters, CHAMBER for the monitor chamber, and dose simulation phantoms, APPLICAT for electron applicators, JAWS for the secondary photon collimators, MLC for the multileaf collimator, MIRROR for the light mirror, and BLOCK for electron cutouts. The actual dimensions and materials used for each of the components were handled by an input data file, which also contained the parameters required for the Monte Carlo transport simulations such as the energy cutoffs for electron (ECUT) and photon (PCUT) transport, minimum energy for the creation of knock on electrons (AE) or bremsstrahlung photons (AP), maximum electron step length (SMAX), maximum energy loss per electron step (ESTEPE), and the incident beam parameters. Several variance reduction techniques were implemented in the BEAM code including electron range rejection, photon interaction forcing, bremsstrahlung splitting, and Russian roulette.¹⁷ The BEAM code uses the default PRESTA electron transport algorithm²⁸ that has demonstrated results comparable (within 2%) to measured results in homogeneous phantoms. The simulated phase-space data can be used as source input for further BEAM simulations or dose calculations using the code DOSXYZ (see below) or analyzed using various software such as BEAM data processor (BEAMDP)²⁹ to derive particle energy spectra, fluence, and angular distributions as well as the parameters used by a beam model (see Sec. II C).

The EGS4/DOSXYZ code system was designed for dose calculations in a 3D rectilinear voxel geometry.²⁵ Voxel dimensions are completely variable in all three directions. Every voxel (volume element) can be assigned to a different material. The cross-section data for the materials used are available in a pre-processed PEGS4 cross-section data file. The density of the material defaults to that in the PEGS4 data file but can be varied in a DOSXYZ calculation for use with the patient's CT data although the density effect corrections for the stopping powers of the material remain unchanged. The voxel dimensions and materials were defined in a DOSXYZ input file together with the transport parameters

such as the energy cutoffs, SMAX, ESTEPE, and the parameters required by PRESTA. For use with CT data, a separate program CTCREATE²⁶ was used to convert the patient's CT data to the desired dimensions, material types, and mass densities (see Sec. II D). An earlier version of DOSXYZ had CTCREATE inside DOSXYZ as a subroutine, requiring more memory to run DOSXYZ because of the large data arrays used for the CT data conversion. Different source configurations can be used with DOSXYZ, such as a simple point source, a parallel beam, etc. The phase-space data obtained from a BEAM simulation can also be used as a source input to imitate all possible beam positions and directions from the linear accelerator. Dose contributions from different beam components were selectively calculated based on the particle charge or the LATCH settings specified in the BEAM simulation. DOSXYZ produced a data file that contained geometry specifications such as the number of voxels in all three directions and their boundaries as well as the dose values and the associated (1σ) statistical uncertainties in the individual voxels. The dose distributions can be analyzed using a program called STATDOSE³⁰ for rebinning, error analysis, or plotting dose distributions along any major axis.

The programs were installed on a variety of computers including SUN SPARC workstations, SGI workstations, and a network of 22 Pentium Pro 200 MHz PCs [each unit having 128 Mbyte of random access memory (RAM) and 10 Gbyte of disk space]. The PC network was used as a dose-computing engine for the Monte Carlo treatment planning process.

B. Accelerator simulation

Three models of Varian linear accelerators were simulated for the clinical implementation of Monte Carlo treatment planning at our institution. The modeled accelerators were the Clinac 1800, 2100 C, and 2300 CD (Varian Oncology Systems, Palo Alto, CA). The dimensions and materials for the accelerator components were incorporated according to the manufacturer's specifications or measurements. The electron beams emerging from the vacuum exit window were assumed to be monoenergetic and monodirectional with a beam radius of 0.1–0.2 cm. These were found to be reasonable assumptions to achieve a dose calculation accuracy of about 2% of the dose maximum (D_{\max}) in the phantom. The energy of the electrons emerging from the vacuum exit window was determined using an interactive process based on two criteria. First, the incident electron energy was interactively modified until the R_{50} value agreed with the measured value to within 1 mm for the clinical electron beams while, at the same time, the calculated and measured relative central-axis dose curves agreed to within 2% of D_{\max} . The mean electron energy values derived from measured R_{50} or $TPR_{20/10}$ were used as a starting point in the energy determination process but fine tuning by iteration was found necessary to achieve our criteria for good agreement.

We obtained accurate phase-space data for electron beams with nominal energies of 6, 9, 12, 16, and 20 MeV. The phase-space data were generally scored at a plane immedi-

ately before the lowest scraper of an electron applicator. The photon jaw settings for a particular applicator were fixed and the field shape could be modified using a Cerrobend cutout. The latter was simulated using the component BLOCK and the phase-space data were either scored immediately below the cutout or at an extended source-surface distance (SSD). The electron cone sizes included 6 cm×6 cm, 10 cm×10 cm, 15 cm×15 cm, and 20 cm×20 cm. The number of particles (including electrons, photons, and positrons) in a phase-space data file ranged from a few million to 50 million depending on the applicator size and beam energy. Three nominal energies were simulated for photon beams: 4, 6, and 15 MV. The phase-space data were scored at a plane immediately above the photon jaws. The number of particles in a photon beam file was about 50 million. Field shaping by photon jaws, blocks, and the MLC was further simulated using BEAM and the phase-space data could be stored temporarily or used directly for dose calculations. Each of the 22 PCs stored an individual (statistically independent) phase-space file (or phase-space model) for each clinical beam. Dose calculations for a given patient were performed on all of the PCs to reduce the simulation time. The statistical uncertainty of the final dose distribution was determined after combining the results from all 22 PCs.

The energy cutoffs for the accelerator simulation were $ECUT=AE=700$ keV (kinetic+restmass) for charged particles and $PCUT=AP=10$ keV for photons. The ESTEPE value was 0.04. The electron range rejection option was used for electron beams, and bremsstrahlung splitting and Russian roulette were used for photon beams. The ICRU recommended compositions and stopping power values were used for the materials used in the accelerator simulation.³¹ The CPU time required for the BEAM simulation ranged from a few hours to a few hundred hours on a single PC and the corresponding disk requirement ranged from a few hundred Mbyte to a few Gbyte depending on the field size and beam energy. The disk requirement amounted to hundreds of Gbyte for all the beams simulated.

C. Beam characterization

It has been demonstrated that well-designed beam models can be used to represent and reconstruct the beam phase-space data with the advantage of saving disk space and computing time in the accelerator simulation.^{32,33} In this work, we have characterized our beams using a well-tested multiple-source model.^{32,33}

In the multiple-source model, particles coming from different parts of an accelerator were treated as if they originated from different (sub)sources. We used several sub-sources to model the particles from different accelerator components. A point source was used to model the particles coming directly from the vacuum window and traversing the monitor chamber and mirror without hitting any of the beam defining components such as photon jaws or applicator scrapers. For an electron beam, the spatial and energy distribution of these "direct" particles depends on the dimensions and material of the scattering foils, monitor chamber, and

mirror. The effective SSD for an electron point source was determined using the "pinhole" method.^{32,34} For photon beams, the planar fluence distribution on a plane source was specified in annular bins. Each annular bin had its own energy and angular distributions. Separate "extended" photon sources were necessary to simulate the effect of electron and photon scattering in the target, primary collimator, and the flattening filter.³³ The effect of the thickness of the subsource on the angular distribution was negligible and therefore ignored. Particles from secondary collimators (jaws) were simulated by parallel bars of zero thickness. The electron applicators were modeled using square rings of zero thickness. Particles differing in charge were considered to originate from different sub-sources. The origin of a particle was classified using the information recorded in LATCH. The parameter LATCH contains the region (i.e., beam defining component) number(s) where a particle had been, had interacted, or was created if it was a secondary particle. The origin of a photon was considered to be the region where it was created or scattered. For a charged particle, the origin is considered to be the last nonair region in which it had been before it reached the scoring plane. The relative subsource intensity was determined according to the relative number of particles from the individual components (using LATCH) with their weight properly considered. Usually, no more than 10 sub-sources were needed to model a clinical electron or photon beam.

The reconstruction of the phase-space data was composed of the following steps. First, a subsource was randomly selected according to the relative source intensity. The particle energy was then sampled from the energy distribution for the subsource. For an electron beam, a position on the phantom surface was sampled for the particle based on the spatial distributions of the subsource with some parameterization such as the "inverse-square" relation. Because there was a very weak correlation between the particle energy and the position of particles from the same subsource, we sampled the particle position and energy independently. A position on the subsource would then be sampled. The position on the subsource and the position on the phantom surface gave the incident direction of the particle. For photon beams, the particle incident direction was sampled from the angular distributions of the extended photon source (plane source). The planar fluence on the scoring plane was a function of the planar fluence on the plane source and the angular distribution. The final step of the reconstruction was to correct for the effect of charged particles scattering in the air. This was accomplished by creating a small perturbation about each particle's incident direction. However, this angular perturbation has no significant (within statistical uncertainty of 0.5%) effect on the electron depth dose or lateral dose profiles.

The multiple-source model was implemented in BEAM and DOSXYZ. The particle planar fluence, energy spectrum, angular distribution, and other source parameters were derived from the simulated phase-space data using BEAMDP. This code produced a source data file that was read by BEAM or DOSXYZ for the phase-space reconstruction. A source data file usually contained a few hundred kilobytes of

TABLE I. Density range for the four materials used to build the Monte Carlo simulation phantoms (a). Only air, tissue and bone were used if a lung were not present in the regions of interest (b).

(a) Phantom with a lung				
Material	Air	Lung	Tissue	Bone
CT number range	0-70	70-800	800-1250	1250-4000
Density range	0.001-0.07	0.07-0.80	0.80-1.28	1.28-2.88
(b) Phantom without a lung				
Material	Air	Tissue	Bone	
CT number range	0-70	70-1250	1250-4000	
Density range	0.001-0.07	0.07-1.28	1.28-2.88	

data and its size was independent of the original phase-space file size. This resulted in a disk space saving of more than a factor of 1000. For a 10 cm \times 10 cm electron field, 5×10^5 phase-space particles were sufficient to derive the source parameters for the beam model to achieve the same dose calculation accuracy (a factor of 10 less compared to using the raw phase-space data). The number of particles contained in the file determines the uncertainty of a phase-space data set. This implies that, for a given set of phase-space data, the uncertainty in the calculated dose increases with decreasing voxel size because the number of particles traversing a voxel decreases. This problem cannot be resolved by simply recycling the phase-space particles since the statistical uncertainty in the phase-space may become a systematic uncertainty in any further simulations. When the beam model is used, however, all the reconstructed phase-space particles are independent. Therefore, dose calculation accuracy can be retained by simulating more histories if smaller voxels are used.

D. Conversion of CT data and beam setup

Conversion of the CT numbers to materials and mass densities was done using the code CTCREATE.²⁶ The current version of CTCREATE, on the OMEGA BEAM 97 distribution, reads the CT data set in both Pinnacle (ADAC, Sunnyvale, CA) and CADPLAN (Varian Oncology Systems, Palo Alto, CA) formats. Additionally, we developed software to convert CT data from the FOCUS (CMS, Inc., St. Louis, MO) format. Information required to run CTCREATE included the CT format, the CT data file name, and voxel dimensions for the simulation phantom. The user could also sample the CT data set and use various functions to convert CT data to the densities and materials for the simulation phantom. For any material, the mass density and CT number limits were set by the user. The density for a given voxel was assigned by linear interpolation of a mass density versus CT number curve. Table I gives the CT number range and density range for the four materials used in our implementation (Table Ia). These were consistent with the recommendations in an ICRU report.³⁵ The density-effect corrections of the stopping powers for air and tissue were from another ICRU report.³¹ The lung material was only used when a lung was

present. Otherwise, the same CT number range (70-1280) was replaced by tissue with the same density limits (Table Ib). The CT slices were usually scanned at 3 mm intervals. A CT image contained 512 \times 512 pixels with the side of a pixel equal to about 0.94 mm. CTCREATE allowed a subsection of the original CT data to be included in the CT phantom. This enabled the simulation to be performed at a resolution higher than if the calculation used the entire CT volume and enabled the user to trim some of the air surrounding the patient on a typical CT image.

Caution was exercised in converting the beam setups from the FOCUS treatment planning system to DOSXYZ. Although both used a right-hand coordinate system a 270° rotation with respect to the x axis was needed to convert the FOCUS coordinates to the DOSXYZ coordinates for the CT data. Furthermore, the field shape on FOCUS was defined in beam's eye view (BEV) while both BEAM and DOSXYZ used the patient's eye view. This required another conversion (180° rotation with respect to the x axis for the phase space) when BLOCK and MLC components were used. We added additional coding in DOSXYZ to handle field shaping by electron cutouts and the MLC. The cutout shape or the MLC leaf positions were coded in BEV so that the latter conversion could be omitted. This was further facilitated by the symmetry of the phase-space data with respect to the x and y axes because they were either scored at a plane immediately above the lowest scraper for electrons or immediately above the secondary collimators for photons. Other considerations included gantry rotation, collimator rotation, couch rotation, and translation.

E. Details of the dose calculation and measurement

For dose profile calculations in water, the simulation phantom was built using the DOSXYZ input file with voxel dimensions and materials individually defined. The voxel dimensions were variable according to dose gradient in the regions of interest. The x and y dimensions were 1-2 mm on the beam penumbra and 5-20 mm near the field's center and outside the field. The dimension in the z direction was 1-2 mm for electron beams near d_{\max} and in the build-up region for photons and 2-4 mm in the rest of the phantom. For heterogeneity studies, the regions size was also set to 1-2 mm near the interfaces. For central-axis depth dose calculations or output factor calculations, the component module CHAMBER was used with variable ECUT values in different regions and electron range rejection switched on. This resulted in significant CPU time savings compared with the use of DOSXYZ, which does not include any of the variance reduction techniques described previously. The diameter of the scoring region was set as close as possible to that of the sensitive volume of the detector. The z dimensions were 1-2 mm near d_{\max} and in the build-up region. In all the calculations, we set the transport parameters to ECUT=AE=700 keV, PCUT=AP=10 keV, and ESTEPE=0.04. The 1 σ statistical uncertainty for the phantom dose calculation was 1% or better by running a sufficient number

of particle histories (e.g., 5×10^6 phase-space particles for a $10 \text{ cm} \times 10 \text{ cm}$ electron field with 1 cm^3 voxels).

For patient dose calculations, the simulation phantom was built from the patient's CT data with up to $128 \times 128 \times 128$ voxels (uniform in size). The side of a voxel varied from 2 to 5 mm. For single electron beams, a subsection of the CT data was sometimes used to retain the spatial resolution while for photon beams with multiple gantry angles, the entire CT volume was often used. The number of particle histories simulated ranged from a few million for electron beams to up to one billion for photon beams with nine gantry angles for an intensity-modulated radiotherapy (IMRT) treatment. The 1σ statistical uncertainty in the dose was generally 1%–2% of the D_{max} value. The CPU time required for an electron beam calculation was generally at the order of a few minutes and for a photon beam about half an hour on the 22 PC network. A factor of 2–3 more particle histories were needed for an IMRT simulation compared to a conventional treatment plan simulation while the CPU time required was still within an hour since many photons were stopped by the MLC leaves and the average CPU time per history became lower compared to that for a conventional treatment.

All measurements in this work were performed in accordance with the recommendations of the TG-25,³⁴ TG-21,³⁶ and TG-39 (Ref. 37) protocols. Central-axis depth-dose curves were measured in a water phantom using a Scanditronix *p*-type diode detector and a Wellhofer 0.1 cc scanning chamber with WP700 data acquisition software. Dose values in the build-up region were acquired with an Attix parallel-plate chamber in solid water phantoms. The depth-dose curves were normalized to the maximum dose value D_{max} at the depth d_{max} . The transverse profiles at depths of interest were acquired either with the diode detector or with Kodak films that were optically scanned and calibrated. The transverse profiles were normalized to the central-axis values at each depth. The output factor measurement was performed with a PTW/Markus parallel-plate chamber. The water-to-air stopping-power ratios used for the conversion from the measured ionization to the dose to water were calculated in this work using the Monte Carlo simulated beam phase-space data. They differed only slightly (within 1.5%) for small field sizes from the TG-21 values, which were derived from broad beams of monoenergetic electrons. The variation of the perturbation corrections with depth for the PTW/Markus chamber was ignored in the output measurements. The measurement uncertainty was estimated to be 1% or less for large fields where electron lateral equilibrium was established and about 2% for smaller fields. The same experimental procedures as those reported in Ref. 38 were used for the measurement of the inhomogeneity corrections in layered phantoms. The inhomogeneity correction factor was defined as the ratio of the dose in a heterogeneous phantom to that in homogeneous water. A 0.6 cc Farmer chamber was used for the water phantom measurement and a 0.1 cc PTW chamber was used for the heterogeneous phantom measurement. The ionization ratios were converted to the dose ratios using the calculated stopping-power ratios in the phantom. The replacement correction factors were calculated using Monte

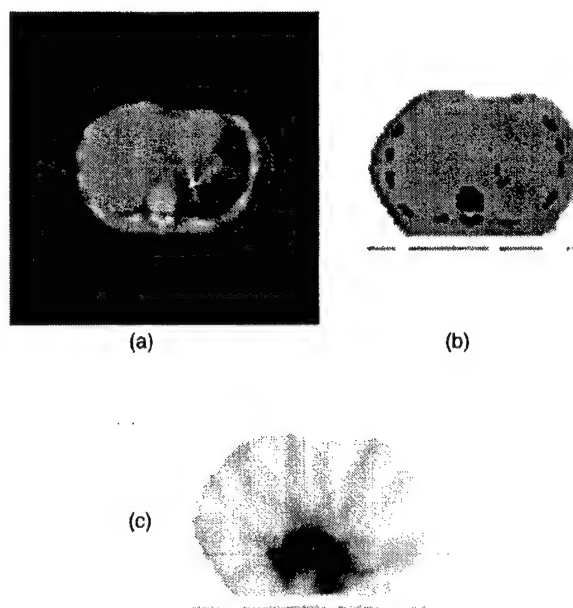


FIG. 1. (a) Mass density map and (b) the material types of a Monte Carlo simulation phantom built from patient CT data. Only three materials were used in this phantom since a lung was not present. A CT artifact caused by a metallic object (or the contrast agent used for magnetic resonance imaging) can be seen. (c) The dose distribution in the same phantom irradiated by nine intensity-modulated 15 MV photon fields calculated by the Monte Carlo method is shown (darker points correspond to higher dose).

Carlo by simulating the dose in water and in a low density cavity of the same volume as the chamber air cavity. The effect of the chamber wall and the central electrode was ignored in the heterogeneity correction factor measurement.

F. Display of the 3D dose data

Software was developed to convert the 3D dose data generated by DOSXYZ for display on a commercial treatment planning system (FOCUS). Rebinning of the 3D dose data was possible. However, the same dose grids were used in this work when comparing with the dose calculations done by the commercial RTP system. Details in the isodose plotting routine and the differences in the dose grids may introduce additional differences in the isodose curves. To be consistent with the commercial system, we also zeroed the dose in the air surrounding the patient's body for the Monte Carlo calculated dose data. The normalization point for the Monte Carlo plan was either at D_{max} or at a specified voxel, consistent with the plan calculated by the commercial system. Figure 1 shows the density and material map used for a patient simulation and the dose distribution for an IMRT plan of nine 15 MV photon fields calculated using the Monte Carlo method.

III. RESULTS AND DISCUSSIONS

A. Comparisons in homogeneous phantoms

We commissioned the radiotherapy beams from our three clinical accelerators, Varian Clinac 1800, 2100C, and 2300CD. The nominal energy of the electron beams ranged from 6 to 20 MeV and the field size ranged from 1 cm \times 1 cm to 20 cm \times 20 cm, shaped using either an electron applicator or a cutout. The nominal energies of the photon beams were 4, 6, and 15 MV. The commissioning procedure included the following steps: (1) verification of the accelerator specifications, (2) measurement of the dose distributions and various correction factors for wedges, blocks, electron applicators, and cutouts, (3) simulation of the phase space for each field/beam, (4) calculation of the dose distributions, and (5) comparison of the calculated and measured dose distributions. Steps (3)–(5) were repeated by changing the simulation parameters in the input file (such as the electron incident energy or the diameter of the pencil beam) until the difference between the Monte Carlo calculated dose distributions agreed with the measurements to 2% of D_{\max} . Detailed descriptions of these results are reported elsewhere.²²

We compared the Monte Carlo calculated output factors with the measured values and obtained good agreement (generally within 2%) for various photon and electron field shapes and sizes. This gave us confidence in computing the monitor units for Monte Carlo calculated treatment plans. Since electron output factors are routinely measured with film at the depth of D_{\max} , the measured output factor for small irregular electron fields might be quite uncertain. For example, a shift of a few mm in the depth of D_{\max} for a 6 MeV beam could result in a change in the measured output factor by 5%–10%. By calculating the output factors using Monte Carlo simulations, we reduced this uncertainty down to about 3%.¹⁹ The D_{\max} for the small irregular field was found by searching the whole simulation phantom. The calculation was completed in 0.5–1 h on the FOCUS treatment-planning computer (an SGI R4400 250 MHz workstation).

The depth-dose curves and lateral profiles calculated using the Monte Carlo method agreed well with the measured data. Both the original phase space and the phase space reconstructed using our multiple-source model were used for the Monte Carlo simulations in this work. The dose distributions were consistent at a 1%–2% level for all the photon and electron beams investigated.^{22,23} The characteristics of the electron beams for the Varian Clinac 2100C accelerator were similar to those reported in Ref. 32 except for the electron incident energy at the vacuum exit window. A separate study³³ also showed that the change in the depth-dose curves or dose profiles due to small variations in electron incident energy (2%–3%) or field size (a few mm) could be predicted using the multiple-source model by varying the corresponding source parameters. This means that the source parameters derived from the phase-space data for a clinical accelerator can be adjusted to reconstruct the phase space of a beam of the same nominal energy and field size for another accelerator of the same type. This can be achieved by comparisons with the measured beam data for the second accelerator.³³

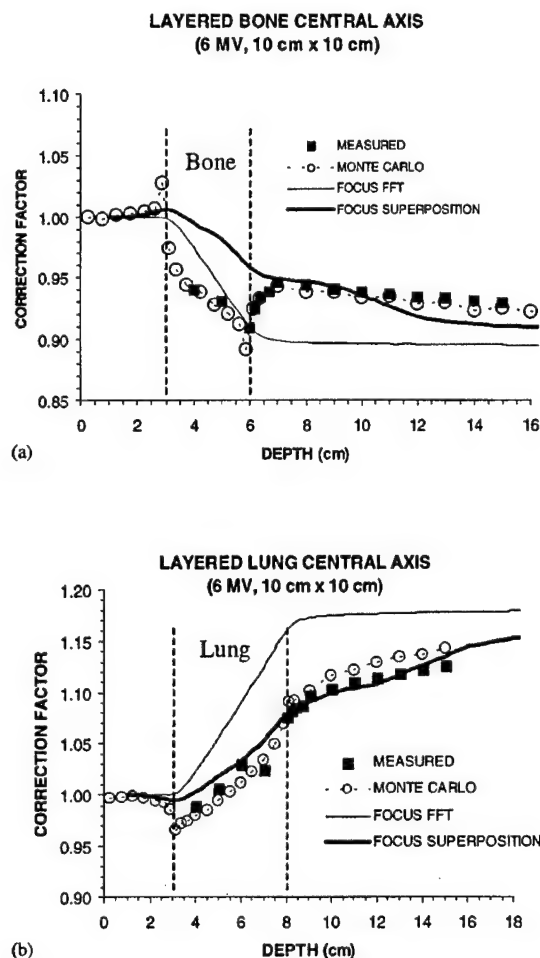


FIG. 2. Comparisons of heterogeneity correction factors calculated by Monte Carlo, by FOCUS (FFT convolution, and by superposition convolution), and by measurements for a 6 MV beam: (a) in a layered-bone phantom for a 10 cm \times 10 cm field and (b) in a layered-lung phantom for a 10 cm \times 10 cm field. The field size is defined at 100 cm SSD.

B. Heterogeneity corrections

Comparisons of dose distributions in heterogeneous phantoms measured using ionization chambers and calculated by Monte Carlo simulations were made for the photon and electron beams available on our accelerators. The heterogeneity corrections, calculated as the ratio of the dose at a point in a heterogeneous phantom to that at the same point in a water phantom, are shown in Fig. 2 for a 6 MV photon beam and in Fig. 3 for a 12 MeV electron beam. The densities of the lung and bone materials were 0.272 and 1.83 g cm⁻³, respectively. The same composition and mass density values were used in the Monte Carlo simulations.

Figure 2(a) shows the correction factor for a water–bone–water phantom. The bone material was 3 cm thick and placed 3 cm below the solid water surface. The solid water behind the bone slab was 12 cm thick. The Monte Carlo calculated correction factors agreed to within 0.5% of the measured values. Similar agreement was achieved for other beam energies (not shown). It is interesting to note that the dose values near the interfaces were significantly perturbed (re-

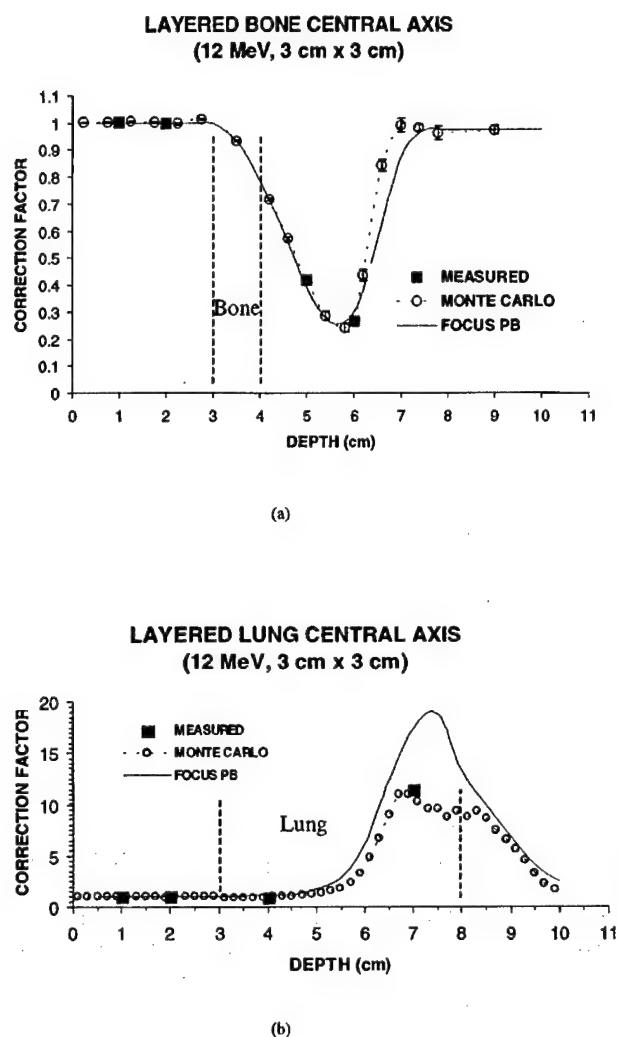


FIG. 3. Comparisons of heterogeneity correction factors calculated by Monte Carlo, by FOCUS (3D pencil beam), and by measurements for a 12 MeV electron beam: (a) in a layered-bone phantom for a 3 cm \times 3 cm field and (b) in a layered-lung phantom for a 3 cm \times 3 cm field. The field size is defined at 100 cm SSD.

quiring up to 10% correction) due to the differences in the photon fluence and electron fluence between the heterogeneous and the water phantoms. The effect of electron disequilibrium diminished at a distance of 1.5 cm from the bone–water interface. Beyond this point, the heterogeneity correction mainly accounted for the perturbation effect caused by the photons. Figure 2(b) shows the heterogeneity correction factors for a layered water–lung–water phantom irradiated by a 6 MV photon beam. The field size was 10 cm \times 10 cm defined at 100 cm SSD. The lung slab was 5 cm thick, and placed 3 cm below the solid water surface. The solid water was 12 cm thick behind the lung slab. The beam axis was centered between the lung blocks. The agreement between the Monte Carlo calculations and the measurements was well within 1%. Our results were consistent with the findings reported in the literature for similar geometry.^{21,38–42}

Recently, a fast fourier transform (FFT) convolution algorithm was implemented and tested in the FOCUS system,

and it showed some improvement in the dose calculations with heterogeneous phantoms over that of the conventional algorithm. However, differences of up to 5%–10% were still found in heterogeneous phantoms between the FFT convolution algorithm and measurements (see Fig. 2). A superposition convolution algorithm is currently being implemented in FOCUS, that can handle the photon scatter component more accurately but still cannot predict the dose in the regions adjacent to the interfaces. It should be noted that the correction factors given in Fig. 2 were calculated as the ratio of the dose to the medium in the heterogeneous phantom to the dose to water in a homogeneous water phantom. While real lung and bone materials were used in the measurement and the Monte Carlo calculations, the FFT and superposition convolution methods used water (with different electron densities) in both phantoms. Thus, comparisons of the correction factors in lung and bone regions could not be made directly without properly converting the dose values to the same medium.

Figure 3(a) shows the heterogeneity correction factors for a layered water–bone–water phantom irradiated by a 12 MeV electron beam. The field was 3 cm \times 3 cm at the phantom surface. The bone slab was 3 cm below the water surface and 1 cm thick. The solid water behind the bone slab was 12 cm thick. Both the Monte Carlo and the FOCUS pencil beam results agreed with the measured data except for deeper depths (6–8 cm) near the practical ranges of the primary electrons. However, the dose values at these depths were small and therefore the actual effect was small. Figure 3(b) shows the corresponding results for a layered water–lung–water phantom irradiated by a 12 MeV electron beam with a 3 cm \times 3 cm field. The lung slab was 5 cm thick and placed 3 cm below the solid water surface. The solid water was 10 cm thick behind the lung slabs. Again, the results were consistent between the calculations and the measurements except for larger depths (5–9 cm) where the FOCUS pencil beam predicted greater corrections compared to Monte Carlo and measurements. In general, the FOCUS pencil beam algorithm worked well for layered heterogeneous phantoms, as has been demonstrated by previous investigators.⁴³

C. Electron beam plans

We now compare the dose distributions for electron beams in different CT phantoms built from patient's CT data computed by a commercial 3D treatment-planning system (the FOCUS system) and by Monte Carlo simulations. The plans were first made on the FOCUS system and then the same beam setup was used in the Monte Carlo simulations. The Monte Carlo calculated 3D dose data were put back into the FOCUS system as separate plans for display.

Figure 4 shows the dose plans for a nasal cavity treatment using a 6 MeV electron beam. The field was 4 cm \times 4 cm defined at 100 cm SSD. Both the FOCUS and the Monte Carlo plans showed hot spots beside the bony structures. However, the locations of the hot spots were shifted a few millimeters. The Monte Carlo calculations also predicted a few more local hot spots which were caused by electron

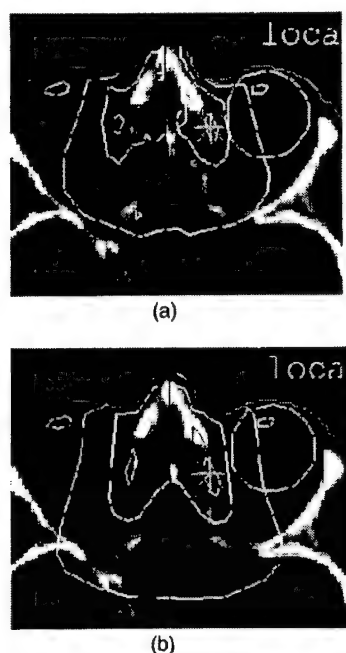


FIG. 4. Treatment plans for a nasal cavity case using a 6 MeV electron beam calculated (a) by Monte Carlo and (b) by the FOCUS 3D RTP system. The electron field is 4 cm \times 4 cm defined at 100 cm SSD (4 cm \times 4 cm cutout on a 10 cm \times 10 cm applicator).

scatter from the bony structures in the upper or lower CT slices. This was not observed in the FOCUS plan. In general, the dose distributions in water calculated by the FOCUS system were consistent with the measurements (at 2%–5% level). However, significant discrepancies (more than 15%) were found for oblique incidence or in the presence of heterogeneities such as lung or bone. The CT phantom in Fig. 4 was much more complex than the layered experimental phantoms used in Figs. 2 and 3. The electron fluence was perturbed by the effect of missing tissue and by the presence of bony structures and air cavities. The overall result was a reduced treatment range, as predicted by the Monte Carlo simulations.

Figure 5 shows another nasal cavity treatment using a 12 MeV electron beam. The field was 4 cm \times 4 cm defined at 100 cm SSD. Again, the dose distributions differed significantly between the FOCUS predictions and the Monte Carlo simulations in terms of the locations of the hot spots and the isodose lines. For example, the 50% isodose lines differed by more than 1 cm. The Monte Carlo calculated dose distributions also showed more variations due to the presence of the air cavities and bony structures whereas the FOCUS dose distributions looked smooth and uniform.

In general, significant discrepancies were found between the Monte Carlo plans and the plans calculated using the 3D pencil beam algorithm implemented in the FOCUS system in the regions near air cavities or/and bones, as well as with oblique incidence, small irregular fields, or/and extended SSDs. Since electron boost fields were not always planned on a RTP system, it was necessary to compute the dose dis-

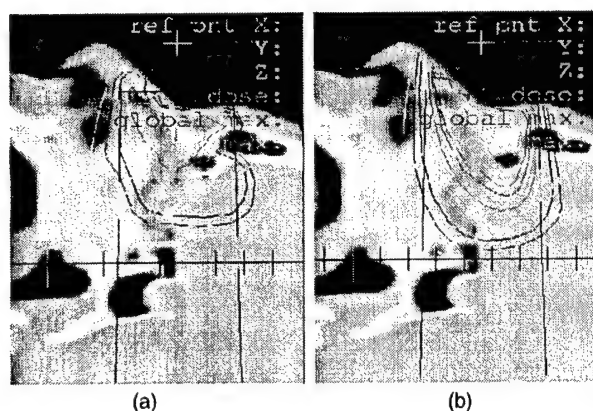


FIG. 5. Treatment plans for a nasal cavity case using a 12 MeV electron beam calculated (a) by Monte Carlo and (b) by the FOCUS 3D RTP system. The electron field is 4 cm \times 4 cm defined at 100 cm SSD (4 cm \times 4 cm cutout on a 10 cm \times 10 cm applicator).

tributions using the Monte Carlo method for some frequently used boost fields. It took from half of an hour to a couple of hours of CPU time on our RTP computer to complete an electron beam Monte Carlo plan. The improvement in the dosimetry accuracy with the use of the Monte Carlo dose calculation was often significant (>5% of the D_{\max} value and a >5 mm shift in the isodose lines). This makes the Monte Carlo dose calculation a valuable component in a RTP system for electron beams despite its CPU time requirement.

D. Photon beam plans

Significant discrepancies between the Monte Carlo calculated patient dose plans and the FOCUS plans were also found for photon beams. The conventional photon dose calculation algorithm used in the current FOCUS system did not properly account for the change in the photon scatter component in the presence of heterogeneities such as lung and bone. The patient dose calculations showed that the doses were often underestimated in the regions behind large bony structures and overestimated in and behind the lung. This is primarily due to the inappropriate treatment of the photon scatter and the lack of electron transport considerations. Figure 6 shows a photon beam plan calculated by Monte Carlo and by the FOCUS system. Part of the target received about 10% less dose compared to the prescribed value. These results were confirmed by our layered water–lung–water phantom measurements (Fig. 2). Our findings were consistent with the results and analysis by previous investigators.^{1,3–5,20,21,38–42,44–47}

To explore the effect of full photon and electron transport in photon beam dose calculations, we show in Fig. 7 an IMRT treatment plan calculated by both Monte Carlo simulation and the CORVUS treatment-planning optimization system (NOMOS Corp., Sewickley, PA). The plan was generated using the CORVUS system for 6 MV photon beams with nine gantry angles. CORVUS also produced the MLC leaf sequence files for operating the Varian dynamic MLC (Varian Oncology Systems, Palo Alto, CA). The same leaf

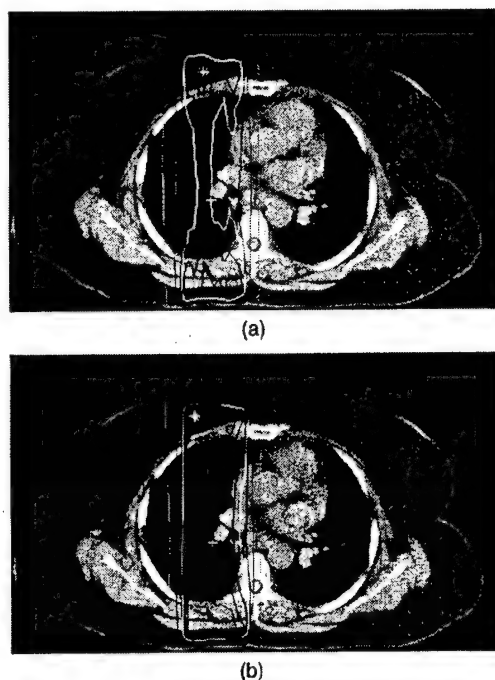


FIG. 6. Treatment plans of an AP/PA lung treatment with a 6 MV photon beam calculated (a) by Monte Carlo and (b) by the FOCUS 3D RTP system using the Clarkson algorithm with pixel-by-pixel heterogeneity corrections applied. The field size is 8 cm \times 9 cm (at 100 cm SSD) and is further defined by Cerrobend blocks. In (a) and (b) the isodose lines given are 10%, 50%, 75%, 80%, 85%, 90%, and 93% of the dose maximum.

sequence files were used in the Monte Carlo simulation to achieve modulation of the photon fluence using the simulated phase-space data. Reasonable agreement was found in the more homogeneous regions between the CORVUS dose distributions and the Monte Carlo predictions while in the regions near large bony structures (such as the spinal cord) differences of more than 10% could be seen. This increase in the dose to the spinal cord was thought to be due to electron scattering from the surrounding bone, which might not be modeled properly by CORVUS using a "finite size pencil beam" algorithm. Although the photon beams were optimized to avoid the cord, electrons could reach the cord and the dose to the cord was enhanced due to the high-density material surrounding it. Each beam going through the vertebra may contribute only a few percent more dose to the cord due to the uncertainty in the beam penumbra. The overall effect from all nine beams was a more than 10% increase in the dose to the cord. Another possible reason was the approximation in the photon leakage correction; the effect of leaf leakage may be underestimated in the regions in a photon field where the beam intensity was supposed to be close to zero.

It should be mentioned that the photon dose calculation algorithm used in the commercial treatment-planning optimization system was demonstrated to be accurate (about 2% for relative dose profiles and 3%–4% for absolute dose) for homogeneous (water) phantoms.⁴⁸ The dose distributions given by the CORVUS system agreed with the Monte Carlo and

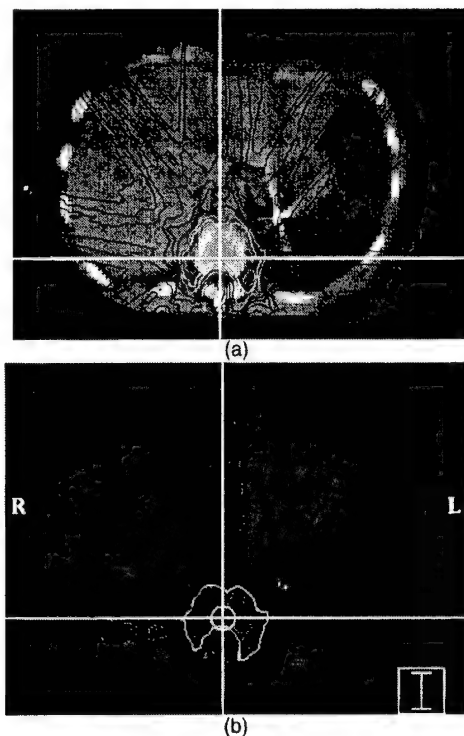


FIG. 7. Dose distributions for an IMRT case with nine intensity-modulated 6 MV photon fields calculated (a) by Monte Carlo and (b) by the CORVUS inverse-planning system. The isodose lines given are 10%, 20%, 30%, 40%, 50%, 60%, 70%, 80%, and 90% of the dose maximum. The patient geometry is the same as that in Fig. 1.

measurements to about 3% in a cylindrical water phantom with various hypothetical target shapes. This indicates that treatment plans for homogeneous phantoms (such as the prostate) may be adequate but they may not be so for treatment sites near heterogeneities such as the air–tissue, lung–tissue, and tissue–bone interfaces. We have verified the "optimized" dose distributions generated by the CORVUS system for treatment sites involving small target volumes and heterogeneities in the case of nasal cavities, head and neck, and the lung using the Monte Carlo simulations. Differences of over 10% were observed in the regions within or near low-density materials such as the lung and air cavities and near large bony structures.

IV. SUMMARY

We have implemented the BEAM and DOSXYZ Monte Carlo codes for radiotherapy RTP dose calculations. The implementation included the simulation and characterization of the clinical radiotherapy beams, the conversion of the patient CT data and beam arrangement for patient dose calculations, and software development for efficient dose calculations and display of the Monte Carlo 3D dose data on the existing treatment-planning system.

Comparisons of the dose distributions in water calculated by Monte Carlo simulations and the measurements showed general agreement within 2% for various clinical beam setups for electron beams as well as for photon beams. Monte

Carlo simulations have been used for computing the monitor units required for small irregular electron fields, which were shown to be more accurate and efficient than routine film or ion chamber measurements (the uncertainty in the output factor was reduced from 5% to 10% using film at a fixed depth to within 3%). The Monte Carlo calculated dose distributions in heterogeneous phantoms were confirmed (within 1%) using specially designed measurements whereas the conventional dose calculation algorithms may underestimate or overestimate by 5%–10% in the regions within or adjacent to the lung or bone materials.

Monte Carlo dose calculations may be more applicable to electron beam treatment planning than to photon beams in terms of computing time and improvement in dose accuracy. The computation time for a typical electron plan was 20 min–2 h on a Pentium Pro 200 MHz PC for 0.5–10 million particle histories. This can be reduced to a few minutes by running the Monte Carlo simulations on today's faster workstations or the multiple-CPU computer systems currently available or being used for treatment-planning and optimization calculations. With Monte Carlo calculations, the uncertainty in the dose for some of these cases may be reduced from 10% to 20% (or a 5–20 mm shift in the isodose lines) to from 3% to 5% (or a 2–3 mm shift in the isodose lines) for the regions of interest. Typical photon plans took 1–20 h of CPU time on a Pentium Pro 200 MHz PC. The computing time was only weakly dependent on the number of beams used since the statistical uncertainty in the dose values was determined only by the number of electron tracks in the volumes of interest, and thus, by the total number of particle histories simulated.

Our results indicate that more accurate dose calculation algorithms than those currently used in the "inverse-planning" systems are needed for intensity-modulated radiotherapy treatment planning. The conventional dose calculation algorithms may not accurately predict the dose distributions in and near inhomogeneities due to the lack of electron transport and charged particle equilibrium. The dose in the target volume may be in error by up to 7% as calculated by the optimization system while the uncertainty in the dose to the critical organ may be over 10% of the maximum target dose for cases involving the head and neck (especially near the nasal cavities), the lung/chestwall, and large bony structures.

ACKNOWLEDGMENTS

The authors are grateful to Dr. A. E. Nahum, Dr. P. Andero, Dr. D. W. O. Rogers, Dr. A. F. Bielajew, Dr. B. A. Faddegon, Dr. T. Holmes, and Dr. M. Miften for useful discussions and valuable comments on the manuscript. They would like to thank Dr. T. R. Mackie, Dr. D. W. O. Rogers, and the OMEGA BEAM team at the National Research Council of Canada, Ottawa, Canada, for the fine-tuned Monte Carlo simulation system. They would like to acknowledge Varian Oncology Systems, Palo Alto, CA, for providing detailed information on the Varian Clinac linear accelerators and CMS, Inc., St. Louis, MO, for information

on the FOCUS 3D treatment planning system. They would like to thank their Stanford colleagues, Gary Luxton, Lei Xing, Lijun Ma, Steve B. Jiang, Jinsheng Li, and Jun Deng, for encouragement and help, and Todd Koumrian, Behrooz Tofighrad, and Michael Luxton for help with the computers and software support. They would like to thank Dr. Moyed Miften of CMS, Inc. for the FOCUS FFT and superposition convolution data in Fig. 2. This investigation was supported in part by Grant Nos. CA78331 and CA43840 from the NIH, by Grant Nos. BC971292 from the DOD, and by the Seed Cycle 1 RSNA Research and Education Fund.

^{a)} Author to whom correspondence should be addressed; electronic mail: cma@reyes.stanford.edu

¹ R. Mohan, *Proceedings of the XIIth International Conference on the Use of Computers in Radiation Therapy*, Salt Lake City, 1997 (Medical Physics Publishing, Madison, WI, 1995), pp. 16–18.

² T. R. Mackie, P. Reckwerdt, and N. Papanikolaou, in *3-D Radiation Treatment Planning and Conformal Therapy*, edited by J. A. Purdy and B. Emami (Medical Physics Publishing, Madison, WI, 1995).

³ J. W. Wong and J. A. Purdy, *Med. Phys.* **17**, 807–814 (1990).

⁴ J. R. Cunningham and J. J. Battista, *Phys. Canada* **51**, 190–218 (1995).

⁵ T. R. Mackie, P. Reckwerdt, T. McNutt, M. Gehring, and C. Sanders, in *Teletherapy: Present and Future*, edited by T. R. Mackie and J. R. Palta (Advanced Medical Publishing, Madison, WI, 1996).

⁶ D. Jette, in *Radiotherapy Physics*, edited by A. R. Smith (Springer-Berlin, 1995), pp. 95–121.

⁷ K. R. Hogstrom and R. E. Steadham, in Ref. 5.

⁸ D. W. O. Rogers, B. A. Faddegon, G. X. Ding, C. M. Ma, J. Wei, and T. R. Mackie, *Med. Phys.* **22**, 503–525 (1995).

⁹ M. Udale-Smith, Ph.D. thesis, University of Leeds, UK, 1990.

¹⁰ R. Mohan, C. S. Chui, and L. Lidofsky, *Med. Phys.* **12**, 592–597 (1985).

¹¹ D. M. Lovelock, C. S. Chui, and R. Mohan, *Med. Phys.* **22**, 1387–1394 (1995).

¹² J. Cygler, J. J. Battista, J. W. Scrimger, E. Mah, and J. Antolak, *Phys. Med. Biol.* **32**, 1073–1083 (1987).

¹³ K. R. Shortt, C. K. Ross, A. F. Bielajew, and D. W. O. Rogers, *Phys. Med. Biol.* **31**, 235–249 (1986).

¹⁴ A. F. Bielajew, D. W. O. Rogers, J. Cygler, and J. J. Battista, *The Use of Computer in Radiation Therapy*, edited by I. A. D. Bruinvis, P. H. van der Giessen, H. J. van Klefens, and F. W. Wittkämper (Elsevier Science, Amsterdam, 1987), pp. 65–68.

¹⁵ A. E. Nahum, in *Monte Carlo Transport of Photons and Electrons*, edited by T. M. Jenkins, W. R. Nelson, and A. Rindi (Plenum, New York, 1988), pp. 523–547.

¹⁶ T. R. Mackie, in *Dosimetry of Ionizing Radiation*, edited by K. Kase, B. Bjargard, and F. H. Attix (Academic, New York, 1990), Vol. III, pp. 541–620.

¹⁷ D. W. O. Rogers and A. F. Bielajew, in Ref. 16, pp. 427–539.

¹⁸ P. Andreo, *Phys. Med. Biol.* **36**, 861–920 (1991).

¹⁹ C.-M. Ma, E. Mok, A. Kapur, and D. Findley, in Ref. 1, pp. 159–1620.

²⁰ C. L. Hatmann-Siantar et al., in Ref. 1, pp. 19–22.

²¹ J. J. DeMarco, T. D. Solberg, and J. B. Smathers, *Med. Phys.* **25**, 1–11 (1998).

²² A. Kapur, C.-M. Ma, E. Mok, D. Findley, and A. L. Boyer, *Phys. Med. Biol.* **44**, 3479–3994 (1998).

²³ A. F. Bielajew, *Proceedings of the XIth International Conference on the Use of Computers in Radiation Therapy*, Manchester, UK, 1994, pp. 2–5.

²⁴ T. R. Mackie et al., in Ref. 23, pp. 152–153.

²⁵ D. W. O. Rogers, C.-M. Ma, G. X. Ding, and B. Walters, *BEAM Users Manual*, National Research Council of Canada Report No. PIRS-0509A (NRCC, Ottawa, Canada, 1995).

²⁶ C.-M. Ma, P. J. Reckwerdt, M. Holmes, D. W. O. Rogers, and B. Geiser, *DOSXYZ Users Manual*, National Research Council of Canada Report No. PIRS-509B (NRCC, Ottawa, Canada, 1995).

²⁷ R. Nelson, H. Hirayama, and D. W. O. Rogers, *The EGS4 Code System*, Stanford Linear Accelerator Center Report, No. SLAC-265 (SLAC, Stanford, CA, 1985).

- ²⁸A. F. Bielajew and D. W. O. Rogers, Nucl. Instrum. Methods Phys. Res. B **18**, 165–181 (1987).
- ²⁹C.-M. Ma and D. W. O. Rogers, *BEAMDP Users Manual*, National Research Council of Canada Report No. PIRS-0509D (NRCC, Ottawa, Canada, 1995).
- ³⁰H. C. E. McGowan, B. A. Faddegon, and C.-M. Ma, *STATDOSE for 3D Dose Distributions*, National Research Council Report No. PIRS-0509F (NRCC, Ottawa, Canada, 1995).
- ³¹*Radiation Dosimetry: Stopping Powers for Electrons and Positrons*, ICRU Report No. 37 (ICRU, Bethesda, MD, 1984).
- ³²C.-M. Ma, B. A. Faddegon, D. W. O. Rogers, and T. R. Mackie, Med. Phys. **24**, 401–417 (1997).
- ³³C.-M. Ma, Radiat. Phys. Chem. **35**, 329–344 (1998).
- ³⁴AAPM TG-25, Med. Phys. **18**, 73–109 (1991).
- ³⁵*Tissue Substitutes in Radiation Dosimetry and Measurement*, ICRU Report No. 44 (ICRU, Bethesda, MD, 1989).
- ³⁶AAPM TG-21, Med. Phys. **10**, 741–771 (1983).
- ³⁷AAPM TG-39, Med. Phys. **21**, 1251–1261 (1994).
- ³⁸Y. P. Zhu and A. L. Boyer, Phys. Med. Biol. **35**, 351–368 (1990).
- ³⁹E. R. Epp, A. L. Boyer, and K. P. Dopke, Int. J. Radiat. Oncol., Biol., Phys. **2**, 613–619 (1977).
- ⁴⁰T. R. Mackie, J. W. Scriger, and J. J. Battista, Med. Phys. **12**, 188–196 (1985).
- ⁴¹C. X. Yu, J. W. Wong, and J. A. Purdy, Med. Phys. **14**, 78–83 (1987).
- ⁴²T. D. Solberg, F. E. Holly, A. A. F. DeSalles, R. E. Wallace, and J. B. Smathers, Int. J. Radiat. Oncol., Biol., Phys. **32**, 235–239 (1995).
- ⁴³R. Muller-Runkel and S.-H. Cho, Med. Phys. **24**, 91–102 (1997).
- ⁴⁴R. Mohan, C. Chui, and L. Lidofsky, Med. Phys. **13**, 64–73 (1986).
- ⁴⁵A. L. Boyer and E. Mok, Med. Phys. **12**, 169–177 (1986).
- ⁴⁶A. L. Boyer, L. Xing, C.-M. Ma, B. Curran, R. Hill, A. Kania, and A. Blier, Med. Phys. **26**, 187–195 (1999).
- ⁴⁷B. Faddegon, J. Balogh, R. Mackenzie, and D. Scora, Radiat. Phys. Chem. **217–228** (1998).
- ⁴⁸L. Wang, C. Chui, and M. A. Lovelock, Med. Phys. **25**, 867–878 (1998).

Calculation of x-ray transmission through a multileaf collimator

Yan Chen,^{a)} Arthur L. Boyer, and C.-M. Ma

Radiation Oncology Department, Stanford University School of Medicine, Stanford, California 94305-5304

(Received 10 November 1999; accepted for publication 10 May 2000)

A ray tracing based method has been developed to calculate the x-ray transmission through a multileaf collimator (MLC) for beam delivery verification and dose calculation in intensity modulated radiotherapy (IMRT). The path length of a ray line in the MLC is accurately calculated using the exact geometry of the MLC leaves. The fluence distribution of an IMRT field is calculated first using a point source. The fluence distribution for a realistic beam model is obtained, as an approximation, by convolving the point source fluence distribution with the distribution of source strength. Full ray tracing calculations are performed using analytic and Monte Carlo simulated beam models to verify the accuracy of the convolution method. The calculation is in better agreement with measurements using either film or a beam imaging system (BIS) than previous calculations for MLC transmission using a simplified model. This ray tracing calculation can be applied to the problem of verifying dynamic MLC leaf sequences as part of a patient-specific quality assurance process for IMRT. © 2000 American Association of Physicists in Medicine. [S0094-2405(00)00508-3]

Key words: IMRT, MLC transmission, Monte Carlo simulation, quality assurance, dose calculation

I. INTRODUCTION

Accurate determination of x-ray transmission through a multileaf collimator (MLC) is important for treatment planning and beam delivery verification, especially in MLC based intensity modulated radiotherapy (IMRT). The number of monitor units (MU) for an IMRT treatment is substantially increased to as large as an order-of-magnitude greater than a conventional treatment. Therefore the leakage dose in IMRT may accumulate to a significant level. Most MLC systems use stepped leaf sides to provide minimized interleaf leakage by overlapping adjacent leaves. This may lead to the so-called "tongue-and-groove" effect with a fluence reduction in the interleaf region due to opening/closing the neighboring leaf pairs at different times. In some designs the leaf ends are rounded to generate roughly the same penumbra width while the leaves travel in straight lines. Many investigators performed experimental studies on the MLC transmission.¹⁻⁵ Boyer and Li derived an analytic solution for the transmission through the round leaf ends using a simplified leaf geometry for the Varian MLC system (Varian Medical Systems, Palo Alto, CA).⁶ An analytic solution for the exact three-dimensional leaf geometry may be formidable. In this work we present a numerical method based on ray tracing for calculating the MLC transmission. The fluence distribution of an IMRT field can be calculated by summing the fluence of a stack of static fields defined by the MLC.

An extended source model has been considered to account for the finite source dimension and scattered photons. The time required to perform a ray tracing calculation with an extended source model may be too long for clinical applications. An approximate method is to convolve the fluence distribution obtained using a point source with the source distribution. The accuracy of the convolution method has

been studied by comparing the results with that obtained by a full ray tracing calculation. Both the analytic source model and a set of Monte Carlo simulated particles above the MLC have been employed. It is demonstrated that the fluence distribution of an IMRT field can be accurately calculated using either source, and the calculation is fast enough for clinical applications. Calculated fluence distribution of an IMRT field can be used as a more accurate reference for comparison with the measurement. Such a comparison is essential for beam delivery quality assurance (QA) in IMRT. It checks both the integrity of the MLC system and the correctness of the treatment plan imported to the beam delivery system. The calculated fluence distribution can also be used for forward dose calculation and inverse planning with accurately modeled leaf leakage.

II. METHODS

A. Calculation of path lengths

The fluence distribution of a field can be calculated by casting a set of ray lines from the x-ray source to a scoring plane. The transmission through an attenuating object represented by each ray line is given by the path length and the linear attenuation coefficient. First, we need a numerical method for path length calculation that can deal with complex geometry of the attenuating object, such as an MLC.

We define the structure function of an object which occupies a 3D region, Ω , as

$$f(\mathbf{r}) = \begin{cases} 1 & \text{if } \mathbf{r} \text{ is inside } \Omega \\ 0 & \text{otherwise} \end{cases}, \quad (1)$$

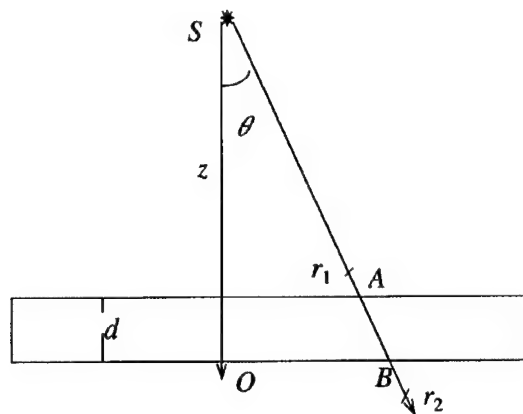


FIG. 1. The path length of the ray line SAB in a slab of thickness d can be calculated by integrating the structure function in the interval $[r_1, r_2]$.

where \mathbf{r} denotes a point in space. Formally, the path length in the object, l , can be expressed by the integral along the ray line,

$$l = \int_{r_1}^{r_2} f(\mathbf{r}) dr, \quad (2)$$

where r_1 and r_2 are arbitrary so long as the integration interval covers the total path length within the object. Equation (2) suggests a numerical approach. The interval $[r_1, r_2]$ can be divided into n subintervals. The structure function is evaluated at one point in each subinterval. An approximated path length is given by the summation of the structure function values at all the subintervals multiplied by the subinterval length.

To demonstrate how the numerical method works let us consider a simple example of calculating the path length in a slab, as shown in Fig. 1. The structure function of the slab is given by

$$f(x, y, z) = \begin{cases} 1 & \text{if } SO - d \leq z \leq SO \\ 0 & \text{otherwise} \end{cases} \quad (3)$$

The origin of the coordinate system is placed at the x-ray source. The path length of a ray line in the slab is given by

$$l(\theta) = \overline{AB} = \frac{d}{\cos \theta}, \quad (4)$$

where θ is the angle of the ray line with respect to the normal incidence. This path length can also be calculated by inte-

grating the structure function along the line SAB. The structure function can be rewritten in the spherical coordinate system as

$$f(r, \theta, \varphi) = \begin{cases} 1 & \text{if } 0 \leq SO - r \cos \theta \leq d \\ 0 & \text{otherwise} \end{cases} \quad (5)$$

The path length is then given by

$$l(\theta) = \int_{r_1}^{r_2} f(r, \theta, \varphi) dr \\ = \frac{r_2 - r_1}{n} \sum_{i=0}^{n-1} f\left(r_1 + \frac{i(r_2 - r_1)}{n}, \theta, \varphi\right), \quad (6)$$

where $r_1 \leq \overline{SA} < \overline{SB} \leq r_2$. The structure function is evaluated at a set of evenly distributed points along the ray line by testing the inequality in Eq. (5). This is a task that can be carried out straightforwardly by a computer. The accuracy of the result depends on the size of the subinterval, $(r_2 - r_1)/n$. The range of integration can be chosen based on the largest region occupied by the attenuating object, which is usually known for a practical problem.

B. Transmission through the MLC with a point x-ray source

A Varian MLC with "1 cm" leaf width consists of either 40 or 26 pairs. Cross-sectional views of a leaf showing the stepped leaf sides and rounded leaf end are depicted in Figs. 2(a) and 2(b). The leaves are arranged focusing to the x-ray source in the direction perpendicular to leaf movement, as shown in Fig. 2(a). Each pair of leaves projects to a 1 cm wide field in the isocenter plane. In a system with 40 leaf pairs, for example, the central axis of the x-ray field passes through the overlapped sides of the 20th and 21st leaves. The midplane of the i th leaf in the direction of x-ray propagation is angled with the beam axis by θ_i with $\tan \theta_i = (i - 20.5)/100$. The Varian MLC leaves have identical shape with a few exceptions. The leaves on the sides of the MLC, i.e., the 1st and 40th leaf pairs, have slightly different shapes, and the difference can be ignored for practical purposes.

The structure function of a leaf can be defined by a set of inequalities in a coordinate system attached to the tip of the leaf end. These inequalities describe the leaf as being boxed by six surfaces, such as the upper and lower surfaces, the rounded leaf end, and the stepped sides. The surface equations can be obtained using piecewise functions following

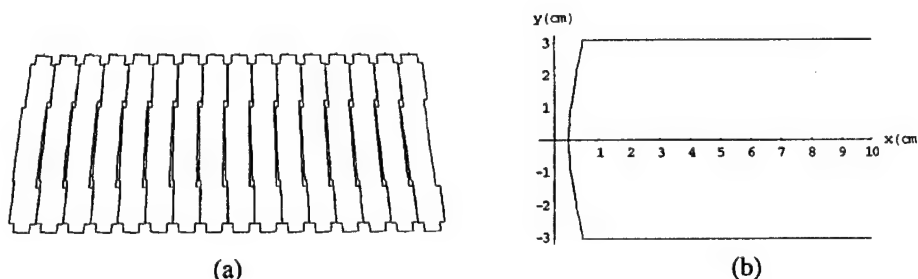


FIG. 2. (a) Cross-sectional view of the MLC. The leaves are arranged focusing to the x-ray source. The leaf sides have a stepped structure to minimize the interleaf leakage. (b) The rounded end of an MLC leaf viewed from side.

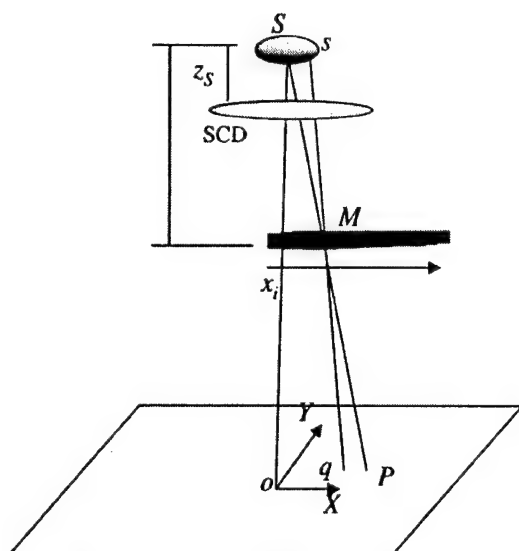


FIG. 3. The fluence distribution is calculated in the isocenter plane. The distance from the level of the MLC to the source is SAD. The extended source is at the level z_s . The position of the i th leaf is denoted by x_i .

the drawings provided by the manufacturer. If the structure functions for the leaves in one bank is given by $f(x, y, z)$, then the structure function for opposing leaves is given by $f(-x, y, z)$, with x the coordinate in the direction of leaf movement. In a coordinate system fixed to the accelerator, the leaf structure function can be obtained by a coordinate translation.

A ray line from a point x-ray source can be specified by its projection on the isocenter plane, (X, Y) , as shown in Fig. 3. The directional cosines of the ray line are given by

$$\begin{aligned} u &= X / \sqrt{X^2 + Y^2 + \text{SAD}^2}, \\ v &= Y / \sqrt{X^2 + Y^2 + \text{SAD}^2}, \\ w &= \text{SAD} / \sqrt{X^2 + Y^2 + \text{SAD}^2}. \end{aligned} \quad (7)$$

Let $I(X, Y)$ be the total path length in the MLC, and $I(X, Y)$ be the fluence at (X, Y) . The primary fluence at the point (X, Y) is given by

$$I_P(X, Y) = I_0(X, Y) e^{-\mu I(X, Y)}, \quad (8)$$

where $I_0(X, Y)$ is the open field intensity, and μ is the linear attenuation coefficient. The MLC is made of tungsten alloys.⁷ Its linear attenuation coefficient will be close to that of pure tungsten. The mass energy coefficient for tungsten has a weak energy dependence on energy in the megavoltage range. For a 15 MV beam, the MLC transmission measured by an ion chamber is 1.8%–1.9% for field sizes from 3 cm×3 cm to 10 cm×10 cm. This is consistent with the published attenuation coefficient data of Hubbell.⁸

Let $f(x, y, z)$ be the leaf structure function in the local coordinate system. Suppose the positions of the ends of the i th leaf pair are given by (x_i^A, y_i^A, z_i^A) and (x_i^B, y_i^B, z_i^B) , respectively. Then, the path length in the MLC can be expressed by

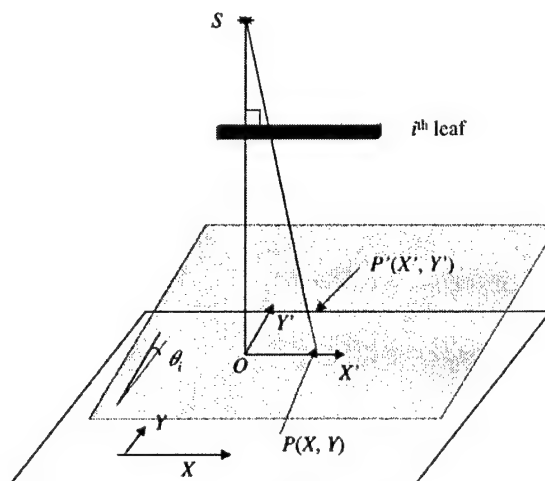


FIG. 4. The path length distribution for a leaf with a given position is calculated in an auxiliary plane, $X'Y'$. θ_i is the angle between the $X'Y'$ plane for the i th leaf pair and the XY plane (isocenter plane). For a ray line the coordinate transformation of the intersection points in the two planes, $P(X, Y)$ and $P'(X', Y')$, is by Eq. (10).

$$I(X, Y) = \sum_{i=1}^N \int_{r_1}^{r_2} [f(ru - x_i^A, rv - y_i^A, rw - z_i^A) + f(-ru - x_i^B, rv - y_i^B, rw - z_i^B)] dr, \quad (9)$$

where r is the length of the radial vector originated from the source and N is the number of leaf pairs. All the leaves have been summed over in Eq. (9) for the sake of generality because a ray line can be intercepted by more than one leaf. For a given ray line, of course, only the leaves that can lie in its path need to be considered. The integration limits are chosen based on the leaf dimensions and the distance from the source to the MLC.

To calculate the path lengths by Eq. (9) is straightforward but time consuming. The path length distributions for various leaf positions can be precalculated in order to speed up the calculation. Because of the focusing leaf arrangement, the path length distribution is pre-calculated in auxiliary planes perpendicular to the leaf orientation with nominal distance to the source (100 cm), as shown in Fig. 4. The auxiliary plane for a leaf pair, denoted as the $X'Y'$ plane, is chosen such that the path length distribution in the $X'Y'$ plane for a given leaf position is the same for all leaf pairs. For the i th leaf pair the incident points of a ray line in the isocenter plane and in the $X'Y'$ plane are related by

$$\begin{aligned} X' &= \frac{\text{SAD} X}{\text{SAD} \cos \theta_i + Y \sin \theta_i}, \\ Y' &= \frac{\text{SAD} (Y \cos \theta_i - \text{SAD} \sin \theta_i)}{\text{SAD} \cos \theta_i + Y \sin \theta_i}, \end{aligned} \quad (10)$$

where θ_i is the angle between the two planes, or the angle of the leaf orientation with respect to the central axis. The path length for a ray line in a leaf can be first calculated in the

auxiliary $X'Y'$ plane for the leaf. Then the fluence contribution of the ray line can be scored in the isocenter plane using Eq. (10).

In general the path length distribution for an MLC leaf in one position cannot be obtained from the path length distribution of the leaf in another position by means of a coordinate translation. However, the path length distribution can be interpolated if the leaf position has changed by a small amount. Suppose that the path length distributions for a leaf with its position at x_i^A and \tilde{x}_i^A are given by $I_i^A(X,Y)$ and $\tilde{I}_i^A(X,Y)$, respectively. $\tilde{I}_i^A(X,Y)$ is given by

$$\tilde{I}_i^A(X,Y) = \int_{r_1}^{r_2} f(ru - \Delta x - x_i^A, rv - y_i^A, rw - z_i^A) dr, \quad (11)$$

where $\Delta x = \tilde{x}_i^A - x_i^A$. Formally, we can write

$$ru - \Delta x = r(X - \Delta X) / \sqrt{X^2 + Y^2 + \text{SAD}^2}, \quad (12)$$

where

$$\Delta X = \frac{\Delta x \sqrt{X^2 + Y^2 + \text{SAD}^2}}{r} \approx \frac{\Delta x \text{SAD}}{\text{SCD}}, \quad (13)$$

and $\text{SCD} = 50.9$ cm is the vertical distance from the source to the MLC. In Eq. (13) we have replaced r by a constant, the length of the radial vector to the midplane of the leaf. The path length distribution for the leaf at \tilde{x}_i^A can then be obtained by

$$\tilde{I}_i(X,Y) \approx I_i(X - \Delta X, Y). \quad (14)$$

Equation (14) is accurate if Δx is smaller than a few millimeters. The path length distributions were precalculated for the physical leaf positions at every 0.5 cm, or the specified leaf position (in the isocenter plane) at about every 1 cm. Grid points with variable spacing were used for precalculation, i.e., 0.025 cm in the penumbra region and 0.5 cm in the central part. Since the path length is not a smooth function in the interleaf region, linear interpolation is used to obtain the path length distribution.

An IMRT field with a fixed gantry angle can be delivered either by a "step-and-shoot" technique or dynamically. With the step-and-shoot method a field consists of a series of segments, each with a fixed portal. Typically the MLC leaves change their positions in 1 or 0.5 cm steps between segments. The number of segments for a field is on the order of 100. A dynamic field can be discretized into a series of fixed segments as an approximation. Using a leaf step size of 0.1 cm, for example, the number of static fields required is on the order of 1000. The fluence distribution of an IMRT field can be calculated by summing over the fluence of each segment. Since there may be only a few leaves with changed positions from one segment to the next, the path length calculation can be performed efficiently by modifying the distribution of the previous segment in the leaf sequence.

C. Transmission through the MLC with an extended source model

The calculated fluence distribution using a point source can be improved by considering a source model that includes the scatter. A dual extended source model assumes that the photons are emitted isotropically from two planar sources, a high intensity, small dimension source at the plane of the x-ray target, and a low intensity, large dimension source at the level of the flattening filter.⁹⁻¹¹ The source distribution for a beam can be obtained by fitting measured or Monte Carlo simulated data. To incorporate an extended source into the ray tracing calculation for MLC transmission, one needs to sum over the ray lines "seen" at the calculation point weighted by the source intensity distribution. A convolution method is discussed in this section, in which the calculated point source fluence distribution is used.

An extended source can be divided into a finite number of elements. The fluence at a point is given by the summation of the contributions from all source elements. A source element contribution to a point in the isocenter plane is determined by the element strength and the path length of the ray line in the MLC. The basic idea of the convolution method is to approximate the path length of a ray line emitted from the extended source by that of an equivalent ray line emitted from the focal point. The path length distribution for the point source has already been calculated. The fluence at a point irradiated by an extended source can then be expressed as a convolution of the point source fluence distribution with the distributed source intensity. This can be shown using a similar argument as for relating the path length distributions of two different leaf positions, discussed in Sec. IIB. Let $l(X,Y,x_s,y_s)$ be the path length of a ray line from a source point (x_s,y_s) in the focal plane ($z=0$) to the point (X,Y) in the isocenter plane, as shown in Fig. 3. $l(X,Y,x_s,y_s)$ is the same as for a ray line emitted from the focal point with both the physical leaf position and the incident point in the isocenter plane translated by a vector (x_s,y_s) . Therefore, using an argument similar to the one that led to Eq. (14), we find

$$l(X,Y,x_s,y_s) \approx l\left(X + x_s \frac{\text{SAD} - \text{SCD}}{\text{SCD}}, Y + y_s \frac{\text{SAD} - \text{SCD}}{\text{SCD}}, 0, 0\right). \quad (15)$$

For a ray line emitted from an extrafocal source, a virtual source point in the focal plane can be determined by back projection, which is given by

$$\begin{aligned} x_s^v &= x_s - (X - x_s) \frac{z_s}{\text{SAD} - z_s}, \\ y_s^v &= y_s - (Y - y_s) \frac{z_s}{\text{SAD} - z_s}, \end{aligned} \quad (16)$$

where (x_s,y_s,z_s) and (X,Y) are the coordinates of the source point and incident point in the isocenter plane, respec-

tively. Using Eqs. (15) and (16), and summing over all source elements, we obtain the fluence at (X, Y) given by a planar source

$$I(X, Y) = \int I_P(X - \Delta X_S, Y - \Delta Y_S) \psi(x_s, y_s) dx_s dy_s, \quad (17)$$

where

$$\begin{aligned} \Delta X_S &= \frac{X z_s - \text{SAD} x_s}{\text{SAD} - z_s} \left(\frac{\text{SAD}}{\text{SCD}} - 1 \right) \\ \Delta Y_S &= \frac{Y z_s - \text{SAD} y_s}{\text{SAD} - z_s} \left(\frac{\text{SAD}}{\text{SCD}} - 1 \right), \end{aligned} \quad (18)$$

$\psi(x_s, y_s)$ is the intensity distribution of the source in the z_s plane, and $I_P(X, Y)$ is the fluence for the point source. Equation (17) is a convolution of fluence distribution for the point source with the source intensity.

The above result can also be derived by assuming that the path length only depends on the location of the intersecting point between the ray line and the $z = \text{SCD}$ plane that represents the MLC. As shown in Fig. 3, a ray line sq intersects with the $z = \text{SCD}$ plane at the point M . The path length of this ray line is approximated by the path length for the ray line SP , which is originated from the focal point and also passes through the point M . It is assumed that all the ray lines passing through the same point in the $z = \text{SCD}$ plane have the same path length in the MLC. Obviously, this is a good approximation only for a small source, so that the ray lines passing through a point in the $z = \text{SCD}$ plane span a small solid angle. Therefore this approximation is to be referred to as the small angle approximation.

Liu *et al.* provided dual source models for 6, 10, and 18 MV photon beams fitted to Gaussians using Monte Carlo simulation data.⁹ For the 10 and 18 MV beams, the radii of the sources, defined as the half width at half maximum, are 0.1 cm for a primary source and 1.05 cm for an extrafocal source. The extrafocal source distributions for the 10 and 18 MV beams are similar. We interpolated the parameters of the two sources to construct a 15 MV source model for our beam. The extrafocal source is 9.5 cm from the x-ray target. For the primary source, we have $z_s = 0$ in Eq. (18). The shift in the isocenter plane for a point with the same path length, as in Eq. (17), is given by

$$\Delta X_S = -0.965x_s, \quad \Delta Y_S = -0.965y_s, \quad (19)$$

which is independent of the incident point. For the extrafocal source, $z_s = 9.5$ cm, and the shift for the equivalent path length is given by

$$\Delta X_S = -1.066x_s + 0.101X, \quad \Delta Y_S = -1.066y_s + 0.101Y. \quad (20)$$

From Eq. (20), we see that the radius of the largest virtual source is about 2 cm for a 20 cm \times 20 cm field. This gives the range in which the small angle approximation is applied.

For an IMRT field, convolution for the extended source needs to be performed only once for the summed point source fluence distributions over all segments. This is because the convolution is a linear operation. The convolution

TABLE I. Results of numerical integration using different subinterval numbers.

N	5	10	50	100	500	1000
I	9.6	10.8	10.56	10.68	10.63	10.64

integrals can be evaluated either directly or using the Fourier technique. In the real domain, only a small area affected by the extended source needs to be considered for each sampling point.

D. Path length calculation for ray lines with arbitrary directions

Ray tracing calculation for the extended source is needed to determine the accuracy of the calculated fluence distribution using the convolution method. The numerical method with the structure function described above can be readily used for a full ray tracing calculation. A ray line from the extended source can be specified by four independent variables, two for its incident point in the scoring plane and two for its direction. The path length is calculated by integrating the structure function for all leaves the ray line intersects. One only needs to consider the leaves in the path of a given ray line, which can be identified by the intersection points of the ray line with the upper and lower surfaces of the MLC. A ray line blocked by a jaw can be disregarded. A planar source with circular symmetry can be divided into a number of rings. A set of evenly distributed ray lines, for example, one in every 15° , are cast from the source to each sampling point in the scoring plane for the path length calculation. The path length of each ray line in the MLC determines the fluence contribution for the represented element of the extended source. For a 10 cm \times 10 cm field, for example, assuming that a point is calculated to sample a 0.1 cm \times 0.1 cm square and the source is divided into 5 rings with 24 rays to sample each ring, there are $5 \times 24 \times 100 \times 100 = 1\,200\,000$ path lengths to be calculated. It may not be practical to use full ray tracing calculation for clinical applications because it is too slow.

Similar ray tracing calculation is performed using the accurate beam phase space data simulated by the Monte Carlo method. The details of the Monte Carlo simulation have been described previously.¹² The transmission probability is calculated for each particle based on its energy and path length in the MLC. The published data of energy dependent attenuation coefficient of Hubbell for tungsten are used.⁸ The path length of a particle can be calculated by integrating the leaf structure function and by interpolating the path length distribution for a point source using the small angle approximation. The approximate calculation is essentially the same as that of the convolution method, in which the path length of a ray line with an arbitrary incident angle is determined by the intercepting point with the plane representing the MLC. The results for using the phase space data as the source are to be compared with the results for analytic source model.

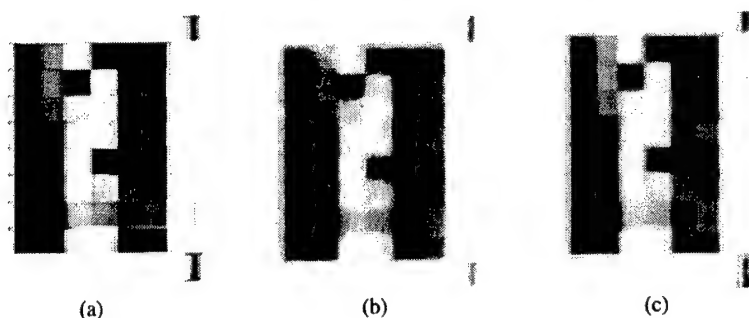


FIG. 5. Fluence distributions of a 15 MV IMRT field with 46 segments. (a) The calculated distribution using a point source. (b) The Wellhöfer BIS measurement. (c) The calculated distribution by convolving over a dual planar source.

E. Correlation with measured fluence distributions

The fluence distributions of IMRT fields are measured using film and a beam imaging system (BIS) (Wellhöfer Dosimetrie, Schwarzenbruck, Germany).¹³ An essential part of IMRT QA is to verify the measured fluence distribution by comparing it with a reference distribution. The comparison actually checks the correctness of the leaf sequences transferred to the beam delivery system and the hardware calibration. In addition to visual inspections, automated image correlation techniques have been employed for beam delivery QA.^{13,14} Quantitatively, the correlation for two images can be defined by

$$\langle AB \rangle = \frac{\sum_i A_i B_i}{\sqrt{\sum_i A_i^2} \sqrt{\sum_i B_i^2}}, \quad (21)$$

where A_i and B_i are the gray scales of the i^{th} pixel of the two images, respectively. The correlation coefficient represents how well two images match, which can be considered as the inner product of the two image vectors. It equals unity for two identical images.

Our calculated fluence distributions can be used as more accurate references for IMRT QA, since the spatial resolution of our calculation is in the order of 0.1 cm, which is comparable to the resolution of the Wellhöfer BIS.

III. RESULTS

Given $d=10$, $SO=100$, and $\theta=20^\circ$ for the example shown in Fig. 1, the exact path length in the slab is 10.64.

Listed in Table I are the numerical results using different subinterval numbers for integrating the structure function. The integration limits are $r_1=95$ and $r_2=107$. The calculated path length converges to the exact result as the subinterval number increases.

As an example, we show the fluence distribution of an IMRT field calculated in the isocenter plane using a point source in Fig. 5(a). The pixel size was $0.1 \text{ cm} \times 0.1 \text{ cm}$ and one ray line was traced in each pixel. In Fig. 5(b) we show the measured fluence using the Wellhöfer BIS. As expected, the fluence distribution shows sharp edges in the area the intensity level changes. This is due to sharp penumbra with the point source. In addition, the interleaf leakage has been overestimated. Shown in Fig. 5(c) is the convolved fluence distribution using the extended source model. The calculated fluence distribution for a realistic source has blurred edges as seen in the measured distribution. In Fig. 6 we show the representative profiles for the point source and the extended source in the directions parallel and perpendicular to the leaf movement. The extended source has a minor effect on the penumbra generated by the rounded lead end, as seen in Fig. 6(a). The difference in the interleaf region between the point source and extended source is much larger, as seen in Fig. 6(b). In Fig. 7, we show the path length profile across the two leaves as a function of the ray line projection in the isocenter plane. A decreased interleaf path length to 4 cm or less is seen in a region of 0.1 cm width. This is due to a small gap between the tongue and groove for clearance between the leaves, as shown in Fig. 2(a). A narrow dip in Fig. 7

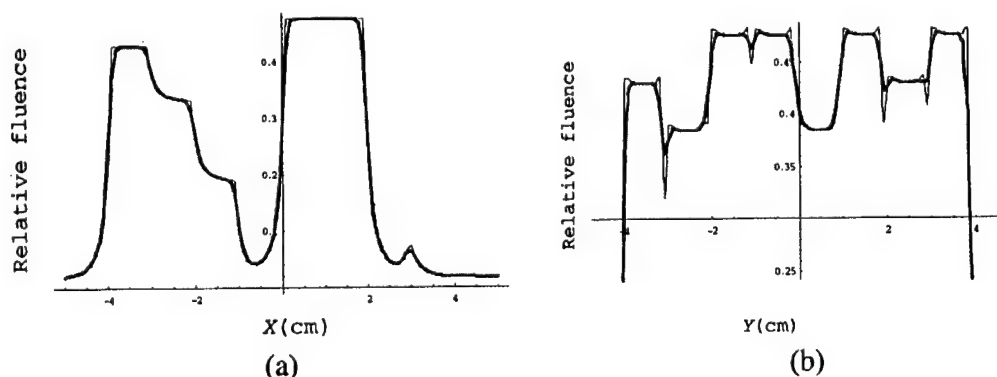


FIG. 6. Calculated fluence profiles with a point source (thin lines) and the convolution method with the extended source (thick lines). (a) Profiles in the direction parallel to leaf movement. (b) Profiles in the direction perpendicular to leaf movement.

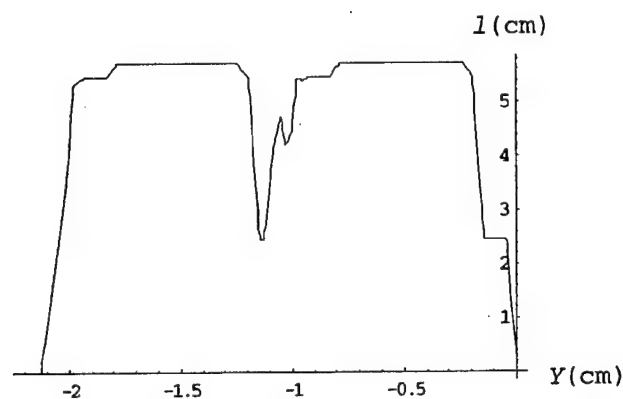


FIG. 7. Path length profile for the overlapping region of two leaves plotted in the direction perpendicular to the leaf movement in the isocenter plane.

corresponds to an interleaf gap of 0.02 cm width in which only the groove is intersected with an overall thickness of 2.5 cm. In a 0.04 cm wide region the thickness is less than 4 cm. For a source with finite dimension, however, only the central part of the source can be "seen" through this gap. Convoluting over an extended source therefore reduces the interleaf leakage as being overestimated with a point source, and thus improves the calculated fluence distribution.

The error of calculated MLC attenuation using the convolution method is estimated by comparison with full ray tracing calculation. One leaf is pulled out in an open field for this study. The difference is seen in the penumbra region with the peak error less than $\pm 5\%$ of the peak attenuation. The magnitude of the error is independent of the leaf position. In Fig. 8 we plot the convolved fluence profiles compared with the profiles calculated by full ray tracing. The largest discrepancy in these profiles is about 7% of the peak intensity, which appeared in a low intensity region.

The calculated fluence profiles using phase space particles of Monte Carlo simulation are shown in Fig. 9 in comparison with the convolved profiles with the analytic source model. There are 6 000 000 particles in the data set. Shown in Figs. 9(a) and 9(b) are the fluence profiles calculated by using the exact path length in the MLC for each particle, and the profiles calculated using the small angle approximation are shown in Figs. 9(c) and 9(d). The results obtained by the two methods agree with each other within the margin of statistical fluctuations.

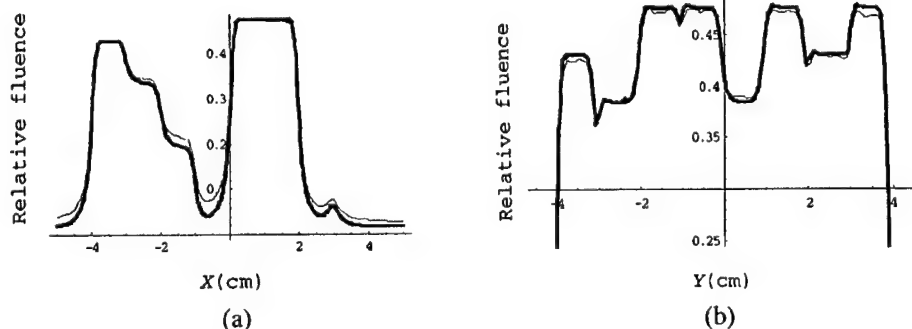


FIG. 8. Comparison between the convolved fluence profiles (thick lines) and full ray tracing calculations (thin lines).

The measured profiles using the Wellhöfer BIS are shown in Fig. 10 in comparison with calculation. The gray scales of the BIS image are normalized to the peak fluence of the field. The BIS image is correlated with the calculated fluence distributions by various methods. For the IMRT field shown in Fig. 5, the global correlation coefficient is 0.96 for the BIS measurement and the calculation using the step function leaf transmission, ignoring the leaf penumbra. For the calculated fluence distribution with a point source the correlation coefficient is 0.989, and for the convolved fluence distribution the correlation is further improved to 0.994. The numerical result is typical for the actual IMRT treatment plans delivered by the step-and-shoot technique on a Varian Clinac 2300CD in our clinic. In fact, the correlation coefficients for all fields were above 0.99 with the convolved fluence distribution, while they were about 0.95–0.96 for the simplified calculation with the step function leaf transmission. Listed in Table II are the correlation coefficients for the subfields defined by each MLC leaf pairs. The 16th and 25th pairs of the leaves were closed. The data reflect the discrepancies between the calculation and measurement in the edges of the field (17th and 24th pairs) and outside the field (16th and 25th pairs).

IV. DISCUSSIONS

The path length of a ray line in an attenuating object is usually calculated by solving the intersecting points between the ray line and the objects. It is impossible to find an analytical solution for a complex 3D geometry. On the other hand, solving simultaneous algebraic equations numerically would involve an iterative process, which can be expensive computationally. Our numerical approach does not require the exact intersecting points of the ray lines and the attenuating object. The accuracy of the results depends on the step size for the numerical integration. The step size is essentially the unit length in a "computer experiment" to measure the path lengths. The limits of integration should be chosen based on the largest region occupied by the attenuating object in order to avoid unnecessary waste of computational time. The numerical approach has an advantage in that no approximation is made on the geometry of the attenuating object. A simple application of the path length calculation is to determine the relation between the physical leaf position and the light field edge projected to the isocenter plane as the

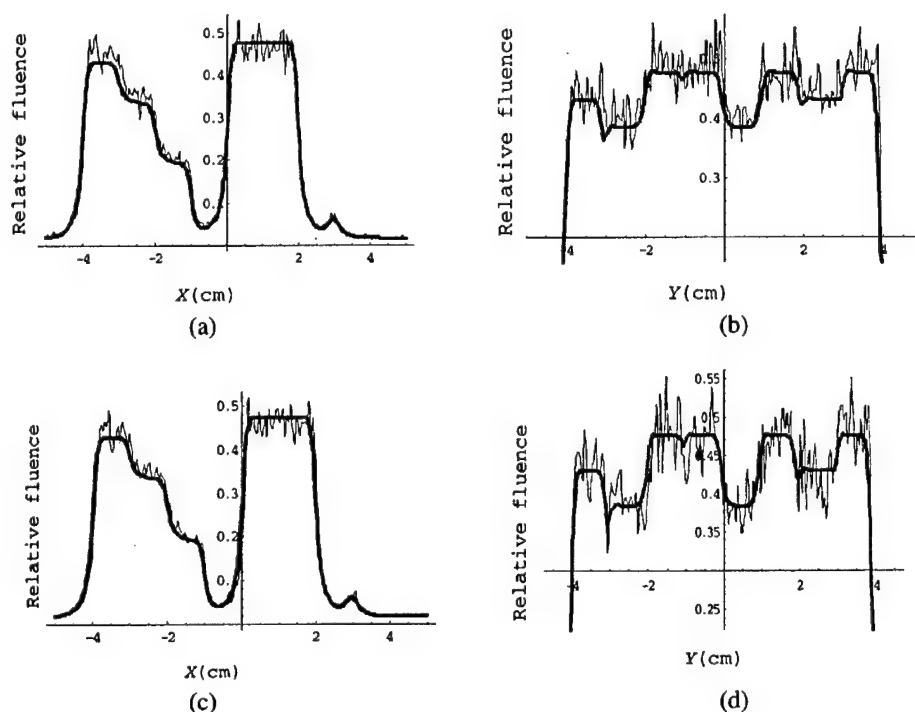


FIG. 9. The fluence profiles calculated using phase space particles of Monte Carlo simulation (thin lines) in comparison with the profiles calculated using the analytic source model (thick lines). The transmitted particles are scored in the isocenter plane with $0.05 \text{ cm} \times 0.05 \text{ cm}$ pixels. The profiles in (a) and (b) are calculated by full ray tracing, and the profiles in (c) and (d) are calculated using the small angle approximation.

specified leaf position. Geometric analysis for such a relation is complicated, and it depends on the specific MLC design. But one can easily generate a look-up table for the physical and specified leaf positions using computer simulation. For a fixed leaf position, the edge of the light field can be determined by interpolating the path length distribution data. By this approach the analytical results of Boyer and Li⁶ can be reproduced with just a few lines of computer code.

The fluence distribution calculation is fast enough for clinical applications. It takes 10 to 30 s on a 400 MHz Pentium PC for a typical step-and-shoot IMRT field depending on its number of segments and field size. The path length distribution for point source geometry is calculated by interpolating precalculated path length distributions. Under the same approximation an extended source can be taken into account by the convolution method. For an IMRT field consisting of many segments, the convolution over the extended source is performed for the summed fluence distributions of individual static fields, since the order of summing the con-

volved fluence distribution and convolving the summed fluence distribution is exchangeable. Consequently, the convolution needs to be performed only once.

The small angle approximation assumes that the path lengths of ray lines as a function of intersecting points in the isocenter plane can be obtained by a coordinate translation when moving the source point or a leaf by a small distance. The approximation is equivalent to the assumption that the path length of a ray line in the MLC only depends on the location of its intersection with the MLC, not on the direction of the ray line. This approximation is bound to break down if the source dimension is too large. This is the case for the extrafocal source. However, the error due to extrafocal source dimension should be small because the extrafocal source only contributes about 10% of the total strength. The approximation can reduce the computation time by at least two orders of magnitude for both the analytic and Monte Carlo simulated source models.

Calculation of the MLC transmission by ray tracing can

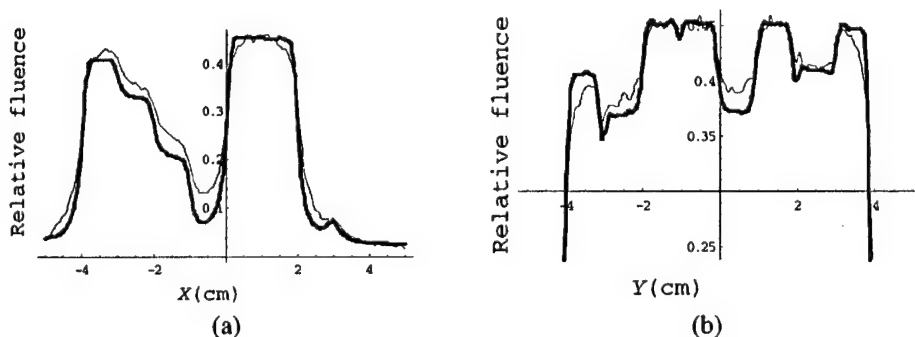


FIG. 10. Measured fluence profiles using the Wellhöfer BIS (thin lines) in comparison with the calculated profiles (thick lines).

TABLE II. Correlation coefficients of the calculated and measured fluence distributions in 10 cm×1 cm areas aligned with the MLC leaves.

Leaf pair	16	17	18	19	20	21	22	23	24	25
Step function	0.876	0.959	0.986	0.974	0.968	0.969	0.969	0.973	0.966	0.877
Point source	0.945	0.989	0.997	0.993	0.993	0.992	0.991	0.995	0.992	0.925
Convolved	0.948	0.993	0.998	0.995	0.995	0.994	0.994	0.997	0.995	0.935

be a useful tool to derive a field specific analytic source model for more efficient Monte Carlo patient dose calculation. The energy spectrum of the source has been ignored in current calculation for the analytic source model, as a measured attenuation coefficient has been used. On the other hand, the energy spectrum with its angular dependence is contained in the data set of the Monte Carlo simulated particles. It is possible to fine tune the analytic source model based on the fluence distribution calculated from the Monte Carlo simulation. This may also take into account the scatter originated from the MLC. Quantitative study of the analytic source model in comparison with Monte Carlo simulation in regard to MLC transmission will be reported along with its effect on dose calculation.

The gray scales of the BIS image are scaled to match the peak fluence of the calculation for comparison. The scaling constant has different values for different fields. This is because the gray scale response of the BIS is field size dependent.¹³ In addition, the relative gray scale of the BIS measurement also depends on the number of monitor units used to acquire the image. The BIS response is affected by the scatter generated in the MLC, which is not considered in the fluence calculation. Because of the nonlinear nature of the response of the BIS or film, it is not possible to use the same gray scale correction curve for all fields to better match the calculation with the measurement.¹⁴ However, the effect of low intensity signals on global correlation can be removed using a threshold. Larger discrepancies between the calculation and the measurement are observed outside the radiation field, as indicated by the data in Table II. With a threshold the global correlation coefficient can be further improved to above 0.995.

The fluence pattern of the IMRT field shown in Fig. 5 with 1 cm×1 cm squares is the result of employing the finite size pencil beam (FSPB) in the inverse planning algorithm. To estimate the reduction of the correlation coefficient due to an error of a leaf position, we assume that the fluence in a 1 cm×1 cm square is wrongfully switched off in a 10 cm×10 cm field. If the average fluence of the field is 0.5, and the norm of the image sampled with 0.1 cm×0.1 cm pixels is $0.5 \times 0.5 \times 100 \times 100 = 2500$, the correlation is reduced to $(2500 - 25) / [(\sqrt{2500 - 25})(\sqrt{2500})] \approx 0.995$. Clearly, the global correlation around 0.95 with a simplified MLC transmission model is not sensitive enough to detect an error involved with one FSPB beamlet. An improved correlation using realistic fluence calculation increases the sensitivity of error detection. The acceptable correlation coefficient can be set to 0.99 for IMRT QA.

V. CONCLUSIONS

We have presented a simple numerical method for calculating the photon transmission through an MLC by ray tracing. It has been developed into a software tool for calculating the fluence distributions for IMRT fields using the MLC. The calculated fluence distributions show better agreement with measurements than the distributions calculated based on simplified MLC transmission model. This is reflected by an improved global correlation with measurement. The software tool can have several clinical applications including beam delivery QA and construction of field specific source models for dose calculation.

ACKNOWLEDGMENTS

We would like to thank Steve Jiang for many helpful discussions and Lijun Ma for the BIS file format. We acknowledge Varian Medical Systems for providing us with detailed information about the MLC construction. This work was supported in part by Grants CA 43840 and CA 78331 from the NCI, BC 971292 from the DOD, and Seed Cycle I by RSNA Research and Education Fund.

^aAuthor to whom correspondence should be addressed. Electronic mail: ychen@reyes.stanford.edu

¹M. S. Huq, Y. Yu, Z. Chen, and N. Suntharalingam, "Dosimetric characteristics of a commercial multileaf collimator," *Med. Phys.* **22**, 241–247 (1995).

²T. J. Jordan and P. C. Williams, "The design and performance characteristics of a multileaf collimator," *Phys. Med. Biol.* **39**, 231–251 (1994).

³J. M. Galvin, A. R. Smith, and B. Lally, "Characterization of a multileaf collimator," *Int. J. Radiat. Oncol., Phys.* **25**, 181–192 (1993).

⁴A. L. Boyer, T. G. Ochrn, C. E. Nyerick, T. J. Waldron, and C. J. Huntzinger, "Clinical dosimetry for implementation of a multileaf collimator," *Med. Phys.* **19**, 1255–1261 (1992).

⁵T. LoSasso, C. S. Chui, and C. Ling, "Physical and dosimetric aspect of multileaf collimation system used in the dynamic mode for implementing intensity modulated radiotherapy," *Med. Phys.* **25**, 1919–1927 (1998).

⁶A. L. Boyer and S. Li, "Geometric analysis of light-field position of a multileaf collimator with curved ends," *Med. Phys.* **24**, 757–762 (1997).

⁷A. L. Boyer, "Basic applications of a multileaf collimator," in *Teletherapy: Present and Future, Proceedings of the 1996 Summer School of the American Association of Physicists in Medicine*, edited by J. Palta and R. Mackie (Medical Physics, Madison, WI, 1996).

⁸J. H. Hubbell, "Photon mass attenuation and energy-absorption coefficients from 1 keV to 20 MeV," *Int. J. Appl. Radiat. Isot.* **33**, 1269–1290 (1982).

⁹H. H. Liu, T. R. Mackie, and E. C. McCullough, "A dual source photon beam model used in convolution/superposition dose calculation for clinical megavoltage x-ray beams," *Med. Phys.* **24**, 1960–1974 (1997).

¹⁰T. C. Zhu, B. E. Bjärngard, and H. Shackford, "X-ray source and the output factor," *Med. Phys.* **22**, 793–798 (1995).

- ¹¹M. B. Sharpe and D. A. Battista, "X-ray sources of medical linear accelerators; Focal and extra focal radiation," *Med. Phys.* **22**, 2065–2074 (1995).
- ¹²C.-M. Ma, E. Mok, A. Kapur, T. Pawlicki, D. Findley, S. Brain, K. Forster, and A. L. Boyer, "Clinical implementation of a Monte Carlo treatment planning system," *Med. Phys.* **26**, 2133–2143 (1999).
- ¹³L. Ma, P. B. Geis, and A. L. Boyer, "Quality assurance for dynamic multileaf collimator modulated fields using a fast beam imaging system," *Med. Phys.* **24**, 1213–1220 (1997).
- ¹⁴L. Dong and A. L. Boyer, "An image correlation procedure for digitally reconstructed radiographs and electronic portal images," *Int. J. Radiat. Oncol., Biol., Phys.* **33**, 1053–1060 (1995).

Electron beam modeling and commissioning for Monte Carlo treatment planning

Steve B. Jiang,^{a)} Ajay Kapur, and C.-M. Ma

Department of Radiation Oncology, Stanford University School of Medicine, 300 Pasteur Drive, Stanford, California 94305-5304

(Received 19 April 1999; accepted for publication 22 October 1999)

A hybrid approach for commissioning electron beam Monte Carlo treatment planning systems has been studied. The approach is based on the assumption that accelerators of the same type have very similar electron beam characteristics and the major difference comes from the on-site tuning of the electron incident energy at the exit window. For one type of accelerator, a reference machine can be selected and simulated with the Monte Carlo method. A multiple source model can be built on the full Monte Carlo simulation of the reference beam. When commissioning electron beams from other accelerators of the same type, the energy spectra in the source model are tuned to match the measured dose distributions. A Varian Clinac 2100C accelerator was chosen as the reference machine and a four-source beam model was established based on the Monte Carlo simulations. This simplified beam model can be used to generate Monte Carlo dose distributions accurately (within 2%/2 mm compared to those calculated with full phase space data) for electron beams from the reference machine with various nominal energies, applicator sizes, and SSDs. Three electron beams were commissioned by adjusting the energy spectra in the source model. The dose distributions calculated with the adjusted source model were compared with the dose distributions calculated using the phase space data for these beams. The agreement is within 1% in most of cases and 2% in all situations. This preliminary study has shown the capability of the commissioning approach for handling large variation in the electron incident energy. The possibility of making the approach more versatile is also discussed. © 2000 American Association of Physicists in Medicine.[S0094-2405(00)03401-5]

Key words: electron beam, treatment planning, Monte Carlo simulation, beam commissioning, source modeling

I. INTRODUCTION

Electron beam radiation therapy is used extensively to treat head and neck cancers to avoid the irradiation of the spinal cord, and to treat chest walls to limit the irradiated volume of lung. The currently available commercial systems for electron treatment planning mostly utilize the Hogstrom algorithm as the dose calculation engine,¹ which is based on Fermi-Eyges theory.^{2,3} Due to the inappropriate treatment of electron transport in inhomogeneous phantoms, large discrepancies (10% or more) in the dose distributions have been observed between the current analytical algorithms and measurements or Monte Carlo simulations in some clinical situations where the treatment volumes encompass air cavities and bone.⁴⁻⁷ Accurate dose calculation is an important factor for the widespread clinical use of electron therapy and the development of new electron therapy techniques, such as electron beam or mixed electron/photon beam intensity modulated therapy, which are expected to improve the conformality of the delivered dose distribution to the target volume for some disease sites.⁸⁻¹⁰

The Monte Carlo method is generally considered to be the most accurate approach for electron dose calculation under all circumstances.¹¹⁻¹⁶ In particular, Monte Carlo simulation can handle electron multiple scattering in the presence of inhomogeneities (such as bone and air cavity) much more

accurately than any existing analytical dose models. The necessity of accurate electron dose calculation has motivated many efforts to develop Monte Carlo electron beam treatment planning systems.^{6,7,17-22} Due to the rapid development of computer technology and the employment of innovative variance reduction techniques, it is expected that treatment planning systems utilizing a Monte Carlo dose engine will begin to serve in routine clinical practice in the next few years.^{6,7,20-29}

The commissioning procedure for a Monte Carlo treatment planning system can be different from that for a conventional planning system, since it requires more detailed and accurate clinical beam data.²² For example, the phase space information (position, direction and energy) is needed to represent particles coming out of the accelerator treatment head. This information is extremely difficult, if not impossible, to acquire experimentally, mainly due to the very high intensity of the therapeutic electron beam.³⁰ Some researchers tried to extract the phase space information from the limited set of measured dose data (such as depth dose curves and dose profiles) by using a simple beam model.³¹ Although the approach may have great potential, at least currently it uses many approximations and the accuracy of the reconstructed phase space cannot be guaranteed. The only method to obtain the accurate electron beam phase space

information is to simulate the accelerator treatment head using the Monte Carlo method.³²⁻³⁴ An EGS4 Monte Carlo user code, OMEGA BEAM, was developed specifically for this purpose.³⁴ Using the BEAM code, the accelerator treatment head and electron applicator can be simulated to yield a data file containing the phase space information for tens of millions of particles exiting the treatment head. The phase space data can then be used as input to calculate dose distributions in a patient's CT phantom.³⁴

However, direct simulation of the accelerator treatment head using the Monte Carlo method is not a viable commissioning approach for Monte Carlo treatment planning. The beam characteristics are usually different due to variation in accelerator designs and on-site beam tuning. The simulated electron beam phase space for one accelerator may not be used directly for another. It is necessary to simulate each accelerator individually to obtain the phase space information. This fact presents three problems for the clinical acceptance of Monte Carlo treatment planning systems. First, the simulation of the accelerator treatment head for every energy/applicator combination takes much more time than the commissioning of a conventional electron planning system. As estimated by Faddegon *et al.*,²² even for users with Monte Carlo simulation experience, it takes about two months of CPU time to generate a complete set of beam data for a single accelerator. Second, the storage of the phase space information requires a lot of computer disk space. For each energy/applicator combination, a phase space file is usually pre-calculated and stored in the treatment planning computer. For accurate treatment planning, a phase space file occupies hundreds of megabytes of disk space. This is certainly a substantial burden for the computer resources at most clinical centers. Third, the generation and quality assurance of the phase space data files by simulating the treatment head requires Monte Carlo simulation experience. Therefore, it is a prohibitive task for general users to perform Monte Carlo simulations for their own accelerators.

In this paper, a hybrid approach for commissioning electron beam Monte Carlo treatment planning systems is proposed. This method combines the advantages of the full Monte Carlo simulation and the method of Janssen *et al.*³¹ It is based on the assumption that accelerators of the same type have very similar electron beam characteristics and the major difference is the electron incident energy at the exit window due to beam tuning during linac acceptance. By simulating a reference accelerator for a particular type of accelerator using the Monte Carlo BEAM code,³⁴ a beam model is constructed using the resultant phase space information. The beam model is a simplified implementation of a previously developed multiple source model which can compress the Monte Carlo phase space data by a factor of 1000 or more.³⁵⁻³⁷ When commissioning another accelerator of the same type, the energy spectra in the beam model are tuned to match standard measured data such as depth doses and dose profiles. Using this approach, we do not have to simulate every accelerator individually. Only one reference accelerator needs to be simulated for a type of accelerator, and this can be done carefully by someone with Monte Carlo exper-

tise. In this paper, a Varian Clinac 2100C accelerator is chosen as the reference machine. The machine is simulated using the BEAM code³⁴ and a four-source beam model is established based on the simulated beam phase space information. The accuracy of the Monte Carlo dose distributions calculated with the model is verified. Then, the model based on the reference beam is used to commission three other electron beams. Two beams are also from the reference machine but with incident energies significantly different from that of the reference beam. The third beam is from another Clinac 2100C machine at a different institution.³⁸ The validity of the proposed commissioning approach is demonstrated by commissioning these three beams.

II. METHODS AND MATERIAL

A. Beam modeling

1. General considerations

Beam modeling is the first step in our hybrid commissioning procedure for a Monte Carlo treatment planning system. A beam model for a type of accelerator is established using the Monte Carlo simulated phase space information for the reference beam. The beam data are modeled using the multiple source model developed by Ma *et al.*,³⁵⁻³⁷ which is modified in the current work for use in the commissioning procedure. The major modifications of the model are discussed here.

The multiple source model is based on the observation that particles from different components of an accelerator have significantly different energy, angular, and spatial distributions, while the particles from the same component have very similar characteristics.³⁵⁻³⁷ Therefore, the particles from different components of an accelerator can be treated as they are from different sub-sources. Each sub-source represents a critical component in the treatment head and its geometrical dimensions are determined by the component dimensions. Each sub-source has its own energy spectrum and planar fluence distribution derived from the simulated phase space data. When the model is used for dose calculation, the incident energy and position of a particle are sampled from the corresponding stored energy spectrum and planar fluence distribution. The incident direction of the particle is reconstructed by sampling the position of the particle on the sub-source and on the phantom surface. The correlation between the particle position and incident angle is naturally retained.

A primary reason to develop the multiple source model was to find a concise way to replace the huge phase space data files generated from Monte Carlo simulations.^{35,36} The emphasis of the current work is to develop a clinically practical commissioning procedure for Monte Carlo treatment planning. The multiple source model is simplified to make the commissioning procedure as simple as possible while trying to maintain dose calculation accuracy under all circumstances of clinical relevance. The number of sub-sources in the model is minimized and only those sub-sources of dosimetric significance are retained. The dependence of the model on the detailed information of accelerators is reduced. Sub-sources are represented by dimensionless geometric ob-

jects, such as points and lines, instead of the actual geometrical shapes and sizes of the treatment head components as used previously.^{35,36}

Ma *et al.* established their multiple source model from the Monte Carlo simulated phase space data on the patient surface (at 100 cm SSD) and the last scraper of the electron applicator was included in the model as a sub-source.^{35,36} In this work, the treatment head is simulated using the BEAM code down to just above the last scraper of the electron applicator,³⁴ where the patient specific cutout is inserted. The last scraper, as well as the field-defining cutout, are simulated together with the patient CT phantom when performing Monte Carlo treatment planning dose calculations. The advantage of this method is that the beam model is patient independent. However, this approach, compared to that of Ma *et al.*,^{35,36} requires more careful beam modeling since an air gap between the last scraper and patient surface is not included in the original BEAM simulation.

In the present paper, the beam modeling approach is applied to a Varian Clinac 2100C machine at Stanford Medical Center, which is chosen as the reference machine to build beam models. At first, a very detailed model for each beam is used as the starting point. All the critical components of the treatment head are modeled as sub-sources. With this model, the phase space information of the electron beam can be precisely reconstructed and the dose distribution in a water phantom can be accurately calculated. Then, the number of sub-sources is gradually reduced while maintaining the accuracy in dose distribution calculation. We find that a point electron source with the energy spectrum obtained from the Monte Carlo simulation is able to give a reasonably accurate depth-dose curve, which is consistent with the previous observation.³⁶ By adding another point photon source, the bremsstrahlung tail in the depth dose distribution can be reproduced accurately. However, it is found that the penumbra at the phantom surface generated with this two point source model is sharper compared to that generated with the full phase space data. In order to get the dose profiles correct, we find that, in addition to the two point sources, two square ring electron sources (which emit electrons isotropically) are needed to represent electrons scattered from the applicator scrapers. (The term *square ring* is used here to represent the edge of a square.) Therefore, the beam model should include four sub-sources: a point electron source for direct electrons (which do not interact with the beam defining system) and electrons scattered from the primary collimator, movable jaws and shieldings, a point photon source for all contaminant photons, and two square ring electron sources for electrons scattered from the first two scrapers of the electron applicator (the third also last scraper is not included in the model).

As described previously, beam modeling consists of two steps, namely, beam representation and beam reconstruction.^{35,36} In beam representation, parameters in the model are extracted from the simulated phase space file. In the current simplified model, these parameters include the positions and relative intensities of the sub-sources, the energy spectra for particles inside and outside the field for each

sub-source, and the planar fluence distributions on the scoring plane (directly above the last scraper) for each sub-source. Beam reconstruction is performed when using the model for dose calculations. The phase space information for each particle, including the energy, position and direction, is reconstructed from the scored source parameters.

2. Beam representation

The positions of the virtual electron and photon point sources can be determined using a method described in Ref. 36, which is analogous to the pinhole method.³⁹ A thin annular aperture is selected on the scoring plane and phase space particles are allowed to pass through the aperture and form an image at a distance below the scoring plane. Ray lines drawn through the center of the aperture and the peak of the aperture image form a virtual focal spot, which is adopted as the position of the point source. This pinhole method is very effective for the photon point source. However, we find that for electrons, this method is only applicable to high energy beams. For lower energy beams, e.g., 6 MeV, the virtual SSD determined with this method is greatly overestimated and dependent on the radius of the thin annular aperture on the scoring plane. This is due to the fact that the in-air multiple scattering of low energy electrons is significant. To overcome this problem we performed another Monte Carlo simulation of the accelerator treatment head by replacing the intervening air with vacuum. Then, based on the new phase space data, this pinhole method can be used to generate the correct position for the virtual electron point source, which is independent of the sampling radius. The effect of in-air multiple scattering is taken into account during beam reconstruction by adding a perturbation to the electron incident direction, as discussed later.

Two square ring sources of electrons are located at the corresponding positions of the two applicator scrapers. The sides of the square rings correspond to the actual openings of the scrapers.

The energy spectrum for each sub-source is derived from the simulated phase space data. It was found that the mean energy of the electrons is relatively uniform inside the field as well as outside the field. The change of mean energy with the distance from the central axis is more like a step function.³⁶ Therefore, in the current model, each sub-source has two different energy spectra, one for electrons inside and the other for electrons outside the treatment field. Parameters stored in the model are the minimum and maximum energies, number of energy bins as well as the relative fluence for each energy bin. The minimum and maximum energies correspond to the cutoff energies (ECUT or PCUT) and the incident energy used in the accelerator simulation. The number of bins is determined by the desired resolution. For example, if we want the uncertainty in the calculated depth of 50% dose, R_{50} , to be less than 1%, the uncertainty in the peak position of the energy spectrum should be within 1% and therefore the bin width should be smaller than 1% of the peak energy. For the 12 MeV beam, we used 128 bins and then the bin width is less than 0.1 MeV. This bin width is

also found to be small enough to represent the peak width of the energy spectrum, which has a significant effect on the slope of the depth dose fall-off.

The planar fluence distribution for each sub-source is also derived from the simulated phase space data and recorded on the scoring plane using a grid scheme. Within each pixel of the grid, the planar fluence is assumed to be uniform. The dimension of a pixel is dependent on field size, usually from 1 to 3 mm. Parameters used to represent the planar fluence distribution include the treatment field dimension, the number of pixels and the relative intensity of each pixel, for each sub-source. It has been found that in general, the mean energy varied from position to position in the treatment field by less than 10% for a given sub-source.³⁶ Thus, it is reasonable to store and then sample the particle energy and position independently.

The angular distributions are not scored explicitly. They are reconstructed during the dose calculation, as described in the next section.

Finally, the simulated phase space information is represented with a set of parameters for each sub-source. The resultant source parameter file is much smaller (about 100 kilobytes) than the original phase space file (>100 megabytes).

3. Beam reconstruction

When performing dose calculation in a patient's CT phantom, the source parameter file is used to reconstruct the phase space information (energy, position and direction) of every incident particle. The beam reconstruction process consists of the following steps:

- (1) Determine from which particular sub-source a particle originates by sampling from the relative source intensity of each sub-source.
- (2) Determine the position on the sub-source (excluding point sources) where the particle is emitted.
- (3) Sample the particle position on the scoring plane from the fluence pattern for the sub-source.
- (4) Sample the particle energy from the energy spectrum for the given sub-source based on the particle position (inside or outside the treatment field).
- (5) Determine the particle incident angle by connecting the position on the sub-source from where the particle is emitted and the position of the particle on the scoring plane.
- (6) Add in-air perturbation on the particle direction if it is an electron.

The sampling from the relative source intensity distribution is done by a table-look-up method.³⁵ All the sub-sources are in turn numbered from 1 to N (here $N=4$ for accelerators with designs similar to the Varian Clinac 2100C machine) and the relative intensity of the i th sub-source is p_i ($i=1, \dots, N$). The accumulative source intensity for the i th sub-source, $P_i (= \sum_{j=1}^i p_j)$, is multiplied by a large integer M . The value of M is determined according to the desired sampling precision of the relative source intensity. For ex-

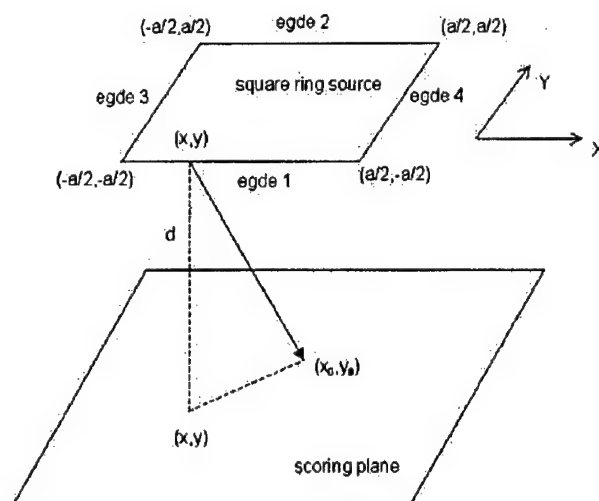


FIG. 1. A diagram for illustrating the sampling algorithm from a square ring source. The origin of the coordinate system is at the center of the square ring.

ample, $M=1000$ corresponds to the precision of 0.1% in sampling from the relative source intensity distribution. Then, a one dimensional array of M elements is prepared by assigning value i to array elements from $INT(MP_{i-1})$ to $INT(MP_i)$, where the operator INT returns the integer part of a real number. During the beam reconstruction, a random integer number K between 1 and M is generated and the value of the K th array element is the sub-source number where the particle is emitted. Such a table-look-up method is of very high sampling speed and efficiency. Its speed is also independent of the number of sub-sources. The sampling precision is usually adequate as long as an large enough array is used.

According to the energy spectra on the scoring plane, the bin number in which the particle energy falls is also sampled using the table-look-up method. An additional uniform sampling is done within the given energy bin to make the particle energy continuous.

The same table-look-up method is also used to sample the pixel number corresponding to a particle position on the scoring plane. Another sampling is performed uniformly to determine the particle's coordinates within the chosen pixel.

For the point sources, the incident angle of the particle is determined by constructing a ray line from the point source to the position of the particle on the scoring plane. For the square ring electron sources, we need to determine where the electron comes from on the ring. This is done in two steps. First, we determine from which edge of the square ring the electron is emitted. Second, we determine from where on the chosen edge the electron comes.

As illustrated in Fig. 1, a square ring of size $a \times a$ is located above the scoring plane at a distance d . We assume that the square ring edge emits electrons uniformly and isotropically. Under this approximation, the probability for an electron on the scoring plane to come from a point on the ring is proportional to the inverse square of the distance be-

tween the points on the ring and plane. This approximation greatly simplifies the sampling process. It is found that the angular distribution of the scattered electrons reconstructed based on the fluence distribution on the scoring plane and the emitting position on the square ring source is reasonably accurate, although electrons scattered from the applicator scraper mainly correspond to electrons incident on the vertical face of the scraper and are dominantly forward directed.⁴⁰ Furthermore, the dose profile at the patient surface is greatly influenced by electrons scattered from the last scraper or cut-outs, which are not included in the source model but will be accurately simulated with the patient CT phantom.

For an electron at position (x_0, y_0) on the scoring plane (see Fig. 1), the probability for it to have come from the i th edge is given as

$$p'_i(x_0, y_0) \sim \frac{1}{C_i} \left[\arctan\left(\frac{x_0 + a/2}{C_i}\right) - \arctan\left(\frac{x_0 - a/2}{C_i}\right) \right] \quad \text{for } i=1,2, \quad (1)$$

$$p'_i(x_0, y_0) \sim \frac{1}{C_i} \left[\arctan\left(\frac{y_0 + a/2}{C_i}\right) - \arctan\left(\frac{y_0 - a/2}{C_i}\right) \right] \quad \text{for } i=3,4, \quad (2)$$

where

$$C_1 = \sqrt{(y_0 + a/2)^2 + d^2}, \quad (3)$$

$$C_2 = \sqrt{(y_0 - a/2)^2 + d^2}, \quad (4)$$

$$C_3 = \sqrt{(x_0 + a/2)^2 + d^2}, \quad (5)$$

$$C_4 = \sqrt{(x_0 - a/2)^2 + d^2}. \quad (6)$$

Using the probabilities given above, the edge from which the electron has come can be sampled. Then, the position (x, y) on the chosen edge is further sampled. For edges 1 and 2,

$$x = x_0 - C_i \cdot \tan \left[(1 - \xi) \cdot \arctan\left(\frac{x_0 + a/2}{C_i}\right) + \xi \cdot \arctan\left(\frac{x_0 - a/2}{C_i}\right) \right] \quad i=1,2, \quad (7)$$

$$y = \begin{cases} -a/2 & \text{for } i=1 \\ a/2 & \text{for } i=2 \end{cases}, \quad (8)$$

and for edges 3 and 4,

$$x = \begin{cases} -a/2 & \text{for } i=3 \\ a/2 & \text{for } i=4 \end{cases} \quad (9)$$

$$y = y_0 - C_i \cdot \tan \left[(1 - \xi) \cdot \arctan\left(\frac{y_0 + a/2}{C_i}\right) + \xi \cdot \arctan\left(\frac{y_0 - a/2}{C_i}\right) \right] \quad i=3,4, \quad (10)$$

where ξ is a random number uniformly distributed from 0 to 1.

After the electron position on the square ring is determined, the connection of this position to the position on the scoring plane gives the electron's incident direction, which needs to be additionally perturbed to address the in-air multiple scattering.

In a previous implementation of this model, the effect of electron multiple scattering in air as well as other materials on its path to the scoring plane was taken into account by sampling the electron perturbation angle from a Monte Carlo simulated angular distribution.³⁶ This angular distribution was stored while performing the Monte Carlo simulation for the accelerator and only included electrons falling into a small region (e.g., of 1 cm radius) around beam central axis. In the current work, the effect of in-air multiple scattering is considered more accurately using the Fermi-Eyges theory.^{2,3} The effect of other materials is considered by adding a parameter to the standard deviation of the angular distribution. The Fermi-Eyges theory is a well-known small-angle theory and can predict the multiple scattering effect of megavoltage electrons in air or other heavier materials as long as the electron effective pathlengths are small.^{41,42}

Assume that an electron initially travels along the z axis. According to the Fermi-Eyges theory, the distributions for the projections of the polar angle, θ , on the $x-z$ plane, θ_x , and on the $y-z$ plane, θ_y , are both Gaussian after electrons travel a distance, and are given as^{3,42}

$$f(\theta_x) = \frac{1}{\sqrt{2\pi}\sigma_{\theta_x}} \exp\left(-\frac{\theta_x^2}{2\sigma_{\theta_x}^2}\right), \quad (11)$$

$$f(\theta_y) = \frac{1}{\sqrt{2\pi}\sigma_{\theta_y}} \exp\left(-\frac{\theta_y^2}{2\sigma_{\theta_y}^2}\right), \quad (12)$$

where σ_{θ_x} and σ_{θ_y} are the standard deviations for each Gaussian distribution, respectively. In a homogeneous material, and without the presence of an electromagnetic field, both standard deviations should be the same, so we let $\sigma = \sigma_{\theta_x} = \sigma_{\theta_y}$. Under the small-angle approximation

$$\theta^2 = \theta_x^2 + \theta_y^2, \quad (13)$$

therefore the polar angle θ obeys a radial Gaussian distribution while the azimuthal angle ϕ is uniformly distributed in $[0, 2\pi]$. Hence the sampling method for these two angles is given as follows:

$$\theta = \sigma \sqrt{-2 \ln \xi_1}, \quad (14)$$

$$\phi = 2\pi \xi_2, \quad (15)$$

where ξ_1 and ξ_2 are random numbers uniformly distributed in $[0, 1]$.

According to the Fermi-Eyges theory, σ can be calculated as^{3,42}

$$\sigma^2 = A_0 - A_1^2/A_2, \quad (16)$$

where

$$A_i = \frac{1}{2} \int_0^l K(l-t)^i dt, \quad i=0,1,2. \quad (17)$$

Here, K is the electron linear scattering power and l is the distance at which electrons travel. The electron linear scattering power can be fitted well using a simple formula proposed by Werner *et al.*:⁴³

$$K(E) = \alpha E^{-\beta}. \quad (18)$$

Using this formula we fitted the linear scattering power data in air supplied by ICRU Report 35⁴⁴ and found that $\alpha = 3.329 \times 10^{-3} \text{ rad}^2/\text{cm}$ and $\beta = 1.638$. E is the electron energy in MeV and sampled from the energy spectrum at the scoring plane. The energy loss of electrons in air is usually very small and can be ignored when they travel from the virtual source to the scoring plane. The mean energy loss of 6 MeV electrons after traveling 100 cm in air is about 4% of its initial energy (estimated using the stopping power) and it is about 2% for 20 MeV electrons. Therefore σ can be given as

$$\sigma^2 = \frac{1}{8} K(E)l, \quad (19)$$

which is a function of electron energy and the distance between the virtual source and the position on scoring plane. During beam reconstruction, according to the sampled electron energy, positions on the scoring plane and on the virtual source, σ can be calculated. Then using Eqs. (14) and (15) θ and ϕ are sampled and a perturbation is added to the electron's incident direction.

The perturbation caused by in-air multiple scattering can be directly calculated using Eq. (19) for electrons from the squaring ring sources. For direct electrons, there are other accelerator components in their paths from the virtual point source to the scoring plane in addition to the intervening air, such as the exit window, scattering foil, monitor chamber, mirror and protection window. The effect of these materials on electron angular distribution has been mainly included in the determination of the virtual electron point source position. We also need to take into account the angular perturbation caused by these materials. If we know precisely the material and thickness of these parts, we can calculate their effect on σ , as done by Keall and Hoban.⁴¹ However, it is usually difficult for users to know this information about their accelerator when commissioning a Monte Carlo treatment planning system. Therefore, we introduce a factor k to account for the effect of these materials. For direct electrons, σ is then given as

$$\sigma^2 = \frac{1}{8} K(E)lk. \quad (20)$$

The factor k is determined by fitting the angular distribution calculated using Fermi-Eyes theory to that simulated with the Monte Carlo method for direct electrons. The introduction of k factor provides a potentially tunable parameter in the source model.

4. Model verification

The four-source model is verified dosimetrically by comparing the dose distributions in a water phantom calculated

using the model with those calculated using the full phase space data. Dose distributions are calculated for various combinations of three electron energies (6, 12, and 20 MeV), three applicator sizes (6×6 , 10×10 , and $20 \times 20 \text{ cm}^2$), and two SSDs (100 cm and 120 cm).

The measurement of electron beam applicator factors (defined as the ratio of the open field dose in water at d_{\max} for a given applicator to that of the reference applicator, typically the 10×10 or $15 \times 15 \text{ cm}^2$, for the same beam energy) is done during accelerator commissioning for all energy/cone combinations. Therefore, the applicator factors will be supplied by the user when performing the model commissioning. Cutout factors (defined as the ratio of the dose in water at d_{\max} for a blocked field to that of the open field for the same applicator and beam energy) are patient specific and not always easy to measure accurately for all clinical situations. Therefore, the model should be able to calculate cutout factors. To demonstrate this, we compare the model calculated cutout factors with those measured and calculated by Kapur *et al.* using a full Monte Carlo simulation.⁴⁵

B. Beam commissioning

The four-source model which is built using a Varian Clinac 2100C accelerator as the reference machine can be used to reconstruct electron beams from other Clinac 2100C accelerators by tuning the energy spectra in the model.

For accelerators with exactly the same design, the major different is the electron incident energy due to the on-site tuning to suit the user. This energy approximately corresponds to the maximum energy of all the stored energy spectra in the source model. It is found that the energy spectra for all sub-sources are very similar for different accelerators of the same type. When the incident energy is changed, the energy spectra can be approximated as stretched or compressed along the energy axis accordingly. The depth dose curve is very sensitive to the electron incident energy and therefore used to adjust the maximum energy, E_{\max} , in the model. The relationship between the incident energy, E_{in} , and R_{50} has been studied by simulating the reference accelerator using a $10 \times 10 \text{ cm}^2$ cone and 100 cm SSD with various incident energies. Then, the variation of E_{in} as a function of the variation of R_{50} is established for this type of accelerator. This relationship is used as a guide to tune the maximum energy in the model to commission a clinical beam.

The proposed commissioning approach can be summarized as follows:

- (1) Chose an accelerator as the reference machine for all other accelerators of the same design, and carefully perform full Monte Carlo simulations for the electron beams of various nominal energies from the reference machine with $10 \times 10 \text{ cm}^2$ applicator.
- (2) Build the source models for the simulated beams based on the Monte Carlo phase space data, perform Monte Carlo dose calculation in water for 100 cm SSD, and record the maximum energy, $E_{\max}^{(\text{ref})}$, in the model and the $R_{50}^{(\text{ref})}$ value for each beam.

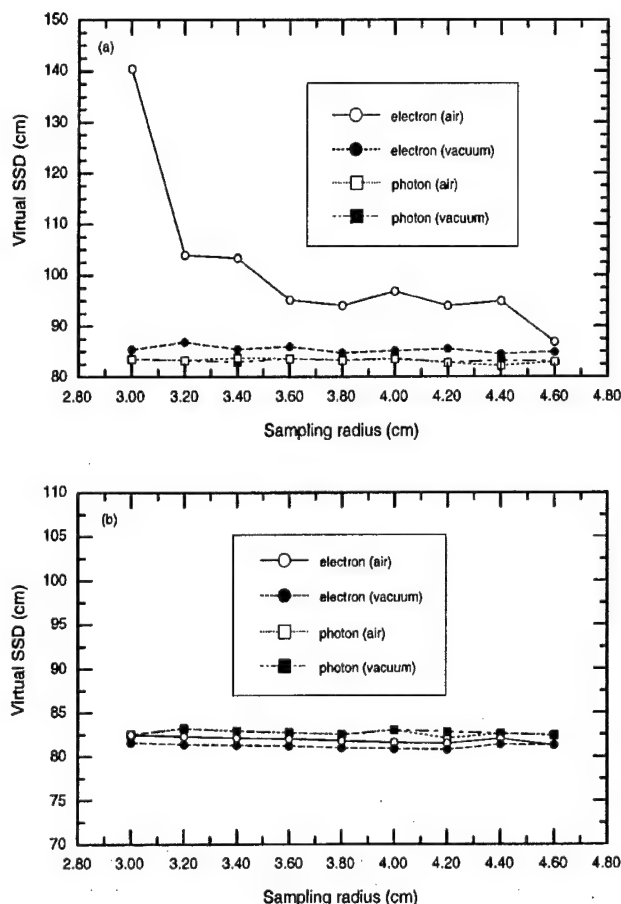


FIG. 2. Effects of intervening air and sampling radius on virtual SSD (defined here as the distance from the point source to the scoring plane) for the electron point source determined with the pinhole method. (a) 6 MeV; (b) 20 MeV.

- (3) For the beam to be commissioned, find the $R_{50}^{(mea)}$ value of the measured depth-dose curve in water for $10 \times 10 \text{ cm}^2$ applicator and 100 cm SSD.
- (4) Select the reference beam which has the same or closest nominal energy as the commissioning beam. Let $i=0$, $E_{\max}^{(i)} = E_{\max}^{(ref)}$, and $R_{50}^{(i)} = R_{50}^{(ref)}$.
- (5) Calculate $\Delta R_{50}^{(i)} = R_{50}^{(i)} - R_{50}^{(mea)}$. If $\Delta R_{50}^{(i)} \leq \epsilon$, where ϵ is the pre-set convergence tolerance, stop iteration and use $E_{\max}^{(i)}$ as the maximum energy in the source model for the commissioning beam; otherwise, go to the next step.
- (6) According to the relationship between ΔE_{\max} and ΔR_{50} , calculate $\Delta E^{(i)}$ using $\Delta R_{50}^{(i)}$ and then calculate $E_{\max}^{(i+1)} = E_{\max}^{(i)} - \Delta E^{(i)}$.
- (7) Calculate the dose distribution using the source model with $E_{\max}^{(i+1)}$ and find the corresponding $R_{50}^{(i+1)}$.
- (8) Let $i \leftarrow i+1$; go back to step 5.

The first two steps only need to be done once for all accelerators of the same design. The convergence tolerance, ϵ , is set by the user, usually according to the estimated measurement error in R_{50} . For example, $\epsilon=1 \text{ mm}$ is good enough in most

clinical situations. The iteration process converges very fast; usually only two or three iterations are needed even for ϵ much smaller than 1 mm.

The commissioning approach has been applied to three electron beams, A, B, and C. The reference beam is the same for all three beams, which is from the reference Clinac 2100C accelerator with $E_{\text{in}}=12.0 \text{ MeV}$. Beam A and beam B are also from the reference machine but with E_{in} as 9.0 MeV and 15.0 MeV, respectively. These two beams are used to mimic two clinical beams of the same nominal energy as the reference beam but with significantly different incident energies. Of course, in reality, the electron incident energy will not be tuned so much ($\pm 3 \text{ MeV}$). These two beams are used as extreme cases to test the commissioning approach. Beam C is a 9 MeV electron beam from another Clinac 2100C accelerator. The dose distributions for beam C are taken from the published data.³⁸

III. RESULTS AND DISCUSSION

Figure 2 shows the effects of intervening air and sampling radius on the electron and photon virtual SSD determined with the pinhole method for 6 MeV and 20 MeV beams. It can be seen that for photons and high energy electrons (20 MeV) effects of intervening air and sampling radius on the positions of virtual point sources are negligible. However, for low energy electrons (6 MeV), these effects are significant. Therefore, to obtain the accurate virtual electron point source position for low energy beams, the phase space simulated without intervening air should be used.

Figure 3 shows the comparison between the angular distributions for direct electrons in 6, 12 and 20 MeV beams calculated with the Fermi-Eyges theory and the Monte Carlo method. We can see that, in general, the fitted angular distributions based on the Fermi-Eyges theory match well with those calculated with the Monte Carlo simulation. We also notice that at large angles the Fermi-Eyges theory slightly

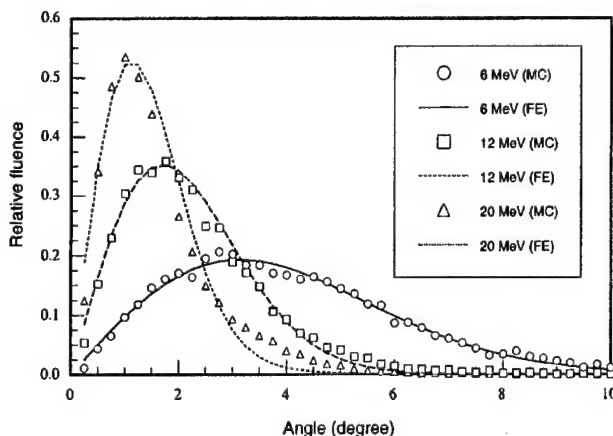


FIG. 3. Angular distributions for direct electrons calculated using the Fermi-Eyges theory and the Monte Carlo method. Beam energies are 6 MeV, 12 MeV and 20 MeV. The fitted k factor is 1.540 for 6 MeV, 1.501 for 12 MeV and 1.571 for 20 MeV. Each distribution is normalized to have unit area under the curve.

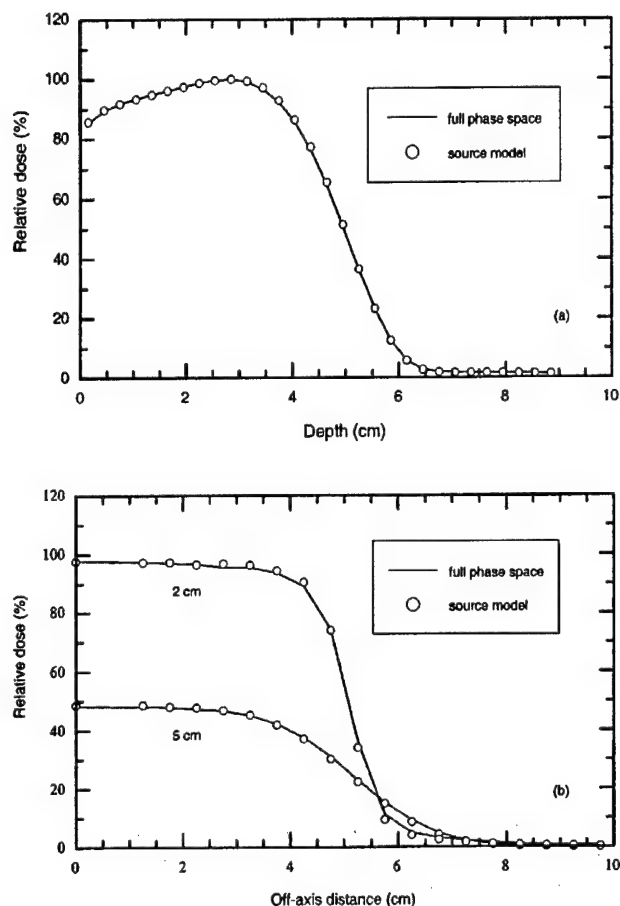


FIG. 4. Dose distributions in water for 12 MeV electron beam with $10 \times 10 \text{ cm}^2$ applicator at 100 cm SSD, calculated with full phase space data and source model: (a) Depth-dose distributions; (b) dose profiles at depths of 2 cm and 5 cm. Curves are normalized to the dose at d_{max} .

underestimates electron fluence due to the fact that it is a small-angle theory. We found that the small discrepancy does not have any significant effect on the final dose distributions. Therefore, the Fermi-Eyges theory with the fitted k factor can be used to account for the angular perturbations of electrons on their way from the source to the scoring plane.

The four-source model was tested by comparing the dose distributions calculated by the model with those calculated by full phase space data for various combinations of three electron energies (6, 12, and 20 MeV), three applicator sizes (6×6 , 10×10 , and $20 \times 20 \text{ cm}^2$), and two SSDs (100 cm and 120 cm). For all the cases tested, the agreement of 1%–2%/1–2 mm has been achieved. Figure 4 shows the comparison for a 12 MeV beam with a $10 \times 10 \text{ cm}^2$ cone at 100 cm SSD. Figure 5 gives the depth-dose curves and dose profiles for 20 MeV beam with $6 \times 6 \text{ cm}^2$ cone at 120 cm SSD, calculated with both the source model and full phase space data. All the curves in Figs. 4 and 5 are normalized to the doses at d_{max} . The Monte Carlo uncertainty is always less than 0.5% and therefore not shown on the curves. In both figures the agreement between the full Monte Carlo simulations and the source model calculations is better than 1%/1 mm. Keep in

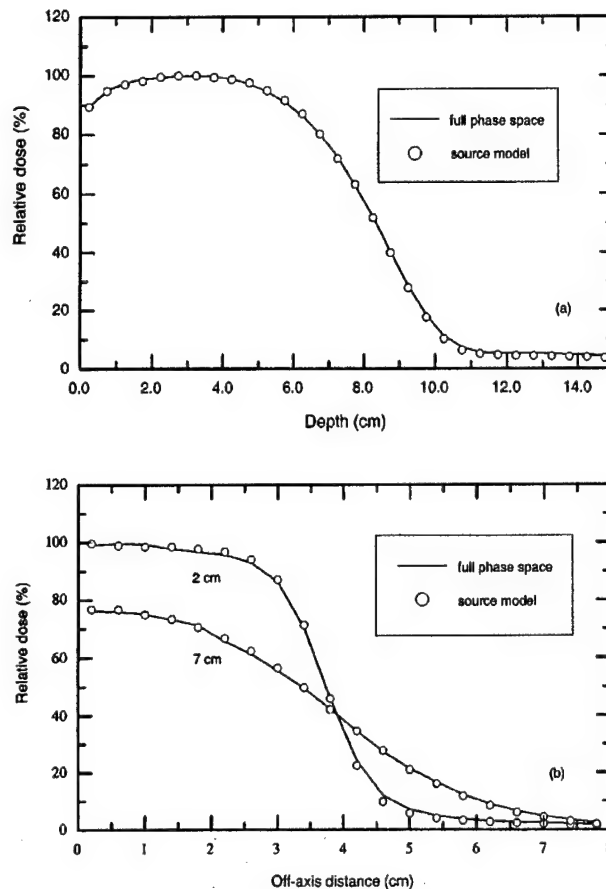


FIG. 5. Dose distributions in water for 20 MeV electron beam with $6 \times 6 \text{ cm}^2$ applicator at 120 cm SSD, calculated with full phase space data and source model: (a) Depth-dose distributions; (b) dose profiles at depths of 2 cm and 7 cm. Curves are normalized to the dose at d_{max} .

mind that 20 cm air gap is rarely used in actual clinical situations. Therefore, we have demonstrated that the simplified four-source model can be used for accurate dose calculations even for extreme cases (such as very large extended SSDs).

The capability of the model for calculating the relative beam output was also tested. Table I shows cutout factors for various square inserts in a $10 \times 10 \text{ cm}^2$ applicator for 6, 12 and 20 MeV electron beams. It is found that the cutout factors calculated with the four-source model are within about $\pm 2\%$ compared to the measured values except for one case where we see 2.5% difference. This is at about the same accuracy level as the full Monte Carlo simulation and considered to be acceptable for clinical use.

The relationship between E_{in} and R_{50} for the reference accelerator with a $10 \times 10 \text{ cm}^2$ cone and 100 cm SSD is shown in Fig. 6. A linear relationship was found and fitted as

$$E_{\text{in}} = 2.597R_{50} + 0.633. \quad (21)$$

It gives the relationship between the variation in the incident energy and the variation in R_{50} as

$$\Delta E_{\text{in}} = 2.597\Delta R_{50}. \quad (22)$$

TABLE I. The electron cutout factors for various square inserts in $10 \times 10 \text{ cm}^2$ applicator for 6, 12, and 20 MeV beams calculated with the source model and the full phase space data and compared with the measurement of Kapur *et al.* (Ref. 45). The values in parenthesis indicate the difference of the data calculated with the source model or the full phase space from the measured data.

Energy (MeV)	Insert (cm^2)	Cutout factor		
		Source model	Full phase space	Measurement
6	2×2	0.803 (2.5%)	0.765 (-1.3%)	0.778
	3×3	0.930 (0.3%)	0.923 (-0.4%)	0.927
	4×4	0.970 (-1.8%)	0.982 (-0.6%)	0.988
	8×8	1.002 (-0.1%)	1.005 (-0.2%)	1.003
12	2×2	0.881 (-0.8%)	0.861 (-2.8%)	0.889
	3×3	0.908 (-2.0%)	0.930 (0.2%)	0.928
	4×4	0.942 (-2.1%)	0.956 (-0.7%)	0.963
	8×8	0.999 (0.8%)	1.002 (1.1%)	0.991
20	2×2	0.963 (-1.1%)	0.957 (-1.9%)	0.976
	3×3	0.989 (-0.4%)	0.968 (-2.5%)	0.993
	4×4	0.993 (-1.8%)	0.993 (-1.8%)	1.011
	8×8	0.999 (-0.5%)	0.993 (-1.1%)	1.004

Equation (22) is used for tuning the maximum energy in the source model to match the measured depth dose curves when commissioning a clinical beam.

Figure 7 shows the dose distributions for the reference beam, beam A, and beam B with the applicator size of $10 \times 10 \text{ cm}^2$ and SSD of 100 cm. All the curves are normalized to the dose at d_{max} . The statistical uncertainty (1σ) in all the Monte Carlo dose calculations was kept to be smaller than 0.5%, therefore, the error bars are smaller than the symbol size and not shown on the curves. The maximum energy in the source model was adjusted to 8.87 MeV to match the dose distributions of the beam A ($E_{\text{in}}=9.0 \text{ MeV}$) and to 15.17 MeV to match the dose distributions of the beam B ($E_{\text{in}}=15.0 \text{ MeV}$). The difference between the depth-dose curves calculated by the adjusted models and the full Monte Carlo simulation is always less than 0.5% for both beam A and beam B. For dose profiles, the difference is usually less than 1% except that in the shoulder region for beam B the difference is about 2%.

Figure 8 shows the dose distributions for the reference beam and beam C with the applicator size of $10 \times 10 \text{ cm}^2$ and SSD of 100 cm. Again, the curves are normalized to the dose at d_{max} and the Monte Carlo uncertainty is lower than 0.5%. In this case, the maximum energy in the source model was adjusted to 11.25 MeV. The dose distributions calculated by the source model with the adjusted maximum energy agree very well (1%/1 mm) with the published data.³⁸

Table II gives E_{in} and R_{50} for the reference and Monte Carlo simulated beams, and E_{max} and R_{50} for the adjusted source models. For the reference beam, E_{max} was directly obtained from the full Monte Carlo simulation. For beam C, E_{in} is unknown. In this study, we set $\epsilon=0.01 \text{ cm}$. Therefore, the R_{50} 's calculated using the adjusted source model match with the full Monte Carlo simulation to within 0.01 cm. Of course, we will not use such a small ϵ in real clinical applications since it is much smaller than the measurement uncertainty in R_{50} . Here, we just want to demonstrate the capa-

bility of the method to reproduce R_{50} accurately.

We have applied the commissioning approach to electron beams from a Clinac 2300C/D accelerator in our institution. The reference machine is still the same Clinac 2100C accelerator. These two machines are sufficiently similar to each other in treatment head geometry. Their dosimetric characteristics are very close to each other due to the beam tuning during linac acceptance. Therefore, it is not surprising to see that the dose distributions calculated with the adjusted source model agree well (within 1%–2% or 1–2 mm) with the measured data.

These preliminary results have shown that the proposed hybrid commissioning approach can be used for accelerators of the same design to account for the dosimetric variations mainly caused by the on-site tuning of the electron incident energy. The capability of the approach to handle large variation in the electron incident energy has been demonstrated. It is believed that for most clinical accelerators of the same type, their treatment head designs are exactly the same or at least very similar, therefore the dosimetric difference can usually be traced back to the difference in the electron incident energy. Therefore, the current approach should be applicable in most clinical situations. In the future work, the method will be evaluated under more critical conditions, such as small field sizes, extended SSD, and heterogeneous phantoms.

The general idea proposed here should also work for other types of accelerators, although we have selected the Varian Clinac 2100C accelerators in the current study. For each type of accelerator, a reference machine should be carefully simulated using the Monte Carlo method. A source model, which may consist of a different number of sub-sources, can be established based on the simulated data. Then, the maximum energy in the model can be adjusted to commission electron beams from other accelerators of the same type.

In some situations, the proposed commissioning approach may not be directly applicable. For example, the measured

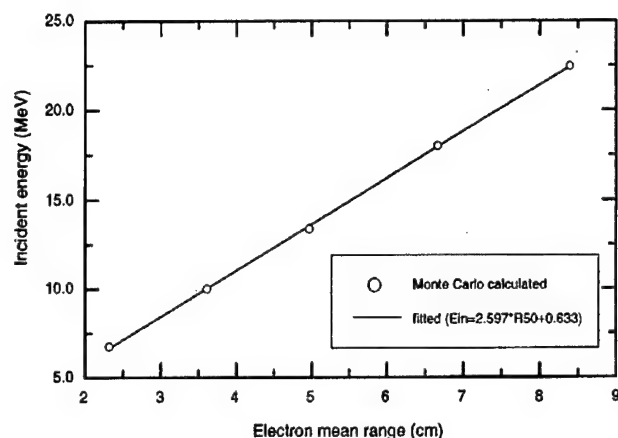


FIG. 6. The relationship between electron incident energy at accelerator exit window (E_{in}) and the depth of 50% dose (R_{50}) for electron beams from the reference accelerator with 10×10 cm² applicator and 100 cm SSD. Symbols are calculated with Monte Carlo simulation of the accelerator treatment head. Solid line is the fitted result with formula $E_{in} = 2.597R_{50} + 0.633$.

dose distributions used for commissioning more or less contain measurement errors, depending on the measurement techniques and the experience of the person who performs the measurements. Since only the maximum energy is the adjustable parameter in the current source model, our approach may not be able to exactly match the measured data. Occasionally, an accelerator used in the clinic may differ from its original design in addition to the electron incident energy. Some parts in the accelerator treatment head may be replaced with nonstandard ones. In this case, we can always perform a full Monte Carlo simulation for this unique accelerator and build its own source model. Alternatively, we can make the present approach more versatile to handle those situations. More parameters in the source model other than the maximum energy, such as the relative intensity of each sub-source, the k factor for in-air perturbation for the direct electrons, and the field size, can be adjusted to match the measured dose distributions. For example, the adjustment of the relative intensity of the photon source will ensure a good match to the bremsstrahlung tail in the depth-dose curve. If some of the materials in the paths of direct electrons, such as the scattering foil, monitor chamber or mirror, are different from those used in the reference accelerator, the adjustment of the k factor can yield a better estimation of the electron angular perturbation. The adjustment of the field size in the source model should recover the measurement error in the width of the dose profiles (e.g., errors of the order of about 1 mm are not rare in a clinical situation). In summary, the introduction of more adjustable parameters in the source model will make the current commissioning approach more powerful. This possibility will be investigated in our future study.

IV. CONCLUSIONS

A hybrid commissioning approach based on a multiple source model has been proposed for Monte Carlo treatment planning. It has been demonstrated that a simplified four-

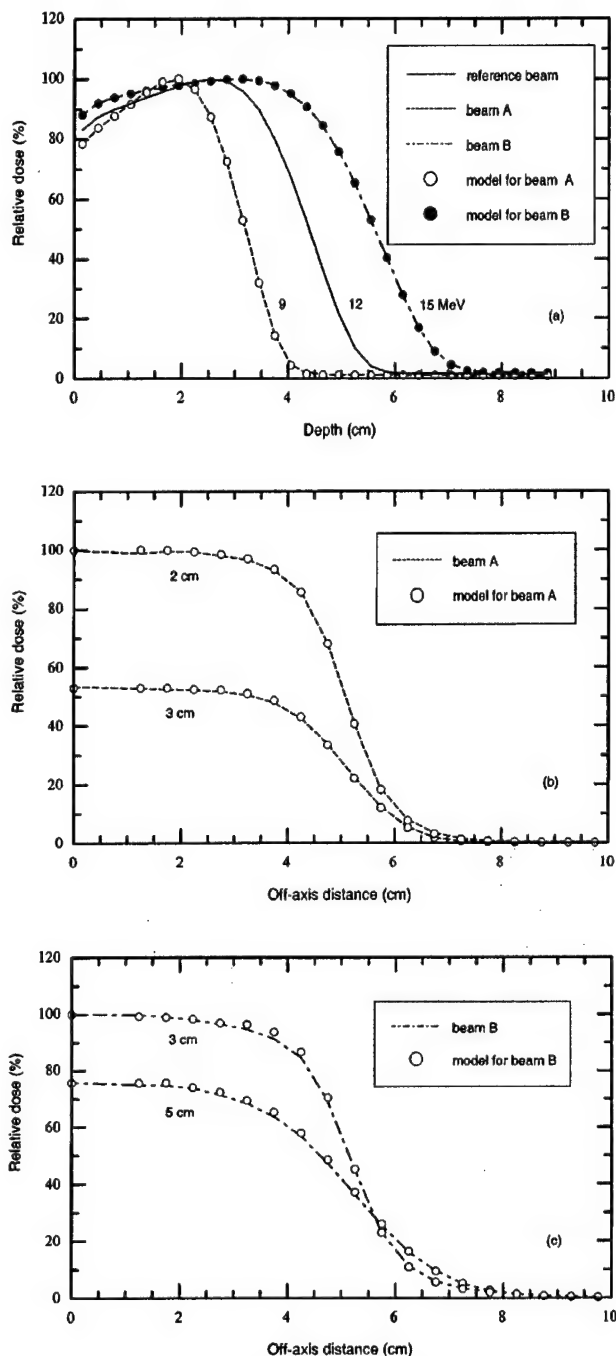


FIG. 7. Dose distributions in water for electron beams from the reference accelerator with 10×10 cm² applicator and at 100 cm SSD. The reference beam has the electron incident energy of 12.0 MeV. A source model was built based on the Monte Carlo simulation of the reference beam. The maximum energy of the energy spectra in the model was adjusted to 8.87 MeV to match the beam A (with $E_{in} = 9.0$ MeV) and 15.17 MeV to match the beam B (with $E_{in} = 15.0$ MeV). Lines are dose distributions from the full Monte Carlo simulations. Symbols are data calculated by the source model with adjusted maximum energies. All data are normalized to the doses at d_{max} . (a) Depth-dose distributions; (b) dose profiles at depths of 2 cm and 3 cm for beam A; (c) dose profiles at depths of 3 cm and 5 cm for beam B.

source model can be used to generate accurate Monte Carlo dose distributions for electron beams from Varian Clinac 2100C accelerators. The model includes a point electron source for direct electrons and electrons scattered from pri-

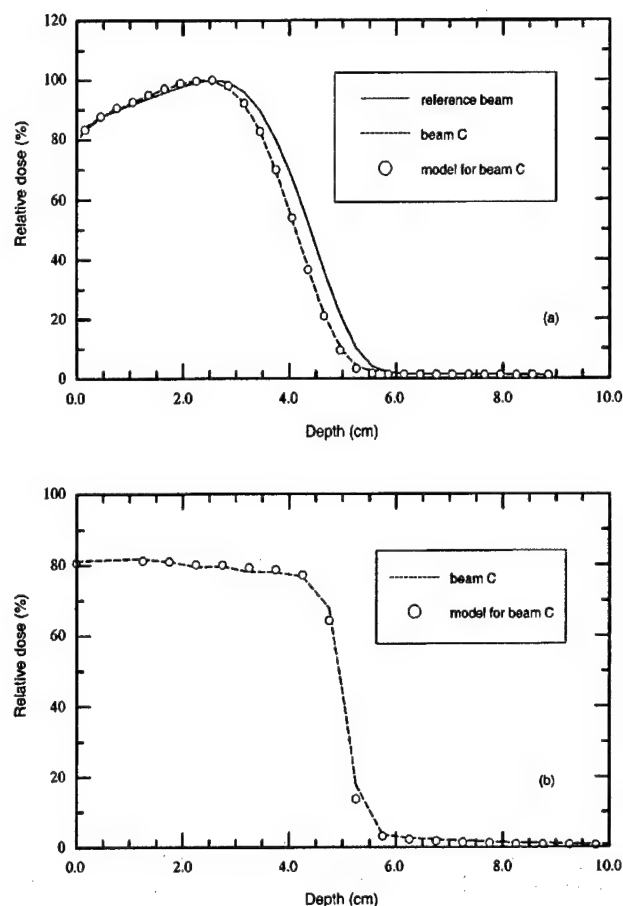


FIG. 8. Dose distributions in water for electron beams with $10 \times 10 \text{ cm}^2$ applicator and at 100 cm SSD. The reference beam (solid line) is from a Clinac 2100C accelerator with $E_{in} = 12.0 \text{ MeV}$. The dose distributions for beam C (dashed lines) is taken from the published data for a 9 MeV beam from another Clinac 2100C accelerator with type III applicator (Ref. 38). A source model built based on the Monte Carlo simulation of the reference beam is used to match beam C by adjusting the maximum energy to 11.25 MeV (open circles). All data are normalized to the dose at d_{max} . (a) Depth-dose distributions; (b) dose profiles at depth of 0.1 cm.

mary collimator and jaws, a point photon source for all contaminant bremsstrahlung photons, and two square ring electron sources representing electrons scattered from two scrapers (other than the last scraper) of the Varian electron applicator (type III). It was found that the position of the virtual point source can be determined accurately using the pinhole method for photons in all cases and electrons in high energy beams. For low energy beams, we should use the Monte Carlo phase space data which are obtained by simulating the treatment head with the intervening air replaced by vacuum. We also found that the in-air perturbation on the electron incident direction can be properly accounted for using the Fermi-Eyges model. The source model which was built based on the simulated phase space data for the reference accelerator can be used for other accelerators of the same type, by simply adjusting the energy spectra in the model. The capability of this commissioning approach for handling large variation in the electron incident energy has been demonstrated.

TABLE II. Some parameters for the full Monte Carlo simulations and the adjusted source models. E_{in} is the electron incident energy at the exit window in the simulation. E_{max} is the maximum energy in the source model. R_{50} is the depth of 50% dose of the depth dose curve in water for $10 \times 10 \text{ cm}^2$ applicator and 100 cm SSD. A source model was built based on the full Monte Carlo simulation of the reference beam. For beams to be commissioned (A, B, and C), E_{max} in the model was adjusted to match the corresponding R_{50} from the Monte Carlo simulation.

Beam tested	MC simulation		Source model	
	E_{in} (MeV)	R_{50} (cm)	E_{max} (MeV)	R_{50} (cm)
Reference	12.0	4.397	12.00	4.397
Beam A	9.0	3.197	8.87	3.192
Beam B	15.0	5.622	15.17	5.624
Beam C	unknown	4.116	11.25	4.119

ACKNOWLEDGMENTS

The authors are grateful to the referees, Drs. Art Boyer, Alan Nahum, Alex Bielajew, David Findley, Gary Luxton, Ed Mok, Todd Pawlicki, and Frank Verhaegen for useful comments on the manuscript. The authors would also like to thank Dr. Sam Brain, Todd Koumian, and Behrooz Tofigh-rad for computer support, Dr. Dave Rogers and his OMEGA/BEAM team at the National Research Council of Canada for the Monte Carlo simulation system, and Eva Papiez for supplying some measured data. The work was supported in part by the U.S. Army breast cancer research program (BC971292), NCI Grant No. CA78331 and a consortium agreement with the Numerix Cooperation.

^aCorresponding author. Tel: (650)498-4074, Fax: (419)498-4015, E-mail: stevej@reyes.stanford.edu

¹K. R. Hogstrom, M. D. Mills, and P. R. Almond, "Electron beam dose calculations," *Phys. Med. Biol.* **26**, 445-459 (1981).

²E. Fermi, in B. Rossi and K. Greisen, "Cosmic-ray theory," *Rev. Mod. Phys.* **13**, 265-268 (1941).

³L. Eyges, "Multiple scattering with energy loss," *Phys. Rev.* **74**, 1534-1535 (1948).

⁴J. Cygler, J. J. Battista, J. W. Scrimger, E. Mah, and J. Antolak, "Electron dose distributions in experimental phantoms: A comparison with 2D pencil beam calculations," *Phys. Med. Biol.* **32**, 1073-1086 (1987).

⁵E. Mah, J. Antolak, J. W. Scrimger, and J. J. Battista, "Experimental evaluation of a 2D and a 3D electron pencil beam algorithm," *Phys. Med. Biol.* **34**, 1179-1194 (1989).

⁶I. Kawrakow, M. Fippel, and K. Friedrich, "3D electron dose calculation using a voxel based Monte Carlo algorithm (VMC)," *Med. Phys.* **23**, 445-457 (1996).

⁷C. M. Ma, E. C. Mok, A. Kapur, T. Pawlicki, D. O. Findley, S. Brain, K. Forster, and A. L. Boyer, "Clinical implementation of a Monte Carlo treatment planning system," *Med. Phys.* **26**, 2133-2143 (1999).

⁸M. A. Ebert and P. W. Hoban, "Possibilities for tailoring dose distributions through the manipulation of electron beam characteristics," *Phys. Med. Biol.* **42**, 2065-2081 (1997).

⁹M. G. Karlsson, M. Karlsson, and B. Zackrisson, "Intensity modulation with electrons: calculations, measurements and clinical applications," *Phys. Med. Biol.* **43**, 1159-1169 (1998).

¹⁰M. Asell, S. Hyödynmaa, S. Söderström, and A. Brahme, "Optimal electron and combined electron and photon therapy in the phase space of complication-free cure," *Phys. Med. Biol.* **44**, 235-252 (1999).

- ¹¹ A. E. Nahum, "Monte Carlo electron transport simulation II: Application to dose planning," in *The Computation of Dose Distributions in Electron Beam Radiotherapy*, edited by A. E. Nahum (Umeå University, Umeå, Sweden, 1985), pp. 319–340.
- ¹² T. M. Jenkins, W. R. Nelson, A. Rindi, A. E. Nahum, and D. W. O. Rogers, *Monte Carlo Transport of Electrons and Photons* (Plenum, New York, 1988).
- ¹³ T. R. Mackie, "Applications of the Monte Carlo method in radiotherapy," in *Vol. III of Dosimetry of Ionizing Radiation*, edited by K. Kase, B. Bjärngård, and F. H. Attix (Academic, New York, 1990), 541–620.
- ¹⁴ D. W. O. Rogers and A. F. Bielajew, "Monte Carlo techniques of electron and photon transport for radiation dosimetry," in *Vol. III of The Dosimetry of Ionizing Radiation*, edited by K. R. Case, B. E. Bjärngård, and F. H. Attix (Academic, New York, 1990), pp. 427–539.
- ¹⁵ D. W. O. Rogers, "The role of Monte Carlo simulation of electron transport in radiation dosimetry," *Int. J. Appl. Radiat. Isot.* **42**, 965–974 (1991).
- ¹⁶ P. Andreo, "Monte Carlo techniques in medical radiation physics," *Phys. Med. Biol.* **36**, 861–920 (1991).
- ¹⁷ C. Manfredotti, U. Nastasi, R. Ragona, and S. Anglesio, "Comparison of three dimensional Monte Carlo simulation and the pencil beam algorithm for an electron beam from a linear accelerator," *Nucl. Instrum. Methods Phys. Res. A* **255**, 355–359 (1987).
- ¹⁸ C. Manfredotti, U. Nastasi, R. Marchisio, C. Ongaro, G. Gervino, R. Ragona, S. Anglesio, and G. Sannazzari, "Monte Carlo simulation of dose distribution in electron beam radiotherapy treatment planning," *Nucl. Instrum. Methods Phys. Res. A* **291**, 646–654 (1990).
- ¹⁹ A. A. al-Beteri and D. E. Raeside, "Optimal electron-beam treatment planning for retinoblastoma using a new three-dimensional Monte Carlo-based treatment planning system," *Med. Phys.* **19**, 125–135 (1992).
- ²⁰ H. Neuenschwander, T. R. Mackie, and P. J. Reckwerdt, "MMC—A high-performance Monte Carlo code for electron beam treatment planning," *Phys. Med. Biol.* **40**, 543–574 (1995).
- ²¹ P. J. Keall and P. W. Hoban, "Super-Monte Carlo: A 3-D electron beam dose calculation algorithm," *Med. Phys.* **23**, 2023–2034 (1996).
- ²² B. Faddegon, J. Balogh, R. Mackenzie, and D. Scora, "Clinical considerations of Monte Carlo for electron radiotherapy treatment planning," *Radiat. Phys. Chem.* **53**, 217–227 (1998).
- ²³ C. M. Ma and A. E. Nahum, "Calculation of absorbed dose ratios using correlated Monte Carlo sampling," *Med. Phys.* **20**, 1189–1199 (1993).
- ²⁴ M. A. Holmes, T. R. Mackie, W. Sohn, P. J. Reckwerdt, T. J. Kinsella, A. F. Bielajew, and D. W. O. Rogers, "The application of correlated sampling to the computation of electron beam dose distributions in heterogeneous phantoms using the Monte Carlo method," *Phys. Med. Biol.* **38**, 675–688 (1993).
- ²⁵ A. F. Bielajew, "Monte Carlo modeling in external electron-beam radiotherapy—Why leave it to chance?," in *Proceedings of The 11th International Conference on The Use of Computers in Radiation Therapy*, edited by A. R. Hounsell, J. M. Wilkinson, and P. C. Williams (Manchester, UK, 1994), pp. 2–5. North Western Medical Physics Department, Christie Hospital NHS Trust.
- ²⁶ R. Mohan, "Why Monte Carlo?" in *Proceedings of The 12th International Conference on The Use of Computers in Radiation Therapy*, edited by D. D. Leavitt and G. Starkschall, Salt Lake City, Utah (Medical Physics Publishing, Madison, 1997), pp. 16–18.
- ²⁷ C. L. Hartmann-Siantar, P. M. Bergstrom, W. P. Chansler, L. Chase, L. J. Cox, T. P. Daly, D. Garrett, S. M. Hornstein, R. K. House, E. I. Moses, R. W. Patterson, J. A. Rathkopf, and A. S. von Wittenau, "Lawrence Livermore National Laboratory's PEREGRINE project," in *Proceedings of the 12th International Conference on the Use of Computers in Radiation Therapy*, edited by D. D. Leavitt and G. Starkschall, Salt Lake City, Utah (Medical Physics Publishing, Madison, 1997), pp. 19–22.
- ²⁸ J. J. DeMarco, T. D. Solberg, and J. B. Smathers, "A CT-based Monte Carlo simulation tool for dosimetry planning and analysis," *Med. Phys.* **25**, 1–11 (1998).
- ²⁹ L. Wang, C. S. Chui, and M. Lovelock, "A patient-specific Monte Carlo dose-calculation method for photon beams," *Med. Phys.* **25**, 867–878 (1998).
- ³⁰ J. O. Deasy, P. R. Almond, and M. T. McEllistrem, "Measured electron energy and angular distributions from clinical accelerators," *Med. Phys.* **23**, 675–684 (1996).
- ³¹ J. J. Janssen, E. W. Korevaar, L. J. van Battum, P. R. M. Storchi, and H. Huizenga, "Clinical electron beam dose calculations with the Phase Space Evolution model," in *Proceedings of the 12th International Conference on the Use of Computers in Radiation Therapy*, edited by D. D. Leavitt and G. Starkschall, Salt Lake City, Utah (Medical Physics Publishing, Madison, 1997), pp. 195–196.
- ³² M. Udale, "A Monte Carlo investigation of surface doses for broad electron beams," *Phys. Med. Biol.* **33**, 939–954 (1988).
- ³³ M. Udale-Smith, "Monte Carlo calculations of electron beam parameters for three Philips linear accelerators," *Phys. Med. Biol.* **37**, 85–105 (1992).
- ³⁴ D. W. O. Rogers, B. A. Faddegon, G. X. Ding, C. M. Ma, J. We, and T. R. Mackie, "BEAM: A Monte Carlo code to simulate radiotherapy treatment units," *Med. Phys.* **22**, 503–524 (1995).
- ³⁵ C. M. Ma and D. W. O. Rogers, "Beam characterization: a multiple-source model," Technical Report PIRS 509d, National Research Council of Canada, Ottawa, Canada, 1995.
- ³⁶ C. M. Ma, B. A. Faddegon, D. W. O. Rogers, and T. R. Mackie, "Accurate characterization of Monte Carlo calculated electron beams for radiotherapy," *Med. Phys.* **24**, 401–416 (1997).
- ³⁷ C. M. Ma, "Characterization of computer simulated radiotherapy beams for Monte-Carlo treatment planning," *Radiat. Phys. Chem.* **53**, 329–344 (1998).
- ³⁸ G. X. Ding and D. W. O. Rogers, "Energy spectra, angular spread and dose distributions of electron beams from various accelerators used in radiotherapy," Technical Report PIRS 0439, National Research Council of Canada, Ottawa, Canada, 1995.
- ³⁹ AAPM TG-25, "Clinical electron beam dosimetry: Report of AAPM Radiation Therapy Committee Task Group No. 25," *Med. Phys.* **18**, 73–109 (1991).
- ⁴⁰ M. A. Ebert and P. W. Hoban, "A Monte Carlo investigation of electron-beam applicator scatter," *Med. Phys.* **22**, 1431–1435 (1995).
- ⁴¹ P. J. Keall and P. W. Hoban, "Calculating the angular standard deviation of electron beams using Fermi-Eyges theory," *Phys. Med. Biol.* **41**, 1511–1515 (1996).
- ⁴² S. B. Jiang, Z. M. Luo, and K. M. Ayyangar, "Incorporation of the electron energy-loss straggling into the Fermi-Eyges equation," *Radiat. Phys. Chem.* **53**, 477–482 (1998).
- ⁴³ B. L. Werner, F. M. Khan, and F. C. Deibel, "A model for calculating electron beam scattering in treatment planning," *Med. Phys.* **9**, 180–187 (1982).
- ⁴⁴ ICRU 35, "Radiation Dosimetry: Electron Beams with Energies Between 1 and 50 MeV," International Commission on Radiation Units and Measurements, Bethesda, MA, 1984.
- ⁴⁵ A. Kapur, C. M. Ma, E. C. Mok, D. O. Findly, and A. L. Boyer, "Monte Carlo calculations of electron beam output factors for a medical linear accelerator," *Phys. Med. Biol.* **43**, 3479–3494 (1998).

Modeling the extrafocal radiation and monitor chamber backscatter for photon beam dose calculation

Steve B. Jiang,^{a)} Arthur L. Boyer, and C.-M. Charlie Ma

Department of Radiation Oncology, Stanford University School of Medicine, 300 Pasteur Drive, Stanford, California 94305-5304

(Received 15 September 1999; accepted for publication 13 October 2000)

A simple analytical approach has been developed to model extrafocal radiation and monitor chamber backscatter for clinical photon beams. Model parameters for both the extrafocal source and monitor chamber backscatter are determined simultaneously using conventional measured data, i.e., in-air output factors for square and rectangular fields defined by the photon jaws. The model has been applied to 6 MV and 15 MV photon beams produced by a Varian Clinac 2300C/D accelerator. Contributions to the in-air output factor from the extrafocal radiation and monitor chamber backscatter, as predicted by the model, are in good agreement with the measurements. The model can be used to calculate the in-air output factors analytically, with an accuracy of 0.2% for symmetric or asymmetric rectangular fields defined by jaws when the calculation point is at the isocenter and 0.5% when the calculation point is at an extended SSD. For MLC-defined fields, with the jaws at the recommended positions, calculated in-air output factors agree with the measured data to within 0.3% at the isocenter and 0.7% at off-axis positions. The model has been incorporated into a Monte Carlo dose algorithm to calculate the absolute dose distributions in patients or phantoms. For three MLC-defined irregular fields (triangle shape, C-shape, and L-shape), the calculations agree with the measurements to about 1% even for points at off-axis positions. The model will be particularly useful for IMRT dose calculations because it accurately predicts beam output and penumbra dose. © 2001 American Association of Physicists in Medicine. [DOI: 10.1118/1.1333747]

Key words: photon beam, extrafocal radiation, monitor chamber backscatter, dose calculation, in-air output factor

I. INTRODUCTION

Photon beam dose calculations usually consist of the calculation of absolute dose for a specific monitor unit setting and the calculation of relative dose distribution. The relative in-air output factor (collimator scatter factor), S_c , is one of the basic quantities required to calculate monitor unit settings. Traditionally, S_c has been determined indirectly from empirical data and tabulated as a function of the square field sizes at the isocenter. The S_c values for rectangular fields are then estimated using the concept of the equivalent square. The collimator exchange effect is often ignored and may introduce errors in the S_c calculation that are as great as 3%.¹⁻⁴ To reduce this error, extensive measurements need to be carried out for rectangular and irregularly shaped fields.

In order to deliver intensity-modulated radiation therapy (IMRT), intensity patterns are usually generated by sweeping a window formed by the multileaf collimator (MLC) leaves across the field, either dynamically or as a step-and-shoot sequence.⁵ An IMRT field can be considered to be a stack of many static fields with irregular shapes, each defined by an MLC. Using a conventional method such as the equivalent square, it is difficult to predict correctly the beam output of each of the windows that form IMRT fields. Since a significant fraction of the dose is accumulated in penumbra regions placed inside an IMRT field, it is necessary to account for the penumbra dose accurately to obtain accurate relative dose distributions.

The radiation backscattered from the collimator jaws to the monitor chamber produces an extraneous signal in the monitor chamber, resulting in a decrease in the delivered dose for a given total monitor unit setting. This effect increases as the field size decreases since the irradiated area on the target side of the jaws is larger for smaller fields. The magnitude of the monitor backscatter (MBS) depends on the design of the monitor chambers, such as the thickness and material of the exit window, and the distance from the chamber to the jaws. Also, an anti-backscatter plate can greatly reduce the size of the MBS effect.^{6,7} For some accelerators, such as the Varian Clinac 2100C with a kapton monitor chamber, the MBS effect contributes significantly to the variation of the beam output as a function of jaw setting. Therefore, it is necessary to model the MBS for accurate output calculations.

In addition to the MBS, it has been found that the change in S_c with field size is dependent on the scattered radiation that can reach the measurement point as the positions of the collimators are varied.⁸ The scattered radiation is also a major contribution to the penumbra dose in the field, resulting in different penumbra dose for different field sizes and for different (X or Y) field edge-defining jaws. The sources of scattered radiation are components inside the accelerator treatment head. It has been demonstrated that the flattening filter and the primary collimator are the major sources for scattered photons.⁸⁻¹⁰ Other components, such as the photon

jaws, contribute a negligible amount to the scattered radiation.¹¹ The scattered radiation can be modeled as a planar source located at the level of the bottom of the flattening filter, which is usually called the extrafocal source, in contrast to the focal spot (or point source at the target) for primary photons which come from the target directly to the measurement point.

In the past decade, many efforts have been made to model the extrafocal radiation (EFR). The EFR can be calculated analytically¹² or by a Monte Carlo simulation of the linac treatment head.⁹ It can also be measured using a tertiary collimator with increasingly larger apertures.^{13,14} Another approach to model the EFR, which may be more useful in clinical practice, is to represent the radial distribution of the extrafocal source using an analytical function and then determine the parameters in the function by fitting the measured S_c values.¹⁵⁻²³

The MBS was usually measured using specially designed experimental approaches. Luxton and Astrahan⁶ assessed the MBS by covering the downstream portion of the monitor chamber with an acrylic plate for a CGR Saturne 25 machine. Kubo²⁴ designed a simple and elegant telescopic method to measure the MBS for an 18 MV beam from a Therac 20 and 6 and 18 MV beams from a Varian Clinac 1800. This method was used later by many other investigators to study MBS effect, such as Duzenli *et al.*,²⁵ Waldron,¹⁷ Yu *et al.*,²⁶ and Lam *et al.*¹⁹ The MBS can also be measured accurately by counting the target current pulses^{14,26,27} or measuring the charge deposited in the target.²⁸ It is also possible to calculate the MBS analytically²⁹ or through the Monte Carlo simulation of the treatment head.^{27,30}

In the present paper, we develop a simple analytic method for modeling both the EFR and MBS for accurate photon beam dose calculations (especially IMRT). In order to be clinically practical, the method does not rely on any special experimental or sophisticated numerical (e.g., Monte Carlo) techniques. The EFR and MBS are represented analytically and determined simultaneously using only conventional measured data, i.e., measured S_c values at the isocenter for fields defined by the photon jaws. The model has been verified extensively using the measured S_c values for various jaw and MLC settings and at various source-detector distances (SDD) and off-axis distances. The model has also been incorporated into a Monte Carlo code for patient dose calculation. The calculated absolute dose values in a water phantom for various MLC-defined irregular fields have been compared with the corresponding measured data.

II. MATERIALS AND METHODS

A. General theory

1. In-air output factor

In the present work, we use the measured linac in-air output factor S_c to determine the EFR and MBS. The S_c factor is usually defined as the ratio of the linac in-air output at the isocenter per monitor unit for a certain field size (fs) to that for a reference field size (fs_{ref}). The field size depen-

dence of the in-air output factor, $S_c(fs)$, is caused by the change of the contributions due to EFR and MBS with the field size. Following Lam *et al.*,¹⁹ we define the term *head scatter factor*, S_h , in a strict sense to represent the part of S_c contributed from the EFR. The effect of the MBS on S_c is considered as the MBS factor, S_b . Then, we have

$$S_c(fs) = S_h(fs) \cdot S_b(fs), \quad (1)$$

where

$$S_h(fs) = [1 + F_{efs}(fs)] / [1 + F_{efs}(fs_{ref})], \quad (2)$$

$$S_b(fs) = [1 - F_{mbs}(fs)] / [1 - F_{mbs}(fs_{ref})]. \quad (3)$$

F_{efs} is the contribution to the beam output from the EFR normalized to the contribution from the primary point source. F_{mbs} is the decrease in the beam output caused by the MBS, normalized to beam output without the presence of MBS. Both F_{efs} and F_{mbs} are dimensionless and can be ratios of either energy fluence, or dose, or charge. For example, F_{mbs} can be the ratio of the dose from backscattered photons to the total dose in the monitor chamber. In the rest of this section, we will discuss our model for EFR and MBS, and how to use the model to calculate F_{efs} and F_{mbs} .

2. Monitor chamber backscatter

The model for the MBS is much simpler than that for EFR, so we will discuss it first. As shown by many other investigators,^{17,19,24-30} it is a good approximation to assume that the backscattered radiation to the monitor chamber has a linear relationship with the irradiated area on the jaw's upper surface. Therefore, under the first-order approximation,¹⁹ F_{mbs} for a rectangular field ($X_1:X_2 \times Y_1:Y_2$, where X_1 and X_2 are the positions of X jaws and Y_1 and Y_2 are positions of Y jaws) can be modeled as

$$F_{mbs}(fs) = \alpha [1 - (Y_1 + Y_2)/fs_{max}] + \beta [1 - (X_1 + X_2)/fs_{max}] \cdot (Y_1 + Y_2)/fs_{max}, \quad (4)$$

where fs_{max} is the maximum jaw opening (40 cm for a Varian accelerator) and is assumed to have zero backscatter to the monitor chamber. α and β give the relative importance of the upper and lower jaws, respectively.

3. Extrafocal source

The primary photons can be modeled as a point source located at the position of the target. The extrafocal radiation is assumed to originate from a planar source with an intensity distribution peaked at the central axis and monotonically decreasing with off-axis distance. The extrafocal source distribution can then be approximated by a series of Gaussian functions

$$f(x, y) = \sum_{i=1}^N \frac{A_i}{2\pi\sigma_i^2} e^{-(x^2+y^2)/2\sigma_i^2}, \quad (5)$$

where A_i and σ_i are the amplitude and standard deviation for the i th Gaussian, respectively. N is determined as the minimum number of Gaussian functions necessary to approxi-

mate the extrafocal source intensity distribution. This number can be different for different machines and different beam energies. A_i gives the relative weight and σ_i characterizes the width of the i th Gaussian. The sum of $A_i, i = 1, \dots, N$, is the total intensity of the extrafocal source relative to the primary point source.

The field size dependence of F_{efs} is caused by the fact that the extent of the extrafocal source visible from the measurement point is different for different collimator settings. It is reasonable to assume that the extrafocal source plane emits photons isotropically over the angle subtended by the primary collimator, since the Klein-Nishina cross section varies slowly over the interval of interest. The distance from a different position on the source plane to the measurement point is different, but the inverse-square-law correction for this effect is very small and can be ignored. Under these approximations, F_{efs} can be calculated by integrating the source intensity distribution over the area of the extrafocal plane visible from the measurement point (it is referred to as *visible area* henceforth).

A visible area with irregular shape can be approximated with a sum of rectangles. The relative contribution to beam output from a rectangular visible area ($x \in [x_{e1}, x_{e2}]$ and $y \in [y_{e1}, y_{e2}]$) can be given as

$$\begin{aligned} F_{\text{efs}}(x_{e1}, x_{e2}, y_{e1}, y_{e2}) &= \int_{x_{e1}}^{x_{e2}} dx \int_{y_{e1}}^{y_{e2}} dy f(x, y) \\ &= \sum_{i=1}^N \frac{A_i}{4} \left[\operatorname{erf}\left(\frac{x_{e1}}{\sqrt{2}\sigma_i}\right) - \operatorname{erf}\left(\frac{x_{e2}}{\sqrt{2}\sigma_i}\right) \right] \\ &\quad \times \left[\operatorname{erf}\left(\frac{y_{e1}}{\sqrt{2}\sigma_i}\right) - \operatorname{erf}\left(\frac{y_{e2}}{\sqrt{2}\sigma_i}\right) \right], \end{aligned} \quad (6)$$

where erf is the error function which can be pre-calculated and stored in a look-up table.

4. Visible area

General case. To use Eq. (6), we need first to determine the visible area. A visible area may be defined by the jaws, MLC, or block. Usually we need to calculate the projections of the edges of the jaws, MLC leaves, or blocks, if they are present, on the extrafocal plane and determine which define the boundary of the visible area.

In a general notation, we assume that the extrafocal plane is perpendicular to the central axis and is located at a distance SED from the target. Similarly the collimation plane is located at a distance SCD (SCD > SED) from the target and is perpendicular to the central axis. The point of measurement is at (x_d, y_d) and SDD away from the target along the central axis. From the view of the measurement point, a point (x_c, y_c) on the collimation plane has a projection on the extrafocal plane

$$x_e = x_d + \frac{\text{SDD} - \text{SED}}{\text{SDD} - \text{SCD}} (x_c - y_d), \quad (7)$$

$$y_e = y_d + \frac{\text{SDD} - \text{SED}}{\text{SDD} - \text{SCD}} (y_c - y_d). \quad (8)$$

Photon jaws. If the visible area is defined by the movable jaws, and if the detector is inside the field, the visible area is limited by the upper edges of the jaws. Assume the distance from the target to the upper edges is SCD_x for the lower (X) jaws and SCD_y for the upper (Y) jaws. A rectangular field ($X_1:X_2 \times Y_1:Y_2$), defined by the jaws at the SAD, corresponds to a rectangular visible area on the extrafocal plane in the view of the measurement point, that is,

$$x \in [x_{e1}, x_{e2}], \quad (9)$$

$$y \in [y_{e1}, y_{e2}], \quad (10)$$

$$x_{e1} = x_d - \frac{\text{SDD} - \text{SED}}{\text{SDD} - \text{SCD}_x} \left(\frac{\text{SCD}_x}{\text{SAD}} X_1 + x_d \right), \quad (11)$$

$$x_{e2} = x_d + \frac{\text{SDD} - \text{SED}}{\text{SDD} - \text{SCD}_x} \left(\frac{\text{SCD}_x}{\text{SAD}} X_2 - x_d \right), \quad (12)$$

$$y_{e1} = y_d - \frac{\text{SDD} - \text{SED}}{\text{SDD} - \text{SCD}_y} \left(\frac{\text{SCD}_y}{\text{SAD}} Y_1 + y_d \right), \quad (13)$$

$$y_{e2} = y_d + \frac{\text{SDD} - \text{SED}}{\text{SDD} - \text{SCD}_y} \left(\frac{\text{SCD}_y}{\text{SAD}} Y_2 - y_d \right). \quad (14)$$

Then F_{efs} for this field size can be calculated using Eq. (6).

If the detector is placed at the central axis, Eq. (6) can be simplified for jaw-defined rectangular fields as

$$\begin{aligned} F_{\text{efs}}(X_1:X_2 \times Y_1:Y_2) &= \sum_{i=1}^N \frac{A_i}{4} \left[\operatorname{erf}\left(\frac{k_x X_1}{\sqrt{2}\sigma_i}\right) + \operatorname{erf}\left(\frac{k_x X_2}{\sqrt{2}\sigma_i}\right) \right] \\ &\quad \times \left[\operatorname{erf}\left(\frac{k_y Y_1}{\sqrt{2}\sigma_i}\right) + \operatorname{erf}\left(\frac{k_y Y_2}{\sqrt{2}\sigma_i}\right) \right], \end{aligned} \quad (15)$$

where

$$k_x = \frac{\text{SDD} - \text{SED}}{\text{SDD} - \text{SCD}_x} \cdot \frac{\text{SCD}_x}{\text{SAD}}, \quad (16)$$

$$k_y = \frac{\text{SDD} - \text{SED}}{\text{SDD} - \text{SCD}_y} \cdot \frac{\text{SCD}_y}{\text{SAD}}. \quad (17)$$

For a symmetric rectangular field ($a \times b$), Eq. (15) can be further simplified as

$$F_{\text{efs}}(a \times b) = \sum_{i=1}^N A_i \cdot \operatorname{erf}\left(\frac{k_x a/2}{\sqrt{2}\sigma_i}\right) \cdot \operatorname{erf}\left(\frac{k_y b/2}{\sqrt{2}\sigma_i}\right). \quad (18)$$

The above discussion of photon jaws is also applicable to blocks and MLCs with flat ends. The only difference is the distance from the target to the collimator.

Multileaf collimator with rounded leaf ends. If all or part of the boundary of the visible area is defined by a MLC with rounded leaf ends, we need to calculate the projection of the leaf ends on the extrafocal plane. This is a two-step process. First, the leaf tip position, X_c , is derived from the light-field size, X , defined by this leaf at the SAD. As shown in Fig. 1, after simple geometric manipulations we have

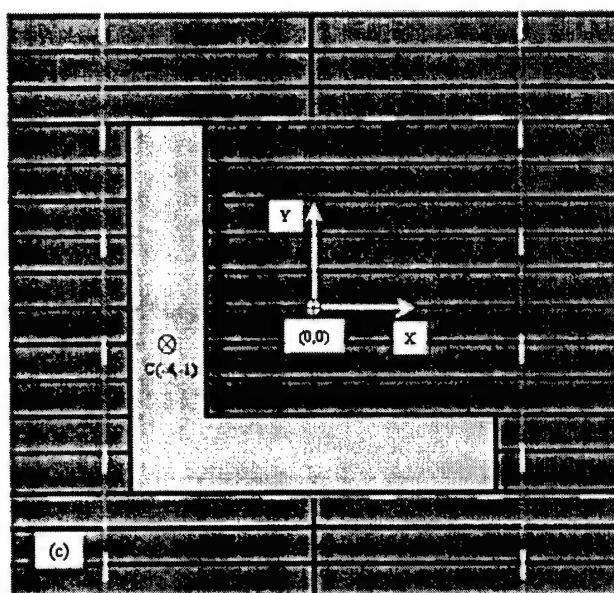
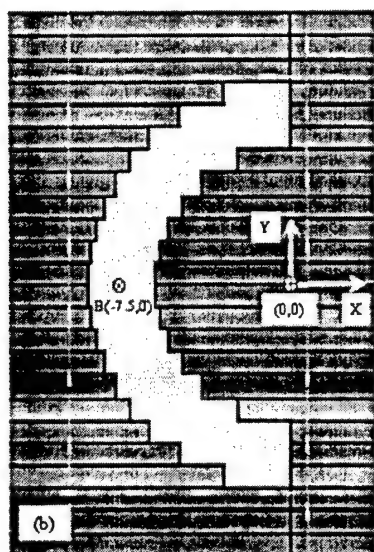
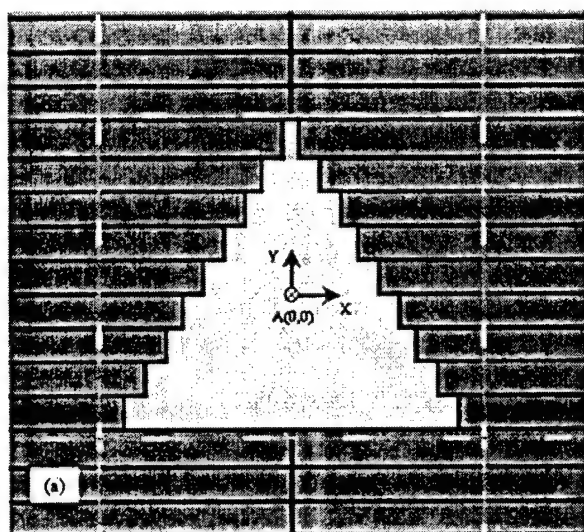


FIG. 2. MLC-defined irregular fields used for model verification: (a) triangular field; (b) C-shaped field; and (c) L-shaped field. The photon jaws are at the recommended positions as illustrated by the dashed lines. Jaw openings (in cm) are $(5.7:5.7 \times 4.2:5.2)$, $(9.7:0.8 \times 9.2:9.2)$, and (11.6×10.4) for triangular, C-shaped, and L-shaped fields, respectively. The calculation/measurement points (A, B, and C) are all at depth 5 cm in a solid water phantom with 100 cm SSD. The coordinates of the points are given in the figures. The origin of the coordinate system is at the central axis.

may have many local minima in the parameter space. Therefore, different initial guesses for the set of fitting parameters may end up with different solutions. A solution reached after a large number of iterations may be physically unrealistic, or may be realistic but not “optimal.” In order to find an “optimal” solution, we combine the Marquardt method with a random search technique and add additional constraints to remove unrealistic solutions. The constraints can be, for example, that $A_i, \alpha, \beta \geq 0$, $F_{cfs} \leq \epsilon_{cfs}$ and $F_{mbs} \leq \epsilon_{mbs}$ for any field size. ϵ_{cfs} and ϵ_{mbs} are the maximum possible values for F_{cfs} and F_{mbs} , respectively. They are set empirically, e.g., $\epsilon_{cfs} = 20\%$ and $\epsilon_{mbs} = 5\%$. There is no constraint on σ_i , because it makes no difference whether positive and negative values of σ_i are used for a Gaussian distribution. What matters is the absolute value of σ_i .

The fitting algorithm used here can be summarized as follows:

- (1) Randomly sample the initial value for each parameter from an empirically pre-set range.
- (2) Run the Marquardt method to get a set of the best-fit parameters.
- (3) Check the constraints. If one of them is violated, abandon this set of fitted parameters and go back to Step 1.
- (4) Store this set of parameters in a stack.
- (5) Check the termination criterion. If it is satisfied, finish the fitting process; otherwise go back to Step 1.

A stack is used to store the best-fit parameters which satisfy all the constraints. The stack is dynamically updated during the fitting process; only the ten best sets of parameters are stored. The best set of parameters gives the minimum value of the χ^2 function. The termination criterion is defined as one of three conditions: (1) all ten best sets of parameters are the same within a tolerance; (2) the pre-set maximum num-

ber of sets of initial values have been sampled; and (3) the pre-set maximum computer CPU time has been reached.

The fitting results should be checked visually by comparing the calculated S_c with measured data for all three sets of fields. The obtained best-fit parameters might be at a local minimum. However, as long as the parameters can produce accurate S_c and satisfy the constraint, they should be clinically acceptable.

C. Model verification

The model was commissioned using S_c values measured at the linac isocenter for square and rectangular fields defined by the jaws. To see if the model worked for situations different than those used for commissioning, we tested the model using the relative in-air output measured at various setups, including measurement points not at isocenter, asymmetric fields, and fields defined by an MLC.

Relative beam in-air outputs were measured using a 0.6 cm³ PTW chamber. Brass build-up caps of 1.76 mm thick for 6 MV beam and 3.17 mm thick for 15 MV beam were used. The long axis of the chamber was oriented parallel to the rotation axis of the collimator. The measurements were taken using the 6 MV and 15 MV x-ray modes of a Clinac 2300C/D accelerator (Varian Oncology Systems, Palo Alto, CA). The reference field size was 10×10 cm² and the maximum field size was 40×40 cm².

The model was incorporated into an in-house developed clinical Monte Carlo dose calculation program, MCDOSE,^{33,34} to calculate the dose distributions in-patient or -phantom. The model was used to generate photons above the MLC and, at the same time, to account for the monitor chamber backscatter effect. The transport of photons through the MLC and in-patient/phantom was simulated in MCDOSE. MCDOSE was carefully benchmarked,³⁵ and the implementation of the model into MCDOSE was described in another publication.³⁶

To verify the model, the Monte Carlo calculated dose data in a water phantom were compared with the corresponding measured data. Three MLC-defined irregular fields were tested, namely, a triangle shaped, a C-shaped, and an L-shaped, as illustrated in Fig. 2. Photon jaws were set to the recommended positions (X jaw opening is 8 mm larger and Y jaw is 2 mm larger than the MLC opening at SAD). The photon jaw opening is illustrated in the figures by the dashed lines. Jaw openings ($X_1:X_2 \times Y_1:Y_2$, in cm) were (5.7:5.7×4.2:5.2), (9.7:0.8×9.2:9.2), and (5.8:5.8×5.2:5.2) for the triangular, C-shaped, and L-shaped fields, respectively. Dose values were calculated and measured in a solid water phantom with 100 cm SSD for both 6 MV and 15 MV beams. For each field, one measurement point was chosen (see Fig. 2). Since the purpose was to verify the model for extrafocal radiation and monitor chamber backscatter, the measurement points were all at a depth of 5 cm in order to exclude the influence of the contaminant electrons.

All the Monte Carlo results were normalized to the calibration point (at d_{\max} for 10×10 cm² field and 100 cm SSD) to give the absolute dose values in cGy/MU. In all calculations, the statistical uncertainty was kept within 0.5%.

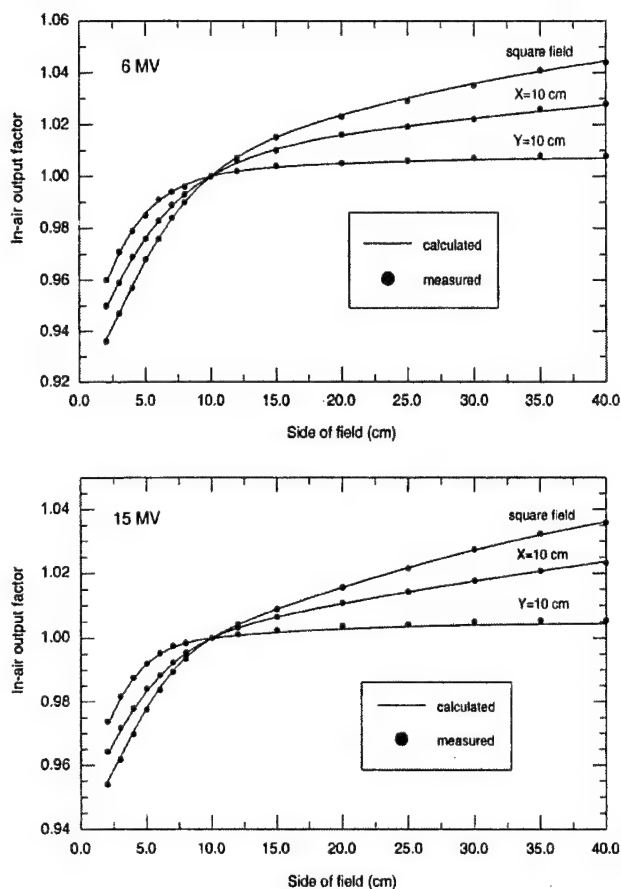


FIG. 3. The comparison between the fitted and measured in-air output factors for 6 MV and 15 MV beams and for three sets of fields: (1) square fields with field sizes from 4×4 cm² to 40×40 cm² ("square field"); (2) rectangular fields with the X jaws at a fixed opening of 10 cm and the Y jaws moving from 4 cm to 40 cm ("X=10 cm"); and (3) rectangular fields with the Y jaws at a fixed opening of 10 cm and the X jaws moving from 4 cm to 40 cm ("Y=10 cm"). The results for jaw openings down to 2 cm are also plotted for comparison.

For the in-phantom measurements, all the measured readings were also normalized to the reading at the calibration point. Therefore, the machine daily output fluctuation and ion chamber correction factors were canceled out. Measurements were performed with a 0.6 cm³ PTW chamber, which was centered at the measurement points and oriented along the Y axis. According to the Monte Carlo calculations, it was found that the dose distributions were uniform around the measurement points for all three fields. Therefore, the averaging effect can be ignored even though a relatively large ion chamber was used.

III. RESULTS

The parameters needed in the model for the calculation, such as the distance from the target to the collimator and flattening filter base, were taken from the manufacturer's specifications.

Three sets of measured S_c values were used to commission the model, using square fields from 4×4 cm² to 40×40 cm², and rectangular fields with one pair of jaws fixed at 10

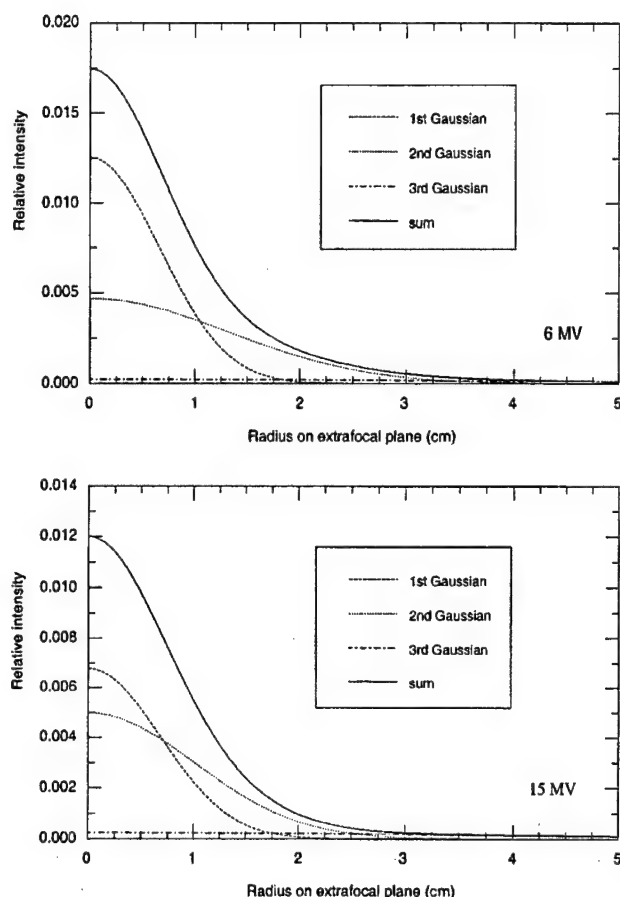


FIG. 4. The relative intensity distributions of the extrafocal source and the three Gaussian components for 6 and 15 MV photon beams. The distributions are normalized to the intensities of primary photons.

cm and the other pair moving from 4 cm to 40 cm. Figure 3 shows the comparison between fitted and measured S_c values. The maximum fitting error is about 0.1% for both 6 MV and 15 MV. The S_c values for jaw openings down to 2 cm were also measured but not used for fitting. These results are compared with the calculated values and shown in Fig. 3. We can see that even for very small field sizes our model can still predict S_c values accurately ($\leq 0.1\%$).

For both beams it was found that three Gaussians were sufficient, because no significant improvement could be achieved with additional Gaussians. The fitted extrafocal source intensity distributions for 6 MV and 15 MV beams are given in Fig. 4. For each distribution we show the three Gaussian components. The best-fit parameters are given in Table I. Using the best-fit parameters, we could easily calculate other quantities of interest. The total intensity of the

extrafocal source, which is relative to the primary point source and is the sum of A_i ($i=1,2,3$), equals 11.7% for the 6 MV beam and 7.7% for the 15 MV beam. The MBS contribution to S_c when the field size increased from 5×5 cm² to 40×40 cm², which can be calculated using Eq. (4), was about 1.2% for the 6 MV beam and 1.6% for the 15 MV beam.

The model was verified using an extensive set of relative in-air outputs measured under various conditions. All calculated and measured in-air outputs were normalized to the reference condition, i.e., at isocenter and for a 10×10 cm² field size. Figure 5 shows the comparison between the calculated and the measured S_c values for 6 MV and 15 MV beams and for four sets of rectangular fields that were defined by setting one pair of jaws at 4 or 40 cm and moving the other pair of jaws from 2 cm to 40 cm. In most situations, the agreement is within 0.1%. The maximum discrepancy is less than 0.2%, even for extremely elongated fields such as 2×40 cm².

Figure 6 shows the calculated and measured S_c data at the isocenter for 6 MV and 15 MV beams and for three sets of asymmetric rectangular fields, i.e., X jaws set to 4, 10, or 40 cm and Y₂ jaw set to 20 cm while Y₁ jaw moving from 1 cm to 20 cm. The calculation agreed with the measurement within 0.2% for 6 MV and 0.1% for 15 MV.

Figure 7 shows the 6 MV beam in-air outputs measured and calculated at 80 cm and 120 cm SDD. The calculation is in good agreement with the measurement (maximum difference is 0.5% for 80 cm SDD and 0.3% for 120 cm SDD).

The model was also tested for fields defined by a MLC. The 6 MV beam in-air outputs, relative to that at isocenter and for jaw-defined 10×10 cm² fields, were measured and calculated for MLC-defined square fields from 2×2 cm² to 28×28 cm² with jaws at a variety of positions including: (1) both X and Y jaws are at the recommended positions for each field; (2) X jaw opening is 30 cm and Y jaws are at the recommended positions; (3) X jaws are at the recommended positions and Y jaw opening is 30 cm; and (4) both X and Y jaw openings are 30 cm. Figure 8 shows a comparison between measurement and calculation. The calculation agrees with the measurement very well (within about 0.1%) for small field sizes ($< 15 \times 15$ cm²) for all jaw settings except for case (4). At larger field sizes, for all jaw settings the calculation underestimated the relative in-air output and the discrepancy increased with the field size. The maximum difference is about 0.3% for jaw setting (1), 0.4% for jaw setting (2), 0.6% for jaw setting (3), and 0.9% for jaw setting (4).

The model was also used to calculate the 6 MV beam in-air outputs for MLC defined off-axis square fields from 2

TABLE I. The best-fit parameters in the extrafocal source and monitor chamber backscatter models for 6 and 15 MV photon beams from a Varian Clinac 2300C/D accelerator.

Beam	A_1	A_2	A_3	σ_1	σ_2	σ_3	α	β
6 MV	0.332e-1	0.517e-1	0.320e-1	0.650e+0	0.133e+1	0.452e+1	0.140e-1	0.181e-4
15 MV	0.192e-1	0.314e-1	0.264e-1	0.671e+0	0.100e+1	0.421e+1	0.185e-1	0.522e-5

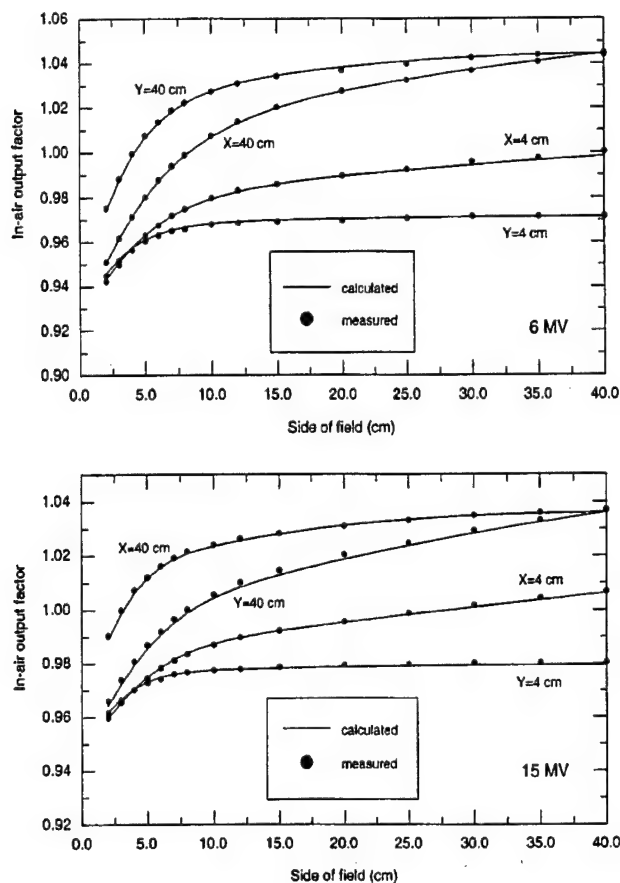


FIG. 5. The comparison between the calculated and measured in-air output factors for 6 MV and 15 MV beams and for four sets of rectangular fields with one pair of jaws setting at 4 or 40 cm and the other pair of jaws moving from 2 cm to 40 cm.

$\times 2 \text{ cm}^2$ to $10 \times 10 \text{ cm}^2$. The calculation point was at the center of the fields as well as 5 cm from both X and Y axes. The beam outputs were calculated and measured for two jaw settings that were: (1) both X and Y jaws at the recommended positions for each field with the limit that the maximum distance over central axis for the X jaws is 2 cm; and (2) Y jaws are opened to 30 cm, X_1 jaw is at 10 cm and X_2 jaw is at 15 cm. The calculated and measured beam outputs were normalized to the reading at isocenter and for a $10 \times 10 \text{ cm}^2$ jaw-defined field. The calculation is compared with the measurement as shown in Fig. 9. For jaws at the recommended positions, the maximum difference between calculation and measurement was about 0.7%. For jaw setting (2), the average difference was about 0.7% but the maximum difference was 1.7% which happened at a field size $2 \times 2 \text{ cm}^2$. We can see that the calculation systematically predicts lower beam outputs.

The absolute dose values in a water phantom at points A, B, and C for three irregular field shapes (see Fig. 2) were calculated by incorporating the current model into MCDOSE.³³ A comparison between the calculated and measured dose values is given in Table II. It can be seen that the agreement is within about 1%. It should be noted that the statistical

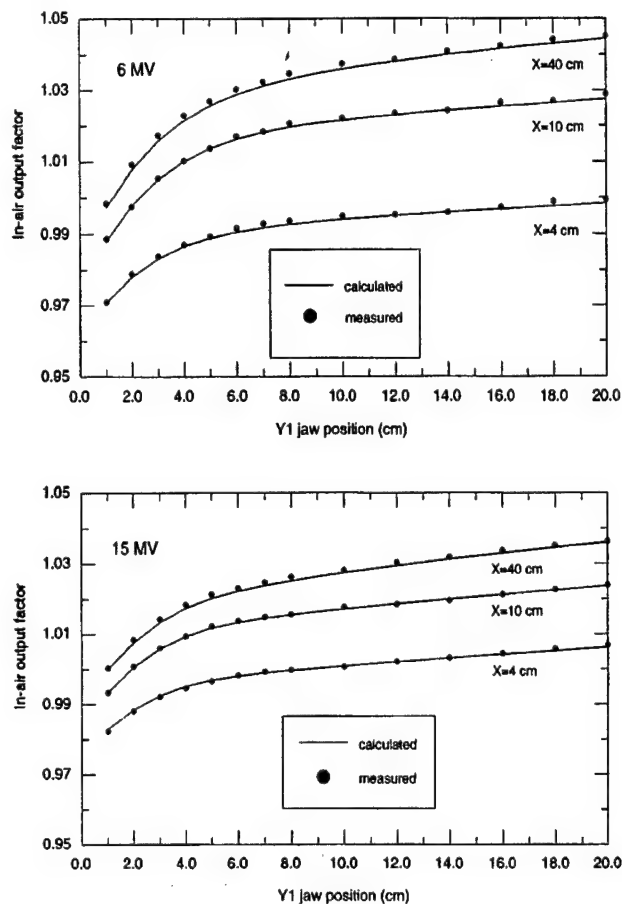


FIG. 6. The comparison between the calculated and measured in-air output factors for 6 MV and 15 MV beams and for asymmetric rectangular fields. X jaws are fixed at 4, 10, 40 cm openings. Y_2 jaw is fixed at 20 cm. Y_1 jaw moves from 1 cm to 20 cm.

uncertainty (1σ) is about 0.5% for the Monte Carlo simulation. It is clear that the difference between calculation and measurement is within the calculation and measurement uncertainties.

IV. DISCUSSION

A model for extrafocal radiation and MBS was derived and commissioned and tested for 6 MV and 15 MV photon beams produced by a medical linear accelerator. For these two beams, we found that three Gaussians are optimal to represent the relative intensity distributions for extrafocal sources. For Varian high energy accelerators, the primary collimator opening at the level of the flattening filter is about 3.1 cm, which limits the radial extent for most scattered photons. We can see in Fig. 4 that the first two Gaussians actually model these photons. A small amount of photons, which are scattered from the treatment head components other than the flattening filter and primary collimator, such as the photon jaws, have a large radial extent when they are back-projected on the extrafocal plane. The relative intensity distribution for these photons is modeled by the third Gaussian and forms a low-intensity long tail of the total distribution.

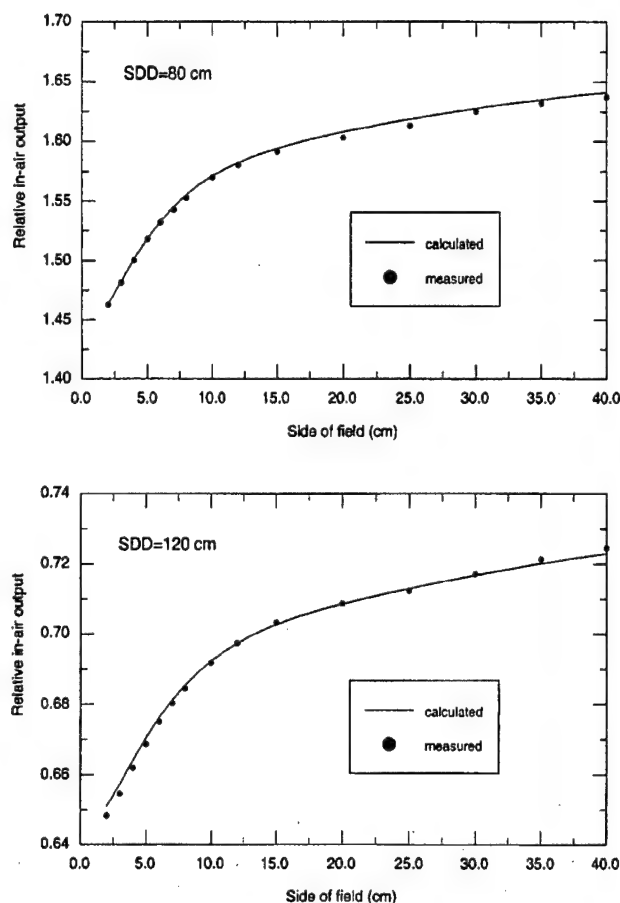


FIG. 7. The comparison between the calculated and measured relative in-air outputs for 6 MV square fields and at 80 and 120 cm SDD. All data are normalized to the beam in-air output at the isocenter for 10×10 cm² field.

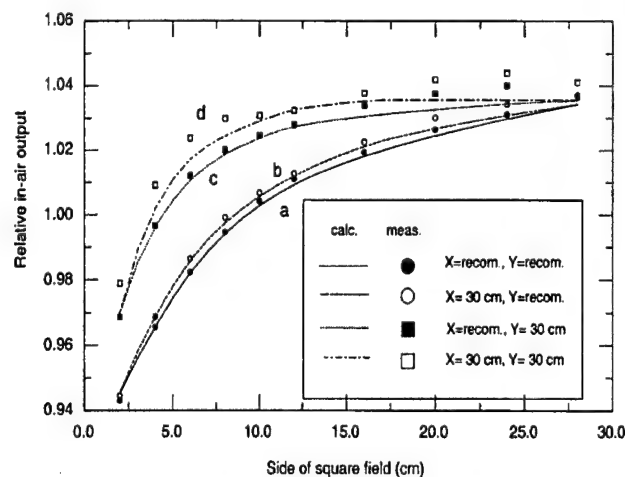


FIG. 8. The comparison between the calculated and measured 6 MV relative in-air output for MLC-defined square fields for four different jaw setups. Lines are the calculated and symbols are measured data. All data are normalized to the beam in-air output at the isocenter for 10×10 cm² jaw-defined field. (a) Both X and Y jaws are at the recommended positions for each field, i.e., X jaw opening is 8 mm wider at SAD than MLC opening and Y jaw is 2 mm wider; (b) X jaw opening is 30 cm and Y jaws are at the recommended positions; (c) X jaws are at the recommended positions and Y jaw opening is 30 cm; (d) both X and Y jaw openings are 30 cm.

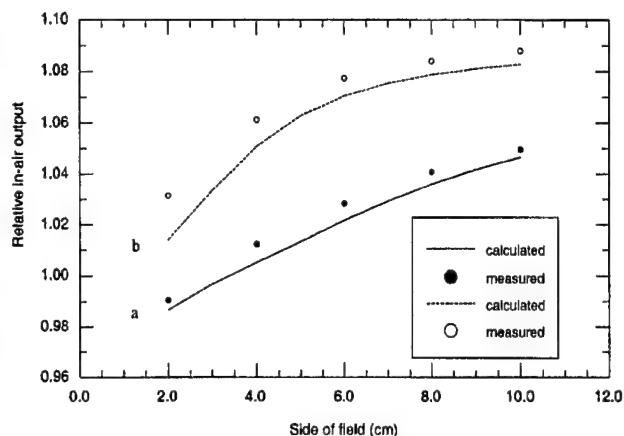


FIG. 9. Comparison between the calculated and measured relative beam in-air outputs for MLC defined off-axis square fields. The detector is placed at the field center and 5 cm away from both X and Y axes. Lines are the calculated and symbols are measured data. (a) Both X and Y jaws are at the recommended positions for each field, i.e., X jaw opening is 8 mm wider at SAD than MLC opening and Y jaw is 2 mm wider. The maximum distance over central axis for X jaws is 2 cm; (b) Y jaws are opened to 30 cm. X₁ jaw is at 10 cm and X₂ jaw is at 15 cm.

The extrafocal source distributions calculated with our model for both 6 MV and 15 MV beams from a Varian Clinac 2300C/D accelerator are qualitatively in agreement with the work of Lam *et al.* (see Fig. 5 in Ref. 19) and the measurement of Jaffray *et al.* (see Fig. 6 in Ref. 13) for the Varian Clinac 2100C machines.

The contribution of the extrafocal source to S_c at the isocenter, relative to that of the primary point source, is 11.7% for the 6 MV beam and 7.7% for the 15 MV beam. Jaffray *et al.*¹³ and Sharpe *et al.*¹⁴ measured the contribution of the extrafocal radiation to the total photon energy fluence at the isocenter for 40×40 cm² field size and 6 MV beams from Varian Clinac 2100C machines. The result of Jaffray *et al.* was 8% and the result of Sharpe *et al.* was 12%. Our result for 6 MV beam from a Varian Clinac 2300C/D accelerator, if normalized to the total photon energy fluence, is 10.5%.

When comparing our results with the Monte Carlo simulation of Liu *et al.*⁹ and Deng *et al.*,¹⁰ we found that the agreement is good for the 6 MV beam but not for the 15 MV

TABLE II. Absolute dose values at points A, B, and C (see Fig. 2) in a water phantom, calculated by incorporating the model for EFR and MBS into a Monte Carlo dose engine. The calculations are compared with the measurements and the relative errors are given.

Point (field shape)	Beam energy (MV)	Dose (cGy/MU)		
		Calculated	Measured	Relative error
A (Triangle)	6	0.843	0.847	-0.4%
	15	0.923	0.933	-1.1%
B (C-shape)	6	0.861	0.869	-0.9%
	15	0.930	0.942	-1.3%
C (L-shape)	6	0.812	0.822	-1.2%
	15	0.897	0.893	0.4%

beam. As pointed out by both groups, the intensity of the extrafocal source increases with beam energy, which is inconsistent with our results (11.7% for 6 MV and 7.7% for 15 MV). To explain this discrepancy, one has to understand the basic assumption used in the model.

Our approach, as well as all other analytical or experimental approaches of deriving the extrafocal source from the variation of S_c with field size (including the experimental techniques of Jaffray *et al.*¹³ and Sharpe *et al.*¹⁴), is based on the assumption that the extrafocal source plane emits photons isotropically over an angle of interest. For a clinical photon beam, scattered photons do not have an isotropic angular distribution. Actually, we can roughly group the scattered photons in a clinical beam into two parts: "directed" part and "isotropic" part. The "directed" part includes those scattered photons that are strongly forward-directed, with directions similar to their primary photons. The "isotropic" part includes those scattered photons with more or less isotropic directions. Our approach, as well as all other approaches based on S_c variation, can model the "isotropic" photons but cannot differentiate the "directed" photons from the primary photons. This is due to the fact that the "directed" photons make no contribution to the S_c variation. Therefore, the extrafocal source intensity, as we have modeled it, is always lower than its true value because the "directed" component has been grouped into the primary photon source. For a low energy beam, we have much more "isotropic" than "directed" photons. Then, the modeled source intensity is close to the result of Monte Carlo simulation. With the increase of beam energy, Compton scattered photons are more and more peaked in the direction of the primary photons. Therefore, for a high energy beam, the source intensity derived using our method or other similar methods can be much lower than that of Monte Carlo simulation. However, the extrafocal source model can still be used to generate accurate beam output and dose distributions since the "directed" part of the scattered photons are naturally considered as part of the primary photons and their angular and energy distributions are very close to those of primary photons.

The MBS contribution to S_c when the square field size changes from $5 \times 5 \text{ cm}^2$ to $40 \times 40 \text{ cm}^2$, which can be calculated using Eq. (4), was about 1.2% for the 6 MV beam and 1.6% for the 15 MV beam. The results are in good agreement with the measurement of Yu *et al.*²⁶ using a target-current-pulse-counting technique for a Varian Clinac 2300C/D machine. Their results were $1.2 \pm 0.3\%$ for 6 MV and $1.8 \pm 0.3\%$ for 15 MV beam when the jaw-defined square field width varied from 5 cm to 40 cm.

The contributions of MBS and EFR to S_c show the same trend as field size varies. It is very difficult, if not impossible, to separate them by only using the measured S_c values. In our method, two sets of measured S_c values for rectangular fields, in addition to one set for square fields, are used for model commissioning. As just mentioned, this approach appears to work well for the 6 and 15 MV beams from a Clinac 2300C/D accelerator by comparing with the measurement of Yu *et al.*²⁶ However, caution should be exercised if one tries

to extrapolate this result to other machines. The obtained absolute values of the MBS contribution may not be accurate. What is more important is that the combination of EFR and MBS generates accurate beam outputs. Our model is accurate in this sense and provides a simple way to account for the MBS in routine clinical use. It may render the specially designed experiments or sophisticated numerical calculations (such as Monte Carlo simulation) unnecessary.

For square or rectangular fields defined by photon jaws, S_c can be accurately calculated using our model. When the calculation point is at the isocenter, for either symmetric or asymmetric fields, the calculation accuracy is within 0.2%. When the calculation point is at an extended SDD, the accuracy is within 0.5%.

For fields defined by an MLC, the accuracy of the calculated in-air outputs using our model is related to the jaw positions. Higher accuracy can be achieved if jaws are at the recommended positions, where most of the time the visible area is limited by jaws instead of by the MLC even though the MLC defines the field shape at the isocenter. If at least one pair of jaws are at the recommended positions, the model can predict the in-air output with an accuracy of about 0.1% for small field sizes (less than $15 \times 15 \text{ cm}^2$). For larger field sizes, the model always underestimates the relative in-air output. For jaws at the recommended positions, the underestimation is less than 0.3%. However, if both jaws are fully open, the underestimation can be 0.9%.

The slightly decreased accuracy for some MLC-defined fields was expected. The model was commissioned for jaw-defined fields, and only accounts for major effects. Some minor effects, such as MLC leaf end scatter, MLC inter-leaf transmission and scatter, and jaw transmission and scatter, may play a role in beam output calculations for large fields defined by an MLC. The influence of electron contamination was studied. We measured the 6 MV data again using the 15 MV buildup cap and found no difference. This result implies that the 6 MV buildup cap was able to screen all contaminant electrons. The influence of leaf carriage position was also investigated. By retracting one pair of the most outside leaves (1A and 1B), we were able to keep both carriages at the same places while the size of the MLC-defined field was varied. No effect was found for leaf carriages. The reason for the underestimation of beam output for large MLC-defined fields is not clear. Our future work will investigate the scatter and leakage from the MLC.

When the calculation point is at about 7 cm off-axis distance, the model underestimates the relative in-air output (by less than 0.7%) for jaw settings at the recommended position. If the jaws are open wide, the average underestimation is about the same, but the maximum is about 1.7% for the smallest field ($2 \times 2 \text{ cm}^2$). At off-axis positions we always underestimate the in-air output. The major reason might be that the isotropic assumption used in the model and the simple analytical form of Eq. (22) are not accurate enough for the off-axis calculation.

For static fields defined by the MLC with jaws at the recommended positions, the in-air output can be predicted using our model to within about 0.2%–0.3% accuracy. For

IMRT fields, since the jaws are usually fixed at the recommended positions for the largest MLC opening while the MLC leaves sweep across the field, the accuracy of the calculated beam output might be slightly worse but still within about 1%. Therefore, the model can be used to predict the beam output not only for static irregular fields shaped with blocks or MLCs, but also for IMRT fields delivered using dynamic jaws or MLCs.

Equation (22) is obviously over-simplified for the calculation of the in-air output factor for off-axis positions and MLC-defined highly irregular fields. To fully utilize the model to generate more accurate beam output and penumbra dose, it should be incorporated into an advanced dose calculation algorithm, such as a pencil beam algorithm or the Monte Carlo method. This would be very useful for IMRT dose calculation since the MLC leaf segments are usually very irregular in shape and a large amount of penumbra dose is accumulated in the field.

In the present work, we have incorporated the model into the MCDOSE Monte Carlo dose calculation code. Photons are generated above the MLC using the model and then transported through the MLC and in the patient/phantom by the Monte Carlo simulation. Comparing to the use of Eq. (22), more accurate results can be achieved since the Monte Carlo simulation is used to take care of all effects downstream from the photon jaws. This has been verified using three irregular fields (see Fig. 2 and Table II).

V. CONCLUSION

A simple and accurate model for both extrafocal source and monitor chamber backscatter has been developed and investigated. We have demonstrated that the relative intensity distribution of the extrafocal radiation can be modeled accurately using a series of Gaussian functions. Both extrafocal source and monitor chamber backscatter can be determined simultaneously using conventional measured data, i.e., S_c values at the isocenter for square and rectangular fields defined by photon jaws. The model can be used to predict accurately the relative in-air outputs analytically. By including the model in a dose algorithm, the penumbra dose will be calculated more accurately than using a point source. The model will be very useful for monitor unit and dose distribution calculations in IMRT.

ACKNOWLEDGMENTS

The authors would like to thank Drs. Michael Sharpe and Kwok Lam for providing some of their results and for helpful discussions. The authors are also grateful to Drs. Frank Verhaegen, Todd Pawlicki, Yunping Zhu, and the referees for useful comments on the manuscript. The work was supported in part by the US Army breast cancer research program (BC971292, BC990213) and the NCI Grants Nos. CA43840 and CA78331.

^{a)}Current address: Department of Radiation Oncology, Massachusetts General Hospital and Harvard Medical School, Boston, MA 02114. E-mail: Jiang.Steve@mgh.harvard.edu

¹K. R. Kase and G. K. Svensson, "Head scatter data for several linear

accelerators (4–18 MV)," *Med. Phys.* **13**, 530–532 (1986).

²P. Vadash and B. Bjarnagard, "An equivalent-square formula for head-scatter factors," *Med. Phys.* **20**, 733–734 (1993).

³M. Tatcher and B. Bjarnagard, "Head-scatter factors in rectangular photon fields," *Med. Phys.* **20**, 205–206 (1993).

⁴M. K. Yu, B. Murray, and R. Sloboda, "Parametrization of head-scatter factors for rectangular photon fields using an equivalent square formalism," *Med. Phys.* **22**, 1329–1332 (1995).

⁵A. L. Boyer and C. X. Yu, "Intensity-modulated radiation therapy with dynamic multileaf collimators," *Semin. Radiat. Oncol.* **9**, 48–59 (1999).

⁶G. Luxton and M. A. Astrahan, "Output factor constituents of a high-energy photon beam," *Med. Phys.* **15**, 88–91 (1988).

⁷A. R. Hounsell, "Monitor chamber backscatter for intensity modulated radiation therapy using multileaf collimators," *Phys. Med. Biol.* **43**, 445–454 (1998).

⁸E. L. Chaney, T. J. Cullip, and T. A. Gabriel, "Monte Carlo study of accelerator head scatter," *Med. Phys.* **21**, 1384–1390 (1994).

⁹H. H. Liu, T. R. Mackie, and E. C. McCullough, "A dual source photon beam model used in convolution/superposition dose calculation for clinical megavoltage x-ray beams," *Med. Phys.* **24**, 1960–1974 (1997).

¹⁰J. Deng, S. B. Jiang, A. Kapur, J. Li, T. Pawlicki, and C.-M. Ma, "Photon beam characterization and modeling for Monte Carlo treatment planning," *Phys. Med. Biol.* **45**, 411–427 (2000).

¹¹A. Ahnesjö, "Collimator scatter in photon therapy beams," *Med. Phys.* **22**, 267–278 (1995).

¹²A. Ahnesjö, "Analytical modeling of photon scatter from flattening filters in photon therapy beams," *Med. Phys.* **21**, 1227–1235 (1994).

¹³D. A. Jaffray, J. J. Battista, A. Fenster, and P. Munro, "X-ray sources of medical linear accelerators: Focal and extra-focal radiation," *Med. Phys.* **20**, 1417–1427 (1993).

¹⁴M. B. Sharpe, D. A. Jaffray, J. J. Battista, and P. Munro, "Extrafocal radiation: A unified approach to the prediction of beam penumbra and output factors for megavoltage x-ray beams," *Med. Phys.* **22**, 2065–2074 (1995).

¹⁵P. B. Dunscombe and J. M. Nieminen, "On the field-size dependence of relative output from a linear accelerator," *Med. Phys.* **19**, 1441–1444 (1992).

¹⁶E. Ihnen and J. M. Jensen, "A new source model for linear accelerators," in *Advances in Radiation Therapy: Tumor Response Monitoring and Treatment Planning*, edited by A. Breit (Springer-Verlag, New York, 1992), pp. 509–513.

¹⁷T. J. Waldron, "Calculation of dynamically-wedged isodose distributions using segmented treatment tables and open-field measurements," Master's thesis, The University of Texas, 1995.

¹⁸M. K. Yu and R. Sloboda, "Analytical representation of head scatter factors for shaped photon beams using a two-component x-ray source model," *Med. Phys.* **23**, 973–984 (1996).

¹⁹K. L. Lam, M. S. Muthuswamy, and R. K. Ten Haken, "Flattening-filter-based empirical methods to parametrize the head scatter factor," *Med. Phys.* **23**, 343–352 (1996).

²⁰P. A. Jursinic, "Clinical implementation of a two-component x-ray source model for calculation of head-scatter factors," *Med. Phys.* **12**, 2001–2007 (1997).

²¹D. Convery and S. Webb, "Calculation of the distribution of head-scattered radiation in dynamically-collimated MLC fields," in *Proceedings of The 12th International Conference on The Use of Computers in Radiation Therapy*, edited by D. D. Leavitt and G. Starkschall, Salt Lake City, Utah, 1997. (Medical Physics Publishing, Madison, 1997), pp. 350–353.

²²S. Kim, J. R. Palta, and T. C. Zhu, "A generalized solution for the calculation of in-air output factors in irregular fields," *Med. Phys.* **25**, 1692–1701 (1998).

²³S. Kim, J. R. Palta, and T. C. Zhu, "The equivalent square concept for the head scatter factor based on scatter from flattening filter," *Phys. Med. Biol.* **43**, 1593–1604 (1998).

²⁴H. Kubo, "Telescopic measurements of backscattered radiation from secondary collimator jaws to a beam monitor chamber using a pair of slits," *Med. Phys.* **16**, 295–298 (1989).

²⁵C. Duzenli, B. McClean, and C. Field, "Backscatter into the beam monitor chamber: Implications for dosimetry of asymmetric collimators," *Med. Phys.* **20**, 363–367 (1993).

²⁶M. K. Yu, R. Sloboda, and F. Mansour, "Measurement of photon beam backscatter from collimators to the beam monitor chamber using target-

- current-pulse-counting and telescope techniques," *Phys. Med. Biol.* **41**, 1107–1117 (1996).
- ²⁷ H. H. Liu, T. R. Mackie, and E. C. McCullough, "Calculating output factors for photon beam radiotherapy using a convolution/superposition method based on a dual source photon beam model," *Med. Phys.* **24**, 1975–1985 (1997).
- ²⁸ K. L. Lam, M. S. Muthuswamy, and R. K. Ten Haken, "Measurement of backscatter to the monitor chamber of medical accelerators using target charge," *Med. Phys.* **25**, 334–338 (1998).
- ²⁹ A. Ahnesjö, T. Knöös, and A. Montelius, "Application of the convolution method for calculation of output factors for therapy photon beams," *Med. Phys.* **19**, 295–301 (1992).
- ³⁰ H. H. Liu, T. R. Mackie, and E. C. McCullough, "Modeling photon output caused by backscattered radiation into the monitor chamber from collimator jaws using a Monte Carlo technique," *Med. Phys.* **27**, 737–744 (2000).
- ³¹ A. L. Boyer and S. Li, "Geometric analysis of light-field position of a multileaf collimator with curved ends," *Med. Phys.* **24**, 757–762 (1997).
- ³² W. H. Press, S. A. Teukolsky, W. T. Vetterling, and B. P. Flannery, *Numerical Recipes*, 2nd ed. (Cambridge University Press, Cambridge, 1992).
- ³³ C. M. Ma, T. Pawlicki, J. S. Li, S. B. Jiang, J. Deng, A. Kapur, E. Mok, G. Luxton, and A. L. Boyer, "MCDOSE—A dose calculation tool for radiotherapy treatment planning," *Med. Phys.* **26**, 1148 (abstract) (1999).
- ³⁴ C. M. Ma, J. S. Li, T. Pawlicki, S. B. Jiang, and J. Deng, "MCDOSE—A Monte Carlo dose calculation tool for radiation therapy treatment planning," in *Proceedings of The 13th International Conference on The Use of Computers in Radiation Therapy*, edited by W. Schlegel and T. Bortfeld, Heidelberg, Germany, 2000 (Springer-Verlag, 2000), pp. 123–125.
- ³⁵ J. S. Li, T. Pawlicki, J. Deng, S. B. Jiang, E. Mok, and C. M. Ma, "Validation of a Monte Carlo dose calculation tool for radiotherapy treatment planning," *Phys. Med. Biol.* **45**, 2969–2985 (2000).
- ³⁶ S. B. Jiang, J. Deng, J. S. Li, T. Pawlicki, A. L. Boyer, and C. M. Ma, "Modeling and commissioning of clinical photon beams for Monte Carlo treatment planning," in *Proceedings of The 13th International Conference on The Use of Computers in Radiation Therapy*, edited by W. Schlegel and T. Bortfeld, Heidelberg, Germany, 2000 (Springer-Verlag, 2000), pp. 434–436.

TOPICAL REVIEW

Monte Carlo modelling of electron beams from medical accelerators

Chang-Ming Ma and Steve B Jiang

Department of Radiation Oncology, Stanford University School of Medicine, Stanford,
CA 94305-5304, USA

E-mail: cma@reyes.stanford.edu

Received 8 June 1999

Abstract. Monte Carlo simulation of radiation transport is considered to be one of the most accurate methods of radiation therapy dose calculation. With the rapid development of computer technology, Monte Carlo based treatment planning for radiation therapy is becoming practical. A basic requirement for Monte Carlo treatment planning is a detailed knowledge of the radiation beams from medical accelerators. A practical approach to obtain the above is to perform Monte Carlo simulation of radiation transport in the medical accelerator. Additionally, Monte Carlo modelling of the treatment machine head can also improve our understanding of clinical beam characteristics, help accelerator design and improve the accuracy of clinical dosimetry by providing more realistic beam data. This paper summarizes work over the past two decades on Monte Carlo simulation of clinical electron beams from medical accelerators.

1. Introduction

The Monte Carlo method is a statistical simulation method. For radiation transport problems, it simulates the tracks of individual particles by sampling appropriate quantities from the probability distributions governing the individual physical processes using machine-generated (pseudo-) random numbers. Average values of macroscopic quantities such as particle fluence, energy spectrum and absorbed dose distribution can be calculated by simulating a large number of particle histories. The Monte Carlo method and its application in medical radiation physics, especially in radiation therapy physics, have been discussed in a number of publications (Burlin *et al* 1973, Raeside 1976, Nelson and Jenkins 1980, Rogers and Bielajew 1984, 1990, Turner *et al* 1985, Nahum 1985, Jenkins *et al* 1988, Mackie 1990, Rogers 1991, Andreo 1991).

The Monte Carlo method can precisely model the physical processes involved in radiation therapy and is powerful in dealing with any complex geometry. It is widely accepted that Monte Carlo simulation of radiation transport is one of the most accurate methods for predicting absorbed dose distributions in radiation therapy. In particular, Monte Carlo simulation can handle backscatter from high-density materials such as bone, or scatter perturbations by air cavities more accurately than any other existing dose calculation model (Rogers and Bielajew 1990, Nahum 1985, 1988, Mackie 1990, Rogers 1991, Andreo 1991, Bielajew 1994, Mohan 1997a). The major shortcoming of the Monte Carlo method, namely being computationally intensive, has become much less severe due to the rapid increase in speed and decrease in cost of computers, and the employment of innovative variance reduction techniques (Ma and Nahum 1993, Holmes *et al* 1993). Monte Carlo simulation is fast becoming the next generation

dose calculation engine for radiation treatment planning systems in routine clinical practice (Manfredotti *et al* 1987, 1990, al-Beteri and Raeside 1992, Neuenschwander *et al* 1995, van der Zee 1996, Kawrakow *et al* 1996, Mohan 1997a, 1997b, Hartmann-Siantar *et al* 1997, Ayyangar and Jiang 1998, DeMarco *et al* 1998, Solberg *et al* 1998, Wallace and Allen 1998, Wang *et al* 1998, Ma *et al* 1999).

A Monte Carlo treatment planning system needs detailed information about the beams incident on the patient. In order to initiate the transport of particles in the patient CT model, accurate phase space information about particles on the patient surface is required. A direct measurement of this information for a clinical beam is very difficult, if not impossible, due to the very high radiation intensities encountered in clinical beams (Deasy *et al* 1996). Calculation of beam phase space parameters using analytical methods is not flexible and usually employs approximations, for example ignoring higher-order Compton scatter events (Desobry and Boyer 1994). Currently, the most practical way to obtain detailed information about the incident radiation beam is the Monte Carlo simulation of the treatment head (Petti *et al* 1983a, b, Mohan *et al* 1985, Han *et al* 1987, Rogers *et al* 1988, 1995a, Udale 1988, Udale-Smith 1990, 1992, Chaney *et al* 1994, Kassaei *et al* 1994, Lovelock *et al* 1994, 1995, Sixel and Faddegon 1995, Ma *et al* 1997a, Lee 1997, Hartmann-Siantar *et al* 1997, Liu *et al* 1997, DeMarco *et al* 1998, Jiang and Ayyangar 1998, Balog *et al* 1999, Faddegon *et al* 1999). In addition, detailed information about radiotherapy beams has a wide variety of applications in clinical physics. Monte Carlo simulation of medical accelerators can increase our understanding of clinical beam characteristics, help accelerator design and improve the accuracy of clinical dosimetry by providing more realistic beam data.

Over the past 20 years or so, many investigations have been carried out on the Monte Carlo simulation of photon beams from medical accelerators or ^{60}Co teletherapy units. McCall *et al* (1978) investigated the effects of various targets and flattening filters on the mean energy of photon beams using the EGS3 code (Ford and Nelson 1978). Patau *et al* (1978) pioneered the Monte Carlo simulation of a complete photon accelerator. They simulated the generation of photons in a W-Cu target, the transport of photons through a flattening filter and the collimators, and the attenuation of photons in slabs of various materials. Nilsson and Brahme (1981) investigated the contaminant photons scattered from flattening filters and collimators. To investigate the electron contamination in photon beams, Petti *et al* (1983a, b) simulated a treatment machine head in great detail using a cylindrical geometry package to approximate various components of the linear accelerator. Mohan *et al* (1985) performed similar detailed simulations based on the EGS3 system to calculate photon spectra and fluence distributions from several accelerators. A special geometry package was also developed to model the exact shape of the flattening filter. Han *et al* (1987) also employed the EGS3 code to simulate in detail the treatment head of a ^{60}Co unit. They approximated the complex geometry of a Theratron-780 ^{60}Co unit as a source capsule, the source housing, and the collimator assembly. Similar studies of clinical photon beams were carried out using the EGS4 code system (Nelson *et al* 1985). Rogers *et al* (1988) investigated the sources of electron contamination in a ^{60}Co beam. Chaney *et al* (1994) simulated a 6 MV photon accelerator to study the origins of head scatter. Lovelock *et al* (1994) simulated the photon beams from a Scanditronix MM50 machine to obtain the beam characteristics needed for treatment planning. An EGS4 user code, McRad, which was a generic Monte Carlo model of a photon linear accelerator, was developed by Lovelock *et al* (1995). Sixel and Faddegon (1995) simulated a Therac-6 treatment head in radiosurgery mode using the cylindrically symmetric EGS4 user code FLURZ with the PRESTA algorithm (Bielajew and Rogers 1987). They calculated the 6 MV radiosurgical x-ray spectra both with and without the flattening filter and compared the results with the Schiff's thin target analytical spectra and the flattened Monte Carlo spectrum calculated by Mohan *et al* (1985). To study

the differential beam hardening effect of the flattening filter, Lee (1997) simulated the 6 MV beam from a Varian Clinac 2100C accelerator using the EGS4 code. Liu *et al* (1995) used a Combinatorial Geometry package to characterize treatment head components, which were modelled as 3D objects and combined using Boolean algebra. Simulations were performed with the ACCEPT code of the ITS 3.0 Monte Carlo system (Halbeib and Mehlhorn 1984). The MCNP Monte Carlo code (Hendricks and Briesmeister 1992, Briesmeister 1993) was also used to model the clinical photon beams. To determine the parameters in their photon source model used for dose calculation in the PEREGRINE system, Hartmann-Siantar *et al* (1997) simulated linacs using MCNP and the EGS4/BEAM code (Rogers *et al* 1995a). DeMarco *et al* (1998) simulated photon beams from Philips SL-15/25 linear accelerators to obtain the phase space information for the dose calculation in a patient's CT phantom. Lewis *et al* (1999) also simulated a Philips SL 75/5 linear accelerator using the MCNP code. Another Monte Carlo system, PENELOPE (Salvat *et al* 1996), has also been used to simulate photon beams from a Saturne 43 accelerator (Mazurier *et al* 1999). The EGS4/BEAM code (Rogers *et al* 1995a) has been extensively used to simulate various types of linear accelerators for photon beams. Liu *et al* (1997) simulated the photon beams from a Clinac 2100C machine and, by analysing the simulation results, developed an extra-focal source model for the dose calculation using a convolution/superposition method (Mackie *et al* 1985). Jiang and Ayyangar (1998) simulated a Varian Clinac 1800 accelerator and studied the perturbation effect of the compensator on photon beam characteristics. Their simulation results were also used to investigate the feasibility and necessity of developing a radiosurgical Monte Carlo treatment planning system (Ayyangar and Jiang 1998) and to study the dose perturbation caused by high-density inhomogeneities in small radiosurgical beams (Rustgi *et al* 1998). A more detailed report on the simulation of clinical photon beams using the EGS4/BEAM code was given by Sheikh-Bagheri (1998). Most recently, Balog *et al* (1999) studied the multileaf collimator (MLC) interleaf transmission by simulating the NOMOS MIMiC MLC attached to a GE Orion 4 MV linear accelerator. Their results were incorporated into the design of an MLC used in a prototype tomotherapy machine (Mackie *et al* 1993, 1995). By simulating the treatment head for a Siemens MXE accelerator, Faddegon *et al* (1999) designed a new flattening filter for the 6 MV photon beam for this machine. Verhaegen *et al* (1999) applied the EGS4/BEAM code to the simulation of radiotherapy kV x-ray units. Some of the above work has been reviewed by Mohan (1988) and Andreo (1991). Ebert *et al* (1996) also reviewed some recent work on the modelling of both clinical photon and electron beams using both analytical and Monte Carlo methods.

In this review paper, we focus on the Monte Carlo simulation of clinical electron beams from medical accelerators. Electron beam Monte Carlo dose calculation was considered to require more detailed beam phase space information on the patient surface than photon beams (Mackie 1990). The difficulty was considered to be that, compared with photon beam simulations, the simulation of electron beams was more sensitive to the details of the accelerator model (Rogers 1991). The work on Monte Carlo simulation of the clinical electron beams can be roughly grouped into two categories. The simulations included in the first category were mainly performed over 10 years ago with limited computation power. A medical accelerator had to be simplified to one or two components of most dosimetric significance in order to perform the Monte Carlo simulation within a reasonable timeframe and acceptable accuracy (Berger and Seltzer 1978, Borrell-Carbonell *et al* 1980, Rogers and Bielajew 1986, Manfredotti *et al* 1987, Andreo *et al* 1989). Even more recently, some studies were still carried out in this way to investigate the influence of an accelerator component on the electron beam characteristics, at a relatively low computing expense (Keall and Hoban 1994, Ebert and Hoban 1995b). The second category includes the Monte Carlo simulation of a complete accelerator (Udale 1988, Udale-Smith 1990, 1992, Kassaei *et al* 1994). This category has been greatly

enhanced since the OMEGA BEAM system was developed (Rogers *et al* 1990, 1995a, b, Mackie *et al* 1990). Since then, the Monte Carlo modelling of medical accelerators has become easier and more systematic. This review is organized to cover these two categories separately. Because of its significance and the large number of applications, the OMEGA BEAM system will be described in detail in a separate section. We also discuss the modelling of Monte Carlo simulated electron beams using different source models, which is one approach to form the link between the Monte Carlo simulation of clinical electron beams and Monte Carlo treatment planning (Ma and Rogers 1995a, b, c, Ma *et al* 1997a, Faddegon *et al* 1998, Ma 1998, Jiang *et al* 1999). Finally, we discuss some existing problems and possible future directions for Monte Carlo simulation of the clinical electron beams generated by medical accelerators.

2. Simulation of the accelerator components

The application of the Monte Carlo technique to the simulation of electron beams has a long history. In the early years, mainly due to the low speed of computers and the relatively simple Monte Carlo codes available, a full simulation of the accelerator geometry was an extremely difficult task. Simulations were usually carried out for treatment heads with great simplification; only one or two components of dosimetric importance, for example the scattering foil or intervening air, in an electron treatment machine head were simulated and the influence of these components on the beam characteristics and dose distributions was studied.

2.1. The work of Berger and Seltzer

Berger and Seltzer (1978) studied the effect of scattering foils on the dose distributions in a water phantom for electron beams with energies from 5 to 40 MeV. A two-step approach was proposed; the accelerator treatment head, simplified as the scattering foil and intervening air, was simulated first and then the simulation results were used for the dose calculation in the phantom. A monoenergetic electron pencil beam was assumed to be incident perpendicularly on the lead scattering foils of thickness between 0.1 mm and 0.6 mm. The effect of 100 cm of air between the scattering foil and the phantom was simulated using a layer of condensed air-equivalent material. The simulation results were recorded at the phantom surface, including the distribution in energy and angle of the electrons and bremsstrahlung photons. The correlation between the energy and direction was ignored, and therefore the energy spectrum and angular distribution were recorded separately. A superposition approach was developed to calculate the dose distribution in the phantom. For both electrons and bremsstrahlung photons, dose kernels for monoenergetic pencil beams were pre-calculated. Then the dose distribution in the phantom was the superposition of different pencil beam dose kernels weighted with different energies, directions and incident positions at the phantom surface. By limiting the summation over directions to certain cones around the central axis, the effect of collimation to finite field size was simulated. Figure 1 shows the energy spectra calculated by Berger and Seltzer (1978) for electrons passing through 0.1 mm lead foil alone or 0.1 mm lead foil plus 100 cm air. It is clear that the effect of intervening air on the electron energy spectrum is significant.

2.2. The work of Borrell-Carbonell *et al*

Borrell-Carbonell *et al* (1980) simulated three GGR MeV/AECL accelerators, i.e. Therac 40 Sagittaire, Therac 20 Saturne and Therac 10 Neptune, using a Monte Carlo code based on the condensed history scheme. Both Sagittaire and Saturne machines generated scanned electron beams controlled by electromagnets while in the Neptune machine electron beam flatness was

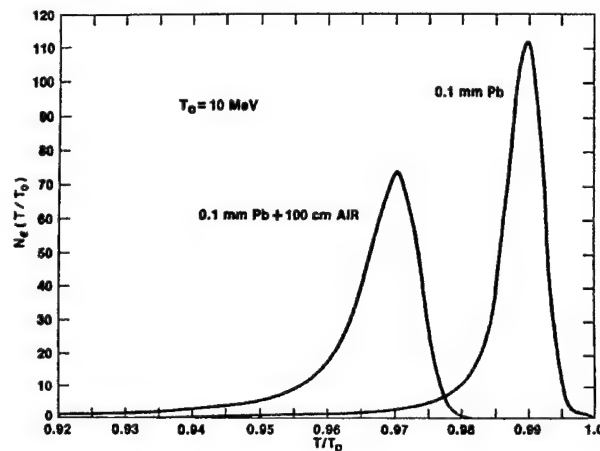


Figure 1. Energy spectra of electrons transmitted through lead foil, or through lead foil plus 100 cm air layer. Electrons with energy T_0 are assumed to be incident perpendicularly onto the foil, and T is the energy with which the transmitted electrons emerge from the foil, or from the layer of air behind the foil. The spectra include all transmitted electrons that emerge with directions within a cone of 20° half-angle around the direction of incidence. The curves are normalized to have unit area under each curve (Berger and Seltzer 1978).

produced by a pencil beam incident on a scattering foil. For all the machines, a simplified treatment head configuration was used in the Monte Carlo simulation. A monoenergetic and isotropic point source was assumed at the exit window of the accelerator. The beam defining system was modelled as a diaphragm with a square opening and zero thickness. Therefore, there was actually no simulation of the interactions of electrons with the components of the treatment machine head, except for the intervening air. Also there was no simulation of the secondary particles generated by electron interactions in the accelerator components.

The transport of the particles through air was simulated for a given collimator opening. In their work, Borrell-Carbonell *et al* (1980) used a two-step approach similar to that proposed by Berger and Seltzer (1978). The simulation results were recorded at the phantom surface, which included the electron energy, direction and position. The electron energy was calculated by subtracting the mean energy loss in air from the initial energy. Using the recorded electron phase space information, the dose distributions in a water phantom were calculated using a superposition approach similar to that of Berger and Seltzer (1978), i.e. by superposition of the pencil beam dose kernels pre-calculated with Monte Carlo simulation.

By comparing the calculated depth dose curves with measured data, Borrell-Carbonell *et al* (1980) checked their simple model for the treatment head. They found that the monoenergetic source was a good approximation for the scanned beams from Therac 40 Sagittaire and Therac 20 Saturne, but not for scattered beams from Therac 10 Neptune. For very high-energy (25 MeV) beams, they found that scattering from the beam defining system contributed significantly to the depth dose distribution, even for the scanned beams; therefore they concluded that the collimating system could not be approximated as a thin diaphragm.

2.3. The work by Rogers and Bielajew

Rogers and Bielajew (1986) calculated electron depth dose curves in a water phantom using the EGS4 Monte Carlo code (Nelson *et al* 1985) by assuming point sources of monoenergetic

electrons passing through 100 cm of vacuum. Compared with the corresponding measured data, they found that the calculation underestimated the dose near the surface and predicted a steeper fall-off beyond d_{\max} , the depth of the maximum dose. Trying to explain the discrepancies, they modelled the clinical electron beam as a monoenergetic beam of electrons passing through the 0.0127 cm Ti exit window of an accelerator, the 0.0127 cm Pb scattering foil, 102 cm of air and 3.9 cm of styrofoam. The electron energy spectrum near the central axis of the beam was scored at the phantom surface. The depth dose curves in the phantom were then calculated for incident broad parallel beams with the scored energy spectra. They found that the calculated depth dose distributions were improved by using the realistic spectrum. They also noticed that the mean energies of the spectra were significantly influenced by the very small low-energy tails. The depth of 50% maximum dose and the practical range were not ideal indices for the electron mean energy and the most probable energy respectively. Comparisons of dose distributions near inhomogeneities between Monte Carlo calculations and measurements were reported in a separate paper (Shortt *et al* 1986), which gave the first clear proof that Monte Carlo could handle electron heterogeneity problems correctly.

2.4. The work of Manfredotti *et al*

Manfredotti *et al* (1987) used the EGS3 code system (Ford and Nelson 1978) to simulate the electron collimator and the intervening air. A source of diameter 2 mm emitting monoenergetic electrons of 17 MeV was used in the simulation. The collimator was simulated with a 10 mm thick slab with a square window to obtain a $10 \times 10 \text{ cm}^2$ field at the phantom surface. The two-step approach was used; the simulated results, including energy, charge, impact points and direction cosines of particles that arrived on the phantom surface, were scored and later used in the three-dimensional phantom dose calculations.

2.5. The work of Andreo *et al*

Andreo *et al* (1989) studied the influence of energy and angular spread on the depth dependence of the stopping power ratio for clinical electron beams using the Monte Carlo method. In a similar way to Berger and Seltzer (1978), the accelerator treatment head was simplified as a lead scattering foil and 100 cm air. The lead thicknesses were chosen to give energy and angular distributions equivalent to those produced by all materials (except for air) within the treatment head. The EGS4 code (Nelson *et al* 1985) was used to simulate a monoenergetic electron pencil beam passing through the lead scattering foil and the air volume. The beam collimation was simulated by restricting the direction of the electrons emitted from the scattering foil to a forward cone, as done by Berger and Seltzer (1978). The electron energy spectrum was scored at the phantom surface and then used for the dose calculation in the phantom by combining with the Gaussian angular distributions of various root mean square angles. The phantom simulation was done using the MCEF Monte Carlo code (Andreo 1980, Andreo and Brahme 1984).

2.6. The work of Keall and Hoban

Keall and Hoban (1994) calculated the energy and angular distributions for primary electrons as well as contaminant bremsstrahlung photons for a Siemens KD2 machine using the EGS4 code (Nelson *et al* 1985). Like Berger and Seltzer (1978) and Andreo *et al* (1989), the accelerator treatment head was simplified as the scattering foils and intervening air while the influence of other components was ignored. For this type of accelerator, the scattering

foil system consists of two foils, i.e. the first scattering foil (stainless steel at 6 MeV and gold at other energies) and the second scattering foil (aluminium of a pyramid shape). The transport of an initially monoenergetic electron pencil beam through the scattering foils and air in the treatment head was simulated and the resulting energy and angular distributions were scored at the phantom surface. The simulated electron angular distribution was found to agree closely to those calculated with the Fermi-Eyges theory (Fermi 1941, Eyges 1948, Keall and Hoban 1996, Jiang *et al* 1998, 1999), indicating that a Gaussian approximation to the incident angular distribution of the primary electron beam might be adequate for use in treatment planning algorithms. The depth dose curve in water for the bremsstrahlung photons alone was calculated using the simulated bremsstrahlung spectrum. They found that the photon component of a 15 MeV electron beam had a similar d_{\max} to the 18 MV photon beam depth dose and similar fall-off to the 10 MV photon beam depth dose. The influence of electron energy and angular spread on the depth dose distribution was also studied. They found that, compared with the measured data with the applicator removed, the calculated depth dose curve using a monoenergetic beam with no angular spread had a lower surface dose and a sharper fall-off. When the simulated energy spectrum was used, excellent agreement in both the build-up and fall-off regions was achieved. The inclusion of the initial angular spread into the phantom dose calculation had a negligible effect on the depth dose curve. However, the initial angular spread was important in determining the penumbral width at the surface.

2.7. The work of Ebert and Hoban

Ebert and Hoban (1995b) performed a detailed study on the effects of electron beam cones and cerrobend cutouts on clinical electron beams using the EGS4 system (Nelson *et al* 1985). The EGS4 user code they used, RTPCART_XYZ, was based on another user code RTPCART (Murray 1990) with elements of XYZDOS (Rogers and Bielajew 1990, Bielajew and Rogers 1992). The energy and angular characteristics of Siemens KD-2 electron beams were taken from the Monte Carlo simulations of Keall and Hoban (1994).

In their study, simulations were performed for a variety of beam energies (6, 12 and 18 MeV) and beam angles incident on elements of the trimming plates or cutouts. The simulated element was a semi-infinite edge of the applicator or cutout in air. The area of the element irradiated by the electron beam was limited by a 5 mm width along the edge, the thickness of the edge and the maximum lateral range of electrons from the edge. They found that there were two processes significant to the dose distribution in the water phantom beneath the edge (see figure 2). One is the scattering of the primary electrons from the vertical face of the edge, the other is contaminant photon transmission through the edge. Other processes, such as transmitted primary electrons, and photons and electrons generated within the edge, etc, are negligible. The effect of the edge on the photon component in the primary beam can be treated as simple attenuation. The electrons scattered from the vertical face of the edge are dominantly forward directed and mostly inside the field. By studying the effect of beam incident angle, they also found that the scattered electron fluence was significantly influenced by the area of the vertical face of the exposed edge; more electrons were scattered from a large exposed area. This finding indicated that cutouts with diverging edges would produce fewer scattered electrons and thus flatter profiles than those with vertical edges. Ebert and Hoban (1995b) also studied the influence of beam energy on the scattered electron fluence, as well as the energy spectrum and mean energy of scattered electrons at various distances from the applicator edge. This information helped them to build a model for applicator scatter (Ebert and Hoban 1995a).

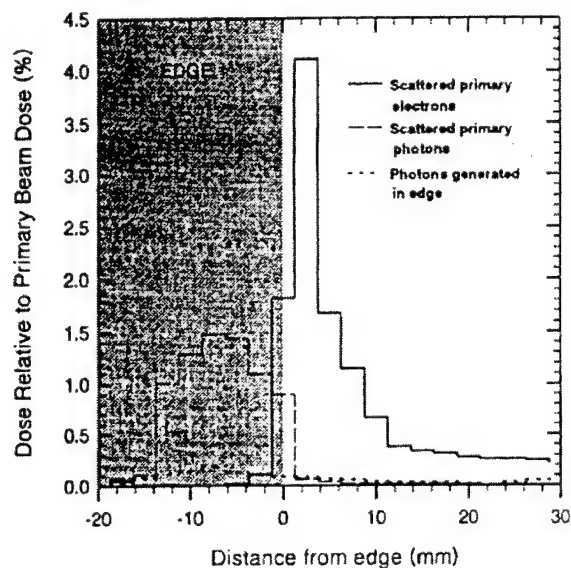


Figure 2. Profiles of dose to water of three components considered (primary beam scattered electrons, primary beam photons, photons generated in the edge by primary beam electrons) for a 12 MeV beam incident on the edge of the applicator or cutout. The edge is 50 mm above the water surface and profiles are taken at the depth of maximum buildup for the component considered, parallel to the line from the beam central axis to the edge. Normalization is to the dose due to primary open beam (Ebert and Hoban 1995b).

3. Simulation of the complete accelerator treatment head

A full Monte Carlo simulation of the medical accelerator geometry is a very difficult task. A large number of physical data (e.g. component dimensions and materials) need to be obtained and validated with high precision. A large amount of careful coding has to be done to accurately and efficiently model the individual accelerator components. Most of all, the simulation results are very sensitive to the details of the model. Therefore, it requires Monte Carlo expertise and deep understanding of electron beam characteristics to obtain good agreement with measurements.

3.1. The work of Udale/Udale-Smith

This difficult problem was first tackled by Udale/Udale-Smith (1988, 1990, 1992), who did very extensive coding (about 18 000 lines of FORTRAN) based on the EGS4 code system (Nelson *et al* 1985). Udale (1988) simulated a 10 MeV electron beam from a Philips SL75-20 accelerator. In this work, all the treatment head components of dosimetric importance were modelled, including the exit window, primary collimator, scattering foil, monitor chamber, mirror, movable jaws, accessory ring and applicator. In order to see the effects of different parts of the treatment head on the beam, she simulated five cases (denoted from case A to case E) at various levels of gradually increasing sophistication (see figure 3). An additional part of the beam defining system was introduced into the simulation in each successive case. In case A, a monoenergetic pencil beam was incident directly on the phantom. In case B a

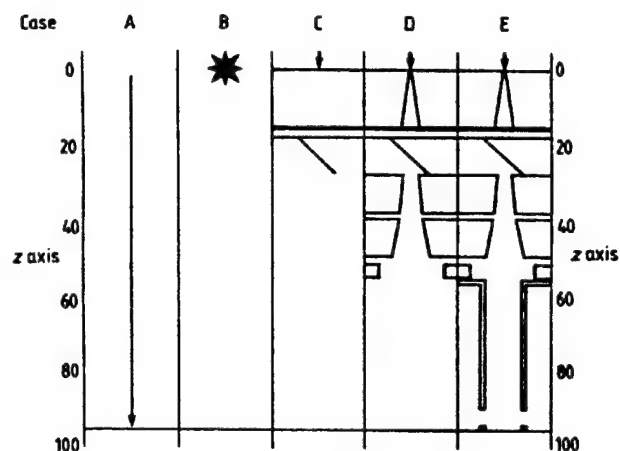


Figure 3. Schematic diagram of five simulation geometries with gradually increased sophistication used by Udale (1988) to study the influence of treatment head components on beam characteristics at the phantom surface. In case A, a monoenergetic pencil beam was incident directly on the phantom. In case B a monoenergetic isotropic point source at 95 cm from the phantom was used and the effect of intervening air was simulated. In case C the simulation was performed for a monoenergetic pencil beam incident on the electron window 95 cm above the phantom and interacting with the scattering foil, ionization chamber, mirror and air. In case D the movable jaws and accessory ring were added to case C and in case E the electron applicator was added.

monoenergetic isotropic point source at 95 cm from the phantom was used and the effect of intervening air was simulated. This was similar to the work of Borrell-Carbonell *et al* (1980). In case C the simulation was performed for a monoenergetic pencil beam incident on the electron window 95 cm above the phantom and interacting with the scattering foil, ionization chamber, mirror and air. In this case everything in the beam's path was simulated, but no collimating components. The geometry used in this case was more complex than that used by Berger and Seltzer (1978), Andreo *et al* (1989) and Keall and Hoban (1994). In case D the movable jaws and accessory ring were added to case C and in case E the electron applicator was added additionally.

Some approximations were made in the modelling of accelerator components in the work of Udale (1988). The primary collimator system was described as a series of concentric cylinders. The monitor ionization chamber and primary collimator extended to infinity radially, and movable jaws were semi-infinite. The initial energy of the pencil electron beam at the exit window for a nominally 10 MeV beam was determined by matching the 50% dose depth (R_{50}) and the electron practical range (R_p) between calculated and measured depth dose curves. Some variance reduction techniques were employed, such as the range rejection technique, i.e. particles were discarded if they did not have enough energy to reach the scoring plane at the bottom of the treatment head.

The two-step approach was adopted in the simulation of Udale (1988). In the first step, the treatment head was simulated and the simulation results (the particle phase space data) were recorded at a scoring plane at the phantom surface. The phase space information included particle type, energy, angle to the beam central axis and position at the phantom surface, which were stored in a four-dimensional array. In the second step, the dose distributions in the phantom were calculated using the scored phase space data as input.

To reduce the number of storage data about the beam exiting the treatment head and to simplify the phantom simulation, Udale (1988) used a so-called *planar approximation*. The energy spectrum was integrated over radius and angle, and the angular distribution was integrated over radius and energy. The angular distribution was defined relative to the beam central axis and there was no dependence on the azimuthal angle at any point. Under this simplification, beam divergence and the correlation among particle energy, angle and position were ignored. The beam was considered to comprise identical pencil beams all incident parallel to the beam central axis. Each pencil beam had the same energy and angular distributions. The dose distribution for each pencil beam was radially symmetric with respect to the beam central axis. A circular field was used to approximate the square field. Using the reciprocity principle, the depth dose to a region centred on the central axis with a radius of 0.25 cm was calculated by simulating a beam of radius 0.25 cm and scoring dose deposition in a cylindrical region with a cross-sectional area equal to that of the cylindrical beam. In this way the calculation efficiency was significantly improved, which was crucial at the time when this work was done.

Another technique used by Udale (1988) to reduce the statistical uncertainty and thus to speed up the simulation was to simulate primary electrons, secondary electrons and contaminant photons separately in a water phantom. The resulting dose distributions were scaled according to the relative numbers of each particle type and summed to give the total distribution. An extra benefit of using this approach was that some correlation between particle energy and angle was retained; for primary and secondary electrons energy spectra and angular distributions were used which were significantly different.

By simulating five cases with gradually increasing sophistication, Udale (1988) studied the influence of treatment head components on beam characteristics at the phantom surface. The effect of cone size on the beam characteristics was also investigated. The contributions to the central axis depth dose from the secondary electron component and photon component were calculated. The calculated depth dose curves were compared with the measurement to verify the simulation. The agreement was better for the smaller fields. Range-energy relationship was also checked.

In a follow-up study, Udale-Smith (1992) extended the EGS4 Monte Carlo simulation to two other Philips machines, the SL75-14/N and SL15, in addition to the SL75-20. One of the purposes of this work was to verify the dosimetric improvement of these two new machines over the SL75-20. The major improvement of the SL75-14/N over the SL75-20 included the use of a dual-foil scattering system rather than the single-foil scattering system, a low-mass ionization chamber and the aperture-plate applicator rather than the tubular electron applicator. As in the previous work (Udale 1988), the information on the component dimensions and materials for all machines was supplied by the manufacturer. But there were two pieces of information which could not be obtained from the manufacturer. One was the source spot size. A monoenergetic pencil beam was assumed. The other was the actual energy of the pencil electron beam at the exit window. Udale-Smith (1992) chose the incident energy, which gave depth-dose curves with practical ranges close to the measured values. As pointed out by Udale-Smith (1992), the introduction of empirical procedures was not satisfactory but could not be avoided.

Some important improvements of the simulation techniques were proposed. For the simulation of the SL75-20 machine, the entire treatment head geometry was treated as a single system. It was extremely complicated to modify the geometry. For SL75-14/N and SL15 machines a modular approach was used. Each treatment head component was treated as an independent module. Along the beam direction there was no overlapping between any two neighbouring components. The transport of particles in each module was independent of the geometry of the neighbouring components. This concept of component module (CM) was later adopted and extended by Rogers *et al* (1995a) in the design of the EGS4/BEAM system.

For the simulations of the SL75-20 and SL75-14/N machines, the planar approximation was used as in the previous work (Udale 1988). Four particle types were scored separately: primary electrons, secondary electrons, photons and positrons. These assumptions were reasonable for the SL75-20 accelerator. However, the simulation of the SL75-14/N machine indicated that they were not adequate for cleaner beams produced by the modified collimating system. Therefore a more realistic model was used in the simulation of the SL15 machine. Five particle types were scored: applicator scattered electrons, jaw scattered electrons, direct electrons (not scattered by the secondary collimating devices), contaminant photons and positrons. For direct electrons, beam divergence and the correlation between energy and direction were taken into account. Five energy bands were used for the direct electrons and for each band there was an appropriate angular distribution. Beam divergence was considered by storing the angle between the electron direction at the scoring plane and a ray from the source incident at the same point on the scoring plane.

The phantom simulations for SL75-20 and SL75-14/N were the same as in the previous work (Udale 1988). The planar approximation was found to be inadequate for SL75-14/N and SL15. Hence, two different approximations were used to include beam divergence into the phantom simulation for the SL15 machine. In one approximation, the central axis depth dose was calculated using the reciprocity principle. Then, an inverse-square correction was applied to the resulting central axis depth dose curve for direct electrons. In the other approximation, a voxel geometry was modelled and then the divergence of the direct electron component was considered explicitly.

The simulations of Udale-Smith (1992) verified the improvement of SL75-14/N and SL15 over SL75-20. For these two new types of Philips accelerator, the beams were cleaner because (a) there were fewer secondary electrons and contaminant photons in the beams, (b) the contaminant photons had much lower mean energy thus contributed less to the dose distributions, (c) there were fewer low-energy electrons in the electron energy spectra, and (d) the electron angular distributions were narrower.

Udale-Smith (1992) benchmarked the simulations by comparing the calculated and measured depth dose distributions. It was found that the introduction of some correlation between energy and direction for direct electrons improved the calculation accuracy. Allowing for the beam divergence also had a beneficial effect. The use of a simple inverse-square correction was shown to be a useful first-order estimate of the effect of beam divergence, allowing quick calculations to be performed and then corrected. Using voxel geometry for phantom simulation took into account the beam divergence explicitly and was shown to give excellent results. It was a useful starting point for the development of CT based Monte Carlo treatment planning as the patient body can be approximated as voxel geometry built from CT numbers.

3.2. Work by other investigators

In addition to the work of Udale-Smith (1990) and the development of the BEAM system (Rogers *et al* 1995a), there were also some other efforts to simulate a complete electron medical accelerator. To evaluate changes in the electron energy spectrum, depth dose and dose profile for two cone designs for Varian Clinac 2100C accelerators, Kassae *et al* (1994) performed Monte Carlo simulation for the treatment head using the cylindrical symmetry CYLTRAN option in ITS Monte Carlo code (Halbeib and Mehlhorn 1984). The treatment head components modelled were scattering foil, photon jaws, electron cones and intervening air. Cones were modelled as a series of circular apertures. Energy spectrum and beam profile were investigated for a 9 MeV monoenergetic electron beam impinging on the 0.025 mm thick Be exit window. Like Udale (1988), to study the influence of different components and

the difference of two cone designs, Kassae *et al* (1994) simulated four cases of different geometrical arrangements of the beam defining system, which were (a) scattering foil only, (b) scattering foil and photon jaws, (c) scattering foil, photon jaws and new cone design, and (d) scattering foil, jaws and old cone design. It was found that the presence of the movable jaws did not significantly modify the electron energy spectrum. The low-energy secondary electron component of the beam exiting the new cone was significantly reduced because the trimming plates were thick enough to absorb all the incident primary electrons, which was verified by Rogers *et al* (1995a) and consistent with the simulation results of Ebert and Hoban (1995b). The dose in the beam penumbral region was lower for the new cones because the leakage of secondary electrons from the cone aperture and housing was appreciably reduced.

Burns *et al* (1995) briefly mentioned a full Monte Carlo simulation of an accelerator treatment head to determine the electron stopping powers and practical ranges for clinical electron beams. An EGS4 user code was developed to model the scattering foil, the collimating system and the intervening air. Unfortunately, no further details were given in the paper.

More recently, Pawlicki (1998) modelled a Varian Clinac 1800 accelerator using the geometry package PENGEO of the PENELOPE Monte Carlo code system (Salvat *et al* 1996). He combined the accelerator simulation with the patient dose calculation in a 3D rectilinear phantom built from CT data.

4. The OMEGA BEAM system

The work of Udale/Udale-Smith (1988,1990,1992) brought the Monte Carlo simulation of electron accelerators to a new stage. Her simulation was no longer restricted to cylindrical symmetry. However, without a large effort, her code could hardly be applied to other types of accelerators, although it was well structured. As pointed out by herself (Udale 1988), 'In many ways the simulation has been very crude'. In order to supply accurate clinical beam information from a wide variety of medical accelerators for electron beam Monte Carlo simulation, a better code system with greater flexibility and extensibility was needed. This led to the development of the BEAM system (Rogers *et al* 1995a,b). Because of the significance of the BEAM code, it is worthwhile devoting this entire section to a description of this code system and its applications.

4.1. Descriptions of the BEAM code

The OMEGA (Ottawa Madison Electron Gamma Algorithm) project was a collaborative effort between the University of Wisconsin, Madison, and the National Research Council of Canada, Ottawa (Mackie *et al* 1990, 1994, Rogers *et al* 1990). The goal was to develop a full 3D electron beam treatment planning system using the Monte Carlo simulation technique to calculate dose distributions in a patient. A major achievement of this project was the development of the BEAM and DOSXYZ code systems (Rogers *et al* 1995a,b, Ma and Rogers 1995a,c, Ma *et al* 1995). Both BEAM and DOSXYZ were based on the PRESTA extension of the EGS4 Monte Carlo system (Nelson *et al* 1985, Bielajew and Rogers 1987, Rogers and Bielajew 1990, Bielajew *et al* 1994).

Although the original emphasis was on the simulation of clinical electron beams from medical accelerators, the BEAM code was equally applicable to all other radiation therapy units, including high-energy photon beams from accelerators, ^{60}Co beams or kilovoltage x-ray beams. The code was also a versatile, general-purpose Monte Carlo transport package, which could be used in a wide variety of applications besides simulating radiation therapy beams. There were many important and useful new features in the BEAM code (Rogers *et al* 1995a).

These included the use of the component modules (CMs), scoring particles' phase space information, tracking each particle's history, applying various variance reduction techniques, setting up a file/structure for parallel processing and developing a user-friendly interface.

The concept of component module was used in the code design of Udale-Smith (1992). In the BEAM code, this method was extended and played a very important role (Rogers *et al* 1995a). Component modules were actually a variety of elementary geometric entities and could be used to represent the components of an accelerator. Each CM dealt with a specific class of geometric shape and was contained between two planes, which were perpendicular to the beam axis. No overlapping between CMs was allowed. Each CM operated completely independently of the other CMs. A CM was defined with a variety of parameters rather than explicit values related to the geometric shape and material type. The parameter values were specified in an input file given by the user to model a specific accelerator component when performing a simulation. Figure 4 shows the diagrams for nine different CMs.

The beauty of this element of the design philosophy of BEAM was that each CM acted like a 'brick' and the model for the whole treatment head could be easily built up by simply putting a series of CMs together according to the technical drawing of an accelerator treatment head. This feature allowed accelerators of different manufacturers and different designs to be modelled at any level of complexity with little effort, even for users without much Monte Carlo coding experience. Also, this feature reduced the chance of making mistakes during the modelling process and made the quality assurance easier. The independence of each component of the geometry package allowed each CM to be tested and debugged in isolation.

Another important element of the basic design philosophy in the BEAM code was the recording of the complete phase space information of each individual particle crossing the scoring planes (Rogers *et al* 1995a). The information included the charge, energy, position, direction and a history tag (see below) for each particle. The phase space data could be recorded at the back plane, perpendicular to the beam axis, of any specified component module in the accelerator model. There could be an arbitrary number of scoring planes and a phase space data file could be created at each plane.

An important parameter in the phase space data file was the history tag variable, LATCH, which was a feature of EGS4 (Nelson *et al* 1985). In the BEAM code, however, each bit of LATCH was manipulated separately to fully utilize this tag. Using LATCH one could easily keep track of each particle's history and the information to score dose components separately, and then analyse the relative dose contributions from various accelerator components. In order to evaluate the influence of different accelerator components, Udale (1988) and Kassaei *et al* (1994) simulated several cases of different levels of complexity. With LATCH, it can be done in one simulation (Rogers *et al* 1995a). The phase space data file could be analysed using various data analysis programs (Ma and Rogers 1995a, b, c). LATCH provided a powerful tool for studying the characteristics of clinical electron beams with these programs.

A phase space file could be re-used by the BEAM code itself (Rogers *et al* 1995a). This allowed the user to simulate a treatment head in separate steps. For example, the user could simulate the treatment head from the exit window down to the upper surface of the last trimming plate of the electron applicator and then re-use the recorded phase space data to simulate the last scraper with various patient-specific cutouts. For an energy/cone combination, the first step of the simulation could be done once and for all, and thus avoid the repetition of the simulation for the subsequent simulation for different electron cutouts (Zhang *et al* 1998, 1999, Kapur *et al* 1998, Jiang *et al* 1999). The phase space data could also be used by the DOSXYZ code (Ma *et al* 1995, Rogers and Bielajew 1990, Bielajew and Rogers 1992), which was designed to perform dose calculations in a 3D rectilinear geometry to simulate various phantoms and the patient geometry built from CT data.

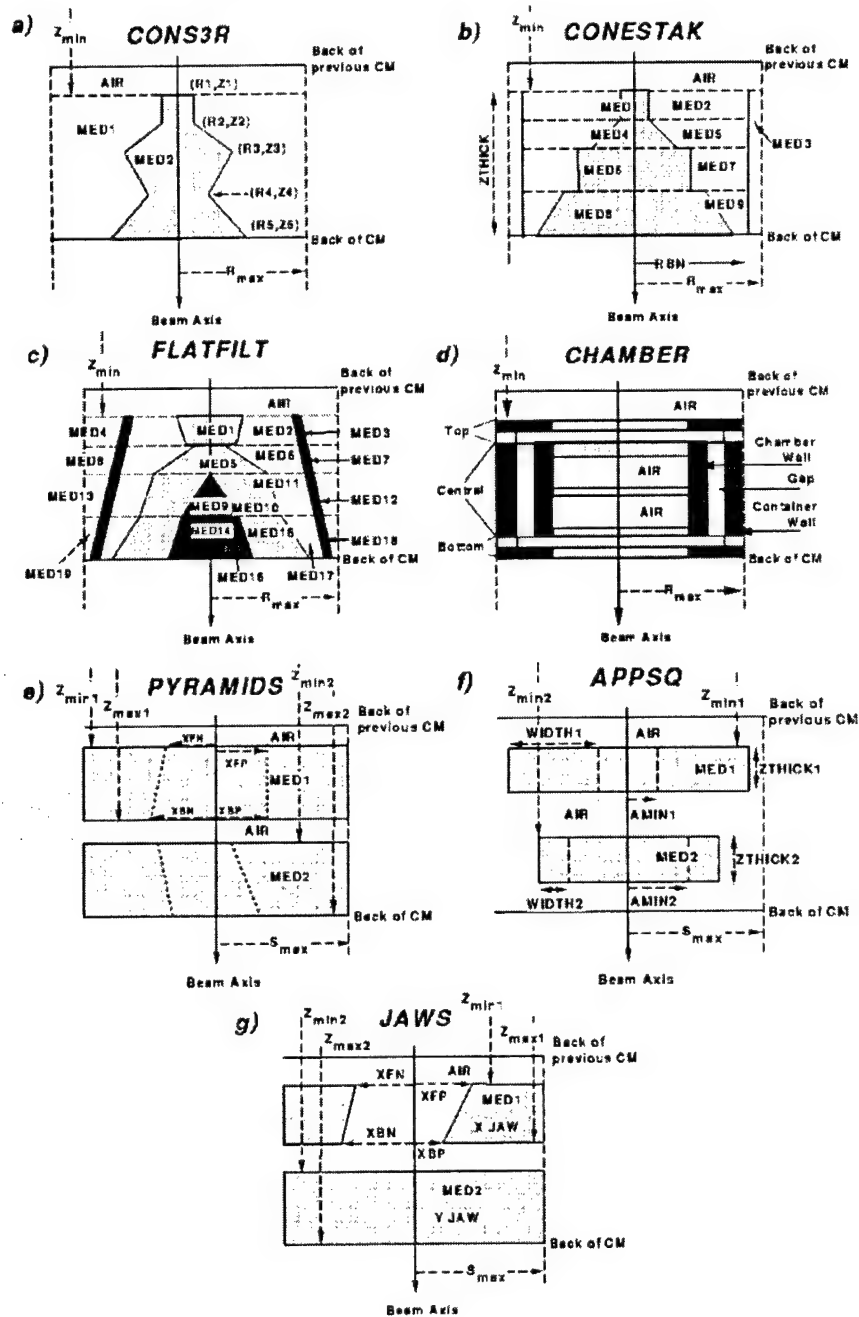


Figure 4. Schematic diagram of some component modules developed for the BEAM code by Rogers *et al* (1995a, b): (a) CONS3R, (b) CONESTAK, (c) FLATFILT, (d) CHAMBER, (e) PYRAMIDS, (f) APPSQ (which was later changed to APPLICAT), (g) JAWS, (h) MIRROR, (i) XTUBE.

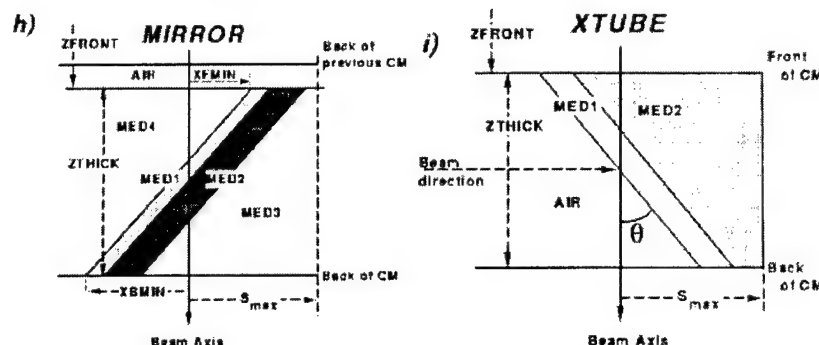


Figure 4. (Continued)

The two-step approach was a common technique for simulating accelerator treatment head and performing phantom dose calculations (Berger and Seltzer 1978, Borrell-Carbonell *et al* 1980, Manfredotti *et al* 1987, Udale 1988, Udale-Smith 1990, 1992). For disk space and other reasons, the correlation between particle energy, direction and position was usually broken, which led to inaccuracies in the reconstructed incident beam as demonstrated by Andreo and Fransson (1989) and in the dose distributions as shown by Udale-Smith (1992). BEAM also used the two-step approach. However, since the full phase space information for each particle was recorded, the correlation was completely retained. Actually, because BEAM used the phase space data file, this two-step approach was almost equivalent to a complete simulation of the treatment head and the phantom; particles were only 'frozen' temporarily at the scoring plane, with all the information to continue for further BEAM simulation or performing phantom dose calculation. The approach of scoring a particle's full phase space information was proved to be not only flexible but also, and even more importantly, a solution to the correlation problem. The major drawback with the approach was that it generated large data files and thus took a large amount of disk space, hundreds of megabytes for an electron beam and several gigabytes for a photon beam (Rogers *et al* 1995a, Kapur *et al* 1998).

Some useful variance reduction techniques were used in the BEAM code (Rogers *et al* 1995a, b). One was the range rejection method. In the BEAM code, however, this technique was further improved. Tables of the residual ranges to the threshold energy (AE) in each medium as a function of electron energy were pre-calculated using the restricted stopping powers. If a charged particle could not escape from the current region or reach a scoring plane, it was terminated. Other variance reduction techniques used in BEAM included photon interaction forcing, bremsstrahlung splitting and Russian roulette. These techniques have been described by Bielajew and Rogers (1988) and can be easily implemented in an EGS4 user code using the Mortran macros included in the EGS4 distribution. When a photon is forced to interact in the phantom the weight of the photon and all its descendents will be reduced to reflect the actual probability for such an interaction in the phantom. This photon forcing method worked for dose calculation in the phantom but failed for fluence scoring, as those photons, which did not interact in the phantom, were not transported. Ma (1992) improved the photon forcing technique by forcing the photons to interact not only in the entire phantom but also in any selected regions of interest. A fictitious photon that carried the remaining weight of the incident photon was transported to ensure the accuracy of both dose and photon fluence calculations (Ma 1992). This new photon forcing technique was implemented in the

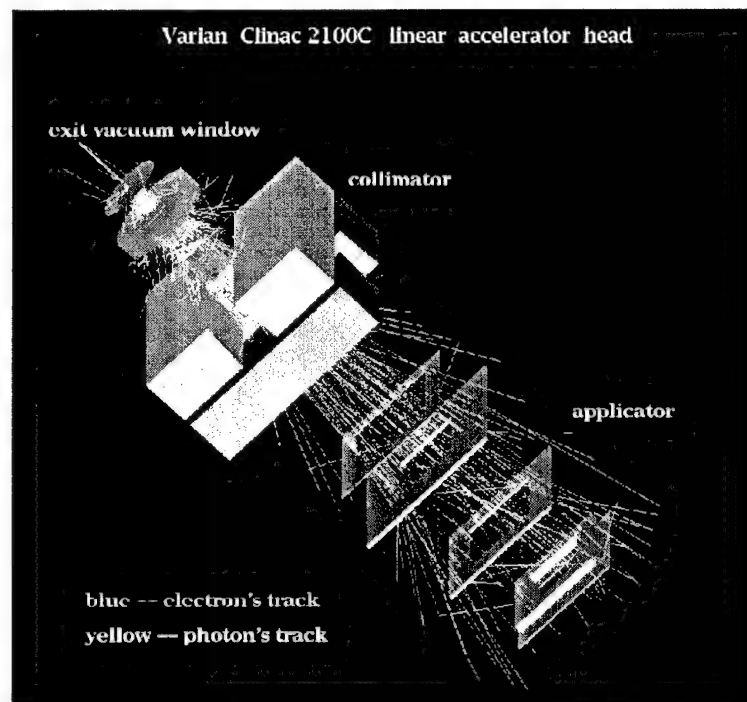


Figure 5. The treatment head of the Varian Clinac 2100C as shown by EGS-windows. About 100 electrons coming from the exit vacuum window are simulated and their tracks are shown in the picture (Rogers *et al* 1995a).

BEAM code and the photons could be forced to interact in any accelerator component as required (Rogers *et al* 1995b). The Russian roulette technique was recommended for use with the bremsstrahlung splitting technique. In a photon beam simulation, the efficiency of the bremsstrahlung photon production can be significantly improved using the particle splitting technique. However, fewer electrons generated by these photons in the treatment head can reach the scoring plane. The simulation efficiency can be significantly improved by applying the Russian roulette technique to these electrons.

Recently, a user interface program, BEAM_GUI, has been written which has greatly simplified the process for writing BEAM input files. A similar user interface was also developed for the DOSXYZ program (Treurniet and Rogers 1998). This has made the BEAM system more user-friendly. Furthermore, the code can be used to score data to produce a 3D display of the accelerator geometry and particle histories using a graphics package called EGS-windows (Bielajew and Weibe 1991). Figure 5 shows a Varian Clinac 2100C machine using EGS-windows and the simulated tracks of some electrons and photons. A file structure can be set up to run the dose calculation in parallel. Different input files can be generated for the same beam and phantom configuration but with different random number seeds to ensure the independence of the individual results. The final results can be combined using the software provided. Many efforts were also made to document the code well, especially in the source code (Rogers *et al* 1995b, Ma *et al* 1995, Ma and Rogers 1995a, b, c).

4.2. Benchmarks and applications of the BEAM code

4.2.1. The work by the NRCC group. The BEAM code has been first benchmarked extensively for electron beams from medical accelerators and used in a wide variety of applications by its developer, the NRCC (National Research Council of Canada) group.

Rogers *et al* (1995a) compared the calculated dose distributions with measurements in a homogeneous water phantom for a wide variety of accelerators, including the NRC 35 MeV research accelerator, a Varian Clinac 2100C, a Philips SL75-20, an AECL Therac 20 and a Scanditronix MM50. The NRC research accelerator has a narrow, well-known electron energy. They found that the calculated and measured depth dose curves and dose profiles were in excellent agreement using no free parameters. The energy and angular distribution of electrons at the exit window of a commercial medical accelerator is usually unknown to the user. Like Udale-Smith (1990), Rogers *et al* (1995a) assumed that all beams in the accelerator vacuum were monoenergetic and on-axis, and selected the incident electron energy by matching the calculated and measured values of the 50% dose depth, R_{50} . The depth dose curves could be calculated with an accuracy better than 2% of D_{\max} for almost any beams simulated. A more detailed benchmark was given in a compilation by Ding and Rogers (1995). In addition to those five linear accelerators studied by Rogers *et al* (1995a), Ding and Rogers (1995) also simulated a Siemens KD2 machine. For each accelerator, they calculated the dose distributions in a water phantom for up to five electron beams with an energy range of 5–50 MeV. For all cases, the calculated and measured dose distributions agreed well.

A detailed study on electron beams from a Varian Clinac 2100C machine was also presented by Rogers *et al* (1995a). The contributions from electrons and photons from different parts of the accelerator to the depth dose curve and dose profiles were analysed. Consistent with the results of Kassae *et al* (1994), they also found that the new applicator design reduced low-energy electrons from the applicator and gave a significantly cleaner beam. As a substitute to the new cone design, they found that an equivalent dosimetric effect could be achieved by adding an additional piece of lead on top of an aluminium scraper. They found that the dose distributions were sensitive to the details of the accelerator. For example, for a Clinac 2100C machine, either using a different monitor chamber or changing the jaw setting slightly would result in distinct changes in the dose distributions.

Ma *et al* (1993a, 1994) used the BEAM code to study the characteristics of the electron beams from three different linear accelerators, Philips SL75-20, AECL Therac 20 and Varian Clinac 2100C. Electron beams of nominal energies 6–20 MeV were simulated using the BEAM code. The results showed that for a Varian Clinac 2100C accelerator, electrons from individual components had distinct energy and angular distributions. The normalized energy spectra for each component varied by less than 5% for the same energy bin within a collimated $10 \times 10 \text{ cm}^2$ field. About 10% of the electrons from the applicator are incident at relatively large angles, peaked at 6 and 15 degrees. These observations led to the development of simplified beam models to replace the simulated phase space data (Ma and Rogers 1995b, c).

A key parameter in the simplified beam model is the virtual point source (VPS) position. Ma *et al* (1997a) simulated electron beams emerging from the treatment head and calculated the dose distributions in a water phantom with varying air gap thicknesses. Dose distributions were also calculated for an ideal point source with various SSD values in order to verify several commonly used methods for VPS position measurements. The results showed that the 'pin-hole' method and the 'full-width half-maximum' (FWHM) method could accurately predict the source positions while the 'inverse square' method usually gave smaller SSD values, especially for lower electron energies. The virtual SSD values obtained using the first two methods were suitable for direct Monte Carlo or analytical calculations, with a point source model, of dose

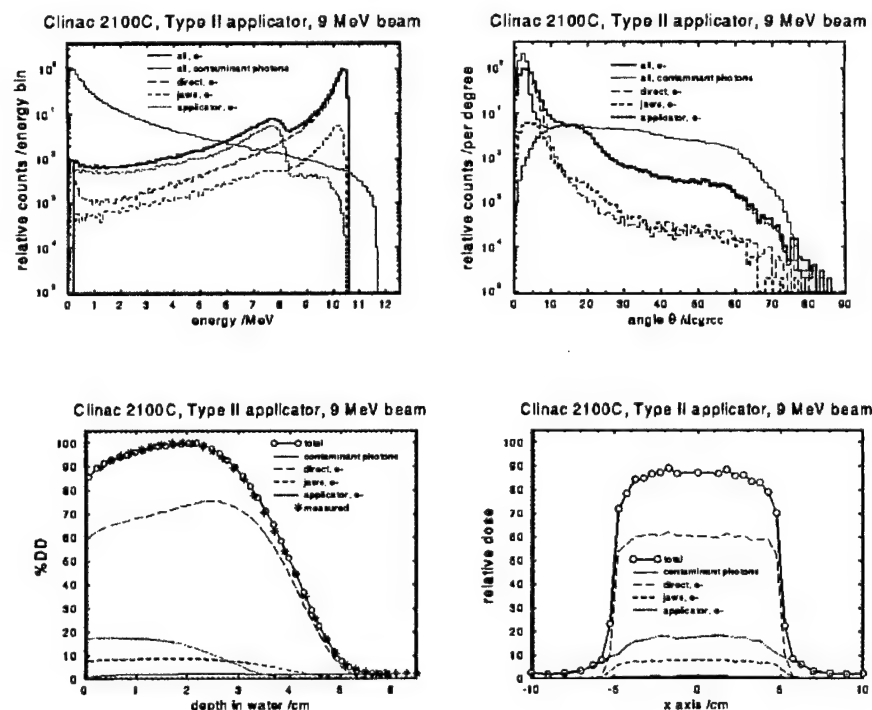


Figure 6. Calculated components of electron energy spectrum, angular distribution (at the phantom surface), depth-dose curve and dose profile (at 0.1 cm depth) for a Clinac 2100C with beam energy 9 MeV, field size = $10 \times 10 \text{ cm}^2$ and SSD = 100 cm, using BEAM and DOSXYZ codes (Ding and Rogers 1995).

distributions with correct FWHM values. Based on these studies, Ma and Rogers (1995b, c) and Ma *et al* (1997a) proposed a multiple source model consisting of a series of sources based on the energy and angular distributions of individual accelerator components. The user could predetermine the complexity of these models so that the full phase space data for these beams could be reproduced with the desired accuracy.

Using the BEAM code, the energy and angular spectra of electrons and photons could be easily obtained. Rogers *et al* (1995a) calculated 18 electron spectra for four different clinical accelerators, including a non-standard Varian Clinac 2100C with a Type II applicator, Philips SL75-20 with a tubular applicator and the scanned beams from the Therac 20 and MM50 Racetrack Microtron. The results for the SL75-20 accelerator were compared with those of Udale-Smith (1990). Some differences were seen for a 10 MeV beam and could be partially attributed to the different values of AE and cutoff energy, as well as different regions from where electrons were included in the spectra. Figure 6 shows the detailed analysis of the components of the electron energy spectrum, angular distribution, depth dose distribution and dose profile for a 9 MeV beam from a Varian Clinac 2100C accelerator. These results showed that most large-angle electrons were contributed by scattered electrons from applicators while scattered electrons from jaws had a relatively smaller angular spread for beams from accelerators with scattering foils. They also found that the contaminant photons were forward directed with a small angular spread because they were mainly produced in scattering foils.

Using the BEAM simulation results for a variety of clinical accelerators, Ding *et al* (1996) studied the mean energy in a water phantom for realistic electron beams from a variety of accelerators. They calculated the Spencer–Attix water/air restricted mass stopping power ratio for realistic electron beams in the energy range from 5–50 MeV and compared the results with those determined according to AAPM and IAEA protocols based on monoenergetic parallel beams (Ding *et al* 1995). A universal correction to the stopping power ratios for electron beam reference dosimetry was presented in terms of per cent depth dose in the photon tail. Ding *et al* (1997) also performed detailed studies of fluence correction factors using the realistic beam data simulated with the BEAM code.

The BEAM code has also been used to study the beam monitor chamber backscatter effect for electron beams. Ding *et al* (1994) found that, for a Clinac 2100C machine, the amount of backscatter decreased from 8% to 3% as the beam energy went from 6 to 18 MeV. They also found that 99% of the backscatter came from a fixed shielding ring downstream of the monitor chamber in the Clinac 2100C. The rest came from the collimator and applicator, and almost none from the water phantom. Using the BEAM code, Zhang *et al* (1998) studied the effects of changes in stopping power ratios with field size on electron beam relative output factors. They simulated electron beams for different field size, energies and machines and then calculated the stopping power ratios. It was found that this effect was negligible, due to error cancellation, as long as the AAPM TG-25 protocol (AAPM 1991) was followed with stopping power ratio data for broad monoenergetic beams (AAPM 1983). Zhang *et al* (1999) calculated the output factors versus size of square cutouts for electron beams with energies between 6 and 13 MeV and from a Siemens MD2 machine. The calculated relative output factors at 100 cm and 115 cm SSD agreed within 1% with the measurements.

4.2.2. The work of the Stanford group. The research group at Stanford University has been actively working on the clinical implementation of the Monte Carlo technique for radiotherapy treatment planning (Ma *et al* 1999). They have investigated the various aspects in the implementation procedure: simulation of electron beams from clinical accelerators (Kapur *et al* 1998, Ma *et al* 1999), beam characterization and modelling for dose calculations (Ma 1998), beam commissioning procedures for clinical implementation (Ma *et al* 1997c, Jiang *et al* 1999); and calculations of electron output factors for small fields (Kapur *et al* 1997, 1998, Ma *et al* 1997b) and extended air gaps (Mok *et al* 1997, Ma *et al* 1999). Further studies were carried out to calculate the dosimetric data required for performing accurate dose measurements for beam commissioning (Kapur and Ma 1999). More studies were reported on the effect of heterogeneous patient anatomy on the dose distributions and comparisons with conventional dose algorithms (Ma *et al* 1999).

Ma *et al* (1999) reported on the simulation of the electron beams (4–20 MeV) from three types of Varian accelerators, namely Clinac 1800, 2100C and 2300C/D, using the BEAM code. The dose distributions in a solid water phantom were calculated using the DOSXYZ code (Ma *et al* 1995) and compared with measured beam data according to specially designed commissioning procedures (Ma *et al* 1997c). The accelerator simulation was refined by adjusting the incident energy and simulating the details of the accelerator components until the difference between the Monte Carlo results and measurements was reduced to within 2% of the maximum dose value. The Monte Carlo calculated isodose curves agreed well with the measured data (using film and ionization chamber) while the results from a commercial treatment planning system with a 3D pencil beam algorithm differed significantly in some typical cases (e.g. >5 mm shift in the depth of the maximum dose, d_{\max} , and the 90% isodose line). The Monte Carlo method accurately predicted the beam output (agreed to within 2% with the measured value) for small irregular fields while the film

measurements at a fixed d_{\max} resulted in an uncertainty of up to 10% for a 6 MeV electron beam.

Mok *et al* (1997) studied the air gap factor for electron fields at extended source distances, the air gap factor being defined as the ratio of the machine output for a field defined by a cutout at an extended SSD to the output of the same field at the standard SSD. They used the BEAM code to simulate the phase space data for the electron beams (6–20 MeV) from a Varian Clinac 2100C accelerator and the DOSXYZ code to calculate the dose values in a water phantom. Comparisons of the Monte Carlo calculations and the measured results showed that the air gap factors could be accurately predicted (within 2%) for square fields of sizes from $10 \times 10 \text{ cm}^2$ to $2 \times 2 \text{ cm}^2$. Similar results were found for elongated fields and irregular fields of various sizes (Mok *et al* 1997, Ma *et al* 1999). They concluded that when set up properly the Monte Carlo program could be used for output factor calculations for small and irregular electron fields by a dosimetrist or a medical physicist with little Monte Carlo knowledge.

Ma *et al* (1997c) reported on the procedures for commissioning the computer simulated clinical beams for the implementation of the Monte Carlo technique for treatment planning. The EGS4/BEAM system was used for the simulation of the beams from several clinical accelerators: Varian Clinac 1800, 2100C and 2300C/D. The EGS4/DOSXYZ code was used for the dose calculations in water and in patients (phantoms built from CT data). The simulated beam data were compared with measurements performed using ionization chambers, diode detectors, TLDs and film. The dosimeter readings were converted using the stopping power ratios calculated for the realistic beams (Kapur and Ma 1999) and the dosimeter perturbation effects were properly corrected. They were able to keep the difference between the calculated and the measured dose, anywhere in the phantom, to about 2% of D_{\max} . The output factor (OF) calculation was more sensitive to the details of the linear accelerator; the photon jaw positions in an electron beam could significantly change the OF values which had to be simulated accurately to match the measured data to within 2%. They have developed procedures and successfully commissioned the beams used at the Stanford Medical Center. As a result, the uncertainty in the OF for small irregular field electrons was reduced from 5–10% to about 3% with Monte Carlo treatment planning.

Output factors for electron beams from a Varian Clinac 2100C accelerator were investigated systematically by Kapur *et al* (1998). Electron beams of 6–20 MeV nominal energy for rectangular and square inserts varying in field size from $1 \times 1 \text{ cm}^2$ to $20 \times 20 \text{ cm}^2$ were simulated using the Monte Carlo calculated phase space files. The calculations for water phantoms yielded values that were consistent with the measured values to within 2% for the range of applicator and square/rectangular insert combinations used on these machines for all the beam energies. The variations of output factors for different applicator–insert combinations were quantitatively assessed by separating the contributions of the direct and indirect particles to the total output factor. Beam characteristics such as the energy spectrum, planar fluence and angular distribution were studied to correlate the observed trends qualitatively. The use of these phase space files to compute output factors for arbitrarily shaped electron cutouts such as those used clinically for electron boosts in breast or head-and-neck cancers was examined. It was found that Monte Carlo calculations reproduced the measured values in water phantoms more accurately than a commercial treatment planning system which uses a 3D pencil beam dose calculation algorithm (Hogstrom *et al* 1981), especially under the conditions of compromised lateral scatter equilibrium.

Kapur and Ma (1999) also studied the restricted mass collision stopping power ratios for clinical electron beams of 6–20 MeV nominal energy from a Varian Clinac 2100C accelerator. The Monte Carlo simulations used for this purpose were performed for a variety of beam geometries including narrow to broad beams, normal to oblique angulation and various SSDs

for homogeneous water phantoms as well as heterogeneous phantoms, for various detector materials. The homogeneous water phantom calculations in this energy range were consistent with protocol recommended values for water-to-air ratios under broad, normal incidence conditions (AAPM 1983). The ratios for narrow realistic clinical beams differed by up to 1% compared with the broad realistic clinical beams, the differences being most significant for water-to-air, film materials and silicon and much smaller for water-to-detector materials such as graphite, ferrous sulphate, PMMA, polystyrene and lithium fluoride. In heterogeneous phantoms comprising water and layered lung- or bone-like plastic materials, stopping power ratios for water-to-detector were compared with the same in identical sized water phantoms using the stopping power ratio correction factors. These factors were found to vary in depth most for water-to-air, film materials and silicon, and to a lesser extent for the other detector materials described above. The extent of variation depended on the actual construction and geometry of the heterogeneous phantoms.

4.2.3. The work of the T-SRCC group. Faddegon *et al* (1998) described their work on implementing Monte Carlo for electron beam treatment planning at the Toronto-Sunnybrook Regional Cancer Center (T-SRCC). Beam data for their current clinical implementation consisted entirely of full phase space data sets simulated using the EGS4/BEAM code (Rogers *et al* 1995a). All 14 beams on a Siemens MXE (5–14 MeV) and a Philips SL20 (4–20 MeV) were commissioned for two applicators, covering nominal $10 \times 10 \text{ cm}^2$ and $15 \times 15 \text{ cm}^2$ fields. After spending substantial effort in commissioning, they still had unresolved discrepancies of 3% (or 2 mm in isodose lines) in the measured and calculated dose distributions (Faddegon *et al* 1998). They considered it likely to be sufficient to weight the beam data with some simple, slowly varying functions of energy and position to improve the calculation accuracy from a clinical perspective. Preliminary work on deriving beam data from measured dose distributions was done using a simple beam model of a point source with spectral distribution (Faddegon 1995). An unfolding technique was utilized to extract appropriate weights for a response matrix of monoenergetic depth doses to yield the measured depth doses. The unfolded spectral distribution had a 50% excess of low-energy electrons to compensate for the assumption of a point source with no angular distribution about the ray lines. Further work was proposed to resolve the level of detail and accuracy required in a beam model to adequately represent a beam, and to determine which concise set of measurements and methodology was most clinically viable for determining the beam model parameters (Faddegon *et al* 1998).

4.2.4. The work of Karlsson *et al*. Karlsson *et al* (1999) investigated the electron beam characteristics for a Varian Clinac 2300C/D accelerator. The purpose was to find out how a conventional treatment head could be modified to use multileaf collimated electron beams. Using the computer controlled multileaf collimator (MLC) for both photon and electron fields, automatic setup would be possible and complex field shapes and beam matching could be achieved. The physical parameters investigated in this work were beam penumbra and virtual/effective source position which were considered to be essential in beam matching and for dosimetry calculations. A 9 MeV nominal electron energy beam was simulated using the EGS4/BEAM code for various geometry combinations. Karlsson *et al* (1999) reported that the beam characteristics would fulfil their preset criteria for clinical use for electron beams of nominal energies down to 9 MeV by replacing the air in the treatment head with helium, changing the primary scattering foil position, using a thinner monitor chamber and lowering the MLC. Another proposal was made based on their Monte Carlo simulations that the electron beam characteristics would still be acceptable by inserting a helium balloon between the MLC and the patient. Thus, no change to the MLC would be necessary.

5. Discussion

During the last two decades, significant efforts have been made in Monte Carlo modelling of the clinical electron beams from medical accelerators. Many major issues have been addressed through detailed Monte Carlo simulations. Such efforts have been facilitated by the development of the BEAM code. Electron beams from various clinical accelerators have been studied more systematically for different purposes by different research groups. The accelerator manufacturers have studied the beam characteristics to improve accelerator design, although they have not published any detailed reports in the literature. The accelerator users have studied the beam phase space information to derive necessary dosimetric data for accurate dosimetry measurement and to perform accurate dose calculations for radiotherapy treatment planning. However, there are still a variety of practical problems associated with the accuracy of the accelerator simulation using the Monte Carlo techniques.

5.1. Simulation accuracy

The most basic information required for a Monte Carlo simulation of a treatment head is the specifications of the accelerator parts, such as their locations, dimensions and materials. Without knowing the component specifications precisely, the simulation results may be of limited usefulness. So far, it seems difficult to get adequate information about a specific accelerator from the manufacturers (Udale-Smith 1992, Rogers *et al* 1995a). Because of the commercial value of the detailed specifications of the accelerator parts, manufacturers are usually reluctant to provide the information with the necessary details for Monte Carlo modelling. Furthermore, newly purchased accelerators are often adjusted on-site for individual users, for example by selection of scattering foils or tuning of the waveguide, to match the beam characteristics of the machine to be replaced, or the existing machines. The situation may be further complicated due to accelerator repair, improvement or update. Accelerators of the same model may not consist of exactly the same components. For example, the same type of accelerator may have different scattering foils, flattening filters, monitor chambers or applicators.

Another practical problem is that it is difficult for users to know the precise phase space information of electrons at the vacuum exit window, such as spot size and location, electron energy distribution and angular distribution. When performing Monte Carlo electron beam simulations it has been common practice to assume a pencil beam of monoenergetic electrons at the accelerator vacuum window. The initial energy of the pencil beam is determined by matching the calculated and measured values of some dosimetric quantities, say, R_{50} or R_p (Udale 1988, Udale-Smith 1990, 1992, Keall and Hoban 1994, Rogers *et al* 1995a, Kapur *et al* 1998, Ma *et al* 1999). It has been found that the final depth dose curve is not sensitive to the width of the incident energy spectrum, unless the spectrum was very broad (Rogers *et al* 1995a). This approach has been demonstrated to be practical and adequate for radiotherapy dose calculations. However, the introduction of these empirical procedures does call into question the accuracy of the simulation results, such as the characteristics of the actual beam phase space data, even though the final dose distribution agrees well with the measured data. For example, the calculated energy spectrum is not necessarily an accurate representation of the realistic spectrum. In addition, as pointed out by Rogers *et al* (1995a), there may be other, more subtle effects, for which this approach may fail. There is a paucity of experimental data on the fluence of clinical electron beams (Deasy *et al* 1996). Thus, there is still rationale for establishing a benchmark for treatment head simulation based on fluence and dose measurements using a research accelerator with well known source and treatment head details (Faddegon *et al* 1998).

It is clear that the required accuracy of accelerator simulation depends on the required accuracy of the end point quantities to be investigated. For Monte Carlo treatment planning, the accuracy of the electron phase space data is usually ensured in such a way that the Monte Carlo calculated dose distributions would be consistent with the measured data to within 2% of the maximum dose (Kapur *et al* 1998, Ma *et al* 1999). This criterion seems to be practical and adequate as the 1σ uncertainty on the dose distributions measured clinically is usually about 2% following the recommended dosimetry procedures (cf IAEA 1987, AAPM 1983, 1991). The 1σ uncertainty in the dose at a point in a phantom in a routine clinical measurement is more likely to be about 3% (Khan 1994). Experience has shown that agreement better than 1% could be achieved between Monte Carlo simulations and measurements by fine-tuning the parameters used in the accelerator simulations (Kapur *et al* 1998, Ma *et al* 1999). High-precision measurements could be predicted to within 0.3% by Monte Carlo simulations (Ma *et al* 1993b, Ma and Seuntjens 1997). Such agreement seems to be overkill for clinical accelerator simulations if the dosimetric uncertainty remains at 2–3% in the dose data used for machine commissioning. Faddegon *et al* (1998) estimated the various uncertainties in electron dose delivery and concluded that an overall accuracy of 5% in dose or 5 mm in the location of the isodose lines, or in shorthand 5%/5 mm, would be achievable if relative doses were calculated to 3%/3 mm (point-to-point variation of dose within a given dose distribution) and the dose in water relative to reference conditions was calculated to 2%/2 mm.

5.2. Simulation time

The major drawback of the Monte Carlo method is the computing time required to obtain an acceptable statistical uncertainty in the simulated quantities. Ma *et al* (1997a) reported that to achieve a 1% statistical uncertainty in the dose distribution in a water phantom consisting of 1 cm^3 cubic voxels, about 1×10^4 phase space electrons were needed for every 1 cm^2 area within the field. The number of particles per unit area would increase for smaller voxels to achieve the same statistical uncertainty. Rogers *et al* (1995a) showed that the ratio of the number of phase space electrons per cm^2 scored at the scoring plane for a $10 \times 10\text{ cm}^2$ field to the number of incident electrons at the vacuum exit window increased with incident electron energy. For a Varian Clinac 2100C accelerator, this ratio was about 0.0002 for a 6 MeV electron beam and 0.0008 for a 20 MeV electron beam. This means that one has to simulate up to 5×10^7 histories in the accelerator simulation in order to achieve the specified 1% statistical uncertainty in the dose calculation. More than 10^8 electron histories will be needed for a 6 MeV, $25 \times 25\text{ cm}^2$ electron field. This may require over 300 h of CPU time on a SGI R4400 200 MHz workstation (Rogers *et al* 1995a) or a few days of CPU time on a Pentium Pro 200 MHz PC (Kapur *et al* 1998). The total CPU time required to simulate five nominal electron energies and five applicators will be close to a month. Because of the iterative process of fine-tuning electron incident energy and other accelerator parameters, the overall CPU time for commissioning all the beams properly may be several months. Clearly, most cancer centres do not possess such computing resources or the necessary Monte Carlo expertise.

5.3. Beam characterization and source modelling

An important reason for simulating the treatment head is to obtain the electron beam phase space information needed for Monte Carlo treatment planning. The phase space data generated with the BEAM code contain almost all the phase space information needed (Rogers *et al* 1995a). However, there are some problems associated with the direct application of such phase space

data in Monte Carlo dose calculations (Ma and Rogers 1995b,c, Ma *et al* 1997a, Ma 1998, Jiang *et al* 1999). Since the beam characteristics are usually different, even for the same type of accelerator, it is necessary to simulate each individual accelerator to obtain the phase space data for Monte Carlo treatment planning. The generation and quality assurance of phase space information by simulating the treatment head is not an easy task, even with the BEAM code. It requires both Monte Carlo simulation experience and much more time than that required for commissioning a conventional electron treatment planning system. This places a practical limit on the clinical implementation of Monte Carlo treatment planning in an ordinary cancer clinic.

Another problem is the storage of the Monte Carlo simulated phase space data. It was found that the beam characteristics for different electron applicators may differ significantly due to the variation of the electrons collimated by the movable jaws and scattered from the applicator scrapers (Zhang *et al* 1998, Kapur *et al* 1998). This means that separate phase space files have to be obtained for each electron energy/applicator combination. In order to achieve a statistical uncertainty of 1–2% in a phantom consisting of 0.1–1 cm³ voxels, 10⁶–10⁷ phase space particles are usually required in a Monte Carlo simulation, depending on the electron beam field size (Rogers *et al* 1995a, Zhang *et al* 1998, Kapur *et al* 1998, Ma *et al* 1999). For a clinical linear accelerator with five nominal energies and five applicator sizes, this means more than 10⁸ phase space particles or a few gigabytes of computer disk space. More disk space is required if photon phase space data are also stored. This represents a significant burden for the limited computer resources at most clinical centres. Obviously a more concise description for the clinical electron beam with sufficient accuracy is necessary for performing routine Monte Carlo treatment planning.

A methodology has been proposed to replace the phase space file with a multiple source model with parameters derived from the simulated phase space data (Ma *et al* 1993a, 1994, 1997a, Ma and Rogers 1995b, Ma 1998, Jiang *et al* 1999). Based on the observations that particles from different components of an accelerator have different energy, angular and spatial distributions while the particles from the same component have very similar characteristics, it was considered that the particles from different parts of an accelerator come from different subsources. Each subsource represented a critical component in the treatment head and its geometrical dimensions were determined by the component in question. Each subsource had its own spectral and planar fluence distributions derived from the simulated phase space data. By sampling the particle position on the subsource and on the phantom surface, the correlation between the particle position and incident angle was naturally retained. A special program, BEAMDP, was written to help derive parameters for the source model from the simulated phase space data using BEAM (Ma and Rogers 1995a, c). This multiple source model has been evaluated against the full phase space data for various accelerators and beam setups (Ma *et al* 1997a, Ma 1998). Figure 7 gives an example which demonstrates the correlation between electron incidence direction and position on the phantom surface as reconstructed using this multiple source model. Figure 8 illustrates that using the multiple source model can reduce the accelerator simulation time by a factor of 10 to achieve the same statistical uncertainty (i.e. requiring a factor of 10 fewer original phase space particles).

A practical commissioning procedure for electron beam Monte Carlo treatment planning was proposed by Ma *et al* (1997c). The idea was to derive the basic source model parameters from the simulated phase space data and then to modify the source model parameters based on the measured beam data for clinical implementation. Ma (1998) demonstrated the feasibility of this approach using a multiple source model developed previously (Ma *et al* 1997a). By varying the bin boundaries of the energy spectra for each subsource, the depth dose distributions calculated using the phase space reconstructed from the multiple source model for one nominal beam energy matched the depth dose distributions for another nominal energy. By varying the

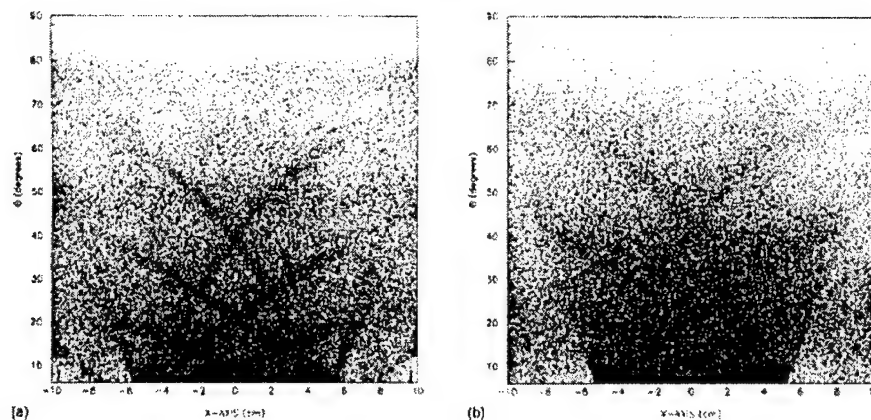


Figure 7. Scatter plot of θ (the angle between the incident direction and the beam central axis) versus x (distance from the central axis along the x -axis) showing correlation between direction of electron incidence and position for an 18 MeV electron beam, Varian 2100C, 10 cm \times 10 cm treatment field defined at 100 cm nominal SSD: (a) from the original phase space data and (b) simulated by the multiple-source model. Each point (x, θ) in the graph corresponds to the incident angle and position of an electron. All the electrons within the 20 cm \times 20 cm scoring field are presented except for those with θ less than 5° (most of them are 'direct' electrons within the treatment field). The arcs are formed by the scattered electrons from the applicator scrapers (Ma *et al* 1997a).

bin boundaries of the planar fluence distribution for each subsource, the lateral dose profiles calculated using the phase space reconstructed from the multiple source model for one field size matched the dose profiles for another field size (Ma 1998).

Jiang *et al* (1999) further improved the methodology for electron beam modelling and commissioning (Ma *et al* 1997a, c, Ma 1998). They improved the source model representation and reconstruction algorithms and investigated the minimum number of subsources of dosimetric significance to obtain the required beam commissioning accuracy. This method was applied to electron beams from a Varian Clinac 2100C machine with a type III applicator. It was found that a four-source model was adequate for all the energy/applicator combinations. The source model consisted of an electron point source, a photon point source and two extended electron sources. The scoring plane was placed directly above the upper surface of the last scraper of the applicator, rather than the phantom surface. The last scraper or a cutout placed on the scraper was not handled by the source model but simulated separately in a further BEAM simulation or in the patient dose calculation. The model was benchmarked by comparing the dose distributions calculated with the source model and the full phase space data. Figure 9 shows an example for a 20 MeV beam with a 6 \times 6 cm² applicator and 120 cm SSD. The chosen Varian Clinac 2100C acted as the reference accelerator. The model established for the reference accelerator was used to commission electron beams from other machines of similar design such as a Varian Clinac 2300C/D by tuning a few parameters in the model. The calculated dose distributions agreed to within 1–2% with the measured data (Jiang *et al* 1999).

6. Conclusions

We have reviewed the work on the simulation of clinical electron beams from medical accelerators using the Monte Carlo method. It is well accepted that the only accurate

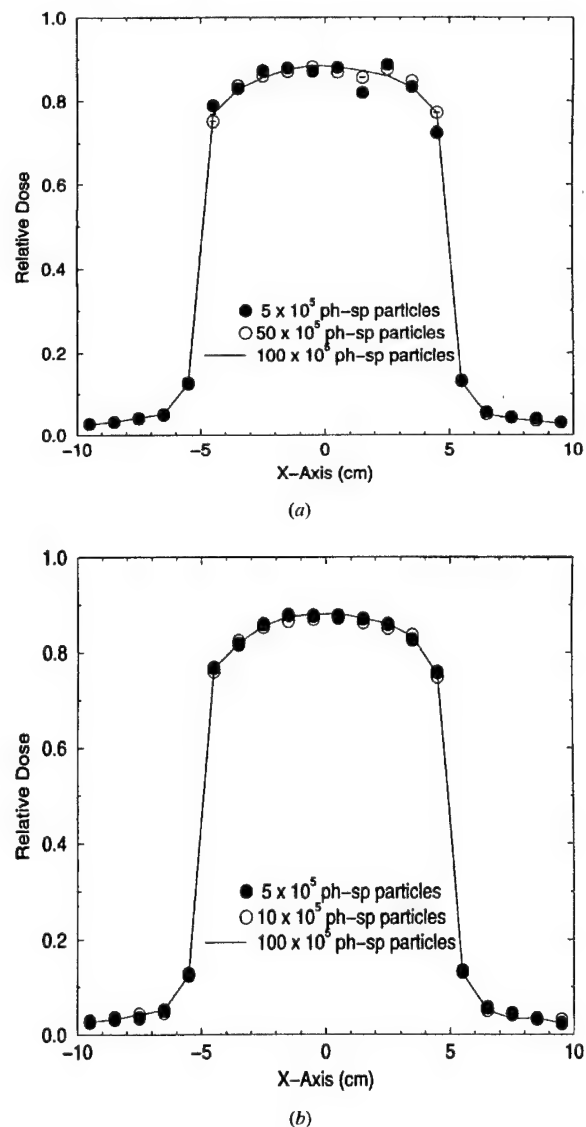


Figure 8. The surface dose profiles along the x-axis calculated using the original phase space data of varying size (a) and using the multiple-source model based on the corresponding phase space data (b) for an 18 MeV electron beam from a Varian Clinic 2100C accelerator. The field is $10 \text{ cm} \times 10 \text{ cm}$ defined at 100 cm SSD. The voxel size in the phantom is 1 cm^3 for the dose calculation. The number of phase space particles in each of the data sets is given in the figures. 10^7 particles are reconstructed for the dose calculations in (b) while the phase space data are recycled (Ma *et al* 1997a).

and practical way to obtain detailed information on a clinical electron beam is the Monte Carlo simulation of the treatment head. Accurate Monte Carlo treatment planning cannot

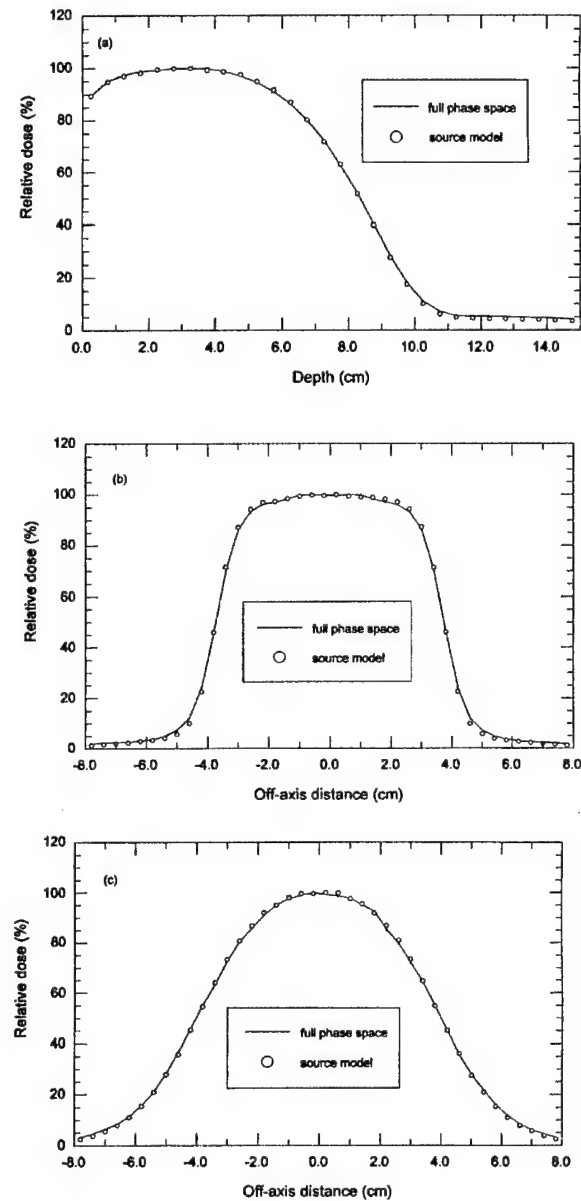


Figure 9. Dose distributions in water for a 20 MeV electron beam from a Varian 2100C machine with 6 cm \times 6 cm applicator at 120 cm SSD, calculated with full phase space data and a four-source model: (a) depth dose distributions, (b) dose profiles at 2 cm depth, (c) dose profiles at 7 cm depth. Each curve is normalized to its own maximum (Jiang *et al* 1999).

be performed without accurate beam phase space data. In addition, detailed information about radiotherapy beams has a wide variety of applications in clinical physics and radiation

dosimetry. Monte Carlo simulation of medical accelerators can increase our understanding of clinical beam characteristics, improve accelerator design and also improve the accuracy of clinical dosimetry by providing realistic beam data.

Optimistically, accurate accelerator simulation will result in accurate dose calculation and eventually in accurate dose delivery. Accurate dose calculation also plays a vital role in dose uniformity or conformity in intensity-modulated radiation therapy. It is exceedingly difficult to match the prescribed dose throughout the treatment volume in fields with heterogeneities due to the large dose discontinuities present in such fields. Treatment plans optimized on the basis of overly simplified dose calculation algorithms can become non-physical due to the uncertainties in the beam profiles. With accurate dose calculations, on the other hand, beam modifiers, mixed beams (electrons and photons) and optimization techniques may be used with confidence to improve the uniformity and conformity of the delivered dose distribution to the ideal prescription.

The following summarizes the current status of the work on electron accelerator simulation:

- (a) Although Monte Carlo simulation of electron medical accelerators has been performed by a number of investigators who focused on the effect of one or two components of dosimetric significance, more detailed beam characteristics and accurate particle phase space did not become available until the complete accelerator geometry could be simulated accurately.
- (b) Since the work of Udale and the development of the EGS4/BEAM system, our knowledge of clinical electron beams has been greatly improved. A large number of scientific findings and important results have been reported based on the EGS4/BEAM studies. However, these studies have only been for a few accelerators and a few beams. Systematic simulations of all the beams on various clinical accelerators need to be carried out.
- (c) The availability of electron beam phase space has led to the clinical implementation of the Monte Carlo technique for radiotherapy treatment planning dose calculations. The Monte Carlo simulated beam data have been used as input to the Monte Carlo code for accurate phantom and patient dose calculations. Accurate beam information has also resulted in more accurate dosimetric data.
- (d) The computing time required to simulate the beam data from a clinical accelerator is significant. This may not be a problem for a once-and-for-all study on some dosimetric data such as the conversion factors or correction factors for radiation dosimeters but will be a burden for a small cancer clinic after major changes in beam parameters due to machine upgrade, replacement of components or any other reasons. Faster computers and parallel processing methods can be used to speed up the simulation in large research centres. Variance reduction techniques are called for to further reduce the CPU time for accelerator simulation and patient dose calculation.
- (e) Accurate simulation of an electron beam from a clinical accelerator requires not only a specifically developed Monte Carlo code but also a great deal of Monte Carlo expertise. As the specifications of the accelerator components are often not known adequately and the machines are also tuned individually at the installation sites (leading to the variation in the incident electron energy), it can be a real challenge to match the Monte Carlo calculated dose distributions with the measured beam data, and dosimeter perturbation effects often need to be well understood to make this possible. Small inaccuracies in the simulation geometry can result in significant changes in the calculated dose distributions. If necessary, accurate energy, angle and fluence distributions should be used for the electrons incident on the vacuum exit window to achieve accurate end-point quantities (such as electron spectrum).

- (f) The phase space data can contain very detailed information about a clinical electron beam. However, the simulation of the phase space of a clinical beam can be time-consuming and it also requires a large amount of disk space. Well-designed beam models can accurately represent the beam characteristics and reconstruct the beam phase space. By using beam models rather than the raw beam phase space data, one can save accelerator simulation time and reduce the disk storage requirement.
- (g) It is probably impossible to simulate the beam phase space for all the clinical electron beams at every cancer clinic because of the lack of computer resources and Monte Carlo expertise. However, it has been demonstrated that well-developed beam models can be used to reconstruct any clinical electron beam. A reference machine needs to be simulated accurately to derive the beam model parameters and these parameters can be further adjusted based on the measured beam data for any machines of the same type. Further studies on source modelling and beam commissioning are needed for widespread clinical application of the Monte Carlo dose calculation technique.

Acknowledgments

We are grateful to Alan Nahum, Pedro Andreo, Dave Rogers, Alex Bielajew, Rock Mackie, Bruce Faddegon, Iwan Kawrakow and Frank Verhaegen for their useful suggestions and detailed comments on the manuscript. We would like to thank Alan Nahum, Dave Rogers, Alex Bielajew, Pedro Andreo, Rock Mackie, Bruce Faddegon, Jan Seuntjens, Iwan Kawrakow and many other colleagues who have directly or indirectly taught us the Monte Carlo simulation technique over the years. We would also like to thank our colleagues at Stanford, Art Boyer, Gary Luxton, Ed Mok, David Findley, Sam Brain, Ajay Kapur, Todd Pawlicki, Jun Deng and Jinsheng Li for encouragement and valuable comments on the manuscript. We acknowledge the financial support of the RSNA Research and Education Fund Seed Cycle 1, DOD BC971292 and NIH CA78331 during the writing of this review.

References

- AAPM 1983 A protocol for the determination of absorbed dose from high-energy photons and electrons *Med. Phys.* **10** 741
- 1991 Clinical electron beam dosimetry: report of AAPM Radiation Therapy Committee Task Group No. 25 *Med. Phys.* **18** 73–109
- al-Beteri A A and Raeside D E 1992 Optimal electron-beam treatment planning for retinoblastoma using a new three-dimensional Monte Carlo-based treatment planning system *Med. Phys.* **19** 125–35
- Andreo P 1980 Monte Carlo simulation and electron transport in water. Absorbed dose and fluence distributions *Report FANZ/80/3* (University of Zaragoza, Spain: Department of Nuclear Physics)
- 1991 Monte Carlo techniques in medical radiation physics *Phys. Med. Biol.* **36** 861–920
- Andreo P and Brahme A 1984 Restricted energy loss straggling and multiple scattering of electrons in mixed Monte Carlo procedures *Radiat. Res.* **100** 16–29
- Andreo P, Brahme A, Nahum A and Mattsson O 1989 Influence of energy and angular spread on stopping-power ratios for electron beams *Phys. Med. Biol.* **34** 751–68
- Andreo P and Fransson A 1989 Stopping-power ratios and their uncertainties for clinical electron beam dosimetry *Phys. Med. Biol.* **34** 1847–61
- Ayyangar K M and Jiang S B 1998 Do we need Monte Carlo treatment planning for Linac based stereotactic radiosurgery?—A case study *Med. Dosim.* **23** 161–7
- Balog J P, Mackie T R, Wenman D L, Glass M, Fang G and Pearson D 1999 Multileaf collimator interleaf transmission *Med. Phys.* **26** 176–86
- Berger M J and Seltzer S M 1978 The influence of scattering foils on absorbed dose distributions from electron beams *Report NBSIR 78-1552* (Gaithersburg: NBS)

- Bielajew A F 1994 Monte Carlo Modeling in external electron-beam radiotherapy—why leave it to chance? *Proc. 11th Int. Conf. on the Use of Computers in Radiation Therapy* ed A R Hounsell, J M Wilkinson and P C Williams (Manchester: North Western Medical Physics Department, Christie Hospital NHS Trust) pp 2–5
- Bielajew A F, Hirayama H, Nelson W R and Rogers D W O 1994 History, overview and recent improvements of EGS4 *Report PIRS-0436* (Ottawa: NRCC)
- Bielajew A F and Rogers D W O 1987 PRESTA: the parameter reduced electron-step transport algorithm for electron Monte Carlo transport *Nucl. Instrum. Methods B* **18** 165–81
- 1988 Variance-reduction techniques *Monte Carlo Transport of Electrons and Photons* ed T M Jenkins *et al* (New York: Plenum) pp 407–19
- 1992 A standard timing benchmark for EGS4 Monte Carlo calculations *Med. Phys.* **19** 303–4
- Bielajew A F and Weibe P E 1991 EGS-Windows—a graphics interface to EGS *Report PIRS-0274* (Ottawa: NRCC)
- Borrell-Carbonell A, Patau J P, Terrissol M and Tronc D 1980 Comparison between experimental measurements and calculated transport simulations for electron dose distributions inside homogeneous phantoms *Strahlentherapie* **156** 186–91
- Briesmeister J F 1993 MCNP—a general Monte Carlo N-particle transport code, version 4A *Report LA-12625* (Los Alamos, NM: Los Alamos National Laboratory)
- Burlin T E, Sidwell J M and Wheatley B M 1973 Applications of Monte Carlo methods in medical radiology *Br. J. Radiol.* **46** 398–9
- Burns D, Duane S and McEwen M R 1995 A new method to determine ratios of electron stopping powers to an improved accuracy *Phys. Med. Biol.* **40** 733–9
- Chaney E L, Cullip T J and Gabriel T A 1994 A Monte Carlo study of accelerator head scatter *Med. Phys.* **21** 1383–90
- Deasy J O, Almond P R and McEllistrem M T 1996 Measured electron energy and angular distributions from clinical accelerators *Med. Phys.* **23** 675–84
- DeMarco J J, Solberg T D and Smathers J B 1998 A CT-based Monte Carlo simulation tool for dosimetry planning and analysis *Med. Phys.* **25** 1–11
- Desobry G E and Boyer A L 1994 An analytic calculation of the energy fluence spectrum of a linear accelerator *Med. Phys.* **21** 1943–52
- Ding G X and Rogers D W O 1995 Energy spectra, angular spread, and dose distributions of electron beams from various accelerators used in radiotherapy *Report PIRS-0439* (Ottawa: NRCC)
- Ding G X, Rogers D W O and Mackie T R 1994 Calculation of backscatter into beam monitor chamber for electron beams (abstract) *Med. Phys.* **21** 923–4
- 1995 Calculation of stopping power ratios using realistic clinical electron beams *Med. Phys.* **22** 489–501
- 1996 Mean energy, energy–range relationship and depth-scaling factors for clinical electron beams *Med. Phys.* **23** 361–76
- 1997 Electron fluence correction factors used in conversion of dose measured in plastic to dose in water *Med. Phys.* **24** 161–76
- Ebert M A and Hoban P W 1995a A model for electron-beam applicator scatter *Med. Phys.* **22** 1419–29
- 1995b A Monte Carlo investigation of electron-beam applicator scatter *Med. Phys.* **22** 1431–5
- Ebert M A, Hoban P W and Keall P J 1996 Modeling clinical accelerator beams: a review *Australas. Phys. Eng. Sci. Med.* **19** 131–50
- Eyges L 1948 Multiple scattering with energy loss *Phys. Rev.* **74** 1534–5
- Faddegon B A 1995 Spectrometry for advanced treatment planning in electron therapy (abstract) *Med. Phys.* **22** 666
- Faddegon B, Balogh J, Mackenzie R and Scora D 1998 Clinical considerations of Monte Carlo for electron radiotherapy treatment planning *Radiat. Phys. Chem.* **53** 217–27
- Faddegon B A, O'Brien P and Mason D L D 1999 The flatness of Siemens linear accelerator x-ray field *Med. Phys.* **26** 220–8
- Fermi E 1941 in Rossi B and Greisen K Cosmic-ray theory *Rev. Mod. Phys.* **13** 265–8
- Ford R L and Nelson W R 1978 The EGS code system: computer programs for the Monte Carlo simulation of electromagnetic cascade showers (version 3) *Report SLAC-210* (Stanford, CA: SLAC)
- Halbeib J A and Mehlhorn T A 1984 ITS: the Integrated Tiger Series of coupled electron photon Monte Carlo transport codes *Report SAND84-0573* (Albuquerque, NM: Sandia National Laboratories)
- Han K, Ballon D, Chui C S and Mohan R 1987 Monte Carlo simulation of a cobalt-60 beam *Med. Phys.* **14** 414–19
- Hartmann-Siantar C L *et al* 1997 Lawrence Livermore National Laboratory's PEREGRINE project *Proc. 12th Int. Conf. on the Use of Computers in Radiation Therapy* ed D D Leavitt and G Starkschall (Madison: Medical Physics Publishing) pp 19–22
- Hendricks J S and Briesmeister J F 1992 Recent MCNP developments *Report LA-UR-91-3456* (Los Alamos, NM: Los Alamos National Laboratory)
- Hogstrom K R, Mills M D and Almond P R 1981 Electron beam dose calculations *Phys. Med. Biol.* **26** 445–59

- Holmes M A, Mackie T R, Sohn W, Reckwerdt P J, Kinsella T J, Bielajew A F and Rogers D W O 1993 The application of correlated sampling to the computation of electron beam dose distributions in heterogeneous phantoms using the Monte Carlo method *Phys. Med. Biol.* **38** 675–88
- IAEA 1987 An International Code of Practice *IAEA Technical Report Series* 277 (Vienna: IAEA)
- Jenkins T M, Nelson W R, Rindi A, Nahum A E and Rogers D W O 1988 *Monte Carlo Transport of Electrons and Photons* (New York: Plenum)
- Jiang S B and Ayyangar K M 1998 On compensator design for photon beam intensity modulated radiation therapy *Med. Phys.* **25** 668–75
- Jiang S B, Kapur A and Ma C-M 1999 Electron beam modeling and commissioning for Monte Carlo treatment planning *Med. Phys.* accepted
- Jiang S B, Luo Z M and Ayyangar K M 1998 Incorporation of the electron energy-loss straggling into the Fermi–Eyges equation *Radiat. Phys. Chem.* **53** 477–82
- Kapur A and Ma C-M 1999 Determined power ratios for clinical electron beams from a scatter-foil linear accelerator *Phys. Med. Biol.* **44** 2321–41
- Kapur A, Ma C-M, Mok E C and Findley D O 1997 Characterization of small field electron beams for radiotherapy using Monte Carlo simulations *Proc. 12th Int. Conf. on the Use of Computers in Radiation Therapy* ed D D Leavitt and G Starkschall (Madison: Medical Physics Publishing) pp 157–8
- Kapur A, Ma C-M, Mok E C, Findley D O and Boyer A L 1998 Monte Carlo calculations of electron beam output factors for a medical linear accelerator *Phys. Med. Biol.* **43** 3479–94
- Karlsson M G, Karlsson M K and Ma C-M 1999 Treatment head design for multileaf collimated high-energy electrons *Med. Phys.* **26** 2161–7
- Kassaei A, Altschuler M D, Ayyalsomayajula S and Bloch P 1994 Influence of cone design on the electron beam characteristics on clinical accelerators *Med. Phys.* **21** 1671–6
- Kawrakow I, Fippel M and Friedrich K 1996 3D electron dose calculation using a voxel based Monte Carlo algorithm (VMC) *Med. Phys.* **23** 445–57
- Keall P J and Hoban P W 1994 The angular and energy distribution of the primary electron beam *Australas. Phys. Eng. Sci. Med.* **17** 116–23
- 1996 Calculating the angular standard deviation of electron beams using Fermi–Eyges theory *Phys. Med. Biol.* **41** 1511–15
- Khan F M 1994 *The Physics of Radiation Therapy* (Baltimore, MD: Williams and Wilkins)
- Lee P C 1997 Monte Carlo simulations of the differential beam hardening effect of a flattening filter on a therapeutic x-ray beam *Med. Phys.* **24** 1485–9
- Lewis R D, Ryde S J S, Hancock D A and Evans C J 1999 An MCNP-based model of a linear accelerator x-ray beam *Phys. Med. Biol.* **44** 1219–30
- Liu H H, Mackie T R and McCullough E C 1997 A dual source photon beam model used in convolution/superposition dose calculations for clinical megavoltage x-ray beams *Med. Phys.* **24** 1960–74
- Liu S, Andreo P, Satherberg A, Gudowska I and Brahme A 1995 Monte-Carlo simulation of therapy accelerators: application to a MM50 Racetrack microtron (abstract) *Radiother. Oncol.* **37** (suppl 1) 119
- Lovelock D M J, Chui C S, Kutcher J and Mohan R 1994 Analysis of the photon beam treatment planning data for a scanning beam machine *Med. Phys.* **21** 1969–77
- Lovelock D M J, Chui C S and Mohan R 1995 A Monte Carlo model of photon beams used in radiation therapy *Med. Phys.* **22** 1387–94
- Ma C-M 1992 Monte Carlo simulation of dosimeter response using transputers *PhD Thesis* University of London (Report ICR-PHY-1/92 (Sutton, UK: ICR))
- 1998 Characterization of computer simulated radiotherapy beams for Monte Carlo treatment planning *Radiat. Phys. Chem.* **53** 329–44
- Ma C-M, Faddegon B A, Rogers D W O and Mackie T R 1997a Accurate characterization of Monte Carlo calculated electron beams for radiotherapy *Med. Phys.* **24** 401–16
- Ma C-M, Kapur A, Mok E and Findley D 1997c Monte Carlo treatment planning: procedures for commissioning computer simulated clinical beams (abstract) *J. Int. Fed. Med. Biol. Eng.* **35** 995
- Ma C-M, Mok E C, Kapur A and Findley D O 1997b Improvement of small-field electron beam dosimetry using Monte Carlo simulation *Proc. 12th Int. Conf. on the Use of Computers in Radiation Therapy* ed D D Leavitt and G Starkschall (Madison: Medical Physics Publishing) pp 159–62
- Ma C-M, Mok E, Kapur A, Pawlicki T, Findley D O, Brain S, Forster K and Boyer A L 1999 Clinical implementation of a Monte Carlo treatment planning system *Med. Phys.* **26** 2133–43
- Ma C-M and Nahum A E 1993 Calculation of absorbed dose ratios using correlated Monte Carlo sampling *Med. Phys.* **20** 1189–99
- Ma C-M, Reckwerdt P, Holmes M, Rogers D W O Geiser and Walters B 1995 DOSXYZ users manual *Report PIRS-0509(b)* (Ottawa: NRCC)

- Ma C-M and Rogers D W O 1995a BEAMDP users manual *Report PIRS-0509(C)* (Ottawa: NRCC)
- 1995b Beam characterization: a multiple source model *Report PIRS-0509(D)* (Ottawa: NRCC)
- 1995c BEAMDP—as a general-purpose utility *Report PIRS-0509(E)* (Ottawa: NRCC)
- Ma C-M, Rogers D W O, Ding G X and Mackie T R 1994 Electron beam characterization: reconstruction models and dose distributions in a homogeneous phantom (abstract) *Med. Phys.* **21** 895
- Ma C-M, Rogers D W O, Faddegon B A, Ding G X, Wei J S, Bielajew A F and Mackie T R 1993a Simplified models of electron beams from a 2100C accelerator (abstract) *Med. Phys.* **20** 1295
- Ma C-M, Rogers D W O, Shortt K, Ross K, Nahum A E and Bielajew A F 1993b Wall correction and absorbed dose conversion factors for Fricke dosimetry: Monte Carlo calculations and measurements *Med. Phys.* **20** 283–93
- Ma C-M and Seuntjens J P 1997 Correction factors for waterproofing sleeves in kilovoltage x-ray beams *Med. Phys.* **24** 1507–13
- Mackie T R 1990 Applications of the Monte Carlo method in radiotherapy *Dosimetry of Ionizing Radiation* vol 3, ed K Kase, B Bjarngard and F H Attix (San Diego, CA: Academic) pp 541–620
- Mackie T R, Holmes T W, Reckwerdt P J and Yang J 1995 Tomotherapy: optimized planning and delivery of radiation therapy *Int. J. Imaging Syst. Technol.* **6** 43–55
- Mackie T R, Holmes T W, Swerdloff S, Reckwerdt P J, Deasy J, Yang J, Paliwal B and Kinsella T 1993 Tomotherapy: a new concept for the delivery of conformal therapy *Med. Phys.* **20** 1709–19
- Mackie T R, Kubsad S S, Rogers D W O and Bielajew A F 1990 The OMEGA project: electron dose planning using Monte Carlo simulation (abstract) *Med. Phys.* **17** 730
- Mackie T R *et al* 1994 The OMEGA project: comparison among EGS4 electron beam simulations, 3D Fermi–Eyges calculations, and dose measurements *Proc. XIth ICCR (Manchester, UK)* (Christie Hospital NHS Trust) pp 152–3
- Mackie T R, Scrimger J W and Battista J J 1985 A convolution method of calculating dose for 15-MV x-rays *Med. Phys.* **12** 188–96
- Manfredotti C, Nastasi U, Marchisio R, Ongaro C, Gervino G, Ragona R, Anglesio S and Sannazzari G 1990 Monte Carlo simulation of dose distribution in electron beam radiotherapy treatment planning *Nucl. Instrum. Methods A* **291** 646–54
- Manfredotti C, Nastasi U, Ragona R and Anglesio S 1987 Comparison of three dimensional Monte Carlo simulation and the pencil beam algorithm for an electron beam from a linear accelerator *Nucl. Instrum. Methods A* **255** 355
- Mazurier J, Salvat F, Chauvenet B and Barthe J 1999 Simulation of photon beams from a Saturne 43 accelerator using the code PENELOPE *Phys. Med.* **15** 101–10
- McCall R C, McIntyre R D and Turnbull W G 1978 Improvement of linear accelerator depth-dose curves *Med. Phys.* **5** 518–24
- Mohan R 1988 Monte Carlo simulation of radiation treatment machine heads *Monte Carlo Transport of Electrons and Photons* ed T M Jenkins *et al* (New York: Plenum) pp 453–68
- 1997a Why Monte Carlo? *Proc. 12th Int. Conf. on the Use of Computers in Radiation Therapy* ed D D Leavitt and G Starkschall (Madison: Medical Physics Publishing) pp 16–18
- 1997b Monte Carlo dose calculations for radiation treatment planning (abstract) *Med. Phys.* **24** 987
- Mohan R, Chui C S and Lidofsky L 1985 Energy and angular distributions of photons from medical linear accelerators *Med. Phys.* **12** 592–7
- Mok E, Ma C-M, Kapur A, Findley D and Boyer A L 1997 Predicting air gap factors for electron fields at extended treatment distances (abstract) *J. Int. Fed. Med. Biol. Eng.* **35** 1026
- Murray D 1990 Using EGS4 Monte Carlo in medical radiation physics *Australas. Phys. Eng. Sci. Med.* **13** 132–47
- Nahum A E 1985 Monte Carlo electron transport simulation II: Application to dose planning *The Computation of Dose Distributions in Electron Beam Radiotherapy* ed A E Nahum (Umeå, Sweden: Umeå University) p 319
- 1988 Overview of photon and electron Monte Carlo *Monte Carlo Transport of Electrons and Photons* ed T M Jenkins *et al* (New York: Plenum) pp 3–20
- Nelson W R, Hirayama H and Rogers D W O 1985 The EGS4 code system *Report SLAC-265* (Stanford, CA: SLAC)
- Nelson W R and Jenkins T M 1980 *Computer Techniques in Radiation Transport and Dosimetry* (New York: Plenum)
- Neuenschwander H, Mackie T R and Reckwerdt P J 1995 MMC—a high-performance Monte Carlo code for electron beam treatment planning *Phys. Med. Biol.* **40** 543–74
- Nilsson B and Brahme A 1981 Contamination of high-energy photon beams by scattered photons *Strahlentherapie* **157** 181–6
- Pataut J P, Vernes C E, Terrisol M and Malbert M 1978 Calcul des caracteristiques qualitatives (TEL, FQ, equivalent dose) d'un faisceau de photons de freinage a usage medical, par simulation de sa creation et de son transport *Proc. 6th Symp. Microdosimetry (1978), Brussels, Belgium (EUR 6064)* ed J Booz and H G Ebert (London: Harwood Academic) pp 579–88
- Pawlicki T 1998 Application of a new mixed-simulation Monte Carlo code system to electron beam radiotherapy treatment planning with computed tomography data *PhD Thesis* Medical College of Ohio

- Petti P L, Goodman M S, Gabriel T A and Mohan R 1983a Investigation of buildup dose from electron contamination of clinical photon beams *Med. Phys.* **10** 18–24
- Petti P L, Goodman M S, Sisterson J M, Biggs P J, Gabriel T A and Mohan R 1983b Sources of electron contamination for the Clinac-35 25-MV photon beam *Med. Phys.* **10** 856–61
- Raesside D E 1976 Monte Carlo principles and applications *Phys. Med. Biol.* **21** 181–97
- Rogers D W O 1991 The role of Monte Carlo simulation of electron transport in radiation dosimetry *Int. J. Appl. Radiat. Isot.* **42** 965–74
- Rogers D W O and Bielajew A F 1984 The use of EGS for Monte Carlo calculations in medical physics *Report PXR-2692* (Ottawa: NRCC)
- 1986 Differences in electron depth-dose curves calculated with EGS and ETRAN and improved energy-range relationships *Med. Phys.* **13** 687–94
- 1990 Monte Carlo techniques of electron and photon transport for radiation dosimetry *The Dosimetry of Ionizing Radiation* vol 3, ed K Kase, B Bjarnagard and F Attix (San Diego, CA: Academic) pp 427–539
- Rogers D W O, Bielajew A F, Mackie T R and Kubsad S S 1990 The OMEGA project: treatment planning for electron-beam radiotherapy using Monte Carlo techniques (abstract) *Phys. Med. Biol.* **35** 285
- Rogers D W O, Ewart G M, Bielajew A F and van Dyk G 1988 Calculation of electron contamination in a Co-60 therapy beam *Proc. IAEA Int. Symp. on Dosimetry in Radiotherapy vol 1* (Vienna: IAEA) pp 303–12
- Rogers D W O, Faddegon B A, Ding G X, Ma C-M, We J and Mackie T R 1995a BEAM: a Monte Carlo code to simulate radiotherapy treatment units *Med. Phys.* **22** 503–24
- Rogers D W O, Ma C-M, Ding G X and Walters B 1995b BEAM users manual *Report PIRS-0509(A)* (Ottawa: NRCC)
- Rustgi S N, Rustgi A K, Jiang S B and Ayyangar K M 1998 Dose perturbation caused by high density inhomogeneities in small beams in stereotactic radiosurgery *Phys. Med. Biol.* **43** 3509–18
- Salvat F, Fernandez-Vera J M, Baro J and Sempau J 1996 *PENELOPE, an Algorithm and Computer Code for Monte Carlo Simulation of Electron-Photon Showers* (Madrid: Informes Tecnicos Ciemat)
- Sheikh-Bagheri D 1998 Monte Carlo study of photon beams from medical linear accelerators: optimization, benchmark and spectra *PhD Thesis* Carleton University, Canada
- Shortt K R, Ross C K, Bielajew A F and Rogers D W O 1986 Electron beam dose distributions near standard inhomogeneities *Phys. Med. Biol.* **31** 235–49
- Sixel K E and Faddegon B A 1995 Calculation of x-ray spectra for radiosurgical beams *Med. Phys.* **22** 1657–61
- Solberg T D, DeMarco J J, Holly F E, Smathers J B and DeSalles A F 1998 Monte Carlo treatment planning for stereotactic radiosurgery *Radiother. Oncol.* **49** 73–84
- Treurniet J R and Rogers D W O 1998 BEAM and DOSXYZ GUI user's manual *Report PIRS-0623* (Ottawa: NRCC)
- Turner J E, Wright H A and Hamm R N 1985 Review article: a Monte Carlo primer for health physicists *Health Phys.* **48** 717–33
- Udale M 1988 A Monte Carlo investigation of surface doses for broad electron beams *Phys. Med. Biol.* **33** 939–54
- Udale-Smith M 1990 A Monte Carlo investigation of high energy electron beams used in radiotherapy *PhD Thesis* Leeds University
- 1992 Monte Carlo calculations of electron beam parameters for three Philips linear accelerators *Phys. Med. Biol.* **37** 85–105
- van der Zee W 1996 Photon beam radiotherapy planning using Monte Carlo systems *MSc Thesis* Utrecht University
- Verhaegen F, Nahum A E, Van de Putte S and Namito Y 1999 Monte Carlo modelling of radiotherapy KV x-ray units *Phys. Med. Biol.* **44** 1767–89
- Wallace S and Allen B J 1998 CT based 3D Monte Carlo radiation therapy treatment planning *Australas. Phys. Eng. Sci. Med.* **21** 41–50
- Wang L, Chui C S and Lovelock M 1998 A patient-specific Monte Carlo dose-calculation method for photon beams *Med. Phys.* **25** 867–78
- Zhang G G, Rogers D W O, Cygler J E and Mackie T R 1998 Effects of changes in stopping-power ratios with field size on electron beam relative output factors *Med. Phys.* **25** 1711–16
- 1999 Monte Carlo investigation of electron output factors versus size of square cutout *Med. Phys.* **26** 743–50

Stopping-power ratios for clinical electron beams from a scatter-foil linear accelerator*

Ajay Kapur† and Chang-Ming Ma

Department of Radiation Oncology, Stanford University School of Medicine, Stanford, CA 94305, USA

E-mail: kapur@reyes.stanford.edu

Received 9 February 1999

Abstract. Restricted mass collision stopping-power ratios for electron beams from a scatter-foil medical linear accelerator (Varian Clinac 2100C) were calculated for various combinations of beams, phantoms and detector materials using the Monte Carlo method. The beams were of nominal energy 6, 12 or 20 MeV, with square dimensions $1 \times 1 \text{ cm}^2$ to $10 \times 10 \text{ cm}^2$. They were incident at nominal SSDs of 100 or 120 cm and inclined at 90° or 30° to the surface of homogeneous water phantoms or water phantoms interspersed with layered lung or bone-like materials. The broad beam water-to-air stopping-power ratios were within 1.3% of the AAPM TG21 protocol values and consistent with the results of Ding *et al* to within 0.2%. On the central axis the stopping-power ratio variations for narrow beams compared with normally incident broad beams were 0.1% or less for water-to-LiF-100, graphite, ferrous sulfate dosimeter solution, polystyrene and PMMA, 0.5% for water-to-silicon and 1% for water-to-air and water-to-photographic-film materials. The transverse variations of the stopping-power ratios were up to 4% for water-to-silicon, 7% for water-to-photographic-film materials and 10% for water-to-air in the penumbral regions (where the dose was 10% of the global dose maximum) at shallow depths compared with the values at the same depths on the central axis. In the inhomogeneous phantoms studied, the stopping-power ratio correction factors varied more significantly for air, followed by photographic materials and silicon, at various depths on the central axis in the heterogeneous regions. For the simple layered phantoms studied, the estimation of the stopping-power ratio correction factors based on the relative electron-density derived effective depth approach yielded results that were within 0.5% of the Monte Carlo derived values for all the detector materials studied.

1. Introduction

In radiotherapy dosimetry protocols (AAPM 1983, IAEA 1987), the use of restricted mass collision stopping-power ratios is recommended for electron beams to convert the absorbed dose to the detector materials to the absorbed dose to the irradiated media. However, the recommended ratios for electron beams commonly used in radiation therapy were calculated by Berger using Monte Carlo techniques for monoenergetic, monodirectional, infinitely wide electron beams that were perpendicular to semi-infinite water phantoms (AAPM 1983). The TG21 protocol (AAPM 1983) suggests periodic revision of these data to accommodate improved calculation procedures. Recent Monte Carlo calculations of these ratios for broad scattered or scanned realistic-electron beams from various linear accelerators indicated

* Presented at the 40th Annual AAPM Meeting (9–13 August 1998, San Antonio, Texas).

† Address for correspondence: Room A-042, Division of Radiation Physics, Department of Radiation Oncology, 300 Pasteur Drive, Stanford University School of Medicine, Stanford, CA 94305, USA.

agreement with the protocol-recommended values to within 1.5% and 0.5% respectively for water-to-air stopping-power ratios at the depth of maximum dose d_{\max} (Ding *et al* 1995). Larger discrepancies were noted at some other depths. The dependence of water-to-air stopping-power ratios on beam characteristics, energy spectra and photon contamination has thus been demonstrated by this and other studies in the literature (Nahum 1978, ICRU 1984a, Andreo 1988, Andreo *et al* 1989, Andreo and Fransson 1989, Klevenhagen 1994, Ding *et al* 1995).

In this paper we extend these studies using Monte Carlo techniques to a variety of electron beam, phantom and detector combinations—in particular for conditions where lateral-scatter equilibrium is degraded compared with broad-beam conditions (ICRU 1984a, AAPM 1991). With the reduction of field size, the associated loss of lateral-scatter equilibrium is known to cause significant spectral changes (Brahme 1977, Nilsson 1985, Andreo *et al* 1989) and cause the absorbed dose profiles to be markedly different than those in broad-beam conditions (Brahme 1977, McGinley *et al* 1979, Hogstrom *et al* 1981, Sharma *et al* 1984, AAPM 1991). Therefore it is not unreasonable to expect changes in the stopping-power ratios due to the associated spectral variations (Ma *et al* 1997, Zhang *et al* 1998). In this paper we quantitatively re-evaluate the AAPM-recommended stopping-power ratios (AAPM 1983, 1991) by incorporating Monte Carlo derived phase-space data (Kapur *et al* 1998) for narrow electron beams. Variations of stopping-power ratios for medium-to-detector in both homogeneous and heterogeneous media, and therefore the relevance of using stopping-power ratio correction factors for dose measurements in heterogeneous phantoms using various detectors, will be discussed.

The AAPM notation of spectrum-averaged restricted mass collision stopping-power ratios for medium 'med' to detector 'det' ($\bar{L}/\rho_{\text{det}}^{\text{med}}$) will be used throughout the text. Except where otherwise indicated they will be referred to as 'stopping-power ratios' for brevity. Calculations are performed for a Varian Clinac 2100C medical linear accelerator that consists of a dual-scattering foil system to flatten the beams at depth in water phantoms. Scatter-foil linacs produce electron beams with a broader spectrum than those from scanning beam linacs so that larger discrepancies from the idealized beams used for the AAPM TG21 stopping-power ratio calculations can be expected with scatter-foil linacs (Ding *et al* 1995). The stopping-power ratios are calculated in accordance with a modified version of the Spencer-Attix formulation (Spencer and Attix 1955) of the Bragg-Gray cavity theory (Bragg 1912, Gray 1936) as recommended by TG21 (AAPM 1983), IAEA (1987) and ICRU (1984a).

2. Theory

2.1. Homogeneous phantoms

When a detector is placed in a medium that is exposed to electron-beam radiation, the primary electrons and secondary electrons generated in the medium deposit energy in the radiation-sensitive region of the detector. From direct or indirect measurement of this deposited energy, the dose to the detector material can be calculated. The dose to the detector material can be related to the dose to the medium in the absence of the detector. Cavity theories in the literature that deal with the dose-conversion range from the simple Bragg-Gray theory (Bragg 1912, Gray 1936) to the Burlin general-cavity theory (Burlin 1966, 1968, Burlin *et al* 1969) and its various modifications (Holt *et al* 1975, O'Brien 1977, Ogunleye and Paliwal 1985). The stopping-power ratios play an integral role in the dose conversion.

According to the Bragg-Gray theory the dose to the medium ' D_{med} ' is related to the dose to the detector material ' D_{det} ' using the unrestricted mass collision stopping-power ratio of

the medium to the detector $(\bar{S}/\rho)_{\text{det}}^{\text{med}}$ as follows:

$$D_{\text{med}} = D_{\text{det}} (\bar{S}/\rho)_{\text{det}}^{\text{med}} \quad (1)$$

Spencer and Attix (1955) replaced $(\bar{S}/\rho)_{\text{det}}^{\text{med}}$ in equation (1) by $(\bar{L}/\rho)_{\text{det}}^{\text{med}}$ (restricted mass collision stopping-power ratio of the medium to the detector) to yield the following expression

$$D_{\text{med}} = D_{\text{det}} (\bar{L}/\rho)_{\text{det}}^{\text{med}} \quad (2)$$

The difference between the theories stems from the different treatment of energy loss processes occurring during radiation transport. While the Bragg-Gray theory assumes continuous energy loss for primary electrons, the Spencer-Attix theory considers energy loss to be continuous for electrons with energy below a certain threshold. In both these theories, however, the underlying assumption is that the detectors are small so that they do not significantly perturb the electron fluence by virtue of their presence.

In the ICRU 35 (ICRU 1984a) and TG21 (AAPM 1983) reports, the dose conversion process applicable to detectors used in radiotherapy dosimetry is decoupled as follows. The perturbation in the fluence of electrons incident on the detector due to the presence of the detector is addressed by calculating a perturbation factor (Harder 1968) and identifying the effective point of measurement (Skaggs 1949) of the detector. The spectrum-averaged mass collision stopping-power ratio of the medium to the detector material is then applied to the perturbation-corrected dose absorbed by the detector. The two-step process yields the dose that would be absorbed by the medium in the absence of the detector. The final expression that can be used for the dose conversion is thus

$$D_{\text{med}} = D_{\text{det}} (\bar{L}/\rho)_{\text{det}}^{\text{med}} P \quad (3)$$

Here $P = \prod_i P_i$ is the product of various terms P_i and equivalent to the perturbation factor (Ma and Nahum 1994) that takes into account the changes in the fluence and mean energy due to the presence of the detector. The final expression thus contains the stopping-power ratio which will constitute the subject of this paper.

In the Spencer-Attix formulation of the Bragg-Gray theory, secondary electrons are further classified based on the choice of an energy threshold ' Δ '. This threshold is selected by comparing the mean chord length (Spencer and Attix 1955) of the detector with the finite range of those electrons that can just cross it. Secondary electrons that have energy below this threshold are treated as 'track-ends' and assumed to deposit all their energy locally through continuous processes within the detector. If equilibrium exists for these secondary electrons, the assumption of local energy deposition is justified. Electrons with energies higher than the cut-off are assumed to originate outside the detector and to deposit part of their energy locally in the detector. The amount of energy deposited locally can be calculated using the restricted mass collision stopping-power for the detector material at these energies. While the use of the same threshold Δ for the medium and the detector is not rigorous since electrons would have different ranges in the two, Burch's attempt (Burch 1955, 1957) to treat it differently and as 'tail-ends' as opposed to 'track-ends' did not yield an analytical solution. Fortunately the water-to-air stopping-power ratios are not critically sensitive to the cut-off energy (AAPM 1983, ICRU 1984a). Thus for practical reasons the Spencer-Attix approach is recommended by standard protocols for the dose conversion process using stopping-power ratios (AAPM 1983, 1991, IAEA 1987). When secondary electronic equilibrium exists, the stopping-power ratios based on Bragg-Gray approach or its approximate formulation by Harder (1965) yield results that are similar to those obtained using the Spencer-Attix approach for water to solid or liquid detector materials (ICRU 1984a).

The spectrum-averaged Spencer-Attix restricted mass collision stopping-power ratio is calculated by adding the track-end contributions from Δ to 2Δ to the integrated fluence-weighted restricted mass collision stopping-power for the energy components greater than 2Δ

for the medium and detector separately and then taking their ratio (Spencer and Attix 1955). Nahum modified the Spencer-Attix approach for the approximate treatment of the track-end terms by obtaining the product of the fluence of electrons with energy less than or equal to Δ and the unrestricted mass collision stopping-power ratio (S/ρ) at the cut-off energy (Nahum 1978). In his approach the lower limit of integration is changed from 2Δ to Δ . The stopping-powers contributed for each energy component greater than the cut-off can be alternatively weighted by the track lengths of the particles. This leads to the same results as the fluence-weighted approach (Berger 1987). The final expression for the stopping-power ratios is thus given as follows

$$(\bar{L}/\rho)_{\text{det}}^{\text{med}} = \frac{\int_{\Delta}^{E_{\text{max}}} \Phi_E^{\text{med}}(E, \Delta) \left(\frac{L}{\rho}(E, \Delta)\right)^{\text{med}} dE + \Phi_{\Delta}^{\text{med}} \Delta \left(\frac{S}{\rho}(\Delta)\right)^{\text{med}}}{\int_{\Delta}^{E_{\text{max}}} \Phi_E^{\text{med}}(E, \Delta) \left(\frac{L}{\rho}(E, \Delta)\right)^{\text{det}} dE + \Phi_{\Delta}^{\text{med}} \Delta \left(\frac{S}{\rho}(\Delta)\right)^{\text{det}}} \quad (4)$$

Here ' E_{max} ' is the maximum energy in the spectrum and ' Φ_E^{med} ' is the fluence of electrons at energy ' E ' in the medium at the region of interest.

2.2. Heterogeneous phantoms

In heterogeneous phantoms, such as those used for the verification of dose calculation algorithms (Shiu *et al* 1992, Ayyangar *et al* 1993), measurements of dose with suitable detectors are required. These detector measurements can be converted to the dose of interest according to equation (3). The dose of interest may be the dose to the actual material of the medium or to a small mass of water contained within that medium. The dose to the medium may be converted to the dose to a small mass of water contained within the medium using the stopping-power ratio of water to the medium. The dose measured in heterogeneous phantoms can be compared with the dose in water phantoms measured using the same detectors to study the effects of the heterogeneities (Prasad *et al* 1984, Prasad and Bassano 1989, El-Khatib *et al* 1992, El-Khatib and Connors 1992) using a heterogeneity correction factor 'HCF'. The HCF is defined as the ratio of dose in a heterogeneous phantom ' D_{het} ' to dose at the same point in a water phantom ' D_{water} '. Using equation (3), this may be expressed as follows:

$$\begin{aligned} \text{HCF}_{\text{water}}^{\text{het}} &= \frac{D_{\text{het}}}{D_{\text{water}}} = \frac{[D_{\text{det}}]_{\text{het}}^{\text{het}} [(\bar{L}/\rho)_{\text{det}}^{\text{het}}]_{\text{het}}^{\text{het}} [P_{\text{det}}^{\text{het}}]_{\text{het}}^{\text{het}}}{[D_{\text{det}}]_{\text{water}}^{\text{water}} [(\bar{L}/\rho)_{\text{det}}^{\text{water}}]_{\text{water}}^{\text{water}} [P_{\text{det}}^{\text{water}}]_{\text{water}}^{\text{water}}} \\ &= (D_{\text{det}})_{\text{water}}^{\text{het}} (\text{SPRCF})_{\text{water}}^{\text{het}} (\text{PCF})_{\text{water}}^{\text{het}} \end{aligned} \quad (5)$$

where

$$(\text{SPRCF})_{\text{water}}^{\text{het}} = \frac{[(\bar{L}/\rho)_{\text{det}}^{\text{het}}]_{\text{het}}^{\text{het}}}{[(\bar{L}/\rho)_{\text{det}}^{\text{water}}]_{\text{water}}^{\text{water}}} \quad (6)$$

and

$$(\text{PCF})_{\text{water}}^{\text{het}} = \frac{[P_{\text{det}}^{\text{het}}]_{\text{het}}^{\text{het}}}{[P_{\text{det}}^{\text{water}}]_{\text{water}}^{\text{water}}} \quad (7)$$

Here the SPRCFs and PCFs are the stopping-power ratio correction factors and perturbation correction factors respectively. The SPRCF at a given voxel for a given detector measurement is defined as the ratio of the stopping-power ratios for the medium-to-detector to water-to-detector evaluated at the corresponding energies in the voxels in the two phantoms. In this notation the phantom is identified in the superscript outside the square brackets. The PCFs will not be addressed in this paper.

3. Materials and methods

3.1. Electron beams

Varian Clinac 2100C (Varian Oncology Systems, Palo Alto, CA) electron beams of 6, 12 and 20 MeV nominal energy, collimated by Type III accessories (that consist of open-walled applicators with matched scattering foils) were used for this study. Beam sizes as projected at a nominal SSD of 100 cm varied from $1 \times 1 \text{ cm}^2$ to $10 \times 10 \text{ cm}^2$. Air gaps of 5 or 25 cm from the lowermost scraper of the applicator were studied. Angles of incidence of these beams as defined by the angle between the central axis of the beams and the surface of the irradiated phantoms were chosen to be either 90 or 30 degrees corresponding to normal or oblique incidence.

In addition broad, mono-directional and mono-energetic beams of energy 6, 12 and 20 MeV incident at 90° to water phantoms were also studied. The stopping-power ratios calculated for these beams were compared with the values tabulated in the TG21 report (AAPM 1983) for similar beams.

3.2. Phantoms

The homogeneous phantoms simulated were composed of water. The heterogeneous phantoms simulated consisted of slabs of lung 'LN4' or bone-like materials 'SB3' (White *et al* 1977, White 1978) thicknesses of 5 and 3 cm respectively, sandwiched between layers of water (see inserts in figure 7). They were placed beneath a 3 cm slab of water. The physical densities of the heterogeneous materials were 0.3 g cm^{-3} and 1.8 g cm^{-3} respectively. The relative electron densities were calculated to be 0.29 and 1.70 respectively. The phantom dimensions were $20 \times 20 \times 10 \text{ cm}^3$.

3.3. Detector materials

The detector materials were air, graphite, ferrous sulfate dosimeter solution, photographic emulsion, silver halides, lithium fluoride (in TLD-100 chips), polymethyl methacrylate (PMMA), polystyrene and silicon. The physical composition of these materials was derived from ICRU Report 37 (ICRU 1984b). For graphite, a bulk density of 1.7 g cm^{-3} as well as a crystallite density of 2.265 g cm^{-3} were studied. For films, to separate the gel and silver halides, both photographic emulsions and silver halides were studied.

3.4. Cross-sectional data

The stopping powers for all these materials were obtained using the code PEGS4 (Nelson *et al* 1985) with the density effect corrections of ICRU Report 37 as implemented by Duane *et al* (1989). The exceptions were the lung and bone-like materials for which density-effect corrections were evaluated with PEGS4 using the in-built Sternheimer-interpolation scheme (Sternheimer *et al* 1982). The ionization potentials for the compounds were evaluated in PEGS4 using Bragg's additivity rule for compounds (Bragg and Kleeman 1905).

3.5. Phase-space files

Phase-space files for the beams studied were obtained from previous calculations (Kapur *et al* 1998) using the Monte Carlo code EGS4/BEAM (Nelson *et al* 1985, Rogers *et al* 1995) for a

nominal SSD of 100 cm at a plane perpendicular to their central axes. The broad-beam phase-space file was calculated for the open $10 \times 10 \text{ cm}^2$ applicator. The narrow-beam phase-space files were calculated for cut-outs on $6 \times 6 \text{ cm}^2$ applicators.

3.6. Calculation procedures: the Monte Carlo code

The code DOSXYZ (Ma *et al* 1995) was modified to score on the fly the mean kinetic energy of charged particles and the stopping-power ratios for the medium to several detectors in voxels of the calculation grid.

In this code, the mean kinetic energy of charged particles with energy greater than the cut-off energy ECUT (Rogers 1984) is calculated for each voxel using a commonly used procedure (Andreo and Brahme 1981, Rogers and Bielajew 1990, Malamut *et al* 1991, Ding *et al* 1996). The procedure is to determine the kinetic energy at the mid-point of the curved tracks of the charged particle and to compute the average of this mid-step kinetic energy over all the track lengths in that voxel.

Stopping-power ratios for the medium-to-detectors are calculated by a similar averaging procedure for each voxel. If the energy of the charged particle exceeds ECUT, the mass restricted stopping-power is obtained at the mid-step energy of the track for the medium in the voxel and is weighted by the track length. The product so obtained is the dose absorbed by the medium from the track being considered in that voxel. It is accumulated in a register for the medium. Simultaneously, the mass restricted stopping-power for each detector of interest for the same mid-step energy is weighted by the same track length and accumulated in registers for each detector. However, if the energy of the charged particle falls below ECUT the register for the medium is incremented by this energy while the registers for the detectors are incremented by the product of this energy and the ratio of the restricted stopping powers for detector-to-medium evaluated at energy Δ . The differences between the use of the cut-off energy or the EGS4 generated energy for the track-end contributions have been ignored. The ratio of the composite values accumulated in the registers for each voxel for the medium to the detectors yields the stopping power ratios.

3.7. Selection of parameters

In this study we chose to use $\text{ECUT} = \text{AE} = 521 \text{ keV}$ and $\text{PCUT} = \text{PE} = 10 \text{ keV}$. These values were used for the calculation of stopping-power ratios for water-to-air in major protocols (AAPM 1983, IAEA 1987) and studies in the literature (ICRU 1984a). The cut-off value of 10 keV kinetic energy corresponds to electrons with a range (continuous slowing down approximation) of approximately 3 mm in air (ICRU 1984b). In order to account for the range of electrons in the continuous slowing down approximation for other detectors considering the typical sizes of the other detectors, separate calculations were also performed for broad clinical beams using $\text{ECUT} = \text{AE} = 611 \text{ keV}$. For the homogeneous phantoms, a value of $\text{ESTEPE} = 0.04$ was employed with the PRESTA algorithm (Bielajew and Rogers 1987). The differences between water-to-air stopping-power ratios calculated using either this value of ESTEPE or a more conservative value of 0.01 were insignificant. For the heterogeneous phantoms $\text{ESTEPE} = 0.01$ was used for more accurate estimations of the stopping-power ratio variations in the interface regions between water and the heterogeneities (Nahum 1987). The voxels in the calculation grids were cubes with 3 mm sides. A sufficient number of histories were accumulated in the calculations to reduce the statistical uncertainties in the water-to-air stopping-power ratios to less than 0.1% at d_{max} .

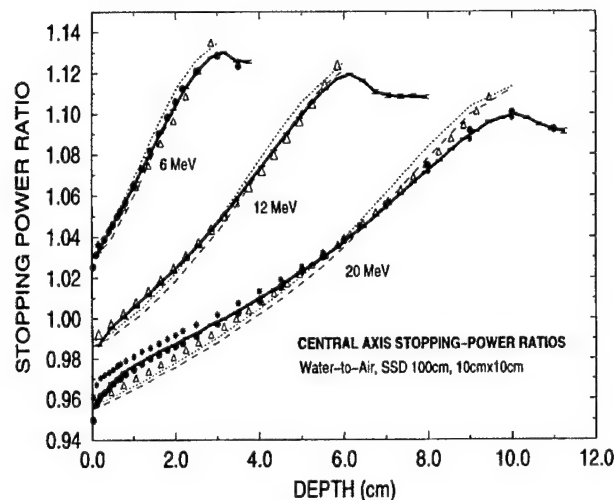


Figure 1. Central axis water-to-air stopping-power ratios for broad beams ($ECUT = AE = 521$ keV). Bold full curves are values obtained from this study for Varian Clinac 2100C 6, 12 and 20 MeV beams (R_{50} calculated 2.33, 4.97 and 8.29 cm respectively). Dotted curves are AAPM TG21 values obtained using $\bar{E}_0 = 2.33R_{50}$. Broken curves are AAPM TG21 values obtained using the Rogers and Bielajew procedure (1986). Triangles are values obtained using the universal equation by Burns *et al.* Full circles are values from NRC, Canada for Siemens KD2 6 and 21 MeV beams with R_{50} of 2.29 and 8.28 cm respectively. Stars are values for a Philips SL75-20 20-MeV beam with R_{50} of 8.06 cm from NRC, Canada.

4. Results and discussion

4.1. Broad electron beams

The dose distributions evaluated for the various beams studied were identical to those obtained previously with the original version of DOSXYZ. Broad-beam water-to-air stopping-power ratios calculated on central axis for 10×10 cm² open-appligator fields for 6, 12 and 20 MeV Varian Clinac-2100C electron beams in homogeneous water phantoms are compared in figure 1 with those obtained from other sources.

4.1.1. Comparison with TG21 stopping-power ratios. Water-to-air stopping-power ratios calculated for broad, monoenergetic (6, 12 or 20 MeV incident energy) and monodirectional beams in this study agreed within 0.1% (1σ) with the values tabulated in the TG21 report (AAPM 1983) except at the surface of the water phantoms. The latter were derived using an older version of the Monte Carlo code ETRAN that has subsequently been improved (Seltzer 1991).

For clinical beams the validity of various procedures to select stopping-power ratios for a given beam based on energy-range relationships has been recently summarized (IAEA 1997). Tabulated TG21 stopping-power ratios were chosen in this study based on either the TG21 ($\bar{E}_0 = 2.33R_{50}$) procedure or the procedure of Rogers and Bielajew (1986) recommended in TG25 (AAPM 1991) to determine the mean surface energy \bar{E}_0 from R_{50} (depth of 50% dose). The largest discrepancy between the calculated and tabulated values is observed for the 20 MeV beams using either procedure and is less than 1.3%. At d_{max} our calculated values are

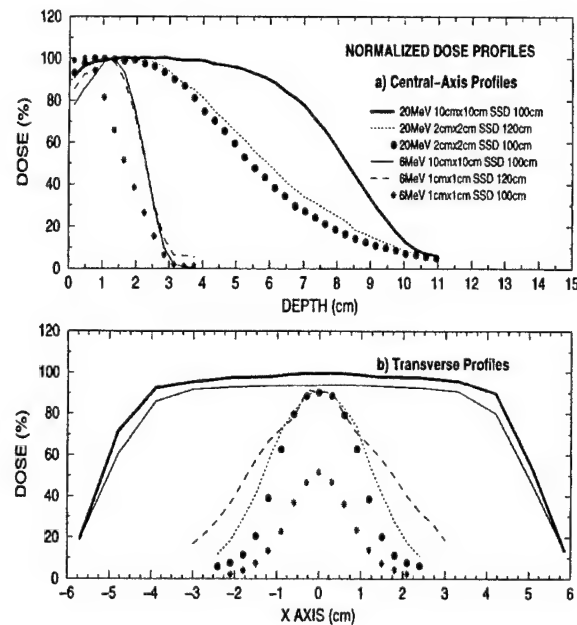


Figure 2. Normalized dose profiles for 6 and 20 MeV beams from Varian Clinac 2100C in a water phantom. Dose is normalized to the maximum value for each beam separately. (a) Central axis profiles and (b) transverse profiles at depth 1.5 cm for 6 MeV and 3 cm for 20 MeV beams. The field size is defined at an SSD of 100 cm.

lower than those of the AAPM TG21 procedure by approximately 0.3% for 6 MeV beams and higher than them by approximately 0.4% and 1.0% for the 12 and 20 MeV beams respectively. They are higher than those calculated using the Rogers and Bielajew (1986) procedure by approximately 0.5%, 0.7% and 1.1% for the 6, 12 and 20 MeV beams respectively.

There is an increase in discrepancies between stopping-power ratios of the monoenergetic beams of TG21 and those of the clinical beams with an increase in energy. Both indirect and direct electrons (which either intersect or do not intersect the collimation devices of the linear accelerator respectively) exist in realistic beams. The higher the nominal energy of the beam, the greater is the absolute difference in mean energy between the indirect and direct electrons (Kapur *et al* 1998). Since water-to-air stopping-power ratios decrease monotonically with an increase in energy, the differences in the stopping-power ratios for the indirect and direct electrons is larger for the 20 MeV beams than it is for the 6 MeV beams. The AAPM TG21 protocol does not consider indirect electrons in the calculation of stopping-power ratios. This explains why our calculated stopping-power ratios exceed the AAPM TG21 values at shallow depths and also why the differences are larger for the higher energy beams. The differences at the surface as explained elsewhere (Malamut *et al* 1991) may be related to the assumption of secondary charged particle equilibrium in the calculations of Berger *et al* (AAPM 1983).

Realistic beams also consist of electrons with energy exceeding \bar{E}_0 and contaminant photons. Thus at deeper depths they are of higher mean energy than the monoenergetic beams. Photon contamination, not considered in the AAPM protocol, plays an increasing role at higher energies (Andreo and Fransson 1989, Klevenhagen 1994, Ding *et al* 1995). This explains why our calculated values are lower than the AAPM values at greater depths.

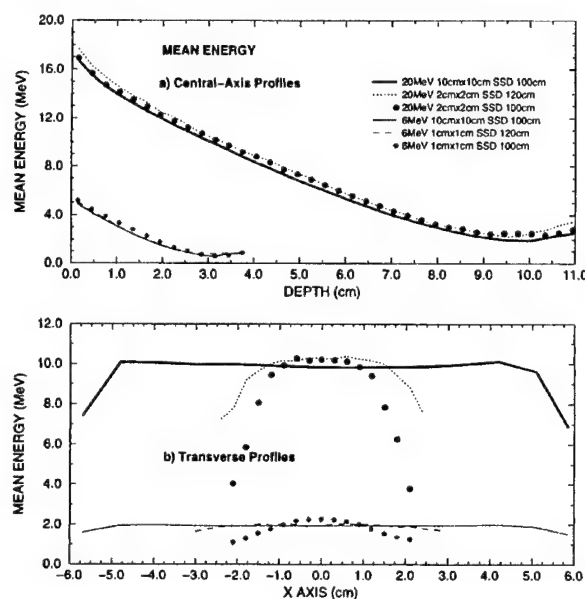


Figure 3. Mean energy profiles (ECUT = AE = 521 keV) for 6 and 20 MeV beams from Varian Clinac 2100C in a water phantom. (a) Central axis profiles and (b) transverse profiles at depth 1.5 cm for 6 MeV and 3 cm for 20 MeV beams. The field size is defined at an SSD of 100 cm.

4.1.2. Comparison with stopping-power ratios from the universal fitting equation of Burns *et al.* The universal fitting equation of Burns *et al* (1996) relates the stopping-power ratios at depth ' z ' for water-to-air to R_{50} . It was based on a fit of the data by Ding *et al* (1995) calculated for 24 realistic clinical beams (both scanned and scattered) which in the range of $0.02 < z/R_{50} < 1.1$ showed a maximum deviation of 1% from the actual data. The maximum deviation is 1.7% if depths upto $1.2R_{50}$ are considered. The deviations of our calculated stopping-power ratios can be seen to be less than the maximum deviation reported by Burns *et al* (1996) based on their universal fitting equation. The data for 6 and 12 MeV agreed in the worst case to within 0.6%, and for 20 MeV to within 0.8% in the range $0.02 < z/R_{50} < 1.1$.

4.1.3. Comparison with stopping-power ratios at a reference depth (Burns *et al.*) The stopping-power ratio at a reference depth given by $d_{\text{ref}} = 0.6R_{50} - 0.1$ was related to R_{50} with another fitting equation by Burns *et al* (1996). The root-mean-square deviation of their data about this fit for the 24 beams they studied was 0.16% and the maximum deviation was 0.26%.

The stopping-power ratios calculated in this study for the 6, 12 and 20 MeV beams at the reference depth defined by Burns *et al* (1996) agreed to within 0.14%, 0.10% and 0.20% respectively with the values obtained from their fitting equation.

4.1.4. Comparison with stopping-power ratios calculated for other scatter foil accelerators. The agreement between our calculations of stopping-power ratios for Varian Clinac 2100C beams and those for beams from a Siemens KD2 machine with very similar R_{50} values (Ding *et al* 1995) is about 0.2%. The difference in R_{50} for the 6 MeV beams is 0.04 cm. For

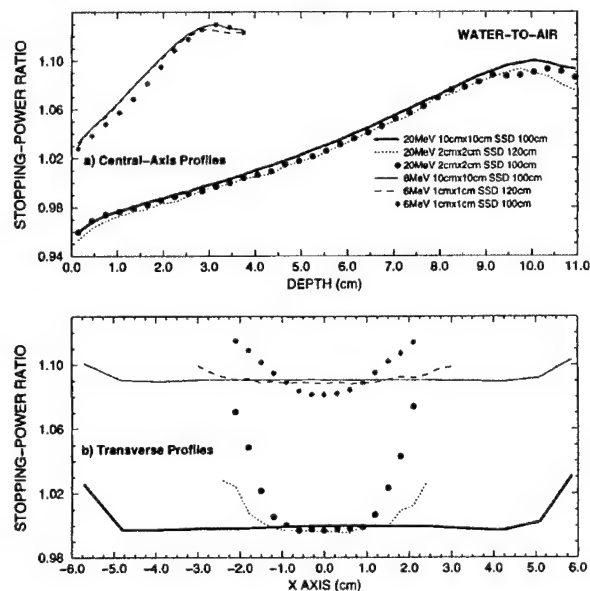


Figure 4. Water-to-air stopping-power ratios ($ECUT = AE = 521$ keV) for 6 and 20 MeV beams from Varian Clinac 2100C in a water phantom. (a) Central axis profiles and (b) transverse profiles at depth 1.5 cm for 6 MeV and 3 cm for 20 MeV beams. The field size is defined at an SSD of 100 cm.

the Varian 20 MeV beam and the Siemens 21 MeV beam, the difference in R_{50} is 0.01 cm. The 20 MeV beam from a Philips SL75-20 accelerator (Ding *et al* 1995) has an R_{50} of 8.06 cm that is 0.23 cm lower than that from the Varian Clinac 2100C 20 MeV beam. Despite this difference, the stopping-power ratios agree to within 1% for shallow depths and 0.2% for greater depths. The discrepancy at the shallow depths may be attributed partially to the differences in spectra of the indirect particles from these machines (Ding *et al* 1995, Ding and Rogers 1995).

4.2. Homogeneous water phantoms

In figure 2 the dose profiles from various beams of 6 and 20 MeV nominal energy are plotted for the central axis and transverse directions. The dose is normalized to the global-maximum dose value in each phantom respectively. The transverse dose profiles are shown for depths of 1.5 and 3 cm for the 6 and 20 MeV beams respectively. In figure 3 the mean kinetic energy of the charged particles in phantom is shown for the same beams along the central axis and transverse directions at the same depths. The mean energy variations as shown in this figure qualitatively explain the trends in the stopping-power ratios for the same beams that are shown in figures 4 through 6 for water-to-air, water-to-silicon and water-to-film-emulsion respectively. The relative importance of stopping-power ratio variations can be assessed with the help of figure 2. The variations for detector materials other than the ones shown in figures 4–6 were all within 1% or much less, with the exception of the silver halides used in photographic-film materials (ICRU 1984b). Calculated broad-beam water-to-detector stopping-power ratios for the clinical beams are listed in tables 1 and 2 for various detectors for 6 and 20 MeV electron beams for two values of AE, namely 521 and 611 keV. The stopping-power ratios are sensitive

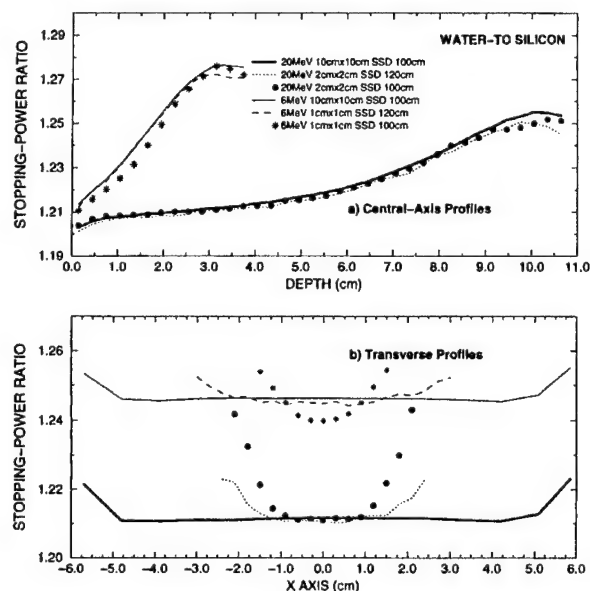


Figure 5. Water-to-silicon stopping-power ratios (ECUT = AE = 521 keV) for 6 and 20 MeV beams from Varian Clinac 2100C in a water phantom. (a) Central axis profiles and (b) transverse profiles at depth 1.5 cm for 6 MeV and 3 cm for 20 MeV beams. The field size is defined at an SSD of 100 cm.

to changes in AE for the photographic materials (up to 5.7% for silver halides and 4.2% for film emulsion) and silicon (up to 2.2%) whereas for the other detector materials studied the differences are within 0.6% for this range of AE values.

4.2.1. Narrow electron beams: variations along the central axis. The observed stopping-power ratio variations are consistent with the mean energy variations seen in figure 3. The narrow beams at a nominal SSD of 100 cm exhibit a consistently higher mean energy on the central axis for both energies compared with the broad beams. At extended SSD, the 20 MeV narrow beam electrons are seen to be more energetic than those at 100 cm; a trend which is reversed for the 6 MeV beam. Consequently the stopping-power ratios vary in a similar manner from the broad-beam data.

The largest variations of the stopping-power ratios studied are seen for water-to-air stopping-power ratios for narrow beams. The stopping-power ratios are within 1% of the broad-beam data within the practical range of the beams. At d_{\max} for the narrow beams, the variation is within 0.5%. For water-to-film-emulsion or the silver halides in photographic films, the variations from corresponding broad-beam data are within 0.8% and 1% respectively. Water-to-silicon ratios are within 0.5% of their corresponding broad-beam data. Minimal variations (at most 0.1%) are seen for the stopping-power ratio variations from broad-beam data for water-to-LiF-100, graphite (the different densities simulated did not indicate any significant differences in the magnitude of these variations), ferrous sulfate dosimeter solution, PMMA and polystyrene. At 6 MeV, water-to-air stopping-power ratios for narrow beams incident at 30° were less than the AAPM TG21 values by up to 0.5%. While this has up to a 0.5% effect

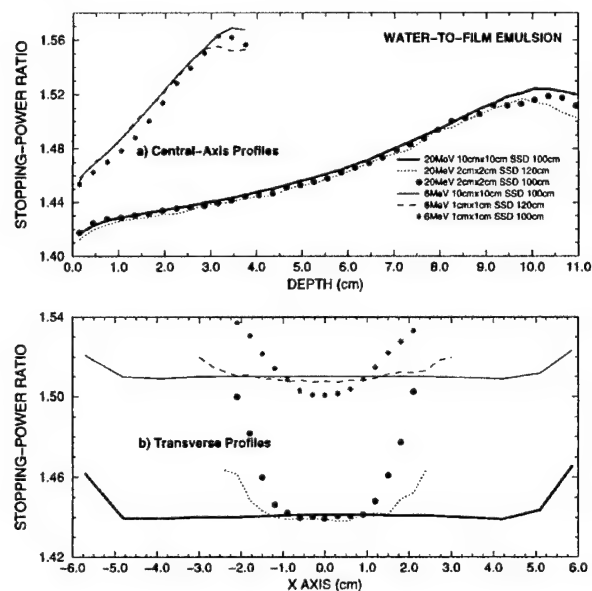


Figure 6. Water-to-film stopping-power ratios (ECUT = AE = 521 keV) for 6 and 20 MeV beams from Varian Clinac 2100C in a water phantom. (a) Central axis profiles and (b) transverse profiles at depth 1.5 cm for 6 MeV and 3 cm for 20 MeV beams. The field size is defined at an SSD of 100 cm.

on the output factor calculations, this angle represents an extreme condition and the effects of obliquity for angles larger than this one will be relatively less significant.

The water-to-air stopping-power ratios for the narrow beams incident normally are consistently lower than those for the realistic-broad beams by a maximum of approximately 1%. This implies that for depths shallower than that where the crossover occurs between the AAPM TG21 values and the broad-beam values (figure 1), they are also within 1.3% of the AAPM-recommended ratios and in fact agree to better than 1%. At greater depths, they are lower than the recommended ratios by up to 2% for the 20 MeV beams. However, the relative-dose is lower at these depths. These findings imply that relative dosimetry based on the use of AAPM-recommended stopping-power ratios will introduce minor discrepancies for such narrow fields.

For narrow monoenergetic beams, the IAEA findings (IAEA 1997) on water-to-air stopping-power ratio variations compared to broad beams are similar. However, due to the upward shift of d_{\max} in small fields (McGinley *et al* 1979, Hogstrom *et al* 1981, Sharma *et al* 1984, ICRU 1984a, AAPM 1991) the determination of output factors for such fields should take the depth-dependent variations of stopping-power ratios into account (Zhang *et al* 1998, Kapur *et al* 1998).

4.2.2. Narrow electron beams: variations in the transverse direction. The variations of the stopping-power ratios in the transverse direction were also found to be consistent with the variations of the mean energy. The increase in the air gap caused a reduction in the variation of the mean energy along the transverse direction for the narrow beams at both 6 and 20 MeV.

Table 1. Calculated stopping power ratios (ECUT = AE = 521 keV) on central axis for water-to-detector material for 6 MeV ($R_{50} = 2.33$ cm) 10×10 cm² Varian Clinac 2100C electron beams at SSD 100 cm. The quantities in parentheses are the stopping-power ratios evaluated using ECUT = AE = 611 keV. AE values correspond to different mean chord lengths of the detectors.

Depth (cm)	Air	Graphite	FeSO ₄	Silver halides	LiF-100	PMMA	Film emulsion	Silicon
0.15	1.032 (1.030)	1.137 (1.136)	1.005 (1.005)	1.598 (1.522)	1.248 (1.242)	1.032 (1.032)	1.457 (1.404)	1.213 (1.190)
0.45	1.044 (1.042)	1.138 (1.137)	1.005 (1.005)	1.613 (1.535)	1.248 (1.242)	1.032 (1.033)	1.468 (1.414)	1.219 (1.196)
0.75	1.055 (1.053)	1.139 (1.138)	1.005 (1.005)	1.626 (1.546)	1.248 (1.242)	1.033 (1.033)	1.477 (1.422)	1.224 (1.201)
1.05	1.067 (1.064)	1.140 (1.139)	1.005 (1.005)	1.640 (1.558)	1.247 (1.242)	1.033 (1.033)	1.487 (1.431)	1.231 (1.207)
1.35	1.078 (1.075)	1.141 (1.140)	1.005 (1.005)	1.655 (1.571)	1.247 (1.242)	1.033 (1.033)	1.498 (1.440)	1.238 (1.214)
1.65	1.091 (1.087)	1.141 (1.141)	1.005 (1.005)	1.673 (1.586)	1.247 (1.242)	1.033 (1.033)	1.510 (1.452)	1.246 (1.221)
1.95	1.102 (1.099)	1.141 (1.141)	1.005 (1.005)	1.690 (1.602)	1.247 (1.241)	1.033 (1.033)	1.522 (1.462)	1.254 (1.229)
2.25	1.112 (1.110)	1.140 (1.140)	1.005 (1.005)	1.706 (1.619)	1.247 (1.241)	1.032 (1.032)	1.533 (1.474)	1.261 (1.236)
2.55	1.121 (1.118)	1.138 (1.138)	1.005 (1.005)	1.724 (1.632)	1.247 (1.240)	1.031 (1.031)	1.544 (1.483)	1.268 (1.242)
2.85	1.128 (1.125)	1.135 (1.134)	1.005 (1.005)	1.740 (1.646)	1.246 (1.240)	1.030 (1.030)	1.554 (1.491)	1.273 (1.246)
3.15	1.130 (1.128)	1.131 (1.130)	1.005 (1.005)	1.755 (1.655)	1.245 (1.239)	1.028 (1.029)	1.563 (1.497)	1.276 (1.248)

With reference to the broad beams, this resulted in the stopping-power ratio variations for the narrow beams at extended SSD being smaller in comparison with those from the narrow beams at an SSD of 100 cm.

Compared with the water-to-air stopping-power ratio at central axis, at the same depth, the stopping-power ratio at an off-axis region where the dose was 10% of the maximum dose was found to be higher because the mean energy of electrons was lower in that region. This difference was more significant for the higher-energy beam. As discussed in section 4.1, the absolute difference in mean energy between the direct and indirect electrons is greater for the higher-energy beam (Kapur *et al* 1998). The off-axis regions contain a larger fraction of these indirect electrons than regions on the central axis. At greater depths in phantom, these differences in mean energy tend to decrease as shown by our calculations of mean energy at various depths, because the mean energy of electrons within the beam drops rapidly with depth. Thus at greater depths these variations in stopping-power ratios are reduced.

The transverse variations quantified this way were up to 4% for water-to-silicon, 6% for water-to-film-emulsion, 7% for silver halide materials used in photographic films and 10% for water-to-air. They were within 0.2% or less for the other materials studied.

4.3. Narrow electron beams: heterogeneous phantoms

The central-axis depth variation of the absolute dose per incident fluence in the layered-lung and bone phantoms (shown on the inserts in figure 7(a)) is plotted in figure 7(a) for the 3×3 cm² beams of 12 MeV electrons incident at an SSD of 100 cm. Also shown for comparison is the dose profile for a water phantom of the same dimensions, which is the reference phantom

Table 2. Calculated stopping power ratios (ECUT = AE = 521 keV) on central axis for water-to-detector material for 20 MeV ($R_{50} = 8.29$ cm) 10×10 cm² Varian Clinac 2100C electron beams at SSD 100 cm. The quantities in parentheses are the stopping-power ratios evaluated using ECUT = AE = 611 keV. AE values correspond to different mean chord lengths of the detectors.

Depth (cm)	Air	Graphite	FeSO ₄	Silver halides	LiF-100	PMMA	Film emulsion	Silicon
0.15	0.959 (0.956)	1.131 (1.130)	1.004 (1.004)	1.545 (1.472)	1.251 (1.245)	1.032 (1.032)	1.416 (1.365)	1.203 (1.180)
1.05	0.976 (0.972)	1.132 (1.131)	1.005 (1.004)	1.560 (1.484)	1.250 (1.244)	1.032 (1.032)	1.428 (1.374)	1.207 (1.184)
1.95	0.986 (0.985)	1.132 (1.132)	1.005 (1.004)	1.567 (1.494)	1.250 (1.244)	1.032 (1.032)	1.433 (1.382)	1.209 (1.186)
2.85	0.996 (0.993)	1.133 (1.132)	1.005 (1.004)	1.575 (1.499)	1.250 (1.243)	1.032 (1.032)	1.439 (1.386)	1.210 (1.187)
3.75	1.007 (1.004)	1.133 (1.133)	1.005 (1.004)	1.584 (1.508)	1.249 (1.243)	1.032 (1.032)	1.446 (1.392)	1.213 (1.190)
4.95	1.023 (1.019)	1.135 (1.134)	1.005 (1.004)	1.599 (1.519)	1.249 (1.242)	1.032 (1.032)	1.457 (1.401)	1.217 (1.192)
5.85	1.035 (1.031)	1.136 (1.135)	1.005 (1.004)	1.609 (1.528)	1.248 (1.242)	1.032 (1.032)	1.464 (1.408)	1.220 (1.196)
6.75	1.048 (1.046)	1.137 (1.136)	1.005 (1.004)	1.623 (1.543)	1.248 (1.242)	1.032 (1.032)	1.475 (1.420)	1.225 (1.202)
7.95	1.071 (1.068)	1.139 (1.138)	1.005 (1.005)	1.650 (1.567)	1.248 (1.242)	1.033 (1.033)	1.494 (1.437)	1.236 (1.211)
8.85	1.087 (1.083)	1.140 (1.139)	1.005 (1.005)	1.672 (1.584)	1.247 (1.241)	1.033 (1.033)	1.509 (1.449)	1.246 (1.220)
9.45	1.095 (1.092)	1.139 (1.139)	1.005 (1.005)	1.685 (1.596)	1.247 (1.241)	1.032 (1.032)	1.518 (1.458)	1.251 (1.226)
10.05	1.098 (1.097)	1.138 (1.138)	1.005 (1.005)	1.691 (1.606)	1.247 (1.240)	1.032 (1.032)	1.522 (1.464)	1.254 (1.230)

for this study. The dose plotted is that to the various phantom materials with no additional conversions. Figure 7(b) shows the variation of the mean kinetic energy along the central axes of the phantoms.

4.3.1. The stopping power ratio correction factors. The central-axis variations of the SPRCFs (equation (6)) at depth in these phantoms is plotted for various detector materials studied including air, graphite, silver halides, LiF-100, photographic emulsion and silicon in figure 8. The SPRCFs plotted are for the actual materials in the heterogeneous media. In both the phantoms, the SPRCFs in the water layers are close to unity for all the detectors throughout the water regions. Within the non-water regions, however, there are significant variations of the SPRCFs for the detector materials with depth.

In the bone-layered phantom, the SPRCFs within the bone region varied by about 2.5% for air, 2.2% for silver halides, 1.3% for silicon and less than 1% for graphite and LiF-100 as seen in figure 8(a). In the lung-layered phantom, the SPRCFs within the lung region varied by about 5% for air and silver halides, 3.5% for photographic emulsions, 3% for silicon and 1% for graphite and LiF-100 as seen in figure 8(b). For both phantoms, the variations of SPRCFs were within 1% in the transverse direction for all the detector materials studied. The mean energy-difference variations in this direction were not as significant as they were along the central axis.

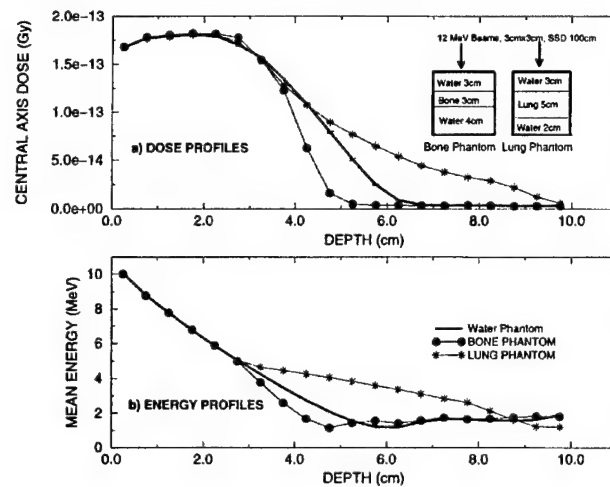


Figure 7. (a) Dose on central axis in water, layered-bone and layered-lung phantoms from 12 MeV beams of $3 \times 3 \text{ cm}^2$ at SSD of 100 cm. (b) Mean energy on central axis for the same phantoms.

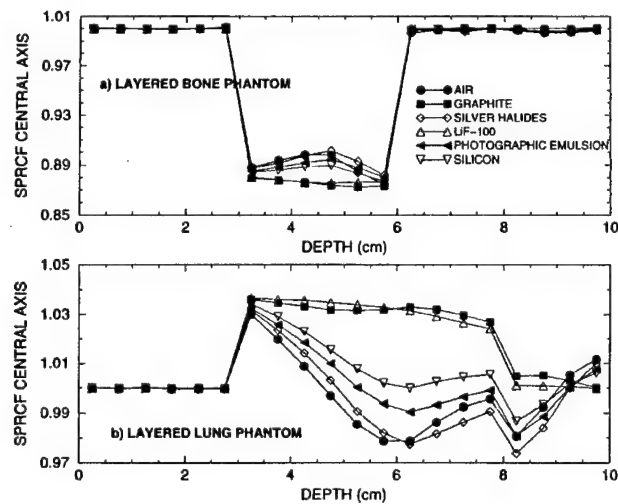


Figure 8. Stopping-power ratio correction factors (SPRCFs) for air, graphite, silver halides, LiF-100, photographic emulsion and silicon, for 12 MeV beams, $3 \times 3 \text{ cm}^2$ in size at SSD of 100 cm for (a) layered-bone and (b) layered-lung phantom using $ECUT = AE = 521 \text{ keV}$.

4.3.2. Effect of heterogeneities and detector materials. From these observations, there appears to be some correlation between the trends followed by the SPRCFs and the difference in mean energy between the heterogeneous phantoms and the water phantoms. In addition there appear to be detector-specific dependences. Based on the initial assumption that Spencer-Attix conditions hold (i.e. the detectors do not perturb the spectra of particles they receive), the difference in mean energies arises because of the difference in radiation transport of electrons

through the two phantoms. A detector placed at the same physical depths in the two phantoms will therefore be exposed to electron beams with these different mean energies. Consequently the response of the detector will be different in the two phantoms.

Because water is a standard reference material in dosimetry (AAPM 1983, IAEA 1987), we proceed to interpret the effects of both the heterogeneities and the detector materials on the SPRCFs by expressing the SPRCFs in terms of heterogeneity or detector-to-water stopping-power ratios, rearranging equation (6) as follows:

$$\begin{aligned} (\text{SPRCF})_{\text{water}}^{\text{het}} &= \frac{[(\frac{\bar{L}}{\rho}(E_h))_{\text{det}}^{\text{het}}]}{[(\frac{\bar{L}}{\rho}(E_w))_{\text{det}}^{\text{water}}]} = \left(\frac{\bar{L}}{\rho}(E_h)\right)_{\text{water}}^{\text{het}} \left[\left(\frac{\bar{L}}{\rho}(E_h)\right)_{\text{det}}^{\text{water}} \left(\frac{\bar{L}}{\rho}(E_w)\right)_{\text{water}}^{\text{det}} \right] \\ &= (\text{SPRCF}_{\text{HET}})(\text{SPRCF}_{\text{DET}}) \end{aligned} \quad (8)$$

where

$$\text{SPRCF}_{\text{HET}} = \left(\frac{\bar{L}}{\rho}(E_h)\right)_{\text{water}}^{\text{het}} \quad (9)$$

and

$$\text{SPRCF}_{\text{DET}} = \left[\left(\frac{\bar{L}}{\rho}(E_h)\right)_{\text{det}}^{\text{water}} \left(\frac{\bar{L}}{\rho}(E_w)\right)_{\text{water}}^{\text{det}} \right]. \quad (10)$$

In equations (8)–(10) the phantom specification by the superscript outside the square brackets has been replaced by the terms ' E_h ' and ' E_w ' which are the mean energies in the corresponding voxels in the heterogeneous and water phantoms respectively. The SPRCF has been expressed as a product of two terms—a heterogeneity term ' $\text{SPRCF}_{\text{HET}}$ ' and a detector term ' $\text{SPRCF}_{\text{DET}}$ '. The heterogeneity term relates the stopping-power ratios for the heterogeneities with respect to water for the mean energy E_h in the heterogeneous phantom. It is independent of the detectors. It reflects the differences in radiation transport at the mean energy E_h that would occur if the material were either water or the heterogeneity. It is useful to compute when the dose of interest is that to the actual material in the medium itself rather than dose to a small mass of water contained within the medium. Such would be the case for example when dose enhancement to bone needs to be evaluated (Prasad and Bassano 1989). The detector term reflects the variation in detector-to-water stopping-power ratios at energies E_h and E_w . The magnitude of this term depends on the difference between E_h and E_w through how much the water-to-detector stopping-power ratios change with energy in this range. Note that if the dose of interest (and hence the HCF of interest) were that to a small mass of water contained within the heterogeneous medium, $\text{SPRCF}_{\text{HET}}$ would be unity and SPRCF would be given by $\text{SPRCF}_{\text{DET}}$ exclusively. Thus $\text{SPRCF}_{\text{DET}}$ is the factor that may be associated with accumulated clinical experience (ICRU 1984a).

The implications of expressing the SPRCF this way are that we can get a qualitative feel for how they will vary for any given combination of phantoms and detectors based on our knowledge of how stopping-power ratios for water-to-various materials vary with energy. Consistent with the results in the previous section (figure 3 and table 1) the SPRCFs vary more significantly for air, film and silicon materials than the others studied, even if the variation of the $\text{SPRCF}_{\text{HET}}$ within the heterogeneous regions is small. Should there be significant variations for $\text{SPRCF}_{\text{HET}}$, the overall variations of SPRCF will be enhanced even further. This is because significant variations in $\text{SPRCF}_{\text{HET}}$ suggest significant differences in radiation transport between the heterogeneity and water which in turn suggests greater differences in mean energies between the two phantoms at specific depths. The greater the mean energy difference, the larger the variation of $\text{SPRCF}_{\text{DET}}$ and hence that of SPRCF. In the bone-layered phantom $\text{SPRCF}_{\text{HET}}$ varied by less than 1% within the bony region. The SPRCF variation was

about 2.5%. In the lung-layered phantom $\text{SPRCF}_{\text{HET}}$ varied by about 1.5% and the SPRCF variation increased to about 5%. Similar results were observed for the other detectors.

4.3.3. Evaluation of $\text{SPRCF}_{\text{DET}}$ at the 'effective' depth. While SPRCFs can be calculated using Monte Carlo techniques, the variety of phantom geometries possible and the extensive computations required per phantom geometry make these calculations cumbersome. For the simple layered geometries studied, the correlation of SPRCFs with mean energy variations between the heterogeneous and homogeneous phantoms seen in this study suggests an alternative approach to predict the SPRCFs at various depths along the central axis. This approach is to find for a depth of interest ' z ' in the heterogeneous phantom, a corresponding depth ' z_{eff} ' in the water phantom where the mean energies are the same or are very similar. Since the stopping-power ratios for water-to-detectors are known for various depths in water phantoms, this alternative procedure would involve evaluating $\text{SPRCF}_{\text{DET}}$ as the ratio of the water-to-detector stopping-power ratios evaluated at depths z_{eff} and z in a water phantom instead—an approach equivalent to that of a lookup-table.

The mean energy of charged particles at a given depth in phantom is affected by the loss of energy of these particles in traversing overlying materials and the directions from which they travel. The latter is governed primarily by scatter events. In this regard, several approaches have been suggested in the literature to obtain scaling factors such as detour factors to obtain z_{eff} (AAPM 1983, ICRU 1984a, Grosswendt and Roos 1989, Sorcini and Brahme 1994, Ding *et al* 1996, Fernandez-Varea *et al* 1996, IAEA 1997).

In this study a simple approach of depth scaling using the relative electron densities is attempted. While the relative electron density scaling method to determine the mean energy variations is not as accurate as other methods such as effective density scaling (AAPM 1983, Ding *et al* 1996), the 2–3% loss in accuracy (Fernandez-Varea *et al* 1996) is not expected to cause a significant loss of accuracy in the determination of stopping-power ratios. Tables 3 and 4 demonstrate this to be the case for the lung and bone phantoms studied along the central axis. In column 1, the actual physical depth z is listed. Column 2 lists the effective depth z_{eff} obtained by electron density scaling. Column 3 lists the mean energy in the heterogeneous phantoms at depth z . Column 4 lists the mean energy in the water phantoms at depth z . Column 5 lists the mean energy in the water phantom at depth z_{eff} . Comparing columns 3 and 5 indicates that the estimated mean energy is typically within 0.2 MeV of the calculated mean energy in the heterogeneous phantom. Columns 6, 7 and 8 list $\text{SPRCF}_{\text{DET}}$ as obtained using the stopping power ratios for water-to-air using the calculated data for $3 \times 3 \text{ cm}^2$, $10 \times 10 \text{ cm}^2$ or AAPM TG21 tables respectively and evaluated at z_{eff} and z . Finally column 9 lists the Monte Carlo calculated values of $\text{SPRCF}_{\text{DET}}$. It is clear from these tables that the relative electron density scaling method can accurately reproduce the Monte Carlo stopping-power ratio correction factors for such phantoms to within 0.4%. Furthermore, any of the available data for water-to-detector stopping power ratios—those calculated in this study for narrow realistic beams or broad realistic beams (tables 1 and 2) or AAPM TG21 (for water-to-air) beams can be used for this purpose.

5. Summary

Restricted mass collision stopping-power ratios calculated for water-to-air on the central axis of broad electron beams from the scatter-foil linear accelerator studied were within 1.3% of those reported by the TG21 protocol for broad monoenergetic, monodirectional beams and were consistent with the results of Ding *et al* to within 0.2%. These values for water-to-air on

Table 3. Calculated $\text{SPRCF}_{\text{DET}}$ on the central axis for air-filled detectors in the layered-lung phantom using a relative electron density scaling approach with stopping-power ratios from calculated narrow ($3 \times 3 \text{ cm}^2$), broad ($10 \times 10 \text{ cm}^2$) and TG21 beams.

Depth, z (cm)	Effective depth, z_{eff} (cm)	Mean energy at depth z in lung phantom (MeV)	Mean energy at depth z in water phantom (MeV)	Mean energy at depth z_{eff} in water phantom (MeV)	$\text{SPRCF}_{\text{DET}}$ using $3 \times 3 \text{ cm}^2$ L/ρ values	$\text{SPRCF}_{\text{DET}}$ using $10 \times 10 \text{ cm}^2$ L/ρ values	$\text{SPRCF}_{\text{DET}}$ using TG21 L/ρ values	$\text{SPRCF}_{\text{DET}}$ from Monte Carlo calculations
1.25	1.25	7.77	7.78	7.78	1.000	1.000	1.000	1.000
3.25	3.07	4.65	4.26	4.54	0.996	0.996	0.995	0.995
4.25	3.36	4.25	2.76	4.09	0.978	0.978	0.975	0.974
5.25	3.65	3.84	1.56	3.64	0.958	0.962	0.960	0.956
6.25	3.94	3.38	1.20	3.21	0.954	0.956	0.952	0.950
7.25	4.23	2.86	1.70	2.79	0.969	0.974	0.975	0.968
8.25	4.70	2.17	1.58	2.18	0.980	0.985		0.981

Table 4. Calculated $\text{SPRCF}_{\text{DET}}$ on the central axis for air-filled detectors in the layered-bone phantom using a relative electron density scaling approach with stopping-power ratios from calculated narrow ($3 \times 3 \text{ cm}^2$), broad ($10 \times 10 \text{ cm}^2$) and TG21 beams.

Depth, z (cm)	Effective depth, z_{eff} (cm)	Mean energy at depth z in lung phantom (MeV)	Mean energy at depth z in water phantom (MeV)	Mean energy at depth z_{eff} in water phantom (MeV)	$\text{SPRCF}_{\text{DET}}$ using $3 \times 3 \text{ cm}^2$ L/ρ values	$\text{SPRCF}_{\text{DET}}$ using $10 \times 10 \text{ cm}^2$ L/ρ values	$\text{SPRCF}_{\text{DET}}$ using TG21 L/ρ values	$\text{SPRCF}_{\text{DET}}$ from Monte Carlo calculations
1.25	1.25	7.80	7.79	7.79	1.000	1.000	1.000	1.000
3.25	3.46	3.79	4.54	3.93	1.005	1.005	1.006	1.010
4.25	5.29	1.69	4.09	1.54	1.029	1.025	1.025	1.025
5.25	7.12	1.44	3.64	1.65	1.005	1.006	1.007	1.009
6.25	8.74	1.43	3.20	1.57	0.994	0.990		0.997

the central axis of narrow electron beams from the scatter-foil linear accelerator studied, using commonly applied geometric conditions were up to 1% lower than the corresponding values for broad beams. They agreed to better than 1% with the AAPM TG21 values at depths shallower than the crossover depth between the AAPM TG21 values and the broad beam values (0.8, 3 and 6 cm for 6, 12 and 20 MeV beams respectively), and underestimated them by up to 2% for larger depths at 20 MeV. The use of the AAPM recommended stopping-power ratios for these beams thus introduces minor errors in relative central-axis dosimetry. The depth dependence of the stopping-power ratios should be incorporated for the calculation of output factors.

The central-axis restricted mass collision stopping-power ratios for narrow-to-broad fields agreed to within 0.1% for water-to-LiF-100, graphite, ferrous sulfate dosimeter solution, polystyrene and PMMA, 0.5% for water-to-silicon and 1% for water-to-photographic-film materials in the same geometric conditions. The stopping-power ratios varied by up to 10% for water-to-air, 7% for photographic silver halide materials and 3% for silicon compared to the central-axis values in the penumbral regions where the dose was 10% of the maximum dose in the phantom. The transverse variations were less than 0.2% for LiF-100, graphite, ferrous sulfate dosimeter solution, polystyrene and PMMA. The stopping-power ratios were sensitive to changes in AE from 521 to 611 keV for water-to-silver-halide, water-to-film-emulsion and water-to-silicon by up to 5.7, 4.2 and 2.2% respectively on the central axes of broad beams.

In heterogeneous phantoms, because radiation transport in general differs from that in water, and water-to-detector stopping-power ratios are energy dependent, the stopping-power ratio correction factors vary with energy for different detectors. The variation of the stopping-power ratio correction factors can be significant when radiation transport in the non-water regions differs significantly from that in water. Of all the detector materials studied, air showed the most marked variations, followed by photographic silver halides, photographic emulsions and silicon. A method for predicting the stopping-power ratio correction factors for simple layered phantoms based on the use of relative electron density scaling has been demonstrated to predict the Monte Carlo calculated values accurately to within 0.5%. This is applicable in the situation when the dose of interest is that to a small mass of water in the heterogeneous medium. Thus these values can be calculated for such phantoms using a simple lookup-table approach at the depth of interest.

Acknowledgments

This work was supported in part by the National Cancer Institute Grant CA43840 and the US Army Breast Cancer Research Program DOD BC971292. The authors would like to thank Dr Pedro Andreo of the International Atomic Energy Agency and Dr Dave Rogers of the National Research Council of Canada for valuable comments that significantly improved the quality of the manuscript. The authors also thank Drs Arthur Boyer, Ralph Nelson, Kenneth Kase and Gary Luxton of Stanford University for useful comments.

References

- AAPM (American Association of Physicists in Medicine) 1983 Task Group 21 Radiation Therapy Committee: a protocol for the determination of absorbed dose from high-energy photon and electron beams *Med. Phys.* **10** 741-71
- 1991 Clinical electron-beam dosimetry: report of AAPM Radiation Therapy Committee Task Group 25 *Med. Phys.* **18** 73-109
- Andreo P 1988 Stopping-power ratios for dosimetry *Monte Carlo Transport of Electrons and Photons* ed T M Jenkins, W R Nelson and A Rindi (New York: Plenum) pp 485-501
- Andreo P and Brahme A 1981 Mean energy in electron beams *Med. Phys.* **8** 682-7
- Andreo P, Brahme A, Nahum A E and Mattsson O 1989 Influence of energy and angular spread on stopping-power ratios for electron beams *Phys. Med. Biol.* **34** 751-68
- Andreo P and Fransson A 1989 Stopping-power ratios and their uncertainties for clinical electron beam dosimetry *Phys. Med. Biol.* **34** 1847-61
- Ayyangar K, Palta J R, Sweet J W and Suntharalingam N 1993 Experimental verification of a three-dimensional dose calculation algorithm using a specially designed heterogeneous phantom *Med. Phys.* **20** 325-9
- Berger M J 1987 Electron stopping powers for transport calculations *Monte Carlo Transport of Electrons and Photons* ed T M Jenkins, W R Nelson and A Rindi (New York: Plenum) pp 57-80
- Bielajew A F and Rogers D W O 1987 PRESTA: the parameter reduced electron-step algorithm for electron Monte Carlo Transport *Nucl. Instrum. Methods B* **18** 165-81
- Bragg W H 1912 *Studies in Radioactivity* (New York: Macmillan) p 94
- Bragg W H and Kleeman R 1905 On the alpha particles of radium and their loss of range in passing through various atoms and molecules *Phil. Mag.* **10** 318
- Brahme A 1977 Electron transport phenomena and absorbed dose distribution in therapeutic electron beams *Book of Abstracts XIV* (Rio de Janeiro: International Congress of Radiology) p 198
- Burch P R J 1955 Cavity ion chamber theory *Radiat. Res.* **3** 361-78
- 1957 Comment on recent cavity ionization theories *Radiat. Res.* **6** 79-84
- Burlin T E 1966 A general theory of cavity ionization *Br. J. Radiol.* **39** 727-34
- 1968 Cavity-chamber theory *Radiation Dosimetry* vol I ed F H Attix and W C Roesch (New York: Academic) pp 331-92

- Burlin T E, Snelling R J and Owen B 1969 The application of general cavity ionization theory to the dosimetry of electron fields *Proc. 2nd Symp. on Microdosimetry* pp 455-71
- Burns D T, Ding G X and Rogers D W O 1996 R_{50} as a beam quality specifier for selecting stopping-power ratios and reference depths for electron dosimetry *Med. Phys.* **23** 383-8
- Ding G X and Rogers D W O 1995 Energy, spectra, angular spread and dose distributions of electron beams from various accelerators used in radiotherapy *NRCC Report PIRS-0439* (Ottawa: National Research Council of Canada)
- Ding G X, Rogers D W O and Mackie T R 1995 Calculation of stopping-power ratios using realistic clinical electron beams *Med. Phys.* **22** 489-501
- 1996 Mean energy, energy-range relationships and depth-scaling factors for clinical electron beams *Med. Phys.* **23** 361-75
- Duane S, Bielajew A F and Rogers D W O 1989 Use of ICRU-37/NBS Collision stopping powers in the EGS4 system *NRCC Report PIRS-0177* (Ottawa: National Research Council of Canada)
- El-Khatib E, Antolak J and Scrimger J 1992 Evaluation of film and thermoluminescent dosimetry of high-energy electron beams in heterogeneous media *Med. Phys.* **19** 317-23
- El-Khatib E and Connors S 1992 Conversion of ionization measurements to radiation absorbed dose in non-water density material *Phys. Med. Biol.* **37** 2083-94
- Fernandez-Varea J M, Andreo P and Tabata T 1996 Detour factors in water and plastic phantoms and their use for range and depth-dose scaling in electron beam dosimetry *Phys. Med. Biol.* **41** 1119-39
- Gray L H 1936 An ionization method for the absolute measurement of γ -ray energy *Proc. R. Soc. A* **156** 578-96
- Grosswendt B and Roos M 1989 Electron beam absorption in solid and in water phantoms: depth scaling and energy-range relations *Phys. Med. Biol.* **34** 509-18
- Harder D 1965 Berechnung der energiedosis aus ionisationsmessungen bei sekundarelektronen-gleichgewicht *Symposium on High-Energy Electrons* ed A Zuppinger and G Poretti (Berlin: Springer)
- 1968 Einfluss der Vielfachstreuung von Elektronen auf die Ionisation in gas-gefüllten Hohlräumen *Biophysik* **5** 157-64
- Hogstrom K R, Mills M D and Almond P R 1981 Electron beam dose calculations *Phys. Med. Biol.* **26** 445-59
- Holt J G, Edelstein G R and Clark T E 1975 Energy dependence of the response of LiF TLD rods in high energy electron fields *Phys. Med. Biol.* **20** 559-70
- IAEA (International Atomic Energy Agency) 1987 Absorbed dose determination in photon and electron beams, an international code of practice for dosimetry *IAEA Technical Report Series 277* (Vienna: IAEA)
- 1997 The use of plane parallel ionization chambers in high energy electron and photon beams, an international code of practice for dosimetry *IAEA Technical Report Series 381* (Vienna: IAEA)
- ICRU 1984a Radiation dosimetry: electron beams with energies between 1 and 50 MeV *ICRU Report 35* (Bethesda, MD: ICRU)
- 1984b Stopping powers for electrons and positrons *ICRU Report 37* (Bethesda, MD: ICRU)
- Kapur A, Ma C-M, Mok E C, Findley D O and Boyer A L 1998 Monte Carlo calculations of electron beam output factors for a medical linear accelerator *Phys. Med. Biol.* **43** 3479-94
- Klevenhagen S C 1994 An algorithm to include the bremsstrahlung contamination in the determination of the absorbed dose in electron beams *Phys. Med. Biol.* **39** 1103-12
- Ma C-M, Mok E, Kapur A and Findley D 1997 Improvement of small-field electron beam dosimetry using Monte Carlo simulation *Proc. 12th Int. Conf. on the use of Computers in Radiation Therapy* ed D D Leavitt and G Starkschall (Madison, WI: Medical Physics Publishing) pp 159-62
- Ma C-M and Nahum A E 1994 Plane parallel chambers in electron beams: Monte Carlo findings on the perturbation factor *Proc. Int. Symp. on Measurement Assurance in Dosimetry* (Vienna: International Atomic Energy Agency) pp 481-93
- Ma C-M, Reckwerdt P, Holmes M, Rogers D W O, Geiser B and Walters B 1995 DOSXYZ users manual *NRCC Report PIRS-0509b*, (Ottawa: National Research Council of Canada)
- Mackie T R 1990 Applications of the Monte Carlo method in radiotherapy *The Dosimetry of Ionizing Radiation* vol III ed K R Kase, B E Bjarngard and F H Attix (New York: Academic) pp 541-620
- Malamut C, Rogers D W O and Bielajew A F 1991 Calculation of water/air stopping-power ratios using EGS4 with explicit treatment of electron-positron differences *Med. Phys.* **18** 1222-8
- McGinley P H, McLaren J R and Barnett B R 1979 Small electron beams in radiation therapy *Radiology* **131** 231-4
- Nahum A E 1978 Water/air mass stopping power ratios for megavoltage photon and electron beams *Phys. Med. Biol.* **23** 24-38
- 1987 Simulation of dosimeter response and interface effects *Monte Carlo Transport of Electrons and Photons* ed T M Jenkins, W R Nelson and A Rindi (New York: Plenum) pp 523-47
- Nelson W R, Hirayama H and Rogers D W O 1985 The EGS4 code system *SLAC Report 265* (Stanford, CA:

- Stanford Linear Accelerator Center)
- Nilsson B 1985 Analysis of quality characteristics of radiotherapeutic photon beams *PhD Thesis* University of Stockholm
- O'Brien 1977 Monte Carlo calculations of the energy response of lithium dosimeters to high energy electrons (<30 MeV) *Phys. Med. Biol.* **22** 836–51
- Ogunleye O T and Paliwal B R 1985 A proposed modification of cavity theory for electrons *Health Phys.* **49** 937–44
- Prasad S C, Ames T E, Howard T B, Bassano D A, Chung C T, King G A and Sagerman R H 1984 Dose enhancement in bone in electron beam therapy *Radiology* **151** 513–16
- Prasad S C and Bassano D A 1989 Comparison of absorbed dose in bone substitute material and water using ionization measurements *Med. Phys.* **16** 81–3
- Rogers D W O 1984 Low energy electron transport with EGS *Nucl. Instrum. Methods* **227** 535–48
- Rogers D W O and Bielajew A F 1986 Differences in electron depth dose curves calculated with EGS and ETRAN and improved energy range relationships *Med. Phys.* **13** 687–94
- 1990 Monte Carlo techniques of electron and photon transport for radiation dosimetry *The Dosimetry of Ionizing Radiation* vol III, ed K R Kase, B E Bjarnagard and F H Attix (New York: Academic) pp 427–539
- Rogers D W O, Faddegon B A, Ding G X, Ma C-M, Wei J and Mackie T R 1995 BEAM: A Monte Carlo code to simulate radiotherapy treatment units *Med. Phys.* **22** 503–24
- Seltzer S M 1991 Electron-photon Monte Carlo calculations: the ETRAN code *Appl. Radiat. Isot.* **42** 917–41
- Sharma S C, Wilson D L and Jose B 1984 Dosimetry of small fields for Therac 20 electron beams *Med. Phys.* **11** 697–702
- Shiu A S, Tung S, Hogstrom K R, Wong J W, Gerber R L, Harms W B and Purdy J A 1992 Verification data for electron beam dose algorithms *Med. Phys.* **19** 623–36
- Skaggs L S 1949 Depth dose of electrons from the betatron *Radiology* **53** 868–73
- Sorcini B B and Brahme A 1994 An accurate energy-range relationship for high-energy electron beams in arbitrary materials *Phys. Med. Biol.* **39** 795–11
- Spencer L V and Attix F H 1955 A theory of cavity ionization *Radiat. Res.* **3** 239–54
- Sternheimer R M, Seltzer S M and Berger M J 1982 Density effect for the ionization loss of charged particles in various substances *Phys. Rev. B* **26** 6067
- White D R, Martin R J and Darlison R 1977 Epoxy resin based tissue substitutes *Br. J. Radiol.* **50** 814–21
- White D R 1978 Tissue substitutes in experimental radiation physics *Med. Phys.* **5** 467–79
- Zhang G G, Rogers D W O, Cygler J E and Mackie T R 1998 Effects of changes in stopping-power ratios with field size on electron beam relative output factors *Med. Phys.* **25** 1711–16

Energy- and intensity-modulated electron beams for radiotherapy

C-M Ma, T Pawlicki, M C Lee, S B Jiang, J S Li, J Deng, B Yi, E Mok and A L Boyer

Department of Radiation Oncology, Stanford University School of Medicine, Stanford, CA 94305-5304, USA

E-mail: cma@reyes.stanford.edu

Received 5 January 2000, in final form 10 April 2000

Abstract. This work investigates the feasibility of optimizing energy- and intensity-modulated electron beams for radiation therapy. A multileaf collimator (MLC) specially designed for modulated electron radiotherapy (MERT) was investigated both experimentally and by Monte Carlo simulations. An inverse-planning system based on Monte Carlo dose calculations was developed to optimize electron beam energy and intensity to achieve dose conformity for target volumes near the surface. The results showed that an MLC with 5 mm leaf widths could produce complex field shapes for MERT. Electron intra- and inter-leaf leakage had negligible effects on the dose distributions delivered with the MLC, even at shallow depths. Focused leaf ends reduced the electron scattering contributions to the dose compared with straight leaf ends. As anticipated, moving the MLC position toward the patient surface reduced the penumbra significantly. There were significant differences in the beamlet distributions calculated by an analytic 3-D pencil beam algorithm and the Monte Carlo method. The Monte Carlo calculated beamlet distributions were essential to the accuracy of the MERT dose distribution in cases involving large air gaps, oblique incidence and heterogeneous treatment targets (at the tissue–bone and bone–lung interfaces). To demonstrate the potential of MERT for target dose coverage and normal tissue sparing for treatment of superficial targets, treatment plans for a hypothetical treatment were compared using photon beams and MERT.

(Some figures in this article are in colour only in the electronic version; see www.iop.org)

1. Introduction

Photon beams have been an effective modality for breast cancer treatment in radiation therapy. Although such conventional treatment with tangential photon fields has been successful, the following two problems (or potential areas of improvement) remain:

- (a) The inclusion of the lung and other normal tissues, and sometimes of a small volume of the heart, in the high-dose volume due to tumour location, patient size or in the case of chest-wall treatments.
- (b) High exit or scatter dose to the normal structures such as the lung, the heart and the contralateral breast.

Advances in the state of the art of computer-controlled medical linear accelerators have recently become available that, along with newly developed treatment planning techniques, may provide significant improvements in the delivery and control of external beam radiation through beam-intensity modulation (Boesecke *et al* 1988, Brahme 1988, Convery and

Rosenbloom 1992, Leibel *et al* 1992, Webb 1992, 1997, LoSasso *et al* 1993, Powlis *et al* 1993, Chui *et al* 1994, Mageras *et al* 1994, Brewster *et al* 1995, Fraass *et al* 1995, Kutcher *et al* 1995, Mackie *et al* 1995, McShan *et al* 1995, Ling *et al* 1996, Boyer *et al* 1997). It is expected that using photon IMRT, the problem (a) above may be significantly improved but (b) may become more serious as treatment time increases with the number of fields/segments used (increased leakage or scattering dose). Using the modulated electron radiotherapy (MERT) technique (Lief *et al* 1996, Hyödynmaa *et al* 1996, Zackrisson and Karlsson 1996, Åsell *et al* 1997, Ebert and Hoban 1997, Karlsson *et al* 1998, 1999), on the other hand, problem (a) may also be significantly improved and problem (b) may almost be eliminated due to the nature of the electron beams.

In the optimization process of MERT, dose conformity along the beam direction can be achieved by modulating the electron incident energy, making use of the sharp dose fall-off feature. A drawback is its large penumbra at large depths. Traditionally, electron beams are shaped using a cutout (or blocks) and beam penetration/intensity may be modified using a bolus. However, it is time-consuming to make such beam modifiers and the treatment time would be significantly increased if such beam modifiers are used for MERT. Efforts have been made to use computer-controlled MLC for electron beam modulation. The recent results by Karlsson *et al* (1999) showed that by replacing the air in the treatment head with a low-cost, custom-made helium balloon, the beam penumbral width (20/80) was reduced from 18 to 11 mm at 80 cm SSD. The beam characteristics are affected by the position of the MLC. However, by replacing the air between the MLC and the patient with a helium balloon, the beam penumbra become almost the same as that achieved by electron beam-shaping with an electron applicator that extends to the patient skin surface (Karlsson *et al* 1999). This means that many of the techniques so far developed with computer-controlled MLC and our experience with MLC photon beam modulation can be adopted for use with MERT.

The calculation of dose distributions for electron beam radiotherapy planning is challenging because electron scattering is strongly affected by changes in density and composition in the patients. The 3D pencil beam algorithm (Hogstrom *et al* 1981) is a fast analytical algorithm which has been adopted by most treatment planning systems. However, it has limitations with small irregular electron fields and in the presence of inhomogeneities (Cygler *et al* 1987, Bielajew *et al* 1987, Mah *et al* 1989, Mackie *et al* 1994, Ma *et al* 1999). The Monte Carlo simulation has been demonstrated to be a viable option for such complex situations, and also the only way to take into account back-scattering from denser materials in a patient (e.g. bone or metal inserts) (Shortt *et al* 1986, Cygler *et al* 1987, Mackie *et al* 1994, Kawrokwaw *et al* 1996, Mohan 1997, Kapur 1999, Ma *et al* 1999). The EGS4/BEAM system was developed for the simulation of radiotherapy beams from various radiotherapy treatment units, such medical accelerators (Rogers *et al* 1995). Excellent agreement (1–3%) has been achieved between the Monte Carlo dose distributions calculated using the simulated particle phase-space data and measurements (Rogers *et al* 1995, Kapur *et al* 1998, Zhang *et al* 1999, Ma *et al* 1999). We have installed a Monte Carlo patient dose calculation tool on a clinical treatment planning system (Ma *et al* 1999) and used Monte Carlo for treatment planning and dose delivery validation. This has reduced the uncertainty of the accelerator output for small irregular field electron beams from up to 10% to about 3% (Ma *et al* 1997, Kapur *et al* 1998).

Conformal radiotherapy was initially used to limit the normal tissue dose by conforming the treatment field to the beam's-eye-view projection of the target volume (Takahashi 1965). For photon beams, the MLC was used to collimate the fields and later to modulate the beam intensity in the field (Boesecke *et al* 1988, Brahme 1988, Convery and Rosenbloom 1992, Leibel *et al* 1992, Webb 1992, 1997, LoSasso *et al* 1993, Powlis *et al* 1993, Chui *et al* 1994, Mageras *et al* 1994, Brewster *et al* 1995, Kutcher *et al* 1995, Mackie *et al* 1995,

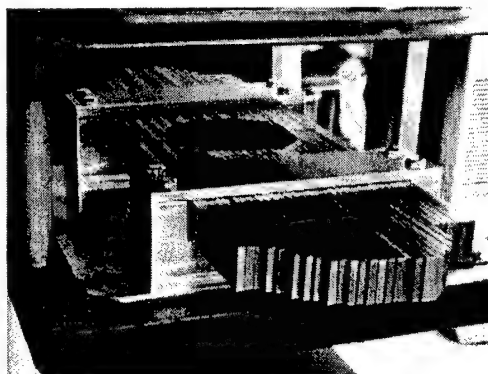


Figure 1. A prototype of an electron MLC mounted on the bottom scraper of a 25 cm \times 25 cm applicator on a Varian Clinac 2100C accelerator. The MLC has 30 pairs of steel leaves and the leaf positions are fixed by the tightening screws.

McShan *et al* 1995, Ling *et al* 1996, Boyer *et al* 1997). There have been a few studies on electron conformal therapy. Tailoring dose distributions using electron beams requires substantial beam manipulation, due to their scattering characteristics. Such manipulation is already possible with radiation sources such as microtrons where preferential energy selection and magnetically scanned pencil beams are possible (Lief *et al* 1996). Both intensity- and energy/intensity-modulated electron beams have been investigated to conform the dose to the target near the surface (Lief *et al* 1996, Hyödynmaa *et al* 1996, Zackrisson and Karlsson 1996, Ebert and Hoban 1997, Karlsson *et al* 1998). More recent work has studied the combination of photon IMRT and MERT for targets at greater depth (Karlsson *et al* 1999). Using the helium-balloon technique together with a computer-controlled MLC, it may be possible to deliver a set of intensity-modulated beams with different energies and incident angles.

In this work, we investigate the feasibility of optimizing energy- and intensity-modulated electron beams for radiotherapy treatment. We report here our Monte Carlo studies of a multileaf collimator specially designed for MERT and some preliminary experimental results. We also report on the dose calculation algorithms and their effects on treatment plan optimization for MERT. We will discuss the differences in the beam characteristics between a photon MLC and an electron MLC. We will compare the dose distributions between a conventional tangential photon treatment plan and a MERT treatment plan for a hypothetical breast treatment to demonstrate the potential of MERT for target dose coverage and normal tissue sparing.

2. Materials and method

2.1. The prototype electron MLC

We have developed a prototype manual-driven electron MLC for the beam delivery for MERT. As shown in figure 1, the electron MLC consists of 30 steel leaf pairs, which were made from the off-the-shelf steel bars for convenience and cost-effectiveness. Each leaf is 0.476 cm wide, 20 cm long and 2.54 cm thick with straight edges and ends. The leaves were mounted on a steel frame, which can be attached to the bottom scraper of a 25 cm \times 25 cm electron applicator on a Varian Clinac 2100C (Varian Oncology Systems, Palo Alto, CA). The leaves can slide in

the steel frame and the leaf positions can be easily set using a pre-cut cardboard for a beam segment. The field shape is maintained by tightening the screws from the side. The largest radiation field available using the electron MLC was 15.7 cm \times 15.7 cm projected at 100 cm source-surface distance (SSD).

Because of the existing electronic device for inserting the electron cutout, the leaves could not be placed at the last scraper level without modifying the existing applicator geometry. Instead, the steel frame was inserted using the electron cutout mount and the leaves were placed immediately above the last scraper. This resulted in a slightly greater air gap (7 cm) between the bottom of the electron MLC leaves and the phantom surface (assuming a 97 cm SSD) compared with that of an electron cutout (5 cm for a 100 cm SSD). The projected leaf width for a 5 cm air gap is 0.5 cm, while for a 7 cm air gap the projected leaf width is 0.51 cm (e.g. for the current configuration at 97 cm SSD). Further modifications are needed to the electron applicator geometry in order to lower the electron MLC leaves. The ideal location for the MLC leaves is the last scraper since electron cutouts will no longer be needed if an electron MLC is in place.

Film measurement was performed to study the characteristics of the electron beams collimated by the electron MLC. The film was calibrated following the AAPM TG-25 recommendations (AAPM 1991) and the exposures were taken by placing film at different depths in a solid water phantom. The film was scanned using a film scanner which has a spatial resolution of about 0.15 cm.

2.2. The Monte Carlo beam simulation

We have used the EGS4 (Nelson *et al* 1985) user code BEAM for the accelerator head simulation. Detailed descriptions of the software can be found in Rogers *et al* (1995). A detailed description of the clinical implementation of the Monte Carlo method at the Stanford Medical Center was given in a previous publication (Ma *et al* 1999).

For this work, we have used the previously simulated Monte Carlo beam data for 6, 12 and 20 MeV electron beams from a Varian Clinac 2100C linear accelerator and for 6 MV photon beams from a 2300CD accelerator (Varian Oncology Systems, Palo Alto, CA). The dimensions and materials for the accelerator components were incorporated according to the manufacturer's specifications. Electron beams emerging from the vacuum exit window were assumed to be monoenergetic and monodirectional with a beam radius of 0.1–0.2 cm (Kapur *et al* 1998). The energy cutoffs for electron transport in the accelerator simulation (ECUT and AE) were 700 keV (kinetic + rest mass) and for photon transport (PCUT and AP) 10 keV. The electron transport step length was confined such that the maximum fractional energy loss per electron step is 4% (i.e. ESTEPE = 0.04). The ICRU recommended compositions and stopping power values were used for the materials in the accelerator simulations (ICRU 1984). The phase-space data were scored at a plane either immediately above the photon MLC or above the lowest scraper. The number of particles was about 2–30 million in an electron beam file and about 50 million in a photon file.

Field shaping by the photon MLC or electron MLC was further simulated using the BEAM component module MLC. MLC could simulate either straight or 'double focused' leaf edges and ends. In this work, we have simulated electron beams collimated by a photon MLC with both straight and double focused MLC leaf shapes. The leaves were 7.5 cm thick and made of tungsten. The leaf center was 49 cm from the isocentre. The intervening air in the accelerator and between the MLC and the isocentre was in some cases replaced with helium to investigate the effect of electron scattering in the air. In the simulations of the electron beams collimated by an electron MLC, the leaves were placed on the bottom scraper of a 25 cm \times 25 cm applicator

with a 7 cm air gap between the bottom surface of the MLC and the isocentre. Tungsten leaves of 1.5 cm thickness with straight edges and ends were used in all the simulations and the phase space data were used in the subsequent dose calculations except for the leaf leakage study where different leaf materials and thicknesses were investigated for the electron MLC.

2.3. The Monte Carlo dose calculation

The EGS4 user code, MCDOSE (Ma *et al* 1999), was used in this work for the dose calculations. MCDOSE was designed for dose calculations in a 3D rectilinear voxel geometry. Voxel dimensions were completely variable in all three directions. Every voxel (volume element) could be assigned to a different material. The cross-section data for the materials used were available in a pre-processed PEGS4 cross-section data file. The mass density of the material in a MCDOSE calculation was varied based on the patient's CT data although the density effect corrections for the stopping powers of the material remain unchanged (Ma *et al* 1999). The voxel dimensions and materials were defined in a MCDOSE input file together with the transport parameters such as the energy cutoffs (ECUT and PCUT), the maximum fractional energy loss per electron step (ESTEPE), and the parameters required by PRESTA (Bielajew and Rogers 1987). Several variance reduction techniques have been implemented in the MCDOSE code to improve the calculation efficiency. These include photon interaction forcing, particle splitting, Russian roulette, electron range rejection and region rejection, particle track displacement and rotation, and correlated sampling. Detailed descriptions of these techniques have been given elsewhere (Rogers and Bielajew 1990, Ma and Nahum 1993, Rogers *et al* 1995, Kawrakow *et al* 1996, Keall and Hoban 1996, Ma *et al* 1999).

For patient dose calculations, the simulation phantom was built from the patient's CT data with up to $128 \times 128 \times 128$ voxels (uniform in any dimension). The side of a voxel varied from 0.2 to 0.4 cm. A separate program was developed to convert the patient's CT data from the FOCUS treatment planning system (Computerized Medical Systems, St Louis, MO) to desired dimensions, material types and densities. The organ contours were also obtained for dose calculation and analysis. The phase-space data obtained from a BEAM simulation were used as a source input with variable source positions and beam incident angles. To simulate the dose distribution of a finite size beamlet used by the inverse planning process, particles were transported to the MLC plane and only those within the beamlet area ($= 1 \text{ cm} \times 1 \text{ cm}$ projected at 100 cm SSD) were allowed to go through. This ignored the bremsstrahlung photon leakage and electron scattering by the leaf ends in the optimization process (the effect was corrected in the final dose calculation, as discussed below). After optimization, a leaf sequence was generated using a modified 'step and shoot' algorithm based on our early work (Ma *et al* 1998). The final MERT dose distribution was computed based on an intensity map (a 2D distribution of particle weighting factors) reconstructed from the leaf sequence. The bremsstrahlung leaf leakage effect was included in the intensity map using the leaf sequence and pre-calculated leaf leakage data for 1.5 cm thick tungsten leaves. MCDOSE produced data files that contained geometry specifications such as the number of voxels in all the three directions and their boundaries as well as the dose values and the associated (1σ) statistical uncertainties in the individual voxels and organs (structures). The EGS4 transport parameters were ECUT = AE = 700 keV, PCUT = AP = 10 keV and ESTEPE = 0.04. The number of particle histories simulated ranged from 2 million to 30 million for a MERT treatment. The 1σ statistical uncertainty in the dose was generally 2% or smaller of the D_{max} value. The CPU time required for a MERT simulation was about 1–3 h on a Pentium III 450 MHz PC with the variance reduction option switched on.

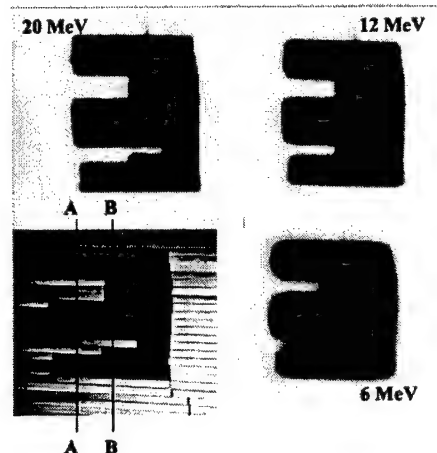


Figure 2. Beam intensity distributions measured by film on the surface of a solid water phantom for 6, 12 and 20 MeV electrons. The MLC leaf positions for the electron fields are also shown (bottom left).

2.4. The optimization process

The treatment planning optimization system used in this work is a home-developed system based on the work by Jiang (1998). First, the planner inputs the patient geometry and defines the treatment setup, such as the beam energy, number and orientations of beams, etc. The target volume and the critical structures are defined by the clinician. A reference monitor unit is assigned to each open rectangular beam and the dose deposition coefficients, which are defined as the dose contribution from a beamlet to a point, are calculated using the MCDOSE code.

Second, using the calculated dose deposition coefficients as input, the optimal intensity profile for each beam is achieved using a gradient method to minimize the objective function. For the target area, a quadratic form of objective function is specified. In addition, two target dose-uniformity constraints are used to ensure a uniform target dose distribution and to distinguish the clinical importance of cold and hot spots. For the critical structures, maximum-dose constraint and several levels of dose-volume constraints are assigned to each structure. For each objective function and constraint, an importance weight relative to the target objective function is assigned. All the constraints are mathematically transformed to the penalty functions of quadratic forms. The augmented objective function, which should be minimized, is a combination of the original objective functions and all penalty functions. The results of the optimization process are the intensity profiles for the individual fields (different incident energies and gantry angles). The same optimizer has been used for photon beam optimization with the Monte Carlo method and a finite-size pencil beam algorithm (Jiang 1998, Jiang *et al* 1999, Pawlicki *et al* 1999).

3. Results and discussion

3.1. Characteristics of electron beams collimated by an electron MLC

Figure 2 shows the electron fields collimated by the prototype electron MLC for 6, 12 and 20 MeV electron beams on a Varian Clinac 2100C machine. For convenience, a photo showing

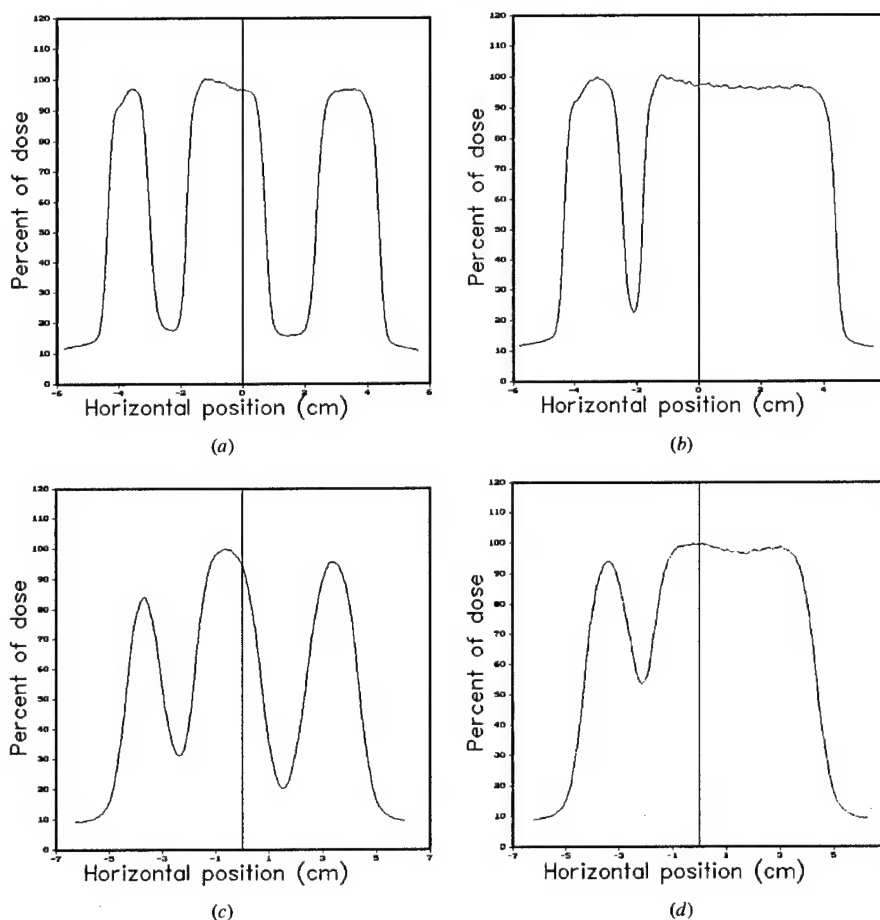


Figure 3. Beam profiles measured by film on the surface of a solid water phantom for the 6 MeV and 20 MeV electron fields shown in figure 2: (a) 20 MeV along A-A; (b) 20 MeV along B-B; (c) 6 MeV along A-A; (d) 6 MeV along B-B.

the MLC leaf positions for the field shape is also included in figure 2. Figure 2 shows the film measurement at the surface of a solid water phantom (97 cm SSD) for 6, 12 and 20 MeV electron beams. Figure 3 shows the measured profiles on the phantom surface along A-A and B-B for the 6 MeV and 20 MeV electron fields shown in figure 2. Figure 4 shows the beam profiles at 2 cm depth in the solid water phantom. It can be seen that for a 20 MeV electron beam, 0.5 cm leaf shapes are still distinguishable on the surface but become very blurred at 2 cm depth. For a 6 MeV electron beam, however, the effect of electron scattering becomes so severe that a leaf width smaller than 1.0 cm will not result in any improvement in the spatial resolution. However, a small leaf width may have the advantage of defining the field more precisely in the direction perpendicular to the leaves.

Based on these experimental results, we further performed Monte Carlo simulations of electron fields collimated by 1 cm wide leaves to study the effect of material type and

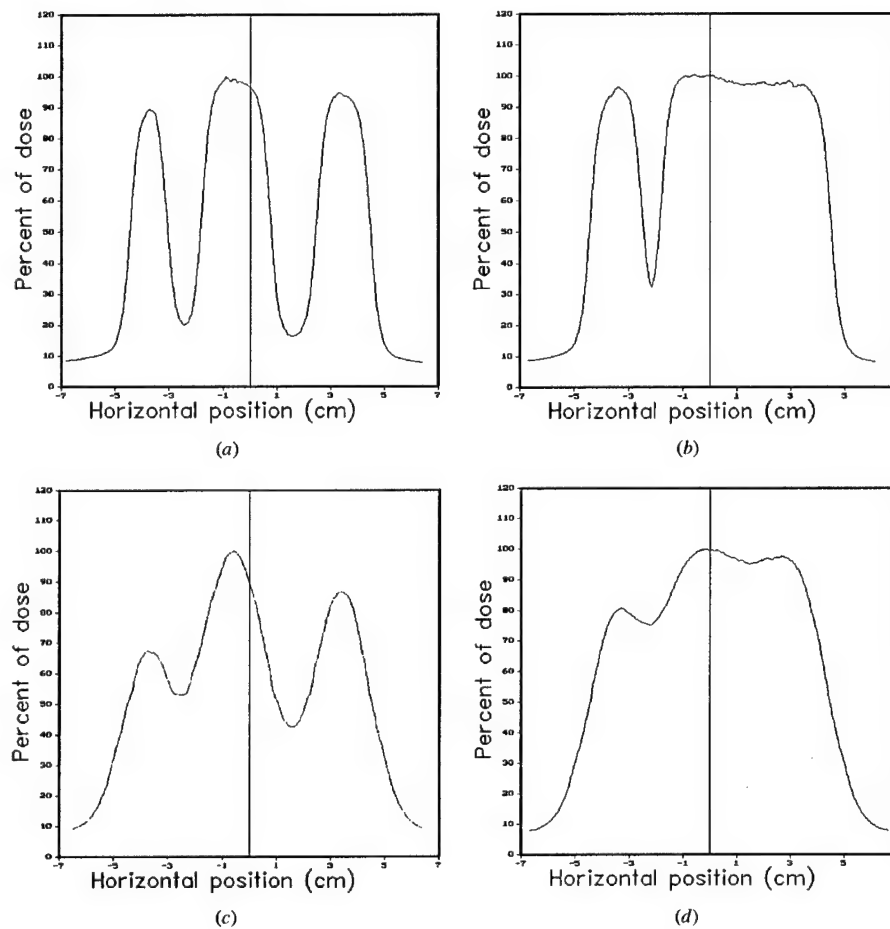
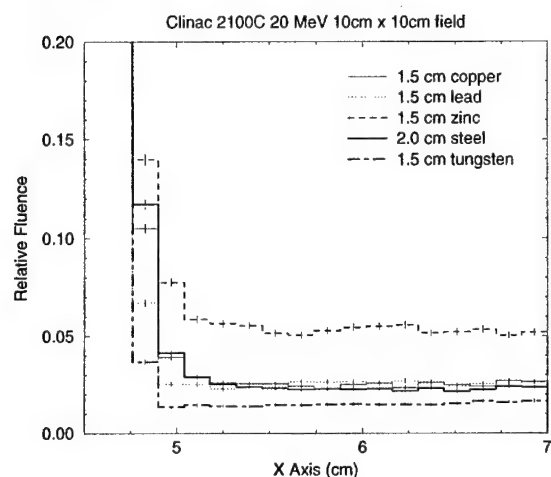
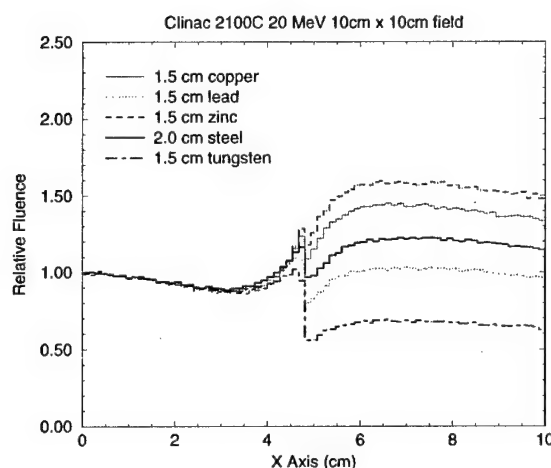


Figure 4. Beam profiles measured at 2 cm depth in a solid water phantom for the 6 MeV and 20 MeV electron fields shown in figure 2: (a) 20 MeV along A-A; (b) 20 MeV along B-B; (c) 6 MeV along A-A; and (d) 6 MeV along B-B.

leaf thickness. Although the beam penumbral widths did not change significantly for leaf thicknesses smaller than 2 cm, the beam intensity outside the field was affected by the leaf thickness and the atomic number of the leaf material. As shown in figure 5 for a 20 MeV electron beam, 1.5 cm thick zinc reduced the electron fluence outside the field to about 5% of the central axis value (figure 5(a)). These electrons were mainly generated by the bremsstrahlung photons in the MLC leaves. This was confirmed by the photon fluence as shown in figure 5(b), where 1.5 cm zinc MLC leaves resulted in about 60% higher photon fluence outside the field compared with the central axis photon fluence. Some electrons were also scattered off the leaf ends and by air. For 1.5 cm copper, 1.5 cm lead and 2 cm steel, the electron fluence was about 2.5% of the central axis value. The electron fluence was reduced to about 1.5% if the leaves were made of 1.5 cm tungsten. This was reflected by the 30% smaller photon fluence under the tungsten MLC leaves compared with the central axis photon fluence. Clearly, tungsten was superior to



(a)



(b)

Figure 5. Monte Carlo simulated electron (a) and photon (b) planar fluence in the penumbral region and outside the treatment field for a Varian Clinac 2100C 20 MeV electron beam collimated by an electron MLC of different leaf materials and thicknesses. The air gap between the electron MLC and the scoring plane is 7 cm.

other materials in terms of leaf leakage. If we increased the tungsten leaf thickness to 2 cm the electron fluence would be reduced to less than 1% of the central axis value and the photon leakage would be reduced to about 50% of the central axis value (not shown).

To study the overall effect of the leaf leakage, leaf scattering, air scattering and the extended source in an electron beam, we compared the dose distributions for single fields and multiple abutting fields collimated by an electron MLC with 1.5 cm thick tungsten leaves. Figure 6 shows the Monte Carlo calculated dose distributions for a single 4 cm \times 4 cm electron field and a multiple abutting field of the same size formed by four 1 cm \times 4 cm electron fields. For

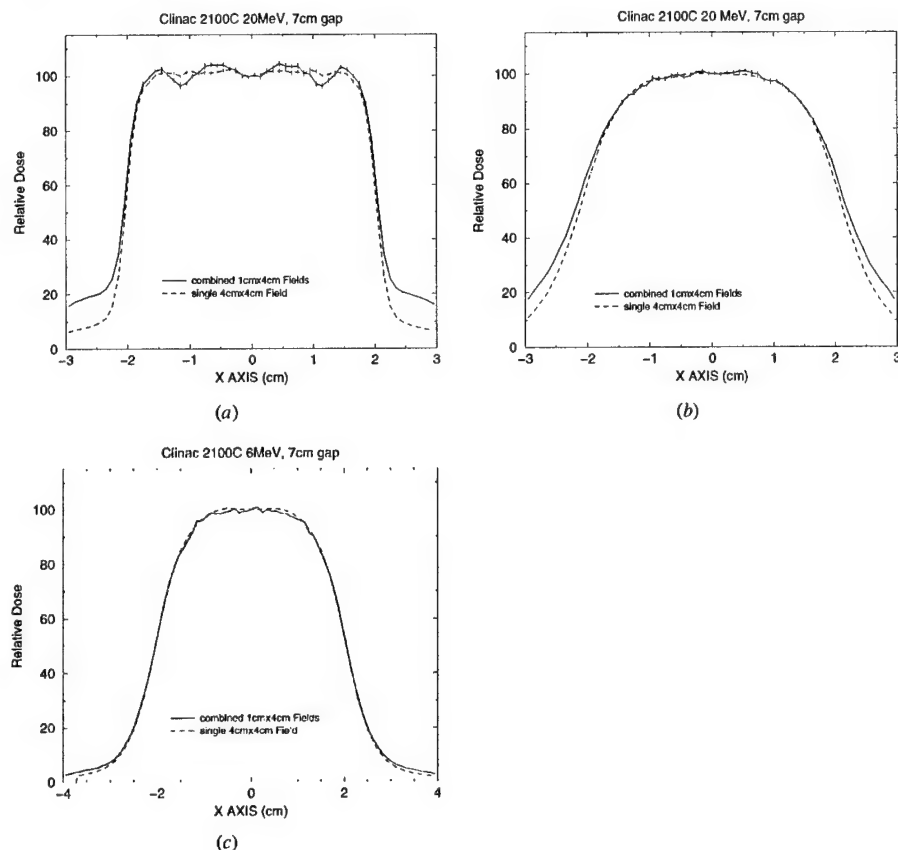


Figure 6. Monte Carlo calculated dose distributions in a water phantom for Varian Clinac 6 and 20 MeV electron beams collimated by an electron MLC of 1.5 cm thick tungsten leaves for a single 4 cm \times 4 cm electron field and a 4 cm \times 4 cm field formed by four 1 cm \times 4 cm electron fields: (a) dose at surface for a 20 MeV beam; (b) dose at 3 cm depth for a 20 MeV beam; (c) dose at surface for a 6 MeV beam.

a 20 MeV electron beam, the dose at the phantom surface for the abutting field shows about 4% fluctuation compared with a single electron field (figure 6(a)). This is potentially due to the effect of leaf shape and extended source. The dose outside the field for the abutting field is about three times higher than that for the single field, which is mainly caused by the leaf leakage due to the longer beam-on time to deliver the four 1 cm \times 4 cm fields and electron scattering off the leaf ends. The dose at 3 cm depth shows little difference between the abutting field and the single field except for the dose near the field edges and outside the field (figure 6(b)). For a 6 MeV electron beam, the dose at the phantom surface for the abutting field is almost the same as that for the single field (figure 6(c)). The dose outside the field for the abutting field is only slightly higher than that for the single field. The effect of leaf leakage is very small for a 6 MeV beam and the dose immediately outside the field is thought to be mainly due to the effect of electron scattering in the air. It seems that field abutting with 1 cm beamlets collimated by an electron MLC can provide adequate beam characteristics for MERT for the beam energies

investigated. However, the dose outside the field needs to be minimized through beam energy and leaf sequence optimization.

3.2. Comparisons of a photon MLC and an electron MLC

There have been studies on electron beam collimation using a photon MLC (Karlsson *et al* 1999). One of the advantages of using a photon MLC is the possibility of combining both photon and electron beams in the same plan. An essential requirement for matching a photon beam and an electron beam at different depths is that both beams share the same source position. Karlsson *et al* (1999) proposed several modifications to the design of a Varian Clinac 2300CD accelerator, one of which was to replace the intervening air with helium. This could significantly reduce the effect of electron scattering in the air on the beam penumbra. However, filling the accelerator head with helium requires major modifications to the existing accelerator design. In this work, we have investigated an alternative solution—a thin leaf MLC at the electron cutout level to reduce the air scattering effect. As can be seen in figure 7, the unfocused MLC leaf ends could scatter the electrons very significantly to degrade the beam characteristics near the field edges. The Varian MLC has rounded leaf ends, which are expected to have similar dosimetric characteristics as the unfocused MLC studied here. Focused leaf ends could greatly improve the beam edges and provided even slightly better dose profiles inside the field for a 20 MeV electron beam compared with an electron MLC (figures 7(a)–(c)), primarily due to the reduction of electron scattering in the accelerator head (helium versus air). The dose outside the field was slightly lower for the electron MLC than for the photon MLC. For a 6 MeV beam, an electron MLC gave slightly better surface dose profiles both inside and outside the field than the focused and unfocused photon MLC. However, the dose profiles became practically similar at the depth of the maximum dose and greater depths (not shown). Note that in these comparisons, we have placed the phantom surface at 20 cm below the photon MLC and 7 cm below the electron MLC to minimize the effect of electron scattering in the air or helium between the MLC and the phantom. It is evident that an electron MLC will have similar dosimetric characteristics as a photon MLC with focused leaf ends but without the need to replace the air in the accelerator head with helium.

3.3. Comparison of beamlet distributions

The accuracy of the beamlet distribution calculation may play an important role in the treatment planning optimization process. Ma *et al* (1999) reported significant differences in the final dose distributions of the optimized treatment plans computed by a commercial inverse treatment planning system with a finite-size pencil beam and the Monte Carlo method. Pawlicki *et al* (1999) demonstrated that inaccurate beamlet distributions may result in under-dosing in the target and over-dosing in the adjacent critical structures, and using the Monte Carlo calculated beamlets could potentially reduce the uncertainty in the photon IMRT dose distributions. This was demonstrated again by Jeraj and Keall (1999) using a Monte Carlo dose calculation based inverse planning algorithm.

It has been shown that the electron beam dose distributions calculated by the pencil beam algorithm as implemented in some commercial treatment planning systems could be fairly uncertain in the regions near material interfaces and inhomogeneities (Cygler *et al* 1987, Shortt *et al* 1986, Mackie *et al* 1994, Ma *et al* 1999). We have computed the beamlet dose distributions using the 3D pencil beam as implemented in the FOCUS treatment planning system (Computerized Medical Systems, St Louis, MO) and compared them with the Monte Carlo calculated beamlets. Figure 8 shows the dose distributions calculated using the Monte

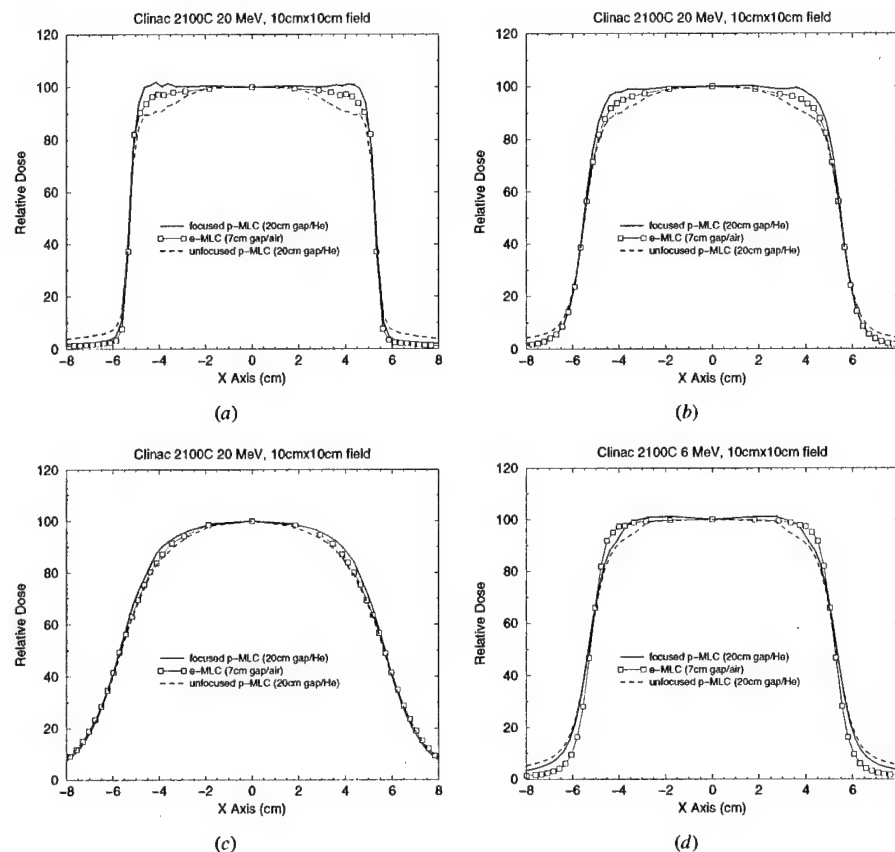


Figure 7. Monte Carlo calculated dose distributions in a water phantom for a 10 cm \times 10 cm field collimated by an electron MLC with 1.5 cm thick tungsten leaves and a photon MLC with 7.5 cm thick leaves on a Varian Clinac 2100C accelerator: (a) surface dose for a 20 MeV beam; (b) dose at 3 cm depth for a 20 MeV beam; (c) dose at 6 cm depth for a 20 MeV beam; (d) surface dose for a 6 MeV beam. The electron MLC has straight leaf ends. The photon MLC has either straight or double-focused leaves.

Carlo method (a, c, e) and the FOCUS 3D pencil beam algorithm (b, d, f) for a 1 cm \times 1 cm 12 MeV beamlet incident on a patient phantom built from CT data. For beamlets with normal incidence (figures 8(a) and (b)), the difference in the dose distributions in the heart was evident: the Monte Carlo calculated isodose lines varied with the heart contour while the pencil beam isodose lines remained symmetrical despite the change in material densities. Figures 8(c) and (d) show the beamlet distributions with a 10 cm air gap. The difference is clearly seen near the surface. The beamlet distributions again differed significantly in the lung for oblique incidence (figures 8(e) and (f)). The axis of the beamlet was intentionally placed to go through soft tissues and bones. The pencil beam isodose lines seemed to stretch according to the beam axis pathlength and showed no signs of electron build-down near the low-density material. These results provided enough evidence to show that to ensure the accuracy of the optimized dose distributions for MERT we should use the Monte Carlo method to compute the electron beamlets for the inverse planning process.

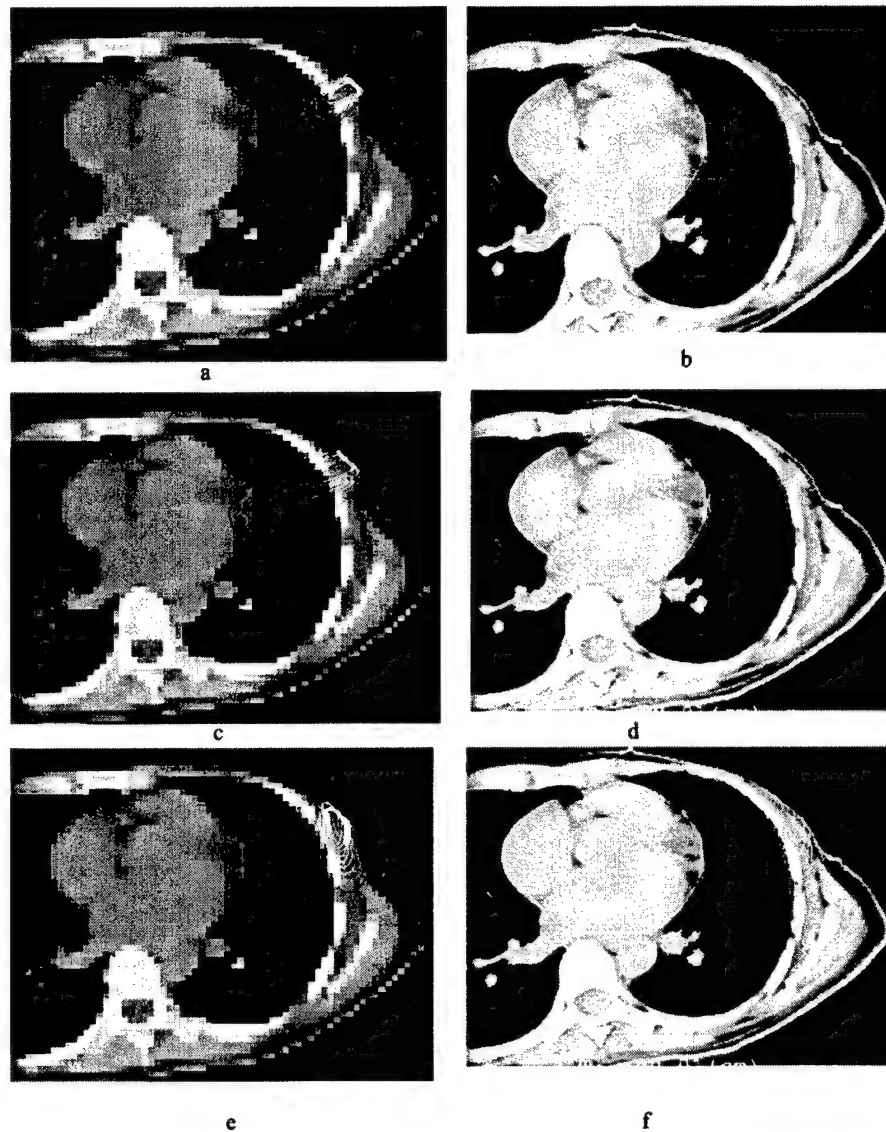


Figure 8. Dose distributions calculated using the Monte Carlo method (*a, c, e*) and the FOCUS 3D pencil beam algorithm (*b, d, f*) for a 1 cm \times 1 cm 12 MeV beamlet with normal incidence (*a* and *b*), normal incidence plus 10 cm air gap (*c* and *d*), and oblique incidence (*e* and *f*). The beamlet size is defined at 100 cm SSD. The isodose lines shown are 10, 20, 30, 40, 50, 60, 70, 80 and 90% of the maximum dose respectively.

3.4. MERT versus photons: a hypothetical treatment plan

Modulated electron radiotherapy is a general purpose technique that should be advantageous in many clinical situations. An exhaustive investigation of the specific advantages of MERT

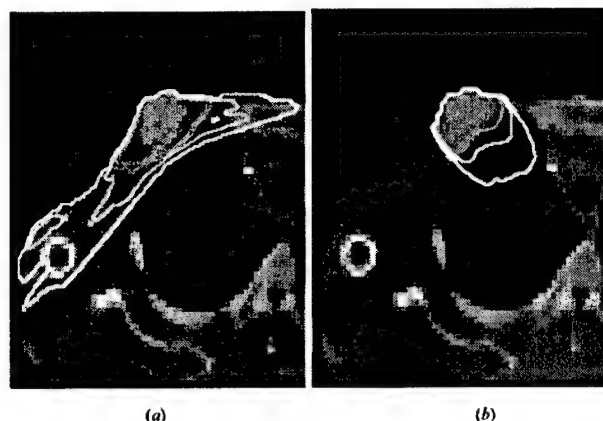


Figure 9. Treatment plans for a hypothetical breast case using tangential 6 MV photon beams (a) and MERT with 6, 12 and 20 MeV electron beams (b). Both plans were calculated using the Monte Carlo method. The isodose lines (90, 70, 50 and 30%) represented 50, 38.9, 25 and 16.7 Gy.

over traditional treatment modalities on a site by site basis is outside the scope of this work. However, to demonstrate the possibility of improving the dose homogeneity in the target and the reduction of the dose in surrounding normal tissues, we compare the dose distributions to treat a hypothetical target using tangential photon beams and MERT. The purpose of the comparison was to illustrate the concept of MERT but not to draw specific conclusions on the use of either technique. Previous investigators have used artificial phantoms and hypothetical targets to mimic different treatment sites (e.g. Hyödynmaa *et al* 1996, Åsell *et al* 1997, Ebert and Hoban 1997). We considered it to be clinically relevant to use a more realistic patient geometry (built from CT data) in our comparison, although the target definition and beam setup are somewhat arbitrary. Figure 9 shows the hypothetical treatment plan using tangential 6 MV photon beams and MERT with normally incident 6, 12 and 20 MeV electron beams. The intensity maps for each electron beam energy are shown in figure 10. The beamlet size was 1 cm \times 1 cm at 100 cm at isocentre. It is worth noting here, that as a matter of practicality, it is impossible to create the intensity maps shown in figure 10 using the conventional electron cutout approach but the electron MLC is a viable alternative. The dose distributions for both plans were calculated using the Monte Carlo method. The isodose lines (90, 70, 50 and 30%) were normalized in such a way that the 90% isodose surface would receive the prescribed target dose of 50 Gy. For the photon plan, the 90% dose line also included a margin in the lung to account for the effect of patient breathing. This was not needed for the electron plan as the electron beams were incident *en face* and the electron beamlet dose distributions do not vary significantly with breathing. Figure 11 shows the dose volume histograms (DVH) for the hypothetical treatment plans shown in figure 9. The target DVH together with the right lung DVH are shown in figure 11(a) (as percentage volume) and the right lung DVH and the 'total body' (including everything inside the external contour) DVH are shown in figure 11(b) (as absolute volume).

It is clear that MERT provided better dose homogeneity in the target region than tangential photon beams. Tangential photon beams produced hot spots in the target and cold spots near the skin (figure 11(a)). MERT significantly reduced the dose to the lung relative to tangential photon beams; the maximum dose to the lung was reduced from 50 Gy for a tangential treatment to 35 Gy for MERT (figure 11(a)). However, MERT increased the volume of the lung that

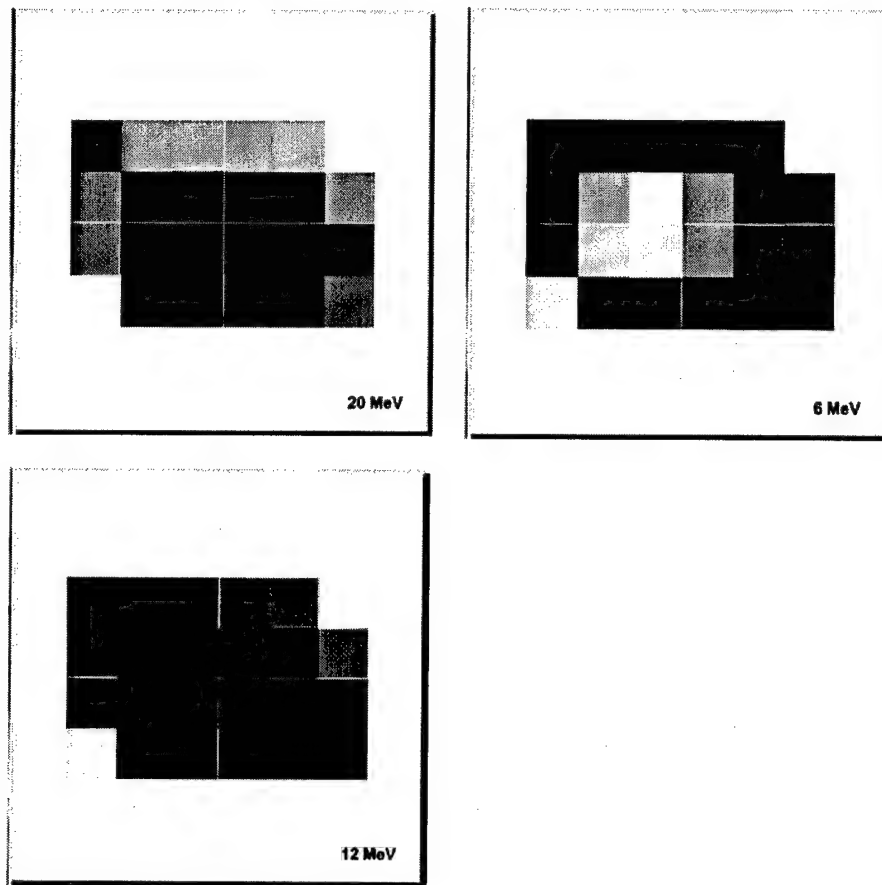


Figure 10. Intensity maps for the three electron beam energies. The beamlet size for each port was $1 \times 1 \text{ cm}^2$. Darker beamlets indicate a higher weight than the lighter beamlets and the grey scale for all three maps is in absolute terms.

received a lower dose (10% more volume received 5 Gy and 20% more volume received 2 Gy) compared with tangential photon beams. The clinical significance of the increased lung volume receiving such a low dose needs to be investigated. On the other hand, over 150 cm^3 of lung received much less dose with MERT compared with tangential photon beams, which could result in reduced lung complications (figure 11(b)). Another clear benefit with MERT is the exclusion of the surrounding normal tissue from the high dose volume (figure 11(b)). Over 1000 cm^3 of normal tissue received 10–30 Gy less dose in a MERT plan compared with this tangential photon beam plan.

4. Conclusions

In this work, we have investigated the feasibility of modulating both energy and intensity of electron beams for radiotherapy. This was achieved by combining electron beams of different

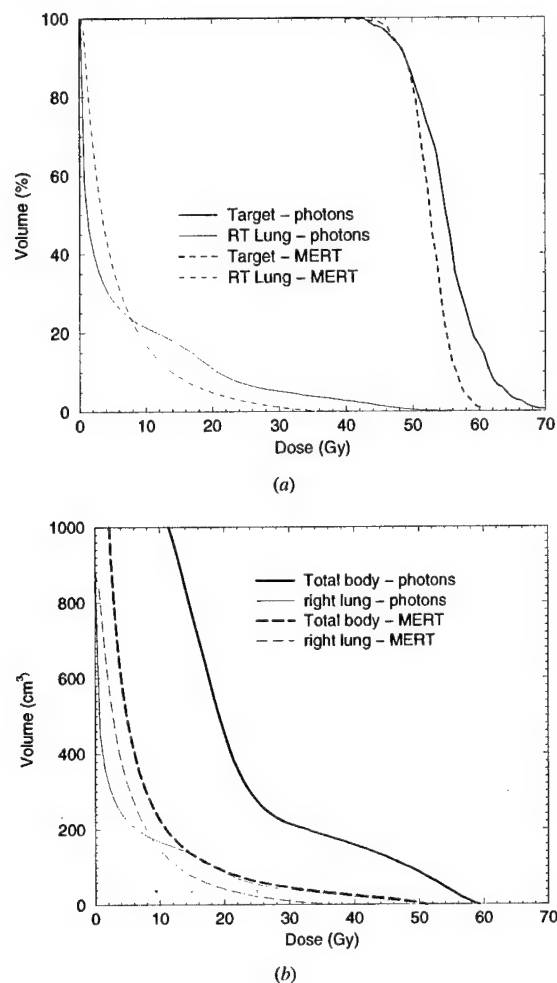


Figure 11. Dose volume histograms (DVH) for the breast treatment plans shown in figure 9: (a) DVH shown as percentage volume for the target (PTV) and the right lung and (b) DVH shown as absolute volume for the right lung and the 'total body' which includes everything inside the external contour.

nominal energies and variable intensity distributions. A prototype electron MLC was built to study the characteristics of MLC-collimated electron beams and the Monte Carlo simulations were used to investigate the effect of MLC leaf material, thickness, shape and location. The beamlet distributions calculated using a 3D electron pencil beam algorithm as implemented in a commercial treatment planning system and the Monte Carlo method were compared for electron beams of different energies, extended air gaps, oblique incidence and heterogeneous geometries. A hypothetical breast case was used to compare the dose distributions using tangential photons and MERT for target coverage (dose homogeneity) and normal tissue sparing (dose reduction in the lung and other surrounding normal tissues).

Our results showed that an electron MLC at the electron cutout location can provide adequate beam collimation for MERT without the need to replace the air in the accelerator head and between the MLC and the phantom with helium. The beam characteristics collimated by an electron MLC are comparable to those collimated by a focused photon MLC. However, the latter requires the accelerator head and between the MLC and the phantom to be filled with helium, which may be impractical for some accelerators because of the major modifications needed to the structure design. An electron MLC can also be used in place of a cutout. The Monte Carlo method can accurately simulate particle transport in cases involving extended air gaps, oblique incidence and heterogeneous anatomy, and is therefore suitable for the beamlet calculation for MERT treatment optimization. Our preliminary results based on a hypothetical breast case demonstrated the potential of MERT for uniform target coverage and normal tissue sparing. To fully explore the potential of MERT, further studies need to be carried out for realistic clinical cases and for other treatment sites such as the head and neck.

Acknowledgments

We would like to acknowledge Varian Oncology Systems, Palo Alto, CA, for providing detailed information on the Varian Clinac linear accelerators. We would like to thank our colleagues Fred van den Haak, for making the prototype electron MLC, and Sam Brain, Todd Koumrian, Behrooz Tofighrad and Michael Luxton for help with the computers and software support. This investigation was supported in part by grants CA78331 from the NIH, BC971292, BC990018 and BC990213 from the DOD, Seed Cycle 1 from the RSNA Research and Education Fund, and a consortium agreement with the NumeriX, LLC.

References

- AAPM 1983 AAPM TG-21, a protocol for the determination of absorbed dose from high-energy photons and electrons *Med. Phys.* **10** 741
- 1991 AAPM TG-25, Clinical electron beam dosimetry: report of AAPM Radiation Therapy Committee Task Group No. 25 *Med. Phys.* **18** 73–109
- Åsell M, Hyödynmaa S, Gustafsson A and Brahme A 1997 Optimization of 3D conformal electron beam therapy in inhomogeneous media by concomitant fluence and energy modulation *Phys. Med. Biol.* **42** 2083–100
- Bielajew A and Rogers D W O 1987 PRESTA—the parameter reduced electron step algorithm for electron Monte Carlo transport *Nucl. Instrum. Methods B* **18** 165–81
- Bielajew A F, Rogers D W O, Cygler J and Battista J J 1987 A comparison of electron pencil beam and Monte Carlo calculational methods *The Use of Computers in Radiation Therapy* ed I A D Bruinvis (Amsterdam: Elsevier) pp 65–8
- Boesecke R, Doll J, Bauer B, Schlegel W, Pastyr O and Lorenz M 1988 Treatment planning for conformation therapy using a multileaf collimator *Strahlenther. Onkol.* **164** 151–4
- Brewster L, Mohan R, Mageras G, Burman C, Leibel S and Fuks Z 1995 Three dimensional conformal treatment planning with multileaf collimators *Int. J. Radiat. Oncol. Biol. Phys.* **33** 1081–9
- Boyer A L, Geis P B, Grant W, Kendall R and Carol M 1997 Modulated-beam conformal therapy for head and neck tumors *Int. J. Radiat. Oncol. Biol. Phys.* **39** 227–36
- Brahme A 1988 Optimal setting of multileaf collimators in stationary beam radiation therapy *Strahlenther. Onkol.* **164** 343–50
- Chui C S, LoSasso T and Spirou S 1994 Dose calculations for photon beams with intensity modulation generated by dynamic jaw or multileaf collimators *Med. Phys.* **21** 1237–43
- Convery D J and Rosenbloom M E 1992 The generation of intensity-modulated fields for conformal radiotherapy by dynamic collimation *Phys. Med. Biol.* **37** 1359–74
- Cygler J, Battista J J, Scrimger J W, Mah E and Antolak J 1987 Electron dose distributions in experimental phantoms: a comparison with 2D pencil beam calculations *Phys. Med. Biol.* **32** 1073–83
- DeMarco J J, Solberg T D and Smathers J B 1998 A CT-based Monte Carlo simulation tool for dosimetry planning and analysis *Med. Phys.* **25** 1–11

- Ebert M A and Hoban P W 1997 Possibilities for tailing dose distributions through the manipulation of electron beam characteristics *Phys. Med. Biol.* **42** 2065–81
- Faddegon B A, Balogh J, Mackenzie R and Scora D 1998 Clinical considerations of Monte Carlo for electron radiotherapy treatment planning *Radiat. Phys. Chem.* **53** 217–28
- Fraass B A, McShan D L, Kessler M L, Matrone G M, Lewis J D and Weaver T A 1995 A computer-controlled conformal radiotherapy system I: overview *Int. J. Radiat. Oncol. Biol. Phys.* **33** 1139–57
- Hogstrom K R, Mills M D and Almond P R 1981 Electron beam dose calculations *Phys. Med. Biol.* **26** 445–59
- Hyödynmaa S, Gastafsson A and Brahme A 1996 Optimization of conformal electron beam therapy using energy- and fluence-modulated beams *Med. Phys.* **23** 659–66
- ICRU 1984 Radiation dosimetry: Stopping powers for electrons and positrons *ICRU Report 37* (Bethesda, MD: ICRU)
- Jeraj R and Keall P 1999 Monte Carlo-based inverse treatment planning *Phys. Med. Biol.* **44** 1885–96
- Jiang S B 1998 Development of a compensator based intensity modulated radiation therapy system *PhD Thesis* Medical College of Ohio, Toledo, OH
- Jiang S B, Boyer A L and Ma C-M 1999 A hybrid system for IMRT inverse planning and dose verification *Int. J. Radiat. Oncol. Biol. Phys.* **41** 123
- Kapur A 1999 Monte Carlo dose calculations for clinical electron and intensity modulated photon beams in radiotherapy *PhD Thesis* Stanford University, Stanford, CA, USA
- Kapur A, Ma C-M, Mok E and Findley D 1997 Characterization of small field electron beams for radiotherapy using Monte Carlo simulations *Proc. 12th Int. Conf. on the Use of Computers in Radiation Therapy (Salt Lake City, Utah)* (Madison, WI: Medical Physics Publishing) pp 157–8
- Kapur A, Ma C-M, Mok E, Findley D and Boyer A L 1998 Monte Carlo calculations of clinical electron beam output factors *Phys. Med. Biol.* **43** 3479–94
- Karlsson M G, Karlsson M K and Ma C-M 1999 Treatment head design for multileaf collimated high-energy electrons *Med. Phys.* **26** 2125–32
- Karlsson M K, Karlsson M G and Zackrisson B 1998 Intensity modulation with electrons: calculations, measurements and clinical applications *Phys. Med. Biol.* **43** 1159–69
- Kawrakow I, Fippel M and Friedrich K 1996 3D electron dose calculation using a voxel based Monte Carlo algorithm *Med. Phys.* **23** 445–57
- Keall P J and Hoban P 1996 Superposition dose calculation incorporating Monte Carlo generated electron track kernels *Med. Phys.* **23** 479–85
- Kutcher G J, Mageras G S and Leibel S A 1995 Control, correction and modeling of setup errors and organ motion *Semin. Radiat. Oncol.* **5** 134–45
- Leibel S A et al 1992 Three-dimensional conformal radiation therapy at the Memorial Sloan-Kettering Cancer Center *Semin. Radiat. Oncol.* **2** 274–89
- Lief E P, Larsson A and Humm J L 1996 Electron dose profile shaping by modulation of a scanning elementary beam *Med. Phys.* **23** 33–44
- Ling C C et al 1996 Conformal radiation treatment of prostate cancer using inversely-planned intensity-modulated photon beams produced with dynamic multileaf collimation *Int. J. Radiat. Oncol. Biol. Phys.* **35** 731–40
- LoSasso T, Chui C S, Kutcher G J, Leibel S A, Fuks Z and Ling C C 1993 The use of multileaf collimators for conformal radiotherapy of carcinomas of the prostate and nasopharynx *Int. J. Radiat. Oncol. Biol. Phys.* **25** 161–70
- Ma C-M, Mok E, Kapur A and Findley D 1997 Improvement of small-field electron beam dosimetry by Monte Carlo simulations *Proc. 12th Int. Conf. on the Use of Computers in Radiation Therapy (Salt Lake City, Utah)* (Madison, WI: Medical Physics Publishing) pp 159–62
- Ma C-M, Mok E, Kapur A, Pawlicki T A, Findley D, Brain S, Forster K and Boyer A L 1999 Clinical implementation of a Monte Carlo treatment planning system for radiotherapy *Med. Phys.* **26** 2133–43
- Ma C-M and Nahum A E 1993 Calculation of absorbed dose ratios using correlated Monte Carlo sampling *Med. Phys.* **20** 1189–99
- Ma C-M, Reckwerdt P, Holmes M, Rogers D W O and Geiser B 1995 DOSXYZ Users Manual *National Research Council Report PIRS-0509(B)* (Ottawa: NRC)
- Ma L, Boyer A L, Xing L and Ma C-M 1998 An optimized leaf setting algorithm for beam intensity modulation using dynamic multileaf collimators *Phys. Med. Biol.* **43** 1629–43
- Mackie T R, Holmes T W, Reckwerdt P J and Yang J 1995 Tomotherapy: optimized planning and delivery of radiation therapy *Int. J. Imaging Syst. Technol.* **6** 43–55
- Mackie T R et al 1994 The OMEGA project: comparison among EGS4 electron beam simulations, 3D Fermi-Eyegs calculations, and dose measurements *Proc. 11th Int. Conf. on the Use of Computers in Radiation Therapy (Manchester, UK)* pp 152–3

- Mageras G S *et al* 1994 Initial clinical experience with computer-controlled conformal radiotherapy using the MM50 microtron *Int. J. Radiat. Oncol. Biol. Phys.* **30** 971-8
- Mah E, Antolak J, Scrimger J W and Pattista J J 1989 Experimental evaluation of a 2D and 3D pencil beam algorithm *Phys. Med. Biol.* **34** 1179-94
- McShan D L, Fraass B A, Kessler M L, Matrone G M, Lewis J D and Weaver T A 1995 A computer-controlled conformal radiotherapy system. II: sequence processor *Int. J. Radiat. Oncol. Biol. Phys.* **33** 1159-72
- Mohan R 1997 Why Monte Carlo? *Proc. 12th Int. Conf. on the Use of Computers in Radiation Therapy (Salt Lake City, UT)* (Madison, WI: Medical Physics Publishing) pp 16-18
- Nelson R, Hirayama H and Rogers D W O 1985 The EGS4 code system *Stanford Linear Accelerator Center Report SLAC-265* (Stanford, CA: SLAC)
- Pawlicki T A, Jiang S B, Deng J, Li J S and Ma C-M 1999 Monte Carlo calculated beamlets for photon beam inverse planning *Med. Phys.* **26** 1064-5
- Powlis W D *et al* 1993 Initiation of multileaf collimator conformal radiation therapy *Int. J. Radiat. Oncol. Biol. Phys.* **25** 171-9
- Rogers D W O and Bielajew A F 1990 Monte Carlo techniques of electrons and photons for radiation dosimetry *Dosimetry of Ionizing Radiation* vol III, ed K Kase, B E Bjarngard and F H Attix (New York: Academic) pp 427-539
- Rogers D W O, Faddegon B A, Ding G X, Ma C-M, Wei J S and Mackie T R 1995 BEAM: a Monte Carlo code to simulate radiotherapy treatment units *Med. Phys.* **22** 503-25
- Shortt K R, Ross C K, Bielajew A F and Rogers D W O 1986 Electron beam dose distributions near standard inhomogeneities *Phys. Med. Biol.* **31** 235-49
- Takahashi S 1965 Conformation radiotherapy-rotation techniques as applied to radiography and radiotherapy of cancer *Acta Radiol. Suppl.* **242** 1-142
- Wang L, Chui C and Lovelock M 1998 A patient-specific Monte Carlo dose-calculation method for photon beams *Med. Phys.* **25** 867-78
- Webb S 1992 Optimization by simulated annealing of three-dimensional conformal treatment planning for radiation fields defined by multi-leaf collimator: II. Inclusion of two-dimensional modulation of x-ray intensity *Phys. Med. Biol.* **37** 1689-704
- 1997 *The Physics of Conformal Radiotherapy: Advances in Technology* (Bristol: Institute of Physics Publishing)
- Yu C X, Symons J M, Du M N, Martinez A A and Wong J W 1995 A method for implementing dynamic photon beam intensity modulation using independent jaws and multileaf collimators *Phys. Med. Biol.* **40** 769-87
- Zackrisson B and Karlsson M 1996 Matching of electron beams for conformal therapy of target volumes at moderate depths *Radiother. Oncol.* **39** 261-70
- Zhang G G, Rogers D W O, Cygler J E and Mackie T R 1999 Monte Carlo investigation of electron beam output factors versus size of square cutout *Med. Phys.* **26** 743-50

Validation of a Monte Carlo dose calculation tool for radiotherapy treatment planning

J S Li, T Pawlicki, J Deng, S B Jiang, E Mok and C-M Ma

Department of Radiation Oncology, Stanford University School of Medicine, Stanford, CA 94305, USA

E-mail: jsli@reyes.stanford.edu

Received 2 March 2000, in final form 26 June 2000

Abstract. A new EGS4/PRESTA Monte Carlo user code, MCDOSE, has been developed as a routine dose calculation tool for radiotherapy treatment planning. It is suitable for both conventional and intensity modulated radiation therapy. Two important features of MCDOSE are the inclusion of beam modifiers in the patient simulation and the implementation of several variance reduction techniques. Before this tool can be used reliably for clinical dose calculation, it must be properly validated. The validation for beam modifiers has been performed by comparing the dose distributions calculated by MCDOSE and the well-benchmarked EGS4 user codes BEAM and DOSXYZ. Various beam modifiers were simulated. Good agreement in the dose distributions was observed. The differences in electron cutout factors between the results of MCDOSE and measurements were within 2%. The accuracy of MCDOSE with various variance reduction techniques was tested by comparing the dose distributions in different inhomogeneous phantoms with those calculated by DOSXYZ without variance reduction. The agreement was within 1.0%. Our results demonstrate that MCDOSE is accurate and efficient for routine dose calculation in radiotherapy treatment planning, with or without beam modifiers.

(Some figures in this article are in colour only in the electronic version; see www.iop.org)

1. Introduction

With the rapid development of computer technology, the Monte Carlo technique, currently the most accurate method for dose calculation (Shortt *et al* 1986, Mackie 1990, Rogers and Bielajew 1990, Andreo 1991, Mackie *et al* 1994, DeMarco *et al* 1998, Ma *et al* 1999a), is becoming more practical for use in radiation therapy treatment planning systems. It has been argued that the outcome of radiation therapy treatment may be improved by using Monte Carlo dose calculation (Mohan 1997, Nahum 1997), especially for intensity modulated radiotherapy (IMRT) treatment planning (Jeraj and Keall 1999, Ma *et al* 1999a, 2000a, b). The Monte Carlo method is being developed for treatment planning dose calculations by several groups (Mackie 1990, Hartmann-Siantar *et al* 1997, Ma *et al* 1997, 1999a, DeMarco *et al* 1998, Wang *et al* 1998, Mubata *et al* 1998, Libby *et al* 1998, Faddegon *et al* 1998).

At present, there are several general-purpose Monte Carlo codes in widespread use for radiation transport simulation, e.g. Electron Gamma Shower version 4 (EGS4) (Nelson *et al* 1985), ETRAN/ITS (Berger and Seltzer 1987) and Monte Carlo *N*-particle (MCNP) (Hendricks 1994) and PENELOPE (Salvat *et al* 1996). It is well known that the EGS4 code system is very well documented and it has been thoroughly benchmarked in the energy region of dosimetric interest (Rogers 1984a, b, Rogers and Bielajew 1984, 1986, 1990). DOSXYZ is

an EGS4 based Monte Carlo simulation code for calculation dose distribution in a rectilinear voxel phantom (Rogers *et al* 1995, Ma *et al* 1995). It is also well benchmarked. Comparisons of the DOSXYZ results with measurements have been reported previously (Rogers *et al* 1995, Kapur *et al* 1998, Ma 1998, Zhang *et al* 1999, Ma *et al* 1999a, 2000a). Unfortunately, these codes are too slow to be acceptable for routine dose calculation in treatment planning systems with existing hardware. Some codes based on the Monte Carlo method have been developed to speed up the dose calculation, such as Macro Monte Carlo (MMC) (Neuenschwander and Born 1992, Neuenschwander *et al* 1995), Voxel Monte Carlo (VMC and XVMC) (Kawrakow *et al* 1996, Fippel 1999) and Super Monte Carlo (SMC) (Keall and Hoban 1996a). Further verification and improvements are needed for routine treatment planning dose calculations.

A new EGS4/PRESTA (Bielajew and Rogers 1987) user code, MCDOSE, has been developed for routine clinical dose calculation (Ma *et al* 1999b, 2000c). MCDOSE was designed as a dose calculation module for easy implementation in a radiotherapy treatment planning system. We have implemented it in an existing commercial RTP system for conventional photon/electron beams (Ma *et al* 1999a) and intensity modulated radiotherapy (IMRT) dose verification (Ma *et al* 2000a). MCDOSE shares similar structure and geometry definition with other EGS4 user codes, such as DOSXYZ. MCDOSE and DOSXYZ have some common features. They can both simulate the transport of photons and electrons (and positrons) in a 3D rectilinear phantom geometry. The volume elements (voxels) in the phantom can have uniform or variable dimensions and the material in the voxel can be specified by the user or determined from the electron density data derived from the patient CT data. Source models are supported in both codes. But there are other features in MCDOSE, which are absent in DOSXYZ:

- (a) Advanced multiple-source models (Ma *et al* 1997, Ma 1998, Deng *et al* 2000, Jiang *et al* 2000a, b) are used as source input for both photon and electron beams in MCDOSE. The multiple-source models implemented in MCDOSE are more accurate and flexible, and easy for commissioning.
- (b) Beam modifiers such as jaws, wedges, blocks, compensators, electron cutouts and bolus are included by MCDOSE in the patient simulation. Both static and dynamic MLC fields can be simulated for conventional and intensity modulated radiotherapy.
- (c) Several variance-reduction techniques have been implemented in MCDOSE. Both codes have range rejection. However, it was implemented in different ways and in different simulation procedures.
- (d) There is an option for selecting the geometry coordinates from two definitions in MCDOSE. One (x, y, z) is the same as that in DOSXYZ for phantom study. The other (x', y', z') is for convenient patient dose calculation corresponding to the treatment system. The relationship between the two coordinates is $x = x'$, $y = -z'$ and $z = y'$.
- (e) Beamlets dose calculation for Monte Carlo inverse planning can be performed by MCDOSE for both photon and electron beams.
- (f) MCDOSE can produce dose volume histograms (DVH) using the patient contour information.

The inclusion of beam modifiers and the implementation of variance reduction techniques makes MCDOSE more practical for routine dose calculation. Beam modifiers play an important role in radiotherapy treatment. They modify the beam shape and/or intensity distribution and therefore change the dose distribution in the patient. They need to be considered for treatment planning dose calculations. It is not sufficient to treat jaws and blocks as apertures and to change the profile using the wedge or compensator factors conventionally. The effect of beam modifiers has been studied by Schach von Wittenau *et al* (2000). It was found

that the scattered electrons generated in jaws could increase the surface dose by several per cent depending on the beam energy and field size. The photon transmission and bremsstrahlung generated in the modifiers need to be considered. To ensure simulation accuracy, these beam modifiers should be simulated with accurate geometry when the Monte Carlo method is used for routine dose calculation. Some codes, like BEAM and PEREGRINE (Walling *et al* 1998), can be used to simulate beam modifiers. But BEAM can only simulate them separately from patient dose calculation. One has to simulate particle transport in the beam modifiers using BEAM first. After scoring the phase space below the modifiers, dose calculation in the patient phantom can then be performed (Ma *et al* 1999a). This two-step method works well but is inconvenient and can be time-consuming. It is not suitable for routine dose calculations. The inclusion of beam modifiers into the patient dose calculation simplifies the simulation procedure in terms of simulation steps and intermediate data storage. Although Monte Carlo is an accurate method, the CPU time needed to perform statistically meaningful dose calculation is always a problem that prevents it from being applied in routine dose calculations. The variance reduction techniques implemented in MCDOSE generally speed up the dose calculation by a factor of 10–30 (Ma *et al* 2000c). This makes the code more practicable for routine application. The dose calculation using MCDOSE for a nine-field IMRT plan (including pre- and post-optimization dose calculation) can be finished in 1 to 4 h on a 450 MHz Pentium III personal computer (Pawlicki *et al* 1999, Ma *et al* 2000b).

Before MCDOSE can be used reliably for clinical dose calculation, it must be extensively validated. The accuracy of the dose calculation depends on the input beam data and the implementation of the user code. Source modelling and beam commissioning have been investigated by Ma *et al* (1997), Ma (1998), Deng *et al* (2000) and Jiang *et al* (2000a, b). Excellent agreement in dose distributions in both homogeneous and heterogeneous phantoms has been achieved between source model, phase space data and measurements. In this work, we focus on the validation of the user code for beam modifiers and variance reduction techniques. The geometry description for beam modifiers and the implementation of variance reduction techniques may affect the simulation accuracy of the code.

The validation of beam modifiers was performed by comparing the simulation results of MCDOSE with those of BEAM/DOSXYZ. The dose distributions in specifically designed homogeneous and inhomogeneous phantoms with different source inputs calculated using MCDOSE and DOSXYZ are presented. Machine data for two Varian accelerators, Clinac 2100C and 2300C/D, were measured as required by the commissioning procedure.

2. Materials and methods

2.1. Simulation of beam modifiers in MCDOSE

In this work, we have implemented beam modifier simulation in MCDOSE. The combination of the modifiers, the geometry parameters and materials can be input by the user. Several different modifiers can be used together. Each of them occupies a slab. For photon beams our multiple-source model covers all the fixed components above the jaws in the accelerator head (Deng *et al* 2000). What we need to consider for routine dose calculations are the jaws, wedges, blocks, compensators, MLC and bolus. For electron beams our multiple-source model covers all the components down to the lowest scraper of the applicator (Jiang *et al* 2000a). Only the electron cutout and bolus need to be considered in MCDOSE.

The x and y jaws are modelled as two pairs. The inner surface of each jaw focuses to the target. The input parameters are x_1 , x_2 , y_1 , y_2 and the material for the jaws. Here x_1 , x_2 , y_1 , y_2 specify the locations of the inner edges of the jaw bars. They correspond to the field size at 100 cm SSD. A schematic diagram for the jaws is shown in figure 1(a).

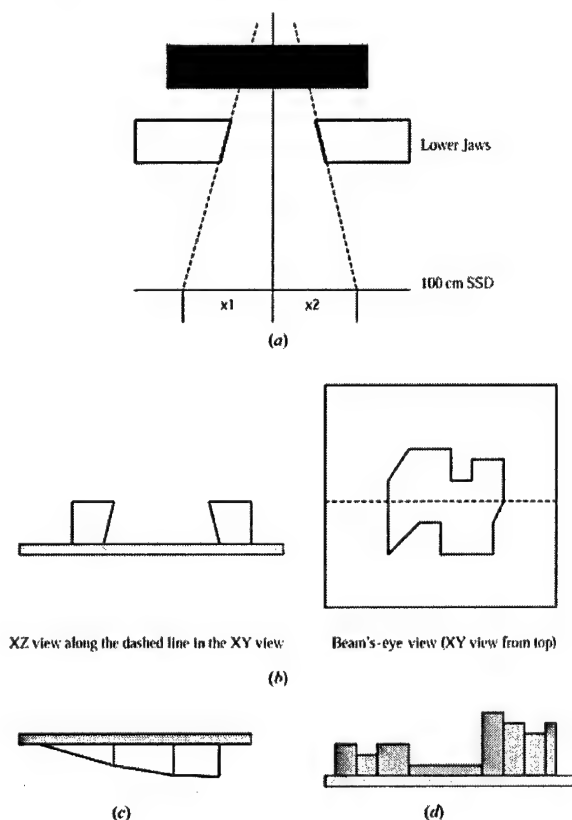


Figure 1. Schematic diagram of the beam modifiers simulated in MCDOSE. (a) X and Y jaws. (b) Photon beam block with tray. (c) Wedge and tray. (d) Compensator and tray.

To simulate the treatment block and the tray, the location, thickness and material of the block and the tray are required. The location is defined as the distance to the isocentre from the bottom surface of the block tray. The user also needs to specify the opening by the coordinates of the vertices that are projected at 100 cm SSD. The planes defining the inner surfaces of the opening are all angled with respect to the Z-axis towards the target as a single focus point. The block opening can be of any shape. The user needs to input the points continuously around the perimeter of the opening. The beam's eye view and X-Z view of the block and tray are shown in figure 1(b).

Wedges can be simulated by MCDOSE using the geometry information about the orientation, location, material and the two-dimensional point coordinates to specify its shape (see figure 1(c)). Full simulation of the particle transport is performed. This approach is similar to the wedge definition for conventional dose calculation algorithms, except for one important point. For the Monte Carlo approach, the user enters the exact wedge specifications without any modifications or adjustments in the parameters so that the final dose calculation matches the measured dose profiles of the wedge under consideration. Thus, in our Monte Carlo approach, the physical transport of particles in the beam modifiers and the

reproduction of the phase space must be accurate to obtain good agreement with measured results.

The compensator including the tray can be simulated by MCDOSE. The location, material and the tray thickness are required. The compensator is divided into different bins in two directions. The coordinates and thickness for each bin (a pixel) are required. An *X-Z* view of the compensator and tray is shown in figure 1(d). This module can also be used as an MLC after setting the tray material to air.

An electron cutout is simulated in a way similar to a photon block except that it does not have a tray. The option to have a diverging or straight and parallel inner planes to define the opening is considered for different clinical applications. The location, material and coordinates of each vertex to specify the opening are required.

The bolus is simulated by adding an extra layer of material to the patient's geometry (outside the patient external contour) according to its material and thickness.

2.2. Simulation of beam modifiers by EGS4/BEAM

In order to validate the code for beam modifier simulation in MCDOSE, EGS4/BEAM was used to simulate block, wedge, compensator and electron cutout. The simulations started with the phase space above the jaws. No variance reduction techniques were used in these simulations. The cut-off energy of electron and photon were set to be 700 keV and 10 keV (total energy). After the phase space data were obtained below the modifiers, DOSXYZ was used to carry out the dose calculation. Comparison between them can prove that our implementation for the simulation of beam modifier is right.

Two component modules, BLOCK and SLABS, were used to simulate the photon blocks and the trays. To simulate the wedge, the left bars of two or more pairs of JAWS were piled up to match the shape. The component modules MLC and SLABS were used to simulate the compensators and trays. The component BLOCK was used to simulate an electron cutout with the phase space above the last scraper as source input. Five subregions were used to specify a butterfly shape for the opening that was simulated for an electron cutout in this paper. The phase space data were scored below the modifiers. Then dose calculations were performed using DOSXYZ in a water phantom.

2.3. Variance reduction techniques and dose calculation details

The goal of MCDOSE is to perform quick and accurate dose calculation for radiation therapy treatment planning. Several variance reduction techniques have been implemented in MCDOSE to speed up the calculation without losing accuracy. These techniques include electron range and region rejection, photon interaction forcing, particle splitting, Russian roulette (Bielajew and Rogers 1988) and electron track repeating (Kawrakow *et al* 1996, Keall and Hoban 1996b). To speed up the simulation in beam modifiers, the electron region rejection technique was applied to the electrons that make little contribution to the dose. For example, when we transport particles in jaws and blocks, we have an option to transport electrons only in a margin around the opening. Variable global cut-off energy (ECUT) has been applied to different regions. The techniques of photon interaction forcing, splitting and Russian roulette are well known and are implemented in some codes, such as BEAM/EGS4 system. They were well described by Bielajew and Rogers (1988) and Rogers *et al* (1995). Electron track repeating is similar to a technique called correlated sampling (Ma and Nahum 1993), in which particle tracks were repeated in different locations or geometries to improve computation efficiency. It was described in great detail by Kawrakow *et al* (1996) and Keall and Hoban (1996b). The main

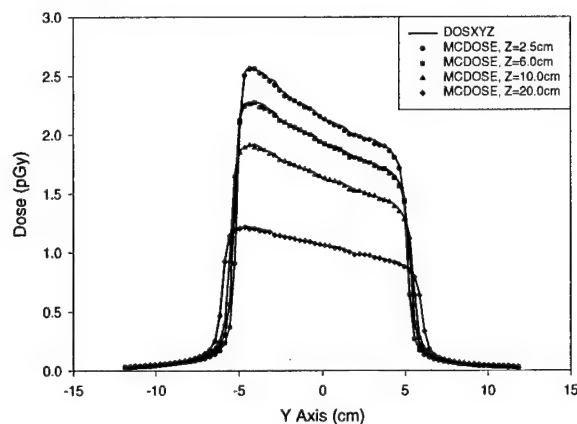


Figure 2. Comparisons of the lateral dose profiles at different depths in a water phantom between MCDOSE and BEAM/DOSXYZ. A 45° wedge were simulated for a 15 MV photon beam, the field size was $10\text{ cm} \times 10\text{ cm}$ defined at 100 cm SSD.

idea is to simulate an electron in a standard phantom such as in water or tissue, recording all the information of the electron transport tracks including the step length, direction, energy deposition, type of collision and generated particles for each step, then repeat the tracks for other electrons with the same energy starting from a different location in the patient. The initial direction for each electron may be different. The length of every step in the electron track is inversely proportional to the material density at that location. Stopping power ratio and scattering power ratio for different materials need to be considered to scale the path lengths and multiple scattering angles. This technique saves the sampling time for multiple scattering and collision for all the repeated electrons but not for the initial one. How many times to repeat the tracks depends on the problem. The number may affect the final efficiency. Our goal was to integrate this technique efficiently with other techniques mentioned above to produce a fast Monte Carlo code. For example, when photons go into the phantom, they are split and forced to have same interactions at different locations. Many electrons are generated and their tracks are repeated at these locations. So time is saved because we do not perform initial simulation for all the electrons. Russian roulette is applied to reduce the number of scattering photons.

To ensure the accuracy of the dose calculation with MCDOSE, specially designed inhomogeneous phantoms, such as layered-lung or layered-bone phantoms, are used. The dose distributions (depth dose curves and lateral dose profiles) calculated by MCDOSE and DOSXYZ for different photon beams and electron beams are compared. DOSXYZ was selected for comparison with MCDOSE because it has already been tested thoroughly and it is also an EGS4 user code. Agreement between MCDOSE and DOSXYZ means that the beam modifier implementation in MCDOSE is correct and the application of variance reduction techniques does not affect the accuracy. Since DOSXYZ has been well benchmarked by other investigators and our previous work (Rogers *et al* 1995, Kapur *et al* 1998, Ma 1998, Zhang *et al* 1999, Ma *et al* 1999a, 2000a), it is not necessary to compare all the MCDOSE results with measurements. In this work, both monoenergetic photon beams and realistic clinical beams of Varian 2300C/D are studied. The goal for use of monoenergetic photon beams is to make sure that the code works well for monoenergetic beams (therefore it should also work

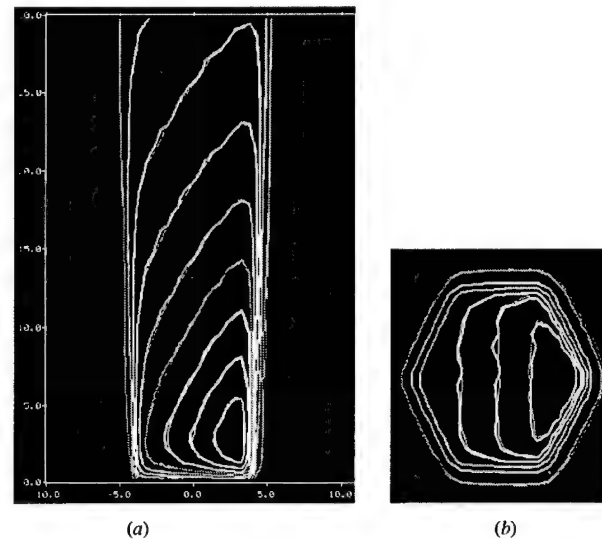


Figure 3. Dose distributions in a water phantom calculated by MCDOSE (thin curve) and BEAM/DOSXYZ (thick curve) for a $10\text{ cm} \times 10\text{ cm}$ field of a 15 MV photon beam. The beam was modified by a hexagonal block and a 60° wedge. (a) The isodose distribution in the X-Z plane through the central axis (beams come from the bottom). (b) The isodose distribution in the X-Y plane at a depth of 3.5 cm.

for polyenergetic beams). This test was done thoroughly in the energy range of interest for dosimetry with an interval of 1 MeV.

3. Results

3.1. Validation of beam modifiers

3.1.1. A 45° wedge. Figure 2 shows the lateral dose profiles at different depths in a water phantom calculated using MCDOSE and BEAM/DOSXYZ for a 45° wedge. Lead was used as the wedge material. The field size was set to $10\text{ cm} \times 10\text{ cm}$ at 100 cm SSD. The voxel size in the water phantom was $1.0\text{ cm} \times 0.3\text{ cm} \times 0.5\text{ cm}$. A 15 MV photon beam from a Varian Clinac 2300C/D machine was used as source input with phase space scored above the jaws. The comparison calculations were performed under the same conditions. The agreement between the results of MCDOSE and BEAM/DOSXYZ is within 1% of the maximum dose. The CPU time comparison between MCDOSE and BEAM/DOSXYZ is shown in table 1. MCDOSE is about 16 times faster than BEAM/DOSXYZ for this simulation.

3.1.2. A hexagonal block and a 60° wedge. Figure 3 shows the dose distributions calculated by MCDOSE and BEAM/DOSXYZ in a water phantom with a hexagonal block and a 60° wedge for a $10\text{ cm} \times 10\text{ cm}$ field of a 15 MV photon beam. The block was made of Cerrobend and its thickness was 7.7 cm. The block tray was made of PMMA and its thickness was 0.7 cm. The wedge was made of lead. The voxel size in the water phantom was $0.5\text{ cm} \times 0.5\text{ cm} \times 0.5\text{ cm}$. Figure 3(a) shows the isodose distribution in the X-Z plane through the central axis and figure 3(b) shows the isodose distribution in the X-Y plane at a depth of 3.5 cm. The difference between the results of MCDOSE and BEAM/DOSXYZ is within 1% of the maximum dose.

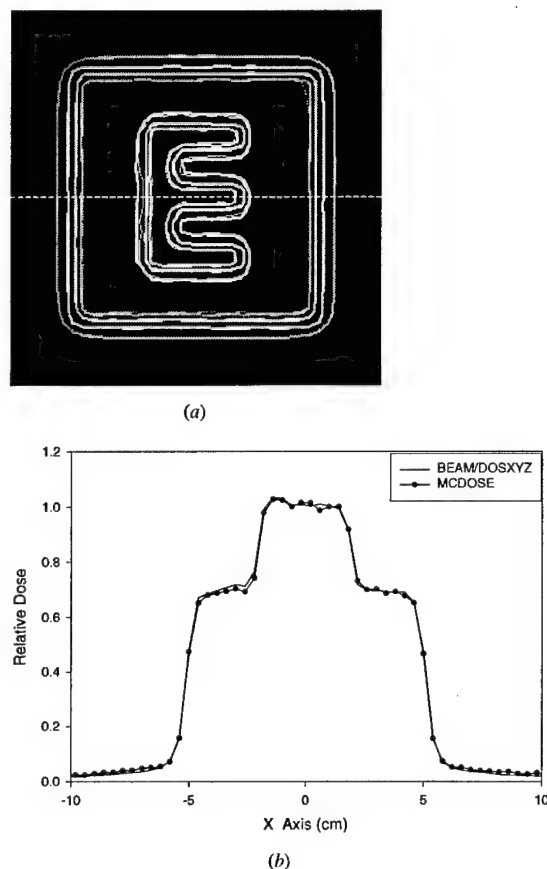


Figure 4. (a) The isodose distributions in *XY* view at a depth of 2.5 cm in a water phantom for a modified 10 cm \times 10 cm 15 MV photon beam using a specially designed compensator. The thick curve is the simulation result of BEAM/DOSXYZ. The thin curve is the result of MCDOSE. (b) The lateral dose profile along the dashed line in (a). The curve with symbols in (b) is the result of MCDOSE.

Table 1. The CPU time (hours) required by MCDOSE and BEAM/DOSXYZ for the beam modifier simulation investigated in this work on a Pentium III 450 MHz personal computer. The statistical uncertainties of the maximum doses are 1%.

	Modifier			
	45° wedge	60° wedge/block	E-shaped compensator	Butterfly-shaped electron cutout
BEAM + DOSXYZ	31.5 \pm 6.1	247.5 \pm 7.9	10.3 \pm 10.9	37.9 \pm 1.4
MCDOSE	2.3	13.0	5.3	2.5
Ratio	16.3	19.4	4.0	15.7

The CPU time needed by MCDOSE and BEAM/DOSXYZ is given in table 1. MCDOSE is about 19 times faster than BEAM/DOSXYZ for this simulation.

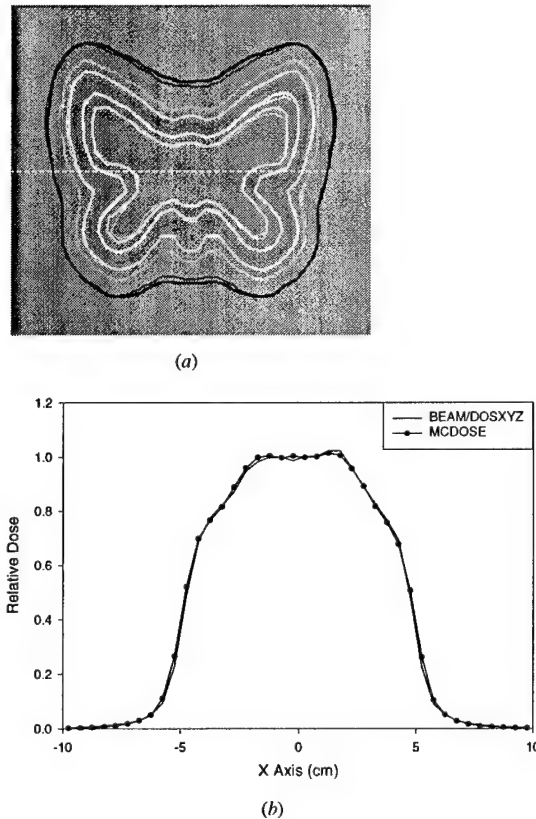


Figure 5. (a) is the isodose distributions in XY view at a depth of 2.25 cm in a water phantom for a modified 10 cm \times 10 cm 12 MeV electron beam using an electron cutout with a butterfly-shaped opening. The thick curve is the simulation result of BEAM/DOSXYZ. The thin curve is the result of MCDOSE. (b) The lateral dose profile along the dashed line in (a). The curve with symbols in (b) is the result of MCDOSE.

3.1.3. Compensator. Figure 4 shows the E-shaped compensator isodose distributions (a) and lateral dose profiles (b) at a depth of 2.5 cm in the water phantom. They were calculated using MCDOSE and BEAM/DOSXYZ respectively. The compensator was made of copper. The thickness in the area of the compensator forming the 'E' shape was 0.5 cm and the thickness in the remaining area was 2 cm. The voxel size in the water phantom was 0.4 cm \times 0.4 cm \times 1.0 cm. Agreement (within 1%) can be observed from the comparison. In the penumbra regions, the separation between the results of MCDOSE and BEAM/DOSXYZ is within 1 mm. The CPU time needed by MCDOSE and BEAM/DOSXYZ is also shown in table 1. MCDOSE is about four times faster than BEAM/DOSXYZ for this simulation.

3.1.4. Electron cutout. Figure 5 shows the isodose distributions (a) and lateral dose profiles (b) in a water phantom calculated using BEAM/DOSXYZ and MCDOSE, for a 12 MeV realistic electron beam from a Varian 2100C machine with a butterfly-shaped cutout. The cutout was made of Cerrobend and its thickness was 1.4 cm. The voxel size in the water phantom

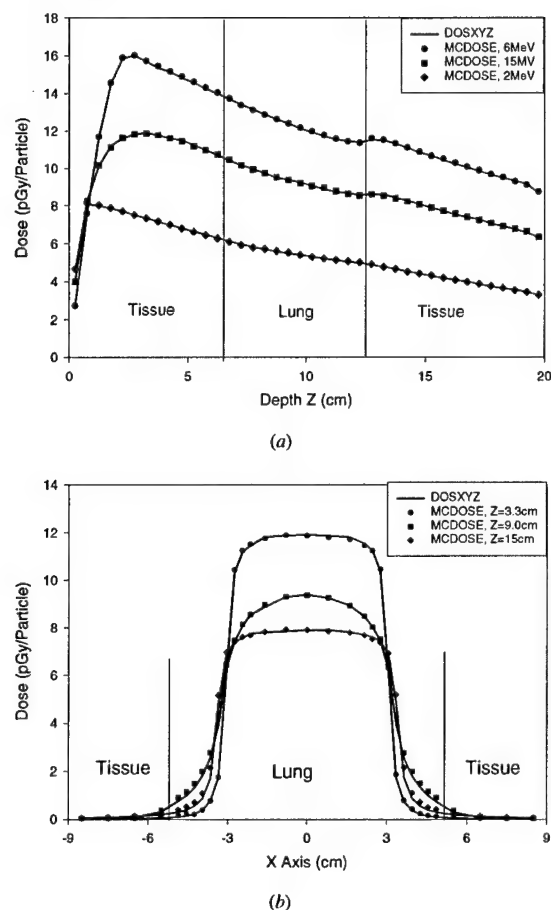


Figure 6. Dose distribution in a tissue-lung-tissue phantom calculated by DOSXYZ and MCDOSE for 6 MeV, 15 MV and 2 MeV photon beams with field size of $6\text{ cm} \times 6\text{ cm}$ defined at 100 cm SSD. The material in the volume of -5.0 cm to 5.0 cm along the X direction, -2.0 cm to 2.0 cm along the Y direction and 7.0 cm to 12.5 cm along the Z direction is lung. (a) The depth dose curves along the central axis for the beams. (b) The lateral dose profiles along the X -axis at depths of 3.3 cm, 9.0 cm and 15.0 cm for the 15 MV photon beam.

was $0.5\text{ cm} \times 0.5\text{ cm} \times 0.3\text{ cm}$. The phase space of an electron beam above the last scraper of a $10\text{ cm} \times 10\text{ cm}$ applicator was used as the source input. Good agreement (within 1%) has been achieved between the results of MCDOSE and BEAM/DOSXYZ. In the penumbra regions, the separation between MCDOSE and BEAM/DOSXYZ is within 1 mm. The CPU time needed by MCDOSE and BEAM/DOSXYZ is shown in table 1. MCDOSE is about 16 times faster than BEAM/DOSXYZ for this simulation.

The electron beam cutout factors calculated using MCDOSE are compared with the published data in table 2. The published data were calculated using BEAM/DOSXYZ with full phase space input and measured by Kapur *et al* (1998). The difference between the MCDOSE data and those calculated with full phase space by DOSXYZ is within 1.0%. The differences

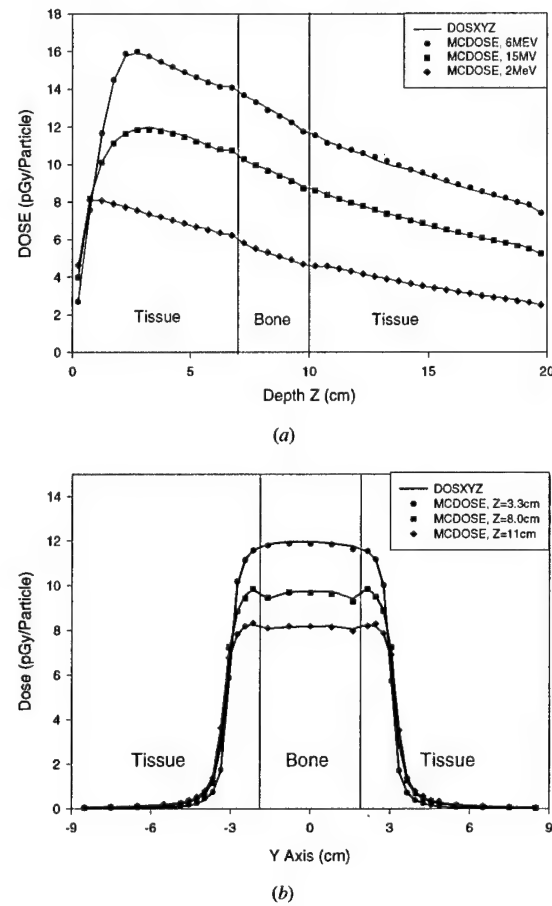


Figure 7. Dose distributions in a tissue-bone-tissue phantom calculated by DOSXYZ and MCDOSE for 6 MeV, 15 MV and 2 MeV photon beams with field size of 6 cm \times 6 cm defined at 100 cm SSD. The material in the volume of -5.0 cm to 5.0 cm along the X direction, -2.0 cm to 2.0 cm along the Y direction and 7.0 cm to 10.0 cm along the Z direction is bone. (a) The depth dose curve along the central axis for the beams. (b) The lateral dose profiles along the Y axis at depths of 3.3 cm, 8.0 cm and 11.0 cm for the 15 MV photon beam.

in the cutout factors between MCDOSE data and measurement is less than 2% except for the cases of 20 MeV electron beams with 3 cm \times 3 cm and 4 cm \times 4 cm inserts.

3.2. Validation of dose distribution in heterogeneous phantoms

To test the accuracy of the dose distribution calculated using MCDOSE with the variance reduction techniques, comparisons are made with the results of DOSXYZ. Each example has been calculated with a source-surface distance of 100 cm and field size of 6 cm \times 6 cm. The global electron cut-off energy (ECUT) was set to 700 keV and photon cut-off energy (PCUT) was set to 10 keV in MCDOSE and DOSXYZ. The maximum fractional energy loss per electron step (ESTEPE) was limited to 4% for both codes. The material compositions and

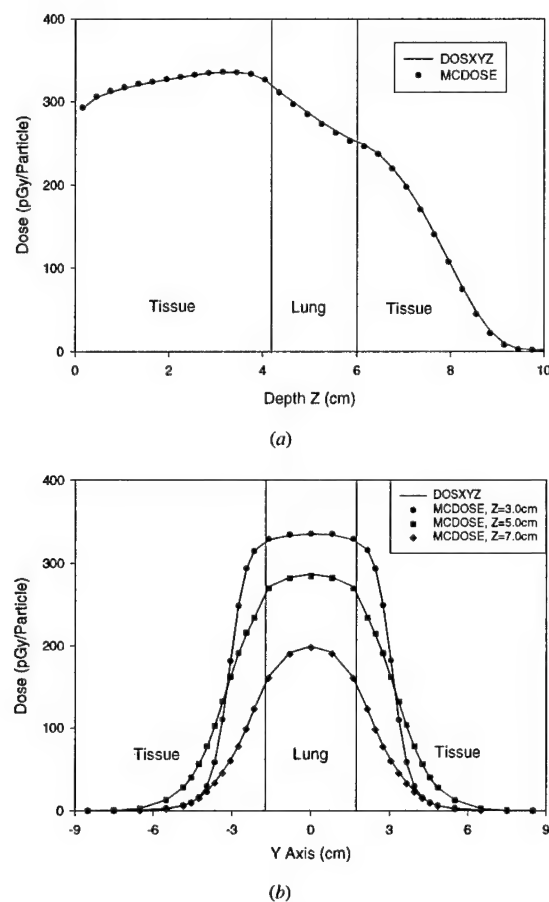


Figure 8. Dose distributions in a tissue-lung-tissue phantom calculated by DOSXYZ and MCDOSE for a 15 MeV electron beam with field size 6 cm \times 6 cm. The material in the volume of -5.0 cm to 5.0 cm along the X direction, -2.0 cm to 2.0 cm along Y direction and 4.2 cm to 6.0 cm along the Z direction is lung. (a) The depth dose curve along the central axis. (b) The lateral dose profiles along the Y-axis at depths of 3.0 cm, 5.0 cm and 7.0 cm.

densities are taken from ICRU (1992). Monoenergetic point sources and phase space files for a 15 MV photon beam of a Varian Clinac 2300C/D linear accelerator were used. Since dose per incident fluence is calculated, absolute dose comparisons are made between MCDOSE and DOSXYZ.

3.2.1. Photon beams. Figure 6(a) shows the depth dose curves along the central axis for 6 MeV and 2 MeV monoenergetic photon beams calculated by DOSXYZ and MCDOSE in a tissue phantom with 3D lung inhomogeneity. At depths from 7 cm to 12.5 cm, the phantom contains a 10 cm \times 4 cm slab of lung in the centre. The depth dose curves for a realistic 15 MV photon beam from a Varian Clinac 2300C/D accelerator calculated by DOSXYZ and MCDOSE in the same phantom are also shown in figure 6(a) and the lateral dose profiles at

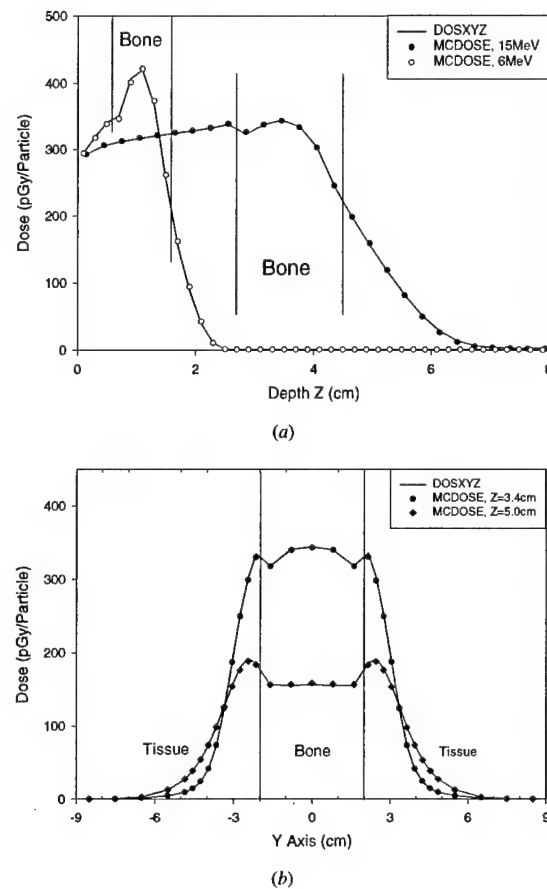


Figure 9. Dose distribution in tissue-bone-tissue phantoms calculated by DOSXYZ and MCDOSE for 15 MeV and 6 MeV electron beams with field size 6 cm \times 6 cm. For the 15 MeV electron beam, the material in the volume of -5.0 cm to 5.0 cm along the X direction, -2.0 cm to 2.0 cm along the Y direction and 2.7 cm to 4.5 cm along the Z direction is bone. For the 6 MeV electron beam, the material in the volume of -5.0 cm to 5.0 cm along the X direction, -2.0 cm to 2.0 cm along the Y direction and 0.6 cm to 1.6 cm along the Z direction is bone. (a) The depth dose curves along the central axis for two beams. (b) The lateral dose profiles along the Y axis at depths of 3.4 cm and 5.0 cm for the 15 MeV electron beam.

different depths are shown in figure 6(b). The phase space for a 15 MV photon beam was generated by BEAM and contains over 5 million particles. The 1σ statistical uncertainty on the dose values for these curves is less than 0.5%.

Dose calculations were also performed for photon beams in an inhomogeneous phantom containing tissue and bone. A 10 cm \times 4 cm slab of bone was placed between 7 cm and 10 cm depth in the centre of the tissue phantom. Figure 7(a) shows the depth dose curves along the central axis for different photon beams. Figure 7(b) shows the lateral dose profiles at different depths for a 15 MV photon beam.

Figures 6 and 7 show good agreement in dose distributions between MCDOSE and DOSXYZ for different photon beams. The absolute doses calculated by these two codes

Table 2. The electron cutout factors for various square inserts in $10 \times 10 \text{ cm}^2$ applicator for 6, 12 and 20 MeV beams calculated by MCDOSE and compared with the full phase space calculation by DOSXYZ and measurement of Kapur *et al* (1998). The values in the parentheses indicate the per cent difference between the MCDOSE calculated data and those measured or calculated with full phase space by DOSXYZ.

Energy (MeV)	Insert (cm \times cm)	MCDOSE	Full phase space	Measurement
6	3 \times 3	0.922	0.923 (−0.1%)	0.927 (−0.5%)
	4 \times 4	0.983	0.982 (0.1%)	0.988 (−0.5%)
	8 \times 8	1.009	1.005 (0.4%)	1.003 (0.6%)
12	3 \times 3	0.930	0.930 (0.0%)	0.928 (0.2%)
	4 \times 4	0.965	0.956 (0.9%)	0.963 (0.2%)
	8 \times 8	0.999	1.002 (−0.3%)	0.991 (0.8%)
20	3 \times 3	0.964	0.968 (−0.4%)	0.993 (−2.9%)
	4 \times 4	0.989	0.993 (−0.4%)	1.011 (−2.2%)
	8 \times 8	0.999	0.993 (0.6%)	1.004 (−0.5%)

in tissue, lung, bone, even at the interface between tissue and bone and tissue and lung agree to within 1% of the maximum dose. Further comparisons of dose calculations for monoenergetic photon beams from 1 MeV to 20 MeV, and also for 6 MV and 10 MV photon beams were performed. Similar agreement between MCDOSE and DOSXYZ was achieved. In most cases, the differences were within the 1σ statistical uncertainty of 1%.

3.2.2. Electron beams. We also performed dose calculations for monoenergetic point source electron beams with field size 6 cm \times 6 cm. The depth dose curves of a 15 MeV electron beam calculated by MCDOSE and DOSXYZ in a tissue–lung–tissue phantom are shown in figure 8(a). The lung material was at a depth from 4 to 6 cm. Figure 8(b) shows the lateral dose profiles at different depths in the phantom. At a depth from 4.2 to 6.0 cm, the lung material was from −5 cm to 5 cm in the *X* direction and from −2 cm to 2 cm in the *Y* direction. The remaining volume was tissue. The difference between the simulation results of MCDOSE and DOSXYZ is within 1% of the maximum dose.

The depth dose curves and lateral dose profiles at different depths for a 15 MeV electron point source beam in a tissue–bone–tissue phantom are shown in figures 9(a) and (b). At a depth from 2.7 to 4.5 cm, there was a 10 cm \times 4 cm slab of bone in the centre surrounded by tissue. The depth dose curve for a 6 MeV electron beam in a tissue–bone–tissue phantom is also shown in figure 9(a). The bone material was at a depth from 0.6 to 1.6 cm. The difference between the simulation results of MCDOSE and DOSXYZ is within 1% of the maximum dose.

3.2.3. CPU time comparison. The CPU times required by MCDOSE and DOSXYZ for dose calculations shown in figures 6 and 9 are listed in table 3 for different photon and electron beams. The calculations were performed on a Pentium III 450 MHz PC. The statistical uncertainty of the maximum dose is 1%. The ratios in the table are the speed-up factors of MCDOSE compared with DOSXYZ for each beam. In general MCDOSE is 20–50 times faster than DOSXYZ for photon beams and 5–10 times faster than DOSXYZ for electron beams.

4. Summary

A new Monte Carlo dose calculation tool has been developed and validated for clinical dose calculation. The main features of MCDOSE include electron and photon beam reconstruction

Table 3. The CPU time (hours) required by MCDOSE and DOSXYZ for the dose calculations shown in figures 6 and 9 on a Pentium III 450 MHz personal computer. The statistical uncertainties of the maximum doses are 1%.

	Beam				
	2 MeV photon	6 MeV photon	15 MV photon	6 MeV electron	15 MeV electron
DOSXYZ	9.44	2.95	4.86	0.78	0.94
MCDOSE	0.25	0.074	0.098	0.08	0.17
Ratio	37.7	39.8	49.6	9.8	5.6

by source models, simulation of beam modifiers together with the patient geometry for dose calculation and application of variance reduction techniques.

Comparisons of dose distribution with wedges, blocks, compensator and electron cutout between MCDOSE and BEAM/DOSXYZ demonstrated that dose calculation with modifiers in MCDOSE is accurate, convenient and efficient. To compare MCDOSE and DOSXYZ dose distributions, 3D heterogeneous phantoms containing lung and bone were used. Excellent agreement between the MCDOSE and DOSXYZ results has been obtained for both photon and electron beams of different energies. Comparing with DOSXYZ, the MCDOSE code runs generally 20–50 times faster for the photon beams and 5–10 times faster for electron beams investigated in this work without beam modifiers.

Acknowledgments

This work is partially supported by an NCI grant no CA 78331, a DOD grant no BC971292 and a consortium agreement with the NumeriX, LLC. We would like to thank Dr Arthur Boyer, Dr Gary Luxton and Dr Sam Brain for valuable discussions and comments on our work. We would also like to thank Todd Koumrian and Michael Luxton for computer hardware and software support.

References

- Andreo P 1991 Monte Carlo technique in medical physics *Phys. Med. Biol.* **36** 861–920
- Berger M J and Seltzer S M 1973 ETRAN, Monte Carlo code system for electron and photon transport through extended media *Documentation for RSIC Computer Package CCC-107* (Oak Ridge, TN: Oak Ridge National Laboratory)
- Bielajew A F and Rogers D W O 1987 PRESTA: the parameter reduced electron-step transport algorithm for electron Monte Carlo transport *Nucl. Instrum. Methods Phys. Res. B* **18** 165–81
- 1988 Variance-reduction techniques *Proc. Int. School of Radiation Damage and Protection Eighth Course: Monte Carlo Transport of Electrons and Photons below 50 MeV* ed T M Jenkins, W R Nelson and A Rindi (New York: Plenum) pp 407–19
- DeMarco J J, Solberg T D and Smathers J B 1998 A CT-based Monte Carlo simulation tool for dosimetry planning and analysis *Med. Phys.* **25** 1–11
- Deng J, Jiang S B, Kapur A, Li J S, Pawlicki T and Ma C-M 2000 Photon beam characterization and modelling for Monte Carlo treatment planning *Phys. Med. Biol.* **45** 411–27
- Faddegon B A, Balogh J, Mackenzie R and Scora D 1998 Clinical considerations of Monte Carlo for electron radiotherapy treatment planning *Radiat. Phys. Chem.* **53** 217–28
- Fippel M 1999 Fast Monte Carlo dose calculation for photon beams based on the VMC electron algorithm *Med. Phys.* **26** 1466–75
- Hartmann-Siantar C L *et al* 1997 Lawrence Livermore National Laboratory's PEREGRINE Project *Proc. 12th Int. Conf. on the Use of Computers in Radiation Therapy* (Salt Lake City, UT) (Madison, WI: Medical Physics Publishing) pp 19–22

- Hendricks J S 1994 A Monte Carlo code for particle transport *Los Alamos Scientific Laboratory Report* **22** 30–43
- ICRU 1992 Photon, electron, proton and neutron interaction data for body tissues *ICRU Report* **46** (Bethesda, MD: ICRU)
- Jeraj R and Keall P 1999 Monte Carlo-based inverse treatment planning *Phys. Med. Biol.* **44** 1885–96
- Jiang S B, Boyer A L and Ma C-M 2000b Modeling the extrafocal radiation and monitor chamber backscatter for photon beam dose calculation *Med. Phys.* accepted
- Jiang S B, Kapur A and Ma C-M 2000a Electron beam modelling and commissioning for Monte Carlo treatment planning *Med. Phys.* **27** 180–91
- Kapur A, Ma C-M, Mok E C, Findley D O and Boyer A L 1998 Monte Carlo calculation of electron beam output factors for a medical linear accelerator *Phys. Med. Biol.* **43** 3479–94
- Kawrakow I, Fippel M and Friedrich K 1996 3D electron dose calculation using a voxel based Monte Carlo algorithm (VMC) *Med. Phys.* **23** 445–57
- Keall P J and Hoban P W 1996a Super-Monte Carlo: a 3D electron beam dose calculation algorithm *Med. Phys.* **23** 2023–34
- 1996b Superposition dose calculation incorporating Monte Carlo generated electron track kernels *Med. Phys.* **23** 479–85
- Libby B, Siebers J and Mohan R 1998 Systematic analysis of Monte Carlo generating beam weights *Med. Phys.* **23** 965–71
- Ma C-M 1998 Characterization of computer simulated radiotherapy beams for Monte Carlo treatment planning *Radiat. Phys. Chem.* **53** 329–44
- Ma C-M, Faddegon B A, Rogers D W O and Mackie T R 1997 Accurate characterization of Monte Carlo calculated electron beams for radio-therapy *Med. Phys.* **24** 401–16
- Ma C-M, Li J S, Pawlicki T, Jiang S B and Deng J 2000c MCDOSE: a Monte Carlo dose calculation tool for radiation therapy treatment planning *Proc. 13th Int. Conf. on the Use of Computers in Radiation Therapy (Heidelberg, Germany)* (Berlin: Springer) pp 123–5
- Ma C-M, Mok E, Kapur A and Findley D 1997 Improvement of small-field electron beam dosimetry by Monte Carlo simulations *Proc. 12th Int. Conf. on the Use of Computers in Radiation Therapy (Salt Lake City, UT)* (Madison, WI: Medical Physics Publishing) pp 159–62
- Ma C-M, Mok E, Kapur A, Pawlicki T, Findley D, Brain S, Forster K and Boyer A L 1999a Clinical implementation of a Monte Carlo treatment planning system *Med. Phys.* **26** 2133–43
- Ma C-M and Nahum A E 1993 Calculation of absorbed dose ratios using correlated Monte Carlo sampling *Med. Phys.* **20** 1189–99
- Ma C-M, Pawlicki T, Jiang S B, Li J S, Deng J, Mok E, Kapur A, Xing L, Ma L and Boyer A L 2000a Monte Carlo verification of IMRT dose distributions from a commercial treatment planning optimization system *Phys. Med. Biol.* **45** 2483–95
- Ma C-M, Pawlicki T, Lee M C, Jiang S B, Li J S, Deng J, Yi B, Mok E and Boyer A L 2000b Energy- and intensity-modulated electron beams for radiotherapy *Phys. Med. Biol.* **45** 2293–311
- Ma C-M, Pawlicki T, Li J S, Jiang S B, Deng J, Kapur A, Mok E, Luxton G and Boyer A L 1999b MCDOSE—A dose calculation tool for radiotherapy treatment planning (abstract) *Med. Phys.* **26** 1148
- Ma C-M, Reckwerdt P, Holmes M, Rogers D W O, Geiser B and Walters B 1995 DOSXYZ users manual *NRCC Report PIRS-0509B*
- Mackie T R 1990 *Dosimetry of Ionizing Radiation* vol 3, ed K Kase, B Bjarnagard and F H Attix (New York: Academic) pp 541–620
- Mackie T R et al 1994 The OMEGA project: comparison among EGS4 electron beam simulations, 3D Fermi-Eyges calculations, and dose measurements *Proc. 11th Int. Conf. on the Use of Computers in Radiation Therapy (Manchester, UK)* pp 152–3
- Mohan R 1997 Why Monte Carlo? *Proc. 12th Int. Conf. on the Use of Computers in Radiation Therapy (Salt Lake City, UT)* (Madison, WI: Medical Physics Publishing) pp 16–18
- Mubata C D, Nahum A E, Rosenberg I and Bielajew A F 1998 Optimization of Monte Carlo simulation in external-beam treatment planning *Med. Phys.* **25** A185
- Nahum A E 1997 Conformal therapy needs Monte Carlo dose computation *Proc. Challenges in Conformal Radiotherapy* (Nice: European Society for Therapeutic Radiology and Oncology) pp 1–11
- Nelson W R, Hirayama H and Rogers D W O 1985 The EGS4 code system *Stanford Linear Accelerator Center Report SLAC-265* (Stanford, CA: SLAC)
- Neuenschwander H and Born E 1992 A macro Monte Carlo method for electron beam dose calculation *Phys. Med. Biol.* **37** 107–25
- Neuenschwander H, Mackie T R and Reckwerdt P J 1995 MMC: a high performance Monte Carlo code for electron beam treatment planning *Phys. Med. Biol.* **40** 543

- Pawlicki T, Jiang S B, Deng J, Li J S and Ma C-M 1999 Monte Carlo calculated beamlets for photon beam inverse planning (abstract) *Med. Phys.* **26** 1064-5
- Rogers D W O 1984a Fluence to dose equivalent conversion factors calculated with EGS3 for electrons from 100 keV to 20 GeV and photons from 11 keV to 20 GeV *Health Phys.* **46** 891
- 1984b Low energy electron transport with EGS *Nucl. Instrum. Methods A* **227** 535
- Rogers D W O and Bielajew A F 1984 The use of EGS for Monte Carlo calculations in medical physics *NRCC Report PXR-2692* (Ottawa: NRCC)
- 1986 Difference in electron depth-dose curve calculated with EGS and ETRAN and improved energy-range relationships *Med. Phys.* **13** 687-94
- 1990 *Dosimetry of Ionizing Radiation* vol 3, ed K Kase, B Bjarnagard and F H Attix (New York: Academic) pp 427-539
- Rogers D W O, Bielajew A F, Mackie T R and Kubsad S S 1990 The OMEGA project: treatment planning for electron-beam radiotherapy using Monte Carlo techniques *Phys. Med. Biol.* **35** 285
- Rogers D W O, Faddegon B A, Ding G X, Ma C-M, We J and Mackie T R 1995 BEAM—a Monte Carlo code to simulate radiotherapy treatment units *Med. Phys.* **22** 503-24
- Salvat F, Fernandez-Vera J M, Baro J and Sempau J 1996 *PENELOPE, An Algorithm and Computer Code for Monte Carlo Simulation of Electron-Photon Showers* (Barcelona: Informes Tècnics Ciemat)
- Schach von Wittenau A E, Bergstrom P M and Cox L J 2000 Patient-dependent beam modifier physics in Monte Carlo photon dose calculations *Med. Phys.* **27** 935-47
- Shortt K R, Ross C K, Bielajew A F and Rogers D W O 1986 Electron beam dose distributions near standard inhomogeneities *Phys. Med. Biol.* **31** 235-49
- Siebers J, Libby B and Mohan R 1998 Trust, but verify: comparison of MCNP and BEAM Monte Carlo codes for generation of phase space distributions for a Varian 2100C *Med. Phys.* **25** A143
- Walling R, Hartmann Siantar C, Albright N, Wieczorek D, Knapp D, Verhey L, May S and Moses E 1998 Clinical validation of the PEREGRINE Monte Carlo dose calculation system for photon beam teletherapy *Med. Phys.* **25** A128
- Wang L, Chui C and Lovelock M A 1998 A patient-specific Monte Carlo dose-calculation method for photon beams *Med. Phys.* **25** 867-78
- Zhang G G, Rogers D W O, Cygler J E and Mackie T R 1999 Monte Carlo investigation of electron beam output factors versus size of square cutout *Med. Phys.* **26** 743-50

Monte Carlo verification of IMRT dose distributions from a commercial treatment planning optimization system

C-M Ma, T Pawlicki, S B Jiang, J S Li, J Deng, E Mok, A Kapur, L Xing,
L Ma and A L Boyer

Radiation Oncology Department, Stanford University School of Medicine, Stanford, CA 94305,
USA

E-mail: cma@reyes.stanford.edu

Received 25 February 2000, in final form 8 May 2000

Abstract. The purpose of this work was to use Monte Carlo simulations to verify the accuracy of the dose distributions from a commercial treatment planning optimization system (Corvus, Nomos Corp., Sewickley, PA) for intensity-modulated radiotherapy (IMRT). A Monte Carlo treatment planning system has been implemented clinically to improve and verify the accuracy of radiotherapy dose calculations. Further modifications to the system were made to compute the dose in a patient for multiple fixed-gantry IMRT fields. The dose distributions in the experimental phantoms and in the patients were calculated and used to verify the optimized treatment plans generated by the Corvus system. The Monte Carlo calculated IMRT dose distributions agreed with the measurements to within 2% of the maximum dose for all the beam energies and field sizes for both the homogeneous and heterogeneous phantoms. The dose distributions predicted by the Corvus system, which employs a finite-size pencil beam (FSPB) algorithm, agreed with the Monte Carlo simulations and measurements to within 4% in a cylindrical water phantom with various hypothetical target shapes. Discrepancies of more than 5% (relative to the prescribed target dose) in the target region and over 20% in the critical structures were found in some IMRT patient calculations. The FSPB algorithm as implemented in the Corvus system is adequate for homogeneous phantoms (such as prostate) but may result in significant under- or over-estimation of the dose in some cases involving heterogeneities such as the air–tissue, lung–tissue and tissue–bone interfaces.

(Some figures in this article are in colour only in the electronic version; see www.iop.org)

1. Introduction

For the last few years, extensive research has been carried out to develop conformal radiotherapy using computer-controlled linear accelerators equipped with multileaf collimators (MLC) (Boesecke *et al* 1988, Leibel *et al* 1992, LoSasso *et al* 1993, Powlis *et al* 1993, Mageras *et al* 1994, Brewster *et al* 1995, Fraass *et al* 1995, McShan *et al* 1995, Yu *et al* 1995). More recently, intensity modulated radiotherapy (IMRT) has been developed (Brahme 1988, Convery and Rosenbloom 1992, Webb 1992, Boyer *et al* 1997) and implemented (Ling *et al* 1996, Boyer *et al* 1998) that uses computer-controlled modulation of x-ray fields by the MLC. It is anticipated that conformal radiotherapy will provide radiation oncologists with a significantly improved tool to deliver high doses of ionizing radiation to some tumour sites while reducing doses to adjacent normal tissue below levels to which they are unavoidably exposed by currently available techniques. Thus, acute and chronic toxicity associated with treatment of a tumour volume by radiation may be significantly reduced or delayed for certain sites of malignant presentations.

The use of conformal radiotherapy, especially with the IMRT technique, is a major departure from the way radiotherapy is currently delivered. Although the use of MLCs provides the possibility of achieving better dose distributions conformed to tumour targets, it also increases the complexity of treatment. The sequences of leaf movement and their associated effects on the dose delivered to the patient may vary significantly depending on the accelerator and the MLC design. Important factors include the variation of the accelerator head scatter component in the MLC-collimated beam (Convery and Webb 1997), the amount of photon leakage through the leaves (Wang *et al* 1996, Webb 1997, Holmes *et al* 1997), the scatter from the leaf ends, the 'tongue and groove' effect (Chui *et al* 1994, Wang *et al* 1996), the effect of back-scattered photons from the moving jaws and MLC leaves on the monitor chamber signal (Hounsell 1998). Traditionally, patient dose calculations in radiotherapy have been based on correcting measured dose distributions. New dose calculation algorithms have been developed to predict the patient dose from 'first principles' using a model of radiation transport (Mackie *et al* 1995). Comparisons of the traditional photon algorithms and the newer ones have been reviewed by Wong and Purdy (1990), Cunningham and Battista (1995) and Mackie *et al* (1996). Due to the lack of electron transport, the conventional dose calculation algorithms often failed to predict the dose distribution accurately near inhomogeneities (Mackie *et al* 1996, Mohan 1997, DeMarco *et al* 1998, Wang *et al* 1998, Ma *et al* 1999). Furthermore, the inverse-planning algorithms for beam optimization have all used approximations to speed up the dose computation that may introduce significant uncertainty in the calculated dose distributions, especially in the presence of heterogeneities. When simple source models are used in the dose computation, the correlation between the calibrated reference dose and the dose related to a beam segment may be lost. All the above imply a potential problem with the prediction of the dose distributions in a patient for an IMRT treatment.

Oldham and Webb (1997) reported differences in excess of 10% in the absolute dose between the optimization dose calculations and measurements (using film) of fields delivered by a dynamic MLC. The differences were attributed partially to the nonlinearity of dose per monitor unit (MU) for small MU deliveries (the actual dose delivered per MU increased by more than 10% from MU = 20 to MU = 1). Wang *et al* (1996) reported that for the Memorial Hospital's dynamic MLC delivery process, the discrepancies between the calculated dose and the measured dose were in excess of 5% if various effects related to the MLC construction, such as accelerator head scatter, were not properly accounted for. The uncertainty in the doses calculated by a conventional dose calculation algorithm was 5–10% in the presence of heterogeneities (Mohan 1997). Our recent Monte Carlo results were consistent with these findings (Ma *et al* 1999).

The purpose of this work was to verify the accuracy of the IMRT dose distributions from a commercial treatment planning optimization system (Corvus, Nomos Corp., Sewickley, PA) using Monte Carlo simulations. We have used the EGS4/BEAM Monte Carlo code system (Nelson *et al* 1985, Rogers *et al* 1995a, b) to simulate the clinical photon beams from two linear accelerators, Varian Clinac 2100C and 2300C/D (Varian Oncology, Palo Alto, CA). The EGS4/DOSXYZ code (Rogers *et al* 1995a, Ma *et al* 1995) was modified to compute the dose in a patient (a three-dimensional phantom built from the CT data) for multiple fixed-gantry fields. Phantom measurements were performed to commission the Monte Carlo system. The dose distributions in the experimental phantoms and in the patients were calculated and used to verify the optimized treatment plans generated by the Corvus inverse-planning system. In the following sections, we will describe the dose calculations in the inverse-planning system and the Monte Carlo simulations. We will show the dose distributions for homogeneous and heterogeneous phantoms and discuss the effect of material density and atomic number on the final dose calculations.

2. Materials and method

2.1. Treatment planning and dose measurement

The treatment planning optimization system used in this work is the Corvus inverse-planning system. The inverse planning process employs a simulated annealing optimization algorithm (Webb 1992). The dose calculation algorithm used for the inverse planning process is a finite-size pencil beam (FSPB) algorithm, which uses predetermined beamlet dose distributions. The beamlet distributions were derived from measured dose distributions and normalized to produce consistent output factors for various field sizes. The patient inhomogeneity correction is made by 'stretching' the beamlet distribution proportionally based on the equivalent pathlength. Some details of the dose calculations have been described by Holmes *et al* (1998) and Boyer *et al* (1999). The monitor unit calculations for a 'step-and-shoot' leaf sequence algorithm have been discussed by Boyer *et al* (1999). The effect of the leaf leakage is accounted for in Corvus by reducing the original beamlet weight by the same amount as the accumulated leakage for a given leaf sequence. This method works well for those beamlets whose weights are greater than the estimated leakage. If the beamlet weights are smaller than the leakage this method will underestimate the dose as any remaining leakage effect cannot be accounted for and the initial dose calculation does not include any leaf leakage effect (which is unknown before a leaf sequence is generated for the field). The Corvus system has been commissioned for clinical IMRT treatment planning (Xing *et al* 1999) and used for treating head and neck patients with IMRT (Boyer *et al* 1998).

In order to test the Corvus system, inverse plans were computed for various target shapes placed in the centre of a cylindrical water phantom having a diameter of 30 cm. Comparisons of the Corvus dose distributions with measurements have been reported in detail by Boyer *et al* (1999). In this work, we have computed the dose distributions for these plans using Monte Carlo methods (see descriptions below). For completeness, we briefly describe the plans and the measurements below. Inverse plans were computed for different hypothetical targets with different numbers of beams directed toward the axis of the cylinder at the centre of the target and spaced at equal angles. The treatments were delivered using a dynamic multileaf collimator (Varian Oncology Systems, Palo Alto, CA). The leaf sequences computed within the Nomos software were written into files with formats conformed to the requirements of the Varian digital control software. The leaf sequences were delivered using the monitor units calculated by the Corvus system. The absolute dose delivered by the leaf sequences was measured in the 30 cm diameter cylindrical water phantom using a 0.147 cm³ ionization chamber (Wellhöfer Dosimetrie, Schwartzenbruck, Germany) following the AAPM TG-21 protocol (AAPM 1983). No corrections were made for the variation in the chamber displacement effect, which depends on the dose gradient at the measurement point and the chamber diameter. This may introduce an up to 2% uncertainty in the measured dose for the 6 mm diameter chamber used (the dose gradient was 5–8% per centimetre at some measurement points). The chamber positioning uncertainty was about 0.1 cm. The overall uncertainty in the measured dose was estimated to be about 3% (1 σ).

2.2. The Monte Carlo simulation

We have used BEAM and DOSXYZ (Rogers *et al* 1995a, b, Ma *et al* 1995) Monte Carlo codes for the accelerator head simulation and dose calculation in the patient respectively. Both codes were EGS4 (Electron Gamma Shower version 4, Nelson *et al* (1985)) user codes, running under the UNIX operating system, developed through the Omega project for Monte Carlo treatment planning dose calculations (Mackie *et al* 1994). Detailed descriptions of the software can be

found from Rogers *et al* (1995a, b). A detailed description of the clinical implementation of the Monte Carlo code system was given in a previous publication (Ma *et al* 1999).

Two types of clinical linear accelerators were simulated for the clinical implementation of Monte Carlo dose verification in this work: Varian Clinac 2100C and 2300C/D (Varian Oncology Systems, Palo Alto, CA). The dimensions and materials for the accelerator components were incorporated according to the manufacturer's specifications. Electron beams emerging from the vacuum exit window were assumed to be monoenergetic and monodirectional with a beam radius of 0.1–0.2 cm. These were found to be reasonable assumptions to achieve an acceptable dose calculation accuracy of about 2% of the dose maximum (D_{\max}) anywhere in the phantom for clinical radiotherapy applications (Kapur *et al* 1998, Ma 1998, Ma *et al* 1999). We obtained accurate phase-space data for photon beams with nominal energies of 4, 6 and 15 MV. The energy cut-offs for electron transport in the accelerator simulation (ECUT and AE) 700 keV (kinetic + rest mass) and for photon transport (PCUT and AP) 10 keV. The maximum fractional energy loss per electron step (ESTEPE) was 0.04. The bremsstrahlung splitting and Russian roulette options were implemented for photon beam simulations (Rogers *et al* 1995b). The ICRU recommended compositions and stopping power values were used for the materials used in the accelerator simulations (ICRU 1984). The phase-space data were scored at a plane immediately above the photon jaws. The number of particles in a photon beam file was about 50 million. Field shaping by photon jaws, blocks and the MLC was further simulated using BEAM and the phase-space data could be stored temporarily or used directly for dose calculations.

The DOSXYZ code was designed for dose calculations in a 3D rectilinear voxel (volume element) geometry (Ma *et al* 1995). Voxel dimensions were completely variable in all three directions. Every voxel could be assigned to a different material. The cross-section data for the materials used were available in a pre-processed PEGS4 cross-section data file. The mass density of the material in a DOSXYZ calculation was varied based on the patient's CT data, although the density effect corrections for the stopping powers of the material remain unchanged (Ma *et al* 1999). The voxel dimensions and materials were defined in a DOSXYZ input file together with the transport parameters such as ECUT, PCUT, ESTEPE and the parameters required by PRESTA (Bielajew and Rogers 1988). The phase-space data obtained from a BEAM simulation was used as a source input with variable source positions and beam incidence angles. Dose contributions from different beam components were selectively calculated based on the particle charge or the LATCH settings specified in the BEAM simulation. DOSXYZ produced a data file that contained geometry specifications such as the number of voxels in all three directions and their boundaries as well as the dose values and the associated (1σ) statistical uncertainties in the individual voxels.

The DOSXYZ code has been modified to read the MLC leaf sequence files for IMRT treatment. For this study, the Varian dynamic MLC leaf sequence files (G-version) generated using a step-and-shoot leaf sequencing algorithm, were used. The monitor units for each leaf sequence were integrated into a two-dimensional map (grids). The dimensions of the map at the isocentre (100 cm from the virtual point source position) are 40 cm in both the x and y directions and the grid sizes were 0.1 cm. The monitor units for the open areas were accumulated for each of the pixels, while for the closed areas a fraction of the monitor units were accumulated based on the measured MLC leakage factor for each beam energy. Thus, the integrated intensity map has included the averaged leaf leakage effect but ignored the influence of the leaf shape (tongue and groove) and the variation of the spatial and spectral distributions due to photon attenuation and scattering in the MLC leaves. This is considered to be a reasonable approach since, unless the effect of organ motion and patient set-up uncertainty has been accounted for properly, the averaged leaf leakage is a more realistic quantity than

the explicit leakage through the leaf and the tongue and groove for estimating the overall dose in a patient during the whole treatment course. The transmission factor for the areas under the photon jaws was assumed to be zero. The dimensions of the photon jaw opening were set according to the actual treatment set-ups. Further modifications were made to simulate several gantry angles in the same run. The leaf sequence files were read sequentially and the gantry angle was changed automatically after the simulation of a photon field was completed.

During the Monte Carlo simulation, the weight of a phase-space particle was altered based on the value of the pixel in the intensity map through which the particle was travelling. To improve the simulation efficiency, two variance reduction techniques were implemented in the DOSXYZ code, particle splitting and Russian roulette (Rogers and Bielajew 1990). The former was applied to the particles with weight greater than unity and the latter was applied to the particles with weight smaller than unity. The splitting and Russian roulette processes were implemented in such a way that the resulting particles would have identical weighting factors. Using uniform weighting factors will generally improve the statistical uncertainty of a simulation.

For patient dose calculations, the simulation phantom was built from the patient's CT data with up to $128 \times 128 \times 128$ voxels (uniform in any dimensions). The side of a voxel varied from 0.2 to 0.4 cm. The EGS4 transport parameters were set to $ECUT = AE = 700$ keV, $PCUT = AP = 10$ keV and $ESTEPE = 0.04$. The number of particle histories simulated ranged from 300 million to 1 billion for up to nine gantry angles for an IMRT treatment. The 1σ statistical uncertainty in the dose was generally 1–2% of the D_{max} value. The CPU time required for an IMRT simulation was 3–15 h on a single Pentium III 450 MHz PC depending on the beam energy and field sizes.

3. Results

3.1. Comparisons in homogeneous water phantoms

Both the inverse-planning system and the Monte Carlo dose calculation system have been commissioned for routine clinical applications (Xing *et al* 1999, Ma 1998, Ma *et al* 1999). Both systems regenerated the PDD curves and the dose profiles at various depths to within 2% of the dose maximum values of the measured beam data for various field sizes and source to surface distances (SSD). The dose distributions given by the Corvus system agreed with measurements to about 3% in a cylindrical water phantom with various hypothetical target shapes (Boyer *et al* 1999). Figure 1 shows the dose distributions in a 30 cm diameter water cylinder irradiated by seven 6 MV intensity-modulated photon beams calculated by Corvus and by the Monte Carlo simulations. The critical structure is in the centre of the water cylinder immediately next to the C-shaped target. A beamlet size of $1 \text{ cm} \times 1 \text{ cm}$ was used in the optimization calculation. The leaf sequencing algorithm used 20 intensity levels. The isodose lines calculated by both systems agreed within about 4% or a shift in isodose lines within about 0.3 cm. These small discrepancies were thought to be partially due to the approximations used by Corvus in accounting for the effect of MLC leaf leakage. Considering that the average leaf leakage is about 1.5% for a 6 MV beam and the total MU required to deliver an IMRT field is about three times more than that required by a conventional field, the estimated accumulated leaf leakage beneath a completely closed leaf pair is about 4.5%. Thus, a few per cent of the observed dose difference may be attributed to the difference in leaf leakage implementation between Corvus and Monte Carlo.

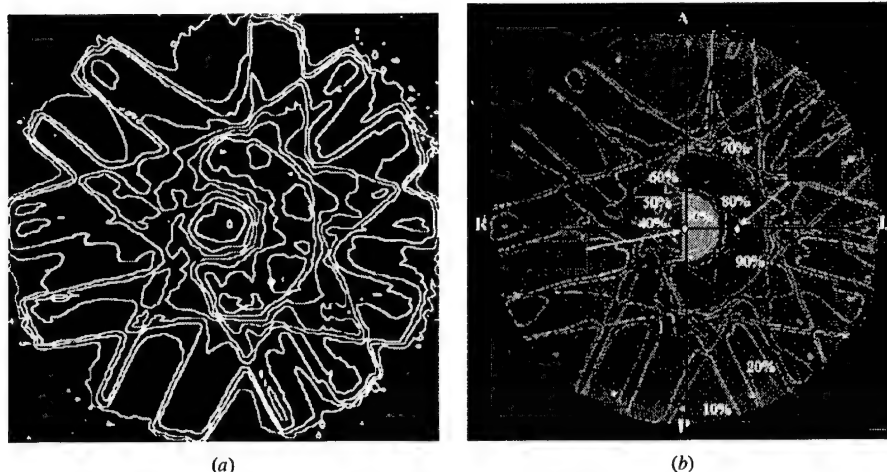


Figure 1. Comparison of 6 MV photon beam (seven co-planar fields at 26, 77, 180, 231, 283 and 334° gantry angles) dose distributions in a water cylinder calculated by Monte Carlo (a) and Corvus (b). The differences between the Corvus calculations and measurements using an ion chamber are shown for certain locations (arrows).

3.2. Comparisons in CT phantoms

In this work, we have compared the dose distributions calculated by Monte Carlo and the Corvus FSPB algorithm for various treatment sites to identify potential treatment situations that may benefit from dose accuracy improvements. In the following examples, we show two typical IMRT treatment plans computed by the Corvus inverse planning system and verified by the Monte Carlo system.

3.2.1. Prostate. To explore the effect of photon and electron transport on IMRT dose calculations, we show in figure 2 an IMRT prostate treatment plan calculated by Monte Carlo simulation and the Corvus system. The plan was generated using the Corvus system for 15 MV photon beams with nine gantry angles (20, 60, 100, 140, 220, 260, 300 and 340°). The beam intensity was modulated using a Varian dynamic MLC with 80 leaves. In both calculations, the isodose lines represent the absolute dose values in the patient. It can be seen that the dose values in the target (the prostate) agreed very well between the Corvus calculations and the Monte Carlo simulations. Similar results were found for six other prostate cases compared (not shown). The difference in the average dose to the target volume was 1.6% between Monte Carlo and Corvus and the maximum dose difference in the target dose was 3.4%. This confirms that both calculation algorithms can predict dose distributions in homogeneous phantoms accurately. The dose values in the nearby critical structures also agreed to 3–7% of the prescribed target dose. For the case shown in figure 2(c), the maximum difference was about 3 Gy in the rectum. However, other cases also showed the maximum differences in the bladder. These differences may be considered to be clinically acceptable.

The dose values in the regions near the bony structures sometimes showed a difference of a few per cent between the Corvus and the Monte Carlo calculations. These discrepancies may be partially explained by the effect of electron backscatter from the bone (high atomic number and high density) to the soft tissue, which was accurately accounted for by the Monte Carlo

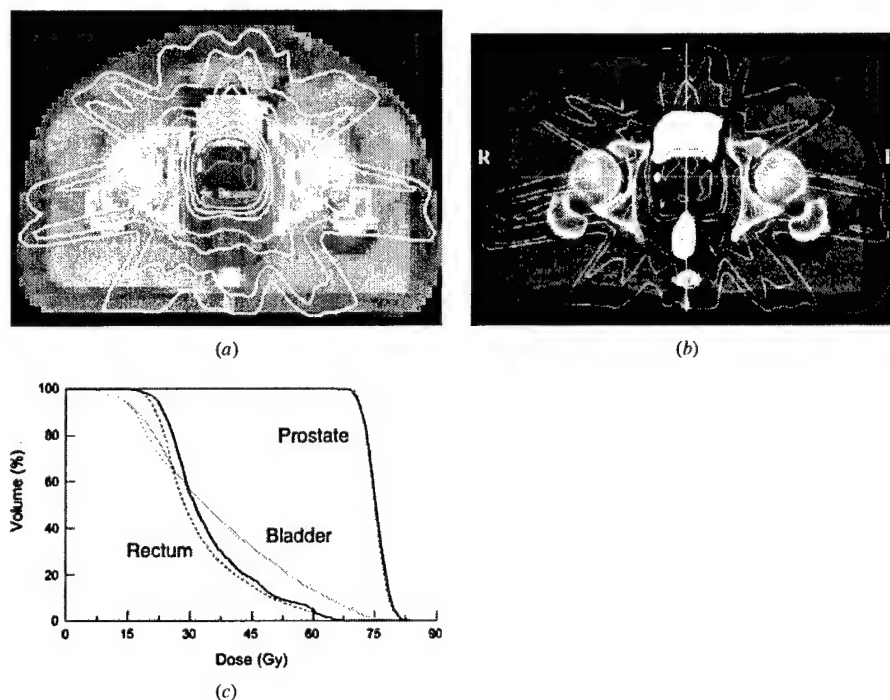


Figure 2. Comparison of 15 MV photon beam (nine co-planar fields) dose distributions for a prostate treatment calculated by Monte Carlo (a) and Corvus (b). The isodose lines are 77.2, 70.0, 56.1, 48.9, 35.0, 27.8, 21.1 and 13.9 Gy respectively in each figure. (c) The dose volume histograms as calculated by Monte Carlo (full curves) and Corvus (broken curves).

simulation but not in a FSPB algorithm. There have been several Monte Carlo studies in the literature showing similar discrepancies between the Monte Carlo algorithm and the correction based calculation algorithms in dose build-up or build-down regions near air cavities, lung and large bony structures (DeMarco *et al* 1998, Mohan 1997, Wang *et al* 1996, Ma *et al* 1999). It should be mentioned that the difference in the dose to the bone was partially due to the fact that the conventional dose calculation algorithms usually used water as the phantom material and the inhomogeneity corrections were computed using varying electron density (based on the CT numbers) while the Monte Carlo algorithm used different materials such as air, tissue, lung and bone with varying mass density calculated from the CT data. If we convert the dose to the bone material to the dose to tissue using the stopping power ratio for bone to tissue (assuming the same electron energy fluence) the dose in the bone regions will be about 3.5% higher for soft bone and about 10% higher for compact bone (ICRU 1984, Siebers *et al* 2000). We will discuss this issue further in section 4. Anyway, the dose in the surrounding tissue regions should not be affected by the conversion, which was mainly caused by the perturbation of the electron fluence by the nearby inhomogeneous anatomy.

3.2.2. Vertebra. Figure 3 shows the dose distributions for the treatment of the vertebra calculated by both Monte Carlo simulation and the Corvus system. The plan was generated using the Corvus system for 15 MV photon beams with nine co-planar gantry angles (20, 55,

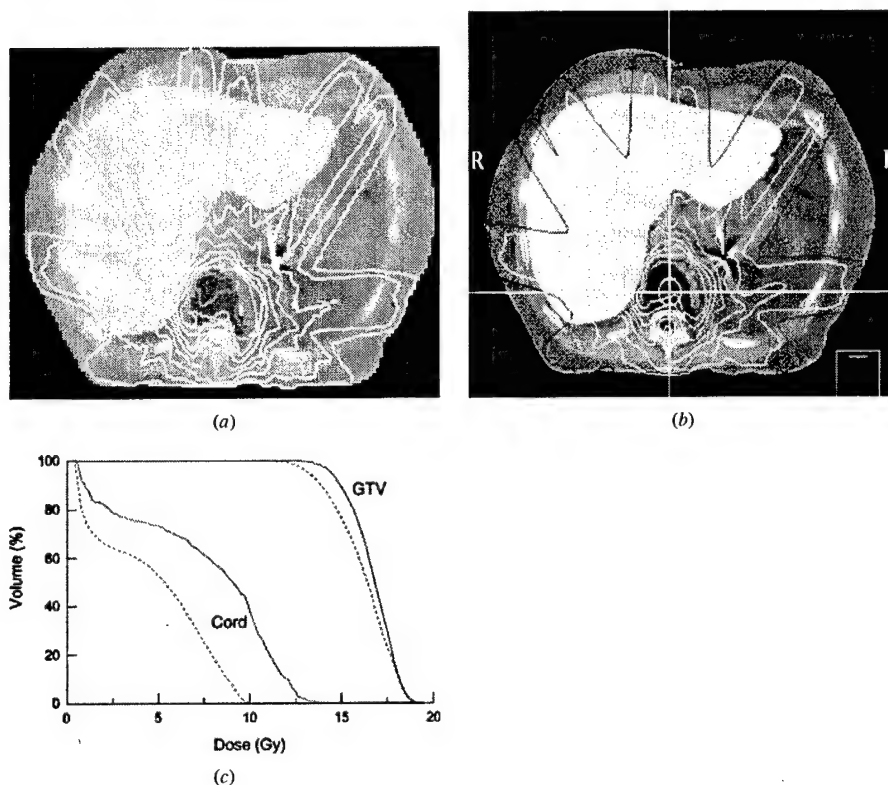


Figure 3. Dose distributions for the treatment of the vertebra calculated by Monte Carlo (a) and by Corvus (b) for 15 MV photons (nine co-planar fields). The isodose lines are 17.6, 15.6, 13.7, 11.7, 9.8, 7.8, 5.9, 3.9 and 2.0 Gy respectively in each figure. (c) The dose volume histograms as calculated by Monte Carlo (full curves) and Corvus (broken curves) for the target and the spinal cord.

90, 140, 180, 220, 260, 300 and 340°). The intensity was modulated using a Varian dynamic MLC with 80 leaves. The prescribed target dose was 18 Gy. The maximum dose in the target showed good agreement between Corvus and Monte Carlo (figure 3(c)). The Monte Carlo dose distribution showed slightly better target coverage than the Corvus dose distribution (a 2 Gy difference in the minimum target dose). Because the cord was sometimes immediately next to the target region the maximum cord dose was expected to be equal to or higher than the minimum target dose. This was confirmed by the Monte Carlo simulations (see figure 3(c)). In the regions near large bony structures (such as the cord) differences of more than 20% of the prescribed target dose could be seen between the Corvus calculation (10 Gy) and the Monte Carlo simulation (14 Gy). The difference in the dose to the cord was thought to be due in part to electron scattering from the surrounding bone, which could not be modelled properly using the FSPB algorithm. Another possible reason might be due to the implementation of the heterogeneity and leaf leakage corrections in the FSPB model. Although the photon beams were optimized to avoid the cord, electrons could reach the cord and the dose to the cord could be enhanced due to the high-density material surrounding it and/or photon leaf leakage that is not included in the dose calculation during the inverse planning process. Further studies are

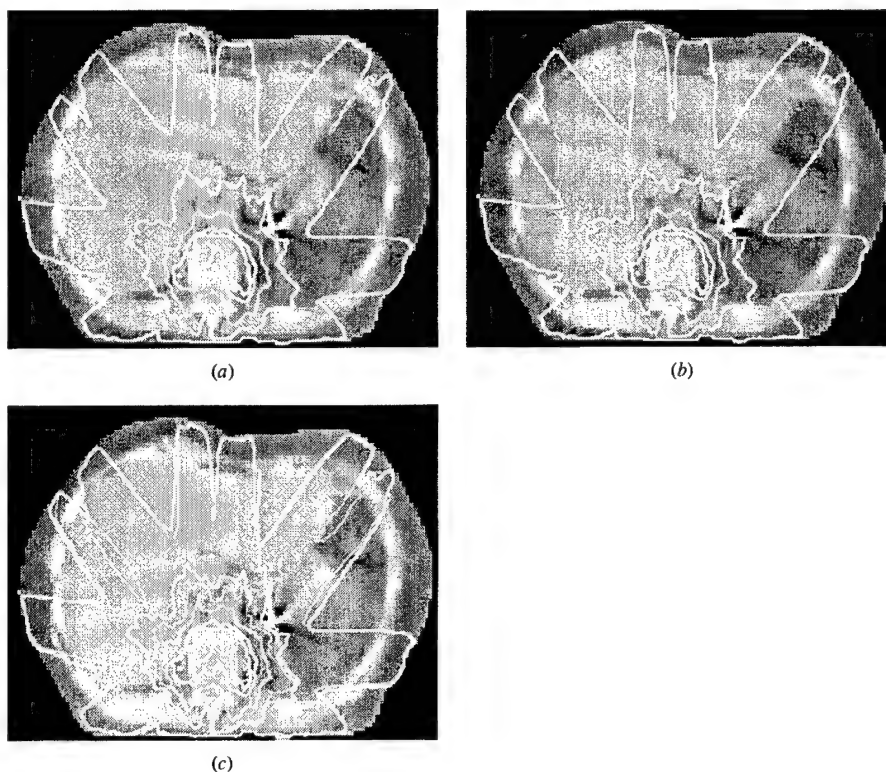


Figure 4. Dose distributions for different tissue types and material densities: (a) tissue and bone with variable density (thick line) and tissue with unity density (thin line); (b) tissue and bone with variable density (thick line) and tissue with variable density (thin line); and (c) tissue and bone with variable density (thick line) and tissue with unity density and bone with 10 g cm^{-3} density (thin line). The phantom geometry and beam arrangements are the same as in figure 3. The isodose lines are given as 10, 30, 50, 70 and 80% of the prescribed target dose.

needed to understand these differences if more access to the FSPB and leaf sequence algorithms in the Corvus system is available.

4. Discussion

Several important factors may affect the Monte Carlo calculated dose distributions and the DVH curves. First, the isodose lines and the DVH curves are affected by the materials used in the patient CT phantom, i.e. whether we plot dose to tissue only or dose to any material (such as air, tissue or bone). It seems reasonable that our previous experience was based on dose to tissue (or dose to water, the difference between the two is within 1%) and therefore the dose values should be expressed as dose to tissue. However, it can also be argued that the real dose to the biological material such as bone should be given whenever possible. Only in this way can the relationship between the 'old' practice and new experience be established.

To understand the effect of the conversion of the dose to different materials, we show in figure 4 the dose distributions calculated using Monte Carlo with different materials and

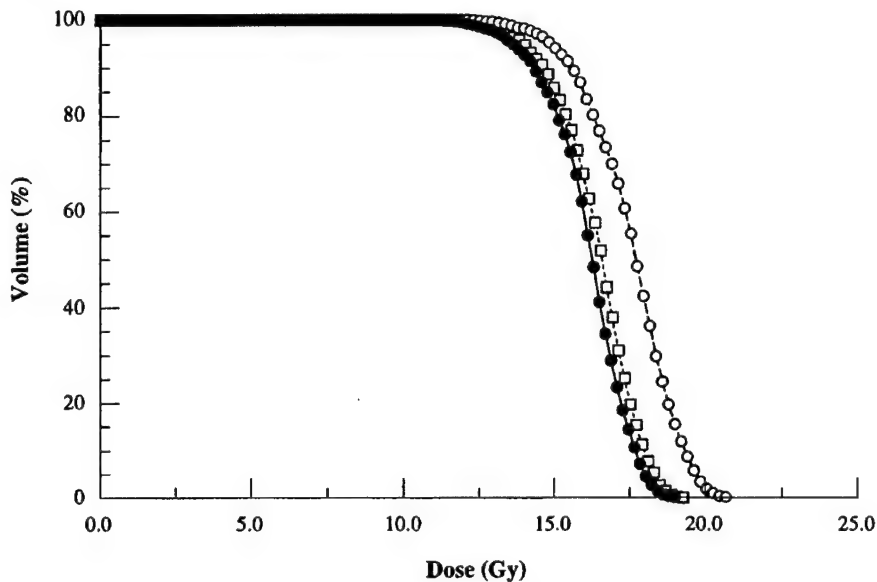


Figure 5. Dose volume histograms for the GTV in figure 3. Full circles are obtained using a CT phantom consisting of air, tissue and bone of variable density with dose calculated for each material. Open circles are obtained using the same phantom with dose converted to tissue using the stopping power ratios of tissue to bone or tissue to air. Open squares are obtained using a phantom consisting of only tissue of variable density.

density configurations for the IMRT case shown in figure 3. In figure 4(a), the dose distribution was calculated using tissue with unit density and air. This phantom should not show any heterogeneity effect due to the change in tissue (or bone) densities. In figure 4(b), the dose distribution was calculated using air and tissue with variable density converted from the CT data. This is similar to the phantom used by the Corvus system. In figure 4(c), the dose distribution was calculated with air, unit density tissue and 10 g cm^{-3} density bone. For comparison, the dose distribution calculated using air, tissue and bone with proper densities converted from the CT data is shown in each figure. The isodose curves were computed by normalizing the dose values to the prescribed target dose. The differences in the isodose lines in figure 4(a) and (b) are small (2–3%). This is also clearly shown in figure 5 for the target DVHs. The difference between dose to tissue and dose to bone would be about 3.5% for soft bone and about 10% for hard bone (Siebers *et al* 2000) if converted using the stopping power ratios for tissue to bone (or soft bone) at these beam qualities, assuming the same electron energy fluence. Clearly, such conversion is not equivalent to performing the Monte Carlo simulation using a water (or tissue) phantom with variable mass (or electron) density. It is known that electron backscattering from the high atomic number materials may perturb the dose in tissue near the tissue–bone interface. This effect is less significant when dose values are averaged over course scoring volumes (0.3–0.4 cm voxels). In figure 4(c), the density of bone was artificially increased to 10 g cm^{-3} which caused significant attenuation of the beams and therefore altered the doses behind the bones. The effects on the surface doses are smaller than for the high dose regions. The maximum dose for the artificially high-density bone geometry is about 15% lower than that for the phantom with normal material density.

Although Monte Carlo dose calculations are time-consuming it is possible to use Monte Carlo calculated dose distributions to verify the IMRT treatment plans in order to detect any cases where the FSPB dose calculation algorithm as implemented in Corvus may fail to predict the dose perturbation effect near inhomogeneities. Monte Carlo simulation may also be used directly for IMRT beamlet distribution calculation as a practical solution to this problem. Our experiences show that a factor of two to three more Monte Carlo particle histories are needed for an IMRT treatment simulation compared with a conventional photon treatment simulation to achieve the same statistical uncertainty. This is because more monitor units are needed to deliver intensity modulated photon fields; more particles will be simulated in a Monte Carlo calculation but many of them will be stopped by the MLC leaves. Therefore, the CPU time per photon history for an IMRT simulation is less than that for a conventional field. Using the existing computing power (8 CPUs) of the Corvus system, the calculation time for a typical 'inverse plan' would be increased from the current 0.5–1 h to 2–4 h with two Monte Carlo calculations. The pre-optimization dose calculation will provide the beamlet distributions for the optimization process, which take into account the effect of the accelerator head scatter and inhomogeneous anatomy of the patient. The post-optimization dose calculation will include the effects due to leaf leakage, leaf scatter and photon backscatter into the monitor chamber after the sequence of MLC leaf movement and jaw positions has been generated. Further studies are under way on a Monte Carlo dose calculation based inverse planning system (Pawlicki *et al* 1999, Ma *et al* 2000).

5. Summary

We have implemented a Monte Carlo system for routine radiotherapy treatment planning dose calculations. In our previous publications we have shown that Monte Carlo simulations agreed with measurements to within 2% for various clinical beam set-ups in homogeneous and heterogeneous phantoms. Based on these results, we have moved one step nearer to using the Monte Carlo simulations to verify the IMRT dose distributions computed by the Corvus system, which employs a FSPB algorithm for beamlet dose calculations, assuming that the Monte Carlo simulations are accurate at the 2% level for patient phantoms built from CT data.

Our results showed that the FSPB algorithm was adequate for most of the IMRT cases where the target was not immediately adjacent to the critical structures. However, the FSPB algorithm may not accurately predict the dose distributions in and near inhomogeneities in some cases. The dose in the target volume calculated by the Corvus system differed from the Monte Carlo results by more than 5%, while the dose to the critical organ differed by more than 20% of the prescribed target dose for a few cases. This suggests that, for such cases, more accurate dose calculation algorithms than that currently implemented in Corvus should be used for intensity-modulated radiotherapy treatment planning.

Acknowledgments

We would like to acknowledge Varian Oncology Systems, Palo Alto, CA, for providing detailed information on the Varian Clinac linear accelerators and Nomos Corp., Sewickley, PA, for the inverse-planning system. We would like to thank our colleagues, Sam Brain, Todd Koumrian, Behrooz Tofighrad and Michael Luxton, for help with the computers and software support. We are grateful to Dr Iwan Kawrakow for the DOSXYZ. SHOW program to plot isodose distributions, and to Jinsheng Li and Michael Luxton for modifications to the program to display structures of interest and to compare two isodose distributions on the same plot.

This investigation was supported in part by grants CA78331 from the NIH, BC971292 from the DOD, Seed Cycle 1 from the RSNA Research and Education Fund, and a consortium agreement with the NumeriX, LLC.

References

- AAPM 1983 AAPM TG-21, A protocol for the determination of absorbed dose from high-energy photons and electrons *Med. Phys.* **10** 741
- Bielajew A F and Rogers D W O 1988 Variance-reduction techniques *Monte Carlo Transport of Electrons and Photons* ed T M Jenkins, W R Nelson, A Rindi, A E Nahum and D W O Rogers (New York: Plenum) pp 407-19
- Boesecke R, Doll J, Bauer B, Schlegel W, Pastyr O and Lorenz M 1988 Treatment planning for conformation therapy using a multileaf collimator *Strahlenther. Onkol.* **164** 151-4
- Boyer A L, Geis P B, Grant W, Kendall R and Carol M 1997 Modulated-beam conformal therapy for head and neck tumors *Int. J. Radiat. Oncol. Biol. Phys.* **39** 227-36
- Boyer A L, Xing L, Ma C-M, Curran B, Hill R, Holmes T and Bleier A 1999 Theoretical consideration of monitor unit calculations for intensity modulated beam treatment planning (abstract) *Med. Phys.* **26** 187-95
- Boyer A L, Xing L, Ma L and Forster K 1998 Verification and delivery of head and neck intensity modulated radiotherapy *Med. Phys.* **25** A200-1
- Brahme A 1988 Optimal setting of multileaf collimators in stationary beam radiation therapy *Strahlenther. Onkol.* **164** 343-50
- Brewster L, Mohan R, Mageras G, Burman C, Leibel S and Fuks Z 1995 Three dimensional conformal treatment planning with multileaf collimators *Int. J. Radiat. Oncol. Biol. Phys.* **33** 1081-89
- Chui C S, LoSasso T and Spirou S 1994 Dose calculations for photon beams with intensity modulation generated by dynamic jaw or multileaf collimators *Med. Phys.* **21** 1237-43
- Convery D J and Rosenbloom M E 1992 The generation of intensity-modulated fields for conformal radiotherapy by dynamic collimation *Phys. Med. Biol.* **37** 1359-74
- Convery D J and Webb S 1997 Calculation of the distribution of head-scattered radiation in dynamically-collimated MLC fields *Proc. 12th Int. Conf. on the Use of Computers in Radiation Therapy (Salt Lake City, UT)* pp 350-3
- Cunningham J R and Battista J J 1995 Calculation of dose distributions for x-ray therapy *Phys. Canada* **51** 190-218
- DeMarco J J, Solberg T D and Smathers J B 1998 A CT-based Monte Carlo simulation tool for dosimetry planning and analysis *Med. Phys.* **25** 1-11
- Fraass B A, McShan D L, Kessler M L, Matrone G M, Lewis J D and Weaver T A 1995 A computer-controlled conformal radiotherapy system. I: overview *Int. J. Radiat. Oncol. Biol. Phys.* **33** 1139-57
- Holmes T M, Bleier A, Carol M, Curran B, DeNisi J, Hill R, Kania A, Lalonde R, Larson L and Sternick E 1998 The Corvus dose model revealed (abstract) *Med. Phys.* **25** 144
- Holmes T M, Bleier A, Carol M, Curran B, Kania A, Lalonde R, Larson L and Sternick E 1997 The effect of MLC leakage on the calculation and delivery of intensity modulated radiotherapy (abstract) *Med. Phys.* **24** 997
- Hounsell A R 1998 Monitor chamber backscatter for intensity modulated radiation therapy using multileaf collimators *Phys. Med. Biol.* **43** 445-54
- ICRU 1984 Radiation dosimetry: stopping powers for electrons and positrons *ICRU Report 37* (Bethesda, MD: ICRU)
- Kapur A, Ma C-M, Mok E and Findley D 1997 Characterization of small field electron beams for radiotherapy using Monte Carlo simulations *Proc. 12th Int. Conf. on the Use of Computers in Radiation Therapy (Salt Lake City, UT)* pp 157-8
- Kapur A, Ma C-M, Mok E, Findley D and Boyer A L 1998 Monte Carlo calculations of clinical electron beam output factors *Phys. Med. Biol.* **43** 3479-94
- Kutcher G J, Mageras G S and Leibel S A 1995 Control, correction and modeling of set-up errors and organ motion *Semin. Radiat. Oncol.* **5** 134-45
- Leibel S A, Kutcher G J and Mohan R et al 1992 Three-dimensional conformal radiation therapy at the Memorial Sloan-Kettering Cancer Center *Semin. Radiat. Oncol.* **2** 274-89
- Ling C C et al 1996 Conformal radiation treatment of prostate cancer using inversely-planned intensity-modulated photon beams produced with dynamic multileaf collimation *Int. J. Radiat. Oncol. Biol. Phys.* **35** 730-41
- LoSasso T, Chui C S, Kutcher G J, Leibel S A, Fuks Z and Ling C C 1993 The use of multileaf collimators for conformal radiotherapy of carcinomas of the prostate and nasopharynx *Int. J. Radiat. Oncol. Biol. Phys.* **25** 161-70
- Ma C-M 1998 Characterization of computer simulated radiotherapy beams for Monte Carlo treatment planning *Radiat. Phys. Chem.* **53** 329-44

- Ma C-M, Mok E, Kapur A and Findley D 1997 Improvement of small-field electron beam dosimetry by Monte Carlo simulations *Proc. 12th Int. Conf. on the Use of Computers in Radiation Therapy (Salt Lake City, UT)* pp 159–62
- Ma C-M, Mok E, Kapur A, Pawlicki T A, Findley D, Brain S, Forster K and Boyer A L 1999 Clinical implementation of a Monte Carlo treatment planning system for radiotherapy *Med. Phys.* **26** 2133–43
- Ma C-M, Pawlicki P, Lee M C, Jiang S B, Li J S, Deng J, Yi B, Mok E and Boyer A L 2000 Energy- and intensity-modulated electron beams for radiotherapy *Phys. Med. Biol.* **45** 2293–311
- Ma C-M, Reckwerdt P, Holmes M, Rogers D W O and Geiser B 1995 DOSXYZ users manual *National Research Council Report PIRS-0509(B)* (Ottawa: NCRC)
- Mackie T R, Holmes T W, Reckwerdt P J and Yang J 1995 Tomotherapy: optimized planning and delivery of radiation therapy *Int. J. Imaging Syst. Technol.* **6** 43–55
- Mackie T R, Reckwerdt P, McNutt T, Gehring M and Sanders C 1996 Photon beam dose calculations *Teletherapy: Present and Future* ed T R Mackie and J R Palta (Madison, WI: Advanced Medical Publishing) pp 103–35
- Mackie T R, Reckwerdt P and Papanikolaou N 1995 3-D photon beam algorithms *3-D Radiation Treatment Planning and Conformal Therapy* ed J A Purdy and B Emami (Madison, WI: Medical Physics Publishing) pp 201–22
- Mackie T R *et al* 1994 The OMEGA project: comparison among EGS4 electron beam simulation, 3D Fermi-eyes calculations and dose measurements *Proc. 11th Int. Conf. on the Use of Computers in Radiation Therapy (Manchester, UK)* pp 152–3
- Mageras G S *et al* 1994 Initial clinical experience with computer-controlled conformal radiotherapy using the MM50 microtron *Int. J. Radiat. Oncol. Biol. Phys.* **30** 971–8
- McShan D L, Fraass B A, Kessler M L, Matrone G M, Lewis J D and Weaver T A 1995 A computer-controlled conformal radiotherapy system. II: sequence processor *Int. J. Radiat. Oncol. Biol. Phys.* **33** 1159–72
- Mohan R 1997 Why Monte Carlo? *Proc. 12th Int. Conf. on the Use of Computers in Radiation Therapy (Salt Lake City, UT)* pp 16–18
- Nelson R, Hirayama H and Rogers D W O 1985 The EGS4 code system *Stanford Linear Accelerator Center Report SLAC-265* (Stanford, CA: SLAC)
- Oldham M and Webb S 1997 Intensity-modulated radiotherapy by means of static tomotherapy: a planning and verification study *Med. Phys.* **24** 827–36
- Pawlicki T A, Jiang S B, Deng J, Li J S and Ma C-M 1999 Monte Carlo calculated beamlets for photon beam inverse planning (abstract) *Med. Phys.* **26** 1064–5
- Powlis W D, Smith A, Cheng E *et al* 1993 Initiation of multileaf collimator conformal radiation therapy *Int. J. Radiat. Oncol. Biol. Phys.* **25** 171–9
- Rogers D W O and Bielajew A F 1990 Monte Carlo techniques of electrons and photons for radiation dosimetry *Dosimetry of Ionizing Radiation* vol 3, ed K Kase, B E Bjarnagard and F H Attix (New York: Academic) pp 427–539
- Rogers D W O, Faddegon B A, Ding G X, Ma C M, Wei J S and Mackie T R 1995a BEAM: a Monte Carlo code to simulate radiotherapy treatment units *Med. Phys.* **22** 503–25
- Rogers D W O, Ma C M, Ding G X and Walters B 1995b BEAM users manual *National Research Council Report PIRS-0509(A)* (Ottawa: NRC)
- Siebers J V, Keall P J, Nahum A E and Mohan R 2000 Converting absorbed dose to medium to absorbed dose to water for Monte Carlo based photon beam dose calculations *Phys. Med. Biol.* **45** 983–95
- Wang L, Chui C and Lovelock M 1998 A patient-specific Monte Carlo dose-calculation method for photon beams *Med. Phys.* **25** 867–78
- Wang X, Spirou S, LoSasso T, Stein J, Chui C and Mohan R 1996 Dosimetric verification of intensity modulated fields *Med. Phys.* **23** 317–28
- Wong J W and Purdy J A 1990 On the methods of inhomogeneity corrections for photon transport *Med. Phys.* **17** 807–14
- Webb S 1992 Optimization by simulated annealing of three-dimensional conformal treatment planning for radiation fields defined by multi-leaf collimator: II. Inclusion of two-dimensional modulation of x-ray intensity *Phys. Med. Biol.* **37** 1689–704
- 1997 *The Physics of Conformal Radiotherapy: Advances in Technology* (Bristol: Institute of Physics Publishing)
- Xing L, Curran B, Hill R, Holmes T, Ma L, Forster K and Boyer A L 1999 Dosimetric verification of a commercial inverse treatment planning system *Phys. Med. Biol.* **44** 463–78
- Yu C X, Symons J M, Du M N, Martinez A A and Wong J W 1995 A method for implementing dynamic photon beam intensity modulation using independent jaws and multileaf collimators *Phys. Med. Biol.* **40** 769–87

Monte Carlo characterization of clinical electron beams in transverse magnetic fields

Michael C Lee and Chang-Ming Ma

Department of Radiation Oncology, Stanford University School of Medicine, Stanford, CA 94305, USA

Received 16 May 2000

Abstract. Monte Carlo simulations were employed to study the characteristics of the electron beams of a clinical linear accelerator in the presence of 1.5 and 3.0 T transverse magnetic fields and to assess the possibility of using magnetic fields in conjunction with modulated electron radiation therapy (MERT). The starting depth of the magnetic field was varied over several centimetres. It was found that peak doses of as much as 2.7 times the surface dose could be achieved with a 1.5 T magnetic field. The magnetic field was shown to reduce the 80% and 20% dose drop-off distance by 50% to 80%. The distance between the 80% dose levels of the pseudo-Bragg peak induced by the magnetic field was found to be extremely narrow, generally less than 1 cm. However, by modulating the energy and intensity of the electron fields while simultaneously moving the magnetic field, a homogeneous dose distribution with low surface dose and a sharp dose fall-off was generated. Heterogeneities are shown to change the effective range of the electron beams, but not eliminate the advantages of a sharp depth-dose drop-off or high peak-to-surface dose ratio. This suggests the applicability of MERT with magnetic fields in heterogeneous media. The results of this study demonstrate the ability to use magnetic fields in MERT to produce highly desirable dose distributions.

1. Introduction

The current trend in radiation therapy towards conformal techniques requires the ability to deposit high dose to a given target region, while sparing surrounding normal tissue. Depth-dose distributions approaching the ideal of a step function are available from the use of protons, heavy ions and exotic particles such as π mesons. However, at present, these treatment modalities are of greatly restricted use due to the extreme expense and technical complexity of the accelerator systems. In contrast, an electron linear accelerator may cost a factor of a hundred less than a proton accelerator, and be orders of magnitude more compact; electron accelerators are thus found in most radiation therapy centres. Furthermore, while photon beam intensity-modulated radiation therapy (IMRT) allows effectively arbitrary dose distributions, the requirement of several centimetres of tissue for electron build-up makes IMRT of shallow tumours difficult. Thus, at present, electron beams hold many advantages for the treatment of shallow tumours such as those in the breast and head and neck.

Additionally, a recent Monte Carlo investigation (Ma *et al* 2000b) into modulated electron beam radiation therapy (MERT) has shown that the use of non-uniform intensity profiles and multiple electron beam energies will allow highly conformal dose delivery to shallow targets. Conformity is achieved laterally via an electron multileaf collimator (Lee *et al* 2000a, b) and in the depth direction by means of energy and intensity modulation. This has been

shown to be particularly useful in treatment of the intact breast. MERT would avoid both the problems of dose delivery to the contralateral breast and the small, very high-dose regions in the lung.

Unfortunately, while electron beams exhibit rapid drops in depth-dose distributions relative to photon beams, the distance between the end of the therapeutically useful range and the practical range of the electrons may still be of the order of centimetres. Thus, while MERT delivers a highly conformal dose to the target, because of the low density of the lung MERT exposes much of the lung to low doses of radiation (less than 50% of the overall maximum.) The biological impact of this low-dose region is as yet unclear; however, it is likely that the clinical outcome will improve if the lung dose is reduced. It is thus of paramount importance to investigate methods that may allow improved depth-dose distributions from electron beams.

Numerous studies have been performed to examine the possibility of using magnetic fields to tailor the dose distributions from electron beams. Two general methods for two distinct purposes have been proposed: magnetic fields directed along the axis of the beam (longitudinal) for lateral confinement of penumbras and stability in the presence of inhomogeneities (Weinhous *et al* 1985, Bielajew 1993), and fields directed orthogonally to the beam (transverse) to reduce the dose penumbra in the depth direction. In this work, only the effects of transverse magnetic fields are considered, as the primary goal is restriction of electron penetration. Transverse fields were suggested by Sempert (1960) and early Monte Carlo studies were performed by Shih (1975), demonstrating the ability to create a sharp depth-dose drop-off. Experimental investigation ensued, including work by Whitmire *et al* (1977), who conducted experiments with 22 and 28 MeV beams in 1 T fields. Nath and Schulz (1978) performed experimental investigations using 2.05 T transverse magnetic fields to increase the dose peak and sharpen the dose drop-off of an electron beam of less than 50 MeV. Further work has explored the effect of inhomogeneities (Paliwal *et al* 1978, Whitmire *et al* 1978). Recent interest in Monte Carlo investigations has been revived by the work of Nardi and Barnea (1999), using the ITS/ACCEPTM system to demonstrate the use of modern Monte Carlo techniques to simulate monoenergetic electron beams in a magnetic field positioned at a fixed depth.

This work aims to use Monte Carlo simulations to investigate the effects of transverse magnetic fields on clinical electron beams, and to examine the possibility of combining this technique with MERT. In particular, the effect of different field strengths and field locations is examined. The changes in dose distributions are quantified with a focus on the effect on surface dose and the dose fall-off. A modified system of MERT is presented in which magnetic fields are used in conjunction with intensity modulation to generate highly conformal dose regions with low surface dose and rapid depth-dose fall-off. The effect of heterogeneities on the dose distribution is also described.

2. Materials and methods

2.1. Principles and theory

When an electron enters a magnetic field, it immediately begins to travel in a curved path as dictated by the Lorentz force and eventually exits the field after moving along a semicircular path. If energy loss is included, then the particle will spiral towards smaller and smaller radii. By this action, an electron can be caused to deposit much of its energy in a localized region. In particular, the electron penetration into the field is approximately restricted to less than a distance defined by the radius of gyration, r_g .

In the limit of constant energy (small step size Δl), in the presence of a magnetic field defined by \vec{B} , a particle direction vector \vec{v}_0 is replaced with (Nelson *et al* 1985)

$$\vec{v} = \vec{B}(\vec{v}_0 \cdot \vec{B}) + [\vec{v}_0 - \vec{B}(\vec{v}_0 \cdot \vec{B})] \cos \frac{\Delta l}{r_g} - \left(\vec{v}_0 \times \vec{B} \sin \frac{\Delta l}{r_g} \right). \quad (1)$$

As Monte Carlo simulated transport occurs in short, discrete steps, this equation is particularly relevant to this study.

It has been shown by Bielajew (1993) that the synchrotron radiation due to the bending of electron paths at the energies of interest is trivial: of the order of 0.1–1 eV additional stopping power. Thus, both this added stopping power and synchrotron photon dose deposition are taken to be zero in this study.

One may generate a simple mathematical description of the expected effect of the magnetic fields on depth-dose distributions, before any Monte Carlo simulations are performed. Putting the unperturbed depth-dose profile in a vector \vec{x} and the depth-dose profile in a magnetic field in a vector \vec{b} , there exists a transformation matrix \mathbf{U} such that

$$\mathbf{U}\vec{x} = \vec{b} \quad (2)$$

with \mathbf{U} upper triangular with columns that sum to unity. The effect of operating on \vec{x} with \mathbf{U} is that below some row of \vec{x} , that is, beyond a given depth, there is a 'folding back' of energy deposition, such that some portion of the energy that would otherwise be deposited at greater depths will now be deposited earlier. However, because the overall energy of the system must be conserved, the columns of the transformation matrix \mathbf{U} must have unit sum. Additionally, the magnetic field cannot cause electrons to deposit energy further downstream than they otherwise would, hence the upper-diagonal nature of the matrix. It will be seen the effect of the magnetic field is a function of the incident energy (spectrum), the depth the magnetic field begins at, and the strength of the field. In principle, if such a function could be derived, the effects of magnetic fields could be computed very rapidly. However, for the purposes of this work, such analytical formulations are considered only to anticipate the form of the depth-dose distributions that will be generated by Monte Carlo simulations.

2.2. Monte Carlo simulations

Note that in all subsequent sections, for brevity and clarity, the term 'beam' will be used to describe the incident flux of electrons, i.e. the electron beam, while 'field' will refer to the magnetic field.

Source-parameter descriptions of electron beams were obtained according to a procedure described elsewhere (Kapur *et al* 1998, Jiang *et al* 2000, Lee *et al* 2000c) and summarized here. Electron beam simulations of a Varian Clinac 2100C (Varian Oncology Systems, Palo Alto, CA) were performed using the EGS4/BEAM user code, (Nelson *et al* 1985, Rogers *et al* 1995) using vendor supplied geometries. The simulation code and geometry employed have been previously shown to provide agreement with measured data of better than 2% in transverse profiles and depth-dose curves for the three nominal energies simulated: 6, 12 and 20 MeV (Kapur *et al* 1998). Phase space files were obtained above the last scraper of electron applicators. Source-parameter files were then obtained by using the BEAMDP program (Ma and Rogers 1997) and used in all future dose calculations. The four-source model used in this study is described in detail in Jiang *et al* (2000). The source-parameter files have also been shown to agree with the measured data to better than 2% in depth-dose and profiles (Lee *et al* 2000c).

The macro package for electromagnetic transport developed by Bielajew (1987, 1993) were implemented into the EGS4/MCDOSE code (Ma *et al* 2000a). The three-dimensional

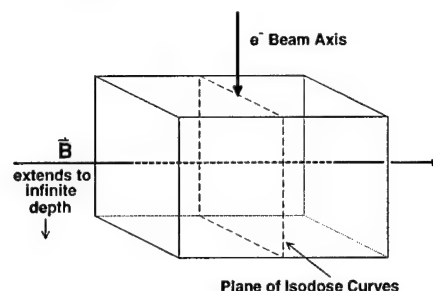


Figure 1. The geometry of the simulated system. The magnetic field vector is orthogonal to the electron beam axis, and is normal to the plane shown in the isodose curves. As shown, the direction of electron deflection is out of the page. The magnetic field region is a semi-infinite slab, i.e. all points below a given depth are assigned the same magnetic field vector.

dose distributions were examined using STATDOSE (McGowan *et al* 1996). Verification of the implementation was performed by computing longitudinal magnetic fields for 20 MeV electrons, as per Bielajew (1993) and 15 MeV monoenergetic beam in fields of varying magnitude, as per Nardi and Barnea (1999) using ITS/ACCEPTM. The agreement was better than 2% in all cases.

Pencil beams were simulated by restricting the particles to a single initial track. Specifically, a monoenergetic parallel beam was used, with a vanishing aperture size. The voxel geometry employed for these calculations was $1 \times 1 \times 1 \text{ mm}^3$. The narrow beams were simulated by using the source-parameter file for a $6 \times 6 \text{ cm}^2$ applicator and transporting particles through a $3 \times 3 \text{ cm}^2$ Cerrobend cut-out before entering the phantom. The $10 \times 10 \text{ cm}^2$ open fields were simulated with the appropriate source-parameter file, with the last scraper included in the MCDOSE simulation. The voxels for the narrow and broad fields were 2 mm in the depth direction, 4 mm in the axis orthogonal to the beam and magnetic field and 10 mm in the direction of the magnetic field. When the effects of inhomogeneities were considered, specific voxels in the phantom were converted to either air, or ICRP standard bone. In all cases, the nominal source-to-surface distance (SSD), defined from the photon target to the phantom surface) was 100 cm.

In all cases, the magnetic field was directed orthogonally to the electron beam axis, and normal to the plane shown in the isodose curves. The geometry is shown in figure 1.

All Monte Carlo simulations were performed on various elements of a suite of 22 Pentium Pro (200 MHz) and 10 Pentium III (450 MHz) CPUs, all running EGS4, BEAM and MCDOSE under the Linux operating system. All simulations utilized an electron cut-off of 0.7 MeV total energy and a photon cut-off of 10 keV, below which all remaining energy was deposited on the spot. PRESTA extensions were employed for step length calculations (Bielajew and Rogers 1987). In general, it was found that 10×10^6 electron histories were sufficient to provide a statistical error of less than 1% (1σ). The overall speed of calculation was reduced by approximately 50% relative to an identical simulation with no magnetic field in place.

2.3. Optimization

A one-dimensional optimization routine was implemented to examine the feasibility of combining fields such that the narrow dose peaks were spread out to several centimetres.

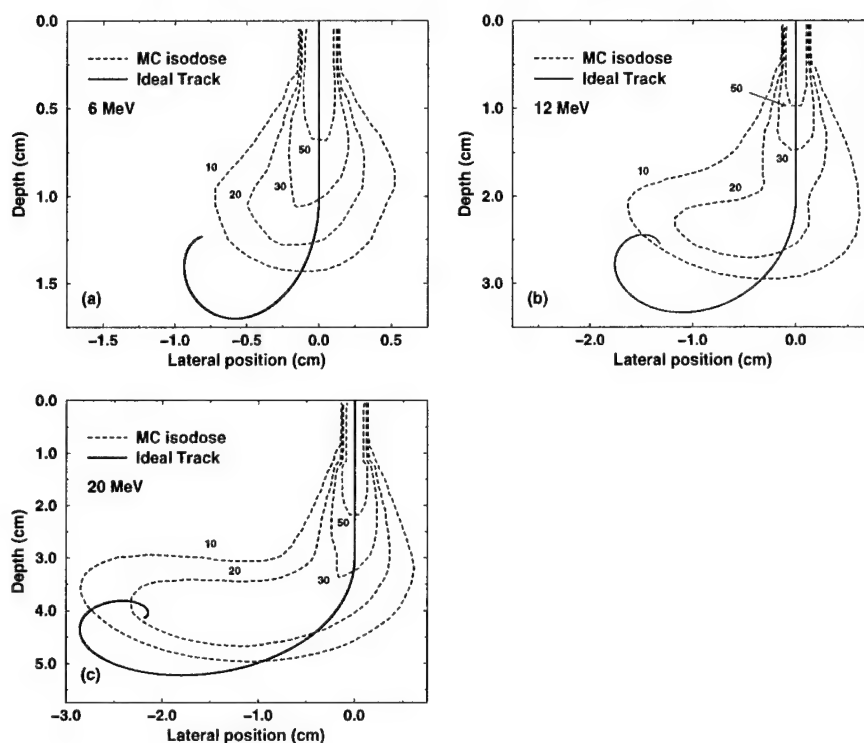


Figure 2. The theoretically derived track of an unscattered electron passing through water in the presence of a 1.5 T magnetic field, overlaid on isodose curves computed using the Monte Carlo method for a pencil beam: (a) 6 MeV with magnetic field beginning at 1 cm depth, (b) 12 MeV at 2 cm depth, (c) 20 MeV at 3 cm depth.

The dose at a given depth in the combined beam, D_{tot} was taken to be a linear combination of the dose at that depth of the individual beams. That is, for n different field/beam combinations

$$D_{\text{tot}}(z) = \sum_{i=1}^n x_i \cdot D_i(z). \quad (3)$$

Each beam i is given a weight x_i , which is determined based on the planned dose profile. To determine the weights $\vec{x} = (x_1, x_2, \dots, x_n)$, depth-dose curves were extracted from the $10 \times 10 \text{ cm}^2$ fields described earlier and each curve placed in the columns of a matrix \mathbf{A} . The desired depth-dose distribution was placed in a column vector \vec{b} and the system

$$\mathbf{A}\vec{x} \approx \vec{b} \quad (4)$$

was solved in a least-squares sense under non-negativity constraints. The method of solution utilized is described in detail in Lawson and Hanson (1974).

3. Results and discussion

The basic characteristics of electron beams in magnetic fields are explored in section 3.1 and section 3.2 by examining isodose curves and depth-dose curves. This demonstrates the

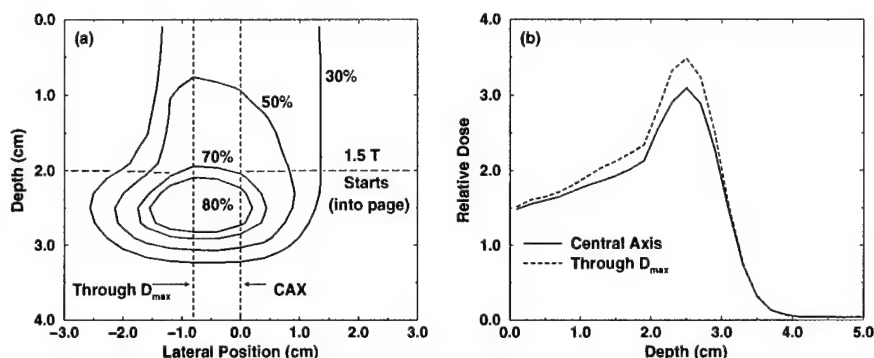


Figure 3. (a) Isodose curves for a 12 MeV electron beam collimated by a $6 \times 6 \text{ cm}^2$ applicator with a $3 \times 3 \text{ cm}^2$ Cerrobend cut-out in the presence of a 1.5 T magnetic field. Dotted lines represent the central axis and the ray passing through the dose maximum. The magnetic field is directed into the page. (b) The corresponding depth-dose curves for the central axis and the ray passing through the D_{max} .

general principles of electron beam therapy with magnetic fields, and provides evidence for the viability of the Monte Carlo transport code. Parameters for describing the depth-dose curves are presented in section 3.3 and the relevance of these parameters to MERT is discussed. An example of the application of MERT techniques to electron beams in magnetic fields is then given in section 3.4. Practical considerations important to actual application of magnetic field MERT are presented in sections 3.5 and 3.6.

3.1. Pencil beams and narrow beams

Monte Carlo calculations were performed in which electrons were constrained to travel down the same initial axis, i.e. a pencil beam. The resultant isodose curves are shown in figure 2. These figures clearly show the curvature of the electron beam dose distribution generally along the expected track. By superposition of many pencil beams along the lateral axis, it is clear that Bragg-peak-like dose peaks can be constructed.

Narrow fields, defined by $3 \times 3 \text{ cm}^2$ Cerrobend cut-outs on $6 \times 6 \text{ cm}^2$ applicators, were also simulated. What is apparent is that there is a significant shift of the dose peak off the central axis, as seen in figure 3. These data are presented primarily as a demonstration of the effects of the magnetic field, i.e. the curvature of the beam and the formation of a dose peak. However, it is difficult to make any definitive statements regarding depth-dose distributions because of the lack of equilibrium, as discussed below.

3.2. Broad beams

3.2.1. Electronic equilibrium. In the $3 \times 3 \text{ cm}^2$ narrow beams and the pencil beams, a state of lateral disequilibrium exists such that along any given axis, many times more particles are removed from the axis by the magnetic field than are replaced, as seen by the displacement of the dose peak in figure 3. In the limit of infinitely broad beams, there is equilibrium along any ray parallel to the beam axis. This is also true in the central region of broad, finite beams. This can be observed by computing the integral dose along a central axis of an unperturbed beam which is inherently large enough for equilibrium to exist. If lateral equilibrium exists, then the total energy deposited along this axis should not change when a magnetic field is applied.

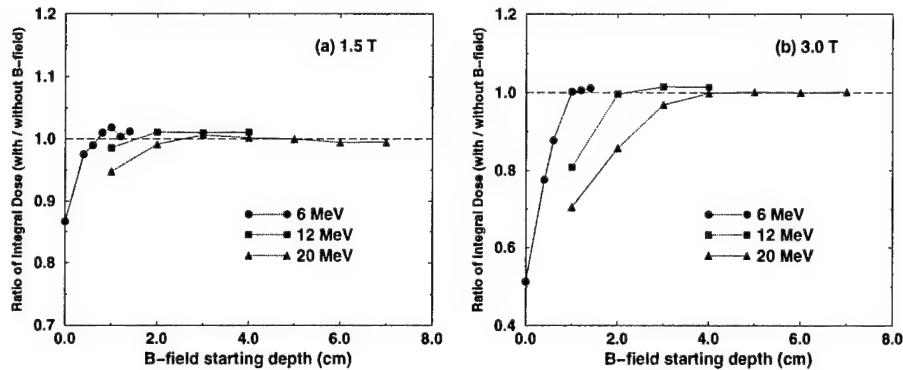


Figure 4. The ratio of energy deposited in the central axis voxels in the presence of a magnetic field to the energy deposited in a field-free system. This ratio is shown as a function of the magnetic field starting depth: (a) 1.5 T magnetic field, (b) 3.0 T.

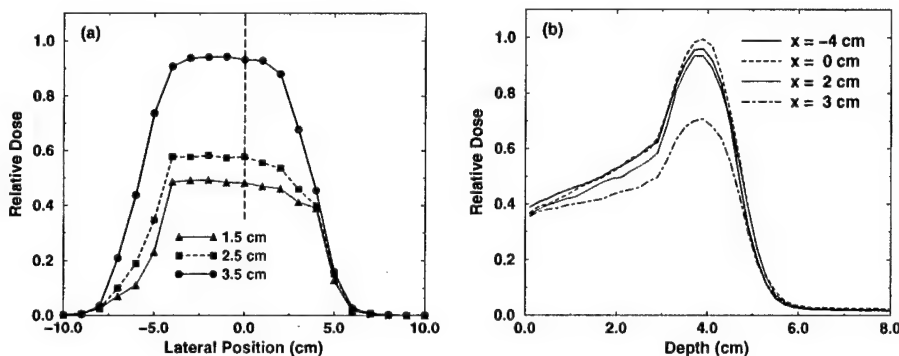


Figure 5. (a) Lateral dose profile for a 20 MeV beam in the presence of a 1.5 T magnetic field beginning at 3 cm depth. The axis being profiled is orthogonal to both the beam axis and the magnetic field. Shown are the profiles at 1.5, 2.5 and 3.5 cm depths. (b) Depth-dose curves for a 12 MeV beam in the presence of a 1.5 T magnetic field beginning at 3 cm depth. Shown are the central axis, and axes at -4, 0, 2 and 3 cm, where the positive direction is defined by $\vec{v} \times \vec{B}$ where \vec{v} is the original beam direction.

The Monte Carlo simulations suggest that for the energies investigated, a $10 \times 10 \text{ cm}^2$ beam is sufficiently broad to overcome the disequilibrium caused by the magnetic fields. As seen in figure 4, when the ratio of the energy deposited along the central axis in the magnetic field to the energy deposited in the zero-field case is less than unity, there is a net flow of electrons out of the field. This is in fact not an issue of lateral equilibrium in the standard sense, but a danger of using high-strength magnetic fields at shallow depths. What is occurring is that the field is strong enough that high-energy electrons are directed back towards the surface, and the primary beam actually exits the phantom via the front surface. Clearly, this situation is highly undesirable from both a treatment and radiation safety standpoint, and it is important to use a parameter such as the integral dose ratio to appreciate the minimum safe depth for a magnetic field. As expected, this depth is shallower at higher field strengths, as more electrons are turned back towards the surface. At 1.5 T, the minimum safe field depths are 0.4, <1 and

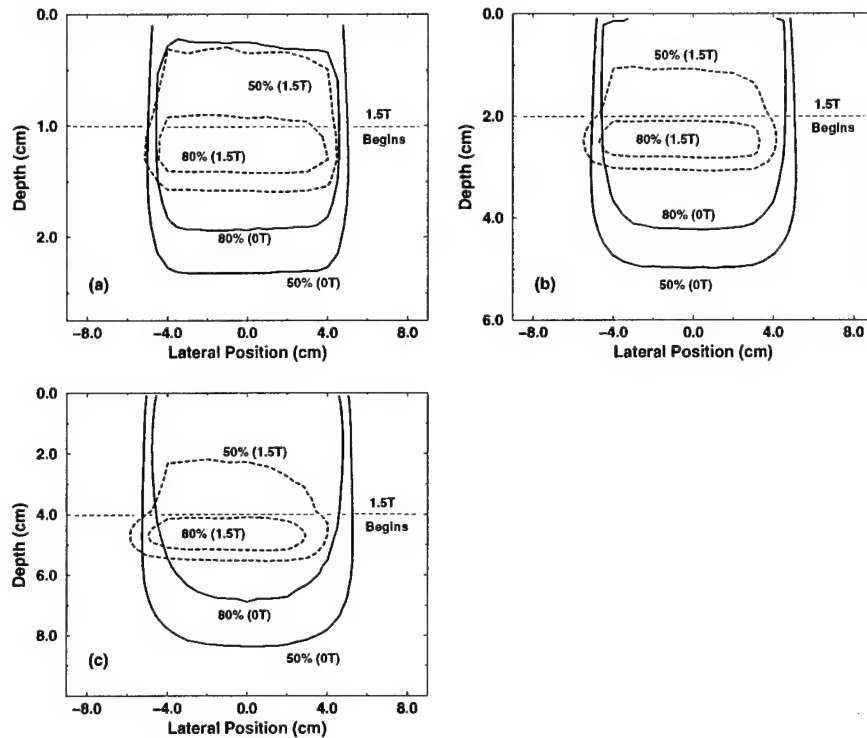


Figure 6. The 80% and 50% isodose curves for $10 \times 10 \text{ cm}^2$ fields. Both the zero-magnetic field case and the curves with a 1.5 T magnetic field directed out of the page are shown: (a) 6 MeV with magnetic field starting at 1 cm depth, (b) 12 MeV at 2 cm, (c) 20 MeV at 4 cm.

1 cm for 6, 12 and 20 MeV respectively. At 3.0 T, the depths are 1, 2 and 3 cm at 6, 12 and 20 MeV. Note that some points have values slightly greater than unity ($\sim 1\%$ higher.) This is partially due to the photon dose: if a magnetic field causes increased electron interactions near the surface, the photon dose curve is shifted towards the surface. Thus, relatively more photon dose will be deposited in the phantom in this case than in the field-free case, in which the photons exiting the phantom retain more energy. This effect in conjunction with statistical uncertainty leads to the slightly higher values.

Once the problem of beam loss is resolved, the original issue of lateral equilibrium can be considered. Evidence for the uniformity of the field is provided by examining the lateral dose profiles, as shown in figure 5(a). These profiles are taken along the axis orthogonal to both the magnetic field and original beam axis. It is seen that within the 7 cm region from -4.5 to 2.5 cm (each voxel was 1 cm in width), the dose was homogeneous to within 5.8% of the average dose in that region. Off-axis depth-dose curves are shown in figure 5(b). Here, the variations in the depth-dose curves caused by moving off of the central axis are comparable with those in open unperturbed $10 \times 10 \text{ cm}^2$ fields while within the equilibrium region (-4.5 to 2.5 cm), but it is clear that there is a rapid drop at 3 cm, where the electron dose has been shifted strongly in the positive direction, as shown. It is noted, however, that even at that position, there still exists a noticeable dose peak and dose drop-off.

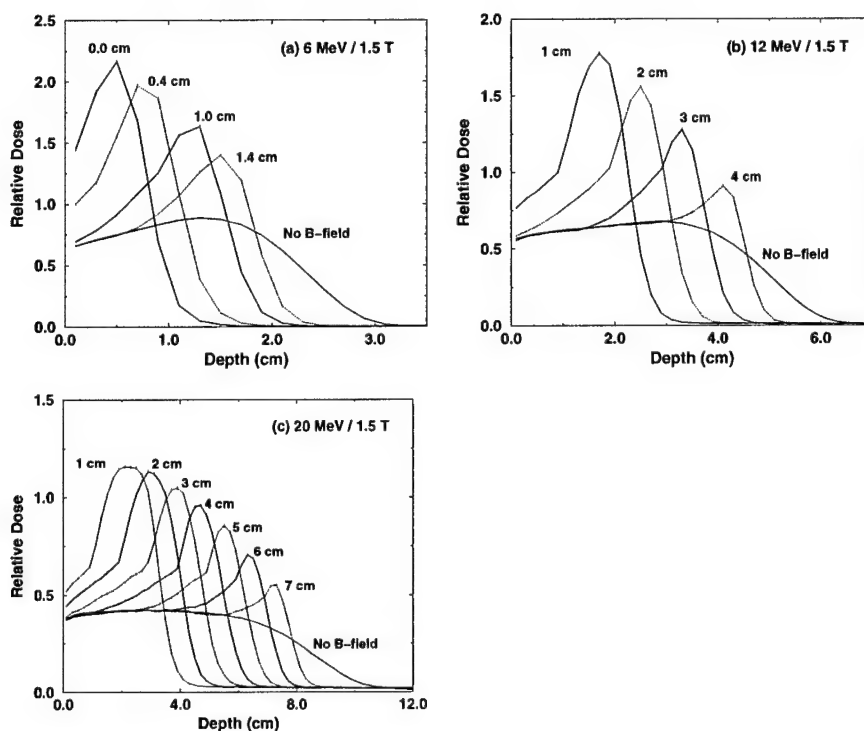


Figure 7. Central axis depth-dose curves for electron beams in the presence of a 1.5 T magnetic field. For each energy, the depth-dose curves are shown for different magnetic field starting depths. The vertical axis represents absolute dose in arbitrary units: (a) 6 MeV, (b) 12 MeV, (c) 20 MeV.

3.3. Dose profile parameters

Having thus established the electronic equilibrium of these systems, it is possible to examine the central-axis dose profiles. Isodose curves for $10 \times 10 \text{ cm}^2$ fields are shown in figure 6. Profiles along the central axis are displayed for 6, 12 and 20 MeV electron beams with the magnetic field positioned at several depths in figure 7 (1.5 T) and figure 8 (3.0 T). These broad electron fields were then characterized by consideration of the following parameters, defined graphically in figure 9:

d_B = the depth at which the magnetic field begins

$d_{80/80}$ = the width of the region bounded below by the 80% dose level

$d_{80/20}$ = the distance between the deepest 80% and the 20% dose levels

$R_{p/\text{eff}}$ = effective practical range, found by extrapolation of the drop-off region

SSF = surface sparing factor, defined by the ratio $D_{\text{max}}^{\text{voxel}} / D_{\text{surface}}^{\text{voxel}}$.

The values of $d_{80/80}$, $d_{80/20}$ and SSF for selected beam and field combinations, as well as the no magnetic field case, are shown in table 1 and are discussed in greater detail in the following sections.

3.3.1. Relationship between field strength and dose curves. Monte Carlo simulations were performed in which the magnetic field position was fixed but the field strength was varied.

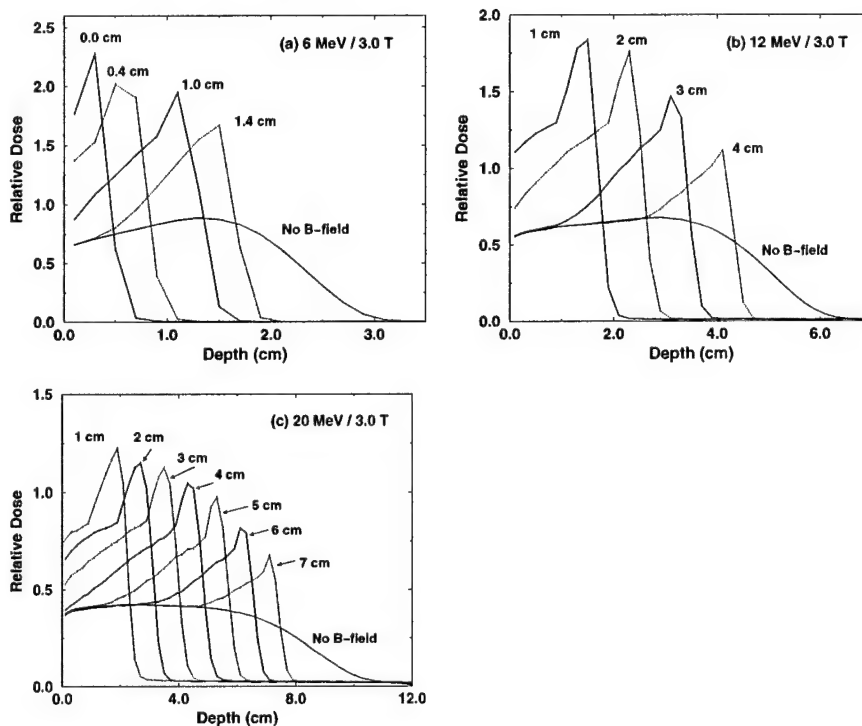


Figure 8. Central axis depth-dose curves for electron beams in the presence of a 3.0 T magnetic field. For each energy, the depth-dose curves are shown for different magnetic field starting depths. The vertical axis represents absolute dose in arbitrary units: (a) 6 MeV, (b) 12 MeV, (c) 20 MeV.

The effect of the changes on $d_{80/20}$ and SSF are shown in figure 10. As expected, the distance between the 80% and 20% dose falls with increasing field strength. While the simple Lorentz force equation may suggest a linear relationship, due to energy straggling and particle scattering, a more complex asymptotic relationship is observed. At approximately 1.5 T, the gains from increasing the magnetic field appear to be minimal.

The SSF shows a sigmoidal behaviour, with a period of rapid increase in SSF between 0.75 and 1.5 T, then a reduction in SSF at higher field strengths. This reduction occurs when the radius of gyration of the electron is too small. In those instances, instead of travelling in a spiral, the electron completes an approximate half-circle and exits the field at some angle, thus depositing dose at depths shallower than the magnetic field.

On the basis of these results, a field strength of 1.5 T was chosen as the primary field of interest. It is noted that the newest generation of interventional magnetic resonance imaging systems produce fields of this magnitude. Generally, simulations were also performed at 3.0 T to illustrate in detail the effects of changing magnetic field strengths.

3.3.2. $d_{80/80}$ —therapeutic range. The value of $d_{80/80}$ was taken as a measure of the portion of the beam that is clinically useful. Values for selected magnetic field positions are shown in table 1. This region is extremely narrow in all cases, with a maximum value of 1.7 cm for a 20 MeV beam with a 1.5 T field beginning at 1 cm depth. As a result, taken as is, these

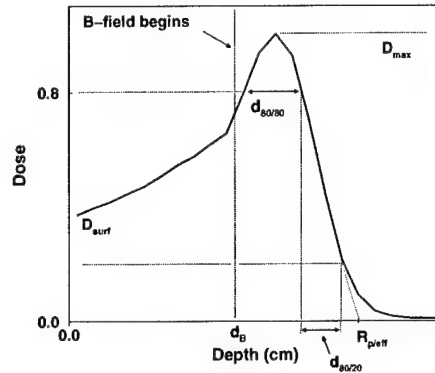


Figure 9. The parameters used to describe the depth-dose curves. $d_{80/80}$ is the distance between the two 80% isodose levels, $d_{80/20}$ is the distance between the deepest 80% and the 20% dose levels, d_B is the depth at which the magnetic field begins (it is taken to continue to infinite depth), D_{surf}^{voxel} and D_{max}^{voxel} are taken as approximate measures of the dose maximum and minimum along the axis, and are used to calculate the surface sparing factor (SSF).

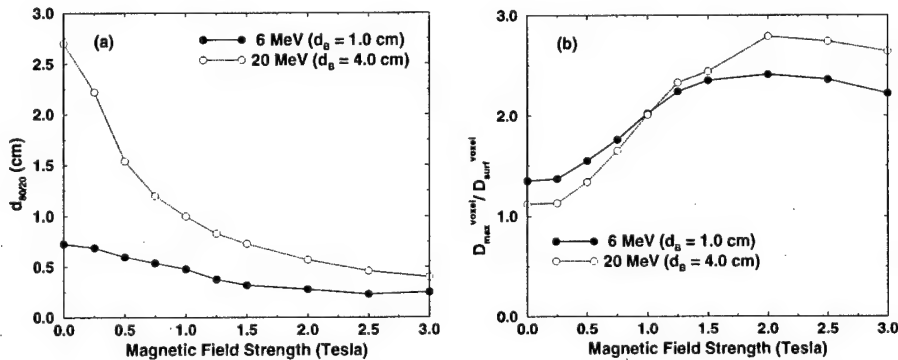


Figure 10. The effects of changing the magnetic field strength was assessed by fixing the field position and incident energy, and observing the effects on two key parameters: (a) the value of $d_{80/20}$ for 6 and 20 MeV at 1.0 and 4.0 cm depth respectively; (b) the ratio of peak to surface dose, SSF, for 6 and 20 MeV at 1.0 and 4.0 cm depth respectively.

irradiation geometries are of limited clinical value. However, this limitation may be overcome using the modified MERT techniques described in section 3.4.

3.3.3. $d_{80/20}$ —dose fall-off. The value of $d_{80/20}$, the width of the 80–20 ‘penumbra’ in the depth direction, is a measure of the ability of the magnetic field to improve the dose drop-off, one of the primary goals of using magnetic fields. It was found that with a 3.0 T magnetic field, $d_{80/20}$ was largely invariant as the depth of the magnetic field was changed, as seen in table 1. The Monte Carlo results show an average $d_{80/20}$ of 2.1 mm at 6 MeV, 2.7 mm at 12 MeV and 3.5 mm at 20 MeV. For comparison, note that without a magnetic field, the $d_{80/20}$ values are 7.3 mm for 6 MeV, 14 mm for 12 MeV and 27 mm for 20 MeV. This indicates a reduction in the drop-off distance of between 71% for 6 MeV to 87% at 20 MeV.

Table 1. Summary of beam parameters for selected electron beams at 1.5 and 3.0 T. Parameters are defined in section 3.3 and are given along the central axis.

Energy (MeV)	\vec{B} -field starting depth (cm)	$\ \vec{B}\ = 1.5 \text{ T}$			$\ \vec{B}\ = 3.0 \text{ T}$		
		$d_{80/80}$ (cm)	$d_{80/20}$ (cm)	SSF	$d_{80/80}$ (cm)	$d_{80/20}$ (cm)	SSF
6	0.0	0.46 [†]	0.32 [†]	1.50 [†]	0.24 [†]	0.17 [†]	1.28 [†]
	1.0	0.49	0.32	2.35	0.32	0.25	2.22
12	1.0	0.84	0.47	2.31	0.53 [†]	0.27 [†]	1.66 [†]
	2.0	0.71	0.51	2.66	0.46	0.27	2.37
	3.0	0.67	0.49	2.25	0.67	0.28	2.62
	4.0	0.93	0.38	1.64	0.73	0.27	2.01
20	1.0	1.66 [†]	0.66 [†]	2.22 [†]	0.91 [†]	0.32 [†]	1.61 [†]
	2.0	1.39	0.72	2.55	0.92 [†]	0.35 [†]	1.74 [†]
	3.0	1.20	0.74	2.71	0.82	0.36	2.12
	4.0	1.06	0.76	2.57	0.76	0.40	2.64
	5.0	0.93	0.72	2.27	0.62	0.37	2.63
	6.0	0.96	0.65	1.88	0.95	0.34	2.19
	7.0	1.19	0.58	1.47	0.84	0.34	1.81
6	None	1.66	0.73	1.35	1.66	0.73	1.35
12	None	4.22	1.40	1.21	4.22	1.40	1.21
20	None	6.96	2.70	1.12	6.96	2.70	1.12

The error on doses (and on all derived values shown above) was in all cases <1% (1σ) of the maximum dose in the volume.

[†] Lateral disequilibrium. Total energy deposited along central axis with \vec{B} -field differs from the unperturbed case by more than 5%. See discussion in section 3.3.

At 1.5 T, the $d_{80/20}$ for the 6 MeV beam is nearly constant at 3.3 mm. However, as seen in table 1, there is a noticeable peak in the $d_{80/20}$ values for 12 and 20 MeV. The rise in $d_{80/20}$ is due to the increased scattering at lower electron energies. As the magnetic fields are positioned deeper in the phantom, the spectrum of the electrons caught in the magnetic field is shifted towards lower energies and the increased scattering at these energies results in a scattering towards greater depths. However, as the magnetic field moves beyond this peak value (2 cm at 12 MeV and 4 cm at 20 MeV), the energies (~ 8 MeV) are too low for the electrons to escape very far from the magnetically defined track.

In the context of MERT, regardless of how many fields are directed along the same port, the $d_{80/20}$ of the combined field will be the $d_{80/20}$ of the deepest penetrating field, given a minimal contribution from the bremsstrahlung tail. Thus, before any combined fields are simulated, there is an *a priori* expectation that combined fields will preserve the rapid dose fall-off seen with the individual fields.

3.3.4. $R_{p/eff}$ —depth of maximum penetration. The third parameter by which the fields were characterized was the effective practical range. This is similar to the standard dosimetric practical range R_p in that it is defined by the intersection of the zero dose level and a linear extrapolation of the dose fall-off region. Physically, $R_{p/eff}$ represents the maximum penetration of electrons in the medium in the presence of the magnetic field. Thus, the distance $R_{p/eff} - d_B$ represents the distance required by the magnetic field to turn the highest-energy electrons back towards the surface.

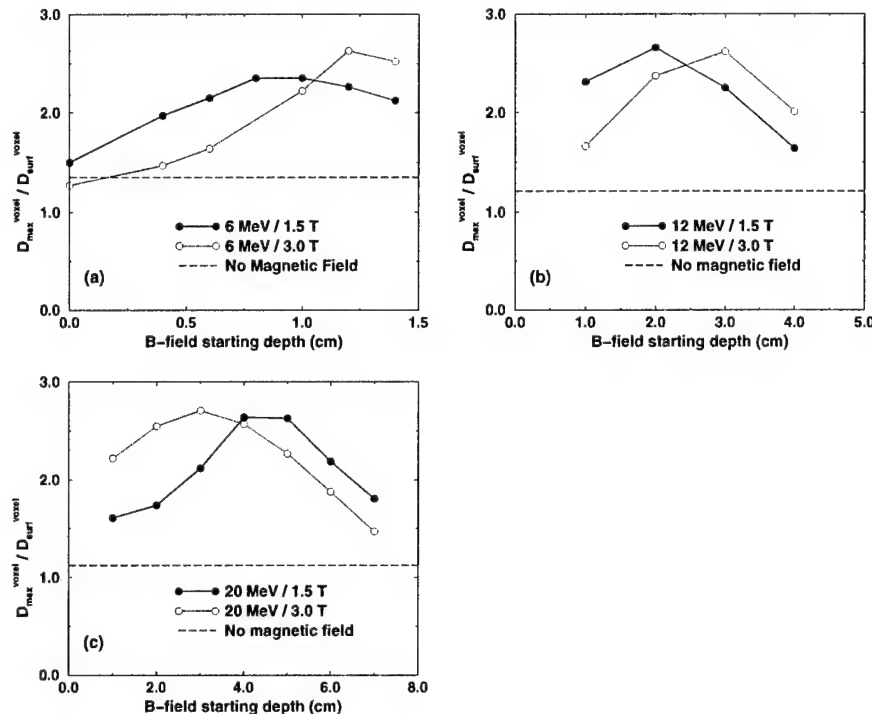


Figure 11. The surface sparing factor (SSF), defined as the ratio ($D_{\max}^{\text{voxel}} / D_{\text{surf}}^{\text{voxel}}$). A higher SSF value suggests lower skin dose for a given target dose. The SSF is shown as a function of magnetic field placement: (a) 6 MeV, (b) 12 MeV, (c) 20 MeV.

As electron energy scales approximately linearly with depth and r_g scales linearly with energy, it follows that the distance between the start of the magnetic field and the effective practical range, $R_{p/\text{eff}} - d_B$, should scale linearly with d_B . Indeed, this was the case as is shown in table 1.

3.3.5. SSF—surface sparing factor. The surface sparing factor is a unitless parameter defined as the ratio of the dose maximum to the dose to a voxel at the surface (i.e. the average dose delivered to the first 2 mm of depth.) However, a high surface sparing factor does not immediately suggest that a high dose may be delivered to a target at several centimetres depth while avoiding a high skin dose. As described above, the dose peak may extend only several millimetres in the depth direction, and would almost certainly not be clinically useful as a single field. Combining fields inevitably leads to a reduced SSF, as will be seen later. Thus it is crucial that the beams that will be used in a magnetic-MERT system exhibit a high starting SSF, before combination with other fields.

As seen in figure 11, at each energy, there is a unique starting depth for the magnetic field that results in a maximal SSF. At 6 MeV, the SSF increases as the magnetic field is moved deeper until a maximum occurs between 0.8 and 0.9 cm at 1.5 T and 1.2 cm at 3.0 T. At 12 MeV, this depth was 1.0 cm at 1.5 T, or 2.0 cm at 3.0 T, and at 20 MeV, this depth was 3 cm at 1.5 T and 4.0 cm at 3.0 T. The existence of a maximal value is related to several factors. The SSF

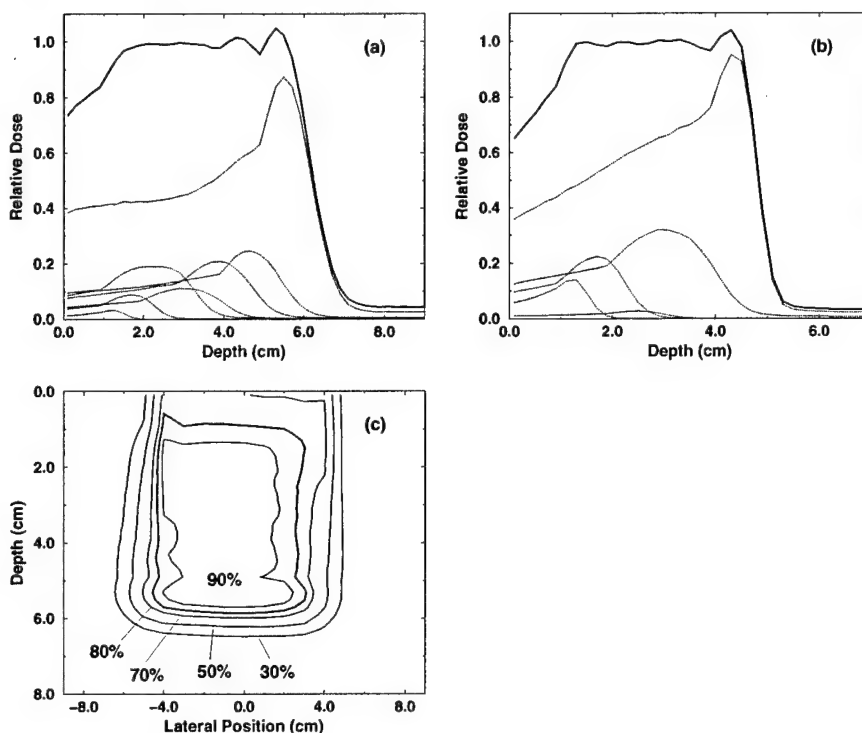


Figure 12. Central-axis depth-dose curves demonstrating how linear combinations of $10 \times 10 \text{ cm}^2$ electron beams in magnetic fields, with different intensities and magnetic field placements, can be used to create homogeneous dose distributions. Note that both the SSF ($D_{\text{max}}^{\text{voxel}}/D_{\text{surf}}^{\text{voxel}}$) and $d_{80/20}$ are significantly improved relative to a field-free situation: (a) 1.5 T only, (b) 1.5 T and 3.0 T, (c) isodose curves for the 1.5 T optimization.

drops dramatically when the magnetic field is introduced at shallower depths, an effect related not so much to the formation of a dose peak as the deposition of energy at the surface. These cases correspond to those which, as discussed earlier, lack electronic equilibrium as electrons exit the beam through the front surface of the phantom. At greater depths, electrons are at a lower energy and so are confined to smaller regions, thus resulting in an increased dose peak. This is offset by the fact that at deeper depths a greater percentage of the energy has already been deposited.

3.4. Combined fields

As seen when examining the depth-dose profiles, the depths at which these magnetically perturbed electron beams are therapeutically useful spans a limited range. Defining a prescription dose of 80% of the dose maximum, the width of the therapeutic region is given by $d_{80/80}$ and can be less than 1 cm, as seen in table 1 and section 3.3.2. Clinical targets are often significantly larger and so a method is required to create wider dose peaks. A similar problem is encountered in proton beam therapy, in which case a system of variable beam attenuation based on a range modulation wheel may be used to create a 'spread-out Bragg peak' of arbitrary

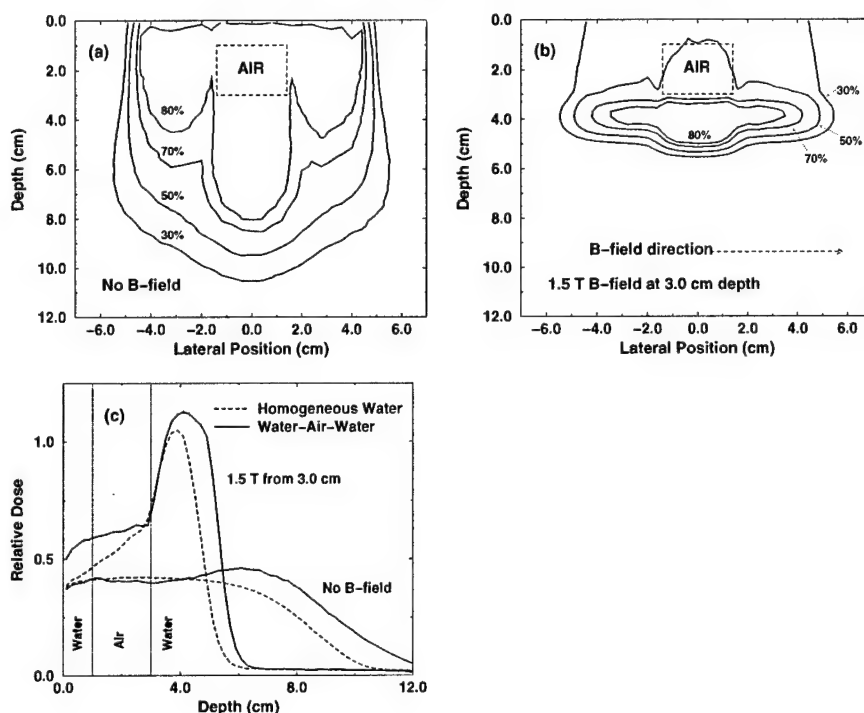


Figure 13. The effect of an air cavity heterogeneities on dose distributions with and without magnetic fields. Note that the heterogeneities do not change the shape of the depth-dose curve significantly when magnetic fields are applied. The direction of electron deflection here is into the page. The heterogeneity extends infinitely into and out of the page. (a) Isodose curves without magnetic field, (b) with 1.5 T magnetic field from 3 cm (directly after the air cavity), (c) corresponding central-axis depth-dose curves. The vertical axis represents absolute dose in arbitrary units.

width. However, for electron beams, any material in the beam path would significantly distort the field shape by causing additional scattering and also risk the production of bremsstrahlung photons in the case of high-Z materials. However, the general principle of beam modulation remains valid, and suggests the use of modulated electron radiation therapy.

Previous discussions of MERT have considered the use of fields with non-uniform energies and intensity distributions. Here, the technique is extended to the use of multiple magnetic field positions, i.e. a single port may include a 20 MeV field with a magnetic field beginning at 3.0 cm depth for a certain number of monitor units, and then another 20 MeV field with the magnetic field located at a depth of 5.0 cm delivered down the same axis, etc. It is instructive to compare this methodology with the more familiar method used in proton beam therapy. In that system, physical blocks of different thicknesses are used to shift the Bragg peak to different depths, and intensity modulation is provided by allowing the beam to dwell on a given modulator for a variable time period. In this case, the only difference is the means of moving the pseudo-Bragg peak, that is, by moving the magnetic field. Beam intensity is modulated simply by changing the number of monitor units delivered with the magnetic field at a given position. It was believed that, as with the proton beam, useful fields can be constructed while maintaining the desirable depth-dose drop-off and low skin dose.

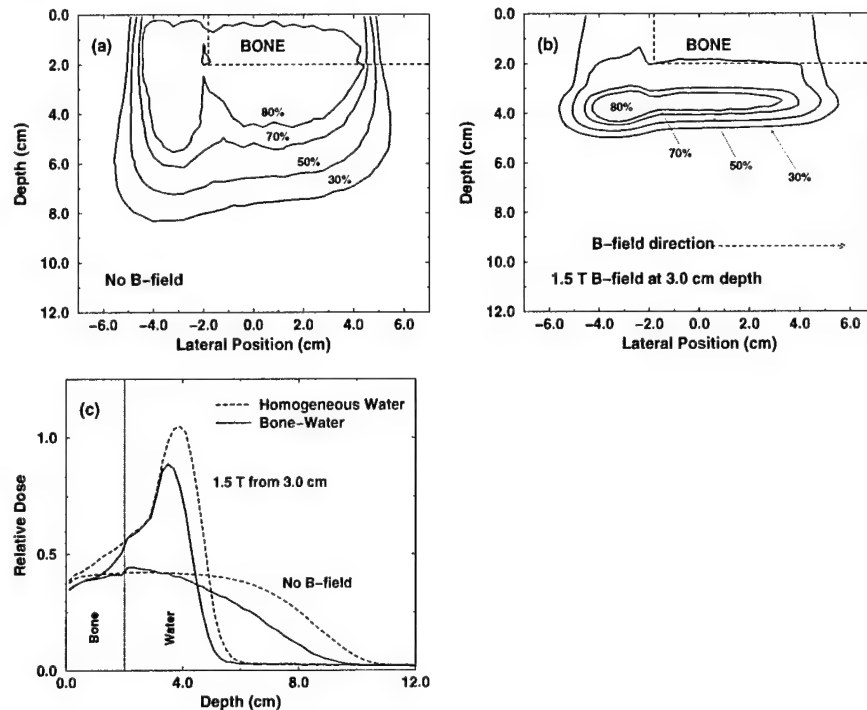


Figure 14. The effect of a bone heterogeneity on dose distributions with and without magnetic fields. The direction of electron deflection here is into the page. The heterogeneity extends infinitely into and out of the page. (a) Isodose curves without magnetic field, (b) with 1.5 T magnetic field from 3 cm, (c) corresponding central-axis depth-dose curves. The vertical axis represents relative dose.

A simple one-dimensional optimization routine was utilized to generate two fields. In one case, a target profile was generated where the dose would rise linearly from 50% at the surface (relative to the maximum along the profiled axis) to 100% at 1.0 cm, then drop to zero at 6.2 cm. The optimized solution was solved numerically, and a linear combination of the 1.5 T fields was generated to match the target values in a least-squares sense. The results are shown in figure 12(a). Using the terminology from section 3.3, the width of the treatment region, $d_{80/80}$, was found to be 5.0 cm, followed by a $d_{80/20}$ drop-off of 0.77 cm. Between the depths of 1.6 cm and 5.6 cm, the dose was homogeneous to within $\pm 5.4\%$ of the average dose. The corresponding isodose curves for this situation are shown in figure 12(c).

A second target profile was also constructed, again rising linearly from 50% at the surface to 100% at 1.0 cm, but then falling to zero dose at a depth of 4.8 cm. In this case, both 1.5 T and 3.0 T magnetic fields were permitted. The results are shown in figure 12(b), with a $d_{80/80}$ of 3.7 cm and a $d_{80/20}$ of 0.43 cm. Between 1.2 cm and 4.6 cm depth, the dose was homogeneous to within $\pm 4.5\%$ of the average dose.

It is noted that to achieve the same target coverage as in figure 12(a) without magnetic fields, a 20 MeV beam would have to be used. Recall that the $d_{80/20}$ for a single 20 MeV beam with a magnetic field is 2.7 cm, or 250% of the $d_{80/20}$ for the 1.5 T field case. Additionally, the surface dose would be higher by approximately 10% of the dose maximum. Similarly,

for figure 12(b), a 12 MeV beam would be used, with a $d_{80/20}$ of nearly 10 times that of the magnetic field case, with a significantly higher surface dose as well. MERT techniques may improve the dose homogeneity within the target region, but cannot improve the depth-dose fall-off.

The small dose inhomogeneities, in particular small peaks near the end of the treatment field, are caused by the limited dataset. The optimization was restricted to setting the magnetic field at the fixed depths used in this study. A full-scale optimization routine would allow the standard non-uniform intensities, in addition to computing optimal magnetic field placements for each segment, with the ability to choose the field placement along a continuum or among a closely spaced set of discrete depths.

Certainly, a real magnetic field/beam profile optimization would have to occur at a minimum in \mathbb{R}^2 , thus accounting for the lateral shift seen in figure 5(a). In an engineering sense, reversing the magnetic field direction is likely to be trivial, and this possibility must also be accounted for. The mathematical and physical nature of this optimization scheme is beyond the scope of this work, but further discussion of practical issues involved in optimization and treatment planning is presented in section 3.6.2.

3.5. Inhomogeneities

The presence of shallow heterogeneities located between the surface and the magnetic field was also investigated. Slabs of bone and air cavities were simulated by replacing the water of some of the voxels with air or ICRP standard bone. The goal was to observe the effect of the changes in electron energy spectra caused by passage through heterogeneous media on the parameters discussed in section 3.3.

The isodose curves with an air cavity, both with and without magnetic fields, are shown in figures 13(a) and 13(b). The corresponding depth-dose curves are shown in figure 13(c). The results of the simulations with a 3 cm slab of bone at the surface are shown in figure 14.

Note that the goal of these simulations differs from previous experimental work, such as that of Paliwal *et al* (1978). In that work, the authors used a magnetic field gradient such that the dose distribution with the inhomogeneity did not differ significantly from the dose distribution without the inhomogeneity. Here, the dose distributions differ radically between the heterogeneous media with the magnetic field and the homogeneous media with no field. Instead, the primary point of interest is that the general *form* of the depth-dose distributions is preserved; that is, a dose peak followed by a sharp dose drop-off with a favourable SSF. Given this, then even in the presence of inhomogeneities treatment fields can be constructed by using the modulation techniques described earlier.

As shown in figure 13(c), with an air cavity present, there is a trivial (1 mm) decrease in the $d_{80/20}$ and a decrease in the SSF from 2.7 to 2.2. With a bone slab, there was no change in $d_{80/20}$ and a drop in SSF from 2.7 to 2.5. Thus, even if the beam passes through inhomogeneities before entering the magnetic field, the advantages of magnetic fields are still preserved. Certainly, with an inhomogeneity present, additional fields may be necessary to cover the entire target region. However, it has been shown elsewhere (Ma *et al* 2000b) that the non-uniform intensity profiles used in MERT can provide highly conformal coverage of a target in the presence of heterogeneities. Based on these results, it is concluded that MERT combined with the techniques shown in the previous section, will exhibit the conformal coverage of MERT with the added ability to reduce surface dose and dose to distal structures, even in inhomogeneous media.

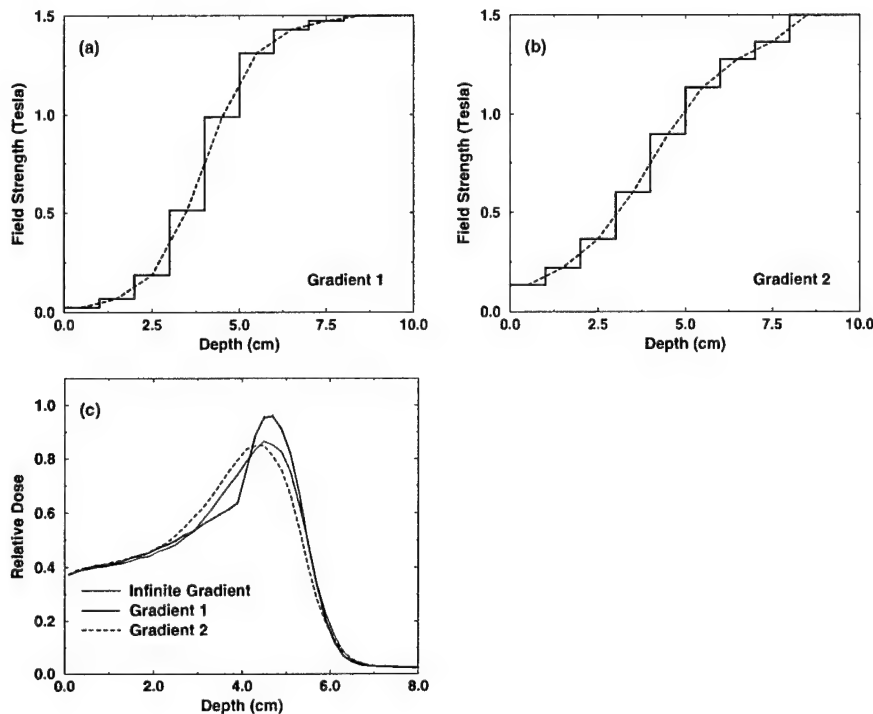


Figure 15. The effect of finite magnetic field gradients on central-axis depth-dose curves. Gradients are displayed as magnetic field strength as a function of depth: (a) gradient 1, (b) gradient 2. (c) The corresponding depth-dose curves with the infinite gradient included for comparison. The vertical axis represents relative dose.

3.6. Practical considerations

3.6.1. Field gradients. For the simulations described thus far, the structure of the magnetic fields have been taken to be a step function, i.e. the field gradient is infinite. However, this cannot be the case in any real system. Similarly, the field strength outside the primary region is typically non-zero, as low-strength fringe fields will inevitably fill the remaining space. Nardi and Barnea (1999) demonstrated that for a 15 MeV monoenergetic beam in a 3.0 T field, the difference between the infinite and finite gradient ($d\|\vec{B}\|/dz \approx 1.25 \text{ T cm}^{-1}$) was not significant. The difference in $d_{80/80}$ was 1 mm while the SSF dropped from 2.43 to 2.27. As demonstrated above, $d_{80/80}$ can be made largely irrelevant by combining fields. Thus, this section focuses on the effects of finite gradients on $d_{80/20}$ and SSF.

To explore the effects of finite gradients and fringe fields, two magnetic fields were constructed with gradients shown in figures 15(a) and 15(b). Considering the semilinear region centred around 4 cm, gradient 1 rises with $d\|\vec{B}\|/dz \approx 0.4 \text{ T cm}^{-1}$ while gradient 2 rises at $\sim 0.2 \text{ T cm}^{-1}$. The resulting central axis dose profiles are shown in figure 15(c), compared with the 20 MeV 4 cm field case (4 cm corresponds to the 50% field level in the gradients.) It can be seen that the $d_{80/20}$ drop-off increases by less than 0.5 mm with gradient 1 (the steeper gradient), and less than 1.5 mm with gradient 2. While this is considered to be an adverse effect, these $d_{80/20}$ values still represent 70.3% and 67.0% improvements over

the zero-field case. The peak dose value was also seen to be diminished while surface dose remained relatively constant. The SSF when the field was defined by a step function was 2.57. With gradient 1 this was reduced to 2.31, and with gradient 2 it was reduced to 2.26. Again, this is undesirable, but the SSF is still more than twice that of the 20 MeV zero-field system.

Thus, it is concluded that while sharper gradients are clearly superior to slower gradients, even an unrealistically 'poor' field of only 0.2 T cm^{-1} still presents significant advantages over the zero-field case.

3.6.2. Other considerations. It is clear that the largest hurdles in the implementation of magnetic fields are not theoretical issues, but rather are of a much more practical nature. In particular, the effect of fringe fields on the electronic equipment of the accelerator and the stability of the electron beam as it travels through the treatment head. This must be investigated thoroughly before any clinical implementation can occur.

Additionally, the use of magnetic fields at multiple depths for different segments of an intensity modulated field requires high-precision computer control. It is feasible that linking the electron-specific MLC to be used in MERT (Lee *et al* 2000a, b) and a magnetic field system to the same controller will allow such delivery to occur. Thus, for example, a single 'step' of a step-and-shoot type algorithm may represent the motion of the leaves to a new pattern as well as motion of the magnetic field to a new position. This would of course necessitate significant changes in the entire treatment planning system. For example, a beamlet-based beam profile optimization routine must have precalculated beamlets not only for different energies, but different field positions (see section 3.4). The leaf sequence algorithm must be extended to also compute the necessary movement of the magnetic field. As has been shown elsewhere (Lee *et al* 2000c), the background dose can rise significantly if too many field segments are used, so the treatment planning system must balance the background dose with trying to achieve maximum conformity. Finally, the issue of magnetic field verification is created, which does not lend itself to as straightforward a solution as leaf sequence verification.

A simplification of the system could conceivably utilize magnetic fields simply as a way of restricting dose to an organ at risk. For example, in an anterior-posterior directed MERT-based breast treatment (Ma *et al* 2000b), the magnetic field could be aligned along the base of the chest wall. This will not improve homogeneity in the breast or reduce skin dose, but will restrict dose to the lung. The advantages of this would have to be compared with the potential dose boost to the distal end of the target structures.

4. Conclusion

It has been demonstrated that transverse magnetic fields can be used effectively to create dose distributions with sharp depth-dose fall-offs and a favourable ratio of peak-to-surface dose. The depth-dose distribution from such a field was qualitatively observed to resemble the Bragg peak seen in proton therapy. The position and size of this peak varied as function of electron energy, field strength and field position. Generally, this peak exhibited only a very narrow therapeutic range, and so a method of broadening this peak was necessary. It was demonstrated that a modified form of MERT could be employed to generate a clinically useful field. The energy and intensity of the electron beam, as well as the position of the magnetic field were varied, thus creating a homogeneous dose distribution several centimetres in depth, while retaining the desired dose fall-off and low surface dose. This could be accomplished with constant magnetic field strength or variable field strength. It was further shown that the primary effect of heterogeneities is to shift the position of the dose peak, but to have minimal effect on the dose

fall-off distance. The effect of magnetic field gradients was seen to adversely affect the drop-off and surface sparing, but only moderately. Nonetheless, it is clear that the sharper gradients are preferred. With recent improvements in the development of compact high-strength magnetic fields, higher- T_c superconductors, the development of variance reduction techniques and rapid Monte Carlo electron dose calculation systems and faster computer systems, it is anticipated that the use of magnetic fields will rapidly become practically feasible. Thus it is concluded that when combined with the emerging modality of MERT, magnetic fields allow significant improvements in dose conformity in the depth direction.

Acknowledgments

We would like to thank our colleagues at Stanford for helpful comments and discussion on this work: Art Boyer, Gary Luxton, Steve Jiang, Todd Pawlicki, Jinsheng Li and Jun Deng. Algorithms for transport in a magnetic field were adapted from Alex Bielajew (University of Michigan) as included in the standard EGS4 distribution. This work was supported in part by grants BC971292 from the US Department of Defense, CA78331 from the NIH, and NIH training grant 5T32GM08294-11.

References

- Bielajew A F 1987 Electron transport in \vec{E} and \vec{B} fields *Monte Carlo Transport of Electrons and Photons* ed T E Jenkins *et al* (New York: Plenum) pp 421–34
- 1993 The effect of strong longitudinal magnetic fields on dose deposition from electron and photon beams *Med. Phys.* **20** 1171–9
- Bielajew A F and Rogers D W O 1987 PRESTA—the parameter reduced electron step algorithm for electron Monte Carlo transport *Nucl. Instrum. Methods B* **18** 165–81
- Jiang S B, Kapur A and Ma C-M 2000 Electron beam modelling and commissioning for Monte Carlo treatment planning *Med. Phys.* **27** 180–91
- Kapur A, Ma C-M, Mok E C, Findley D O and Boyer A L 1998 Monte Carlo calculations of electron beam output factors for a medical linear accelerator *Phys. Med. Biol.* **43** 3479–94
- Lawson C L and Hanson R J 1974 *Solving Least Squares Problems* (Englewood Cliffs, NJ: Prentice-Hall)
- Lee M C, Jiang S B and Ma C-M 2000a Monte Carlo and experimental investigations of multileaf collimated electron beams for modulated electron radiotherapy *Med. Phys.* **27** accepted
- Lee M C, Jiang S B, Yi B and Ma C-M 2000b Monte Carlo simulations of multileaf collimated electrons *Proc. 13th Int. Conf. on the Use of Computers in Radiation Therapy* ed W Schlegel and T Bortfeld (Heidelberg: Springer) pp 126–8
- Lee M C, Kapur A, Jiang S B and Ma C-M 2000c Characterization of electron beams for modulated electron beam radiotherapy *Proc. World Congress on Medical Physics and Biomedical Engineering (23–28 July, 2000)* (CD-ROM)
- Ma C-M, Li J S, Pawlicki T, Jiang S B and Deng J 2000a MCDOSE—a Monte Carlo dose calculation tool for radiation therapy treatment planning *Proc. 13th Int. Conf. on the Use of Computers in Radiation Therapy* ed W Schlegel and T Bortfeld (Heidelberg: Springer) pp 123–5
- Ma C-M, Pawlicki T, Lee M C, Jiang S B, Li J, Deng J, Yi B, Mok E, Luxton G and Boyer A L 2000b Energy- and intensity-modulated electron beams for radiotherapy *Phys. Med. Biol.* **45** 2293–311
- Ma C-M and Rogers D W O 1997 BEAMDP users manual *National Research Council of Canada Report PIRS-0509c* (Ottawa: NRC)
- McGowan H C E, Faddegon B A and Ma C-M 1996 STATDOSE for 3D distributions *National Research Council of Canada Report PIRS-0509f* (Ottawa: NRC)
- Nardi E and Barnea G 1999 Electron beam therapy with transverse magnetic fields *Med. Phys.* **26** 967–73
- Nath R and Schulz R J 1978 Modification of electron-beam dose distribution by transverse magnetic fields *Med. Phys.* **5** 226–30
- Nelson W R, Hirayama H and Rogers D W O 1985 The EGS4 code system *SLAC Report 265* (Stanford, CA: Stanford Linear Accelerator Center)

- Paliwal B R, Wiley A L, Wessels B W and Choi M C 1978 Magnetic field modification of electron-beam dose distributions in inhomogeneous media *Med. Phys.* **5** 404-8
- Rogers D W O, Faddegon B A, Ding G X and Ma C-M 1995 BEAM: a Monte Carlo code to simulate radiotherapy treatment units *Med. Phys.* **22** 503-24
- Sempert M 1960 New developments in high-energy electron beam therapy with the 35 MeV Brown Boveri betatron *Radiology* **74** 105-7
- Shih C C 1975 High energy electron radiotherapy in a magnetic field *Med. Phys.* **2** 9-13
- Weinhous M S, Nath R and Schulz R J 1985 Enhancement of electron beam dose distributions by longitudinal magnetic fields: Monte Carlo simulations and magnet system optimization *Med. Phys.* **12** 598-603
- Whitmire D P, Bernard D L, Peterson M D and Purdy J A 1977 Magnetic enhancement of electron-dose distribution in a phantom *Med. Phys.* **4** 127-31
- 1978 Magnetic enhancement of electron-dose distribution in tissue and lung phantoms *Med. Phys.* **5** 409-17

Monte Carlo based treatment planning for modulated electron beam radiation therapy

Michael C Lee, Jun Deng, Jinsheng Li, Steve B Jiang¹ and C-M Ma

Radiation Physics Division, Department of Radiation Oncology,
Stanford University School of Medicine, Stanford, CA 94305-5304, USA

E-mail: mclee@reyes.stanford.edu

Received 5 March 2001

Published 19 July 2001

Online at stacks.iop.org/PMB/46/2177

Abstract

A Monte Carlo based treatment planning system for modulated electron radiation therapy (MERT) is presented. This new variation of intensity modulated radiation therapy (IMRT) utilizes an electron multileaf collimator (eMLC) to deliver non-uniform intensity maps at several electron energies. In this way, conformal dose distributions are delivered to irregular targets located a few centimetres below the surface while sparing deeper-lying normal anatomy. Planning for MERT begins with Monte Carlo generation of electron beamlets. Electrons are transported with proper in-air scattering and the dose is tallied in the phantom for each beamlet. An optimized beamlet plan may be calculated using inverse-planning methods. Step-and-shoot leaf sequences are generated for the intensity maps and dose distributions recalculated using Monte Carlo simulations. Here, scatter and leakage from the leaves are properly accounted for by transporting electrons through the eMLC geometry. The weights for the segments of the plan are re-optimized with the leaf positions fixed and bremsstrahlung leakage and electron scatter doses included. This optimization gives the final optimized plan. It is shown that a significant portion of the calculation time is spent transporting particles in the leaves. However, this is necessary since optimizing segment weights based on a model in which leaf transport is ignored results in an improperly optimized plan with overdosing of target and critical structures. A method of rapidly calculating the bremsstrahlung contribution is presented and shown to be an efficient solution to this problem. A homogeneous model target and a 2D breast plan are presented. The potential use of this tool in clinical planning is discussed.

¹ Present address: Department of Radiation Oncology, Massachusetts General Hospital and Harvard Medical School, Boston, MA 02114, USA.

1. Introduction

In an increasing number of centres, the treatment of tumours in close proximity to critical organs or targets possessing complex geometries is performed via intensity modulated radiation therapy (IMRT) with photon beams. While this technique is an extremely powerful tool for treating tumours that are located more than a few centimetres below the surface, the physics of x-ray energy deposition suggests that photon IMRT is not well suited to the treatment of shallow targets. Furthermore, in many cases the slow attenuation of photon beams makes conventional photon IMRT a poor choice for some targets with distal critical structures. In contrast, electron beams, with their comparatively higher surface doses and more rapid depth-dose fall-offs, are well suited to these targets. However, conventional electron beam delivery and treatment planning systems are ill-equipped for the delivery of complex dose distributions.

Modulated electron beam radiation therapy (MERT) is a new electron modality that has been developed to deliver highly conformal doses to shallow targets (Lief *et al* 1996, Hyödynmaa *et al* 1996, Zackrisson and Karlsson 1996, Åsell *et al* 1997, Ebert and Hoban 1997, Karlsson *et al* 1998, 1999, Åsell *et al* 1999, Ma *et al* 2000b). Dose conformality in the beam direction may be achieved by energy modulation, while lateral uniformity and conformity may be achieved by intensity modulation via a variable collimator. Many of the studies into MERT have used microtron based scanned beam systems. In principle, energies should be selectable with relative ease on these systems, while intensity modulation could be achieved by scanning the narrow electron beam. Studies using these systems have shown MERT to be feasible and potentially of great value; however, the cost and availability of such machines have greatly restricted research and development of scanned beam based MERT. Investigations into the use of the photon MLCs on accelerators that broaden electron beams with scattering foils have also been performed, including the possibility of using helium along the beam axis to reduce deleterious air scatter (Karlsson *et al* 1999, Lee *et al* 2000a).

As an alternative to these systems, an electron-specific multileaf collimator (eMLC) has been proposed (Lee *et al* 2000a, Ma *et al* 2000b). It has been demonstrated that a collimator consisting of 1.5 cm thick tungsten leaves located at the level of the last scraper of a 25×25 cm² electron applicator allows shaping of the field to a higher degree of resolution than is possible using the photon MLC. By superposition of a number of different field shapes, an intensity modulated field may be delivered. However, a system for generating such a plan required further research.

Any planning system requires the ability to perform accurate dose calculations. Because electron transport and scatter in matter is strongly influenced by density and material composition, dose calculation in heterogeneous media is extremely challenging. Conventional algorithms typically utilize variants of the 3D Hogstrom pencil beam algorithm, based on Fermi-Eyges transport theory (Hogstrom *et al* 1981). However, it has been well documented that in heterogeneous phantoms and small irregular fields, this algorithm results in large regions of dose error (Cygler *et al* 1987, Bielajew *et al* 1987, Mah *et al* 1989, Mackie *et al* 1994, Ma *et al* 1999). It has been demonstrated that the Monte Carlo method can provide accurate dose estimations under all circumstances (Cygler *et al* 1987, Mackie *et al* 1994, Kawrakow *et al* 1996, Mohan 1997, Kapur 1999, Ma *et al* 1999). Additionally, Monte Carlo transport algorithms can be used to accurately assess the perturbations to the electron fluence caused by beam modifiers, such as multileaf collimators (assuming an accurate source model). The combined effects of field size, shape, and collimator on absolute doses can then be included as planning considerations with a high degree of accuracy. Thus, while the need for Monte Carlo dose computation of photon IMRT plans has been debated, the importance of Monte Carlo in conventional electron plans is well established, and it follows that more complex MERT plans will also benefit from Monte Carlo computation.

Most photon IMRT planning systems divide a radiation field into small spatial elements, or beamlets, and separate out the dose contribution from each beamlet as the first step in planning. This beamlet simulation may be performed by analytical methods or by the Monte Carlo method (Boyer and Mok 1985, Pawlicki *et al* 1999, Laub *et al* 2000). By optimizing on the dose distributions, weights or intensities for each beamlet may be obtained and the resulting 2D intensity maps may be converted into an MLC leaf sequence for delivery. The assumption is that the dose computed on a beamlet-by-beamlet basis is the same as the dose delivered via the actual leaf sequence. Even in photon IMRT this is not the case, the MLC tongue-and-groove effect being the most notable violation (van Santvoort *et al* 1996, Yu 1998), with transmission through leaf ends and edges also being a factor (Chen *et al* 2000). In these instances, an additional correction must be applied to leaf sequences or simply during dose reconstruction so that planners may evaluate the true dose rather than an ideal dose.

This difference between beamlet and delivered doses is the primary challenge encountered in developing a MERT planning system. During delivery, electrons (and contaminant photons) have the opportunity to scatter off or through leaf ends and sides to a much greater degree than photons. Additionally particles incident on the closed portions of the leaves may generate secondary particles, in particular bremsstrahlung photons (Lee *et al* 2000a). These effects result in a leaf-delivered dose that may differ significantly from the beamlet predicted dose. The magnitude of this effect depends on the specific plan and cannot be known *a priori*.

Holmes (2001) has proposed a tomotherapy planning system that accounts for aperture-dependent non-idealities such as leakage and head scatter. In that system, leaf sequencing occurred as part of the optimization procedure, and thus aperture-dependent leakage and head scatter could be included for each 'field' delivered by the tomotherapy system. This work seeks to apply the same concept to MERT planning, though in this case Monte Carlo calculated aperture-dependent non-idealities are incorporated via a *post hoc* procedure rather than during the optimization.

The objective of this study was first to examine the differences between beamlet deliveries and dose distributions from simulations in which particles were transported in the eMLC. A Monte Carlo based treatment planning system was then developed in which the bremsstrahlung leakage and leaf-end scatter and transmission could be properly accounted for in the optimization process. A method of implicitly including the effect of particle transport in the leaves was developed, allowing for faster calculations. Using this system, a plan is generated for an artificial homogeneous phantom and for a CT phantom of an intact breast. Based on these results, potential directions for further research are discussed.

2. Methods

2.1. Monte Carlo simulations

Source parameter descriptions of 6, 9, 12, 16 and 20 MeV (nominal energy) electron beams were obtained using a procedure described elsewhere and summarized here. Electron beam simulations of a Varian Clinac 2100C (Varian Oncology Systems, Palo Alto, CA) were performed using the EGS4/BEAM code (Nelson *et al* 1985, Rogers *et al* 1995). A 25×25 cm² type III (open walled) applicator was used in these simulations. Vendor supplied geometries were used to define the component modules in the BEAM simulation, with photon jaw settings adjusted according to the nominal beam energy. It has been shown elsewhere that the resulting phase space data from these simulations, when used in EGS4/DOSXYZ or MCDOSE dose calculations, provide agreement with measured data to within 2% on depth-dose and transverse profiles, as well as output factor calculations (Kapur *et al* 1998, Kapur 1999, Lee *et al* 2000c).

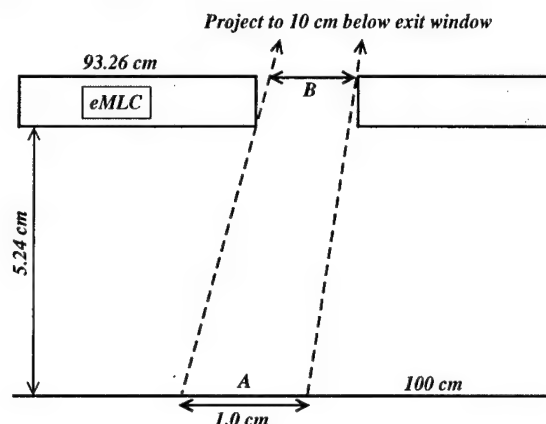


Figure 1. A schematic diagram of the beamlet and electron MLC geometry. The beamlet is defined as having a width of exactly 1.0 cm at 100 cm from the photon target, regardless of where the phantom surface is actually located. This is shown in A. The source plane is reconstructed at 93.26 cm, coincident with the upper surface of the eMLC. The beamlets are then defined at this plane B by ray tracing from the approximate location of the electron virtual source, 10 cm below the exit window. Only particles within B are reconstructed and beamlet simulation occurs without any collimation. When leaves are simulated, their positions are set based on the geometric projections of the leaf edges, as shown. Thus there is an inherent difference in beamlet simulation and actual delivery.

During the simulation, 'latch bit' settings were used to delineate particles originating or scattering off the first two scrapers of the applicator (source 1 and 2), and electrons (source 3) and photons (source 4) that were well described by a virtual point source (Ma *et al* 1997, Ma and Rogers 1997, Jiang *et al* 2000). This four-source model has been shown to provide agreement with both the direct phase-space simulation and measured data (Jiang *et al* 2000). During dose calculations particles were generated according to this source model, thus eliminating the need for calculation and storage of large phase-space data files.

Unless otherwise noted, electrons were transported down to 0.70 MeV total energy (ECUT) and photons transported to 10 keV energy (PCUT), at which point the remaining energy was deposited on the spot. It has been documented that an ECUT of 0.70 MeV, corresponding to a residual continuous slowing down approximation range in water of <0.5 mm, is sufficient for most dosimetric purposes (Rogers *et al* 1995). Transport through the leaves and in air was performed using PRESTA for step-length calculations (Bielajew and Rogers 1987). For transport in the phantom, photon splitting and electron track repetition were employed as variance reduction techniques (Kawrawkow and Fippel 2000, Ma *et al* 2000a).

Dose calculations were performed using the EGS4 user code MCDOSE (Nelson *et al* 1985, Ma *et al* 2000a). This code has been described in detail elsewhere and has been shown to provide agreement with DOSXYZ and measured data to within 2% (Li *et al* 2000b). The code was modified and used for MERT planning as described in the following sections.

2.1.1. Electron beamlets. For each energy and port, electron beamlets were simulated for use in the inverse planning algorithm in a manner analogous to Monte Carlo based photon IMRT planning (Pawlicki *et al* 1999). Beamlet size was set at the level of isocentre, with a resolution of 1 cm. The beamlet was then defined by a virtual aperture located at the position of the upper surface of the electron MLC, 93.26 cm below the photon target. The beamlet size was defined

to be given by projections taken from the plane containing the isocentre to the approximate location of the electron virtual source, 10 cm below the photon target as determined during beam commissioning. This geometry is shown schematically in figure 1. The virtual aperture could be simulated in one of two ways:

- (a) By taking the beamlet to be an opening in a perfectly absorbing infinitely thin collimator, that is, sampling from the full $25 \times 25 \text{ cm}^2$ field and transporting only those particles that land in the beamlet.
- (b) Sampling directly within the beamlet itself, and never generating any particles in the remaining regions.

For efficiency, method (b) was selected with weighting factors defined as follows.

Let us consider a subset of a two-dimensional fluence profile ('beamlet') defined by $x = x_1$ to x_2 and $y = y_1$ to y_2 with area A_{beamlet} . If we sample within this beamlet according to the true distribution, then each particle can be given a weighting factor equal to the ratio of the integral fluence within the beamlet to the overall integrated fluence. If, however, we sample *uniformly* within this region, then we must apply an additional weighting factor to remove the biasing due to the uniform sampling. If the intensities (number of particles in a bin) are given as $F(x, y)$ and we consider a point (x', y') , then

$$w(x', y') = \frac{A_{\text{beamlet}}}{A_{\text{bin}}} \frac{F(x', y')}{\sum_x \sum_y F(x, y)} \quad (1)$$

where A_{bin} is the area of the spatial bin to convert number of particles to fluence and the summation represents the total number of particles in the source parameter file.

As mentioned above, each source parameter file contains fluence information for four subsources. Because spatial bins are defined in the same way for each subsource, it is possible to assign a cumulative distribution function (CDF) for each bin, describing the relative intensities of each source. Particles are sampled according to this CDF and hence no additional weighting factor is needed for subsources. Note that contaminant photons from the treatment head are included in the source reconstruction during both beamlet and eMLC simulation. Particle origins are uniformly sampled on each subsource (i.e. an electron has an equal probability of coming from each edge of an electron scraper). The reader is referred to Jiang *et al* (2000) for complete details on source reconstruction for this four-source model, with the aforementioned weighting factors for beamlet sampling.

During beamlet simulation, particles are reconstructed at the upper surface of the eMLC at a distance 93.26 cm below the nominal photon target position. The remaining air gap to the phantom is then explicitly simulated, thus accounting for the in-air scatter, such that the final fluence at the phantom surface is essentially a convolution of the original fluence and the scatter kernel.

2.1.2. Electron MLC simulation. A proposed design for an electron specific MLC (eMLC) has been described elsewhere and is summarized below (Lee *et al* 2000a). Based on measurements with a prototype system and Monte Carlo simulations, it has been shown that 1.5 cm thick tungsten leaves located at the level of the last scraper provide adequate electron collimation for MERT. Leaf ends and sides may be unfocused, though in this study leaf sides were considered to be focused to a point 10 cm below the photon target (for the 2D targets studied here, this has no significant effect). Note that while this study utilized this specific eMLC design, the results are general to any collimator in which leaf end scatter and transmission and bremsstrahlung leakage are non-trivial.

The MCDOSE code was modified to include the simulation of particle transport in such a collimator, placed according to arbitrary table, collimator and gantry angles, with leaves set

according to a leaf sequence file. The geometry coding routines were based upon macros used for block simulations (Li *et al* 2000a, b). In all simulations, a region extending from the field edge 5 mm into the leaves of the eMLC was subject to explicit simulation of all particles, up to the global transport cut-offs. Margins of thickness greater than 3 mm have been shown to be adequate for accounting for edge effects in cut-outs (Mubata *et al* 2000). Outside this region, one of two rejection methods was used to accelerate the simulations. In one method all particles in this region were rejected, while in the second method electrons were discarded based on a 2 MeV total energy cut-off while photons were transported explicitly. An alternative method for computing bremsstrahlung leakage was investigated and is described separately in section 2.1.3.

Each segment of the MERT plan was given a different number of histories based upon the number of monitor units to be delivered. Note, however, that the absolute dose is decoupled from the number of histories delivered, because the absolute dose for each field is separately computed assuming a single monitor unit delivery, and then rescaled to the correct value. However, for increased speed, the number of particles simulated was proportional to the number of MU to be delivered. In particular, the overall statistical uncertainty at a point after N segments with relative intensities w is given by

$$\sigma_{\text{tot}}^2 = \sum_{i=1}^N (w_i \sigma_i)^2. \quad (2)$$

If we express all the intensities in units of the minimum intensity, w_{min} , such that $w_i = \alpha_i w_{\text{min}}$, we may write

$$\sigma_{\text{tot}}^2 = \sum_{i=1}^N (\alpha_i^2 w_{\text{min}}^2 \sigma_i^2). \quad (3)$$

If we desire to have all segments provide an equal contribution to the overall uncertainty, then $(\alpha_i^2 \sigma_i^2)$ must stay constant over i . This implies that the square of the uncertainties should scale linearly with the square of the intensities, or equivalently, the number of histories for a field should scale with the square of the intensities. The uncertainty in the final plans was less than 1% at 1σ for the voxels with a dose $D > 0.5 D_{\text{max}}$. By using a low uncertainty (at the cost of high computation time), the noise-convergence issue of Monte Carlo based inverse planning can be minimized (Jeraj and Keall 2000, Keall *et al* 2000).

2.1.3. Bremsstrahlung background approximation. In a subset of the simulations, leakage photons were included in the calculations without explicit transport through the leaves. Using the EGS4/BEAM system, two phase space files were generated, one directly above and one directly below a 1.5 cm tungsten slab. Only particles passing through a $10 \times 10 \text{ cm}^2$ square centred on the slab's upper surface were transported and scored. The photons in the lower phase space were placed into angular bins of 1.0° (taken with respect to the central axis) and within each angular bin, particles were separated into energy bins of 0.5 MeV. A 'total photon yield' S was defined as the number of photons in the lower phase space divided by the total number of particles in the upper phase space. Note that this differs from the standard definition of bremsstrahlung yield in that all photons are scored including, for example, transmission, rather than only bremsstrahlung, and the yield is given per incident particle rather than per incident electron.

The Monte Carlo simulation employed the bremsstrahlung production cross sections of Koch and Motz (1959). The validity of the Monte Carlo method for studying thick-target bremsstrahlung has been discussed at length in the literature (e.g. Seltzer and Berger 1985, Faddegon *et al* 1990, 1991).

During source reconstruction, electrons that would be incident upon the upper surface of the eMLC are discarded (recall that the source plane and the top of the eMLC are coincident). A random number η is selected in the interval (0, 1], and if $\eta < (S/N_{\text{split}})$ then a photon of weight N_{split} is generated according to the joint angular/spectral distribution and simulated beginning from the bottom surface of the MLC. In these simulations, N_{split} was set at 10, thus utilizing a Russian roulette-style variance reduction technique. The assumption was made that the bremsstrahlung phase space was invariant across the field, and that at a given point the photon distribution was radially symmetric. The low-energy electrons produced in the leaves were also ignored. This greatly simplifies and accelerates both source model generation and reconstruction, and it is shown in section 3.1.3 that these assumptions allow for sufficient accuracy for treatment planning.

2.1.4. Absolute dose calibration. In general, Monte Carlo results are given in dose per incident particle. To convert to absolute dose, the dose distribution from a $15 \times 15 \text{ cm}^2$ field is calculated (for each separate energy) and the central axis maximum taken to be a calibration factor, $D_{\text{ref}}^{\text{ref}}$ (here, subscripts refer to fields and superscripts refer to measurement points). This value is given in cGy/particle. Then, an arbitrary point A in the reference field may be converted to absolute dose per monitor unit D , given in cGy MU^{-1} by

$$D = \frac{D_{\text{ref}}^A}{D_{\text{ref}}^{\text{ref}}} \quad (4)$$

Because some particles are ignored for various reasons during conversion from phase space to source parameter (particles going backwards, positrons, field size limits, etc), this simple calculation is only valid for a single source parameter file. To be used in any field (in particular, here, the $25 \times 25 \text{ cm}^2$ field), equation (4) may be expanded as

$$\frac{D_{25 \times 25}^A}{D_{\text{ref}}^{\text{ref}}} = \frac{D_{25 \times 25}^A}{D_{25 \times 25}^{\text{ref}}} \times \frac{D_{25 \times 25}^{\text{ref}}}{D_{\text{ref}}^{\text{ref}}} \quad (5)$$

The term $D_{25 \times 25}^{\text{ref}}$ can be calculated directly by simulating a $25 \times 25 \text{ cm}^2$ field. The second factor, $D_{25 \times 25}^{\text{ref}}/D_{\text{ref}}^{\text{ref}}$ cannot be taken from source parameter based Monte Carlo calculations, for reasons described above, i.e. some particles are not included during source parameter generation. However, this energy-dependent parameter may be taken from Monte Carlo simulations based on complete phase-space data or from measured applicator factors, defined as the ratio of absolute doses at the central axis maxima.

2.2. Optimization

The optimization method used was developed by Jiang (1998) and the salient features are described here. The system utilizes a steepest descent search algorithm, with a quadratic objective function augmented by dose-volume constraints. As usual, deviations from the prescribed dose p_0 contribute to the objective function in the following form

$$F_{\text{target}} = \sum_{i \in T} (d_i - p_0)^2 \quad (6)$$

with T denoting points in the target. The soft dose-volume constraints are given by Zangwill's penalty function (Buchanan and Turner 1992). In particular,

$$F_{\text{target}}^{\text{penalty}} = w_{\text{target}}^{\text{low}} \sum_{i \in T} \xi_i^{\text{low}} (d_i - p_1)^2 + w_{\text{target}}^{\text{high}} \sum_{i \in T} \xi_i^{\text{high}} (d_i - p_2)^2 \quad (7)$$

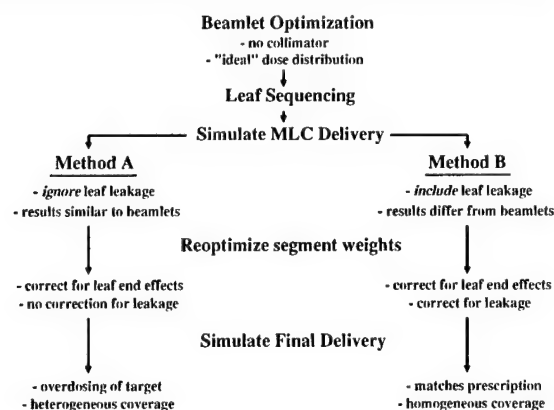


Figure 2. A schematic summary of the overall treatment plan. Each stage is discussed in detail in the text. 'Method A' utilizes a simplified leaf model and is shown to result in an inferior plan. 'Method B' utilizes either explicit particle transport in the leaves or a bremsstrahlung approximation, and results in a delivered doses that match well with prescriptions.

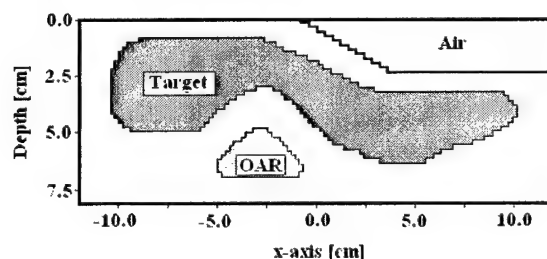


Figure 3. Schematic diagram of the test phantom. The target structure and organ at risk (OAR) are shaded and labelled accordingly. An extended air gap exists in the positive x region with the accelerator isocentre located at the origin of the diagram. The phantom material is ICRU tissue. The phantom extends 10 cm above and below the plane of the page.

where d_i is the dose at a point i , p_1 and p_2 are the upper and lower limits on target dose, w are the weights for the constraints and ξ_i is defined as 1 if the point i is too high/low and the volume constraint (number of points already in violation) has been reached. Similarly, critical structures are protected by adding upper-limit penalties in a dose-volume fashion. The overall objective function is then defined as

$$F_{\text{obj}} = F_{\text{target}} + r(F_{\text{target}}^{\text{penalty}} + F_{\text{critical}}^{\text{penalty}}) \quad (8)$$

where r rises with each Zangwill iteration. Further details on this method of optimization may be obtained from Jiang (1998).

3. Results and discussion

The general outline of the treatment planning procedure is given in figure 2. On occasion, the text will refer to 'method A' or 'method B'. These will correspond with the appropriate branch of the flowchart in figure 2.

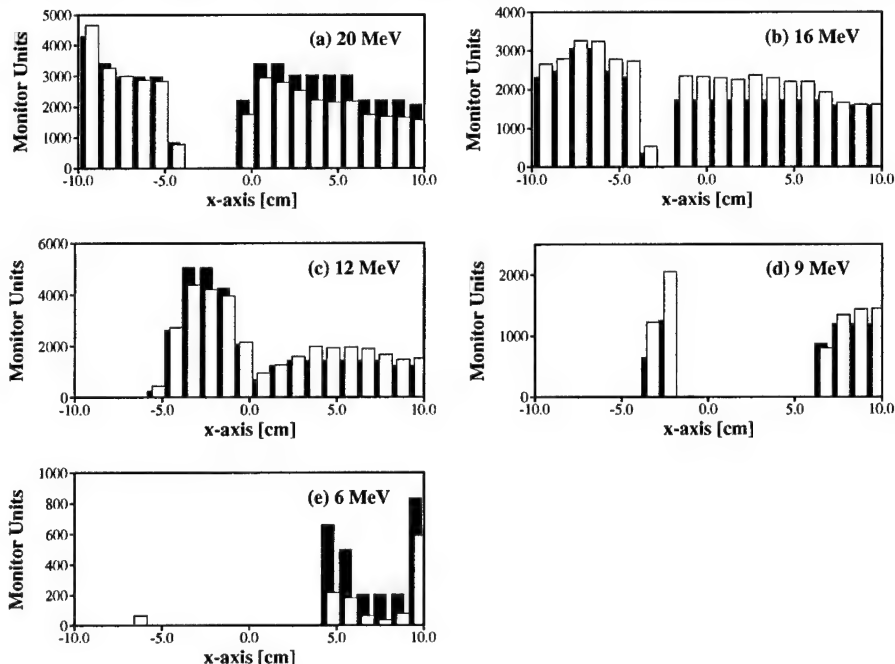


Figure 4. Intensity maps generated for the homogeneous phantom by optimization of electron beamlets: (a) 20 MeV, (b) 16 MeV, (c) 12 MeV, (d) 9 MeV, (e) 6 MeV. Shown are □, after initial beamlet optimization and ■, after final segment optimization. Note that the intensities shown for beamlets are prior to rebinning.

3.1. Homogeneous phantom

3.1.1. Geometry and beamlets. The first phantom geometry to be considered was a two-dimensional homogeneous phantom with a sloped surface, shown schematically in figure 3. The two-dimensional system was chosen so that beamlet weights and dose distributions could be more easily assessed. The target was chosen to be concave with a critical structure placed within the concavity. A small region around the target was chosen to represent the normal tissue dose. The lateral extent of the target was approximately 20 cm. In the third dimension, i.e. out of the page, as shown, the target region was 4 cm wide and was surrounded by homogeneous ICRU tissue to a total width of 20 cm. The isocentre was placed at the surface of the phantom, centred on the x-axis.

An array consisting of 20 beamlets, each with an area of $1 \times 7 \text{ cm}^2$, was delivered into the phantom at each of the five available energies, covering the area from $x = -10.0$ to 10.0 cm . The 7 cm beamlet size along the y-axis was chosen to be sufficiently large such that the central target voxels were covered by a uniform field.

The beamlet weights were optimized to provide the intensity map shown in figure 4. The general trend is as expected based on energies and depths. That is, the higher (20 and 16 MeV) beams are restricted to the deeper target regions, while the lower energies are used in regions where sparing of the critical structure is necessary. The resulting cumulative dose-volume histogram (DVH) is shown in figure 5. Note that the target is well covered at the level of dose prescription and the coverage is uniform to within the statistics given in table 1.

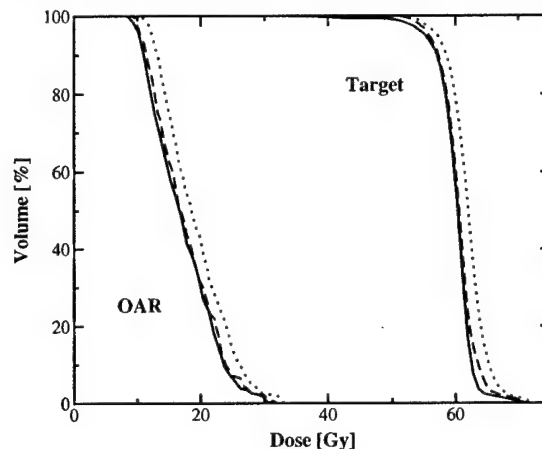


Figure 5. Cumulative DVHs for the homogeneous phantom based on a leaf sequence derived from the beamlet optimization (before the second optimization). Shown are DVHs for target and critical structures. The results are for beamlet simulation (—), full simulation of leaves (· · · · ·), and with leaf end scatter but no leakage (---). The full simulation is what would actually be delivered, including a significant overdosing because of bremsstrahlung from the leaves. This overdose is not predicted by the other simulations.

Table 1. Dose constraints used during optimization of plans. For the target, a prescription dose of 60 Gy was assigned for the homogeneous phantom and 50 Gy for the breast phantom. In both cases, the average dose met this prescription to within 1%. Dose volume constraints are given as maximum or minimum dose allowed for a given volume (Prescr.). When this constraint is violated, penalties are assessed according to equation (7).

	Structure	Dose (Gy)	Relative weight	% Volume exceeding dose limit		
				Prescr.	Initial opt.	Final opt.
Homogeneous phantom	Target	>61.0	100.0	1.0	35.7	35.1
		<59.0	100.0	0.0	25.9	27.6
	OAR	>30.0	50.0	5.0	1.5	2.4
		>20.0	50.0	25.0	29.7	32.1
		>5.0	50.0	75.0	100.0	100.0
Breast phantom	Target	>50.5	100.0	0.0	38.0	34.6
		<49.5	100.0	0.0	38.7	33.7
	Rt Lung	>1.0	25.0	50.0	61.8	100.0
		>3.3	25.0	30.0	43.6	55.4
		>9.2	25.0	20.0	19.1	22.7

3.1.2. Simulation of the leaf sequence. This intensity profile was converted to a step-and-shoot leaf sequence (for a single, wide leaf) via the close-in method (Bortfeld *et al* 1994). The leaf sequencing method was chosen arbitrarily, but it is expected that the results should be general to any given leaf sequencing system (see section 3.2, for example). The delivery of this leaf sequence was then simulated with the leaves accounted for using two different methods: (A) no particles transported in leaves and consequently, no bremsstrahlung production in the leaves, and (B) explicit transport of electrons down to 2.0 MeV (ECUT) and photons to

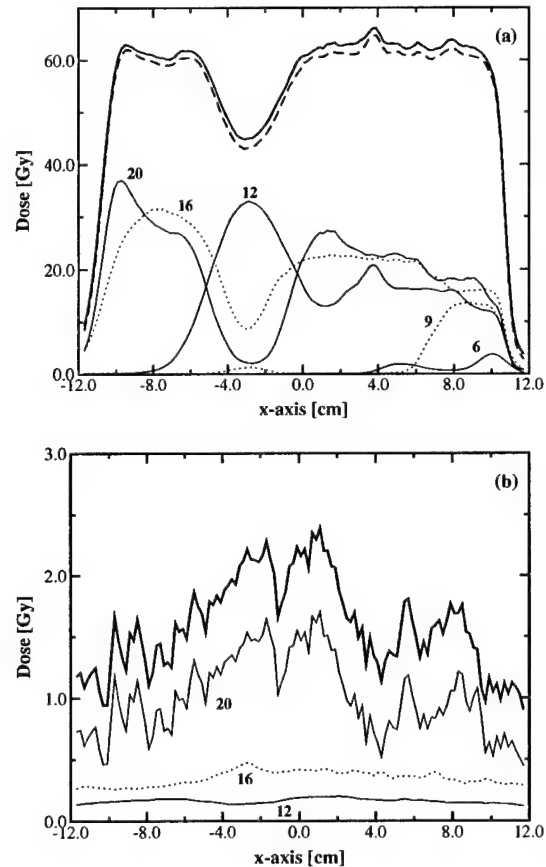


Figure 6. Dose profile from the simulated delivery of a plan based on beamlet optimization results (before the second optimization). (a) Dose profile taken at a depth of 4.0 cm below isocentre. Thin curves (full and dotted for clarity) represent individual energies while the thick curves indicate total dose, — with, - - - without bremsstrahlung. (b) A difference plot representing the bremsstrahlung contribution for each energy and the total plan (thick curve). For clarity, 9 and 6 MeV have been omitted. These low energies result in considerably less bremsstrahlung leakage than the energies displayed.

10 keV (PCUT). In all cases, complete simulation of all particles down to the global cut-offs was performed in an area within 5 mm of the leaf boundaries.

The DVHs for these deliveries are shown in figure 5. There are significant differences in the DVHs based on the type of leaf simulation. When bremsstrahlung is ignored (method A), the delivered DVH closely matches the DVH generated during beamlet delivery, with small differences caused by the finite thickness of the leaves and scatter off the leaf ends. The similarity between these two curves suggests that the beamlets and leaf delivery are implemented properly both in relative and absolute dose calculation. The difference between the beamlet optimization result and simulation via method A is due to the combined effects of leaf end scatter and rebinning the weights into 10 intensity levels. These effects are observed to have only a small impact on the resulting DVHs for this case.

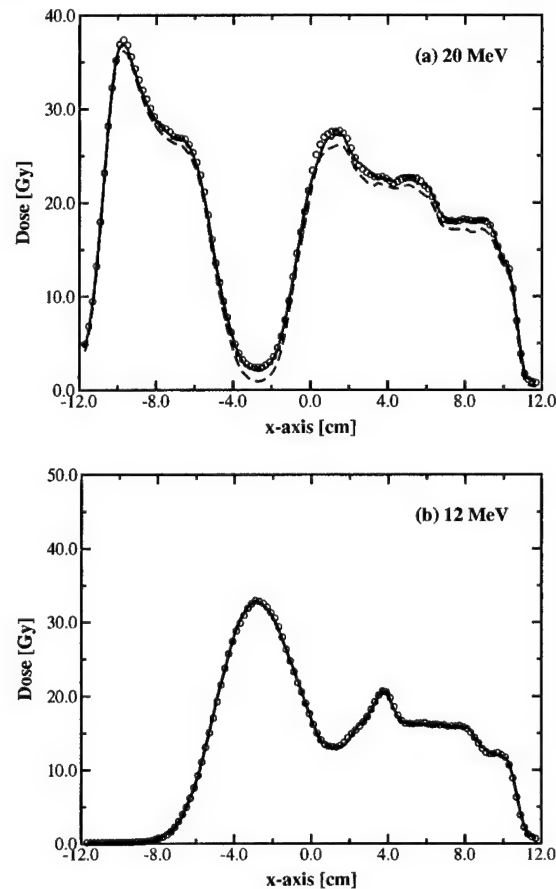


Figure 7. Dose profiles taken at a depth of 4.0 cm below isocentre for (a) 20 MeV and (b) 12 MeV. Shown are explicit simulation (—), no bremsstrahlung production in leaves (---), and approximated leakage (○). Note the magnitude of the bremsstrahlung dose (the difference between no transport and explicit simulation) at 20 MeV and the agreement between the approximate and explicit simulation.

This, however, represents only the ideal case and one that cannot be delivered with a real collimator system. When the actual eMLC delivery is simulated, including bremsstrahlung production in the leaves (method B), it is apparent that a significant increase in dose occurs in both the critical structure and target. This suggests that bremsstrahlung leakage is an essential element in the dose calculation.

Figure 6(a) shows the contribution of each energy to the total dose at a depth of 4.0 cm. As expected, the dose distribution of each energy roughly follows the intensity maps of figure 4. The difference in absolute dose between the complete plan delivered with and without bremsstrahlung leakage, taken at the same depth, is shown in figure 6(b). What is immediately apparent is that, as expected, the primary contributor to bremsstrahlung background is the 20 MeV field. Profiles at different depths show similar results. It is also observed that the

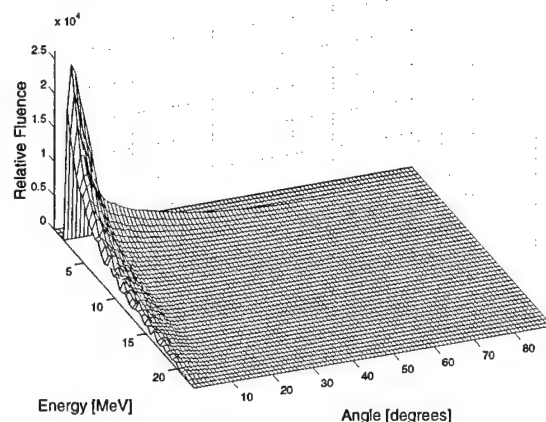


Figure 8. The joint angular/spectral distribution for bremsstrahlung photons generated in a 1.5 cm tungsten slab irradiated by the 20 MeV field of a Varian Clinac 2100C. The distribution is given as an average over the entire field. The z-axis is presented in arbitrary units of planar fluence. Integrated over all angles, the most probable energy for this distribution is 2.25 MeV with a mean energy of 5.06 MeV.

effect is not uniform, and is thus not likely to be corrected by a global change in monitor units delivered.

This leaf effect can be studied in more detail by examining dose profiles for individual energies, as shown for 20 and 12 MeV in figure 7. Examining the 20 MeV profile in figure 7(a), taken at a depth of 4.0 cm, it can be seen that the full leaf simulation gives a slightly higher dose across the field, especially in the region corresponding to the critical structure. In this region, adequate coverage was achieved by the use of the 12 MeV field because the target stopped at a shallower depth. Because the 20 MeV would penetrate into the critical structure, it was blocked in this region. However, while primary electrons are blocked, bremsstrahlung is generated by the electron interactions in the leaves.

Thus, there exists here a situation where the open field (12 MeV) delivers dose as predicted by the beamlet simulation, but leakage dose from closed fields (20 MeV) is not accounted for during beamlet optimization. In this case, an appropriate correction can be found by inspection: the intensity of the portions of the 12 MeV overlaying the critical structure should be reduced in such a way as to (at least partially) offset the dose being delivered by the bremsstrahlung from the 20 MeV field. Of course, this only offers an approximate correction to one region which may not be the optimal correction even for this limited problem, and does not correct for leaf end scatter. As noted, leaf end scatter plays a small role in this case, but situations may arise in which it has a larger impact than bremsstrahlung production, especially if low-energy fields are delivered with higher intensities. A more robust and automated solution is necessary for use in treatment planning. This can be achieved by the optimization of segment weights.

3.1.3. Bremsstrahlung approximation. These results clearly indicate that the effect of bremsstrahlung leakage must be included during treatment planning. However, transporting particles through the leaves becomes prohibitively slow when multisegment, multienergy plans are considered. A method to approximate the leakage was then developed to circumvent this problem.

Table 2. A comparison of the three different methods of leaf simulation. All values are taken at a depth of 2.5 cm. The open portion of the field extended from the central axis towards the +x direction. The 'dose out of field' was computed as the average of the dose from -10.0 cm to -3.5 cm. Relative speeds are presented normalized to the full, or explicit, simulation. See section 2.1.3 for details on each simulation method. The same number of initial particles were simulated in each case. The statistical uncertainty was approximately 0.5% at 1σ .

Field	Leaf simulation method	Relative speed	Max. dose in field		Dose out of field	
			(Gy)	Rel. error	(Gy)	Rel. error
20 MeV $5 \times 7 \text{ cm}^2$	Explicit	1.0	10.05	—	0.16	—
	No trans.	5.1	9.98	<1%	0.01	-92.4%
	Approx.	4.3	10.01	<1%	0.16	<1%
20 MeV $1 \times 7 \text{ cm}^2$	Explicit	1.0	8.27	—	0.15	—
	No trans.	13.3	8.14	-1.54%	0.01	-96.3%
	Approx.	8.2	8.50	+1.03%	0.16	<1%

Just as a source model is used to generate electrons and photons from the treatment head, a bremsstrahlung source model was used to re-create photons at the lower surface of the eMLC, as described in section 2.1.3. The joint angular/spectral distribution for a 20 MeV field as generated by EGS4/BEAM simulation is plotted in figure 8. As expected, the photons are primarily forward directed with a significant low-energy portion. The approximation was tested on simple static fields and found to reproduce full simulation results to within 2%. The improvement in speed and specific dose values can be found in table 2. In particular, for the 1 cm field where only about 3% of the eMLC is open (as is the case in many plan segments), the simulation could be accelerated by approximately a factor of 8.

A second set of simulations was executed for these leaf settings, again with full leaf simulation. The BLCMIN parameter of the PRESTA algorithm was set to 1.5 to maintain smaller step sizes than are necessary for accurate transport (Bielajew and Rogers 1987). It has been reported that this may lead to a small but significant change in the bremsstrahlung yield in thick targets (Faddegon *et al* 1990, 1991). However, no significant changes were observed in the bremsstrahlung dose distributions, and so the default PRESTA values were retained (for speed) in all subsequent simulations. However, it is noted that the true bremsstrahlung spectrum, yield and angular distributions may indeed differ significantly from the approximate source used here, though the effect on the resulting dose is trivial compared with the primary electron dose.

In section 3.1.2, it was proposed that optimizing segment weights may correct for bremsstrahlung leakage. This will be most effective if the bremsstrahlung angular spread is sufficiently narrow such that open regions received only trivial photon dose during the delivery of that segment. Indeed, this assumption is validated by the results shown in table 2. For the 1 cm wide field, the difference between maximum doses with explicit leakage and no leakage is approximately 1.6% on a statistical uncertainty of 1.0%. The overdose caused by the approximation in the open field region is similarly within 2%. This error is due to the approximation that the bremsstrahlung angular distribution is the same at all points, rather than tilted away from the central axis (as the incident electrons are). However, especially as this effect decreases with increasing field size, it was considered an acceptable level of error.

The method presented is one possible method to simulate the effect of the leaves in an acceptable time frame, and was used for the CT phantom in section 3.2. For the homogeneous phantom currently under discussion, DVHs and isodose lines for simulations performed using

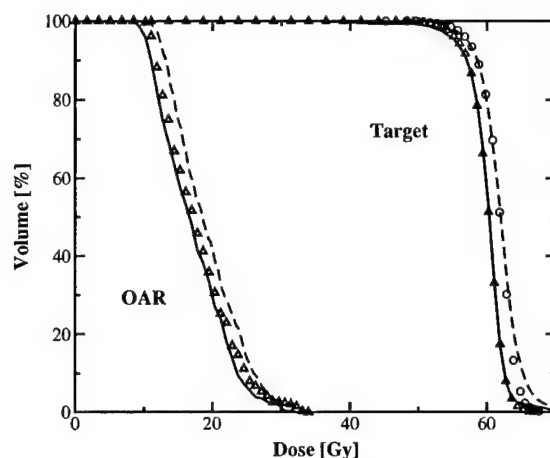


Figure 9. Cumulative DVHs for the homogeneous phantom for target and critical structure, after beamlet optimization (—), simulated delivery of this plan with leaves in place, i.e. without second optimization (---), and simulated delivery with leaves after segment optimization, i.e. final plan (Δ). Note that the original beamlet optimization and the final plan are nearly indistinguishable in target coverage. Also shown is the delivered target DVH for a plan in which a second optimization occurred, but in which segments only included leaf scatter, and not bremsstrahlung (O).

this approximation and explicit full leaf simulation were found to be indistinguishable. Thus, unless otherwise specified, figures and discussion regarding explicit simulation of leaves are equally applicable to the approximate bremsstrahlung approach.

3.1.4. Optimization of segment weights. During the simulated delivery of the leaf sequence, the dose distribution from each segment was stored separately. A segment was defined as the beam delivered by a field defined by a set of leaf positions, that is, a single static field in a step-and-shoot sequence. Treating each of these segments as if they were beamlets, the weights, or monitor units delivered per segment, were re-optimized with the same parameters as before. The initial conditions for the optimization were taken from the original monitor unit settings, i.e. those derived from the first beamlet optimization. The results of this second optimization are shown in table 1.

It is crucial to recall that this second optimization is based on a realistic geometry and includes such details as leaf end transmission and bremsstrahlung leakage. In contrast, the results of the first optimization are based on idealized beamlets, i.e. with no real collimator geometry involved. This first optimization gives the best dose distribution with a given optimization (given a perfectly absorbing and infinitely thin collimator), while the second optimization is the actual delivered dose. What is observed is that if the non-idealities caused by the eMLC are included in the second stage optimization (i.e. the segment optimization), the final result does not deviate far from the ideal case (i.e. the beamlet optimization). The target dose and coverage are very similar, with a slight increase in dose to critical structures. Note that of course the bremsstrahlung dose cannot be completely negated, and that there is a small increase in dose to normal tissues as a result, but this occurs deeper than the target and critical structure and thus represents doses of less than 2% of the prescription dose.

These results are further detailed in figure 9, where the DVHs are shown after various stages of planning. Idealized beamlets are optimized to give a dose distribution that agrees very well

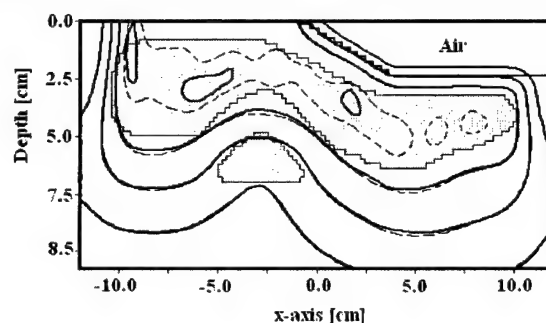


Figure 10. Isodose lines for the homogeneous phantom. Shown are the simulated deliveries of plans generated accounting for leaf effects (—) and plans that ignored the effect of the leaves (---). The structures are labelled in figure 3. Lines represent absolute doses: starting closest to the target and moving outwards, 62.5, 50, 30, 10 Gy. Recall that the prescription dose was 60 Gy. Target doses in both cases satisfied the minimum prescription dose requirements, but there is significant overdosing of the target in the plan that did not account for leaf effects.

with the prescription on table 1, shown as full curve in the figure. However, actually delivering this plan adds the effect of the collimator leakage and scatter. The resulting DVH is shown as a broken curve, and is right shifted and also has a change in the slope, suggesting much poorer target coverage than was predicted by the idealized plan. However, once segment weights are re-optimized, the DVHs, shown as symbols, indicate that target coverage is very similar to that of the ideal beamlets, despite the non-idealities of the real collimator. The dose to critical structures rises slightly with the addition of the leaves, due to the leakage, but the final optimization does reduce this effect somewhat. The resulting intensity maps are shown in figure 4.

It is noted that this optimization is a somewhat smaller problem than the initial optimization. In particular, whereas the initial optimization was in 100 dimensions (20 beamlets \times 5 energies), this second optimization has a dimensionality equal to the total number of segments in all ports: in this case, 33. Additionally, the initial values of the segment weights are much closer to the optimal solution than the initial beamlet weights, which were set to zero.

3.1.5. Final dose distributions. As implemented, the optimization procedure involves storage of complete information about dose in structures (target, OAR) but only stores dose for a limited set of healthy tissue voxels. Thus, while the DVHs generated in the second optimization are complete, plotting isodose lines and a full accounting of normal tissue dose requires a final dose calculation based upon the entire plan. While it is possible that this step could be avoided in a clinical implementation (given sufficient computer resources), it was also a necessary step for this study to fully quantify the error introduced by ignoring the leaf transport.

Figure 9 shows the DVHs for the final deliveries planned based on full leaf transport simulations and also a plan generated with only leaf scatter accounted for. Both plans were based on an intensity map generated by the same ideal beamlets. This initial optimization result gave the leaf positions for the deliveries. At this point, both simulations are identical. Then, the delivery of the leaf sequence was simulated with leaf leakage included in one case and ignored in the other. In the case where bremsstrahlung from the leaves was ignored, the finite thickness of the leaves and end scatter and transmission was still included. The segment weights for these two simulations were then re-optimized, such that a final set of leaf positions

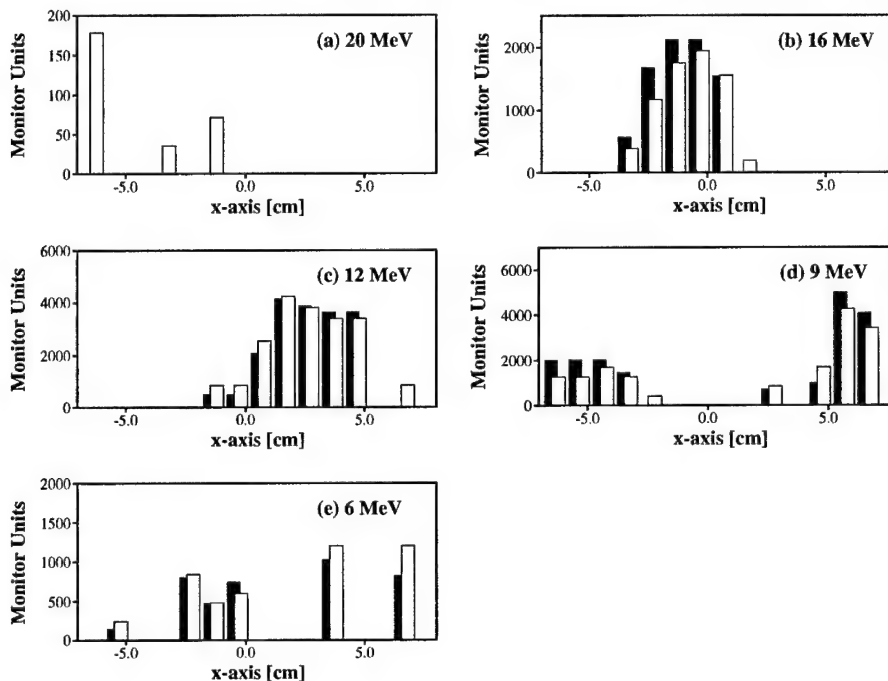


Figure 11. Intensity maps for the AP field of the 2D breast plan, generated by optimization of electron beamlets, for the AP directed port: (a) 20 MeV, (b) 16 MeV, (c) 12 MeV, (d) 9 MeV, (e) 6 MeV. Shown are □, after beamlet optimization and ■, after segment optimization.

(based on the first optimization) and monitor units (based on the second optimization) were obtained. These were then simulated with complete simulation of the collimator system, to observe the dose distributions from actual deliveries based on these planning procedures.

As expected, figure 9 shows that the delivery that was planned without leaf leakage resulted in an overdose to the target and critical structures. This is expected to be true for any situation in which the leaf transport and leakage is not properly included in the simulation, not just simulations in which all transport is ignored. Note that the DVHs for the plan generated with the bremsstrahlung approximation are virtually indistinguishable from the full simulation DVHs, and are thus not shown.

Isodose plots are shown in figure 10 for the plans generated with the leaf effect included in the optimization and for plans that did not take this leaf effect into account. What is apparent is that failing to include leaf effects in planning leads to an overdosing, shown by the 62.5 Gy isodose line.

3.2. Two-dimensional breast CT phantom

As a demonstration of this method in a more realistic scenario, a plan was generated for irradiation of an intact breast. For this proof-of-principle study, the breast was taken as a single CT slice. Extension to 3D cases requires further study on the effect of leaf sequences on MERT planning, and will be addressed in future research. Details of the planning parameters and results can be seen in table 1.

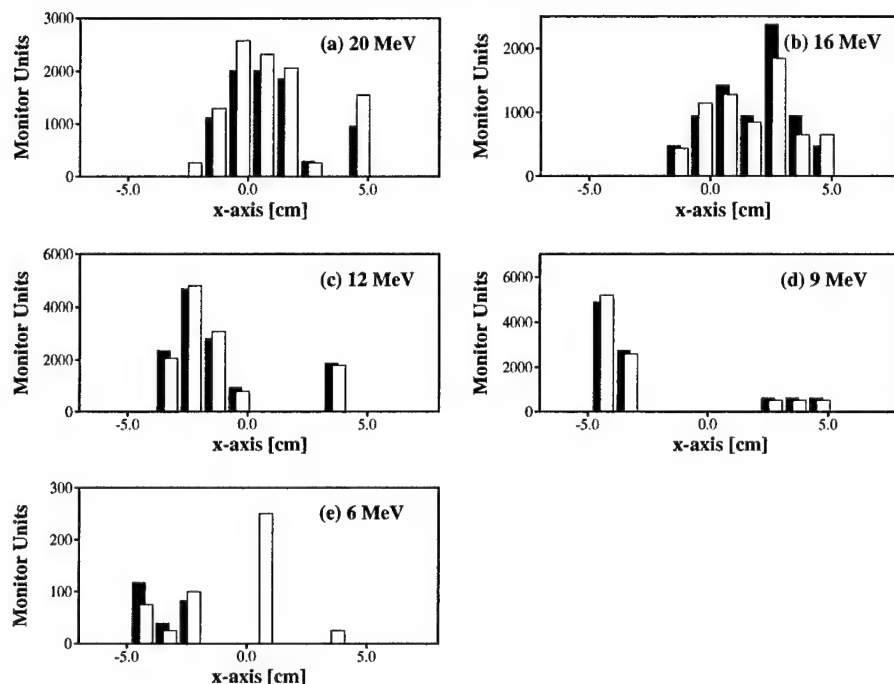


Figure 12. Intensity maps for the RL field of the 2D breast plan, generated by optimization of electron beamlets, for the right lateral port: (a) 20 MeV, (b) 16 MeV, (c) 12 MeV, (d) 9 MeV, (e) 6 MeV. Shown are \square , after beamlet optimization and \blacksquare , after segment optimization.

For this plan, two ports with different gantry angles and isocentres were employed, with five energies delivered through each port. One port is directed in the anterior-posterior (AP) direction while the second port was directed from the right lateral (RL) direction. The planning proceeded using the method developed in the discussion of the homogeneous phantom (i.e. via method B). Beamlets were delivered and optimized, a leaf sequence was derived for the eMLC, delivery was simulated using the bremsstrahlung approximation and the segment weights were re-optimized. While the homogeneous leaf sequence was generated using the close-in method, this leaf sequence was generated using the intensity solid paradigm method of Siochi (1999), as a demonstration of the generality of the planning procedure. No other modifications to the planning scheme described above were necessary for simulation of this multiport/multi-isocentre plan.

The intensity maps for the AP fields are shown in figure 11 and the RL fields are shown in figure 12. Unlike the single-port homogeneous plan discussed earlier, the intensity maps are less intuitive and are, in a qualitative sense, less smoothly varying than the homogeneous phantom discussed earlier. The addition of a second gantry angle and homogeneous material makes this optimization more similar to photon IMRT in that intensity maps can only be roughly estimated by inspecting the geometry. However, the general trend of reducing 20 MeV field intensities and compensating for this with increased intensity at the lower energies is maintained. Further research will examine the effect of smoothing these profiles, as has been suggested for photon IMRT.

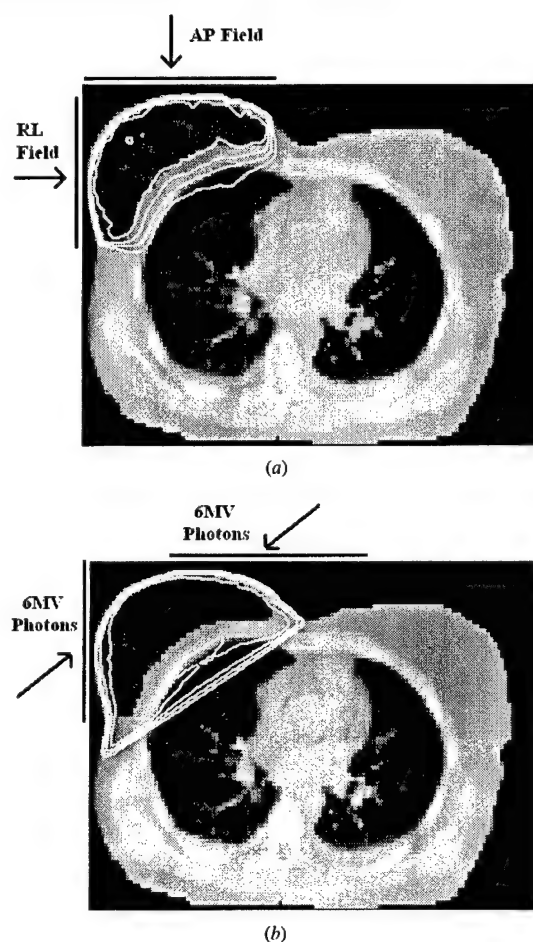


Figure 13. Isodose lines for the 2D breast plan. (a) MERT final delivery after both beamlet and segment optimization are complete. (b) A pair of tangential photon beams. Starting closest to the target and moving outwards, 48, 40, 30, 20 Gy.

(This figure is in colour only in the electronic version, see www.iop.org)

The resulting dose distribution for the MERT plan is shown in figure 13(a). A second set of isodose lines are plotted in figure 13(b) for a pair of 6 MV tangential photon beams directed onto the breast as per standard protocols. The lateral photon field utilized a 45° wedge and the relative weights of the two fields was optimized. The corresponding DVHs are shown in figure 14. The low lung dose in the MERT plan is a combination of two factors: the two-port set-up and the use of lower-energy beams for the thinner portions of the breast. Note that achieving a homogeneous dose with two electron ports necessitates intensity modulation. Note, also, that the DVH volumes are presented as percentages of this slice only, and not as a percentage of the entire lung.

This represents a case where conventional treatments are often non-optimal, as tangential photon beams often result in heterogeneous dose, scatter dose to the contralateral breast and

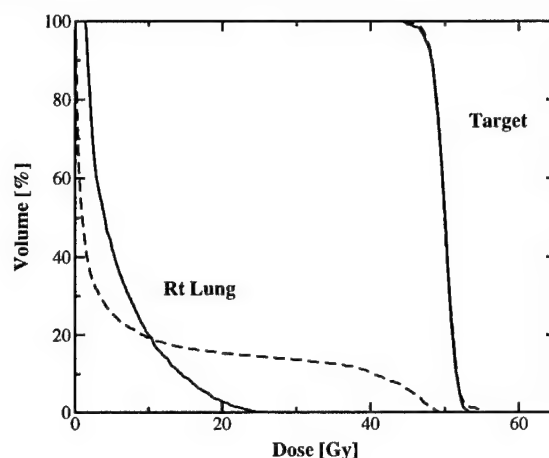


Figure 14. Cumulative DVHs for the 2D breast plan. —, simulation of final delivery plan with leaves in place and - - -, tangential 6 MV photon beams. Note that volumes actually represent area in this slice, as the plan was conducted in two dimensions.

the necessity of a large margin to compensate for breathing motion. In this case, the breathing motion was assumed to be primarily expansion in the direction normal to the tangential beams. While this two-port MERT plan is also affected by breathing motion, the effect is somewhat lessened as the beams still retain an acute angle of incidence relative to the breathing motion. In contrast, the photon plan includes a much larger region of the breast in the high-dose region, as a large margin must be included because breathing motion is in a direction largely orthogonal to the beam angles. A complete study of the impact of breathing motion on the two treatment modalities will be of significant interest, but is beyond the scope of this work. Regardless of the margin, the curvature of the chest wall and the lateral extent of the clinical target region dictate that some amount of normal tissue and lung will be included in the high-dose region.

Note that this case has been presented as a proof-of-principle for both the potential role of MERT in a clinical scenario and of the efficacy of this planning scheme. Examining the utility of MERT at different anatomical sites and a full comparison with other treatment modalities is beyond the scope of this paper.

4. Conclusions

This study has demonstrated the feasibility of MERT with a scattering foil linear accelerator. Two primary objections voiced against MERT have been that the in-air scatter is too great to have an acceptable resolution and that this scatter will hinder the optimization process. The scattering problem has been minimized by the design of the electron MLC. There is certainly an appreciable amount of air scatter, especially at the lower energies; however, it has been shown that this does not significantly affect dose distributions in the model targets. Furthermore, optimization of electron beamlets will be inherently inaccurate if poor electron transport algorithms are used to account for in-air transport. This problem has been overcome with the use of Monte Carlo transport algorithms. The beamlet dose profiles may have wide penumbras or other non-ideal characteristics, but as long as this information is incorporated into optimization, the final result will be physically correct.

While this study has employed a specific model of an electron MLC and a specific Monte Carlo dose calculation system and optimization software, it should be noted that these results can be generalized to other situations. That is, the effect of any real collimator that perturbs the delivered beam away from the idealized beamlets can be at least partially accounted for by this two-step optimization procedure. Also, any dose calculation system and optimization software may be used, provided that transport in non-patient regions such as the air gap and eMLC can be performed accurately.

With rapidly increasing Monte Carlo calculation speeds and improvements in computer hardware, it is likely that calculating MERT plans in the manner described will soon be possible on a time scale easily comparable to advanced analytical photon planning algorithms. Thus it is important to pursue additional research in MERT planning, focusing on development of three-dimensional planning techniques. Currently, three-dimensional plans may be generated using the methods presented. However, it is anticipated that the method used to organize individual leaves into a synchronous leaf sequence will have some bearing on the ability to compensate for leakage. Further research will also examine specific treatment planning considerations, such as changing the number of energy and intensity levels, as well as adding additional gantry angles or isocentres, and combining photons and electrons in a single plan.

Acknowledgments

We would like to thank our colleagues A L Boyer, G Luxton, B Shahine, T Pawlicki, T Guerrero and J Jolly for their support and helpful discussions regarding this work. We would also like to thank S Brain, B Tofighrad and T Koumrian for help with computer and software support. This work has been funded in part by grants CA78331 from the NIH, BC971292 and BC000838 from the US Department of Defense, and NIH Training Grant 5T32GM08294-11.

References

- Åsell M, Hyödynmaa S, Gustafsson A and Brahme A 1997 Optimization of 3D conformal electron beam therapy in inhomogeneous media by concomitant fluence and energy modulation *Phys. Med. Biol.* **42** 2083-100
- Åsell M, Hyödynmaa S, Söderström S and Brahme A 1999 Optimal electron and combined electron and photon therapy in the phase space of complication-free cure *Phys. Med. Biol.* **44** 235-52
- Bielajew A F 1994 Monte Carlo modelling in external-beam radiotherapy—why leave it to chance? *Proc. 11th Int. Conf. on the Use of Computers in Radiation Therapy* ed A R Hounsell, J M Wilkinson and P C Williams (Manchester: North Western Medical Physics Department, Christie Hospital NHS Trust) pp 2-5
- Bielajew A F and Rogers D W O 1987 PRESTA—the parameter reduced electron step algorithm for electron Monte Carlo transport *Nucl. Instrum. Methods B* **18** 165-81
- Bielajew A F, Rogers D W O, Cygler J and Battista J J 1987 A Comparison of electron pencil beam and Monte Carlo calculational methods *The Use of Computers in Radiation Therapy* ed I A D Bruinvis (Amsterdam: Elsevier) pp 65-8
- Bortfeld T R, Kahler D L, Waldron T J and Boyer A L 1994 X-ray field compensation with multileaf collimators *Int. J. Radiat. Oncol. Biol. Phys.* **28** 723-30
- Boyer A L and Mok E C 1985 A photon dose distribution model employing convolution calculations *Med. Phys.* **12** 169-77
- Buchanan J L and Turner P R 1992 *Numerical Methods and Analysis* (New York: McGraw-Hill)
- Chen Y, Boyer A L and Ma C-M 2000 Calculation of x-ray transmission through a multileaf collimator *Med. Phys.* **27** 1717-26
- Cygler J, Battista J J, Scrimger J W, Mah E and Antolak J 1987 Electron dose distributions in experimental phantoms: a comparison with 2D pencil beam calculations *Phys. Med. Biol.* **32** 1073-83
- Ebert M A and Hoban P W 1997 Possibilities for tailoring dose distributions through the manipulation of electron beam characteristics *Phys. Med. Biol.* **42** 2065-81
- Faddegon B A, Ross C K and Rogers D W O 1990 Forward directed bremsstrahlung of 10-30 MeV electrons incident on thick targets of Al and Pb *Med. Phys.* **17** 773-85

- Faddegon B A, Ross C K and Rogers D W O 1991 Angular distribution of bremsstrahlung from 15 MeV electrons incident on thick targets of Be, Al and Pb *Med. Phys.* **18** 727–39
- Hogstrom K R, Mills M D and Almond P R 1981 Electron beam dose calculations *Phys. Med. Biol.* **26** 445–59
- Holmes T W 2001 A method to incorporate leakage and head scatter corrections into a tomotherapy inverse treatment planning algorithm *Phys. Med. Biol.* **46** 11–27
- Hyödynmaa S, Gustafsson A and Brahme A 1996 Optimization of conformal electron beam therapy using energy- and fluence-modulated beams *Med. Phys.* **23** 659–66
- Jansson T, Lindman H, Nygård K, Dahlgren C V, Montelius A, Öberg-Kreuger C, Asplund S and Bergh J 1998 Radiotherapy of breast cancer after breast-conserving surgery: an improved technique using mixed electron-photon beams with a multileaf collimator *Radiother. Oncol.* **46** 83–9
- Jeraj R and Keall P 2000 The effect of statistical uncertainty on inverse treatment planning based on Monte Carlo dose calculation *Phys. Med. Biol.* **45** 3601–13
- Jiang S B 1998 Development of a compensator based intensity modulated radiation therapy system *PhD Thesis* Medical College of Ohio, Toledo, OH
- Jiang S B, Kapur A and Ma C-M 2000 Electron beam modelling and commissioning for Monte Carlo treatment planning *Med. Phys.* **27** 180–91
- Kapur A 1999 Monte Carlo dose calculations for clinical electron and intensity modulated photon beams in radiotherapy *PhD Thesis* Stanford University, Stanford, CA
- Kapur A, Ma C-M, Mok E C, Findley D O and Boyer A L 1998 Monte Carlo calculations of electron beam output factors for a medical linear accelerator *Phys. Med. Biol.* **43** 3479–94
- Karlsson M G, Karlsson M K and Ma C-M 1999 Treatment head design for multileaf collimated high-energy electrons *Med. Phys.* **26** 2125–32
- Karlsson M K, Karlsson M G and Zackrisson B 1998 Intensity modulation with electrons: calculations, measurements and clinical applications *Phys. Med. Biol.* **43** 1159–69
- Kawrakow I and Fippel M 2000 Investigation of variance reduction techniques for Monte Carlo photon dose calculation using XVMC *Phys. Med. Biol.* **45** 2163–83
- Kawrakow I, Fippel M and Friedrich K 1996 3D electron dose calculation using a voxel based Monte Carlo algorithm *Med. Phys.* **23** 445–57
- Keall P J, Siebers J V, Jeraj R and Mohan R 2000 The effect of dose calculation uncertainty on the evaluation of radiotherapy plans *Med. Phys.* **27** 478–84
- Klein E E, Li Z and Low D A 1996 Feasibility study of multileaf collimated electrons with a scattering foil based accelerator *Radiother. Oncol.* **41** 189–96
- Koch H W and Motz J W 1959 Bremsstrahlung cross-section formulas and related data *Rev. Mod. Phys.* **31** 920–55
- Korevaar E W, Heijmen B J M, Woudstra E, Huizenga H and Brahme A 1999 Mixing intensity modulated electron and photon beams: combining a steep dose fall-off at depth with sharp and depth-independent penumbras and flat beam profiles *Phys. Med. Biol.* **44** 2171–81
- Laub W, Alber M, Birkner M and Nüsslin F 2000 Monte Carlo dose computation for IMRT optimization *Phys. Med. Biol.* **45** 1741–54
- Lee M C, Jiang S B and Ma C-M 2000a Monte Carlo and experimental investigations of multileaf collimated electron beams for modulated electron radiotherapy *Med. Phys.* **27** 2708–18
- Lee M C, Jiang S B, Yi B and Ma C-M 2000b Monte Carlo simulations of multileaf collimated electrons *Proc. 13th Int. Conf. on the Use of Computers in Radiation Therapy* ed W Schlegel and T Bortfeld (Heidelberg: Springer) pp 176–8
- Lee M C, Kapur A, Jiang S B and Ma C-M 2000c Characterization of electron beams for modulated electron beam radiotherapy *CD-ROM Proc. of the World Congress on Medical Physics and Biomedical Engineering* (23–28 July 2000)
- Li J S, Pawlicki T, Deng J, Jiang S B and Ma C-M 2000a Simulation of Beam Modifiers for Monte Carlo Treatment Planning *Proc. 13th Int. Conf. on the Use of Computers in Radiation Therapy* ed W Schlegel and T Bortfeld (Heidelberg: Springer) pp 437–9
- Li J S, Pawlicki T, Deng J, Jiang S B, Mok E and Ma C-M 2000b Validation of a Monte Carlo dose calculation tool for radiotherapy treatment planning *Phys. Med. Biol.* **45** 2969–85
- Lief E P, Larsson A and Humm J L 1996 Electron dose profile shaping by modulation of a scanning elementary beam *Med. Phys.* **23** 33–44
- Ma C-M, Faddegon B A, Rogers D W O and Mackie T R 1997 Characterization of Monte Carlo calculated electron beams for radiotherapy *Med. Phys.* **24** 401–16
- Ma C-M, Li J S, Pawlicki T, Jiang S B and Deng J 2000a MCDOSE—A Monte Carlo dose calculation tool for radiation therapy treatment planning *Proc. 13th Int. Conf. on the Use of Computers in Radiation Therapy* ed W Schlegel and T Bortfeld (Heidelberg: Springer) pp 123–5

- Ma C-M, Mok E, Kapur A, Pawlicki T, Findley D, Brain S, Forster K and Boyer A L 1999 Clinical implementation of a Monte Carlo treatment planning system for radiotherapy *Med. Phys.* **26** 2133-43
- Ma C-M, Pawlicki T, Lee M C, Jiang S B, Li J, Deng J, Yi B, Mok E, Luxton G and Boyer A L 2000b Energy- and intensity-modulated electron beam radiotherapy for breast cancer *Phys. Med. Biol.* **45** 2947-67
- Ma C-M and Rogers D W O 1997 BEAMDP users manual *National Research Council of Canada Report PIRS-0509c* (Ottawa: NRC)
- Mackie T R *et al* 1994 The OMEGA project: comparison among EGS4 electron beam simulations, 3D Fermi-Eyges calculations, and dose measurements *Proc. 11th Int. Conf. on the Use of Computers in Radiation Therapy* ed A R Hounsell, J M Wilkinson and P C Williams (Manchester: North Western Medical Physics Department, Christie Hospital NHS Trust) pp 152-3
- Mah E, Antolak J, Scrimger J W and Pattista J J 1989 Experimental evaluation of a 2D and 3D pencil beam algorithm *Phys. Med. Biol.* **34** 1179-94
- Mohan R 1997 Why Monte Carlo? *Proc. 12th Int. Conf. on the Use of Computers in Radiation Therapy* ed D D Leavitt and G Starkschall (Madison, WI: Medical Physics Publishing) pp 16-18
- Mubata C D, Verhaegen F and Nahum A E 2000 Speeding up Monte Carlo simulation of electron cut-outs in treatment planning *Proc. 13th Int. Conf. on the Use of Computers in Radiation Therapy* ed W Schlegel and T Bortfeld (Heidelberg: Springer) pp 440-2
- Nelson W R, Hirayama H and Rogers D W O 1985 The EGS4 code system *SLAC Report 265* (Stanford, CA: Stanford Linear Accelerator Center)
- Pawlicki T A, Jiang S B, Deng J, Li J S and Ma C-M 1999 Monte Carlo calculated beamlets for photon beam inverse planning *Med. Phys.* **26** 1064-5
- Rogers D W O 1991 The role of Monte Carlo simulation of electron transport in radiation dosimetry *Int. J. Appl. Radiat. Isot.* **42** 965-74
- Rogers D W O, Faddegon B A, Ding G X and Ma C-M 1995 BEAM: a Monte Carlo code to simulate radiotherapy treatment units *Med. Phys.* **22** 503-24
- Seltzer S M and Berger M J 1985 Bremsstrahlung spectra from electron interactions with screened atomic nuclei and orbital electrons *Nucl. Instrum. Methods B* **12** 95-134
- Siochi R A C 1999 Minimizing static intensity modulate delivery time using an intensity solid paradigm *Int. J. Radiat. Oncol. Biol. Phys.* **43** 671-80
- van Santvoort J P C and Heijmen B J M 1996 Dynamic multileaf collimation without 'tongue-and-groove' underdosage effects *Phys. Med. Biol.* **41** 2091-105
- Yu C X 1998 Design considerations for the sides of multileaf collimator leaves *Phys. Med. Biol.* **43** 1335-42
- Zackrisson B and Karlsson M 1996 Matching of electron beams for conformal therapy of target volumes at moderate depths *Radiother. Oncol.* **39** 261-70

The MLC tongue-and-groove effect on IMRT dose distributions

Jun Deng¹, Todd Pawlicki, Yan Chen, Jinsheng Li, Steve B Jiang and C-M Ma

Department of Radiation Oncology, Stanford University School of Medicine, Stanford, CA 94305, USA

E-mail: jun@reyes.stanford.edu

Received 19 May 2000, in final form 9 January 2001

Abstract

We have investigated the tongue-and-groove effect on the IMRT dose distributions for a Varian MLC. We have compared the dose distributions calculated using the intensity maps with and without the tongue-and-groove effect. Our results showed that, for one intensity-modulated treatment field, the maximum tongue-and-groove effect could be up to 10% of the maximum dose in the dose distributions. For an IMRT treatment with multiple gantry angles (≥ 5), the difference between the dose distributions with and without the tongue-and-groove effect was hardly visible, less than 1.6% for the two typical clinical cases studied. After considering the patient setup errors, the dose distributions were smoothed with reduced and insignificant differences between plans with and without the tongue-and-groove effect. Therefore, for a multiple-field IMRT plan (≥ 5), the tongue-and-groove effect on the IMRT dose distributions will be generally clinically insignificant due to the smearing effect of individual fields. The tongue-and-groove effect on an IMRT plan with small number of fields (< 5) will vary depending on the number of fields in a plan (coplanar or non-coplanar), the MLC leaf sequences and the patient setup uncertainty, and may be significant ($> 5\%$ of maximum dose) in some cases, especially when the patient setup uncertainty is small (≤ 2 mm).

(Some figures in this article are in colour only in the electronic version; see www.iop.org)

1. Introduction

Intensity-modulated radiotherapy (IMRT) has generated intense and widespread interest in radiation treatment of cancers due to its many advantages over conventional radiotherapy. First of all, IMRT optimally assigns weights to individual beamlets in a photon field as opposed to a single weight to the whole photon field, which allows IMRT to produce dose distributions that are more conformal than those possible with standard 3D conformal radiotherapy (3DCRT).

¹ Addressee for correspondence.

Secondly, IMRT has the potential to be a more efficient form of treatment than the standard 3DCRT. There are no secondary field shaping devices other than the computer-controlled multi-leaf collimator (MLC).

Although the use of MLC provides the possibility of achieving better dose distributions conformed to tumour targets, there are many factors that need to be considered carefully in the use of an MLC. For example, the 'tongue-and-groove' effect may become a significant issue when underdosage occurs between two adjacent leaf pairs due to the fact that the region in between is always covered by the tongue, or the groove or both (Chui *et al* 1994, Wang *et al* 1996). Algorithms have therefore been developed to either minimize or remove this effect when MLC leaf sequences are generated (Van Santvoort and Heijmen 1996, Webb *et al* 1997, Dirx *et al* 1998, Siochi 1999). There are also some other important factors associated with the use of an MLC, which include the variation of the accelerator head scatter component in the MLC-collimated beam (Brahme 1988, Convery and Rosenbloom 1992), the amount of photon leakage through the leaves (Wang *et al* 1996, Webb 1997), and the effect of back-scattered photons from the moving jaws and MLC leaves on the monitor chamber signal (Hounsell 1998, Boyer *et al* 1998). In addition, the sequences of leaf movement and their consequential effects on the dose delivered to the patient may vary significantly depending on the accelerator and the MLC design. Therefore, in order to fully utilize the power of IMRT delivered by an MLC, we need to investigate extensively all these factors. In this work, we concentrate on the 'tongue-and-groove' effect on the IMRT dose distributions by comparing IMRT treatment plans for two typical clinical cases.

The tongue-and-groove design was introduced to reduce the inter-leaf leakage between adjacent leaves in an MLC, as shown in figure 1(a). The tongue-and-groove effect is demonstrated in figures 1(b)–(d) showing the intensity profiles after the beam travels through the MLC leaves. The intensity profile in 1(b) results when the upper shaded leaf stays in the beam and the lower shaded leaf is retracted fully. Conversely, when the upper shaded leaf is retracted fully and the lower shaded leaf is in the beam, the resultant intensity profile is shown in figure 1(c). When the two profiles are added together, the resultant intensity profile is shown in 1(d) and there is a low dose region centred between two adjacent leaves, which indicates the tongue-and-groove effect. In an IMRT treatment using an MLC, the tongue-and-groove effect will occur when the overlapping region between two adjacent pairs of leaves is covered by the tongue, or the groove or both for the most of time during beam delivery.

The tongue-and-groove effect has been considered a possible limitation of the IMRT method. As pointed out by many investigators, the tongue-and-groove effect can result in an underdose of as much as 10–15% (Galvin *et al* 1993, Chui *et al* 1994, Wang *et al* 1996). Recently, Sykes and Williams (1998) carried out an experimental investigation on the tongue-and-groove effect for the Philips multileaf collimator and found that the dose reduction of the tongue-and-groove effect recorded on radiographic film could be as much as 15–28% when adjacent leaves were studied.

Although the tongue-and-groove effect can be significantly reduced by synchronization of the leaves, the cost of synchronization is usually an increase in the total number of monitor units, and therefore longer time is needed to deliver the required dose (Van Santvoort and Heijmen 1996, Xia and Verhey 1998). So far, no Monte Carlo IMRT simulations have been performed to study the tongue-and-groove effect on the dose distributions using actual clinical cases. Whether the tongue-and-groove effect is clinically important, how important it is and under what circumstances this effect will be prominent are questions with no clear answers yet.

An EGS4 user code, MCDOSE, has been developed for radiotherapy treatment planning dose calculations (Nelson *et al* 1985, Ma *et al* 1999). MCDOSE can be used for both

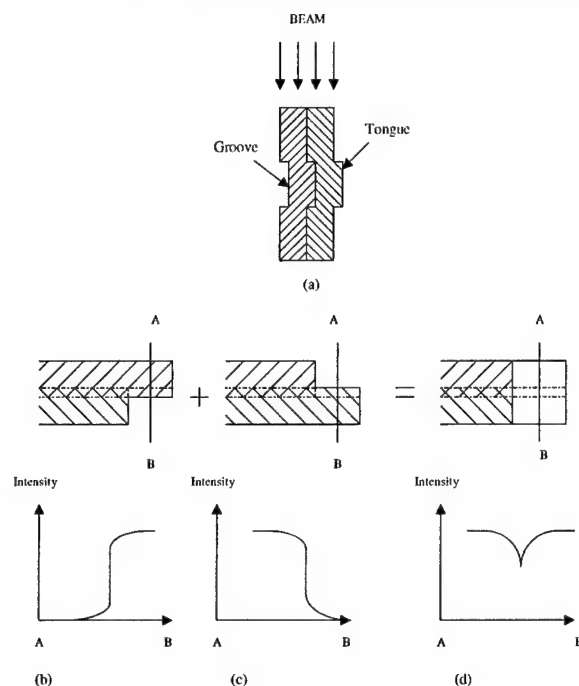


Figure 1. Schematic diagram of the tongue-and-groove effect in an MLC. (a) The design of the MLC tongue and groove is to reduce inter-leaf leakage. (b)–(d) Schematic diagrams of two fields and their superposition defined by two adjacent leaves. The region centred between two leaves in (d) is underdosed.

conventional and IMRT photon/electron beam dose calculations. In addition, separate programs have been developed to transform the MLC leaf sequence files into intensity maps by taking into account the leaf transmission properly. Therefore, the goal of this paper is to use the Monte Carlo method to investigate the tongue-and-groove effect on the IMRT dose distributions and show how significant this effect is in the clinic.

2. Materials and method

This section is organized as the following: we first describe how MCDOSE and MLC2MAP generate intensity maps without and with the tongue-and-groove effect, then the Monte Carlo dose calculation by MCDOSE that we have developed and applied in this work. Then we discuss the convolution approach to approximate the patient setup uncertainty when the final IMRT dose distributions are displayed and compared. Finally, the two clinical cases are described in detail.

2.1. MCDOSE generates intensity maps without the tongue-and-groove effect

For IMRT cases, MCDOSE used the patient's leaf-sequence files from the CORVUS planning system (NOMOS Corp., Pittsburgh, PA) to build an intensity map of each field for Monte Carlo simulation. The intensity map had a resolution of 0.1 cm at the isocentre. The monitor units

in each step of the leaf sequence were accumulated for the open beamlets in the map. The leaf transmission was accounted for by adding a fraction of the monitor units in each leaf step to the intensity map. This fraction corresponded to the average measured leaf transmission and varied with beam energy. Since there is no consideration of the geometry of the tongue and groove of an MLC in MCDOSE, the tongue-and-groove effect is not considered. During the simulation, the weight of a particle traversing the map at the MLC level was set equal to the intensity value at the position where it crossed the map. The extra-focal radiation is handled in the multiple-source model and the only physical aspect not accounted for is the scatter off the leaf ends.

2.2. MLC2MAP generates intensity maps with the tongue-and-groove effect

MLC2MAP was originally developed by Chen *et al* (2000) for beam delivery verification and Monte Carlo dose calculations for IMRT. MLC2MAP utilized a raytracing-based method to calculate the x-ray transmission through a multileaf collimator. The path-length of a rayline in the MLC is accurately calculated using the exact geometry of the MLC leaves. The calculation has been verified and is in good agreement with measurements using both film and a Wellhöfer beam imaging system (Wellhöfer Dosimetrie, Schwarzenbruck, Germany). The intensity distribution generated by MLC2MAP will be used by MCDOSE for forward dose calculation. Our approach of calculating doses using the intensity distributions generated by MLC2MAP is accurate enough to yield some important results, although it is not as accurate as simulating the electron and photon transport through the MLC leaves via the Monte Carlo method, which takes a much longer time.

2.3. Monte Carlo dose calculations by MCDOSE

MCDOSE is an EGS4 user code developed for radiation therapy treatment planning dose calculations. It can be used to simulate the transport of photons and electrons in a patient geometry built from CT data. Realistic clinical accelerator beams can be used for any combinations of gantry angles, couch angles, collimator rotations, source-skin distances and beam modifiers. It can be used to compute dose distributions for conventional treatment with photon and electron beams, beamlet distributions for inverse treatment planning and the final dose distributions for intensity modulated radiotherapy using the multileaf collimator leaf sequences generated by a treatment planning optimization system.

For patient dose calculations, the simulation phantom was built from the patient's CT data with up to $128 \times 128 \times 128$ voxels (uniform in any dimension). The side of a voxel varied from 0.2 to 0.4 cm. A separate program was developed to convert the patient's CT data from the FOCUS treatment planning system (Computerized Medical Systems, St Louis, MO) to required dimensions, material types and densities. The organ contours were also obtained for dose calculation and dose-volume histogram analysis.

In MCDOSE, a multiple-source model was developed and used to recover the phase space of a photon beam for Monte Carlo simulation (Ma 1998, Deng *et al* 2000). The source model approach was adopted as a convenient method to handle the huge photon beam phase space files created by a full BEAM simulation and also provided an infinite number of incident particles for patient-specific simulation.

All the Monte Carlo simulation parameters, such as the electron and photon energy cutoffs (ECUT and PCUT), the low energy thresholds for δ -ray and bremsstrahlung production (AE and AP), the maximum fractional energy loss per electron step (ESTEPE) and the parameters required by PRESTA (Bielajew and Rogers 1987), have been specified in the MCDOSE input file. For all the simulations in this work, the energy cutoffs were $ECUT = AE = 700$ keV

and PCUT = AP = 10 keV. ESTEPE was set to 0.1 and the default parameters were used for the PRESTA algorithm.

Absolute doses were determined by simulating a calibration measurement. For each photon beam energy, the maximum dose on the central axis was calculated for a 10 cm × 10 cm calibration field. For any arbitrary field size, the dose per monitor unit was obtained as the ratio of the dose for this field to the dose for the 10 cm × 10 cm calibration field. Monte Carlo calculated IMRT treatment plans were ultimately converted to the absolute dose based on the monitor units for all the fields used. It has been demonstrated that for a 1 σ statistical uncertainty of less than 2%, there is no significant uncertainty in Monte Carlo dose-volume information due to the statistical concerns in the Monte Carlo results (Jiang *et al* 2000, Keall *et al* 2000). In this work, our Monte Carlo doses were calculated with a statistical uncertainty of about 1% in the mean target dose.

2.4. Convolution approach to approximate the patient setup uncertainty

During the course of an IMRT treatment, patient setup errors are inevitable. The overall effect is equivalent to blurring the original IMRT dose distributions with a setup error distribution. As reported by Schewe *et al* (1996), setup errors were observed to be primarily random, with standard deviations of 5–6 mm for each of three translational motions. They have treated 49 patients in the abdomen, chest and pelvic regions over the course of 20 months, and have determined the setup errors using a curve-matching graphical interface to compare digitized port films to digitized simulation films. However, in order to prevent the choice of large setup uncertainty from smearing out the optimized intensity modulations, we have used a Gaussian of a sigma of 2 mm instead of 5 mm to be convolved with the original IMRT dose distributions to simulate the effect of patient setup errors.

2.5. Study of two clinical cases

In this paper, we present a comparison of IMRT dose distributions of two patients with and without the tongue-and-groove effect. One case is a prostate cancer treated by IMRT with eight gantry angles delivered by a 80-leaf MLC, while the other is a vertebra cancer treated by IMRT with nine gantry angles delivered by a 52-leaf MLC. Dose-volume histograms (DVHs) are also compared for the two cases.

Multiple-source models were used to model the 4 MV photon beam from a Varian Clinac 2100C and 15 MV photon beam from a Varian Clinac 2300C/D accelerator (Varian Medical Systems, Palo Alto, CA). Beam modifiers such as jaws, physical and dynamic wedges are simulated in MCDOSE together with a 3D rectilinear patient geometry model built from patient CT data. The 2300C/D is equipped with an 80-leaf MLC and the 2100C is equipped with a 52-leaf MLC.

In order to study the tongue-and-groove effect, we start with an eight-field IMRT prostate treatment plan. The plan has been optimized by the CORVUS inverse planning system and the leaf sequence files for the eight fields have been generated by CORVUS with the tongue-and-groove effect present.

Starting with the same eight-field leaf sequence files generated by CORVUS, we generated two prostate plans. For plan 1, we run MCDOSE to read in these eight-field leaf sequence files and produce the accumulated intensity maps one by one without considering the tongue-and-groove effect.

In comparison, for plan 2, we first use a separate program MLC2MAP to convert each of the same eight-field leaf sequence files to a transmission intensity map with the tongue-and-groove

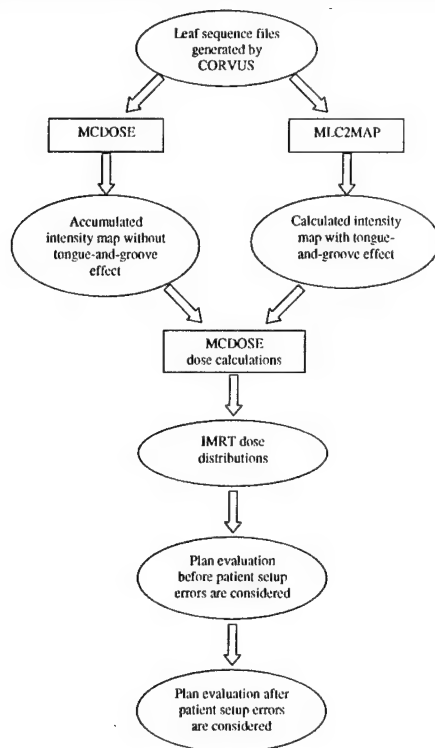


Figure 2. Illustration of procedures in the study of the MLC tongue-and-groove effect on the IMRT dose distributions.

effect incorporated. Then we use these calculated intensity maps to replace the original intensity maps generated by MCDOSE in plan 1. The rest of the Monte Carlo dose calculation process is identical for the two plans. Finally, the two plans are evaluated to demonstrate the tongue-and-groove effect on the dose distributions in this prostate case. The two plans were further evaluated with the consideration of the patient setup errors, that is, both dose distributions were convolved with a Gaussian distribution with a sigma of 2 mm. The whole procedures are illustrated in figure 2.

3. Results and discussion

3.1. Single-field comparison

Before we proceed to perform the dose calculations of the two plans, we have performed a comparison between plans 1 and 2 using just one of the eight fields. Dose calculations were performed in a uniform water phantom of 17 cm × 17 cm × 17 cm with voxel size of 1 mm × 1 mm × 1 mm.

Shown in figure 3(a) is an accumulated intensity map of one of the eight fields of the prostate plan. Each square is 1 cm × 1 cm in the isocentre plane, with darker grids representing higher intensity. It is generated by MCDOSE from reading in the corresponding

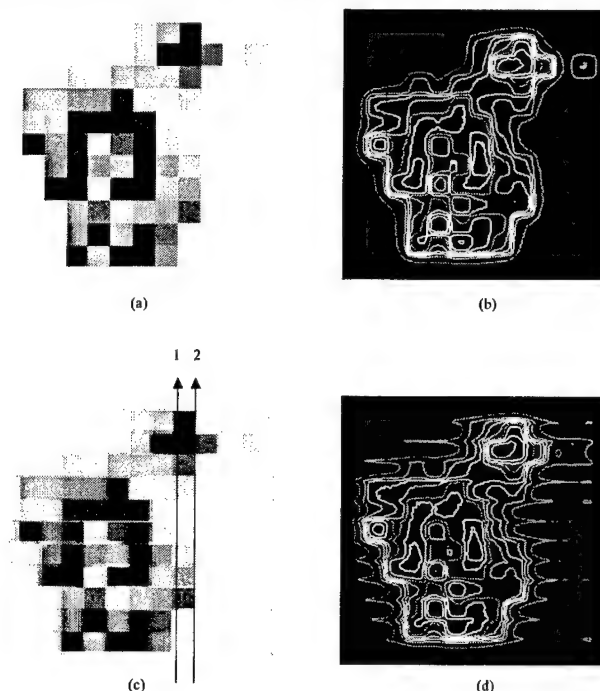


Figure 3. (a) An accumulated intensity map for one field of an IMRT plan by MCDOSE. The tongue-and-groove effect has not been considered. (b) The corresponding Monte Carlo dose calculations by MCDOSE. (c) A calculated intensity map for the same field by MLC2MAP. The tongue-and-groove effect has been considered. (d) The corresponding Monte Carlo dose calculations by MCDOSE. The arrows 1 and 2 are for figures 4 and 5.

leaf sequence file and ignoring the tongue-and-groove effect. For comparison, the Monte Carlo dose calculation in a water phantom by MCDOSE is shown in figure 3(b). The doses were scored at 2.95 cm depth in water.

Shown in figure 3(c) is a calculated intensity map of the same field. It is obtained by using MLC2MAP, which properly accounts for the geometry of MLC leaves, the physical path of the photons and the photon transmission property through the tungsten leaves. Its corresponding Monte Carlo dose calculation results at depth of 2.95 cm in water are shown in figure 3(d). As we can see, figure 3(a) is sharp while figure 3(c) is fuzzy with lighter strips between dark squares and darker strips between light squares along the leaf movement direction. This is due to the fact that MCDOSE reads in leaf sequence files without considering the tongue-and-groove design of the MLC while MLC2MAP has considered the tongue-and-groove design of the Varian MLC in an appropriate way to generate figure 3(c). Shown in figures 3(b) and (d) are 5%, 10%, 20%, 30%, 40%, 50%, 60%, 70%, 80% and 90% isodose lines respectively.

Although both dose distributions in figures 3(b) and 3(d) reflect the intensity maps of figures 3(a) and 3(c) quite well, there are some differences. One of the differences comes from the observation that the high dose lines (80% and up) in figure 3(d) usually lie within the corresponding isodose lines in figure 3(b) while the low dose lines in figure 3(d) usually extend outside corresponding isodose lines in figure 3(b).

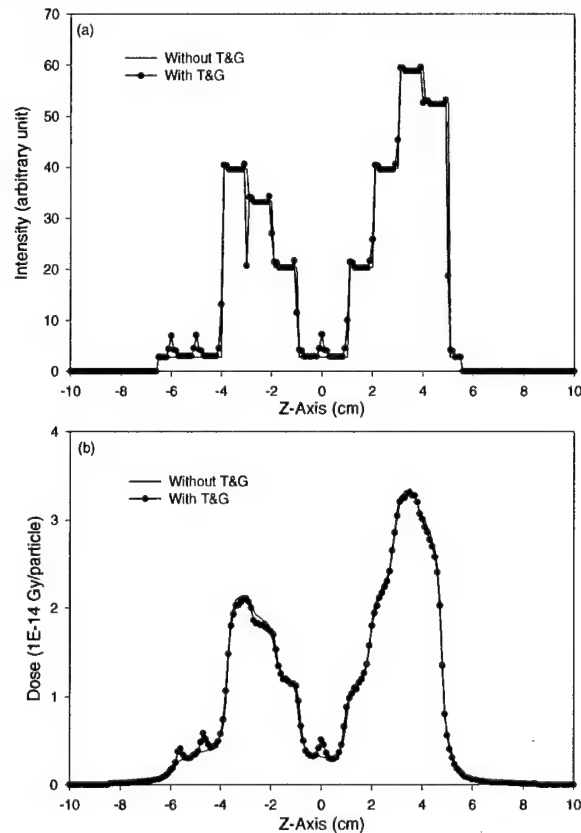


Figure 4. (a) The intensity profile comparison along arrow 1 between the same field as in figure 3 with and without the tongue-and-groove effect. (b) The corresponding Monte Carlo dose calculation comparison in water by MCDOSE.

Another difference lies in the dose distributions around the field edge along the direction of leaf movement. In figure 3(b), since there is no tongue-and-groove effect incorporated, the low dose lines around the field edges are smooth and clean. But in figure 3(d), the low dose lines are zigzagged on both sides, and the pattern is coincident with the intensity distributions on the edge of the intensity map shown in figure 3(c). The appearance of zigzagged isodose lines in figure 3(d) are most apparent for the three outermost lines (5%, 10% and 20%): the rest of the isodose lines are basically the same shape as those in figure 3(b). Also, from the gradient between the two adjacent isodose lines, we can determine that the wiggling caused by the tongue-and-groove design in the dose distributions is about 4%.

In figures 4 and 5, we have shown the dose and intensity comparison with and without the tongue-and-groove effect considered at two locations. One was along arrow 1, while the other was along arrow 2, as depicted in figure 3(c). As demonstrated clearly in figures 4(a) and 5(a), without considering the tongue-and-groove effect, the intensity profiles are steplike. If we consider the tongue-and-groove effect, at high intensity area where the tongue-and-groove effect occurs, the intensity profile will be lower than that without the tongue-and-groove effect,

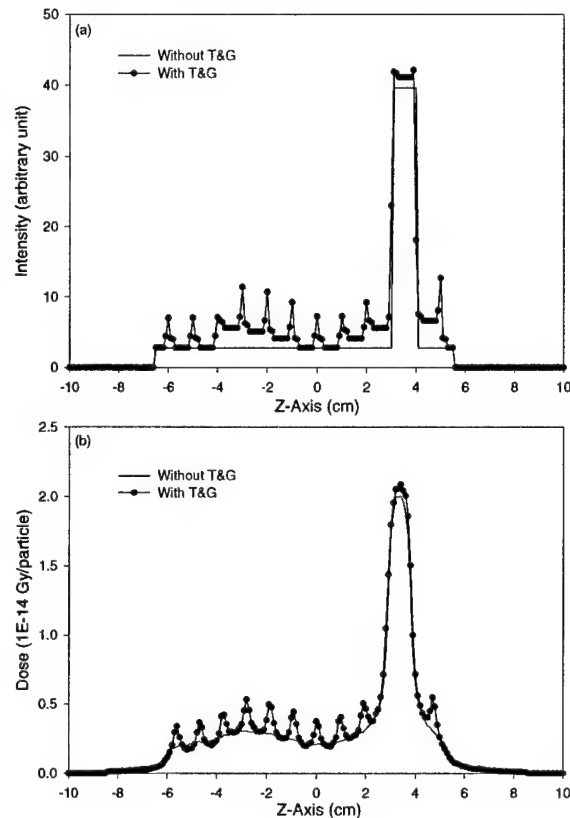


Figure 5. (a) The intensity profile comparison along arrow 2 between the same field as in figure 3 with and without the tongue-and-groove effect. (b) The corresponding Monte Carlo dose calculation comparison in water by MCDOSE.

and at low intensity area, the intensity profile will be higher with peaks located right between two leaves. But at some high intensity areas where there is no tongue-and-groove effect, the intensity profile generated by MLC2MAP will be slightly higher than that generated by MCDOSE due to the enhanced leakage from the rounded leaf ends of the Varian MLC, which is accounted for in MLC2MAP. The dose comparisons in a water phantom at two locations are also shown in figures 4(b) and 5(b). From the figures 4(b) and 5(b), we can see the tendency very clearly, that is, on one hand, at the low intensity area, due to the tongue-and-groove design, the intensity is larger, and therefore the doses are higher as shown by the peaks in figure 5(b). On average, the dose increment due to the tongue-and-groove design in the low intensity area is about 4.5% of the maximum dose in the projected tongue-and-groove region over 1 mm voxels, as determined from figure 5(b). On the other hand, when the tongue-and-groove underdosage occurs at the high intensity region, the corresponding doses are lower than those without the tongue-and-groove effect. As determined from figure 4(b), the tongue-and-groove effect can cause about 3.2% underdosage in the projected tongue-and-groove region over 1 mm voxels.

Also, it is worth noting that in figures 4 and 5 the dose profiles shown in figures 4(b) and 5(b) are scored at a plane in water with source-to-plane distance of 94.45 cm due to the

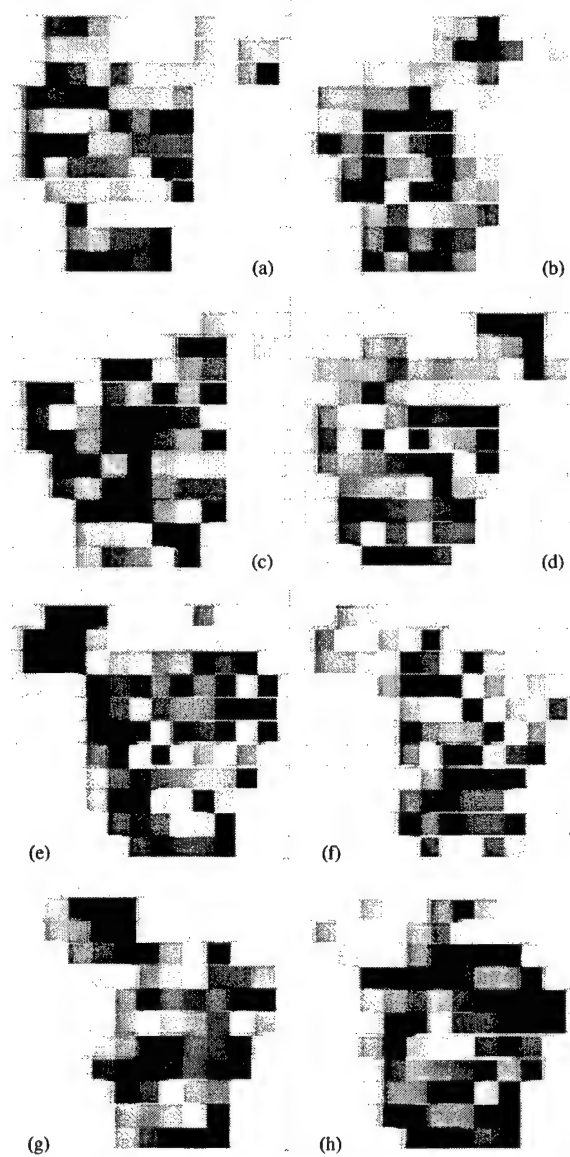


Figure 6. The calculated intensity maps by MLC2MAP for all the eight fields of the prostate plan. The IMRT plan is generated by CORVUS with the tongue-and-groove effect present in the leaf sequences. The gantry angles are (a) 45° , (b) 85° , (c) 115° , (d) 145° , (e) 215° , (f) 245° , (g) 275° and (h) 315° .

phantom design, while the intensity profiles shown in figures 4(a) and 5(a) are projected from the MLC plane to 100 cm. Therefore, the dose profiles are squeezed compared to the intensity profiles with the scale down ratio of 94.45/100.

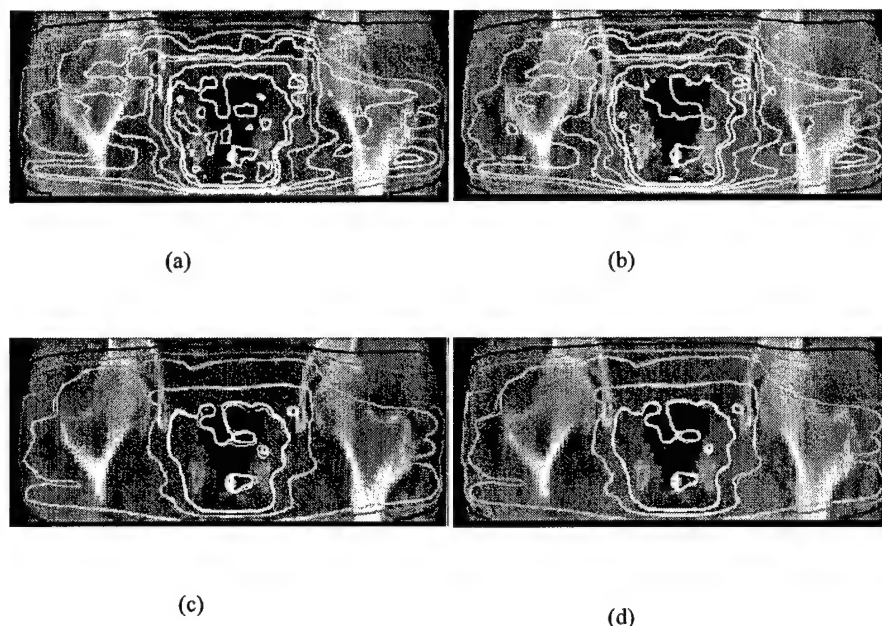


Figure 7. XZ view of IMRT dose distributions. (a) An IMRT prostate plan without the tongue-and-groove effect before blurring. (b) The same plan with the tongue-and-groove effect considered before blurring. From the outermost to innermost, the isodose lines are 5%, 10%, 20%, 30%, 40%, 50%, 60%, 70%, 80% and 90%, respectively. (c) After blurring the two IMRT prostate plans are superposed and compared. The thick lines are for plan 1 without the tongue-and-groove effect while the thin lines are for plan 2 with the tongue-and-groove effect. Only 5%, 10%, 20%, 50% and 80% isodose lines are displayed for clarity. (d) Identical to (c) except that the doses for plan 2 have been renormalized so that the DVHs for plan 1 and 2 agreed.

For the prostate case, the patient was treated by IMRT with eight gantry angles: 45, 85, 115, 145, 215, 245, 275 and 315 degrees. The collimator angle is 180 degrees for all eight fields. Shown in figure 3(c) is just one of the eight gantry angles. In figure 6, we show the calculated intensity map of all the eight fields. All the intensity maps have been confirmed by exposing the film using a 15 MV photon beam. As we can see, although the tongue-and-groove effect appeared in multiple locations in each field, these locations did not coincide spatially in the same plane for all the fields. Even if the tongue-and-groove effect appeared in the same locations for all the fields, the overall tongue-and-groove effect of this IMRT plan should be equal to or smaller than the largest effect seen in one single field. Therefore, the overall tongue-and-groove effect of an IMRT plan is no greater than the largest effect in one single field.

It has been shown from figures 3 to 6 that, if only one field (for the case investigated) is engaged in an IMRT treatment delivered by an MLC, the final dose distributions can differ by as much as 3.2% depending on whether or not the tongue-and-groove effect is considered, indicating that the tongue-and-groove effect cannot be neglected and must be considered carefully in the use of MLC. In the case of multiple fields, the tongue-and-groove effect on the dose distributions is discussed in the following for two clinical cases.

3.2. An eight-field IMRT treatment plan for prostate cancer

We then use MCDOSE to calculate the dose distributions of an eight-field prostate case using two different intensity maps, as illustrated in figure 2. The voxel sizes of the patient CT phantom are $2.8 \text{ mm} \times 1.6 \text{ mm} \times 3.0 \text{ mm}$. Figures 7(a) and (b) show the XZ view of the IMRT dose distribution comparison between plan 1 in 7(a) (without the tongue-and-groove effect) and plan 2 in 7(b) (with the tongue-and-groove effect) before considering patient setup errors. The isodose lines shown in figures 7(a) and (b) are 5%, 10%, 20%, 30%, 40%, 50%, 60%, 70%, 80% and 90%, respectively. There are some minor differences between the two distributions around the target, but the tongue-and-groove effect is not clearly and prominently present in the dose distributions in 7(b). We have also found that in general, the high dose contours (80% and up) cover a slightly larger area in figure 7(a) than in figure 7(b). This is due to the tongue-and-groove effect, which lowers the dose to the region where the effect occurs and causes less volume to receive the same high dose.

As mentioned above, incorporating patient setup errors can be approximated by blurring the dose distributions with a setup error distribution (a Gaussian distribution with a sigma equal to 2 mm has been used here). After we blurred the distributions in figures 7(a) and (b), we put the two dose distributions together in figure 7(c) and only compared 5%, 10%, 20%, 50% and 80% isodose lines for clarity. Figure 7(d) is identical to 7(c) except that the dose distributions for plan 2 have been renormalized so that the DVHs for plan 2 in figure 10 have been shifted horizontally by 1.6% to agree with the DVHs for plan 1. In figures 7(c) and (d), the thick lines are for plan 1 without the tongue-and-groove effect while the thin lines are for plan 2 with the tongue-and-groove effect. As shown in figures 7(a)–(d), the discrepancies seen in figures 7(a) and (b) between plan 1 and plan 2 have been reduced in figure 7(c) to about 1.6%.

We have also found similar observations from the XY and YZ views of the same IMRT dose distribution comparison as shown in figures 8 and 9. Figures 8(a), 8(b), 9(a) and 9(b) all have the same isodose line format as that in figures 7(a) and 7(b). Figure 8(d) is identical to 8(c) and figure 9(d) is identical to 9(c) except that the dose distributions for plan 2 have been renormalized so that the DVHs for plan 2 in figure 10 have been shifted horizontally by 1.6% to agree with the DVHs for plan 1. Being consistent with figures 7(c) and (d), in figures 8(c), 8(d), 9(c) and 9(d), the thick lines are for plan 1 without the tongue-and-groove effect while the thin lines are for plan 2 with the tongue-and-groove effect.

In addition, we have found three major characteristics common to figures 7–9. First, thin dose lines are usually on the outer side of thick dose lines in the low dose region, meaning that the doses for plan 2 (with the tongue-and-groove effect) are slightly larger than doses for plan 1 (without the tongue-and-groove effect) in the low dose region. Secondly, in the high dose regions such as around the target, thin dose lines are usually on the inner side of thick dose lines, indicating that the dose distributions for plan 2 covers a smaller area than dose distributions for plan 1 in high dose regions. Thirdly, the two dose distributions agreed slightly better in figures 7(d), 8(d) and 9(d) than those in figures 7(c), 8(c) and 9(c), which has been consistent with the DVHs in figure 10. Therefore, after the patient setup errors are considered during the IMRT treatment, the tongue-and-groove effect can cause minor differences (1.6% shift) in DVHs and the differences in the final dose distributions (about 1.6% underdosage around the target) are insignificant.

The cause of the reduced discrepancies in figures 7 to 9 between plans 1 and 2 is the smearing effect of the IMRT treatment plan. The more treatment fields there are, the less chance that the tongue-and-groove effect will show up at the same location in the final dose distributions. We can understand the whole problem as this: although there may be an underdose in each individual field for an IMRT treatment, since the underdose regions do not always coincide with each other for all the treatment fields, especially when we take

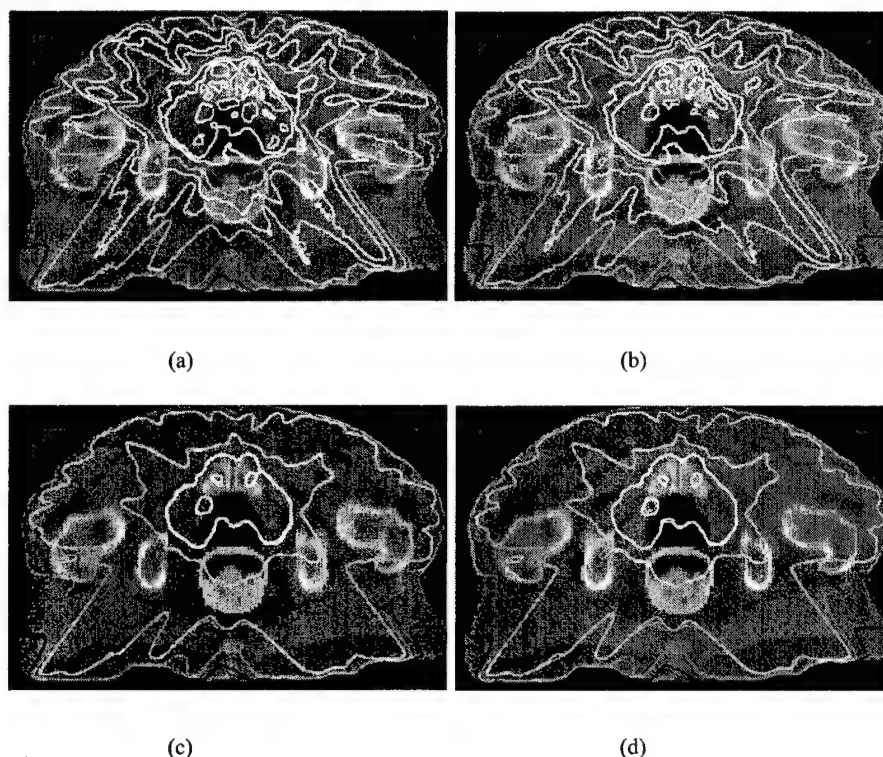


Figure 8. XY view of IMRT dose distributions. (a) An IMRT prostate plan without the tongue-and-groove effect before blurring. (b) The same plan with the tongue-and-groove effect considered before blurring. From the outermost to the innermost, the isodose lines are 5%, 10%, 20%, 30%, 40%, 50%, 60%, 70%, 80% and 90%, respectively. (c) After blurring the two IMRT prostate plans are superposed and compared. The thick lines are for plan 1 without the tongue-and-groove effect while the thin lines are for plan 2 with the tongue-and-groove effect. Only 5%, 10%, 20%, 50% and 80% isodose lines are displayed for clarity. (d) Identical to (c) except that the doses for plan 2 have been renormalized so that the DVHs for plan 1 and 2 agreed.

the patient setup errors into account, the dose distributions in those underdose regions are smeared around the neighbouring regions, and the final overall dose distributions will show no significant tongue-and-groove effect.

The cumulative dose-volume histograms (DVHs) are plotted in figure 10, showing the comparison between plan 1 without the tongue-and-groove effect considered and plan 2 with the tongue-and-groove effect considered. Different lines are used to represent the DVHs of different organs exposed to the radiation during the whole IMRT treatment for plan 1, such as prostate, seminal vesicle, lymph node etc. For comparison, different lines and symbols are used to represent the DVHs of corresponding organs for plan 2. As shown, for all the six organs studied, there are no significant differences between plan 1 and plan 2 for lymph node, skin and rectum. The bladder in plan 2 received low dose for a slightly larger area and high dose for a slightly smaller area. For the seminal vesicle and prostate, that are exposed to high doses, the tongue-and-groove effect causes the underdose to some areas in those two organs, and therefore the DVHs are always slightly shifted toward lower doses by 1.6%.

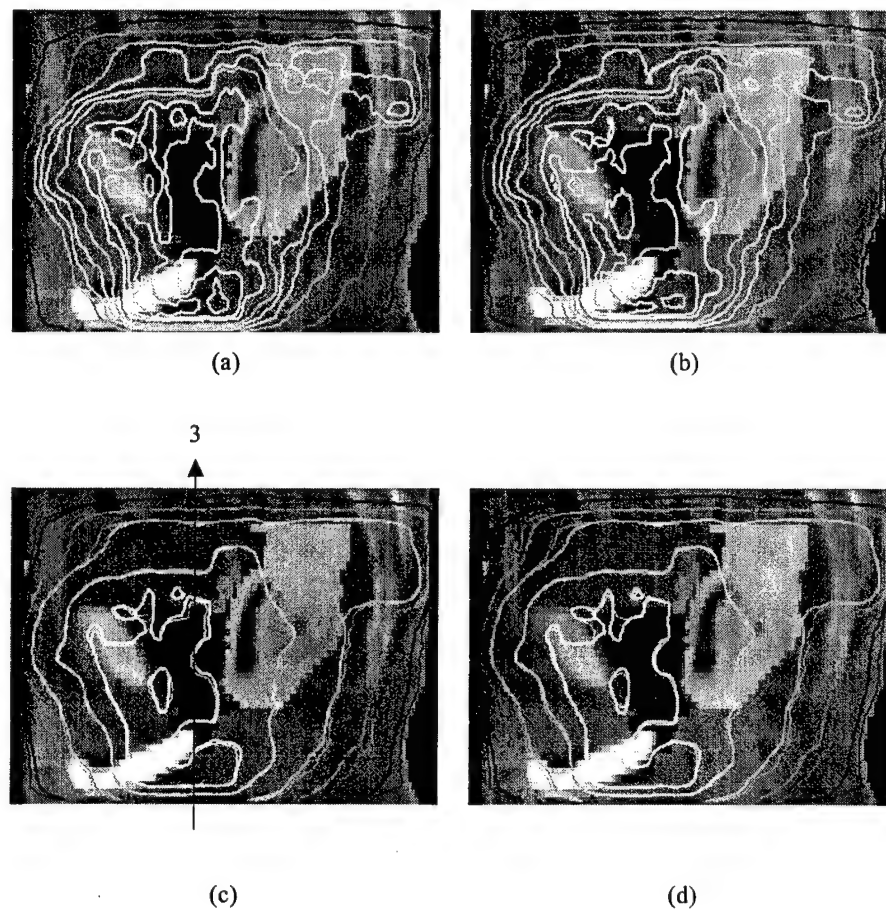


Figure 9. YZ view of IMRT dose distributions. (a) An IMRT prostate plan without the tongue-and-groove effect before blurring. (b) The same plan with the tongue-and-groove effect considered before blurring. From the outermost to innermost, the isodose lines are 5%, 10%, 20%, 30%, 40%, 50%, 60%, 70%, 80% and 90%, respectively. (c) After blurring the two IMRT prostate plans are superposed and compared. The thick lines are for plan 1 without the tongue-and-groove effect while the thin lines are for plan 2 with the tongue-and-groove effect. Only 5%, 10%, 20%, 50% and 80% isodose lines are displayed for clarity. (d) Identical to (c) except that the doses for plan 2 have been renormalized so that the DVHs for plan 1 and 2 agreed. The arrow 3 is for figure 11.

In order to explore the dose profiles in actual clinical cases treated by IMRT as compared to the dose profiles shown in figures 4(b) and 5(b) for a single field, we have compared the dose profiles between the plan without the tongue-and-groove effect and the plan with the tongue-and-groove effect in figure 11. Shown in figure 11(a) is the dose profile comparison along arrow 3 as illustrated in figure 9(c). The location is chosen so that the dose profile will go through the target and be as close to the centre of the target as possible. As we can see, the doses for the plan with the tongue-and-groove effect are generally smaller around the target, but equal to or larger than the doses for the plan without the tongue-and-groove effect around the field edges. If we increase the doses for the plan with the tongue-and-groove effect by 1.6%, we will obtain

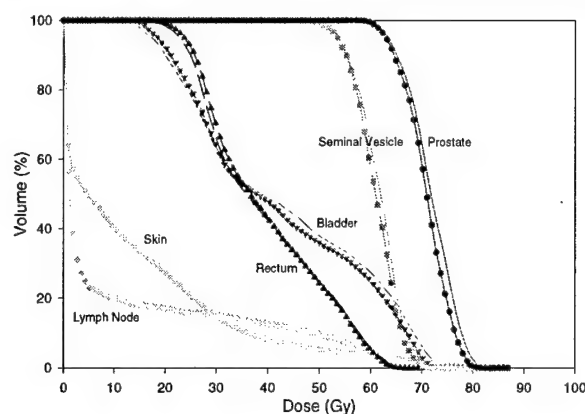


Figure 10. The cumulative dose-volume histogram comparison between (a) an IMRT prostate plan without the tongue-and-groove effect represented by lines and (b) the same plan with the tongue-and-groove effect represented by lines and symbols.

a better agreement between the dose profiles for the two plans as shown in figure 11(b). This 1.6% shift has been consistent with the observations in the DVH results shown in figure 10.

3.3. A nine-field IMRT treatment plan for vertebra cancer

We have also calculated the dose distributions of a nine-field vertebra case using the same method. The voxel sizes of the patient CT phantom are $3.7 \text{ mm} \times 1.8 \text{ mm} \times 4.0 \text{ mm}$. Figures 12(a) and (b) show the XY view of the IMRT dose distribution comparison before blurring between plan 1 in 12(a) (without the tongue-and-groove effect) and plan 2 in 12(b) (with the tongue-and-groove effect). The isodose lines shown here are 5%, 10%, 20%, 30%, 40%, 50%, 60%, 70%, 80% and 90%, respectively. There are very little differences between the two distributions, and the tongue-and-groove effect is not clearly present in the dose distributions in 12(b). After we blurred the distributions in figures 12(a) and (b), we have put the two dose distributions together in figure 12(c) and only compared 5%, 10%, 20%, 50% and 80% isodose lines for clarity. Figure 12(d) is identical to 12(c) except that the dose distributions for plan 2 have been renormalized so that the DVHs for plan 2 in figure 13 have been shifted horizontally by 1.0% to agree with the DVHs for plan 1. In figures 12(c) and (d), the thick lines are for plan 1 without the tongue-and-groove effect while the thin lines are for plan 2 with the tongue-and-groove effect. After we consider the patient setup errors, the dose distributions in 12(c) and (d) are very similar, yet the dose distributions of two plans agreed slightly better in 12(d) than in 12(c).

The DVH plot, as shown in figure 13, also demonstrated that for all the five organs studied, there are no significant differences between plan 1 and plan 2. The largest difference seen in DVHs comes from the DVHs for GTV, with 1% lower doses for plan 2 than for plan 1. If we increase the doses for plan 2 by 1%, we will obtain a very good agreement between the two plans.

3.4. The number of fields in an IMRT treatment plan

Although we have studied two actual clinical cases treated by IMRT with multiple fields (≥ 5) to investigate the tongue-and-groove effect, it is still unknown whether the tongue-and-groove effect is significant when small number of fields (< 5) are used in an IMRT treatment plan.

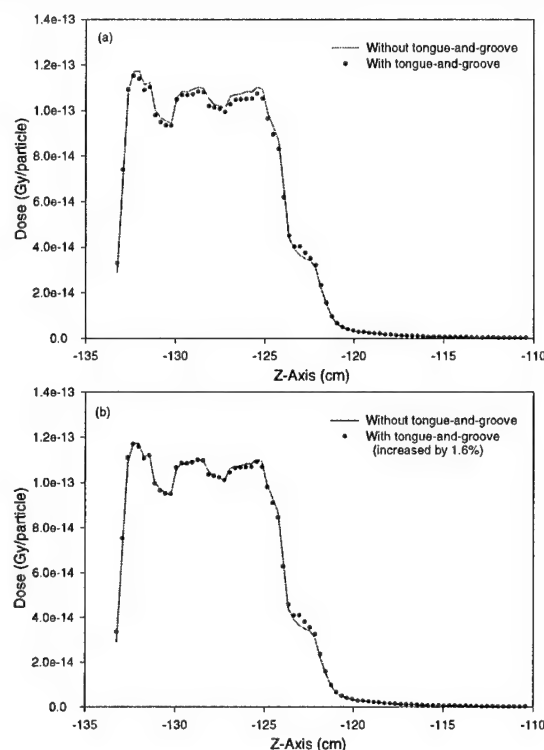


Figure 11. (a) The Monte Carlo dose calculation comparison in a patient by MCDOSE along arrow 3 between the two prostate plans with and without the tongue-and-groove effect. (b) The doses for the plan with the tongue-and-groove effect are increased by 1.6% to agree with the doses for the plan without the tongue-and-groove effect. This is consistent with our observation in figure 10 where the DVHs for the plan with the tongue-and-groove effect need to be shifted horizontally by 1.6% to match with the DVHs for the plan without the tongue-and-groove effect.

There have been reports on the usage of fewer IMRT fields for prostate cancer (Mohan *et al* 2000, Zelefsky *et al* 2000). In order to obtain an optimized treatment plan, the IMRT plan often consists of five non-coplanar fields, e.g., one anterior (or posterior), two lateral and two anterior (or posterior) oblique. Although we anticipate the tongue-and-groove effect will be more prominent in an IMRT plan with small number of fields, it is virtually impossible to tell how significant the tongue-and-groove effect will be in all IMRT plans from a case-by-case basis. However, we can apply the Monte Carlo method to study the maximum difference we expect to encounter in the clinic when the tongue-and-groove effect is maximum present in an IMRT plan with small number of fields.

Therefore, we have carried out a conceptual study (figure 14). We first performed Monte Carlo simulations on the tongue-and-groove effect for a simple MLC configuration as depicted in figure 1, where for the first 100 monitor units we exposed even numbered leaves and retracted odd numbered leaves, while for the second 100 monitor units we exposed odd numbered leaves and retracted even numbered leaves. The dose calculations have been performed using MCDOSE in a uniform rectilinear water phantom. With this configuration, we observed the dose profiles similar to figure 1(d) with 10% underdosage in the leaf gap regions for 1 mm

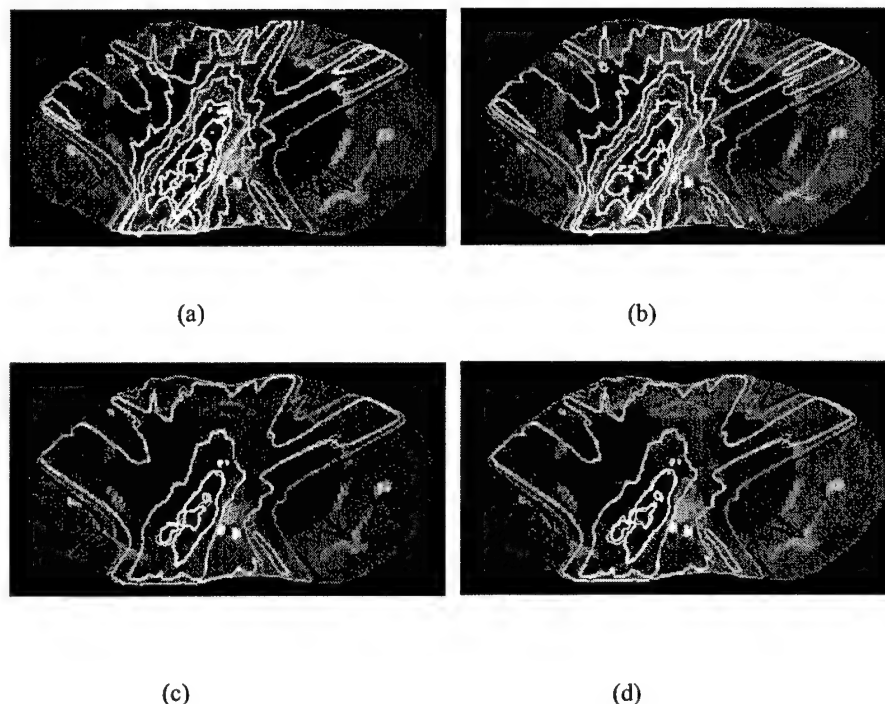


Figure 12. XY view of IMRT dose distributions. (a) An IMRT vertebra plan without the tongue-and-groove effect before blurring. (b) The same plan with the tongue-and-groove effect considered before blurring. From the outermost to innermost, the isodose lines are 5%, 10%, 20%, 30%, 40%, 50%, 60%, 70%, 80% and 90%, respectively. (c) After blurring the two IMRT vertebra plans are superposed and compared. The thick lines are for plan 1 without the tongue-and-groove effect while the thin lines are for plan 2 with the tongue-and-groove effect. Only 5%, 10%, 20%, 50% and 80% isodose lines are displayed for clarity. (d) is identical to (c) except that the doses for plan 2 have been renormalized so that the DVHs for plan 1 and 2 agreed.

voxels, as shown in figure 15(a). Therefore, as shown very clearly in figure 15(a), the maximum underdosage due to the tongue-and-groove effect is 10% of the maximum dose when the dose is scored in $1\text{ mm} \times 1\text{ mm} \times 1\text{ mm}$ voxels. It also shows that, due to different MLC leaf sequences, the tongue-and-groove effect will vary from 3.2% in our previous calculation using one of the eight fields of an IMRT prostate plan to 10% in the current case (the worst case).

We then created a hypothetical four-field coplanar IMRT treatment plan where the gantry angles are 0, 90, 180 and 270 degrees respectively and the leaf sequence is identical for the four fields as in the single-field case. In so doing, we would expect the maximum tongue-and-groove effect for the following two reasons: first, the tongue-and-groove underdosage occurs in all the leaf gap regions; second, due to the fact that it is a coplanar plan, the tongue-and-groove effect from the four fields will coincide with each other in the same plane, making the worst underdosage. The dose calculations have been performed using MCDOSE in a water phantom of $10\text{ cm} \times 10\text{ cm} \times 10\text{ cm}$ with $1\text{ mm} \times 1\text{ mm} \times 1\text{ mm}$ voxel size. As determined from the Monte Carlo dose calculations and shown in figure 15(b), the tongue-and-groove effect has caused an underdosage of 6.5% of the maximum dose in the leaf gap regions.

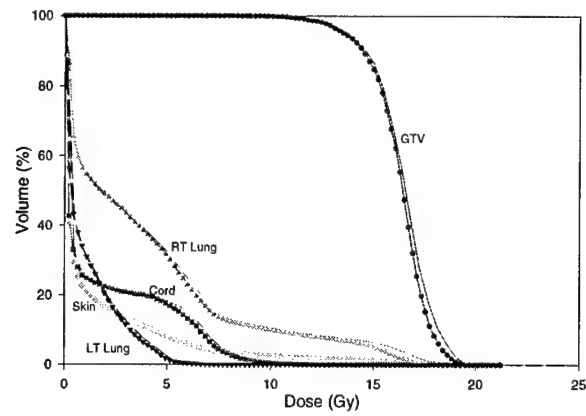


Figure 13. The cumulative dose-volume histogram comparison between (a) an IMRT vertebra plan without the tongue-and-groove effect represented by lines and (b) the same plan with the tongue-and-groove effect represented by lines and symbols.

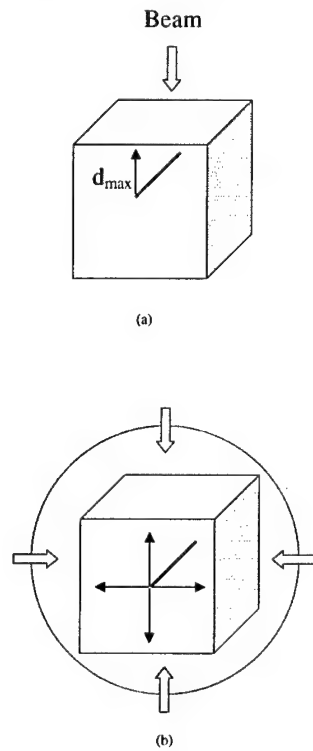


Figure 14. Conceptual studies on the dependence of the MLC tongue-and-groove effect on the number of fields in an IMRT plan for (a) an IMRT plan with only one field and (b) an IMRT plan with four fields. The water phantom is uniform in three directions with $1\text{ mm} \times 1\text{ mm} \times 1\text{ mm}$ voxels. The centre of the water phantom is at the isocentre. The z-axis shown in (a) is at depth of d_{max} while it is at the centre in (b); they are for figure 15.

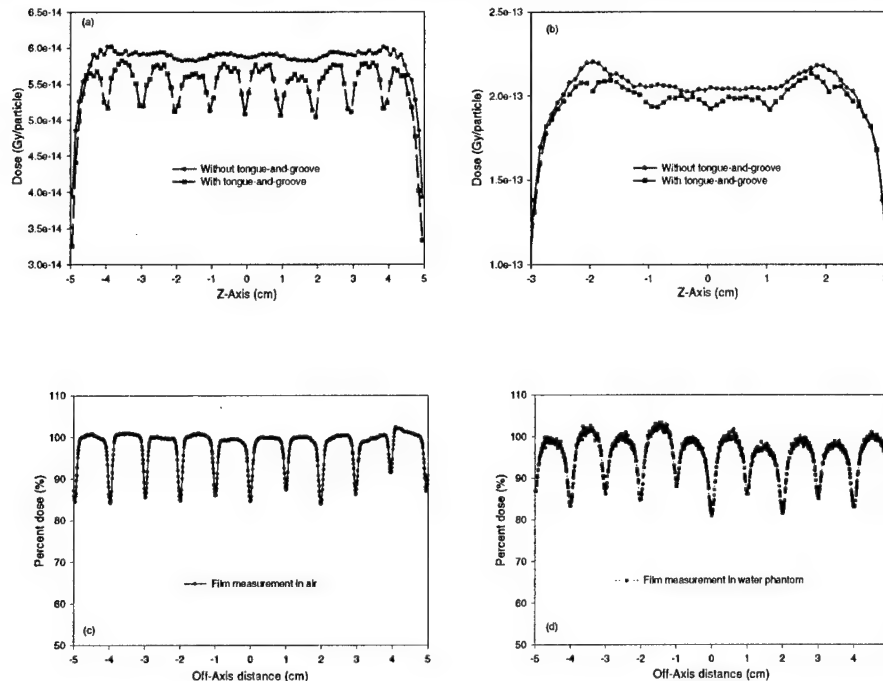


Figure 15. The Monte Carlo dose calculation comparison along the z-axis in the water phantom between the plans with and without the tongue-and-groove effect. (a) An IMRT plan with a single field; (b) an IMRT plan with four fields. Film measurements corresponding to the leaf sequences in (a) for a 15 MV photon beam are shown in (c) with the film in air and in (d) with the film at 3 cm depth in a solid water phantom. The source-to-surface distances are 100 cm for both film measurements.

Since the MLC configuration being investigated corresponded to the worst situation, we can therefore argue that in an IMRT plan with only one field the underdosage caused by the tongue-and-groove effect will not exceed 10% of the maximum dose. For an IMRT plan with four fields, the maximum underdosage due to the tongue-and-groove effect is about 6.5% of the maximum dose. However, in real clinical cases, the tongue-and-groove underdosage does not occur everywhere along the leaf gap regions, and does not coincide with each other in the same plane from different fields. For non-coplanar plans, the tongue-and-groove effect will be smaller than that for coplanar plans. Furthermore, when the patient setup uncertainty (± 2 to 5 mm) is considered, the tongue-and-groove underdosage will be much reduced.

We have also made film measurements in air and a solid water phantom for the case of single field IMRT using 6 and 15 MV photon beams to study the tongue-and-groove effect. Shown in figure 15(c) is the relative dose profile across the MLC leaves in air while figure 15(d) shows the relative dose profile in a solid water phantom for the 15 MV beam. As shown clearly, the tongue-and-groove effect is prominent in both film measurements with roughly 10–15% underdosage in the tongue-and-groove regions, but the tongue-and-groove underdosage in figure 15(d) is a little smaller and the dose profile is more rounded with wider dips than those in figure 15(c). This is due to electron transport in the film and solid water so that the resultant dose profile recorded in the film is blurred (corresponding to the electron fluence profile in solid

water); in air, with electron transport only in the film, the dose profile is sharper (corresponding to the photon fluence profile in air). This explains why a large tongue-and-groove effect (more than 10%) has been reported in the in-air film measurements while a smaller tongue-and-groove underdosage (about 10%) has been observed in the in-water dose calculations. The results for the 6 MV photon beam are more significant than those of the 15 MV photon beam.

It is interesting to compare the two approaches when dealing with the tongue-and-groove effect. On one hand, one can apply the leaf synchronization algorithm to reduce the tongue-and-groove effect when generating the leaf sequences. However, there are several disadvantages with this technique. Van Santvoort and Heijmen (1996) have reported that for all the intensity-modulated beams they studied, the observed increase in treatment time was typically 5% to 15% due to the leaf synchronization algorithm. Xia and Verhey (1998) have also pointed out that in order to reduce the tongue-and-groove effect 20% to 35% more segments were needed when generating MLC leaf sequences. So, the increase in treatment time will be 5% to 35% depending on the leaf sequencing algorithms used. Secondly, longer treatment time means larger leakage through the MLC leaves. For some short IMRT treatment courses this 2% average leakage through the leaves is not a problem, but for some long IMRT treatment courses the increased leakage must be considered in the synchronization algorithm. However, when it comes to the situation where the desired dose is less than the increased leakage through the leaves due to synchronization, then this leakage cannot be accounted for by the leaf synchronization algorithm. Thirdly, due to the accuracy of MLC leaf end positioning, synchronized leaf sequences may result in some underdose and overdose regions along the direction perpendicular to the leaf movement, which imposes another problem for using leaf synchronization.

On the other hand, our studies have shown that the tongue-and-groove effect on the IMRT dose distributions is not significant when multiple fields (≥ 5) are engaged. For a single field, the tongue-and-groove effect can cause 3.2% to 10% underdosage in the leaf gap regions depending on the MLC leaf sequences. However, due to the smearing effect of a multiple field IMRT, the tongue-and-groove effect has been observed to be 1.6% underdosage around the prostate and seminal vesicle for the prostate case, and 1% underdosage around GTV for the vertebra case. The DVHs for the plan with the tongue-and-groove effect can be shifted horizontally by 1.6% for the prostate case and 1% for the vertebra case and match very well with the DVHs for the plan without the tongue-and-groove effect.

Therefore, on one hand, for a multiple-field IMRT plan (≥ 5), our studies have suggested that instead of reducing the tongue-and-groove effect via leaf synchronization, we can compensate for the effect by assigning a slightly higher dose to the target, say 1–2%, though it is probably clinically insignificant. By doing this, we avoid the disadvantages of leaf synchronization and the final dose distributions and DVHs are almost identical to those without the tongue-and-groove effect.

On the other hand, for an IMRT plan with small number of fields (< 5), the tongue-and-groove effect on the IMRT dose distributions may or may not be clinically significant depending on whether the plan is coplanar or non-coplanar, and whether the tongue-and-groove underdosage is present everywhere along the leaf gap regions. It also depends on whether the tongue-and-groove underdosages coincide with each other in the same plane, and how much the patient setup uncertainty is. Therefore, the tongue-and-groove effect should be considered carefully when a small number of fields (< 5) are used in an IMRT plan.

4. Conclusions

We have investigated the tongue-and-groove effect on the IMRT dose distributions. We have compared the dose distributions calculated using the intensity maps with and without the

tongue-and-groove effect. Our results show that, if only one treatment field is engaged, the maximum tongue-and-groove effect can be up to 10% of the maximum dose in the final dose distributions. For a multiple-field IMRT case, the overall effect should be less than that in a single field. Due to the fact that the tongue-and-groove effect does not always occur in the same plane for a multiple-field IMRT case, the overall tongue-and-groove effect should be much smaller (less than 1.6% for the two typical clinical cases studied). After considering the patient setup errors, the tongue-and-groove effect was further reduced. Therefore, for a multiple-field IMRT plan (≥ 5), the tongue-and-groove effect on the IMRT dose distributions will be generally clinically insignificant due to the smearing effect of individual fields. The tongue-and-groove effect on an IMRT plan with a small number of fields (< 5) will vary depending on the number of fields in a plan (coplanar or non-coplanar), the MLC leaf sequences and the patient setup uncertainty, and may be significant ($> 5\%$ of maximum dose) in some cases, especially when the patient setup uncertainty is small (≤ 2 mm).

Acknowledgments

We would like to thank Sam Brain, Todd Koumrian and Michael Luxton for computer hardware and software support. This work was supported in part by a grant from the Department of Defense US Army Breast Cancer Research Program BC971292, a National Institute of Health (NIH) grant CA78331 and a consortium agreement with the NumeriX, LLC.

References

- Bielajew A F and Rogers D W O 1987 PRESTA: the parameter reduced electron-step transport algorithm for electron Monte Carlo transport *Nucl. Instrum. Methods B* **18** 165–81
- Boyer A L, Xing L, Ma L and Forster K 1998 Verification and delivery of head and neck intensity modulated radiotherapy [abstract] *Med. Phys.* **25** A200–A201
- Brahme A 1988 Optimal setting of multileaf collimators in stationary beam radiation therapy *Strahlenther. Onkol.* **164** 343–50
- Chen Y, Boyer A L and Ma C-M 2000 Calculation of x-ray transmission through a multileaf collimator *Med. Phys.* **27** 1717–26
- Chui C S, LoSasso T and Spirou S 1994 Dose calculations for photon beams with intensity modulation generated by dynamic jaw or multileaf collimators *Med. Phys.* **21** 1237–43
- Convery D J and Rosenbloom M E 1992 The generation of intensity-modulated fields for conformal radiotherapy by dynamic collimation *Phys. Med. Biol.* **37** 1359–74
- Deng J, Jiang S B, Kapur A, Li J, Pawlicki T and Ma C-M 2000 Photon beam characterization and modeling for Monte Carlo treatment planning *Phys. Med. Biol.* **45** 411–27
- Dirkx M L P, Heijmen B J M and van Santvoort J P C 1998 Leaf trajectory calculation for dynamic multileaf collimation to realize optimized fluence profiles *Phys. Med. Biol.* **43** 1171–84
- Galvin J M, Smith A R and Lally B 1993 Characterization of a multi-leaf collimator system *Int. J. Radiat. Oncol. Biol. Phys.* **25** 181–92
- Hounsell A R 1998 Monitor chamber backscatter for intensity modulated radiation therapy using multileaf collimators *Phys. Med. Biol.* **43** 445–54
- Jiang S B, Pawlicki T and Ma C-M 2000 Removing the effect of statistical uncertainty on dose–volume histograms from Monte Carlo dose calculations *Phys. Med. Biol.* **45** 2151–61
- Keall P J, Siebers J V, Jeraj R and Mohan R 2000 The effect of dose calculation uncertainty on the evaluation of radiotherapy plans *Med. Phys.* **27** 478–84
- Ma C-M 1998 Characterization of computer simulated radiotherapy beams for Monte Carlo treatment planning *Radiat. Phys. Chem.* **53** 329–44
- Ma C-M, Pawlicki T, Li J, Jiang S, Deng J, Kapur A, Mok E, Luxton G and Boyer A L 1999 MCDose—a dose calculation tool for radiotherapy treatment planning [abstract] *Med. Phys.* **26** 1148
- Mohan D S, Kupelian P A and Willoughby T R 2000 Short-course intensity-modulated radiotherapy for localized prostate cancer with daily transabdominal ultrasound localization of the prostate gland *Int. J. Radiat. Oncol. Biol. Phys.* **46** 575–80

- Nelson R, Hirayama H and Rogers D W O 1985 The EGS4 code system *Stanford Linear Accelerator Center Report SLAC-265*
- Schewe J E, Balter J M, Lam K L and Ten Haken R K 1996 Measurement of patient setup errors using port films and a computer-aided graphical alignment tool *Med. Dosim.* **21** 97–104
- Siochi RAC 1999 Minimizing static intensity modulation delivery time using an intensity solid paradigm *Int. J. Radiat. Oncol. Biol. Phys.* **43** 671–80
- Sykes J R and Williams P C 1998 An experimental investigation of the tongue and groove effect for the Philips multileaf collimator *Phys. Med. Biol.* **43** 3157–65
- Van Santvoort J P C and Heijmen B J M 1996 Dynamic multileaf collimator without tongue-and-groove underdosage effects *Phys. Med. Biol.* **41** 2091–105
- Wang X, Spirou S, LoSasso T, Stein J, Chui C and Mohan R 1996 Dosimetric verification of intensity modulated fields *Med. Phys.* **23** 317–28
- Webb S 1997 *The Physics of Conformal Radiotherapy: Advances in Technology* (Bristol: Institute of Physics Publishing)
- Webb S, Bortfeld T, Stein J and Convery D 1997 The effect of stair-step leaf transmission on the 'tongue-and-groove problem' in dynamic radiotherapy with a multileaf collimator *Phys. Med. Biol.* **42** 595–602
- Xia P and Verhey L 1998 Multileaf collimator leaf sequencing algorithm for intensity modulated beams with multiple static segments *Med. Phys.* **25** 1424–34
- Zelevsky M J, Fuks Z, Happersett L, Lee H J, Ling C C, Burman C M, Hunt M, Wolfe T, Venkatraman E S, Jackson A, Skwarchuk M and Leibel SA 2000 Clinical experience with intensity modulated radiation therapy (IMRT) in prostate cancer *Radiother. Oncol.* **55** 241–9

Derivation of electron and photon energy spectra from electron beam central axis depth dose curves

Jun Deng, Steve B Jiang, Todd Pawlicki, Jinsheng Li and C-M Ma

Department of Radiation Oncology, Stanford University School of Medicine, Stanford, CA 94305, USA

E-mail: jun@reyes.stanford.edu

Received 9 October 2000, in final form 21 February 2001

Abstract

A method for deriving the electron and photon energy spectra from electron beam central axis percentage depth dose (PDD) curves has been investigated. The PDD curves of 6, 12 and 20 MeV electron beams obtained from the Monte Carlo full phase space simulations of the Varian linear accelerator treatment head have been used to test the method. We have employed a 'random creep' algorithm to determine the energy spectra of electrons and photons in a clinical electron beam. The fitted electron and photon energy spectra have been compared with the corresponding spectra obtained from the Monte Carlo full phase space simulations. Our fitted energy spectra are in good agreement with the Monte Carlo simulated spectra in terms of peak location, peak width, amplitude and smoothness of the spectrum. In addition, the derived depth dose curves of head-generated photons agree well in both shape and amplitude with those calculated using the full phase space data. The central axis depth dose curves and dose profiles at various depths have been compared using an automated electron beam commissioning procedure. The comparison has demonstrated that our method is capable of deriving the energy spectra for the Varian accelerator electron beams investigated. We have implemented this method in the electron beam commissioning procedure for Monte Carlo electron beam dose calculations.

1. Introduction

The Monte Carlo dose calculation algorithm has received more attention for electron beam dose calculation (Jenkins *et al* 1988, Mackie 1990, Rogers and Bielajew 1990, Rogers 1991, Andreo 1991, Ma *et al* 1999a) than the pencil beam algorithm, which has been implemented in several commercial treatment planning systems currently available for radiotherapy treatment planning (Hogstrom *et al* 1981). Due to the inappropriate electron transport in inhomogeneous phantoms, the dose distributions calculated using the pencil beam algorithm may deviate significantly (10% or more) from the measurements or the Monte Carlo simulations in some

clinical cases, where air cavities and bone are present (Cygler *et al* 1987, Mah *et al* 1989, Ma *et al* 1999a). In contrast, the Monte Carlo method can handle multiple electron scattering in the presence of inhomogeneities much more accurately than any existing analytical dose models. In particular, with the development of computer technology and variance reduction techniques, the Monte Carlo method is becoming an accurate and practical approach in the clinic for electron as well as photon dose calculations.

In order to perform dose calculations using the Monte Carlo method, large phase space files are needed to record the particles coming out of the accelerator treatment head. However, it is neither efficient to generate these huge phase space data files of hundreds of megabytes nor convenient to store or access them. The necessity of generating one phase space file for every beam energy (for photon beams) or applicator (for electron beams) of a linear accelerator treatment head makes this approach even more impractical in the clinic. Therefore, we have developed multiple source models to accurately reconstruct the phase space data while keeping the storage requirement low (Ma *et al* 1997, Jiang *et al* 2000, Deng *et al* 2000). For Varian accelerator electron beams, it is found that a multiple-source model consisting of an electron point source, a photon point source and two square ring electron sources is accurate enough to reconstruct the phase space data from the linear accelerator treatment head (Jiang *et al* 2000). As the Monte Carlo dose calculation method is becoming available for clinical application, it is therefore our primary concern to derive the multiple-source model parameters from a 'standard' set of measurement data rather than from Monte Carlo simulated phase space data. The former can be easily measured in the clinic and is often available for commissioning treatment planning systems while the latter cannot be obtained without significant investment in software, hardware and training for Monte Carlo simulations.

The electron energy spectrum is an important component of any dose calculation code used for electron beam radiotherapy. As demonstrated by Ma *et al* (1997), the electron energy spectrum has a dominant effect on the central axis depth dose curves. When the beam passes through the treatment head and undergoes some discrete energy-loss events such as bremsstrahlung and δ -ray production, the sharp peak of the electron energy spectrum is broadened. The resultant electron energy spectrum is a broadened peak located at the most probable energy E_p with a low-energy tail. The photon energy spectrum in a clinical electron beam will be similar to that in a clinical photon beam with a dominant low-energy component and a smoothly descending distribution up to the maximum energy of electrons in the beam, but somewhat softer since there is no beam hardening effect caused by the flattening filter.

Great efforts have been made to study and derive the electron and photon energy spectra in clinical electron beams. Jiang *et al* (2000) used a hybrid approach to tune the Monte Carlo calculated energy spectra of electrons and photons in clinical electron beams according to the R_{50} (the depth of 50% of maximum dose) variation between the measured central axis PDD and the Monte Carlo simulated central axis PDD. Faddegon and Blevis (2000) used a public domain code FERDO to unfold the electron energy spectra from the measured depth dose distributions with the photon background subtracted. Their approach yielded smooth but wide spectra with an average resolution of $16 \pm 3\%$ of the mean peak energy for the 27 beams studied. Luo and Jette (1999) studied a regularization method to determine an effective energy spectrum for electrons in clinical electron beams from PDD data. Deasy and Almond (1994) carried out Monte Carlo simulations to study the spectral dependence of electron central axis depth dose curves and found that the energy spread has only a small effect on the shape of the central axis depth dose curve.

In this work, a multiple source model has been created based on our previous study (Jiang *et al* 2000). A 'random creep' algorithm has been developed to derive the energy spectra of electrons and photons from clinical electron beams. The precalculated monoenergetic electron

and photon central axis PDD data are obtained from the Monte Carlo simulations. The photon depth dose contributions are determined first and subtracted before applying the random creep algorithm to derive the energy spectra for electrons and photons. The derived spectra were compared with the spectra obtained from the Monte Carlo full phase space simulations to assess our method. Comparison has also been made for the head-generated photon depth dose distributions between the full phase space simulations and calculation results obtained with our multiple-source model. The central axis depth dose curves and dose profiles at different depths for 6, 12 and 20 MeV electron beams have been compared as a result of our beam commissioning procedure.

2. Materials and method

In this work we have used a four-source model to reconstruct the beam phase space. The source model includes an electron point source, a photon point source and two square ring electron sources. All the four sources have been specified in a source parameter file, which contains a numerical description of the source type, the source position, the charge of the source, the relative source intensity, the energy distributions and the fluence distributions for each source. We have developed an automated electron beam commissioning procedure to facilitate the generation of source parameter files from a set of standard measurement data for a clinical linear accelerator. The resulting source parameter files can be used to perform the Monte Carlo dose calculations using the code MCDOSE (see descriptions below).

2.1. Photon depth dose curves in clinical electron beams

There are two types of contributions to the photon doses in a clinical electron beam. One is from the photons generated in the treatment head of a linear accelerator when the electrons interact with the beam scattering devices and the beam defining system. The other is from the photons generated in the phantom when the electrons travel through and interact with the phantom material. Figure 1 shows the total depth dose distribution and the corresponding photon dose contribution of a 20 MeV electron beam in a water phantom. As we can see, the total photon doses $D_{x,\text{total}}$ (short dashed curve) consist of head-generated photon doses $D_{x,h}$ (full curve) and phantom-generated photon doses $D_{x,p}$ (dotted curve).

Many investigations have been carried out for various electron beam energies and applicator sizes to study the contribution of the photon dose to the final central axis depth doses (Rustgi and Rodgers 1987, Klevenhagen 1994, Sorcini *et al* 1995, 1996, 1997). In general, the phantom-generated photon doses are negligible while the head-generated photon doses dominate the total photon dose contributions for beam energies less than 18 MeV in water (Rustgi and Rodgers 1987). However, as the beam energy and atomic number of phantom materials increase, the phantom-generated photon doses will increase and may no longer be ignored (Sorcini *et al* 1996). In addition, the head-generated photon depth dose distributions in clinical electron beams have been found to be very similar to the photon depth dose distributions in clinical x-ray beams, with characteristics such as a buildup region near the surface and a broad maximum followed by a region of exponential attenuation with depth.

Our Monte Carlo studies have shown that for each combination of electron beam energy and applicator size, the depth dose curve of the photons in the electron beam follows a similar shape, which can be expressed by a biexponential function given by Brahme and Svensson (1979)

$$D(z) = D_c(e^{-\mu_p z} - v e^{-\mu_r z}) \quad (1)$$

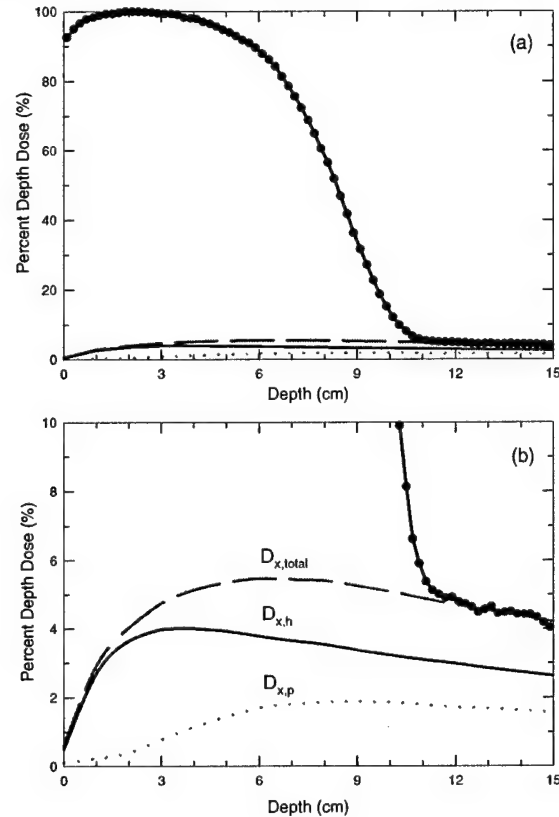


Figure 1. The total central axis depth dose distribution of a 20 MeV electron beam in a water phantom (a) and the corresponding photon dose distributions (b). The total photon dose distribution $D_{x,\text{total}}$ (dashed curve) consists of head-generated photon dose distribution $D_{x,h}$ (full curve) and phantom-generated photon dose distribution $D_{x,p}$ (dotted curve).

where D_c is a normalization constant, μ_p is the mean attenuation coefficient of primary and high-energy scattered photons, μ_e is the mean attenuation coefficient of the secondary electrons and low-energy secondary photons and $1 - \nu$ is a factor related to the surface dose. Although both head-generated and phantom-generated photon dose distributions can be expressed in forms of equation (1), we are more interested in the head-generated photon doses due to the fact that the head-generated photon dose distributions are needed in order to determine the electron and photon energy spectra in our method. Therefore, our goal is to determine the four parameters in equation (1) so as to represent the portion of the head-generated photon doses in the central axis PDD curves in clinical electron beams.

We utilized an iterative process to determine the parameters in equation (1). First, for each combination of electron beam energy and applicator size, we have initialized the values of μ_p , μ_e and ν while leaving D_c as a variable. The initial values of μ_p , μ_e and ν have been obtained from our Monte Carlo full phase space simulations. Then, we figure out the head-generated photon doses in the photon tail according to the ratios of head-generated photon doses to the

total photon doses in the tail. Since the total central axis depth doses at a depth of 1–2 cm beyond the practical range of the electrons can be attributed to the pure photon contributions, which contain both the head-generated and the phantom-generated photon contributions, we can use the Monte Carlo full phase space simulations to determine these ratios. Finally, by fitting the least chi-square between the results calculated by equation (1) and the determined head-generated photon doses from the measurement at depths, D_c can be determined iteratively until the best match has been achieved. The whole distribution of the head-generated photon depth doses is thus determined when all the parameters of equation (1) are known. The determined photon background will then be subtracted from the total central axis depth dose distribution. The subtracted central axis depth dose distribution will serve as a basis to start the random creep process to determine the electron energy spectrum.

2.2. Monte Carlo simulations of monoenergetic depth dose curves

Before we proceed to fit the subtracted central axis depth dose distribution, we perform Monte Carlo simulations of 100 monoenergetic electron beams and 100 monoenergetic photon beams. The electron beam energy range is from 0.0 to 25.0 MeV with an interval of 0.25 MeV. The electron energy is set in such a way that it represents the average value of the whole energy bin. For example, 24.875 MeV is used to represent the energy bin with an energy between 24.750 and 25.000 MeV. For all the monoenergetic electron beam simulations, we employ an electron point source located 90 cm above the phantom surface with a square collimation to define the field size. Since different applicator sizes will have different effects on the central axis PDD due to electron scattering in air and in water, we have performed Monte Carlo simulations with field sizes from 6 cm \times 6 cm to 20 cm \times 20 cm defined at the phantom surface. In figure 2(a), we show monoenergetic central axis PDDs for two field sizes, 6 cm \times 6 cm and 15 cm \times 15 cm. The energies for the five groups of data in figure 2(a) are 4.875, 9.875, 14.875, 19.875 and 24.875 MeV respectively. As shown clearly, for higher electron energies (above 10 MeV), the central axis PDD for the 6 cm \times 6 cm collimation is shifted toward a shallower depth than for the 15 cm \times 15 cm collimation. This is caused by a lack of electron lateral equilibrium. Based on our results, we found that the 15 cm \times 15 cm collimation is adequate to cover the 15 cm \times 15 cm, 20 cm \times 20 cm and 25 cm \times 25 cm applicators while for 6 cm \times 6 cm and 10 cm \times 10 cm applicators, separate monoenergetic beam data are needed with corresponding collimation for the Varian accelerator beams investigated in this work.

Likewise, we have performed Monte Carlo simulations of 100 monoenergetic photon beams. The photon beam energy is up to 25.0 MeV with an interval of 0.25 MeV. The energy is set in the same way as it is for the monoenergetic electron beams. For all the monoenergetic photon beam simulations, we use a photon point source located at 100 cm above the phantom surface with different field sizes. Since the photon central axis depth dose distribution is not sensitive to the field size, we only use one set of monoenergetic photon beam simulations with 6 cm \times 6 cm collimation. This has been illustrated in figure 2(b) where there are essentially no differences for the central axis depth dose distributions of 4.875 MeV and 19.875 MeV photon beams between the 6 cm \times 6 cm collimation and the 15 cm \times 15 cm collimation. All the Monte Carlo calculations for the 100 monoenergetic electron beams and for the 100 monoenergetic photon beams have a statistical uncertainty (1σ) less than 0.5%.

2.3. Random creep algorithm

The random creep algorithm is an iterative optimization process used to determine a best set of weighting factors of monoenergetic electron and photon energy bins. Figure 3 is a schematic

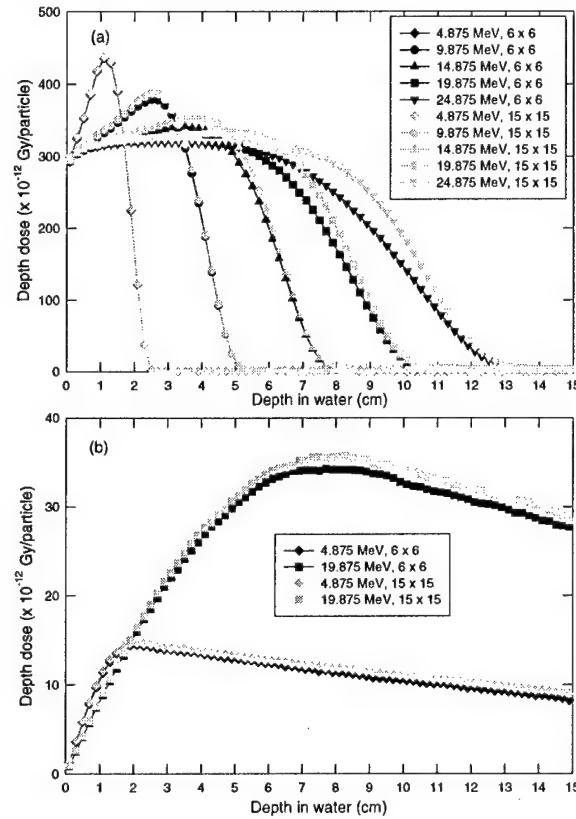


Figure 2. The monoenergetic beam central axis depth dose comparison between the $6 \text{ cm} \times 6 \text{ cm}$ collimation and $15 \text{ cm} \times 15 \text{ cm}$ collimation for (a) electron beams of 4.875, 9.875, 14.875, 19.875 and 24.875 MeV and (b) photon beams of 4.875 and 19.875 MeV. The black symbols and curves are for $6 \text{ cm} \times 6 \text{ cm}$ collimation while the grey symbols and curves are for $15 \text{ cm} \times 15 \text{ cm}$ collimation.

flow-chart demonstrating how it works. It starts with the initialization. The goal of the initialization process is to obtain a reasonably good guess of the relative weighting factors of individual energy bins according to the R_{50} of the measured central axis PDD curve. Then the algorithm initiates an iterative search process to fit the measured central axis PDDs using the precalculated monoenergetic central axis PDDs from Monte Carlo simulations. Within each iteration, a certain energy bin is randomly chosen and its relative weight is either increased or decreased by a small amount called the 'creep constant'. The objective function for the optimization process is the correlation coefficient between the measured PDD curve and the calculated PDD curves based on the fitted spectrum. The correlation coefficient is computed using the following formula:

$$\text{correlation coefficient} = \frac{\sum_i F_i M_i}{\sqrt{\sum_i F_i^2} \sqrt{\sum_i M_i^2}} \quad (2)$$

where F_i and M_i are the PDDs of the i th point in the fitted and measured central axis PDD curves respectively. For each variation, a correlation coefficient is computed and compared

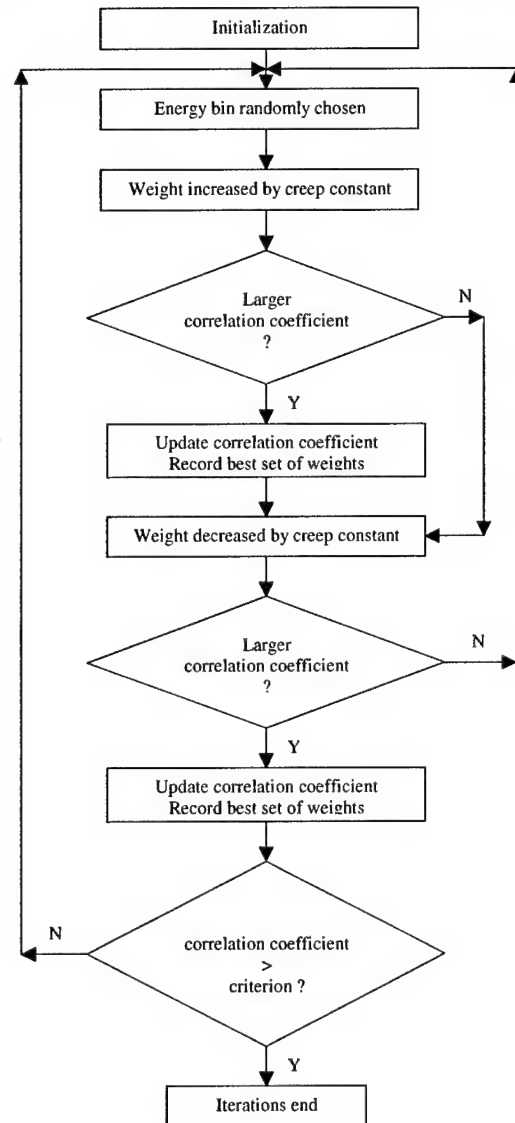


Figure 3. Illustration of the procedures used in the random creep method to fit the electron and photon energy spectra.

with the old correlation coefficient. If the new correlation coefficient is larger than the old one, the algorithm will update the best set of weighting factors. If not, the variation is discarded and a new variation is initiated. It is always the set of weighting factors which corresponds to the largest correlation coefficient that gets chosen. The algorithm will iterate until the preset correlation coefficient is achieved. The details of the algorithm for electron and photon spectrum fitting are discussed below.

2.4. Fitting of the electron energy spectrum

The electron energy spectrum can be determined by fitting the central axis PDDs of 100 monoenergetic electron beams to match the measured central axis PDDs excluding the head-generated photon background.

Basically, there are two major processes involved: initialization and random creep. A detailed description of the initialization process is given below. From the central axis PDD provided, we can determine its R_{50} . Knowledge of R_{50} , the most probable energy E_p and the cutoff energy E_{cutoff} (the maximum energy of electrons) for a certain electron beam can also be obtained via the Monte Carlo simulations. From our Monte Carlo simulations, the E_p as a function of the R_{50} and the E_{cutoff} as a function of the R_{50} have found to be linear as summarized in equations (3) and (4) below:

$$E_p = 2.524R_{50} - 0.252 \quad (3)$$

$$E_{\text{cutoff}} = 2.597R_{50} + 0.633. \quad (4)$$

The most probable energy E_p and the cutoff energy E_{cutoff} for the measured data are therefore determined via equations (3) and (4) accordingly. Thus, we can set the relative weighting factor to be 1.0 for the energy bin that covers the obtained most probable energy E_p . The relative weighting factors of those energy bins whose energy is larger than the obtained cutoff energy E_{cutoff} are set to be 0.0. We also set the relative weighting factors of the energy bins adjacent to the most probable energy E_p to be 0.5 and the next neighbouring energy bins to be 0.25. The remaining energy bins have the relative weighting factors of 0.1 except that the weighting factor for the first energy bin is set to be 0.0 due to the usage of ECUT of 700 keV in all of our Monte Carlo simulations.

The initialization in our random creep algorithm is associated with the choice of a 'creep constant'. The creep constant is a small positive number by which, for every iteration, the weight for the randomly selected energy bin is to be changed. By this analogy, we name our algorithm the 'random creep' algorithm. The creep constant we choose for our work is 0.001. For larger creep constants, the initial weights for the energy bins should also be increased. Our studies have shown that the fitting time of our random creep algorithm, for the same correlation coefficient criterion, is approximately inversely proportional to the magnitude of the creep constant, i.e. the product of fitting time and creep constant is approximately a constant.

Following the initialization process, the random creep process will go on until the preset criterion is satisfied. First, an integer is randomly generated and this number corresponds to a certain energy bin number ordered from 1 to 100. Then the weight for the selected energy bin will be modified by the amount of the creep constant, either positively or negatively. For either positive or negative change of the weighting factor, a correlation coefficient is computed and compared with the old correlation coefficient. The method prohibits any weight to be less than 0.001, the creep constant. By doing this, we can avoid negative weights in the energy spectrum.

Although the selection of the energy bin in the iteration process is random, since our initialization has basically locked into a reasonably good energy spectrum it does not take a long time for the algorithm to reach a best set of weighting factors for all 100 energy bins. A typical fitting process lasts less than 10 s on a Pentium III 450 MHz PC with the preset correlation coefficient tolerance of 0.00001. That is to say, the final correlation coefficient will be equal to or larger than 0.99999, which will give us a very good fitting between the measured central axis PDDs and the fitted central axis PDDs (within 1% of dose maximum or less than 1 mm shift in isodose lines for all the dose values).

In our work we have preset the correlation coefficient tolerance to be 0.00001 primarily for the following two reasons. If the tolerance is set to be too stringent, the program may

take a long time or never reach the criterion if the measurement data have large uncertainties. The second, and also the more important reason, is that, by setting a stringent tolerance, the program may find a solution with a resultant energy spectrum which is no longer realistic. We have found that a creep constant with a value between 0.000 001 and 0.0001 will generally lead to a solution with a relatively smooth electron energy spectrum while keeping a very high correlation between the fitted central axis PDD and the measured central axis PDD. Generally, the smaller the tolerance is, the more zigzagged the fitted spectrum is, and the longer it takes to reach the criterion.

2.5. Fitting of the photon energy spectrum

We have applied the same random creep algorithm to fit the photon energy spectrum. The photon energy spectrum can be determined by fitting the central axis PDDs of 100 monoenergetic photon beams to match the head-generated photon dose distribution determined using equation (1) before the fitting of electron energy spectrum. The major difference comes from the initialization process. Due to the nature of photon attenuation in the phantom, unlike the steep fall-off of the electron central axis PDD curve, the photon central axis PDD curve consists of a build-up region and a gradually descending fall-off region after d_{\max} (the depth of the maximum dose). The photon energy spectrum in a clinical electron beam has a dominant low-energy component with a long and gradually descending tail extended up to the maximum energy of electrons.

We have used a log-normal function to initialize the photon energy spectrum. The function takes the following form:

$$W(E) = e^{-(\ln(E/E_p)/\alpha)^2/2} \quad (5)$$

where E_p is the energy at which the peak in the spectrum is located and α is the width of the peak. The values of E_p and α have been found from our Monte Carlo simulations for each combination of electron beam energy and applicator size. After the initialization, the rest of the process is the same as the process to determine the electron energy spectrum. The correlation coefficient tolerance for photon energy spectrum fitting is usually set to be between 0.000 01 and 0.0001 in the random creep algorithm in order to obtain a relatively smooth photon energy spectrum.

2.6. Central axis depth dose comparison via MCDOSE

The determination of energy spectra for electrons and photons in clinical electron beams is part of an automated commissioning procedure that we have developed to commission clinical electron beams for Monte Carlo dose calculations. The output of the commissioning procedure is a source parameter file that will be used by MCDOSE for particle phase space reconstruction in order to calculate the dose distributions in a water phantom or in a patient geometry built from CT data. After the dose calculations, the central axis PDDs and dose profiles at various depths can be compared to evaluate our random creep algorithm.

MCDOSE is an EGS4 user code developed for dose calculations in radiation therapy treatment planning (Nelson *et al* 1985, Ma *et al* 1999b). It can be used to simulate the transport of photons and electrons in a patient-specific CT phantom. It can also be used to compute the dose distributions for conventional treatment with photon and electron beams, beamlet distributions for inverse treatment planning and the final dose distributions for intensity modulated radiotherapy. In order to perform the Monte Carlo dose calculations, MCDOSE needs an input file which specifies all the Monte Carlo simulation parameters, such as the

Table 1. Comparison of the peak widths for 6, 12 and 20 MeV electron beams between the fitted spectra using the random creep method and the Monte Carlo simulated spectra.

Nominal beam energy (MeV)	Random creep				Monte Carlo			
	E_p (MeV)	FWHM (MeV)	FWHM/ E_p	ΔE	E_p (MeV)	FWHM (MeV)	FWHM/ E_p	ΔE
6	5.625	0.9	16.0%	0.25	5.6875	0.3	5.3%	0.175
12	12.375	0.66	5.3%	0.25	12.375	0.5	4.0%	0.375
20	20.875	0.63	3.0%	0.25	20.875	0.81	3.9%	0.25

electron and photon energy cutoffs for particle transport (ECUT and PCUT), the maximum fractional energy loss per electron step (ESTEPE) and the parameters required by PRESTA (Bielajew and Rogers 1987). For all the simulations in this work, the energy cutoffs were ECUT = 700 keV and PCUT = 10 keV. The energy threshold for δ -ray production (AE) and for bremsstrahlung production (AP) were 700 keV and 10 keV respectively. ESTEPE was set to 0.04 and the default parameters were used for the PRESTA algorithm.

3. Results and discussion

3.1. Electron energy spectrum comparison

Figure 4 shows the comparison between the fitted results and the Monte Carlo simulations of the energy spectra for 6, 12 and 20 MeV electron beams. The symbols are from our random creep method while the full curves are from the Monte Carlo phase space simulations of the electron beams generated from a Varian Clinac 2100C (Varian Oncology Systems, Palo Alto, CA). All the curves have been normalized so that the area underneath each curve is unity. As shown, our fitted spectra are sharp and similar to the Monte Carlo spectra. The fitted energy peak is located within ± 0.125 MeV of the Monte Carlo simulated peak. The slight difference is due to the energy interval ΔE of 0.25 MeV in our fitted energy spectra, which is much larger than the energy bin size of the Monte Carlo simulated spectra. In fact, it is found that if a bin size of 0.25 MeV is used for scoring the Monte Carlo simulated spectra, a better agreement is achieved between our fitted energy spectra and the Monte Carlo simulated energy spectra. According to figure 4, the peak width in terms of FWHM (full width at half maximum)/ E_p of our fitted spectra is 16.0% for 6 MeV, 5.3% for 12 MeV and 3.0% for 20 MeV while the peak width of the Monte Carlo simulated spectra is 5.3% for 6 MeV, 4.0% for 12 MeV and 3.9% for 20 MeV respectively.

From table 1 we can see that the peak width determined by the random creep method for 6 MeV is larger than that determined from the Monte Carlo simulations, while for 12 MeV and 20 MeV beams, the peak width determined by the random creep method is about the same as that determined from the Monte Carlo simulations. This is due to two reasons. First, the energy interval of our random creep method is 0.25 MeV while it is 0.175 MeV for the Monte Carlo spectrum of the 6 MeV beam. Second, the peak energy E_p for the Monte Carlo simulated 6 MeV beam is 5.6875 MeV, which is between 5.625 MeV and 5.875 MeV. So as shown clearly in figure 4(a), our random creep algorithm tries to increase the weight for the 5.875 MeV, 6.125 MeV and 6.375 MeV energy bins in order to obtain a good match between the measured central axis depth dose distribution and the fitted central axis depth dose distribution. By doing so, our fitted energy spectrum for 6 MeV beam becomes wider in terms of the peak width.

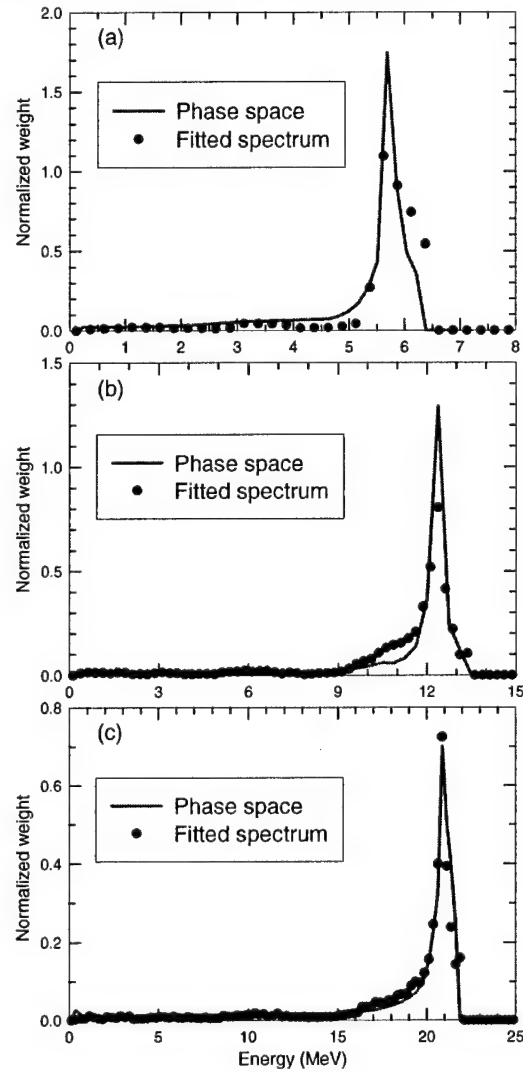


Figure 4. Comparison of the electron energy spectra for the fitted results and the Monte Carlo simulations for (a) a 6 MeV electron beam, (b) a 12 MeV electron beam and (c) a 20 MeV electron beam. The symbols are for the fitted results and the curves are for the Monte Carlo simulations. The fitted energy spectra have a fixed energy interval $\Delta E = 0.25$ MeV.

In our studies, we have observed that the peak width in terms of FWHM/E_p is dependent on the choice of the energy interval of the spectrum. In general, the smaller the energy interval ΔE , the smaller the peak width, but it will not be narrower than the default peak width of the spectrum. Therefore, in order to study the effect of the choice of energy interval on our fitted energy spectrum, we have increased the resolution of our fitted spectra. That is, by fitting 200 monoenergetic electron central axis depth dose distributions to match the measured central axis

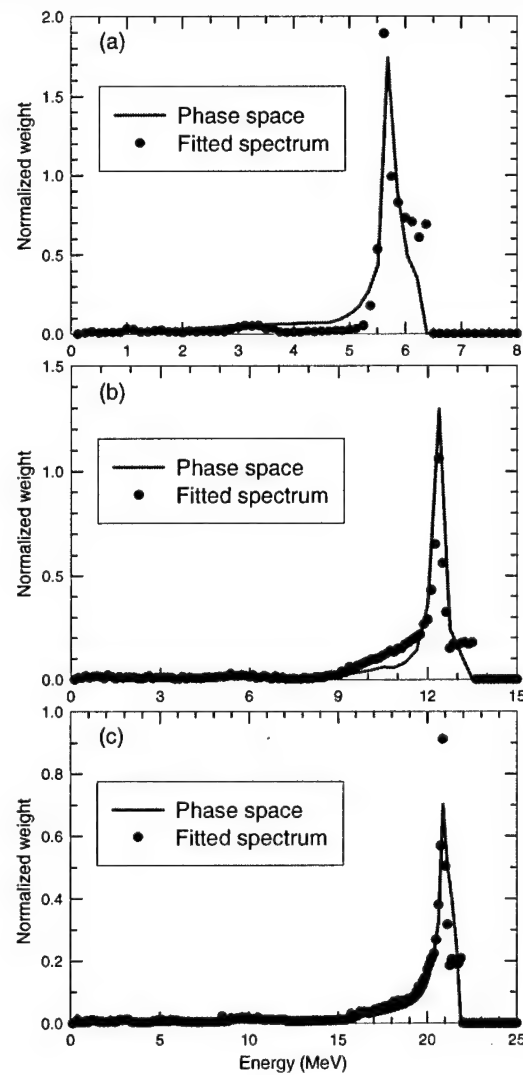


Figure 5. Comparison of the electron energy spectra for the fitted results and the Monte Carlo simulations for (a) a 6 MeV electron beam, (b) a 12 MeV electron beam and (c) a 20 MeV electron beam. The Monte Carlo simulated spectra are identical to those in figure 4 while the fitted spectra are obtained using a finer energy interval $\Delta E = 0.125$ MeV.

depth dose distribution using our random creep method, we can obtain spectra with an energy interval of 0.125 MeV. The results of the test are shown in figure 5 and included in table 2 below.

Table 2 lists the results of the test where the resolution of our fitted spectra has been doubled. As shown, the peak widths for 6, 12 and 20 MeV beams determined by our random creep method are all narrower than those of the Monte Carlo spectra. The smaller energy interval of 0.125 MeV used in our fitting procedure definitely decreases the peak widths for all

Table 2. Comparison of the peak widths for 6, 12 and 20 MeV electron beams between the fitted spectra using the random creep method and the Monte Carlo simulated spectra. The energy interval ΔE is 0.125 MeV for the fitted spectra.

Nominal beam energy (MeV)	Random creep				Monte Carlo			
	E_p (MeV)	FWHM (MeV)	FWHM/ E_p	ΔE	E_p (MeV)	FWHM (MeV)	FWHM/ E_p	ΔE
6	5.625	0.24	4.3%	0.125	5.6875	0.3	5.3%	0.175
12	12.375	0.33	2.7%	0.125	12.375	0.5	4.0%	0.375
20	20.875	0.36	1.7%	0.125	20.875	0.81	3.9%	0.25

the beam energies. Compared with the results in table 1, the peak width has been reduced by a factor of 3.72, 1.96 and 1.76 for 6, 12 and 20 MeV beams respectively. Figure 5 illustrates the comparison for the three energy beams. Besides the sharper peaks, the fitted spectra using a higher resolution also exhibit some fine structures that do not show in the lower-resolution spectra. However, there are no noticeable differences in the PDD curves calculated using the spectra of two different energy intervals.

Regarding our fitting procedure, the following issues deserve some further discussion. One is the choice of energy interval in the fitting procedure. As demonstrated clearly in figures 4 and 5 and in tables 1 and 2, for a small spectrum peak width a small energy interval ΔE is needed. Our random creep method is capable of fitting sharp peaks as long as the energy interval is small enough. It appears that a 0.125 MeV energy interval is better for 6 MeV beams while a 0.25 MeV energy interval is good enough for 12 and 20 MeV beams although the PDD curves calculated with the two different energy intervals are essentially the same (well within the 1σ statistical uncertainty of 0.5% of the maximum dose). We actually used 0.25 MeV for spectrum fitting in our automated beam commissioning procedure.

The second issue is the accurate location of the most probable energy E_p . Assume that the energy resolution of the fitted spectrum is 0.25 MeV, which is 1% of 25 MeV, the maximum electron energy used for the fitting procedure. Since the initial position of the energy peak is determined by the R_{50} value, the difference between the final peak location and the initial location is not expected to be significant unless the beam spectrum is significantly different from the commonly available clinical beams (the difference in the spectral shape of the beam for the same nominal energies between the Varian accelerators is very small). However, the accuracy of the measured R_{50} value may be affected by the quality of the measured PDD curves. To test the robustness of our fitting procedure, we have deliberately changed the R_{50} values of the central axis PDD curves so as to offset the initial energy peak positions by up to 1% of their real value. Our method can always converge back to the correct locations of the energy peak. Another test was done with a flat spectrum (initial weight values equal to 0.1 for all of the energy bins) and the fitting procedure also converged to an identical spectrum. We have also implemented some quality checks in the fitting software. If the final energy peak position is significantly different from the initial energy peak position, i.e. if it corresponds to $|R_{50(\text{measured})} - R_{50(\text{fitted})}| > 1.0$ mm, a warning message will be generated to caution the user. This means that the 50% isodose lines may shift by more than 1 mm, which does not satisfy our commissioning criterion for spectrum fitting. For all the beam energies studied in this work, the fitted energy peaks are located within 0.5% of the Monte Carlo calculated values except for some of the 6 MeV beams where a 1.1% difference in peak location is observed due to the 0.25 MeV energy interval used in the fitting procedure. The fitted R_{50} values, however, are within 0.1 mm of the corresponding R_{50} of the Monte Carlo phase space data.

The third issue is the choice of the creep constant and the correlation coefficient tolerance used in the random creep method. In our approach, we have chosen the weight for the most probable energy to be 1 and the creep constant to be 0.001. After the fitting, the quotient of the maximum weight for the most probable energy to the minimum weight in the low-energy part is of the same order as that of the Monte Carlo simulated spectrum. Generally, the final fitted spectrum will not change too much in shape from the originally initialized spectrum near the peak energy because the creep constant is small and our objective function is sensitive to the shape of the spectrum near the peak energy (a small change from the correct spectrum shape near the peak may cause sizable degradation in the correlation coefficient). Yet the random selection of energy bins in the search process explores all possibilities for a satisfactory correlation between the fitted and the measured central axis PDDs. Our objective function has a maximum value of 1, which implies a perfect match between the PDDs calculated with the Monte Carlo spectrum and the fitted spectrum. However, the solution may not be unique, and it is well known that many different spectra may result in the same PDDs (within statistics). To make sure the final fitted spectrum resembles the realistic spectrum of a clinical electron beam, we initiate our random search with a set of energy bin weights that closely match the energy peak and low-energy tail (see above). The resulting energy spectra may vary slightly depending on the energy interval and the tolerance of the correlation coefficient. This small variation has not been found to affect the calculated dose distributions significantly. It is found from our studies that when the tolerance of the correlation coefficient is set to be 0.0001 or less, the maximum difference in the PDD curves between the fitted spectra and Monte Carlo calculated spectra is less than 1% of the maximum dose or within a 1 mm shift of the isodose lines (whichever is smaller). Therefore, our choice in this work of a small correlation coefficient tolerance (between 0.000001 and 0.0001) ensures that the fitted PDD curves will match the PDD curves from the Monte Carlo phase space data to within 1%/1 mm.

3.2. Photon energy spectrum comparison

The fitted photon energy spectra for 6, 12 and 20 MeV electron beams are shown in figure 6 in comparison with the corresponding Monte Carlo simulated photon energy spectra. All the curves have been normalized so that the area under each curve is unity. As we can see, the fitted photon energy spectra agree very well with the Monte Carlo simulated energy spectra of phase space in terms of shape, width and smoothness. Both of them have a dominant low-energy component and are monotonically decreasing toward high energy. But the FWHMs of our fitted spectra are slightly larger than those of Monte Carlo phase space spectra. This may be due to two reasons. One is the fixed resolution of 0.25 MeV in our fitting procedure, which is larger than the energy intervals of the Monte Carlo spectra shown in figure 6. Another reason is the approximation in our procedure that all photons are from a point source.

In addition, we have observed in our studies that the photon central axis depth dose distributions are not so sensitive to the photon energy spectrum. In other words, the fitted photon energy spectra may be somewhat different from those of Monte Carlo simulations but the photon central axis depth dose distributions in the phantom can still be very similar. Although the photon central axis depth dose distributions can be very similar, they do exhibit some apparent differences. Since different shapes of photon energy spectra will have different mean energies, the slopes of the photon central axis depth dose distributions after d_{\max} will be apparently different. Therefore, in this work the slope of the central axis depth dose distribution after d_{\max} has been used as an indicator to find whether the photon energy spectrum is fitted correctly or not.

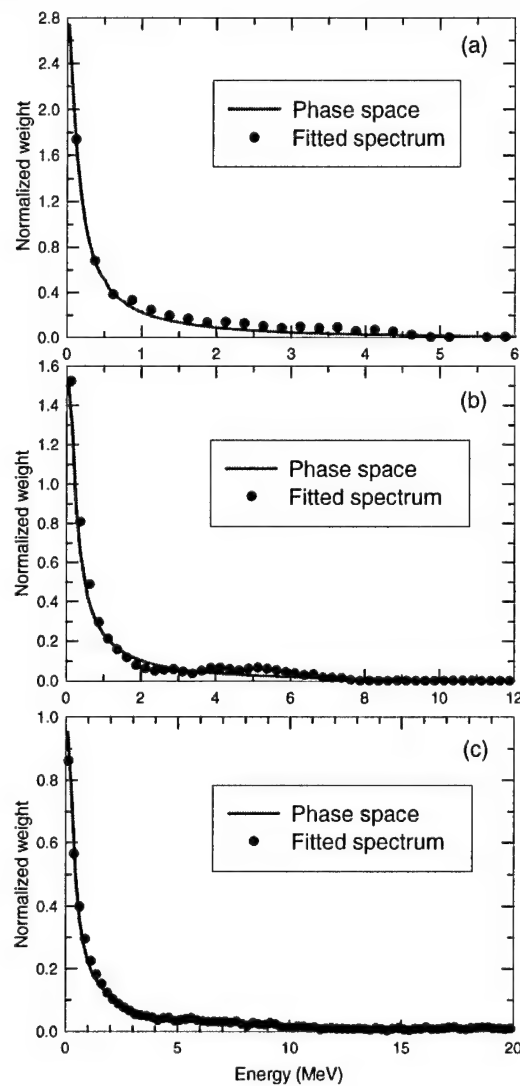


Figure 6. Comparison of the photon energy spectra for the fitted results and the Monte Carlo simulations for (a) a 6 MeV electron beam, (b) a 12 MeV electron beam and (c) a 20 MeV electron beam. The symbols are for the fitted results and the curves are for the Monte Carlo simulations.

3.3. Photon contribution to the central axis depth doses in electron beams

As pointed out by previous investigators (Rustgi and Rodgers 1987, Klevenhagen 1994), the contribution of photons to the final central axis PDD becomes more and more important as the electron beam energy increases. As electron energy increases, more and more photons are generated by the bremsstrahlung process. These bremsstrahlung photons have a dominant low-energy component with a monotonically descending tail extended up to the cutoff energy of

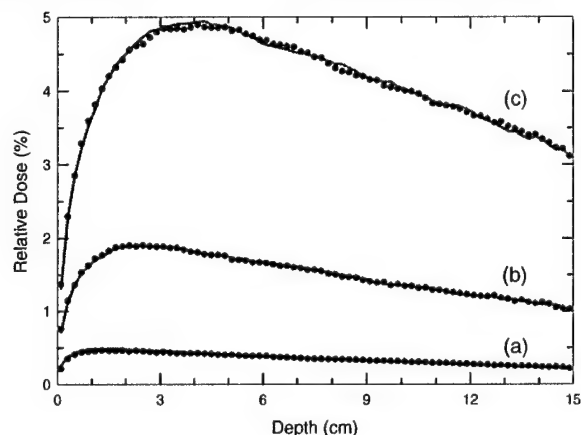


Figure 7. Comparison of the head-generated photon central axis depth dose for the fitted results and the Monte Carlo simulations for (a) a 6 MeV electron beam, (b) a 12 MeV electron beam and (c) a 20 MeV electron beam. The symbols are for the fitted results and the curves are for the Monte Carlo simulations.

electron beams. The central axis depth dose curve of these photons will follow the characteristic shape of the central axis PDD of the megavoltage x-ray beams with a region of build-up and a maximum followed by a nearly straight descending line.

Our studies have shown that the maximum contribution of photon dose to the final central axis PDD from the head-generated photons can be as much as 5.0% of the maximum dose for 20 MeV electron beams, 1.9% for 12 MeV electron beams and 0.6% for 6 MeV electron beams. Figure 7 shows the contribution of head-generated photons to the dose for clinical electron beams of 6, 12 and 20 MeV calculated using our fitted photon spectra. In comparison, the Monte Carlo simulated head-generated photon doses using phase space data are plotted. The curves have been normalized to their d_{\max} of the total doses (electrons plus photons). As demonstrated, the surface doses, the d_{\max} and the slope of the dose distributions in the fall-off region agree well with those of Monte Carlo simulations, which also means that our fitted photon energy spectra are in good agreement with the Monte Carlo simulated photon energy spectra.

3.4. Central axis depth dose comparison for 6, 12 and 20 MeV electron beams

The central axis depth dose distributions are compared in figure 8 between the Monte Carlo simulations and the commissioning results for 6, 12 and 20 MeV electron beams with applicator sizes of 6 cm \times 6 cm and 20 cm \times 20 cm. The central axis PDDs agreed very well between the two for all the cases tested with differences of less than 1%/1 mm. Since we also accounted for the photon background accurately, good agreement is achieved in the tail part of depth dose distributions. Due to the adoption of separate sets of monoenergetic electron beam central axis PDDs for different field sizes, good agreement is also achieved around the R_{50} region where the dose falls off rapidly.

As shown in figure 2(a), the monoenergetic electron central axis depth dose distributions are dependent on field size. As beam energy increases, the central axis depth dose distributions will differ more significantly around the R_{50} region between the 15 cm \times 15 cm collimation

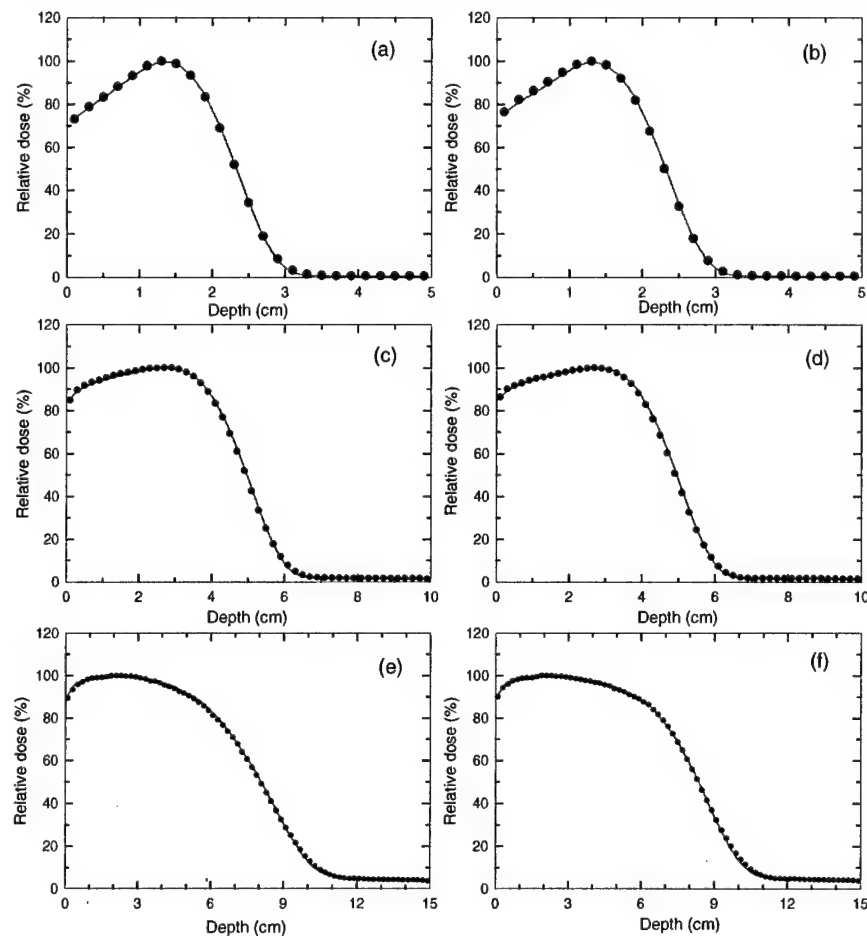


Figure 8. Comparison of the central axis depth dose for the fitted results and the Monte Carlo simulations for (a) a 6 MeV electron beam with a 6 cm × 6 cm applicator, (b) a 6 MeV electron beam with a 20 cm × 20 cm applicator, (c) a 12 MeV electron beam with a 6 cm × 6 cm applicator, (d) a 12 MeV electron beam with a 20 cm × 20 cm applicator, (e) a 20 MeV electron beam with a 6 cm × 6 cm applicator and (f) a 20 MeV electron beam with a 20 cm × 20 cm applicator. The symbols are for the fitted results and the curves are for the Monte Carlo simulations.

and 6 cm × 6 cm collimation. Therefore, we cannot commission the data for small fields (e.g. 6 cm × 6 cm) using the monoenergetic beam central axis depth dose distributions of large fields (e.g. 15 cm × 15 cm). Even though we can get a perfect match from our fitting procedure, the dose distributions in the phantom calculated using the wrongly fitted spectra would not be correct. In this work, we have adopted 6 cm × 6 cm and 10 cm × 10 cm monoenergetic PDDs for the corresponding applicators, and one set of 15 cm × 15 cm monoenergetic PDDs for 15 cm × 15 cm, 20 cm × 20 cm and 25 cm × 25 cm applicators to commission the electron beams of the investigated Varian Clinac accelerators.

Table 3. The electron cut-out factors for various square inserts in a $10 \times 10 \text{ cm}^2$ applicator for 6, 12 and 20 MeV electron beams calculated with the four-source model and the full phase space data, and measured by Kapur *et al* (1998). The values in parenthesis indicate the difference between the data calculated with the source model or the full phase space and the measurement data.

Energy (MeV)	Insert (cm^2)	Cut-out factor		
		Source model	Full phase space	Measurement
6	2×2	0.793 (0.015)	0.765 (−0.013)	0.778
	3×3	0.923 (−0.004)	0.923 (−0.004)	0.927
	4×4	0.990 (0.002)	0.982 (−0.006)	0.988
	8×8	1.004 (0.001)	1.005 (0.002)	1.003
12	2×2	0.898 (0.009)	0.861 (−0.028)	0.889
	3×3	0.932 (0.004)	0.930 (0.002)	0.928
	4×4	0.960 (−0.003)	0.956 (−0.007)	0.963
	8×8	0.993 (0.002)	1.002 (0.011)	0.991
20	2×2	0.968 (−0.008)	0.957 (−0.019)	0.976
	3×3	0.990 (−0.003)	0.968 (−0.025)	0.993
	4×4	1.003 (−0.008)	0.993 (−0.018)	1.011
	8×8	0.995 (−0.009)	0.993 (−0.011)	1.004

3.5. Dose profile comparison at two depths for 6, 12 and 20 MeV electron beams

Besides the central axis depth dose distributions, dose profiles at two different depths for various combinations of beam energy and applicator size are shown in figure 9. Depths are 1.1 and 2.1 cm for 6 MeV beams, 2.1 and 4.9 cm for 12 MeV beams and 3.5 and 6.9 cm for 20 MeV beams. All the curves in figure 9 are normalized to the doses at d_{max} . The Monte Carlo uncertainty is less than 0.5% of the maximum dose and not shown on the curves. As shown, the agreement between the Monte Carlo full phase space simulations and the beam commissioning results is less than 1%/1 mm, which means that our random creep algorithm together with the beam commissioning procedure are acceptable for clinical use.

3.6. Comparison of electron cut-out factor for 6, 12 and 20 MeV electron beams

The capability of our multiple source model for calculating the relative beam output has also been tested. Table 3 shows electron cut-out factors for various square inserts in a $10 \times 10 \text{ cm}^2$ applicator for 6, 12 and 20 MeV electron beams. It is found that the cut-out factors calculated with our four-source model are within 2% of the measured values. This is at about the same level of accuracy as the Monte Carlo full phase space simulations and is therefore considered to be acceptable for clinical use.

4. Conclusions

We have employed a random creep algorithm to determine the energy spectra of electrons and photons from the central axis PDD curves of clinical electron beams. The PDD curves for 6, 12 and 20 MeV electron beams obtained from Monte Carlo full phase space simulations of the Varian linear accelerator treatment head have been used to test the method. The fitted electron and photon energy spectra have been compared with the corresponding spectra obtained from the Monte Carlo simulated phase space data. Our fitted electron and photon spectra are in good agreement with the Monte Carlo simulated spectra in terms of peak position, peak

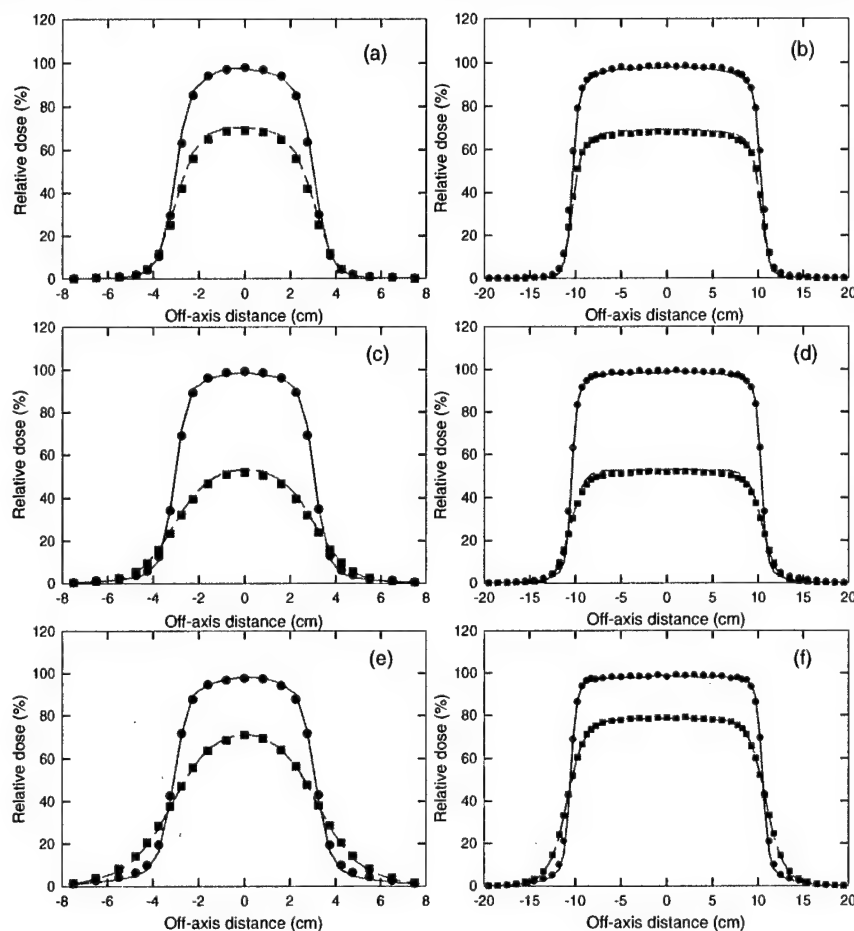


Figure 9. Comparison of the dose profile for the fitted results and the Monte Carlo simulations at two depths for (a) a 6 MeV electron beam with a 6 cm \times 6 cm applicator, (b) a 6 MeV electron beam with a 20 cm \times 20 cm applicator, (c) a 12 MeV electron beam with a 6 cm \times 6 cm applicator, (d) a 12 MeV electron beam with a 20 cm \times 20 cm applicator, (e) a 20 MeV electron beam with a 6 cm \times 6 cm applicator and (f) a 20 MeV electron beam with a 20 cm \times 20 cm applicator. Depths are 1.1 and 2.1 cm for 6 MeV, 2.1 and 4.9 cm for 12 MeV and 3.5 and 6.9 cm for 20 MeV. The symbols are for the fitted results and the curves are for the Monte Carlo simulations.

width and smoothness of the spectrum. In addition, the derived photon depth dose curves for head-generated photons agree well in both shape and amplitude with the Monte Carlo simulations of the contribution of head-generated photons to the dose in clinical electron beams. The central axis depth dose curves and dose profiles at various depths calculated using Monte Carlo simulated phase space spectra and those from the fitted spectra agreed to within 1%/1 mm for 6, 12 and 20 MeV electron beams. The electron cut-out factors calculated with our four-source model are within 2% of the measured values and the values calculated using the Monte Carlo phase space data. It has been demonstrated that our method is capable of deriving the energy spectra for clinical electron beams from the Varian Clinac 2100C and

2300C/D accelerators. Further studies will be carried out to use this method for other types of medical accelerators used in radiation therapy. The method has been implemented as part of an electron beam commissioning procedure for Monte Carlo electron beam dose calculations for clinical treatment planning.

Acknowledgments

We would like to acknowledge Varian Medical Systems, Palo Alto, CA, for providing detailed information on the Varian Clinac linear accelerators. We would like to thank our colleagues Sam Brain and Todd Koumrian for computer hardware and software support. This work was supported in part by grants from the Department of Defense US Army Breast Cancer Research Program BC971292, BC990213 and BC990018, a National Institute of Health (NIH) grant CA78331 and a consortium agreement with the NumeriX, LLC.

References

- Andreo P 1991 Monte Carlo technique in medical physics *Phys. Med. Biol.* **36** 861–920
- Bielajew A F and Rogers D W O 1987 PRESTA: The parameter reduced electron-step transport algorithm for electron Monte Carlo transport *Nucl. Instrum. Methods B* **18** 165–81
- Brahme A and Svensson H 1979 Radiation beam characteristics of a 22 MeV microtron *Acta Radiol. Oncol.* **18** 244–72
- Cygler J, Battista J J, Scrimger J W, Mah E and Antolak J 1987 Electron dose distributions in experimental phantoms: a comparison with 2D pencil beam calculations *Phys. Med. Biol.* **32** 1073–86
- Deasy J O and Almond P R 1994 The spectral dependence of electron central-axis depth-dose curves *Med. Phys.* **21** 1369–76
- Deng J, Jiang S B, Kapur A, Li J, Pawlicki T and Ma C-M 2000 Photon beam characterization and modeling for Monte Carlo treatment planning *Phys. Med. Biol.* **45** 411–27
- Faddegon B A and Blevis I 2000 Electron spectra derived from depth dose distributions *Med. Phys.* **27** 514–26
- Hogstrom K R, Mills M D and Almond P R 1981 Electron beam dose calculations *Phys. Med. Biol.* **26** 445–59
- Jenkins T M, Nelson W R, Rindi A, Nahum A E and Rogers D W O 1988 *Monte Carlo Transport of Electrons and Photons* (New York: Plenum)
- Jiang S B, Kapur A and Ma C-M 2000 Electron beam modeling and commissioning for Monte Carlo treatment planning *Med. Phys.* **27** 180–91
- Kapur A, Ma C M, Mok E C, Findley D O and Boyer A L 1998 Monte Carlo calculations of electron beam output factors for a medical linear accelerator *Phys. Med. Biol.* **43** 3479–94
- Klevenhagen S C 1994 An algorithm to include the bremsstrahlung contamination in the determination of the absorbed dose in electron beams *Phys. Med. Biol.* **39** 1103–12
- Luo Z and Jette D 1999 On the possibility of determining an effective energy spectrum of clinical electron beams from percentage depth dose (PDD) data of broad beams *Phys. Med. Biol.* **44** 177–82
- Ma C-M, Faddegon B A, Rogers D W O and Mackie T R 1997 Accurate characterization of Monte Carlo calculated electron beams for radio-therapy *Med. Phys.* **24** 401–16
- Ma C-M, Mok E, Kapur A, Pawlicki T, Findley D, Brain S, Forster K and Boyer A L 1999a Clinical implementation of a Monte Carlo treatment planning system *Med. Phys.* **26** 2133–43
- Ma C-M, Pawlicki T, Li J, Jiang S, Deng J, Kapur A, Mok E, Luxton G and Boyer A L 1999b MCDOSE—a dose calculation tool for radiotherapy treatment planning *Med. Phys.* **26** 1148 (abstract)
- Mackie T R 1990 Applications of the Monte Carlo method in radiotherapy *Dosimetry of Ionizing Radiation* vol 3, ed K Kase, B Bjarngard and F H Attix (New York: Academic) pp 541–620
- Mah E, Antolak J, Scrimger J W and Battista J J 1989 Experimental evaluation of a 2D and a 3D electron pencil beam algorithm *Phys. Med. Biol.* **34** 1179–94
- Nelson R, Hirayama H and Rogers D W O 1985 The EGS4 code system *Stanford Linear Accelerator Center Report SLAC-265* (Stanford, CA: SLAC)
- Rogers D W O 1991 The role of Monte Carlo simulation of electron transport in radiation dosimetry *Int. J. Appl. Radiat. Isot.* **42** 965–74
- Rogers D W O and Bielajew A F 1990 Monte Carlo techniques of electron and photon transport for radiation dosimetry *Dosimetry of Ionizing Radiation* vol 3, ed K Kase, B Bjarngard and F H Attix (New York: Academic) pp 427–539

- Rustgi S N and Rodgers J E 1987 Analysis of the bremsstrahlung component in 6–18 MeV electron beams *Med. Phys.* **14** 884–8
- Sorcini B B, Andreo P, Bielajew A F, Hyödynmaa S and Brahme A 1995 An improved energy–range relationship for high-energy electron beams based on multiple accurate experimental and Monte Carlo data sets *Phys. Med. Biol.* **40** 1135–59
- Sorcini B B, Hyödynmaa S and Brahme A 1996 The role of phantom and treatment head-generated bremsstrahlung in high-energy electron beam dosimetry *Phys. Med. Biol.* **41** 2657–77
- 1997 Quantification of mean energy and photon contamination for accurate dosimetry of high-energy electron beams *Phys. Med. Biol.* **42** 1849–73

Comparison of RTP dose distributions in heterogeneous phantoms with the BEAM Monte Carlo simulation system

Moyed Miften,^{1,*} Mark Wiesmeyer,^{2,†} Ajay Kapur,^{3,‡}
and C.-M. Charlie Ma^{3,§}

¹Department of Radiation Oncology, Duke University Medical Center, Durham,
North Carolina 27710

²Computerized Medical Systems, Inc., St. Louis, Missouri 63132

³Department of Radiation Oncology, Stanford University School of Medicine,
Stanford, California 94305

(Received 18 April 2000; accepted for publication 9 October 2000)

Therapeutic treatment plan evaluation is often based on examining the radiotherapy treatment planning (RTP) system dose distributions in the target and surrounding normal structures. To study the effects of tissue inhomogeneities on photon dose distributions, we compared FOCUS RTP system dose distributions from the measurement-based Clarkson and model-based MultiGrid Superposition (MGS) algorithms with those from the BEAM Monte Carlo code system in a set of heterogeneous phantoms. The phantom inhomogeneities mimic relevant clinical treatment sites, which include lung slab, lung-bone slab, bone-lung slab, mediastinum, and tumor geometries. The benchmark comparisons were performed in lung densities of 0.20 and 0.31 g/cm³, and a bone density of 2.40 g/cm³ for 5×5 cm² and 10×10 cm², 6- and 15-MV photon beams. Benchmark comparison results show that the MGS model and BEAM doses match better than 3% or 3 mm, and the MGS model is more accurate than the Clarkson model in all phantoms. The MGS model, unlike the Clarkson model, predicts the build-down and build-up of dose near tissue interfaces and penumbra broadening in lung associated with high energy beams. The Clarkson model overestimates the dose in lung by a maximum of 10% compared to BEAM. Dose comparisons suggest turning-off the effective path length inhomogeneity correction in the Clarkson model for lung treatments. © 2001 American College of Medical Physics. [DOI: 10.1120/1.1328616]

PACS number(s): 87.53.-j, 87.53.Bn

Key words: dose, heterogeneous, BEAM, superposition, Clarkson

INTRODUCTION

External beam radiotherapy treatment planning (RTP) is a complex process, which involves the use of information from CT and/or MRI examinations in order to localize the target volume and surrounding normal structures. One then determines the treatment technique and beam setup, performs the dose calculation, evaluates and optimizes the plan, and verifies the plan on the simulator and treatment machine. Dose calculation and treatment plan evaluation depend strongly on the accuracy of the dose calculation algorithm in the RTP system.¹

Dose calculation algorithms in RTP systems can be broadly classified into measurement-based and model-based approaches. Measurement-based models, such as the Clarkson algorithm,² compute dose based on measurements in water. These models usually correct the homogeneous water distributions to account for treatment aids, patient contours, and tissue inhomogeneities. Unlike measurement-based approaches, model-based approaches, such as the convolution/superposition algorithm,³ compute the dose in water or patient from physics principles. The dose calculation accounts for beam energy, treatment aids, the transport of primary and secondary radiation inside the patient, and the effects of tissue inhomogeneities on the dose distributions.

When commissioning RTP dose calculation algorithms, the goal is often to achieve agreement between calculated and measured doses within 1–2 % for open and wedge fields in water. While this is possible to achieve using both measurement-based and model-based algorithms in water phantoms, such an agreement is usually not possible for measurement-based algorithms in phantoms with heterogeneities. This is due to the fact that measurement-based models are able to account for the effect of tissue inhomogeneities on the primary radiation. However, correcting for the scatter radiation is difficult since it depends on field size, beam energy and shape, location and density of the inhomogeneities.⁴ In contrast, model-based algorithms can account for the effect of tissue inhomogeneities on the scatter radiation using the density scaling method^{5,6} or other approaches.^{7,8}

Many RTP research and commercial systems still use measurement-based models for dose calculations. The accuracy of dose calculation algorithms in heterogeneous phantoms has previously been investigated by comparing calculations with measurements. Comparisons were mainly limited to the central-axis due to the complexity of performing accurate full three-dimensional (3D) measurements.^{4,9,10} Therefore, there is a need for a detailed study and examination of 3D dose distributions in heterogeneous phantoms, since many studies have debated the use of inhomogeneity corrections in treatment planning, especially for lung treatments.^{11–14} In this work, we compared FOCUS RTP system dose distributions from the measurement-based Clarkson² and model-based MultiGrid Superposition¹⁵ (MGS) algorithms with those from the BEAM¹⁶ Monte Carlo (MC) code system in a set of heterogeneous phantoms. The phantom and beam geometries simulate clinical treatment situations. We present results that suggest turning-off the effective path length inhomogeneity correction in the Clarkson model for lung treatments. While the methods presented are specific to the FOCUS Clarkson and FOCUS MultiGrid Superposition models, results should apply to other implementations of the Clarkson and Superposition models in other treatment planning systems.

METHODS

The Clarkson and MGS models of the FOCUS RTP system are used (version 2.5.0, Computerized Medical Systems, St. Louis, MO). Calculated dose distributions are compared to BEAM Monte Carlo dose distributions for a Varian Clinac 2300C/D accelerator (Varian Oncology Systems, Palo Alto, CA). Dose distributions are normalized to the value from the BEAM simulation, at the depth of maximum dose (d_{\max}) along the central axis. Distributions for 6- and 15-MV beams are compared for $5 \times 5 \text{ cm}^2$ and $10 \times 10 \text{ cm}^2$ fields.

In order to compare the BEAM and RTP dose calculation models, corresponding dose values are extracted from the 3D dose data from each model. The dose values from the corresponding planes are read into a comparison utility. The utility compares both sets of plane data and produces the percent-difference relative to the dose at d_{\max} , distance to agreement (distance to agreement to the nearest point exhibiting the same dose level) and percent passing information. The output is then read by another utility which allows the visualization of isodose distributions and various information.

Heterogeneous phantoms

The five heterogeneous phantom geometries studied in this work are shown in Fig. 1. All phantoms have external dimensions of $30 \times 30 \times 30 \text{ cm}^3$. A build-up layer of water with a thickness of 3 cm for the 6-MV beam and 5 cm for the 15-MV beam is used in order to achieve electronic equilibrium before entering the low or high density layers. The heterogeneities are assumed to have the same atomic composition as water.

The lung and bone slab geometries have been used to verify dose calculation algorithms along the central-axis in many research articles.^{4,9,10} The slab-based phantoms are used to examine doses inside the inhomogeneities, beyond them, and near material interfaces. Figure 1(a) is a lung slab in a water phantom with a density of 0.31 g/cm^3 . The lung slab has a dimension of

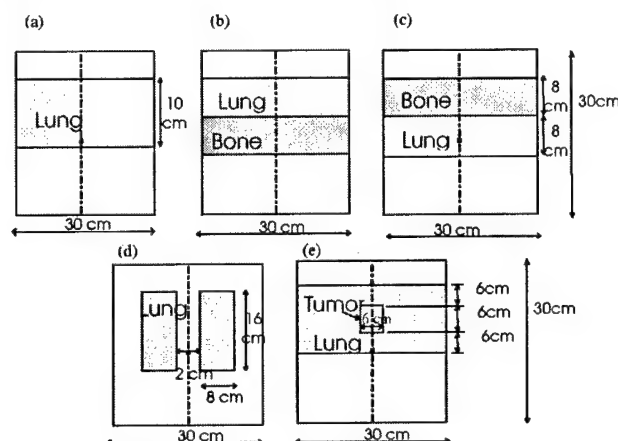


FIG. 1. Schematic of the (a) lung slab phantom, (b) lung-bone slab phantom, (c) bone-lung slab phantom, (d) mediastinum phantom and (e) tumor phantom.

$30 \times 30 \times 10 \text{ cm}^3$. Figures 1(b) and 1(c) are a lung-bone and bone-lung slab in a water phantom with 0.2 and 2.4 g/cm^3 density for lung and bone, respectively. The lung and bone slabs have a dimension of $30 \times 30 \times 8 \text{ cm}^3$ each. To achieve full scatter conditions, the lateral extent of the slabs is larger than the $5 \times 5 \text{ cm}^2$ and $10 \times 10 \text{ cm}^2$ field sizes used in this work.

Figure 1(d) is a mediastinum geometry (two lung geometry).¹⁷ Each lung dimension is $8 \times 30 \times 16 \text{ cm}^3$ and has a density of 0.31 g/cm^3 ; the two lungs are separated by water of 2 cm thickness. For this geometry, the dose will change inside in the lungs. The scatter dose contribution to the central axis will also change without affecting the primary dose. The tumor geometry is shown in Figure 1(e) with a tumor density of 1 g/cm^3 and a $6 \times 6 \times 6 \text{ cm}^3$ dimension centered in a lung thickness of 18 cm . The tumor geometry is designed to simulate the treatment of a patient lung tumor, which is often located inside the lung.⁴ The setup is used to examine the dose distributions inside the tumor, lung and near interfaces.

BEAM setup

BEAM is a Monte Carlo based system for modeling radiotherapy treatment unit heads for 3D RTP.¹⁶ The BEAM code is developed based on the EGS4 code system¹⁸ which has been demonstrated to accurately simulate the coupled transport of electrons and photons in matter.^{19,20,22} The EGS4 system has been used to calculate beam data for many clinical linear accelerators and dose distributions in both homogeneous and heterogeneous phantoms.¹⁹

The BEAM code generated the full phase-space of all particles for the 6- and 15-MV beams that emerge from the simulated Varian Clinac 2300C/D treatment unit. The phase-space file contains information about particle type, energy, position, direction, weight, and a tag that records the particle history at any specified plane in the simulated geometry.

To commission the Monte Carlo simulated phase-space data, the dose distributions calculated using the Monte Carlo method were compared with the measured beam data for the 6- and 15-MV beams. The incident beam parameters, which include the incident electron energy, the spatial and the angular distributions at the target surface, were altered so that the calculated dose distributions can match the measured values within 2% of the maximum dose everywhere in the phantom.^{22,24,25} Sufficient number of particle histories were simulated to ensure the 1-sigma statistical uncertainty on the calculated dose values was less than 1% of the maximum dose for all voxels.

DOSXYZ in the BEAM/EGS4 system is a code for simulating electron and photon transport in a Cartesian volume and scoring the energy deposition in the designated voxels. The geometry is a rectilinear volume with voxel dimensions which are variable in all three dimensions. Each voxel can have different materials with varying densities for use with CT data. DOSXYZ was used to calculate the dose in the heterogeneous phantoms, depicted in Fig. 1, on $0.5 \times 0.5 \times 0.5$ -cm grid size using the 6- and 15-MV beam phase-space source distributions.

Dose calculation algorithms

The Clarkson sector integration algorithm uses patient data, treatment machine data, and setup information to simulate dose distributions inside the patient. The patient information consists of relative electron density data which represents a section of the patient. The relative electron density values can be calculated from either the CT data or the assigned structure densities. The algorithm takes into account primary dose corrections for inhomogeneities in the patient, transmission by the wedge, and scatter modifications of blocks and collimators resulting from field shaping. The algorithm does not take into account scatter modifications due to differences in field intensity (e.g., wedges), patient density, surface curvature and missing tissue.

In the Clarkson algorithm, the dose is calculated at a point (x, y) in a plane at depth d as the sum of primary and scatter dose:

$$D(x, y, d) = \Phi(x, y) [\text{TAR}(0, d_{\text{eff}}) + \text{SAR}(x, y, d_{\text{eff}})]. \quad (1)$$

TAR is the central-axis tissue-to-air ratio at the radiological depth d_{eff} extrapolated to zero field size. SAR is the scatter-to-air ratio at d_{eff} at the dose point. Here, the Clarkson algorithm accounts for the effects of tissue inhomogeneities by calculating the primary and scatter dose along each beam "effective path length" fan line. Note that the Clarkson algorithm, unlike the MGS algorithm, does not model the effect of tissue inhomogeneities on scatter dose distribution.

The MGS algorithm uses fundamental physics principles to calculate dose distributions inside the patient rather than providing reproductions or modifications of measured data. Specifically, the MGS algorithm computes the dose by convolving the total energy released in the patient with Monte Carlo generated energy deposition kernels.²⁰ The MGS model accounts for beam hardening, missing tissue and the effects of tissue inhomogeneities on the dose distributions. A detailed description of the implementation and commissioning of the MGS model has recently been reported.¹⁵ In the MGS algorithm, the total energy released per unit mass (TERMA²¹), T , at the interaction point may be calculated as

$$T(\underline{r}', E) = \frac{\mu}{\rho}(E, \underline{r}') E \Phi(\underline{r}_o) \exp(-\mu |\underline{r}' - \underline{r}_o|), \quad (2)$$

where μ/ρ is the mass attenuation coefficient, E is the beam energy, μ is the linear attenuation coefficient, \underline{r}_o is a point at the patient surface, Φ is the primary fluence along the beam fan line through the position \underline{r}_o . The dose at a point \underline{r} is calculated by convolving TERMA with a density scaled energy deposition kernel,

$$D(\underline{r}) = \int \int T(\underline{r}', E) \frac{\rho(\underline{r}')}{\bar{\rho}} K(\bar{\rho} l(\underline{r} - \underline{r}'), \underline{r} - \underline{r}', E) d^3 r' dE, \quad (3)$$

where K is the energy deposition kernel, $\bar{\rho}$ is the average density along the path between the interaction and dose deposition sites, $l(\underline{r} - \underline{r}')$, $\underline{r} - \underline{r}'$ is the distance between interaction and dose deposition sites, and $\rho(\underline{r}')$ is the density of the interaction site. K is distorted by the radiological distance $\bar{\rho} l(\underline{r} - \underline{r}')$ from dose deposition point. The density scaling method was used to scale the energy deposition kernels to account for the effect of tissue inhomogeneities on the dose distribution.

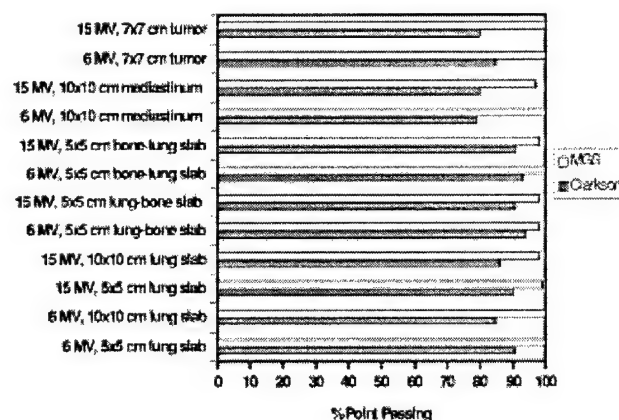


FIG. 2. (Color) A histogram showing the total number of Clarkson and MGS dose calculation points passing a 3% or 3 mm accuracy criteria versus BEAM.

RESULTS AND DISCUSSION

Figure 2 shows the total number of points that passed a 3% or 3 mm accuracy criteria for the Clarkson and MGS models, compared to BEAM, for all study beam setups and test phantoms. This is an overall quantitative assessment of the accuracy through reporting the total number of calculation points passing a 3% or 3 mm criteria. In general, the MGS model is more accurate than the Clarkson model in all phantoms with an average of 99% versus 87% for the Clarkson model.

Next, we will discuss the results of the quantitative evaluation for a qualitative evaluation. Specifically, the depth dose and isodose distributions in each test phantom were examined individually to study the effects of tissue inhomogeneities on dose distributions and to determine the accuracy of the algorithms under these various clinical situations. For the sake of brevity, we decided to present only the MGS model isodose results.

Lung slab phantom

Figures 3(a) and 3(b) show the Clarkson, MGS, and BEAM depth dose distributions and Figs. 3(c) and 3(d) show the MGS and BEAM isodose distributions in the lung phantom for the 5×5 cm², 6- and 15-MV beams. Figures 4(a)–4(d) show the same information for the 10×10 cm², 6- and 15-MV beams. Note that the BEAM MC dose distributions are not smooth as a consequence of the inherent random errors, or statistical uncertainty, contained in the calculations.²³

For this type of setup, the MGS results are within 3% or 3 mm of BEAM results. Note however, that the Clarkson model overestimates the dose by a maximum of 10% and 4%, compared to BEAM, in the lung for the 5×5 cm² and 10×10 cm² field sizes, respectively. The overestimation arises from the use of the effective path length correction which tends to boost the primary dose in the low density region without accounting for loss of scatter.

In reality, a deficit in dose in the lungs occurs, mainly due to two conditions presented inside the lungs: (i) the loss of scatter and (ii) electronic disequilibrium, especially for higher energies and small field sizes as shown in Fig. 3. This is due to the increase of the ratio of primary to scatter radiation. With higher energy beams, there is a reduction in the number of scattered photons. Further, more energy is carried away by primary electrons from the low density lung region than re-enters from the off-axis direction. The increase of primary photons in lung also results in an increase (build-up) in the dose when radiation penetrates through the water region below the lung slab as shown in Fig. 3(b). The effect of lung inhomogeneity along central-axis dose distribution increases with smaller field sizes and higher energies.

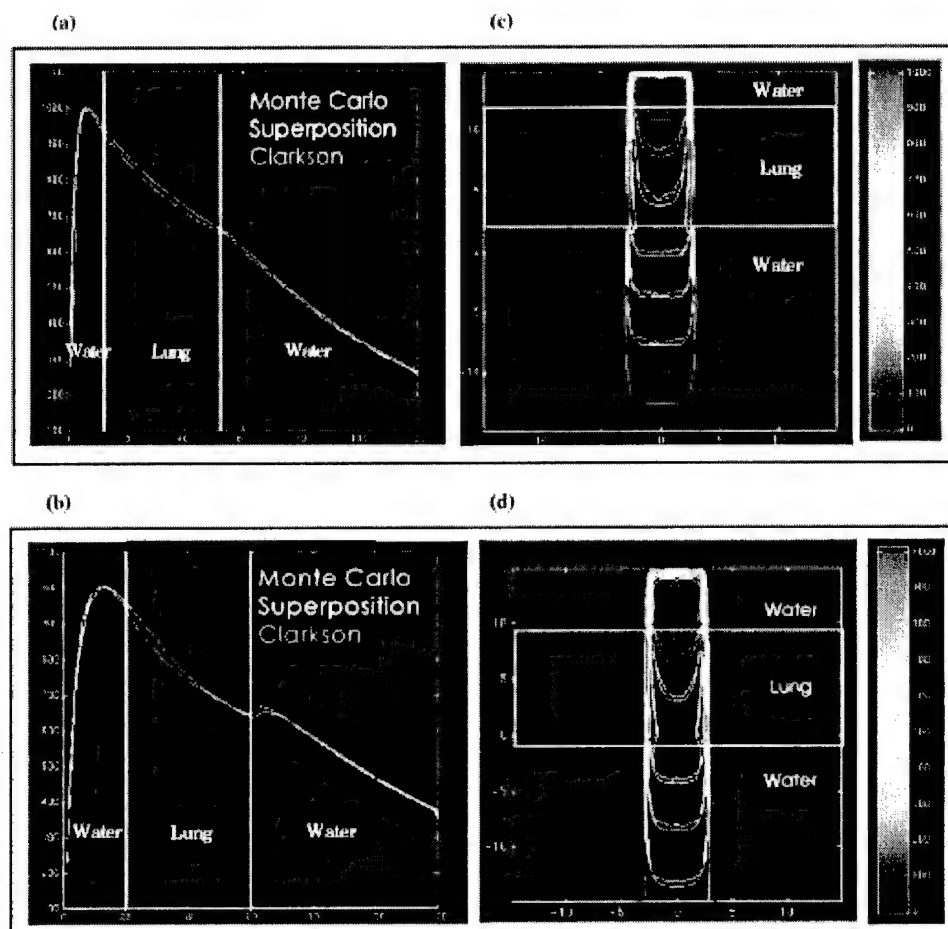


FIG. 3. (Color) Depth dose distributions for the Clarkson, MGS, and BEAM in the lung phantom, (a) 5×5 cm², 6-MV beam, (b) 5×5 cm², 15-MV beam. Isodose distributions for the MGS and BEAM along a central-axis transverse plane, (c) 5×5 cm², 6-MV beam, (d) 5×5 cm², 15-MV beam.

The MGS model can account for most of these effects by scaling the energy deposition kernels using the density scaling method as we observed in the figures. The Clarkson model, using only the effective path length correction for the primary radiation, does not account for these scatter effects and therefore yields inaccurate results.

The protuberance of the 3% and 5% isodose lines in lung, as shown in Figs. 3(c) and 3(d), is modeled correctly using the MGS algorithm. The bulge of low isodose lines is due to the fact that higher energy photons set primary electrons in motion with higher energy resulting in an increased electron range, especially in low density materials. The increase in the lateral range of electrons and scattered photons in low density regions causes an increase in the lateral range of dose. This usually results in penumbra broadening in low density regions such as lung, especially for small field sizes and higher energy beams.

Lung-bone and bone-lung slab phantoms

Figures 5(a) and 5(c) show the depth dose distribution and isodose lines for 5×5 cm², 15-MV beams in the lung-bone slab phantom. Figures 5(b) and 5(d) show the dose distributions for the same beam setup in the bone-lung slab phantom.

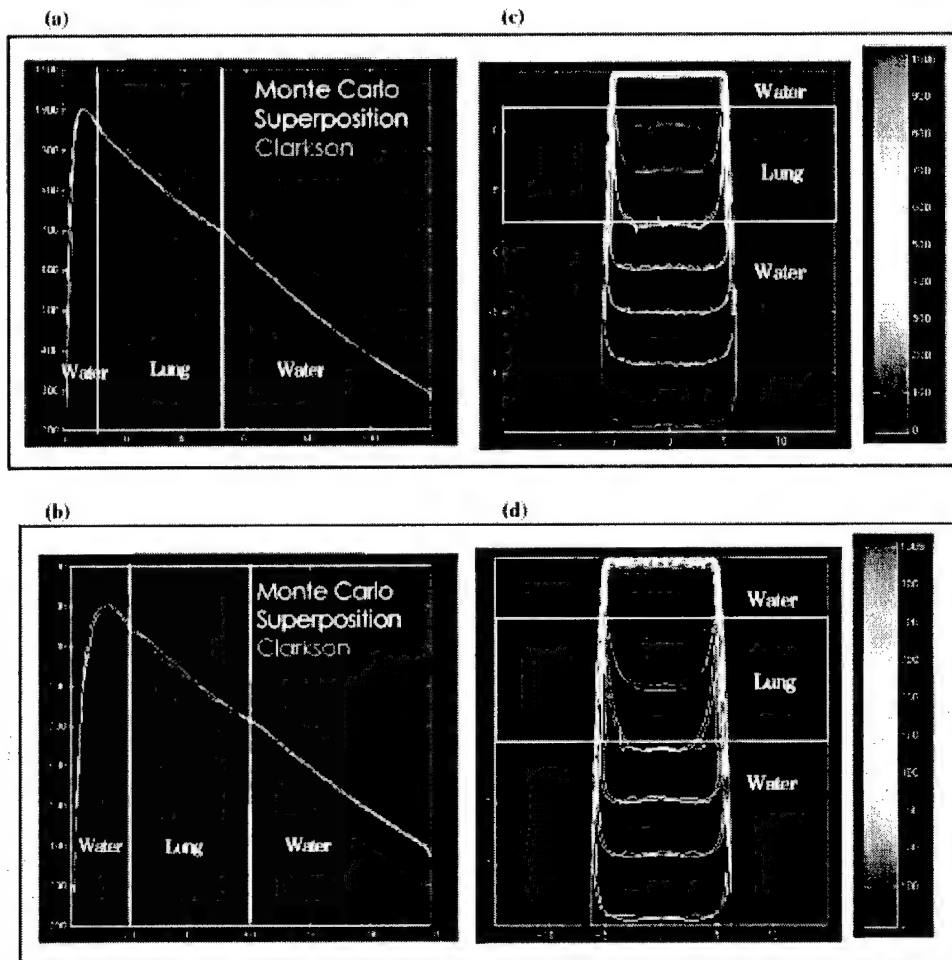


FIG. 4. (Color) Depth dose distributions for the Clarkson, MGS, and BEAM in the lung phantom, (a) $10 \times 10 \text{ cm}^2$, 6-MV beam, (b) $10 \times 10 \text{ cm}^2$, 15-MV beam. Isodose distributions for the MGS and BEAM along a central-axis transverse plane, (c) $10 \times 10 \text{ cm}^2$, 6-MV beam, (d) $10 \times 10 \text{ cm}^2$, 15-MV beam.

In these phantoms, the MGS model is more accurate than Clarkson in the lung and bone structures. The increased accuracy for the MGS model is due to the correct modeling of the inhomogeneities effects on scatter radiation in the MGS algorithm, using the density scaling method. In the bony structure, both models generate results within 3% of BEAM. The reason for this agreement is that most electrons set in motion by photons deposit the energy locally due to the high density of bone which limits electron range. Note that the Clarkson model, MGS model, and BEAM assume that the bone material is equivalent to water (i.e., same atomic properties) in the dose calculations. Larger differences between the MGS and BEAM would be expected if we had modeled the materials as nonwater equivalent in the BEAM calculations, especially near bone interfaces.

The differences observed in the lung slab phantom, using the Clarkson model, in the build-down and build-up regions are also observed in the lung-bone and bone-lung phantoms. There are no interface effects after the radiation penetrates the water below the bone in the lung-bone phantom. The reason for this behavior is the reduction of both primary and scatter radiation in bone due to attenuation.

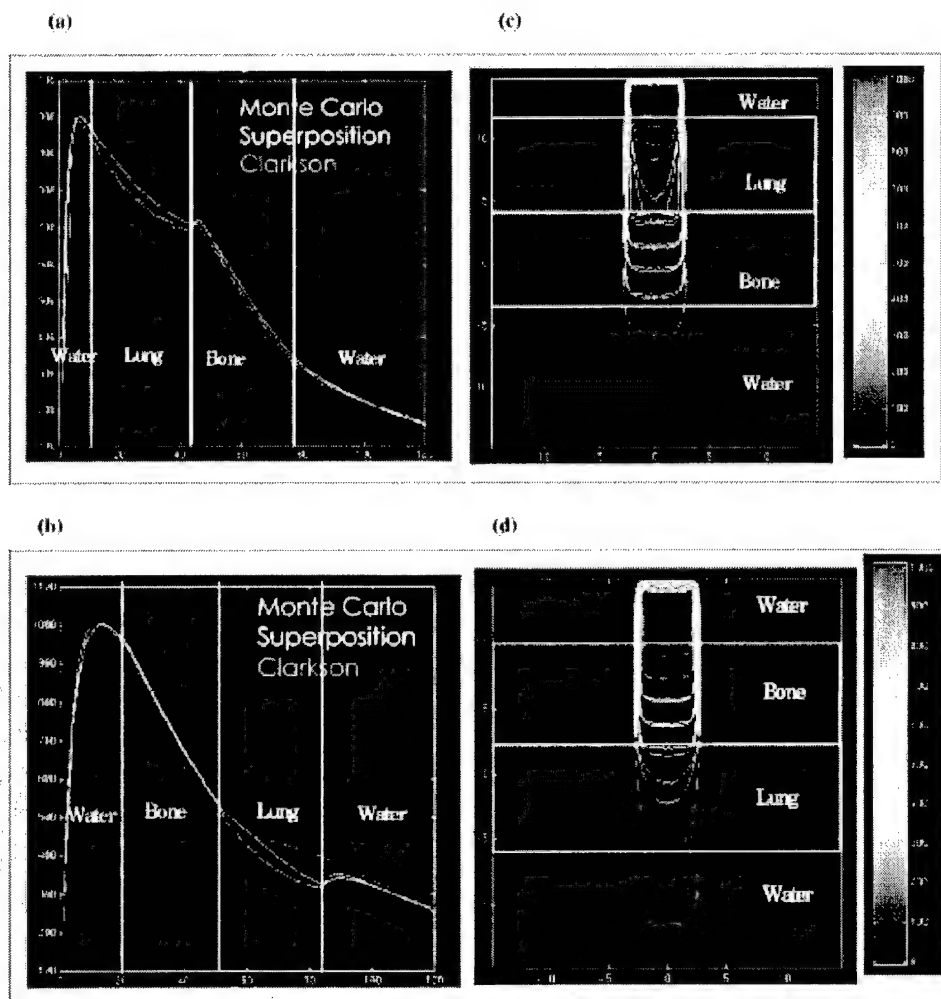


FIG. 5. (Color) Depth dose distributions of the Clarkson, MGS, and BEAM for $5 \times 5 \text{ cm}^2$, 15-MV beam in the (a) lung-bone phantom, (b) bone-lung phantom. Isodose distributions for the MGS and BEAM along a central-axis transverse plane for $5 \times 5 \text{ cm}^2$, 15-MV beam in the (c) lung-bone phantom, (d) bone-lung phantom.

Mediastinum phantom

Figures 6(a)–6(d) show the depth dose and isodose lines in the two-lung geometry for $10 \times 10 \text{ cm}^2$ 6-MV and 15-MV beams. The phantom shape alters the scatter contribution to the central-axis without modifying the primary radiation along the central axis. Therefore, comparing dose calculation models along the central axis only for such type of phantom may lead to incorrect conclusions on the accuracy of models.

The MGS model agrees with BEAM along the central-axis and the Clarkson model overestimates the dose. The dose distributions inside the lung and at the lateral interfaces show that the MGS model predicts the penumbra broadening inside the lung and the build-down and build-up along the interfaces, especially for the 15-MV beam.

Tumor phantom

The tumor geometry shown in Figures 7(a)–7(d) depicts a clinical setting of treating a tumor inside the lung using a $7 \times 7 \text{ cm}^2$ field. The MGS model is more accurate than the Clarkson along

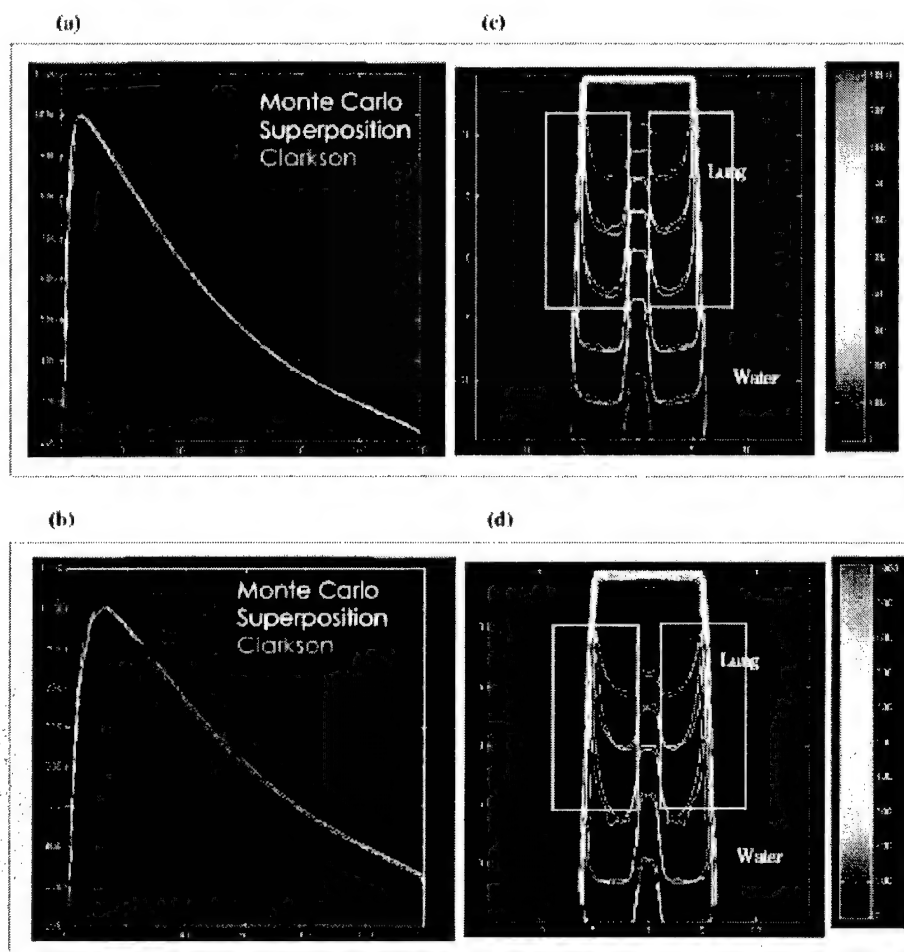


FIG. 6. (Color) Depth dose distributions for the Clarkson, MGS, and BEAM in the mediastinum phantom, (a) 10×10 cm², 6-MV beam, (b) 10×10 cm², 15-MV beam. Isodose distributions for the MGS and BEAM along a central-axis transverse plane, (c) 10×10 cm², 6-MV beam, (d) 10×10 cm², 15-MV beam.

the central axis. The results show the MGS model is within 2% for 6 MV and 3% for 15 MV, compared to BEAM. Further, the isodose distributions in Figures 7(c) and 7(d) show that the MGS predicts the doses correctly along and beyond the inhomogeneity in the lateral direction. In contrast, the Clarkson model overestimates the dose in the lung by a maximum of 6% in the tumor and by a maximum of 10% in lung for the 15-MV beam.

These results clearly show that using the Clarkson model (with only the effective path length correction) overestimates the dose in lung and target. This may lead the "treatment planner" to reduce the dose in order to reduce lung complications. Consequently, this may result in underdosing the target. Therefore, inhomogeneity correction, based only on the effective path length correction, should not be used for Clarkson-type algorithms in lung treatments because it may lead to inaccurate calculations. The results and analysis presented so far suggest treating the patient as a unit density medium in order to avoid underdosing the target. Furthermore, the results indicate that using model-based algorithms for heterogeneous calculations, such as the MGS model, is necessary to achieve accurate dose distributions in lung treatments.

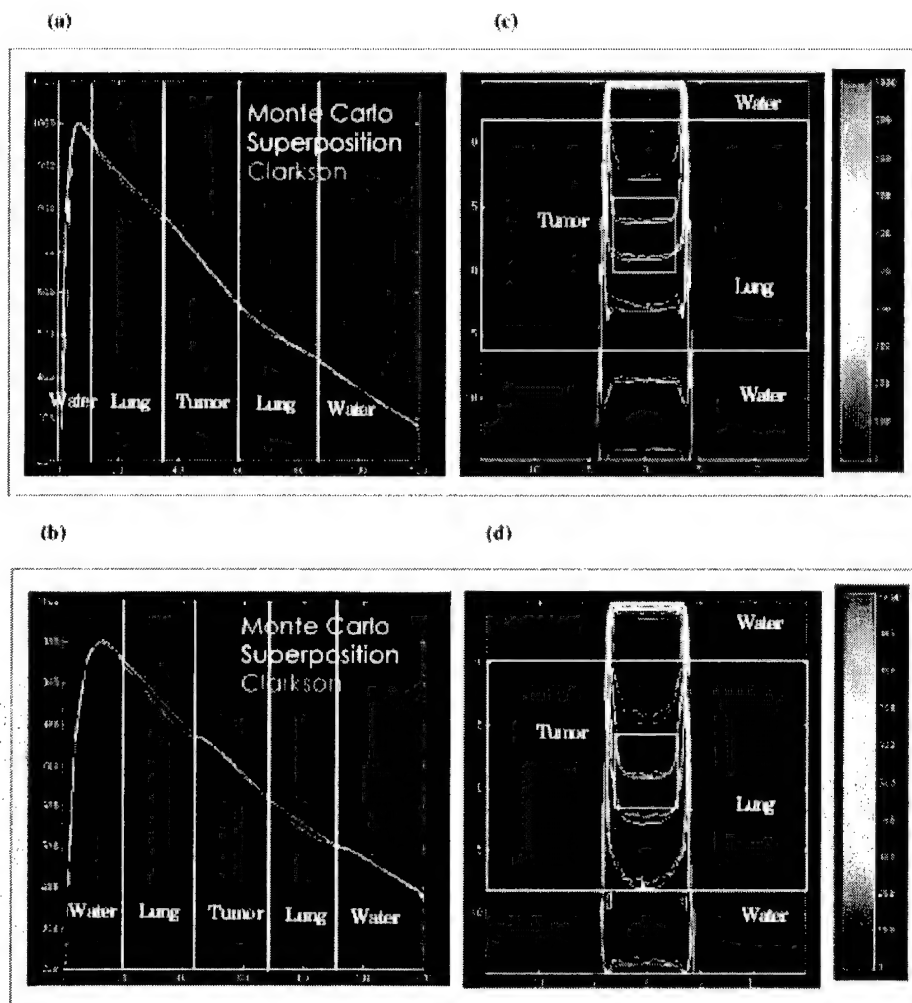


FIG. 7. (Color) Depth dose distributions for the Clarkson, MGS, and BEAM in the tumor phantom, (a) 7×7 cm², 6-MV beam, (b) 7×7 cm², 15-MV beam. Isodose distributions for the MGS and BEAM along a central-axis transverse plane, (c) 7×7 cm², 6-MV beam, (d) 7×7 cm², 15-MV beam.

CONCLUSIONS

Accurate dose calculation models in RTP systems are a vital link in the radiotherapy treatment planning process. We compared dose distributions from the FOCUS Clarkson and FOCUS MultiGrid Superposition (MGS) models with those from the BEAM Monte Carlo simulation system in heterogeneous phantoms. The results confirmed that the MGS model and BEAM doses are within 3% or 3 mm, and the MGS model is more accurate than the Clarkson model in heterogeneous phantoms. Furthermore, the results suggest turning-off the effective path length inhomogeneity correction for lung treatments using the measurement-based Clarkson model and demonstrate the importance of using the model-based MGS algorithm for heterogeneous dose calculations.

*Email address: miften@radonc.duke.edu

†Email address: markw@cms-stl.com

‡Current address: GE Corporate Research and Development, Clifton Park, NY 12065. Email address: kapur@crd.ge.com

§Email address: cma@reyes.stanford.edu

- ¹R. Mohan, in *Proceeding of the XIIth International Conference On the Use of Computers in Radiation Therapy*, edited by Leavitt and Starkschall (Medical Physics Publishing, Salt Lake City, 1997), pp. 16–18.
- ²J. R. Cunningham, P. N. Shrivastava, and J. M. Wilkinson, "Program IRREG-calculation of dose from irregularly shaped radiation beams," *Comput. Programs Biomed.* **2**, 192 (1972).
- ³T. R. Mackie, J. W. Scrimger, and J. J. Battista, "A convolution method of calculating dose for 15 MV x-rays," *Med. Phys.* **12**, 188–196 (1985).
- ⁴R. K. Rice, B. J. Mijneer, and L. M. Chin, "Benchmark measurements for lung dose corrections for x-ray beams," *Int. J. Radiat. Oncol., Biol., Phys.* **15**, 399–409 (1988).
- ⁵J. E. O'Connor, "The variation of scattered x-rays with density on an irradiated body," *Phys. Med. Biol.* **1**, 352–369 (1957).
- ⁶M. K. Woo and J. R. Cunningham, "The validity of density scaling method in primary electron transport for photon and electron beams," *Med. Phys.* **17**, 187–194 (1990).
- ⁷P. Keall and P. Hoban, "Accounting for primary electron scatter in x-ray beam convolution," *Med. Phys.* **22**, 1413–1418 (1995).
- ⁸M. Miften, M. Wiesmeyer, and K. Krippner, "A Fermi-Eyges based 3D kernel scaling model to account for primary electron transport in superposition photon dose calculations," *Med. Phys.* **25**, A188 (1998).
- ⁹T. R. Mackie, E. El-Khatib, J. Battista, J. Scrimger, J. Van Dyk, and J. R. Cunningham, "Lung dose corrections for 6- and 15-MV x-rays," *Med. Phys.* **12**, 327–332 (1985).
- ¹⁰J. W. Wong and J. A. Purdy, "On methods of inhomogeneity corrections for photon transport," *Med. Phys.* **17**, 807–814 (1990).
- ¹¹C. G. Orton, P. M. Mondalek, J. T. Spicka, D. S. Herron, and L. I. Anders, "Lung corrections in photon beam treatment planning: are we ready?," *Int. J. Radiat. Oncol., Biol., Phys.* **10**, 2191–2198 (1984).
- ¹²W. G. McKenna, K. Yeakel, A. Klink, B. A. Fraass, J. Van de Geijn, E. Glatstien, and A. Lichter, "Is correction for lung density in radiotherapy treatment planning necessary?," *Int. J. Radiat. Oncol., Biol., Phys.* **13**, 273–278 (1987).
- ¹³K. Mah and J. Van Dyk, "On the impact of tissue inhomogeneity corrections in clinical thoracic radiation therapy," *Int. J. Radiat. Oncol., Biol., Phys.* **21**, 1257–1267 (1991).
- ¹⁴E. E. Klein, A. Morrison, J. A. Purdy, M. V. Graham, and J. Matthews, "A volumetric study of measurements and calculations of lung density corrections for 6 and 18 MV photons," *Int. J. Radiat. Oncol., Biol., Phys.* **37**, 1163–1170 (1997).
- ¹⁵M. Miften, M. Wiesmeyer, S. Monthofer, and K. Krippner, "Implementation of FFT convolution and multigrid superposition models in the FOCUS RTP system," *Phys. Med. Biol.* **45**, 817–833 (2000).
- ¹⁶D. W. O. Rogers, B. A. Faddegon, G. X. Ding, C. M. Ma, J. We, and T. R. Mackie, "BEAM: A Monte Carlo code to simulate radiotherapy treatment units," *Med. Phys.* **22**, 503–524 (1995).
- ¹⁷J. W. Wong and R. M. Henkelman, "A new approach to CT-pixel-based photon dose calculations in heterogeneous media," *Med. Phys.* **10**, 199–208 (1983).
- ¹⁸W. R. Nelson, H. Hirayama, and D. W. O. Rogers, "The EGS4 code system," Stanford Linear Accelerator Center, Publication No. 265, 1985.
- ¹⁹R. Mohan, C. Chui, and L. Lidofsky, "Energy and angular distributions of photons from medical linear accelerators," *Med. Phys.* **12**, 592–597 (1985).
- ²⁰T. R. Mackie, A. F. Bielajew, D. W. O. Rogers, and J. J. Battista, "Generation of photon energy deposition kernels using the EGS Monte Carlo code," *Phys. Med. Biol.* **33**, 1–20 (1988).
- ²¹A. Ahnesjö, P. Andreo, and A. Brahme, "Calculation and application of point spread functions for treatment planning with high energy photon beams," *Acta Oncol.* **26**, 49–55 (1987).
- ²²C.-M. Ma, E. Mok, A. Kapur, T. Pawlicki, D. Findley, S. Brain, K. Forster, and A. L. Boyer, "Clinical implementation of a Monte Carlo treatment planning system," *Med. Phys.* **26**, 2133–2143 (1999).
- ²³P. J. Keall, J. V. Siebers, R. Jeraj, and R. Mohan, "The effect of dose calculation uncertainty on the evaluation of radiotherapy plans," *Med. Phys.* **27**, 478–484 (2000).
- ²⁴C. M. Ma, "Characterization of computer simulated radiotherapy beams for Monte Carlo treatment planning," *Radiat. Phys. Chem.* **53**, 329–344 (1997).
- ²⁵A. Kapur, "Monte Carlo dose calculations for clinical electron and intensity modulated photon beams in radiotherapy," Ph.D. Thesis, Stanford University, Stanford, USA, 1999 (unpublished).

Modulated Electron Radiation Therapy (MERT): A Novel Treatment Modality for Parotid Cancers

Yulin Song, Ph.D.¹, Arthur L. Boyer, Ph.D.^{1*}, Todd Pawlicki, Ph.D.¹, Lei Xing, Ph.D.¹,
Steve Jiang, Ph.D.², Yulong Yan, Ph.D.¹, C-M Charlie Ma, Ph.D.⁴, and Michael C. Lee, Ph.D.³

¹Department of Radiation Oncology
Stanford University School of Medicine
300 Pasteur Drive, Stanford, CA 94305

²Department of Radiation Oncology
Massachusetts General Hospital
Harvard Medical School
100 Blossom Street, Boston, MA 02114

³Department of Radiology
University of California at San Francisco
505 Parnassus Avenue, San Francisco, CA 94115

⁴Department of Radiation Oncology
Fox Chase Cancer Center
7701 Burholme Avenue, Philadelphia, PA 19111

Running Title Header: Radiotherapy for Parotid Cancers

Keywords: Monte Carlo, IMRT, MERT, EMLC, MLC, and Parotid Cancer

***Address Correspondence to:**

Arthur L. Boyer, Ph.D., Director and Professor
Division of Radiation Physics
Department of Radiation Oncology
300 Pasteur Dr., Room H0144
Stanford University School of Medicine
Stanford, CA 94305-5304
Tel: (650)-723-5549
Fax: (650)-498-5008
E-mail: boyer@reyes.stanford.edu

Abstract

In this study, we investigated treating parotid cancers using modulated electron radiation therapy (MERT) and compared MERT plans with photon beam intensity-modulated radiation therapy (IMRT) in terms of target dose coverage and normal tissue sparing. To deliver MERT plans effectively, we developed a prototype MERT delivery device – an electron multileaf collimator (EMLC) for routine clinical implementation of MERT.

The prototype electron multileaf collimator was fabricated by modifying a conventional 25 x 25 cm² electron applicator (Varian Medical Systems, Palo Alto, CA). Electron beams produced by a medical linear accelerator (Clinac 2100C, Varian Medical Systems, Palo Alto, CA) and collimated by this EMLC were simulated using the EGS4/BEAM code. The simulations were based on the manufacturer's specifications of the beam production system and the electron applicator design. The MERT plans with three coplanar beams (205⁰, 235⁰, and 255⁰) and five nominal energies (6, 9, 12, 16, 20 MeV) were created using modified EGS4/MCDOSE code. The corresponding IMRT plans with five coplanar beams were computed using a commercial treatment planning system (CORVUS, NOMOS Corp, Sewickley, Pennsylvania). Our preliminary data indicated that MERT was able to provide at least similar or better target dose coverage and uniformity compared with photon beam IMRT. However, MERT can significantly reduce the dose to critical structures. In the cases we studied, the maximum doses to the orbits, brainstem, optic chiasm, and spinal cord were reduced by 3.0, 16.2, 11.5, and 19.6 Gy, respectively, for a 50.0 Gy target dose, suggesting a distinct normal tissue sparing advantage for MERT.

Introduction

Each year, about 70,000 new head and neck cases were diagnosed in the United States (1) and tumors of the parotid gland are the most frequently encountered salivary gland tumors, accounting for about 3% of total head and neck cancers (2). Currently, the most widely used treatment is a combination of surgery and adjuvant postoperative radiotherapy for the malignant salivary tumors (3, 4). The minimally required operation for tumors of the parotid gland is a superficial parotidectomy with careful identification and preservation of the facial nerve (5). The parotid gland has two lobes, a superficial lobe and a deep lobe. Most tumors are located in the superficial lobe of the parotid gland and can be excised easily. Retrospective studies have indicated that this combined modality treatment can reduce the local recurrence rate by 5 - 40% (6, 7).

However, in certain situations, such as high surgical risk of damage to the facial nerve, advanced inoperable cancers, unfavorable cosmetic outcome after surgery, lymph node metastases, and deep-lobe malignant tumors, radiotherapy should be the preferred treatment (5). Because of its proximity to many critical structures, such as the oral cavity, brainstem, auditory apparatus, spinal cord, optical nerves, and the lenses of the eyes, parotid cancer treatment using radiation still remains a very challenging task. Currently, the most commonly used radiotherapy techniques for the treatment of the parotid cancers are: 1) an ipsilateral wedged pair of 6 MV photon beams oriented at oblique angles to encompass the entire parotid bed, 2) an ipsilateral field treated with high energy electrons (12, 16 or 20 MeV), and 3) a combination of high energy photon and electron beams (6 MV + 12 or 16 or 20 MeV) with proper weighting (8, 9, 10) (Figure 1). However, all these techniques have drawbacks. The first technique gives a low radiation dose to the contra-lateral parotid gland and high doses to the oral cavity, brainstem, cochlea, optical nerves, the lenses of the eyes, and spinal cord. In addition, because relatively high energy photon beams are used, the slow build-up effect of the photon beams results in a low skin dose. This is not acceptable for the treatment of the majority of the parotid cancers

because most parotid cancers are located in the superficial lobe of the parotid gland. Although high energy electrons may be the best in terms of normal tissue sparing, it is impossible to achieve depth dose conformity with a single electron energy only. The third technique typically employs a high energy electron beam (12-20 MeV) and a single 6 MV photon beam. However, good matching of photon and electron beams is not easy to achieve and poor matching may produce areas of high inhomogeneity within the tumor dose distribution.

Recently, with the availability of photon beam intensity modulated radiation therapy (IMRT) and computer-controlled multileaf collimators (MLC), there has been wide interest in using photon beam IMRT to treat head and neck cancers and parotid cancers in particular (9, 11-16). A common feature of the head and neck cancers is their complex geometry. IMRT has shown potential to produce a highly conformal dose distribution around the concave-shaped target volumes and a steep dose gradient near the organs at risk (OAR). These characteristics can spare radiosensitive normal structures and reduce complication rates (17-19). In addition, there has been an effort to exploit IMRT to improve local-regional tumor control through dose escalation. Now, many commercial inverse treatment planning systems and MLCs are available.

Although the photon beam IMRT is a powerful tool for treating the parotid tumors that extend deeply into tissue below the skin surface, it is not suitable to treat very shallow targets due to the low surface doses and large depth of photon beam penetration. For photon beam IMRT, the slow attenuation of photon beams can still deliver a high dose to the critical structures that are far from the target. A promising alternative approach is modulated electron radiation therapy (MERT) (20-21). The rapid dose falloff of electron beams makes electron therapy an attractive treatment modality for some shallow targets such as parotid tumors. Conceptually, each MERT plan consists of multiple ports (gantry angles) with different electron energies (energy modulation) and optimized beam intensity (intensity modulation). Dose conformity in the depth direction

may be achieved by electron energy modulation, which is unique to MERT. Dose conformity and uniformity in the lateral direction may be achieved by intensity modulation using an electron-specific MLC (EMLC). Through both intensity and energy modulations, MERT is capable of delivering highly conformal doses to targets with complex shapes and of sparing surrounding normal tissue, particularly, the distal critical structures.

However, because of severe electron in-air scattering, the conventional photon beam MLC is not suitable for the delivery of MERT plans. To deliver MERT plans effectively, we designed and manufactured a prototype EMLC based on the results of Monte Carlo simulations and a conventional Varian 25 x 25 cm² electron applicator (22). Based on the manufacturer's specifications of the beam production system and the EMLC design, electron beams collimated by this EMLC were simulated for a Varian Clinac 2100C linear accelerator using the EGS4/BEAM code (23, 24). Subsequently, using the simulated electron beams, MERT plans for parotid cancers were created. In the present study, we investigated the possibility of treating parotid tumors using modulated electron radiation therapy by comparing MERT plans with corresponding photon beam IMRT plans in terms of target dose coverage and normal tissue sparing.

Materials and Methods

Electron MLC

We have previously reported a prototype manually-driven electron specific MLC for the delivery of MERT plans (20, 21). Ideally, the EMLC leaves should be placed in such a position that the bottom of the leaves is as close to the patient skin as possible in order to produce a clinically acceptable field. However, because of the existing electronic circuitry used to detect the insertion of the electron cutout at the last scraper of a standard Varian 25 x 25 cm² electron applicator, it was impossible to place the EMLC leaves at that position without changing the existing electron applicator design significantly. Thus,

initially, the steel frame of the EMLC leaves was temporally inserted into the electron cutout mount and the leaves were placed about 1 cm above the last scraper. This configuration resulted in a 10 cm air gap between the bottom of the EMLC leaves and the patient skin for a nominal 100 cm source-surface distance (SSD) (**Figure 2 (A)**). To further lower the EMLC leaves and, thus, reduce in-air electron scattering and the penumbra, we have now removed the entire last scraper of the electron applicator and its electronic accessories. The EMLC frame was placed at the bottom of the modified electron applicator and stabilized with eight screws. This modification reduced the air gap to 5.0 cm between the bottom of the EMLC leaves and the patient skin (**Figure 2 (B)**). Since the electronic circuitry for detecting the electron cutout was completely removed, we were able to avoid activating interlocks associated with electron beam accessory malfunction while inserting the EMLC assembly into the linac treatment head. Thus, even if the linac was in the electron mode, the gantry could still be rotated, making the delivery of MERT plans with multiple beam angles possible.

MERT Plans

Based on manufacturer's specifications of the beam production system and the electron applicator design, electron beams produced by a Varian Clinac 2100C linear accelerator and collimated by the EMLC were simulated using the EGS4/BEAM code. Monte Carlo simulations were carried out using a group of 22 Pentium Pro CPUs (200 MHz) and 10 Pentium III CPUs (450 MHz), all running EGS4/BEAM, MCDOSE (**23**, **24**), and their utilities under the Linux operating system. All simulation parameters, such as the electron and photon energy cutoffs (ECUT and PCUT), the maximum fractional energy loss per electron step (ESTEPE), and the number of initial electron histories, were specified in the EGS4/BEAM input file. In this study, we used ECUT = 700 KeV and PCUT = 10 KeV, below which all remaining energy was assumed to deposit on the spot. ESTEPE was set to 0.04. The EMLC was included in the EGS4/BEAM simulations as an MLC component module. The number of initial electron histories ranged from 2-30 million, depending on the electron energy. Phase space data were scored at a plane of 100

cm SSD after the particles had transported through the linac treatment head, the EMLC, and the air gap beneath it. Based on this simulated electron beam, the MERT plans were then created using our modified EGS4/MCDOSE code.

The CT scans of representative parotid cancer patients were obtained from our department's patient database. The CT images were acquired with the patients in supine position. During CT scanning, a thermoplastic facial mask with three fiducials was used for the purpose of patient immobilization and target localization for the subsequent treatments. For each patient, about 90 images with a slice thickness of 3.0 mm were acquired over the entire treatment area. Each CT image had an in-plane resolution of 512 x 512 pixels, with each voxel being $0.94 \times 0.94 \times 3.0 \text{ mm}^3$ in size. The CT images were transferred to an AcQSim system (Marconi Medical Systems, Inc., Cleveland, OH) for further processing. The clinical tumor volume (CTV) and critical structures were contoured on the axial CT images by a radiation oncologist using the AcQsim workstation. The gross tumor volume (GTV) was defined based on diagnostic imaging and clinical findings. It consisted of gross primary and nodal tumors. The CTV was constructed by expanding the GTV 1.0 cm in all directions to cover microscopic extension of the tumor. The PTV was obtained by adding a 0.5 cm margin uniformly to CTV to account for patient setup uncertainty and organ shift. Like photon beam IMRT, any structures whose dose needed to be kept below a certain limit or whose statistics were to be calculated in the MERT plan had to be contoured. Only those targets and structures that were contoured were considered in the plan and included in the final statistics. In addition, in order for our MERT inverse planning programs to work properly, all regions of interest were delineated as separate structures. No structure overlapping was allowed for the current version of our programs. In this study, the critical structures to be protected were the spinal cord, brainstem, optical chiasm, optical nerve, and orbits. The CT images, along with the outlined structures, were transferred to a workstation using the DICOM 3.0 format and then converted into a format that was compatible with EGS4/MCDOSE code so that they could be sent to our designated

Monte Carlo treatment planning machines. The final CT images used in MERT planning had an in-plane resolution of 128×128 pixels with a voxel size of $0.35 \times 0.35 \times 0.30 \text{ cm}^3$ that balanced resolution with the Monte Carlo dose calculation time. Additionally, the CT numbers were converted into mass densities and material types for Monte Carlo simulations. Based on the CT numbers, each voxel was designated as being one of the three materials: air, tissue or bone. This provided the approximate effective atomic numbers, cross-sections, and stopping powers for each voxel.

Figure 3 shows the simplified MERT planning flowchart. To facilitate the description of the flowchart, we will use the term *field* to specify each beam angle/electron energy combination and reserve the term *port* to indicate a single beam orientation (gantry angle). Thus, a plan in which five electron energies are delivered at a single gantry angle may be said to have one port and a total of five fields. In this study, the MERT plans consisted of three ports and a total of fifteen fields, as summarized in **Tables 1 and 2**. Like the photon beam IMRT, the first step in creating a MERT plan was to select a set of suitable beam orientations, i.e., gantry angles, to fully cover the target volume while sparing the adjacent critical structures as much as possible. Each port was then divided into $1.0 \times 1.0 \text{ cm}^2$ beamlets, i.e., the smallest beam elements for dose calculation. This means that beam intensity within a $1.0 \times 1.0 \text{ cm}^2$ beamlet could not be further differentiated. The beamlet size was defined at the isocenter plane. The goal of this step was to determine how many beamlets were required to simulate for each port. The user specified the isocenter, gantry, collimator, and couch angles, the desired beamlet size, and the dimension of the search space. A program calculated which beamlets intersected the target and created a text file containing these beamlets and their coordinates. This file was used by MCDOSE to pre-calculate the beamlet dose kernels. The total number of beamlets was the sum of the beamlets over all ports. A beamlet could be turned off, i.e., assigned a weight of zero, but continued to remain active throughout optimization. After the selection of a proper set of beam angles, we needed to decide which electron energies to use for each beam angle. To do so, we computed a tumor

depth map for each beam angle, whose pixel size was the same as that of a beamlet, i.e., $1.0 \times 1.0 \text{ cm}^2$. Based on the tumor depth distribution and assuming that the electrons lost energy at about 2 MeV/cm in tissue, we were able to determine a suitable set of electron energies for each beam angle. Since, in most of the cases, the target was not spherical in shape, different beam angles could have different sets of electron energies. The obvious advantage of this approach was the removal of those electron energies that contributed less to the target dose and, thus, the reduction in the number of fields used and delivery time.

The next step was to calculate beamlet dose kernels using MCDOSE. The beamlet dose kernel was the Monte Carlo calculated dose array for all structures due to a single beamlet. Each element of the dose kernel represented the dose delivered to a dose calculation point or voxel assuming a unit beamlet weight. These values are also referred to as dose deposition coefficients. Thus, the purpose of this step was, given a set of unit beamlet weights, to calculate the dose distribution in every structure that we were interested in. To optimize beamlet weights or intensity maps, a quadratic objective function augmented with dose-volume constraints was constructed. This was based on the assumption that there existed a quadratic relationship between the delivered dose and the biological effect. The overall objective function contained a linear component for each structure. Within each structure, each of the individual constraints contributed linearly to the objective function. Following the construction of the objective function, the optimization of beamlet weights was initiated. The core of the optimization procedure was the well-known conjugate gradient search algorithm. A complete description of the conjugate gradient search algorithms may be found in any number of sources. The major advantage of the gradient search technique was its fast convergence speed, as compared to stochastic optimization techniques, such as simulated annealing. We believe that the gradient search algorithm was a good choice for future routine clinical implementation of MERT. During the optimization, care was exercised to avoid negative weights. These non-physical results were eliminated by scaling step sizes to avoid stepping over the

boundary of the acceptable solution space and by projecting gradients onto the boundaries.

Following the beamlet weight optimization, the resulting fifteen optimized continuous intensity maps were stratified into five discrete intensity levels in preparation for leaf sequencing. The fifteen discrete intensity maps were then converted to fifteen step-and-shoot leaf sequences (26) based on the technique proposed by Bortfeld et al. (27). Since the dose distribution delivered by the ideal beamlets could be different from that delivered by the leaf sequences, A Monte Carlo dose calculation was performed again based on the fifteen discrete intensity maps reconstructed from the corresponding fifteen leaf sequences. With these new dose kernels, the leaf sequence segment weights were re-optimized. This second optimization differed from the first one in two aspects. The first optimization was entirely based on idealized beamlets, without considering the EMLC geometry, while the second optimization took into account not only the EMLC geometry, but also leaf end transmission and Bremsstrahlung leakage. Thus, the first optimization produced the best dose distribution possible, while the second one gave the actual delivered dose.

The MERT plans with three coplanar beams (gantry angles: 205° , 235° , and 255°) were created using our modified EGS4/MCDOSE treatment planning system. The schematic layout of the beam orientations is shown in **Figure 4A**. The beam orientations were selected based on the goodness of target coverage by the beams. Each gantry angle or port was treated with five nominal electron energies (6, 9, 12, 16, and 20 MeV) separately. The intensities of each energy for each particular gantry angle were determined by the optimizer. The prescribed dose to the target was 50.0 Gy, with a conventional fractionation scheme of 2.0 Gy per fraction, 5 fractions per week, and 25 fractions in total. The goal of the treatment planning was to cover the entire target with isodose lines between 95% and 107% of the prescribed dose as recommended by ICRU Report No. 50 (25). Isodose lines were normalized to 55.0 Gy for all plans.

IMRT Plans

The CT images, together with the outlined structure set, were transferred from the AcQSim system to a commercial treatment planning system (CORVUS, NOMOS Corp, Sewickley, Pennsylvania). The corresponding photon beam IMRT plans were computed using our standard clinical protocol. As in the MERT planning, the PTV was defined by adding a 0.5 cm immobilization and localization uncertainty to the CTV. The CORVUS IMRT system allows the target volume to grow based on a user-specified positional uncertainty caused by tissue motion and setup errors. The isocenter of the beams was placed approximately at the geometric center of the target. The goal dose to the target was 50.0 Gy, with the minimum and maximum doses being 49.0 Gy and 54.0 Gy, respectively. The CORVUS IMRT system also allows the user to specify a percent target volume allowed below the goal dose. In this study, we used 4% for this value. For the critical structures, the limit dose ranged from 37.0 to 42.0 Gy, with the volume allowed above the limit dose being 5%. The maximum allowable dose to the critical structures was set to be 40.0 Gy. IMRT plans using other combinations of the dose volume constraints were also tried. It was found that above-described constraints optimized target dose coverage and conformity against critical structure sparing. The final IMRT plans consisted of five coplanar gantry angles, each being treated with a 4 MV photon beam. The gantry angles and beam energy were selected in such a way as to minimize unnecessary normal tissue and critical structure irradiation. However, in this study, beam orientations were not optimized. IMRT plans of different beam number and angle combinations were generated. Each of the plans was carefully reviewed and evaluated on the basis of target dose coverage and normal tissue sparing. Plan evaluation indicated that the plans with coplanar beams: 0° , 205° , 235° , 270° , and 320° gave the best results. Therefore, this beam arrangement was used in this study. Isodose lines were also normalized to 55.0 Gy for all IMRT plans. **Figure 4B** shows the IMRT beam orientations.

Tissue heterogeneity correction was performed during the beamlet intensity optimization and final dose calculation. Like the MERT planning system, the CORVUS IMRT system also uses an integral dose volume histogram-based cost function. The current version of the CORVUS IMRT software supports only one optimization technique, simulated annealing (28). To obtain the best possible beamlet intensities and thus, the optimal dose distribution, the optimizer mode was set to continuous. This mode determines the internal representation of the beamlet intensities and is, in general, the best choice for most treatment plans. All IMRT plans used in this study were created based on a Varian Clinac 2100C linear accelerator and delivered in the step-and-shoot mode. The machine was equipped with a 26-leaf pair photon MLC, capable of producing $1.0 \times 1.0 \text{ cm}^2$ beamlets.

Results and Discussion

Electron MLC

Figure 5 shows a photo of the EMLC assembly inserted on the treatment head of a Varian Clinac 2100C linear accelerator. The EMLC had 30 steel leaf pairs, with each leaf being 0.476 cm wide, 20.0 cm long, and 2.54 cm thick. Both sides and ends of the leaves were made parallel with the central beam axis. The maximum opening was $14.2 \times 15.5 \text{ cm}^2$ when all leaves were completely retracted, giving the largest radiation field of $15.0 \times 16.3 \text{ cm}^2$ projected at 100 cm SSD. The EMLC leaves could be pushed in and pulled out easily. For each of the beam segments, the corresponding field shape was obtained by manually positioning the leaves according to their coordinates, which were computed from the electron beam leaf-sequencing program. To set the field shapes more efficiently, currently, we first drew the field shapes on a piece of hard cardboard at a ratio of 1:1 and cut them out. The field shapes were then set using these pre-cut cardboard templates. In the near future, we will develop a faster and more accurate technique of setting field shapes.

In the past, attempts have been made to use a photon MLC for electron beam collimation (30). Using a photon MLC in this circumstance has its obvious advantages. On one hand, treatment planners could easily make plans that consist of both photon and electron beams. On the other hand, the plans could be delivered using the existing linear accelerators without any further capital investment. Unfortunately, because of the severe electron scattering in the air, the quality of the electron beam collimated by a photon MLC is significantly degraded and is no longer clinically useful. Here, we present a practical and viable approach to the electron beam collimation — an electron-specific MLC. Our results indicated that the newly modified EMLC was able to provide sufficient beam collimation for MERT plan delivery.

Intensity Maps

Figure 6A shows a 3-D beam's eye view of a representative parotid tumor viewed at the beam angle of 235° . **Figure 6B** shows the corresponding tumor depth map at the same beam angle, in which different pixel gray scale levels represent different depths of the target. Darker pixels indicate the area where the tumor extended deeper into the tissue at this particular beam angle. As clearly demonstrated in the tumor depth map, this case was a good candidate for a MERT treatment because the target was superficial and, in addition, it had an irregular boundary. Based on the tumor depth map, a histogram was created, showing the tumor depth distribution (**Figure 7**). Out of 115 pixels, 2 pixels had a mean depth of greater than 5.0 cm, 2 pixels had a mean depth between 4.0 and 5.0 cm, 20 pixels had a mean depth between 3.0 and 4.0 cm, and 43 pixels had a mean depth between 2.0 cm and 3.0 cm, 37 pixels had a mean depth between 1.0 and 2.0 cm, and 11 pixels had a mean depth between 0.0 and 1.0 cm. Thus, the electron beams of 12, 16, and 20 MeV would be the best choices for this case in terms of depth dose conformity at this beam angle.

However, for this preliminary study, we chose to use all available electron energies. **Figures 8A to 8E** show representative beam intensity maps for a MERT plan

for the 6, 9, 12, 16, and 20 MeV fields at the beam angle of 235^0 . In all figures, each pixel represents a $1 \times 1 \text{ cm}^2$ beamlet projected at the isocenter. Darker pixels indicate higher beam intensity levels, which correspond to a longer beam on time. White background indicates zero beam intensity. These are areas where beams were blocked all the time by the EMLC leaves. In reality, however, there was about 1% radiation leakage through the EMLC leaves. As can be seen in the intensity maps, the optimizer gave significant weights to the 12, 16, and 20 MeV fields, while small weights were assigned to the 6 and 9 MeV fields. It was these different electron energy weights that brought about the energy modulation. By carefully examining the intensity maps and the tumor depth map, we noticed that the MERT intensity maps largely reflected the tumor depth distribution. The superposition of these intensity maps yielded not only the optimal lateral dose conformity, but more importantly the optimal depth dose conformity. The numbers of segments needed to produce these intensity maps were 18 (for 6 MeV), 18 (for 9 MeV), 12 (for 12 MeV), 18 (for 16 MeV), and 14 (for 20 MeV), giving a total of 80 segments for this port. This number was comparable to the number of segments for a photon field in a typical IMRT head and neck plan. For comparison, the corresponding optimized photon beam IMRT intensity map for the 4 MV field at the same beam angle is shown in **Figure 8F**. This intensity map, actually consisting of two separate maps, was combined together manually. This was because the size of the target in the anterior-posterior direction was fairly large, the MLC leaves could not cover the entire target with one field only. Thus, this 235^0 port split into two sub-fields. Like the MERT intensity maps, each pixel in the photon beam IMRT map represents a $1 \times 1 \text{ cm}^2$ beamlet projected at the isocenter. Compared to its MERT counterparts, the photon beam IMRT intensity map shows a relatively uniform intensity distribution, indicating a lack of depth dose modulation. The combined photon beam IMRT intensity map required a total of 120 segments to deliver, divided into 62 and 58 segments for each sub-field, respectively. For both the MERT and the IMRT plans, we counted both “step” and “shoot” that were listed in the step-and-shoot leaf sequence files as a segment. Thus, in the case of the combined photon beam IMRT intensity map, it required 60 steps and 60 shoots to produce. Since

the delivery time is linearly proportional to the number of segments in a leaf sequence file, we can say that the MERT plan required relatively less time to deliver. It is worth pointing out that in this study, we used all five available electron energies, which, in most cases, is not necessary. Let us take the 6 and 9 MeV electron beams as examples. As shown in **Figures 8A and 8B**, the optimizer gave them very low weights. Their contributions to the dose distribution in the final MERT plan were not significant. Therefore, they could have been deleted from the plan, leaving only three electron beams in the plan. The final three leaf sequence files would have had less number of segments. The total delivery time would have been even less.

Dose Distributions

Figures 9A and 9D show the comparison of the MERT and IMRT isodose distributions for the central axial slices from a representative parotid cancer case. **Figures 9B and 9E** show the comparison of the isodose distributions for the central coronal slices from the same example. **Figures 9C and 9F** show the comparison of the isodose distributions for the central sagittal slices also from the same example. The isodose distributions are shown in color lines. In both plans, the isodose curves were normalized to 55.0 Gy, representing 10, 20, 30, 40, 50, 60, 70, 80, 90, and 100%, respectively. Only selected isodose lines are labeled in the figures. The red colored target in the IMRT plan represents the PTV, while the red colored target in the MERT plan represents the CTV. The final MERT dose distribution was computed based on 15 intensity maps reconstructed from corresponding 15 step-and-shoot leaf sequences. The beamlet size was $1 \times 1 \text{ cm}^2$ for both plans. It is evident from the isodose distributions that higher isodose lines covered the target fairly well in terms of conformity in both plans, with the MERT plan showing an overall better conformity for all isodose lines in all three anatomical planes. As to the lower isodose lines, the photon beam IMRT plan exhibited a relatively poor conformity. As anticipated, the exit doses of the photon beams penetrated much deeper regions than the doses delivered by the electron beams. This resulted in significant, but unnecessary doses to distal areas, including some of the critical structures.

This was clearly demonstrated in the axial and coronal slices of the IMRT plan, in which the 30% isodose line covered the spinal cord fully and the 40% isodose line covered the brain stem and the orbits partly,. In contrast, the corresponding MERT plan showed an excellent critical structure sparing because of the rapid falloff of the electron beams. The 30% isodose line covered only small portions of the spinal cord, the brain stem, and the right orbit. The left orbit was almost completely spared, as shown in **Figures 9D and 9E**. Thus, it is very clear that the MERT plan provided a better target dose coverage and homogeneity than the photon beam IMRT plan.

Dose-Volume Histograms (DVH)

To evaluate the plans objectively, we analyzed the cumulative dose-volume histograms (DVH) of the plans. The cumulative dose-volume histograms displayed quantitative statistical information about the target dose coverage and homogeneity and normal tissue sparing. Each cumulative DVH curve represents the fractional volume that received a particular dose or higher for that structure. It provides radiation oncologists and medical physicists with a very effective tool to evaluate completing treatment plans created with different parameters or even with different treatment planning systems (TPS). The DVHs for the target and the critical structures considered in this study from a representative parotid cancer case are shown in **Figure 10**. Based on the DVHs, it is evident that the MERT plan provided a more homogenous dose coverage to the target than the corresponding photon beam IMRT plan as the former's DVH is more vertical than the latter's. In the MERT plan, the maximum, minimum, and mean doses delivered to the CTV were 55.82, 40.50, and 50.32 Gy, respectively, while the corresponding doses delivered to the CTV in the IMRT plan were 60.38, 17.30, and 50.24 Gy, respectively, resulting in some undesirable hot and cold spots. Obviously, the photon beam IMRT plan exhibited some degree of dose inhomogeneity. In addition, in the photon beam IMRT plan, about 3% of the CTV received a dose of greater than or equal to 55 Gy and 5 % of the CTV received a dose of less than or equal to 45 Gy. In contrast, the MERT plan gave much better statistics. Less than 0.5% of the CTV received a dose of greater than or equal

to 55 Gy and approximately 1.5% of the CTV received a dose of less than or equal to 45 Gy. All these suggest that the MERT plan provide a better dose homogeneity. It has been known that conventional treatment modalities using electron beams exhibit a higher degree of dose inhomogeneity in comparison with photon beam techniques. In part, this is caused by tissue heterogeneity and skin surface irregularity. Here, we see that with electron energy and intensity modulations, it is possible to reduce the degree of dose heterogeneity and achieve a satisfactory dose distribution and uniformity.

Significant differences between the two DVHs for the critical structures indicated that the MERT plan also delivered much less doses to the critical structures than the photon beam IMRT plan. It is undoubtedly clear from **Figure 10** that the MERT plan showed a superior normal tissue sparing. The maximum, minimum, and mean doses to the spinal cord in the MERT plan were 16.62, 0.02, and 5.24 Gy, respectively, while the corresponding doses in the photon beam IMRT plan were 36.22, 0.60, and 17.50 Gy. Only 16% of the spinal cord volume in the MERT plan received a dose of greater than or equal to 10 Gy compared to 97% in the IMRT plan. Similar sparing for other structures were also observed in the MERT plan. The maximum, minimum, and mean doses given to the brainstem in the MERT plan were 13.65, 0.45, and 2.66 Gy, respectively. In contrast, the corresponding doses given in the photon beam IMRT plan were 29.88, 8.45, and 16.66 Gy, significantly higher than the doses delivered in the MERT plan. As to the orbits, both the MERT and the photon beam IMRT plans gave very low doses. Especially, the MERT plan delivered an extremely low dose to the contra-lateral orbit, with the maximum, minimum, and mean doses being 0.15, 0.01, and 0.05 Gy, respectively. This is very significant and clinically relevant since the tolerance dose for the lenses is only 10 ~ 15 Gy. In the cases we studied, the contra-lateral parotid gland was not contoured as an independent critical structure. However, based on the isodose distributions shown in **Figure 9**, it is clear that the dose delivered to the contra-lateral parotid gland for the MERT plan was well under the established tolerance dose of 20 ~ 30 Gy (29). Even if we increased the prescribed dose to 60 Gy, the dose delivered to the

contra-lateral parotid gland for the MERT plan would be still kept well within the tolerance. It is very important to point out that the mean dose to the non-target tissue in the photon beam IMRT plan was 7.54 Gy as compared with 3.95 Gy in the MERT plan. This is of clinical significance as the MERT plan could significantly reduce low radiation doses to large normal tissue volume.

For many years, parotid cancers have been largely treated using one of these three radiotherapy techniques: an ipsilateral wedged pair of photon beams oriented at oblique angles, an ipsilateral field treated with high energy electrons, and a combination of high energy photon and electron beams with carefully chosen weights. Unfortunately, because of the intrinsic limitation of the underlying physics, all these techniques are not able to produce treatment plans that provide both a high degree of target dose conformity and a significant normal tissue sparing. Recently, the photon IMRT has shown some success in treating certain head and neck cancers, but it is still not suitable to treat shallow tumors due to extremely low surface dose and excessively high exit dose. The low surface dose is not effective in killing tumor cells in superficial tissues. The high exit dose constitutes a significant risk to the normal function of the distal critical structures, such as the spinal cord and the contra-lateral orbit and parotid gland. Therefore, it would be desirable to develop a technique that can eliminate these drawbacks. As the results presented here indicate, through both electron intensity and energy modulations, MERT was able to deliver highly conformal doses to targets with complex shapes. In the mean time, it provided sufficient protection of the critical structures and substantial normal tissue sparing. Considering the radiation side effects and the quality of life limiting organs at risk like the contra-lateral parotid gland and orbit, it is necessary to keep the dose to the healthy tissue to a minimum and preserve the organ normal function as much as possible. In this respect, MERT had an undisputable advantage and a great potential.

Conclusions

Based on the results of this comparative dosimetric study, we conclude that EMLC was able to provide sufficient beam collimation for MERT treatments and for superficial targets, such as parotid cancers, MERT offered not only a better target dose coverage and uniformity, but also a superior normal tissue sparing. Therefore, it could become the treatment of choice for superficial tumors. As the development of the computer-controlled EMLC is underway, we believe that the widespread routine implementation of this novel technique for superficial tumors should be investigated.

Acknowledgements

This study was supported in part by grants DAMD17-00-1-0443 (Yulin Song and Steve Jiang), DAMD17-00-1-0444 (Todd Pawlicki), and DAMD17-01-1-0635 (Lei Xing) from the US Department of Defense. In addition, we would like to express our sincere thanks to Varian Medical System, Palo Alto, CA, for providing electron applicators for this study.

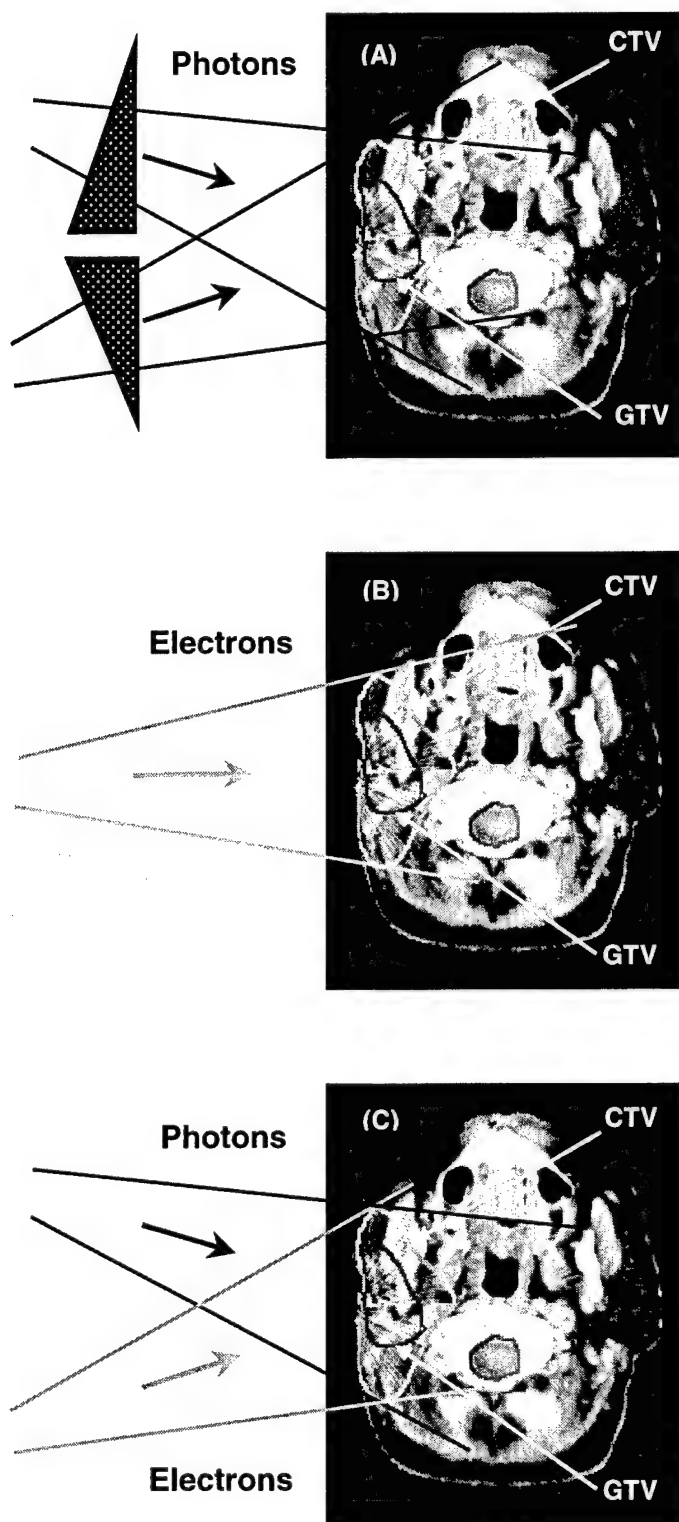


Figure 1

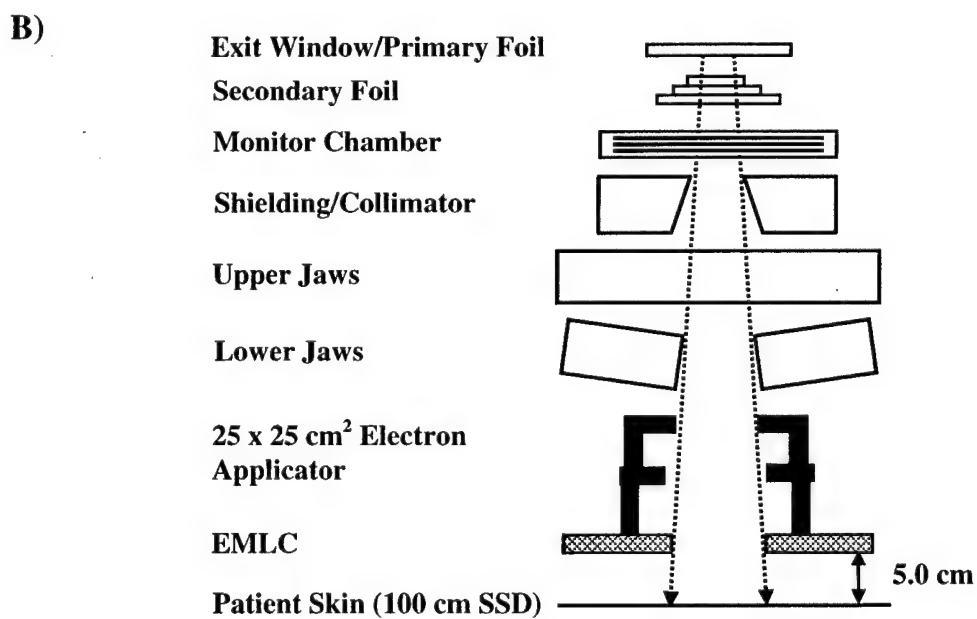
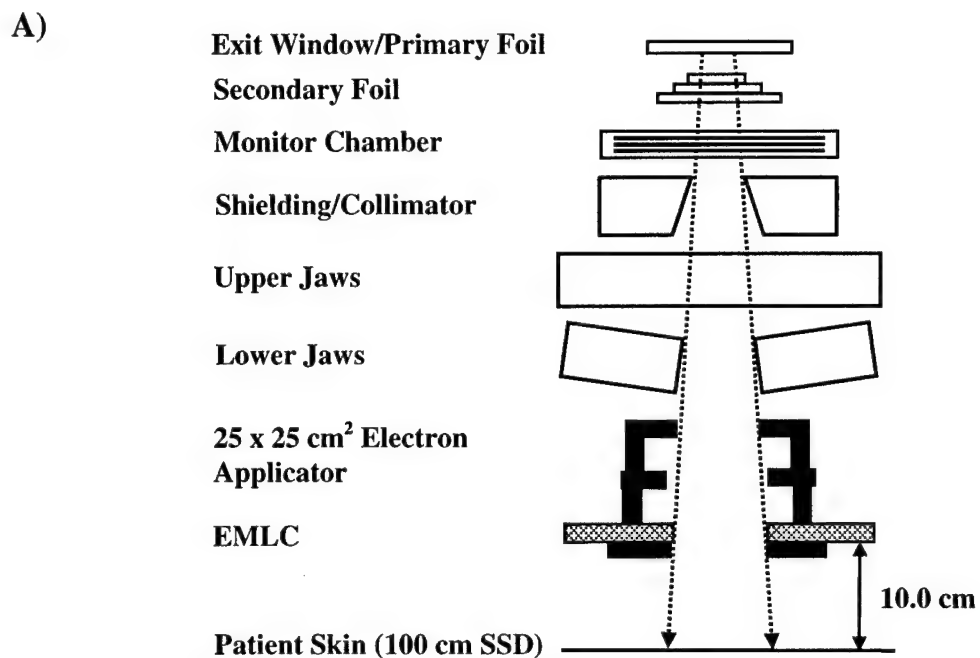


Figure 2

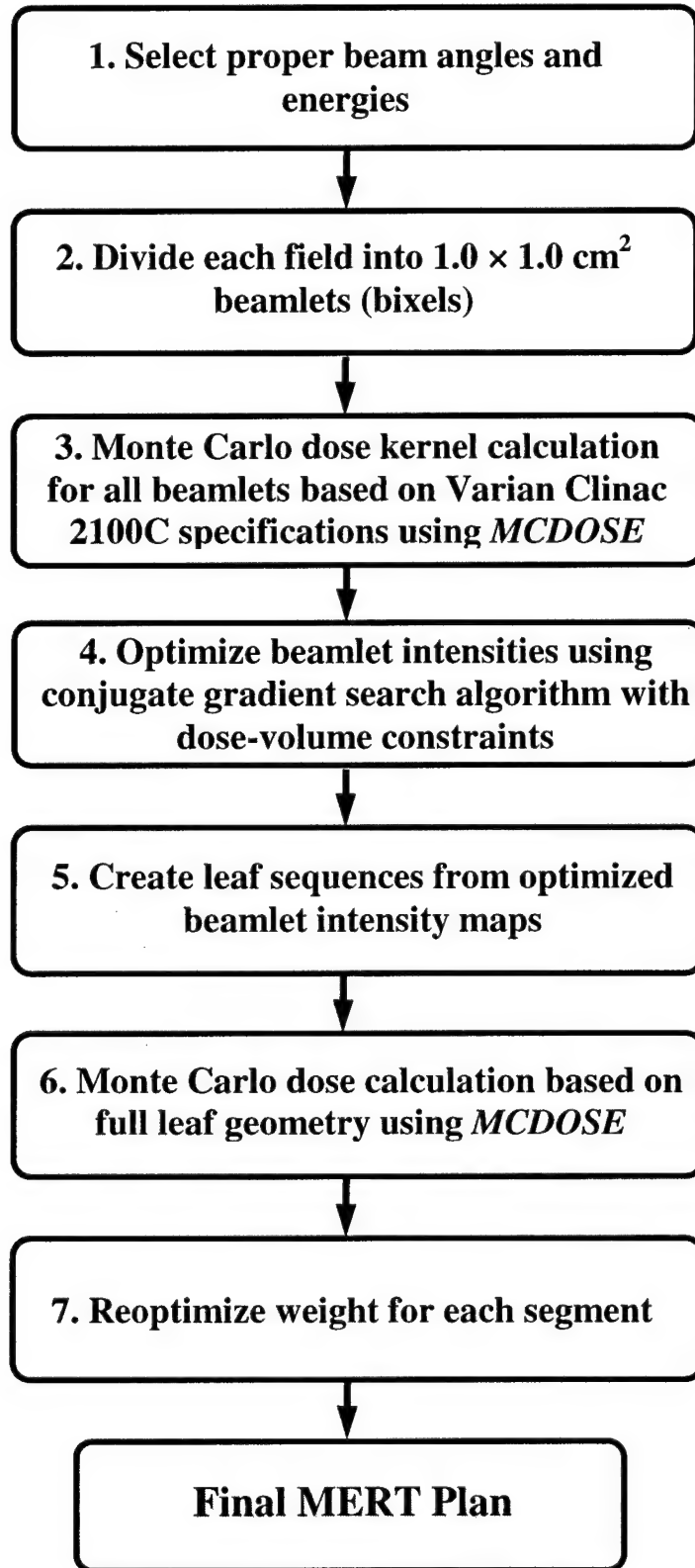


Figure 3

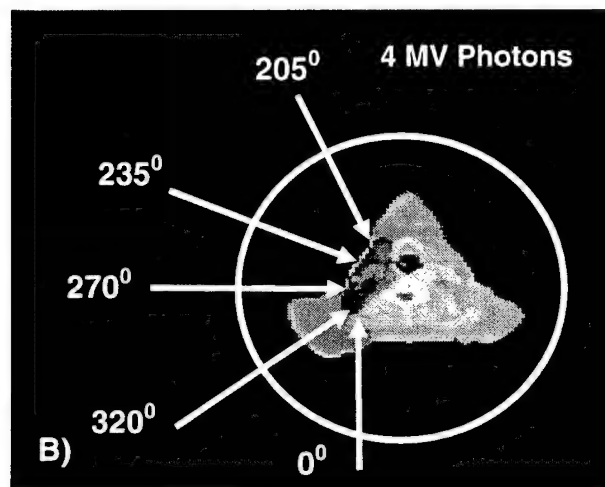
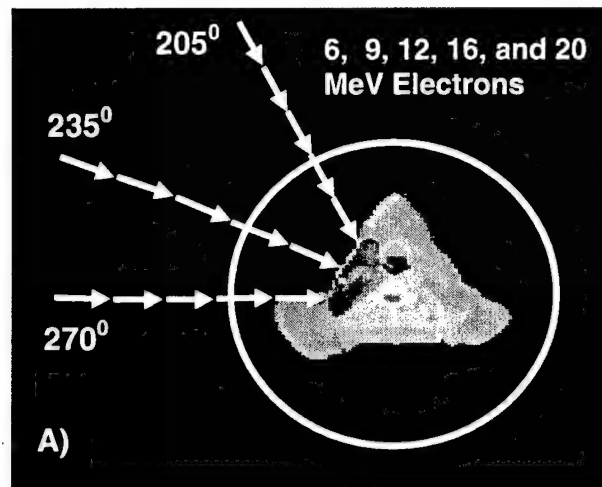


Figure 4

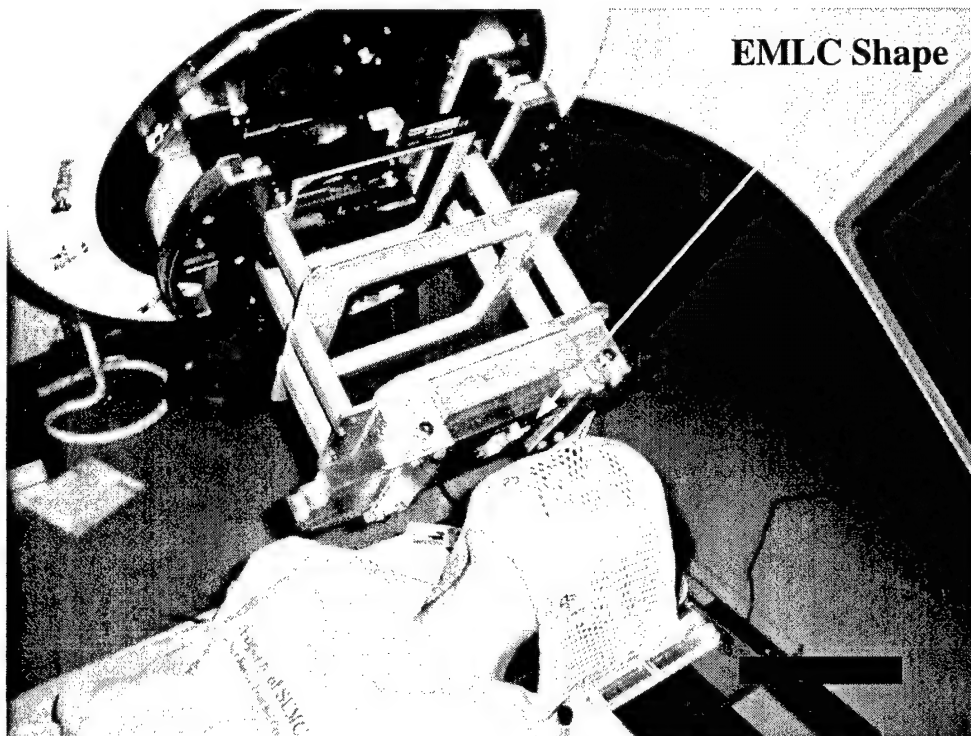
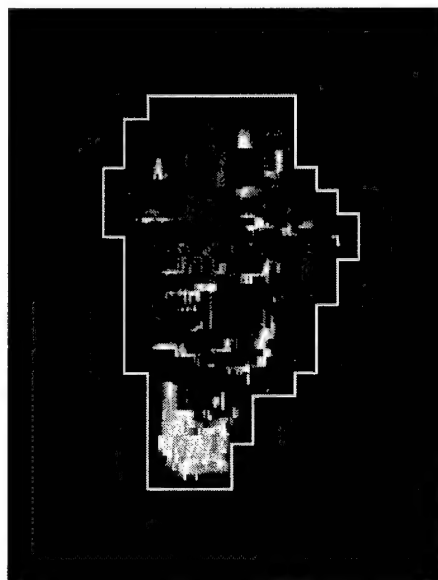


Figure 5

A



B

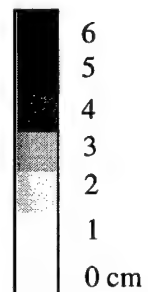
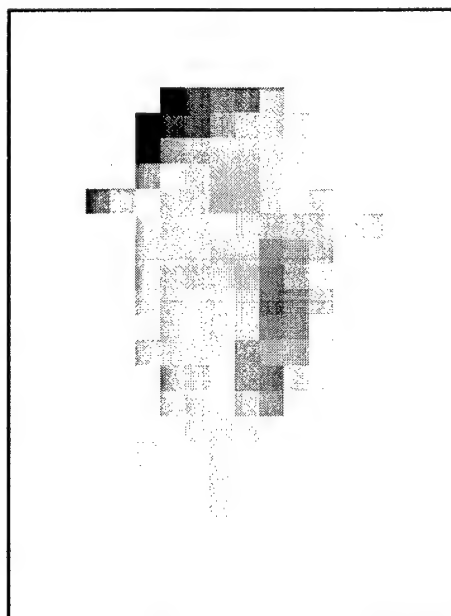


Figure 6

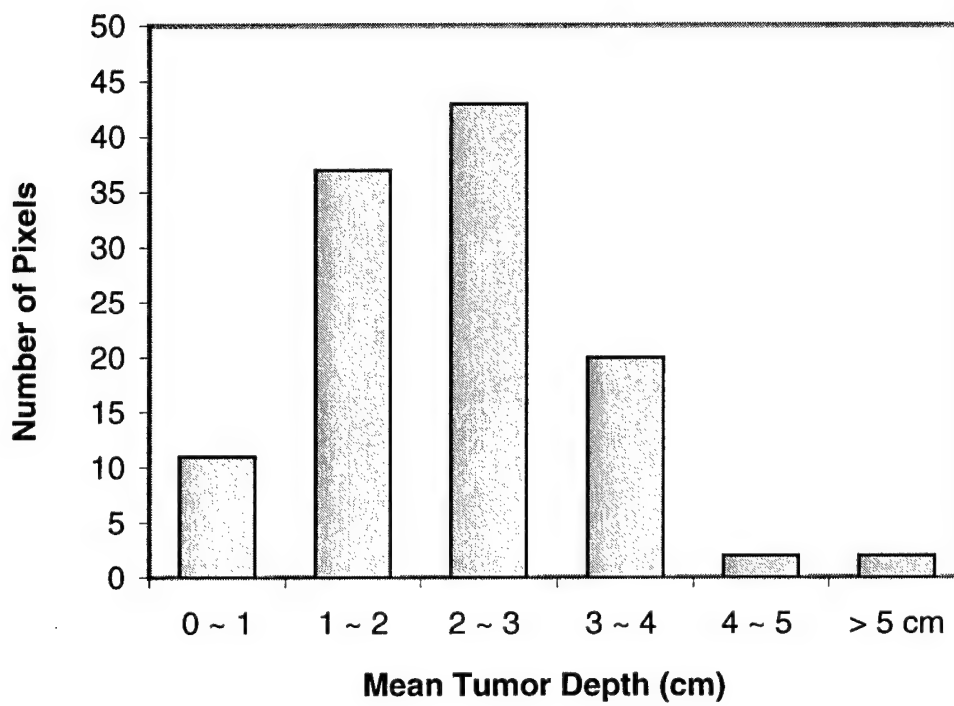
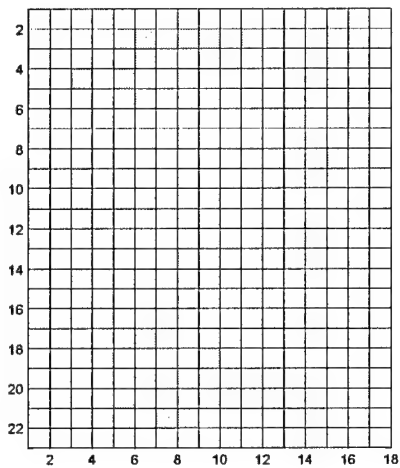
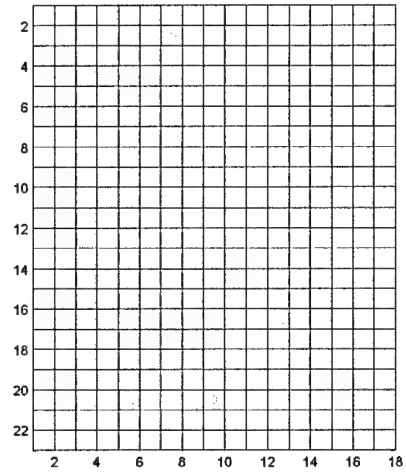


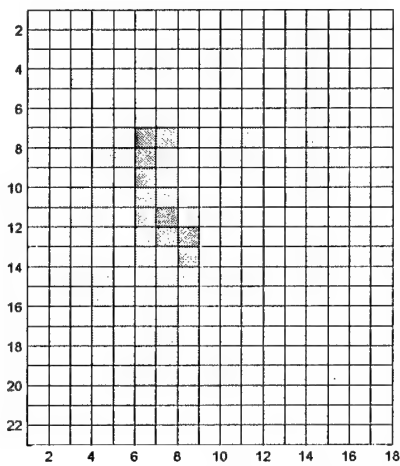
Figure 7



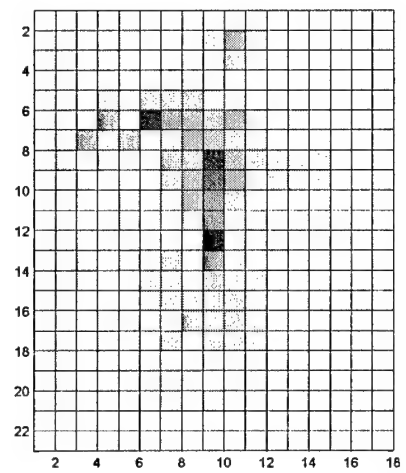
A. MERT plan 6 MeV field



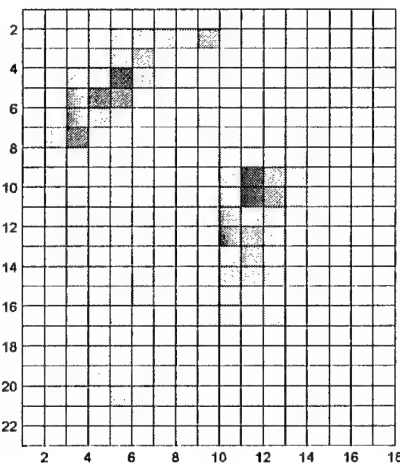
B. MERT plan 9 MeV field



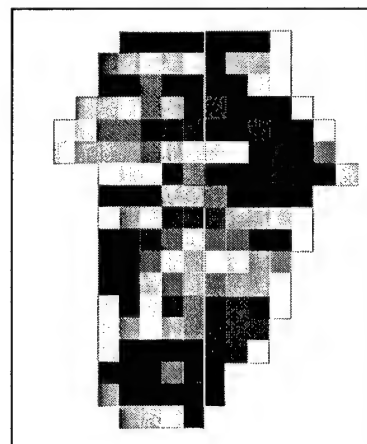
C. MERT plan 12 MeV field



D. MERT plan 16 MeV field



E. MERT plan 20 MeV field



F. IMRT plan 4 MV field

Figure 8

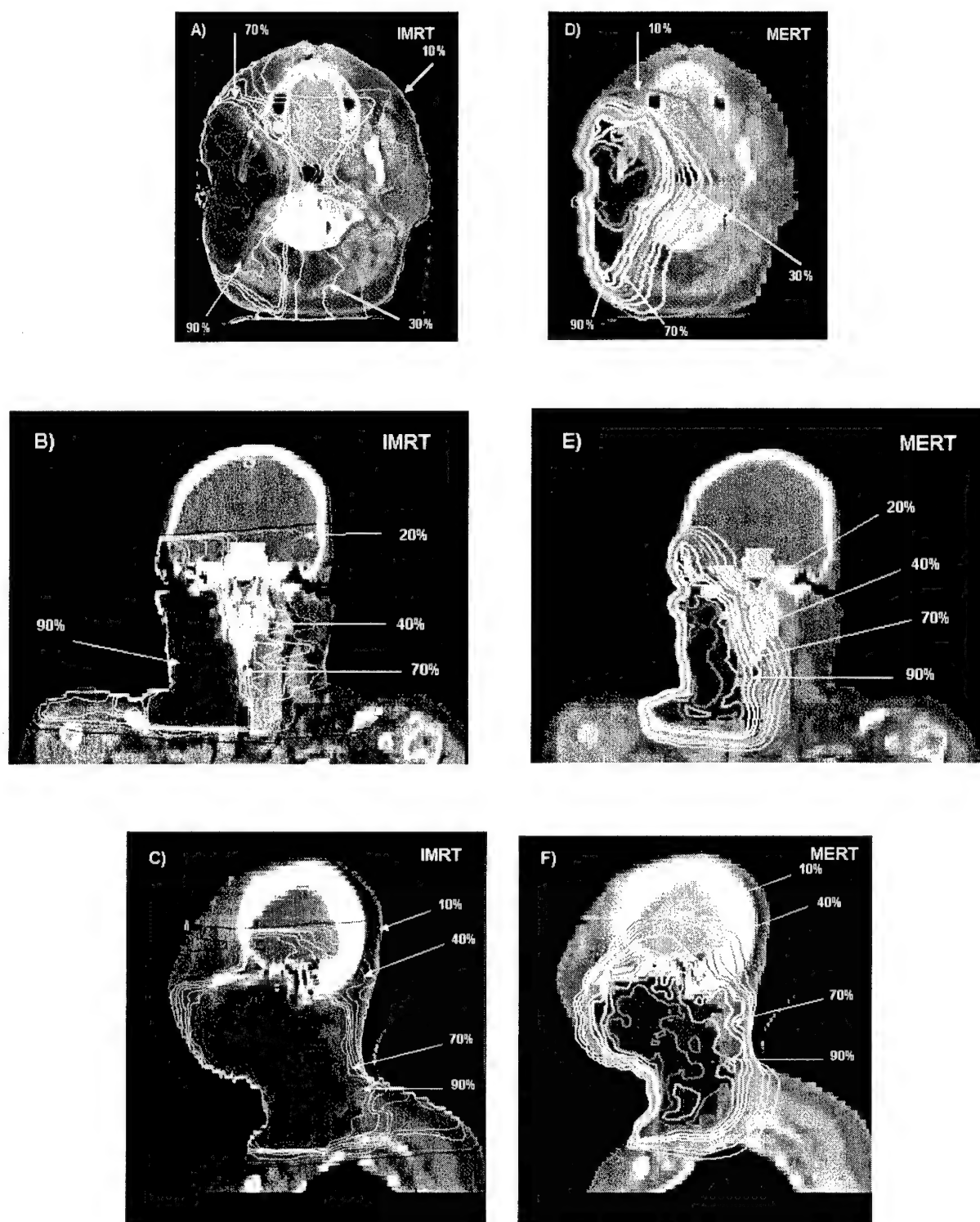


Figure 9

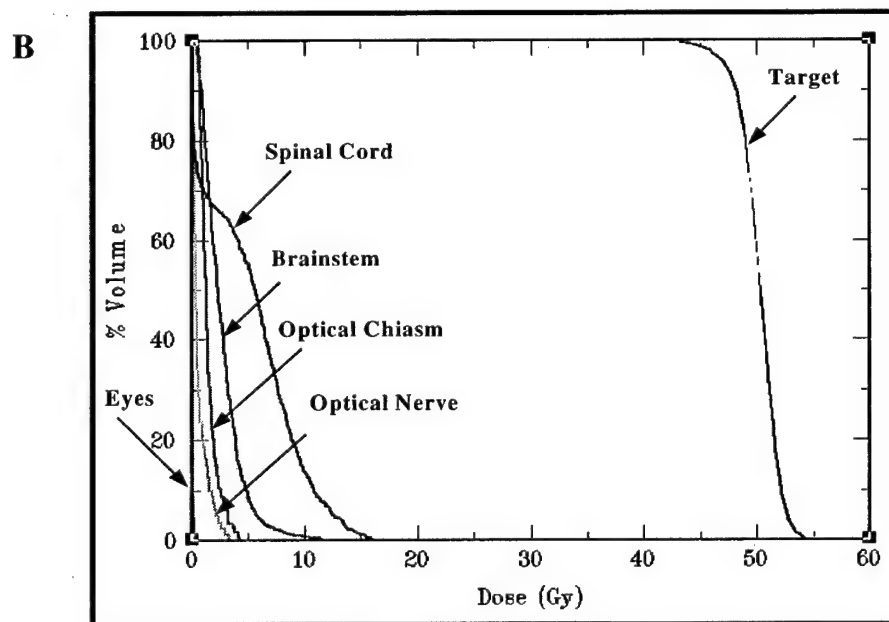
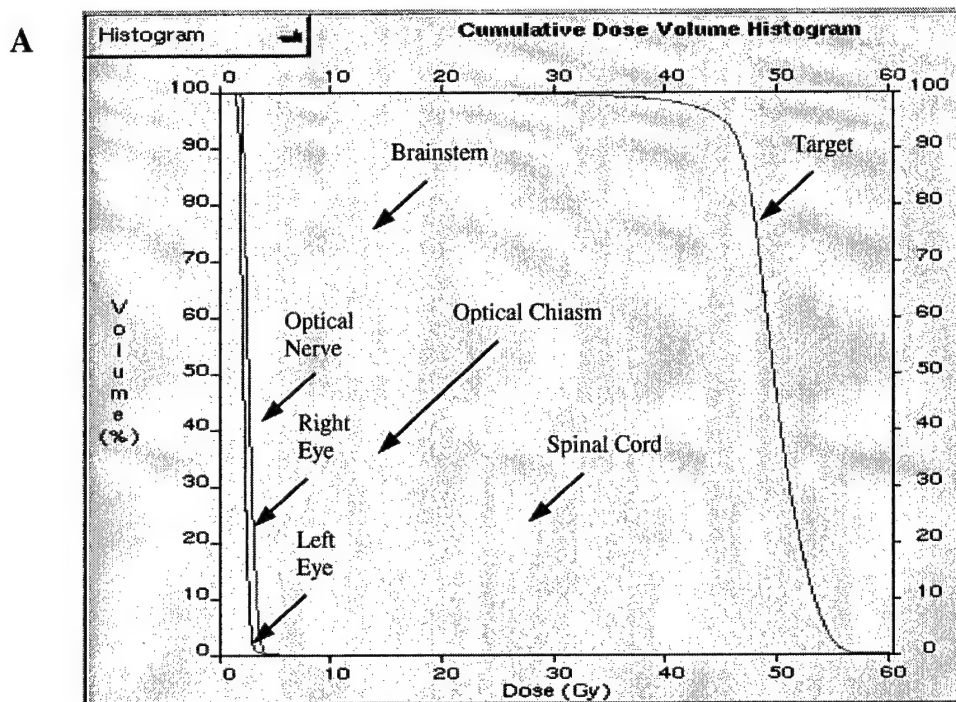


Figure 10

FIGURE LEGENDS

Figure 1

Conventional radiotherapy techniques for the treatment of parotid tumors. (A) An ipsilateral wedged pair of 6 MV photon beams oriented at oblique angles to cover the entire parotid bed, (B) An ipsilateral field treated with high energy electrons (12, 16 or 20 MeV), and (C) A combination of high energy photon and electron beams (6 MV + 12 or 16 or 20 MeV) with proper weighting.

Figure 2

Schematic drawings of the EMLC and a Varian Clinac 2100C treatment head. (A) The manually-driven EMLC was originally placed at the last scraper of a standard Varian 25 x 25 cm² electron applicator. This resulted in a considerably large air gap (10 cm) between the bottom of the EMLC leaves and the patient skin for a nominal 100 cm SSD. (B) To further lower the EMLC leaves, we have now removed the entire last scraper of the electron applicator and its electronic circuitry. The EMLC was placed immediately at the bottom of the modified electron applicator and stabilized with eight screws. This modification reduced the air gap to 5.0 cm between the bottom of the EMLC leaves and the patient skin.

Figure 3

The MERT treatment planning flowchart.

Figure 4

Schematic layouts of the beam orientations. (A) Each MERT plan consisted of three coplanar ports, oriented at 205⁰, 235⁰, and 255⁰, respectively. Each port was treated with five nominal electron energies (6, 9, 12, 16, and 20 MeV) consecutively. (B) Corresponding photon beam IMRT plan had five coplanar ports: 0⁰, 205⁰, 235⁰, 270⁰, and 320⁰, with each port being treated with a 4 MV photon beam.

Figure 5

A photo of the EMLC assembly mounted on a Varian Clinac 2100C linear accelerator. The air gap between the bottom of the EMLC leaves and the patient skin was 5.0 cm. The gantry angle was 235° .

Figure 6

A representative parotid tumor and corresponding tumor depth map. (A) A 3-D beam's eye view of a parotid tumor at the beam angle of 235° . (B) Corresponding tumor depth map, with darker pixels indicating the deeper parts of the tumor at this viewing angle.

Figure 7

A representative tumor depth histogram. The histogram was created based on Figure 6B, showing the number of pixels distribution as a function of mean tumor depth. Based on this distribution, a suitable set of electron energies were selected for this particular beam angle.

Figure 8

Representative beam intensity maps. (A-E) Intensity maps for the MERT plan for the 6, 9, 12, 16, and 20 MeV fields at the beam angle of 235° . (F) Corresponding photon beam IMRT intensity map for the 4 MV field at the same beam angle. This intensity map consisting of two separate intensity maps and combined together manually.

Figure 9

Comparison of the MERT and IMRT plan isodose distributions. (A, D) Isodose distributions for the central axial slices for a representative parotid cancer case. (B, E) Isodose distributions for the central coronal slices from the same case. (C, F) Isodose distributions for the central sagittal slices from the same case. The isodose curves,

normalized to 55.0 Gy, represent 10, 20, 30, 40, 50, 60, 70, 80, 90, and 100%, respectively. Only selected isodose lines are labeled here.

Figure 10

Comparison of dose volume histograms (DVH) for the photon beam IMRT (A) and MERT (B) plans. Clearly, the MERT plan shows a superior normal tissue sparing and a better dose distribution.

Table I. List of ports used in the MERT plans

Port No	Gantry Angle
1	205 ⁰
2	235 ⁰
3	270 ⁰

Table II. List of fields used in the MERT plans

Field No	Gantry Angle	Beam Energy (MeV)
1	205 ⁰	6
2	205 ⁰	9
3	205 ⁰	12
2	205 ⁰	16
5	205 ⁰	20
6	235 ⁰	6
7	235 ⁰	9
8	235 ⁰	12
9	235 ⁰	16
10	235 ⁰	20
11	270 ⁰	6
12	270 ⁰	9
13	270 ⁰	12
14	270 ⁰	16
15	270 ⁰	20

References

1. Parker, S., Tong, T., Bolden, S., and Wingo, P., "Cancer Statistics", *CA Cancer J Clin*, **47**:5-27, 1997.
2. Seifert, G., Brocheriou, C., Cardesa, A., and Eveson, J. W., "WHO International Classification of Tumors. Tentative Histological Classification of Salivary Gland Tumors", *Pathol Res Pract*, **186**(5):555-581, 1990.
3. Garden, A. S., El-Naggar, A. K., et al, "Postoperative Radiotherapy for Malignant Tumors of the Parotid Gland", *Int J Radiat Oncol Biol Phy*, **37**:79-85, 1997.
4. Spino, I. J., Wang, C. C., and Montgomery, W. W., "Carcinoma of the Parotid Gland. Analysis of Treatment Results and Patterns of Failure After Combined Surgery and Radiation Therapy", *Cancer*, **71**:2699-2705, 1993.
5. Lenhard, Jr., R. E., Osteen, R. T., and Gansler, T., "Clinical Oncology", *American Cancer Society*, 297-329, 2001.
6. North, C. A., Lee, D-J, Piantedosi, S., Zahurak, M. S., Johns, M. E., "Carcinoma of the Major Salivary Glands Treated by Surgery Plus Postoperative Radiotherapy", *Int J Radiat Oncol Biol Phy*, **18**:1319-1326, 1990.
7. Sykes, A. J., Logue, J. P., Slevin, N. J., Gupta, N. K., "An Analysis of Radiotherapy in the Management of 104 Patients with Parotid Carcinoma", *Clin Oncol*, **7**:16-20, 1995.
8. Yaparpalvi, R., Fontenla, D. P., Tyerech, S. K., Boselli, L. R., and Beitler, J. J., "Parotid Gland Tumors: A Comparison of Postoperative Radiotherapy Techniques Using Three Dimensional (3D) Dose Distributions and Dose-Volume Histograms (DVHS)", *Int J Radiat Oncol Biol Phy*, **40**(1):1319-1326, 1990.

9. Nutting, C. M., Rowbottom, C. G., Cosgrove, V. P., Henk, J. M., Dearnaley, D. P., Robinson, M. H., Conway, J., and Webb, S., "Optimization of Radiotherapy for Carcinoma of the Parotid Gland: A Comparison of Conventional, Three-Dimensional Conformal, and Intensity-Modulated Techniques", *Radiother Oncol*, **60**:163-172, 2001.
10. Garden, A. S., El-Naggar, A. K., Morrison, W. H., Callender, D. L., Ang, K. K., and Peters, L. J., "Postoperative Radiotherapy for Malignant Tumors of the Parotid Gland", *Int J Radiat Oncol Biol Phy*, **37**(1):79-85, 1997.
11. Boyer, A. L., Geis, P., Grant, W., and Carol, M., "Modulated Beam Conformal Therapy for Head and Neck Tumors", *Int J Radiat Oncol Biol Phy*, **39**:227-236, 1997.
12. Bragg, C. M., Conway, J., and Robinson, M. H., "The Role of Intensity-Modulated Radiotherapy in the Treatment of Parotid Tumors", *Int J Radiat Oncol Biol Phy*, **52**(3):729-738, 2002.
13. Wu, Q., Manning, M., Schmidt-Ullrich, R., and Mohan, R., "The Potential for Sparing of Parotids and Escalation of Biologically Effective Dose with Intensity-Modulated Radiation Treatments of Head and Neck Cancers: A Treatment Design Study", *Int J Radiat Oncol Biol Phy*, **46**(1):195-205, 2000.
14. Cozzi, L., Fogliata, A., Lomax, A., and Bolsi, A., "A Treatment Planning Comparison of 3D Conformal Therapy, Intensity Modulated Photon Therapy and Proton Therapy for Treatment of Advanced Head and Neck Tumors", *Radiother Oncol*, **61**:287-297, 2001.
15. Vineberg, K. A., Eisbruch, A., Coselmon, M. M., McShan, D. L., Kessler, M. L., and Fraass, B. A., "Is Uniform Target Dose Possible in IMRT Plans in the Head and Neck?", *Int J Radiat Oncol Biol Phy*, **52**(5):1159-1172, 2002.

16. Rowbottom, C. G., Nutting, C. M., Webb, S., "Beam-Orientation Optimization of Intensity-Modulated Radiotherapy: Clinical Application to Parotid Gland Tumors", *Radiother Oncol*, **59**:169-177, 2001.
17. Boyer, A. L., "The Physics of Intensity-Modulated Radiation Therapy", *Phys Today*, 38-44, September 2002.
18. Boyer, A. L., *et al*, "Intensity-Modulated Radiation Therapy: Current Status and Issues of Interest", *Int J Radiat Oncol Biol Phy*, **51**(4):880-914, 2001.
19. Xing, L., Cotrutz, C., Hunjun, S., Boyer, A. L., Adalsteinsson, E., and Spielman, D., "Inverse planning for functional image-guided IMRT", *Phys Med Biol*, **47**:3567-3578, 2002.
20. Lee, M. C., Deng, J., Li, J., Jiang, S. B., and Ma, C-M, "Monte Carlo Based Treatment Planning for Modulated Electron Radiation Therapy", *Phys Med Biol*, **46**:2177-2199, 2001.
21. Ma, C-M, Pawlicki, T., Lee, M. C., Jiang, S. B., Li, J., Deng, J., Yi, B , Mok, E., and Boyer, A. L., "Energy-and Intensity-Modulated Electron Beams for Radiotherapy", *Phys Med Biol*, **45**:2293-2311, 2000.
22. Song, Y., Jiang, S. B., Lee, M. C., Ma, C-M, and Boyer, A. L. "A Multileaf Collimator for Modulated Electron Radiation Therapy (MERT) for Breast Cancer", the Department of Defense Breast Cancer Research Program Meeting, Proceedings Volume I:17-5, 2002.
23. Nelson, W. R., Hirayama, H., and Rogers, D. W. O., "The EGS4 Code System", SLAC-Report-265, Stanford Linear Accelerator Center, 1985.

24. Rogers, D. W. O., Faddegon, B. A., Ding, G. X., Ma, C-M., Wei, J., and Mackie, T. R., "BEAM: A Monte Carlo Code to Simulated Radiotherapy Treatment Units", *Med Phys*, **22**:503-524, 1995.
25. ICRU, "Prescribing, Recording, and Reporting Photon Beam Therapy-Report 50", Washington, DC, *International Commission on Radiation Units and Measurements*, 1993.
26. Bortfeld, T., Kahler, D. L., Waldron, T. J., and Boyer, A. L., "X-ray Field Compensation with Multileaf Collimators", *Int J Radiat Oncol Biol Phy*, **28**:723-730, 1994.
27. Boyer, A. L., and Yu, C. X., "Intensity Modulated Radiation Therapy with Dynamic Multileaf Collimators", *Semin Radiat Oncol*, **9**:48-59, 1999.
28. Webb, S., "Optimization of Conformal Radiotherapy Dose Distribution by Simulated Annealing", *Phys Med Biol*, **34**:1349-1370, 1989.
29. Chao, K. S. C, Low, D. A., Perez, C. A., and Purdy, J. A., "Intensity Modulated Radiation Therapy in Head and Neck Cancers: The Mallinckrodt Experience", *Int J Cancer (Radiat Oncol Invest)*, **90**:92-103, 2000.
30. Karlsson, M. G., Karlsson, M. K., and Ma, C-M, "Treatment Head Design for Multileaf Collimated High-Energy Electrons", *Med Phys*, **26**:2125-2132, 1999.



SCIENCE @ DIRECT

Register or Login: Password: [Home](#)[Search](#)[Journals](#)[Abstract Databases](#)[Reference Works](#)[My Alerts](#)[My Profile](#)Quick Search: within [This Issue](#) 7 of 13 [results list](#) [previous](#) [next](#)**Medical Dosimetry**

Volume 26, Issue 2, Summer 2001, Pages 157-168

doi:10.1016/S0958-3947(01)00061-9

Copyright © 2001 American Association of Medical Dosimetrists. Published by Elsevier Science Inc.

Monte Carlo simulation for MLC-based intensity-modulated radiotherapyTodd Pawlicki^a, ^a and C. -M. Charlie Ma^a^a Department of Radiation Oncology, Stanford University School of Medicine, Stanford, CA, USA

Accepted 8 March 2001 Available online 4 June 2001.

This Document**Abstract****Actions**

- [Cited By](#)
- [Save as Citation Alert](#)
- [E-mail Article](#)
- [Export Citation](#)

Abstract

This article describes photon beam Monte Carlo simulation for multi leaf collimator (MLC)-based intensity-modulated radiotherapy (IMRT). We present the general aspects of the Monte Carlo method for the non-Monte Carloist with an emphasis given to patient-specific radiotherapy application. Patient-specific application of the Monte Carlo method can be used for IMRT dose verification, inverse planning, and forward planning in conventional conformal radiotherapy. Because it is difficult to measure IMRT dose distributions in heterogeneous phantoms that approximate a patient, Monte Carlo methods can be used to verify IMRT dose distributions that are calculated using conventional methods. Furthermore, using Monte Carlo as the dose calculation method for inverse planning results in better-optimized treatment plans. We describe both aspects and present our recent results to illustrate the discussion. Finally, we present current issues related to clinical implementation of Monte Carlo dose calculation. Monte Carlo is the most recent, and most accurate, method of radiotherapy dose calculation. It is currently in the process of being implemented by various treatment planning vendors and will be available for clinical use in the immediate future.

Author Keywords: Monte Carlo; IMRT; MLC; Dose calculation

Reprint requests to: Todd Pawlicki, Ph.D., Department of Radiation Oncology, Stanford University School of Medicine, 300 Pasteur Drive, Stanford, CA 94305-5304; email: tpaw@reyes.stanford.edu

Medical Dosimetry

Volume 26, Issue 2, Summer 2001, Pages 157-168

This Document**Abstract****Actions**

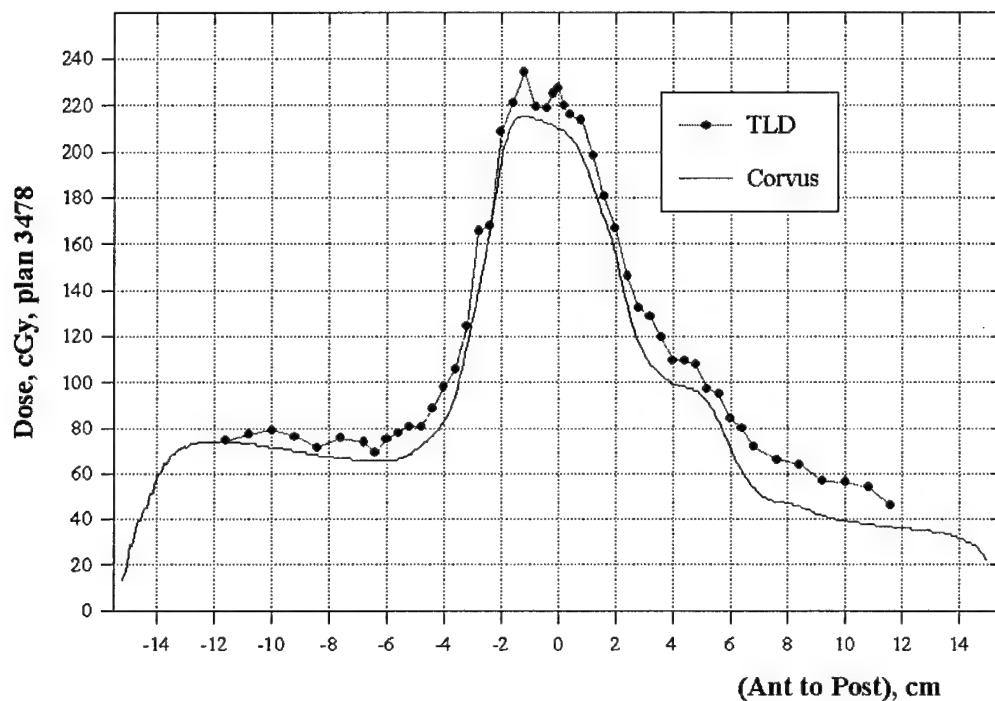
- [Cited By](#)
- [Save as Citation Alert](#)
- [E-mail Article](#)
- [Export Citation](#)

AbstractID: 8116 Title: TLD measurement system for comprehensive dosimetric quality assurance in IMRT

TLD measurement system for comprehensive dosimetric quality assurance in IMRT

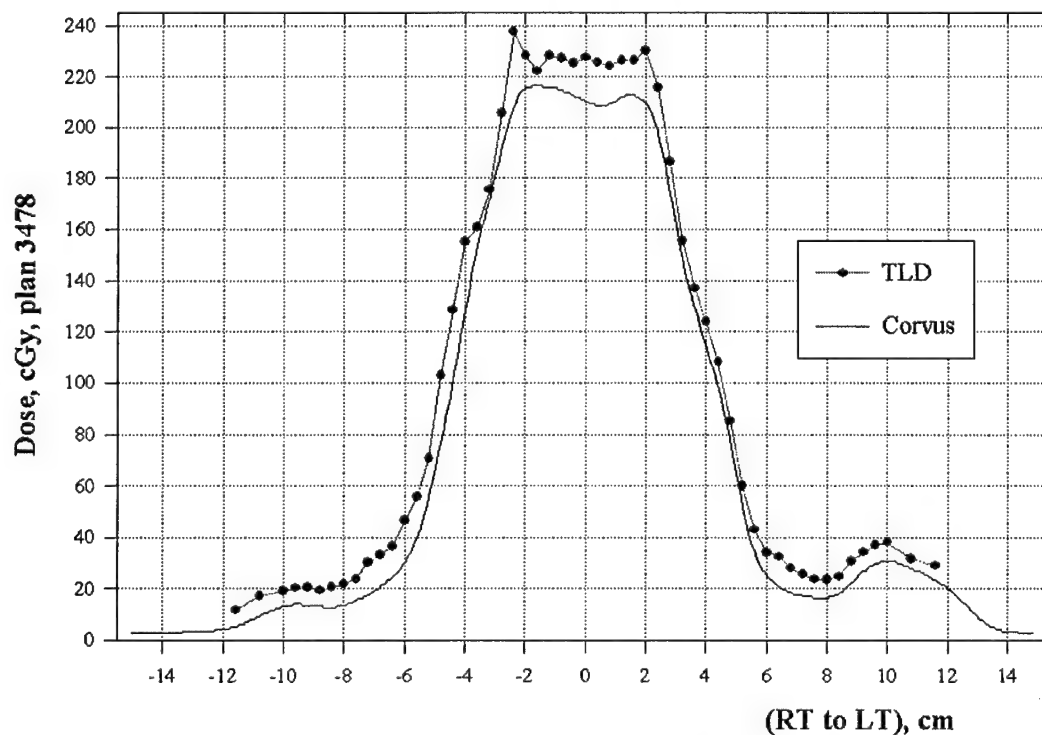
Intensity-modulated radiotherapy (IMRT) provides a technique for improving dose distributions by using inverse planning computer treatment plan optimization and computer-controlled dynamic delivery of complex planned intensity distributions. IMRT places unique demands on capabilities of treatment planning and delivery systems, strongly suggesting a need for a method of systematic quality assurance that includes detailed testing and verification of dose delivery. A multi-slab Plastic Water™ phantom was constructed to accommodate measurement in different planes of 2-D dose distributions from complete IMRT treatment plans with millimeter resolution, using 1-mm thermoluminescent dosimeter (TLD) cubes. The phantom can accommodate single-point ionization chamber measurement as well. The 30 x 30 cm axial cross section phantom was imaged with 1.5-mm spacing between CT slices, and the data set exported to a commercial IMRT treatment planning system (Corvus™) with an accompanying DICOM structure of idealized 30 x 30 axial contours to represent idealized surface anatomy. The planning system assigned the phantom a bulk density of that of water. Using Corvus utilities, clinical patient treatment plans were calculated as though they were applied to the slab phantom unchanged. Numerical data was extracted in matrix form from axial plane dose computation files by following a procedure documented by the manufacturer to convert dose images to 'tif' format, and a utility available within MATLAB™ software to interpret these files. Results were compared with TLD measurements. Initial data show general agreement of the shape of the calculated dose distributions, but with systematic relative deviations appearing in the lower-dose regions.

Dose profile: TLD vs. corvus, 15X, A-P, (avg 2 meas.)



Small-field plan, 15X

Dose profile: TLD vs. corvus, 15X, RT-LT.(avg 2 meas.)



Energy and Intensity Modulated Electron Radiotherapy: A Comparative Dosimetric Study of MERT and IMRT for Head & Neck Cancer

Y. Song, M. C. Lee, and A. L. Boyer

Department of Radiation Oncology, Stanford University School of Medicine, Stanford, CA

In this study, we investigated treating head and neck cancers using modulated electron radiation therapy (MERT) by comparing MERT plans with x-ray intensity-modulated radiation therapy (IMRT) in terms of target coverage and normal tissue sparing.

An experimental electron multi-leaf collimator was fabricated by modifying a conventional electron cone (Varian Medical Systems, Palo Alto, CA). Electron beams produced by a linac (Clinac 2100C, Varian Medical Systems) and collimated by this electron MLC were simulated using the EGS4/BEAM code. The simulations were based on the manufacturer's specifications of the beam production system and the electron cone design. The MERT plans with three coplanar beams (205^0 , 235^0 , and 255^0) and five nominal energies (6, 9, 12, 16, 20 MeV) were created using modified EGS4/MCDOSE code. The doses were checked against a commercially available Monte Carlo dose calculation engine (NXEGS, NumeriX LLC, New York, NY) and measurements. The IMRT plans with five coplanar beams were computed using a commercial treatment planning system (CORVUS, NOMOS Corp, Sewickley, Pennsylvania).

Our preliminary data indicated that MERT is able to provide similar target dose coverage compared with photon beam IMRT. However, MERT can significantly reduce the dose to critical structures. In the cases we studied, the maximum dose to the orbits, brainstem, optic chiasm, and spinal cord were reduced by 3.0, 16.2, 11.5, and 19.6 Gy, respectively, for a 50Gy target dose, suggesting a distinct normal tissue sparing advantage for MERT.

This work was supported in part by DOD grant DAMD17-00-1-0443 and by NumeriX LLC

Energy and Intensity Modulated Electron Radiotherapy: A Comparative Dosimetric Study of MERT and IMRT for Head & Neck Cancer

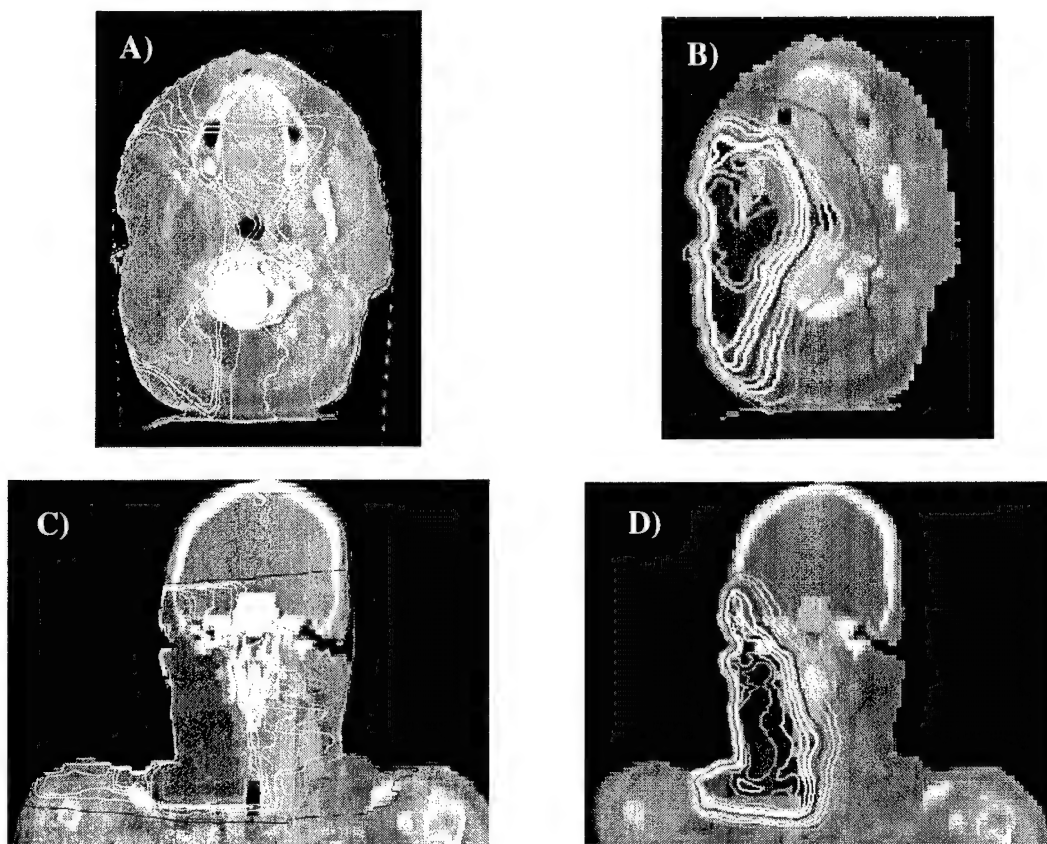
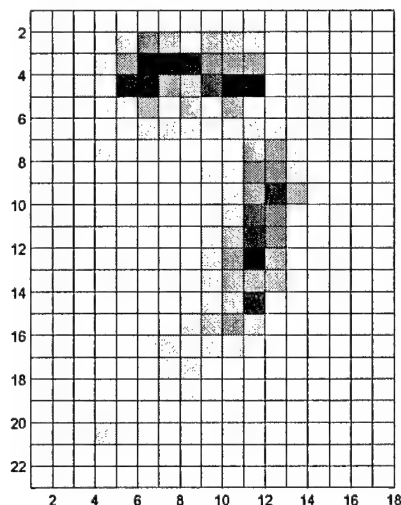


Figure 1. Comparison of dose distributions between the x-ray IMRT plan (A, C) and the MERT plan (B, D). The IMRT plan was computed using NOMOS CORVUS treatment planning system with five coplanar 4 MV beams. The MERT plan was computed using the modified EGS4/MCDOSE system with three coplanar beams (205° , 235° , and 255°), with each beam being energy and intensity modulated. The final MERT dose distribution was computed based on 15 intensity maps reconstructed from corresponding 15 leaf sequences. The beamlet size is 1x1 cm for both plans. The isodose curves, normalized to 55 Gy, represent 10, 20, 30, 40, 50, 60, 70, 80, 90, and 100%, respectively. As shown here, the MERT plan offers at least similar or better target dose coverage and uniformity.

Figure 2. A representative MERT intensity map. The intensity map was generated with a 205° gantry angle and a 20 MeV electron beam. For this particular map, five different intensity levels were used, with darker beamlets indicating a higher intensity level.



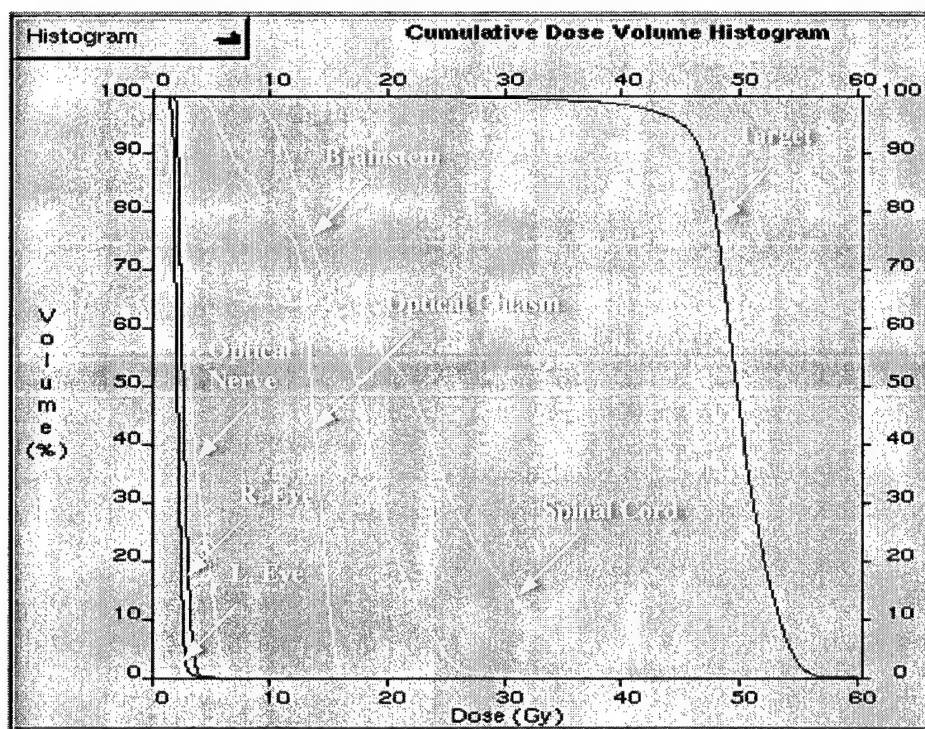
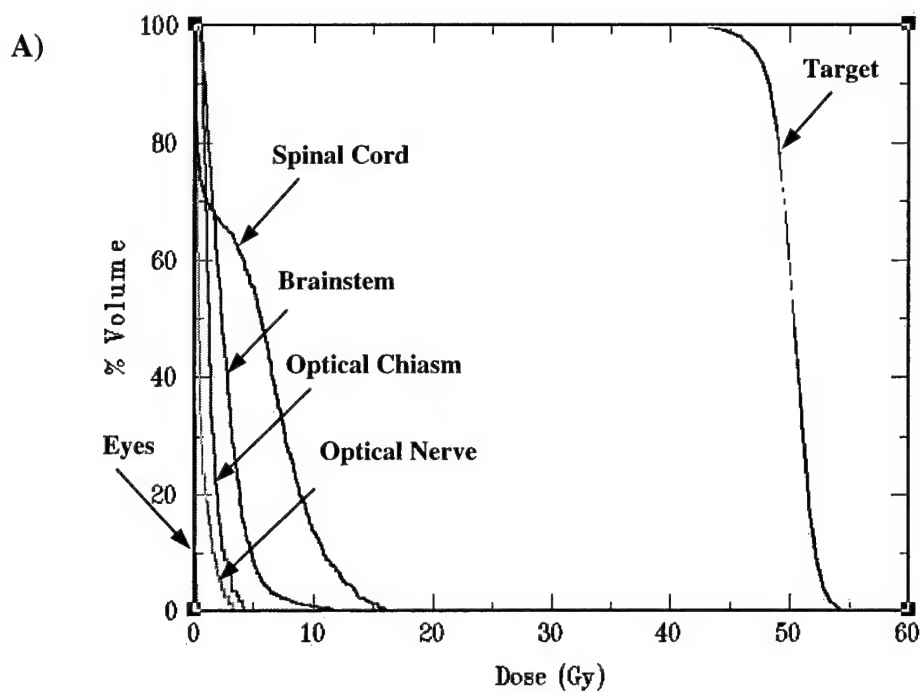


Figure 3. Comparison of dose volume histograms (DVH) for a representative head and neck case. **A)** DVH of the MERT plan. **B)** DVH of the corresponding IMRT plan. Clearly, the MERT plan shows superior normal tissue sparing.

Dose Matching of Two IMRT Plans or an IMRT and a 3D Conformal Treatment plan

L Xing, Z. Shou, J.G. Li, Y. Song, T. Pawlicki, A.L. Boyer, Q.-T. Le,

Purpose: IMRT is being increasingly adopted in radiation therapy community as a viable modality for radiation therapy of various cancers. One of the important problems related to its clinical application is the matching of an IMRT dose distribution for the treatment of part of the target volume(s) with a conventional 3D or another IMRT dose distribution for the treatment of the other portion of target volume(s). The purpose of this work is to develop an effective method for optimally matching the two sets of dose distributions and to demonstrate its clinical utility.

Methods and Materials: The two plans that need to be matched are dealt sequentially. First, the 3D conformal radiation therapy plan or the 1st IMRT plan used for treating part of the tumor volume(s) is obtained. To reduce the sensitivity of the final matching to the potential setup errors, attempt needs to be made to "blur" the penumbra or dose gradient in the direction perpendicular to the general matchline. Specifically, instead of having a sharp dose gradient, we let the dose to extend by additional 1.5~5cm in the direction perpendicular to the matchline and in this transition region, the dose is forced to fall-off linearly. The overlap is generally determined by the desired sensitivity against the setup error. After the first plan is done with the extended transitional dose gradient region, we proceed to optimize the 2nd IMRT plan with consideration of the existing doses of the first treatment plan. The goal of the 2nd dose optimization is to obtain an IMRT that yields a uniform composite dose distribution in the target volume(s) and (including the transitional regions) while sparing the sensitive structures. The technique is applied to the treatment of head and neck cancer, where matching of a conventional supraclavicular field for the irradiation of supraclavicular lymph nodes and an IMRT plan for the irradiation of the nasopharynx tumor and cervical lymph nodes is required. The matching between breast IMRT treatment and the supraclavicular field is also investigated. Finally, the method is demonstrated by the combining radiotherapy of intensity modulated photon and electron beams.

Results: To test the technique, the matching of two pairs of parallel opposed fields is first performed on a cubic phantom. A comparison with conventional approach shows significant improvement in target dose homogeneity and the sensitivity against a few intentionally introduced errors. A similar phantom test based on the matching of an intensity modulated photon beam and an electron beam also shows more dramatic improvement. Without intensity modulating the photon beam, overdosing/underdosing on the electron/photon side of the matchline was found to be +19% and -16%, respectively. The dose becomes almost perfectly uniform at the target region with the help of intensity modulation. The hybrid dose distribution also shows a ~50% reduction in the sensitivity with respect to the setup error. For each of the clinical cases investigated here, satisfactory matching between the different treatment regimes is found. Most importantly, with the implementation of the composite dose optimization technique, the matching becomes much controllable and transparent to the clinicians.

Conclusion: A general method for matching an IMRT dose distribution with a 3D conformal or another IMRT treatment is proposed. The approach takes advantage of the state-of-the-art intensity modulation and dose optimization techniques and provides an effective solution to the timely clinical problem of IMRT dose matching. In addition to better dose uniformity in the target volumes in the matchline region, we found that the sensitivity of the doses in the matchline region is significantly improved.

Concurrent Boost Using Forward Multiple-Segment Planning and Step-and-Shoot Delivery: A Novel Technique of Breast-Conserving Radiation Therapy

Yulin Song, Penny Peng, Arthur L. Boyer, and Lei. Xing

Department of Radiation Oncology, Stanford University School of Medicine,
Stanford, California 94305-5304

Purpose: Currently, most-widely used breast radiation therapy employs two opposed tangential photon beams with either uniform or wedge-shaped intensity profiles, followed by an electron boost field. Since plans created using this technique are not optimized, a certain portion of the ipsilateral lung and, in the case of the left breast treatment, a small volume of the heart is inevitably included in the treatment fields, resulting in high radiation doses to these areas. Recently, tangential field treatment using intensity-modulated fields has shed some light on breast cancer treatment. Although the dosimetric advantage of IMRT with opposed tangential beam configuration is obvious, its wide clinical application has not been realized. This is, in part, due to the fact the current IMRT planning and treatment procedure deviate significantly from the conventional approach and require additional steps in planning, delivery, quality assurance, and intensive personnel training. The goal of this study was to establish a variant of IMRT, multiple segment radiation therapy (MSRT), for concurrent breast boost treatment using forward planning and step-and-shoot delivery and address several untouched clinical issues related to the technique.

Materials and Methods: Five right-sided and five left-sided breast cancer patients, who had previously undergone lumpectomy, were selected for the study. The patients were CT scanned in the conventional treatment position supported by an Alpha Cradle immobilization device. Radiopaque markers were placed on the patients' chest to indicate the medial and lateral borders of the palpable breast tissue and the location of the lumpectomy scar. The critical structures, including the left and right lungs, the heart, and the contralateral breast, were delineated by a radiation oncologist. It is, however, not required to outline the structures in general MSRT concurrent boost planning. Treatment planning was performed using a 3D treatment planning

system. A uniform dose of 4,500 cGy or 5,040 cGy was prescribed to the entire target volume and a concurrent boost dose of 1,800 cGy was prescribed to the surgical region of the target volume. All plans were delivered in 180-cGy fractions. For comparison, three plans were created for each patient. One was the standard opposed tangential field (OTF) plan and the other two were the MSRT concurrent boost plans with different constraints. The standard plans employed a medial and a lateral tangential field with 6 or 15 MV photon energy. A wedge filter was used in the lateral beam. The MSRT concurrent boost planning started with a standard OTF plan. After the initial wedged plan was obtained, an additional MLC field segment was added to one or both beam directions to boost the surgical region under the guidance of dose distributions and DVH. If necessary, more segments were added to boost the "cold" or to remove the "hot" regions in the target. A segment may also be needed to reduce the dose to the ipsilateral lung and the heart. Once the plan was completed, the static MLC files were exported and concatenated to form a step-and-shoot delivery file. The intensity map, MU, and the maximum boundary of the MLC were independently checked prior to the first treatment.

Results: Compared with the OTF plans, the MSRT concurrent boost plans showed a much better dose uniformity in the target and a significant dose reduction in the ipsilateral lung and heart. In addition, the target volume receiving high dose irradiation was significantly reduced. Furthermore, it was found that the overall planning, treatment, and delivery overhead was insignificant and was more time efficient than the current conventional IMRT planning.

Conclusions: A clinical challenge in IMRT breast treatment is how to modulate breast irradiation without increasing the treatment complexity. In this study, we investigated MSRT concurrent breast boost treatment and demonstrated its clinical utility. When dose conformity can be realized using MLC beam shaping devices, the addition of a few extra segments could often improve the dose distribution significantly. The manual forward planning technique is a competitive approach compared with computerized inverse planning. MSRT is particularly efficient in incorporating prior and posterior knowledge and physical constraints into the treatment planning process. It is thus a more natural way to evolve from the conventional radiation therapy to the more sophisticated IMRT treatment. MSRT is likely to be beneficial for any radiation treatment where a simple beam configuration is used and where it is difficult to achieve a desired dose distribution within the target volume.

This study was supported in part by grant DAMD17-00-1-0443 from the US Department of Defense

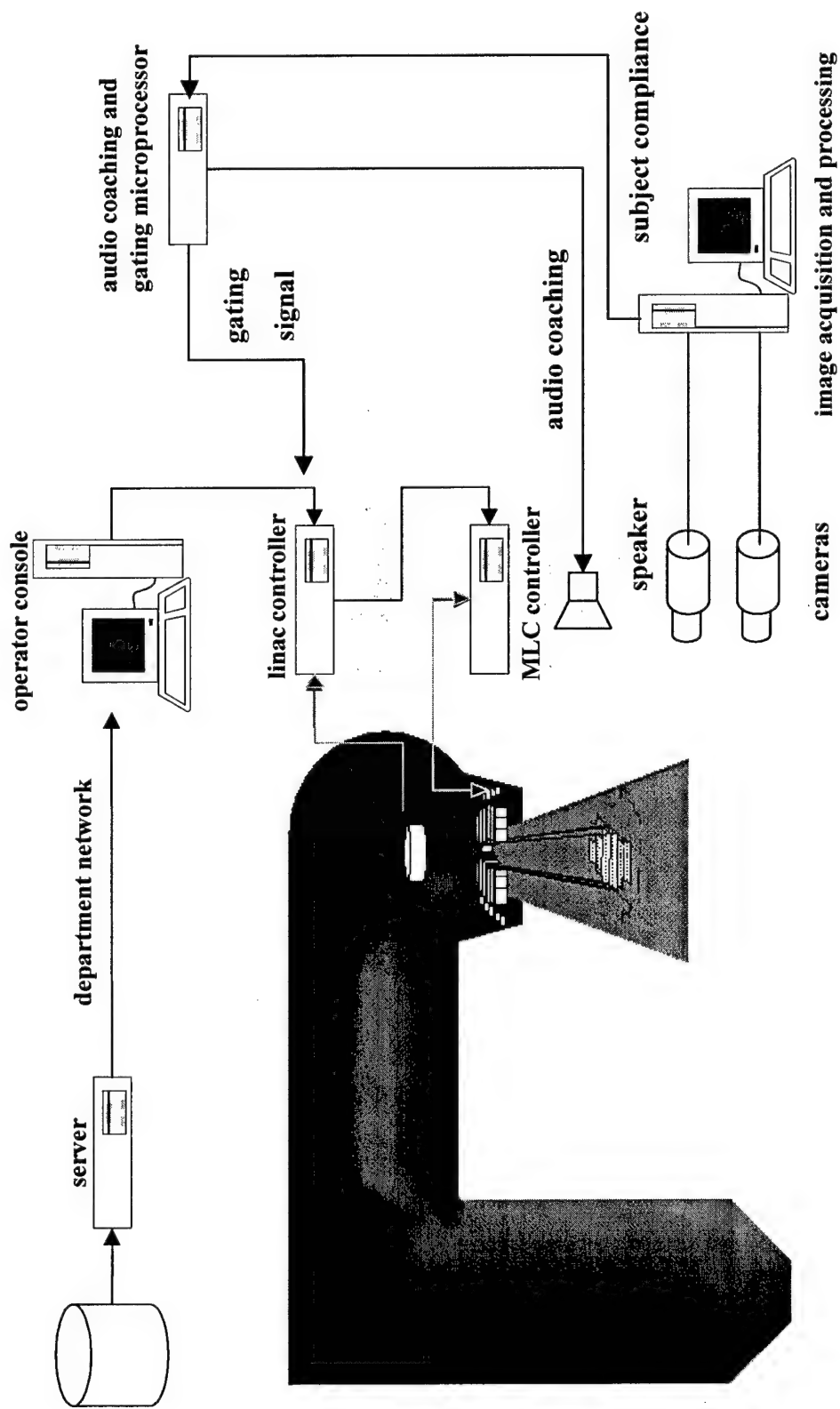
IMRT Using Audio and Optical Respiration Gating

Arthur L. Boyer, Todd Pawlicki, Carlos Cardenas, and Yulin Song

Department of Radiation Oncology
Stanford University School of Medicine,
Stanford, California 94305-5304

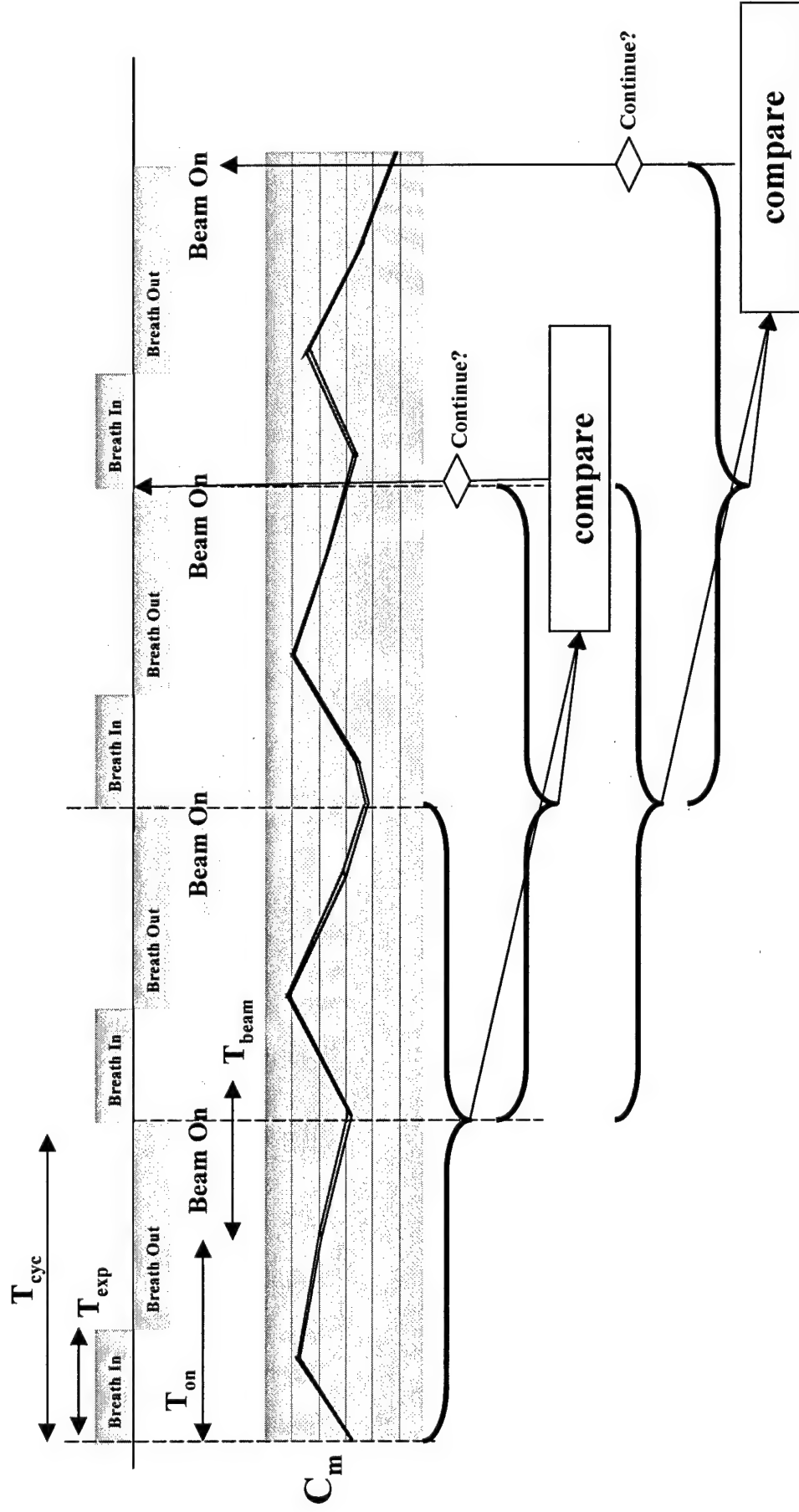
We report on an investigation of beam gating to compensate for respiration. We have studied audio coaching synchronized to a gating signal to the linear accelerator as the primary timing method while using a secondary respiration monitor to confirm that the patient (subject) is complying with the audio coaching. We asked whether this approach provides a more regular gating pattern for the linear accelerator and therefore a more consistent daily treatment than physical measures of the subject respiration. We studied optical observation of the subject with a video camera as a respiration monitor. A fixed field of view centered on the treatment isocenter was established for two cameras viewing the patient from the right and left lateral directions. The video signals produced by the cameras were digitized by an image processing board in a personal computer (Sony XC-73 camera, Matrox Meteor-II/Multi-Channel video board, Pentium III CPU, 864MHz, 256M RAM, Microsoft Windows 2000, Matrox Imaging Library). Respiration was monitored by the correlation of a region-of-interest within the field of view that was acquired and correlated once every 200 milliseconds. The correlation value yielded an adequate measure of chest wall motion and served as a respiration phase parameter. A means was sought to use this time-dependent correlation value as a measure of subject compliance with the audio coaching. A two-standard deviation, phase-dependent threshold was tested using a gating pattern that was found to be adequate for compensating for lung or kidney motion.

IMRT Using Audio and Optical Respiration Gating



IMRT Using Audio and Optical Respiration Gating 2

Microprocessor Clock



Combining IMRT and MERT for Breast-Conserving Radiation Therapy

Anthony Lo, Yulin Song, Arthur L. Boyer, Todd Pawlicki, and Lei. Xing

Department of Radiation Oncology, Stanford University School of Medicine,
Stanford, California 94305-5304

Purpose: The conventional opposed tangential photon beam treatment for breast cancer has two major limitations. Firstly, part of the lung and heart (in the case of the left breast treatment) may be exposed to a high radiation dose. Secondly, the contralateral breast may receive a significant amount of scatter dose. To reduce radiation side effects, we have investigated the strategy of treating breast cancer by combining intensity modulated radiation therapy (IMRT) and modulated electron radiation therapy (MERT). The objective of this study was to fully utilize the desirable characteristics of electron beams and intensity-modulated photon beams to achieve an optimal dose distribution in the target and minimize the exit and scatter doses to the critical structures.

Materials and Methods: Five early-stage breast cancer patients, who had previously undergone lumpectomy, were chosen for this combined-modality study. The patients were CT scanned in the conventional treatment position supported by an Alpha Cradle immobilization device. Radiopaque markers were placed on the patients' chest to indicate the medial and lateral borders of the palpable breast tissue and the location of the lumpectomy scar. The clinical target volume (CTV) and critical structures, including the left and right lungs, the heart, and the contralateral breast, were delineated on the axial CT images by a radiation oncologist. The PTV was obtained by adding a 1.0 cm margin uniformly to the CTV to account for patient setup uncertainty and organ shift. A uniform dose of 50.4 Gy was prescribed to the PTV in 1.8-Gy fractions. For comparison, two plans were computed for each patient. One was the standard opposed-tangential-field plan and the other the composite plan using the combined IMRT and MERT technique. The standard plan consisted of a medial and a lateral tangential field treated with a 6 MV photon beam. A 45° wedge was used in the lateral beam to obtain the desired dose distribution. The combined IMRT and MERT plan was computed using modified

EGS4/MCDOSE code. It was composed of five coplanar fields: two medial and two lateral IMRT fields (6 MV) and one perpendicular MERT field ($\sim 20^\circ$ from the anterior-posterior direction). The MERT field was treated with three nominal electron energies (6, 12, and 20 MeV). To deliver the MERT field effectively, we designed and manufactured a prototype electron MLC based on the results of Monte Carlo simulations and a conventional Varian 25 x 25 cm² electron applicator. The intensities of each electron energy were determined by the optimizer. Each of the photon and electron fields was divided into 1.0×1.0 cm² beamlets for the purpose of intensity optimization. The prescribed dose to the target was 50.4 Gy in 1.8 Gy fractions. For comparison, isodose lines were normalized to 50.0 Gy for all plans.

Results: The dose coverage to the PTV was similar for both techniques. However, the combined IMRT and MERT plans showed a much better dose homogeneity than the conventional opposed-tangential-field plans, which often exhibited extensive “hot” spots in the superior and inferior regions of the target. The dose to the ipsilateral lung, the heart, and, particularly, the contralateral breast was significantly reduced. In addition, the volume of normal tissue receiving low dose irradiation was significantly reduced.

Conclusions: Based on the results of this comparative dosimetric study, it seems that the combined IMRT and MERT technique offered a viable treatment option for breast cancer therapy. It is especially suitable to patients with large breasts, where a homogeneous dose distribution is difficult to achieve using the conventional opposed-tangential-field technique. As the IMRT treatment planning systems become more easily available and the development of the computer-controlled electron MLC is underway, we believe that the widespread routine implementation of this technique for breast cancer treatment should be investigated thoroughly.

This study was supported in part by grant DAMD17-01-1-0635 (Lei Xing) from the US Department of Defense.

Sweeping Window Arc Therapy (SWAT)

Arthur L. Boyer, Yulin Song, David Yong, Lei Xing
Stanford University
Stanford, California

Abstract

A novel variant of intensity-modulated radiation therapy is proposed in which the dose distribution is delivered with a single rotation of the accelerator gantry while multi-leaf collimator leaves modulate the x-ray beam. The leaves move along horizontal leaf tracks parallel to the axis of rotation of the gantry. The leaf sequence is derived from an initial leaf sequence produced by sweeping windows that lead to all voxels in the target volume being alternately irradiated at some gantry angles and then shielded from the parallel-opposed gantry angles. The result is a uniform irradiation of the target volume identical to that delivered by the classical Takahashi arc, but employing twice as many monitor units. This sequence was used to initiate an optimization algorithm that sought to minimize a traditional cost function by testing variations from the initial sweeping window sequence. An overshoot of a leaf beyond the initial window boundary can be used to produce regions where dose is reduced to spare a structure. An undershoot of a leaf back from the initial window boundary can be used to produce a region of additional dose to compensate for the target dose inhomogeneity produced by shielding. Prototype optimization codes were used to test the procedure for three-dimensional target volumes and adjacent organs-at-risk structures. The results with these simple preliminary tests approached the results of more sophisticated fixed-gantry intensity-modulated radiation therapy calculations. The delivery sequences have been verified by film dosimetry using a computer-controlled linear accelerator equipped with a multi-leaf collimator.

Comparison of Takahashi arcs with current IMRT techniques.

Arcs with a micro-MLC.

Experience with commercially available treatment planning systems indicates that continuous arcs with intensity modulation should be investigated further. Implementation of the Takahashi arc technique has been promising. Quite excellent results can be achieved with commercially available MLCs. The example in Figure 1 was delivered with a MLC with leaves that project to 3mm at isocenter (Xia et.al., 1999). The conformation of the isodose curves to the butterfly-shaped Gadolinium enhanced lesion can be appreciated. This case was treated using a computer-controlled MLC (MM3, Brainlab GbH, Munich, Germany). An "inverse treatment planning" algorithm is available with this commercial system that provides some normal structure sparing over the arc. We compared the results of the Brainlab inverse planning algorithm with stereotactic treatments planned with circularly collimated fields produced by cones on a robotic linear accelerator (Cyberknife, Accuray Inc., Sunnyvale, California). We used three clinical cases that had been treated with the Cyberknife and recomputed the treatment plans using the Brainlab inverse planning software. The stereotactic technique used three to five coronal arcs delivered in a step-and-shoot fashion by the Cyberknife robotic delivery system. Continuous arcs were mimicked by the use of 100-200 individual beams all using the same circular collimation. The MLC treatments were not delivered, but were only calculated for purposes of comparison. Four cases were studied. The MLC-collimated strategy were found to be superior to the circularly collimated strategy. In this study we found that IMRT was more conformal in 3 of the 4 cases

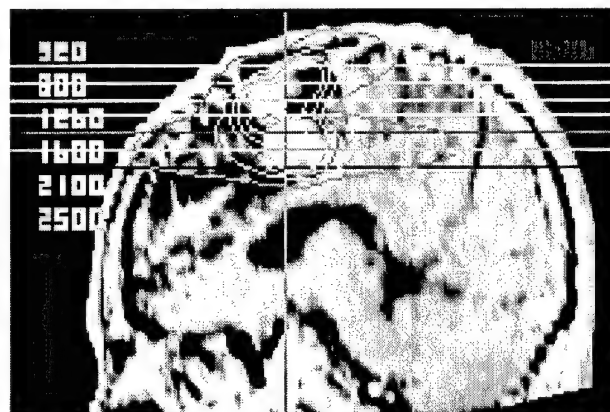


Figure 1. Sagittal view of brain tumor treated with Takahashi arcs implemented with a mini-MLC.

studied - depending on the priority given to normal structures. In addition, IMRT plans achieved superior sparing of organs at risk in 5 of 7 structures that were analyzed in the study. The MLC inverse planning in the Brainlab system is heuristic and attempts to minimize the dose to normal structures by shielding the normal structure projections over portions of the arcs. The algorithm allows the user to weight the amount of shielding to either fully protect the normal structure (similar to shielding the central structure in the Figure 1) or to maximizing the dose uniformity to the target volume. The results suggest that some extension of the Takahashi arc technique to intensity modulation during the arc can produce dose distributions superior to arcing alone. The problem is to determine the sequence of leaf settings over the course of the arc that will provide for the most uniform treatment of the tumor volume while achieving acceptable sparing of the normal structure. The selection of these leaf settings must be such that it can be done automatically by a computer in one to ten minutes for a particular case with a minimum of selection of parameters by the operator.

Comparisons of Takahashi arcs with current IMRT

We have studied the selection of the leaf settings manually using a conventional three-dimensional treatment planning system (Focus, Computerized Medical Systems, St. Louis, Missouri). We used prostate treatments that were currently being planned by another commercial IMRT treatment planning system (Corvus, NOMOS Corporation, Sewickley, Pennsylvania). These cases were chosen because a large volume of bowel was included in the plan. Continuous arcs were computed with the MLC field shapes selected manually to optimize the DVHs by trial and error. This was a relatively labor-intensive exercise, but it yielded interesting results. A characteristic example is shown as a DVH in Figure 2 to the right. The DVH curves for the prostate are nearly identical. The arc DVH for the bladder is significantly lower than the IMRT DVH curve for the same maximum dose, but the modified Takahashi arc curve is always significantly lower than the IMRT curve. The same pattern is observed for the bowel curve. If these results can be obtained with intuitive guesses of leaf trajectories and aperture patterns, then there is strong reason to expect that there are algorithmic processes that can lead to similar and superior results.

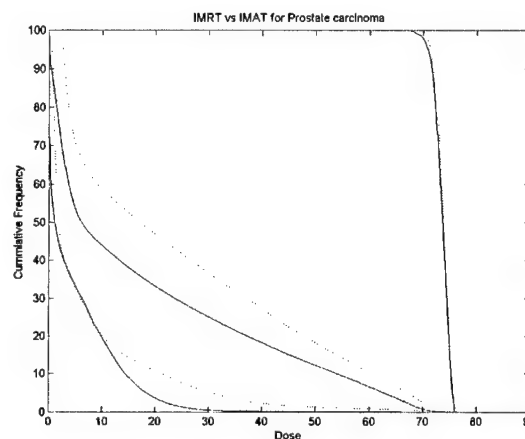


Figure 2. Comparison of a plan using manual quasi-Takahashi cone-beam arcs with fixed-gantry IMRT treatment plans. The arced plan is plotted with thick lines, and IMRT plan is plotted with thin lines.

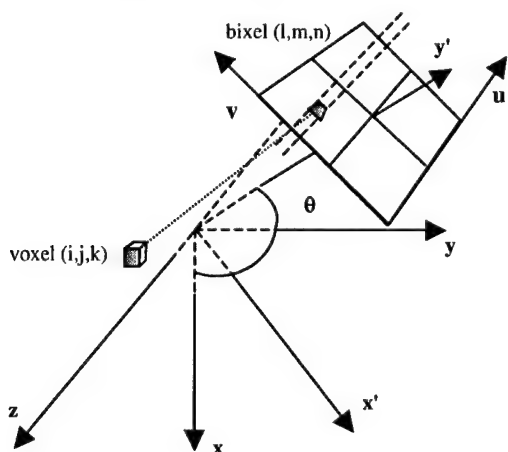


Figure 3. Illustration of the orientation of the MLC leaves and the coordinate system used in this discussion. Parallel dashed lines indicate a leaf track.

Arc therapy with a dynamic MLC.

Technical potentials.

There are installed software packages and hardware components capable of delivering exposures with a computer-controlled linear accelerator during gantry rotation while moving the MLC leaves in a prescribed fashion. The MLC leaf positions are specified in a computer file written in an ASCII format. The control system reliably interprets the file and moves the gantry and leaves accordingly. Software is available to simulate the sequence on a PC before applying it on the linear accelerator. The files consist of a series of aperture specifications at sequential gantry angles. The motion of the leaves is linear between aperture specifications at the selected number of gantry angles. The number of gantry angles used can easily be set to specify apertures every 5° to every 10°. We have developed algorithms to write the leaf-sequence files required by the control system and have demonstrated that our

specifications are delivered. We can fix the collimator such that either the leaves move in a direction parallel to the direction of rotation (between x-y planes in Figure 3) or in a direction parallel to the axis of rotation (parallel to the z-axis in Figure 3). The gantry can rotate slowly as the sequence is delivered providing for delivery times of one to five minutes. The maximum size of the leaf sequence is not a practical technical limitation. The

leaves move at a maximum velocity of 2cm/sec. This technical capability has not been investigated intensely as a means of delivering IMRT with multiple fixed gantry fields.

At a given gantry angle θ the MLC will form a window using a series of gaps between the opposing leaves along each track. A track centered at coordinate v in Figure 4 creates a gap from position u_m^A for what will be the a-leaf extending into the field from the patient's inferior to position u_m^B for the b-leaf extending into the field from the patient's superior. This forms a single gap of width $W_m(\theta)$ centered about a point at $u = M_m(\theta)$ as depicted in Figure 4. The bixel at (l,m) in Figure 3 either passes full fluence to voxels in the treatment field, such as the voxel (i,j,k) in Figure 3, or the fluence is attenuated by the leaf depending on whether the bixel falls within the gap.

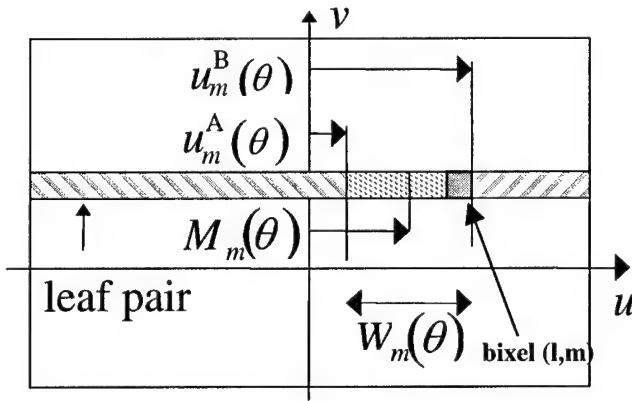


Figure 4. Representation of a single gap between opposed MLC leaves $W_m(\theta)$ is the width of the gap.

Sweeping arc.

We investigated leaf sequence optimizations that began with a leaf sequence that delivered dose to a volume while the leaves formed a window that swept across the target volume as the gantry rotated. A Takahasi arc sets the leaves to conform to the projection of the target volume throughout the rotation. For a spherical target volume centered on the axis of rotation, the Takahasi arc technique would set the leaves to a fixed circle throughout the entire arc. The results of a Takahasi arc are a nearly uniform dose in the circle and a cylindrically symmetric skirt of dose outside the target.

However, one can also achieve a uniform dose to the target volume using a sweeping window that can be described with the aid of Figure 5. This figure represents schematically the positions of complimentary leaf tracks as a function of gantry angle. The position for some leaf track centered a distance $v(m)$ from the aperture center is given on the left panel for gantry angles from 0° to 180° . The positions for the complimentary leaf track at $v(m_c)$ is shown in the right panel for the parallel-opposed gantry angles between 180° and 360° . The index of the complimentary leaf track is calculated by $m_c = m_{max} - m + 1$ where m_{max} is the maximum number of leaf tracks. In the left panel the right most leaf (let us assume it is the superior leaf of a pair) tracks the superior projection of the

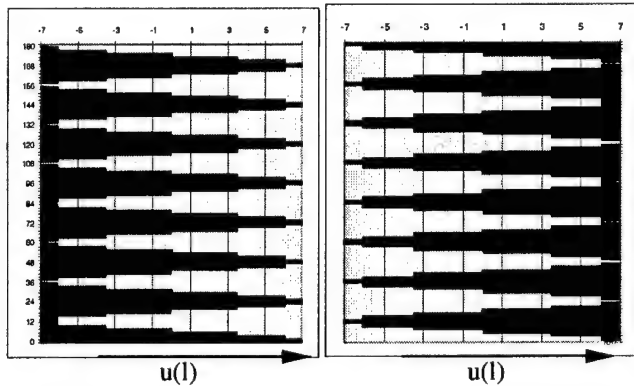


Figure 5. Dark areas represent relative extension of the leaves between the superior and inferior margins of the target volume. Left column represents gantry angles between 0° (bottom) and 180° (top). Right column represents the parallel opposed angles.

the target volume for the first 180° of gantry rotation (note that 0° is at the bottom of the column and 180° is at the top). This is depicted as a straight line running along the right side of the left column in Figure 5. The left leaf (let us assume it is the inferior leaf of the same pair) starts extended entirely across the target volume. As the gantry rotates, the inferior leaf retracts to the inferior projection of the target volume and then sweeps back to meet the superior leaf at the superior projection. This pattern is repeated (seven and one-half times in Figure 5) until the gantry reaches the 180° angle where the sweeping leaf in is the retracted state. For the next 180° of

gantry rotation, the inferior leaf tracks the inferior projection of the target (depicted as the left straight vertical side of the right column in Figure 5) while the superior leaf executes the sweeping pattern, arriving at a fully extended condition at 360°. Inspection of the patterns in Figure 5 shows that the patterns complement one another. Attenuation of a voxel from one side is complemented by irradiation from the other. The result is a sum-zero deviation from uniform irradiation of the target volume. The total irradiation is reduced by one-half that of an open, unswept field delivered with the same number of monitor units. The advantage of this strategy is that it provides opportunities for the leaves to deviate from the sum-zero sweep in order to modulate the dose delivery over the arc.

By deviating from the sum-zero pattern, the relative dose to portions of the target volume (or adjacent structures) can be increased or decreased.

Figure 6 contains the axial and sagittal plane films exposed by such a sweeping arc pattern. The circular target volume was uniformly irradiated while the leaves moved continuously during the arc in the manner of the

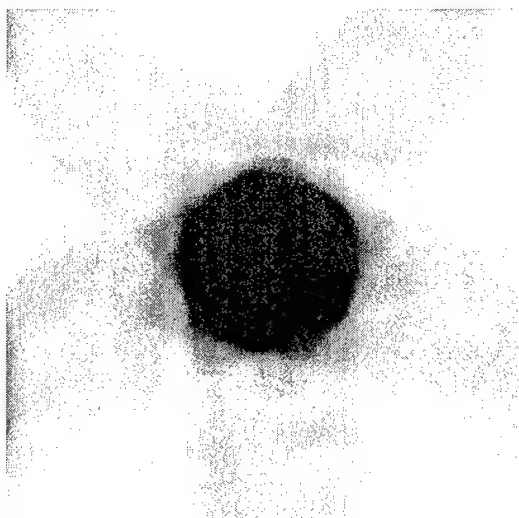


Figure 6a. Dose delivered by MLC leaves producing sweeping window in 360° arc in axial plane measured with film.



Figure 6b. Dose delivered by MLC leaves producing sweeping window in 360° arc in sagittal plane measured with film.

The transit dose outside the target volume is not uniform as is the case for a pure Takahashi arc, but contains a heterogeneous pattern with a number of arms determined by the frequency of the sweeping pattern over the gantry rotation (in this case five total sweeps). The sweeping window is proposed as the starting condition for the optimization process described in the next section.

Fast calculations using pointer arrays.

Pointer arrays for optimization. Preliminary investigations of optimization of continuous sweeping window arcs have used a calculation schema illustrated in Figure 7. The prototype calculations were based on a dose score array consisting of voxels, and a sequence of MLC windows as a function of gantry angle consisting of bixels. A voxels were defined as cubic volumes centered around the regularly-spaced calculation points. The voxels used in the prototype calculations were 5mm on a side. The bixels were defined as square areas bounded in one dimension by the leaf widths and bounded in the direction of travel of the leaves by an arbitrary step size. The calculations and measurements were carried using 5mm wide leaves and 5mm step sizes for 5mmx5mm bixels. The pointer arrays were a fast method of pointing between bixels and voxels. For a given gantry angle, each voxel was assigned one bixel by determining the bixel center most closely approached by the ray line from the voxel center to the radiation source. In the cases in which ray lines intersected bixel boundaries, a single bixel was arbitrarily

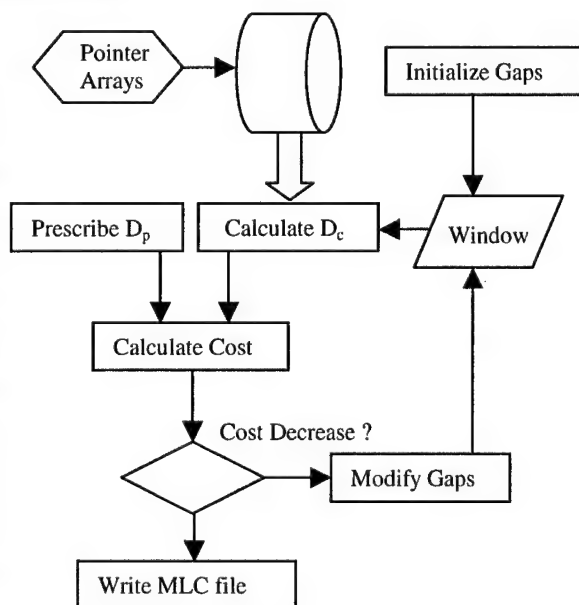


Figure 7. Diagram depicting modification of leaf sequence in Figure 5 by optimization using cost function.

assigned. The voxel-to-bixel integer pointers were computed once for the chosen array geometry and saved as a file. The size of the array was determined by the size of the calculation array (in these tests, a 32x32x32 element array representing a cube 16cm on a side), the maximum size of the MLC aperture considered (in these tests, a 46x46 element array representing a maximum window size of 23cmx23cm) and the number of gantry angles chosen (in these tests 36 gantry angles at every 10° of gantry angle). The voxel-to-bixel test array used for the preliminary tests required 6.87 MB of storage. The ray line passing through the center of a single bixel within the MLC space at a given gantry angle passes through a sequence of voxels. The previously defined voxel-to-bixel array was used to determine the sequence of voxels projected to the selected bixel. The number of voxels determined in this manner is maximal along a ray passing obliquely through the calculation matrix. This dimension of the bixel-to-voxel array was set at one and one-half times the dimension of the calculation array. The bixel-to-voxel array was computed for the geometry selected for the tests and saved as a 31.8 MB file. These array sizes are not a practical limitation for dose calculations. The three-dimensional dose and fluence arrays can themselves be represented as long vectors. This operation on the fluence is usually represented by the matrix symbolism as

$$\vec{D}_c = \vec{F} \cdot |H|$$

where $|H|$ is the matrix whose elements are zero if a bixel element does not contribute to the dose in the voxel element, and some ratio if the ray in \vec{F} strikes the voxel in the vector \vec{D}_c . The general form of the optimization scheme used in the initial tests is given in Figure xx. A prescribed dose distribution was determined for a target volume and limiting structures, represented by D_p in the schematic in Figure 7. An initial sequence of windows or apertures, defined by the MLC leaves, was selected, using the sweeping window approach. This is indicated by the "Initialize Gaps" box in Figure 7. Unattenuated fluence reaching the voxels was the zero-order surrogate for dose in these initial tests. A more accurate dose calculation is proposed for the investigations to be conducted during the funded research using Monte Carlo computations to determine the exact fluence-to-dose ratios that are the nonzero matrix elements of $|H|$. The computed surrogate dose, D_c in Figure 7, was used with the prescribed dose, D_p , to compute a least-squares cost value, $C = \sum_x \sum_y \sum_z |D_p(x, y, z) - D_c(x, y, z)|^2$. The

initial sweeping window gaps composing the elements of \vec{F} were then modified such that the cost value was reduced. Two strategies were tested in the preliminary tests to modify the gaps in the window sequence. One strategy was and *ad hoc* intuitive selection of gap changes. The other was an application of the Simplex technique. Once modified, the dose distribution and associated cost were recomputed to determine whether the modified windows produced a reduced cost. If the cost decreased, the modifications were accepted. Otherwise they were rejected and another set of modifications was chosen to be tested. Modifications for single gaps along each leaf track intersecting the projection of the target volume were tested in each cycle through this loop. Thus the dose was recalculated repeatedly, and required a fast assessment of the consequence of the gap modifications.

Test cases with *ad hoc* search. The results of this prototype calculation produced by the intuitive gap modification strategy are given in the following paragraph. Tests were carried out using artificial target structures and organ-at-risk structures. In the example given here the target volume was a 12-cm diameter sphere with a 5-cm diameter cylindrical structure embedded in its periphery. The initial zero-sum swept window pattern was modified to account for a sensitive structure by initially keeping it always shielded from every angle. Two strategies were tested in the preliminary tests to modify the gaps in the window sequence. One strategy was and *ad hoc* intuitive selection of gap changes tested within 7 bixels of the window track. The other was an application of the Simplex technique. Once modified, the fluence distribution and associated cost were recomputed to determine whether the modified windows produced a reduced cost. If the cost decreased, the modifications were accepted. Otherwise they were rejected and another set of modifications was tested.

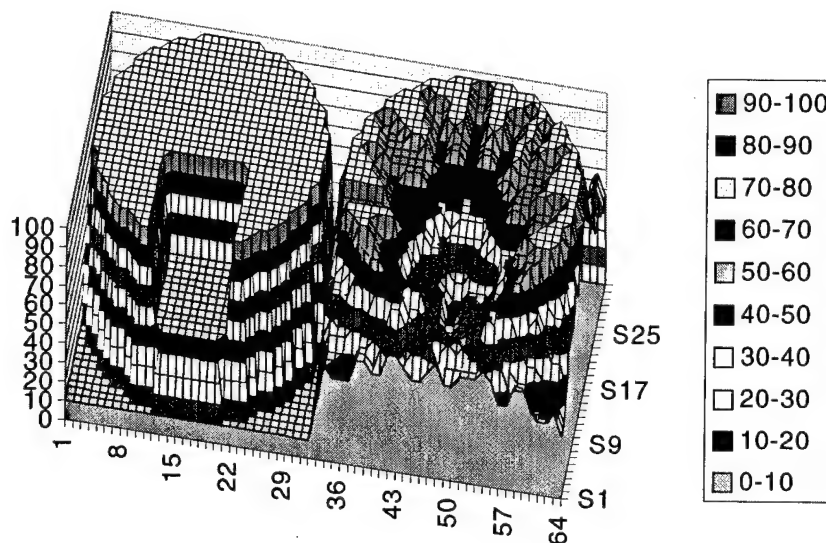


Figure 8. Comparison of the prescribed fluence (left) with the computed SWAT fluence (right).

The results of this prototype calculation produced by the intuitive gap modification strategy are given in Figure 8. The prescribed dose on the left consisted of a 12-cm diameter spherical target structures with a 5-cm diameter cylindrical critical structure embedded in its periphery. The dose constraint to the critical structure was 50%. An isometric three-dimensional plot of the final computed fluence in the central axial plane of the target volume is given the right side in Figure 8. The target volume had about 20% inhomogeneity, similar to what is achieved with fixed-gantry IMRT. The computed distribution was verified with film measurements.

SWAT Implementation

The goal of the investigation is to determine the best algorithm for computing the set of MLC leaf trajectories,

$$W_m(\theta) \quad m = 1, 2, \dots, m_{\max}$$

$$M_m(\theta)$$

(see Figure 4) for a multileaf collimator with m_{\max} leaves as a function of the gantry angle θ in order to deliver a conformal radiation dose. These trajectories are to produce dose distributions that are equal to or superior to those that can be obtained by presently available commercial systems that use multiple fixed-gantry cone beam IMRT implemented with dynamic and step-and-shoot delivery techniques. The algorithms would be considered to be superior if dose distributions can be achieved that are equivalent to the fixed-gantry sweeping window approaches, but with a significantly shorter delivery time and a simplified planning process. A key element of this investigation is on the use of a sweeping window arc as the starting point of iterative searches. The motivation for this focus is the notion that such a sweeping window will achieve intensity modulation over the course of a single arc. The technique will therefore be referred to as a sweeping window arc therapy or SWAT. Preliminary investigations indicate that the approach has considerable potential, but the investigations detailed here are needed to clarify the practicality of implementation.

Refine computation of dose in the spatial domain using pointers.

Application of Monte Carlo techniques to dose calculation matrix. The computation of the three-dimensional dose distribution due to an arc pattern must be fast, but it must also be accurate. The symbolic representation of the dose calculation from the swept window sequence is

$$\bar{D}_c = \bar{F} \cdot |H|$$

where H is the matrix of ratios of dose to a voxel per fluence in a bixel. In the preliminary work, these elements were crudely approximated using a parallel ray approximation and neglecting both attenuation and scatter. The parallel-ray approximation can be easily removed by tracing rays along the slant lines given by

$$v = \frac{SAD(y \cos \theta - z \sin \theta)}{SAD - z \cos \theta - y \sin \theta}$$

$$u = \frac{xSAD}{SAD - z \cos \theta - y \sin \theta}$$

In addition, a number of better approximations can be made to improve the dosimetric accuracy of the computation. We propose to use Monte Carlo methods to compute the nonzero elements of the H matrix. Monte Carlo code has been developed at Stanford that can be easily adapted to carry out this part of the project. For a particular patient, the CT data of the patient in treatment position will be used to compute the matrix

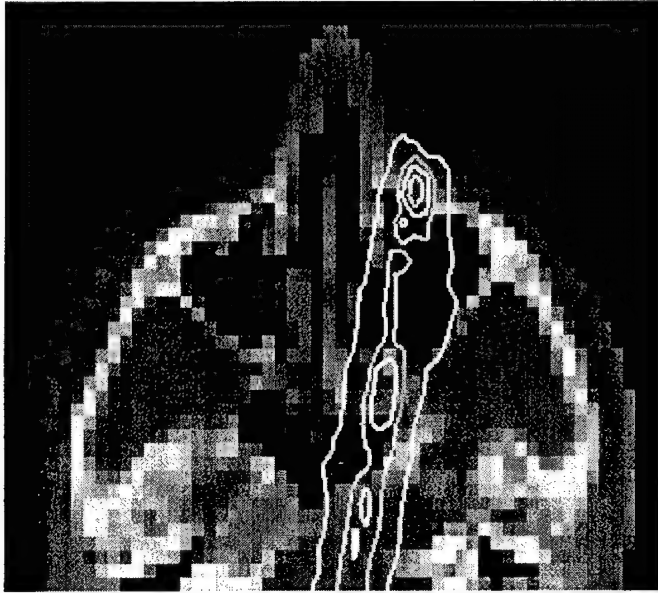


Figure 9. Dose along the track of a single bixel ray computed by a Monte Carlo simulation illustrating accounting for both bone and air heterogeneities.

elements taking into account the attenuation up to each voxel and electron transport and scatter from the upstream voxels along the ray path from the bixel to the voxel. All voxels that receive a significant amount of scatter will be added to the list of voxels to which the pointer points. An example of this type of pencil beam Monte Carlo calculation is given in Figure 9. The time required to compute these matrix elements may seem excessive, but in fact it is not. Each element need only be calculated to a precision sufficient to give a cumulative precision when all elements are used in the summation. For example, a given voxel may require 2.5 million Monte Carlo histories to achieve a standard deviation of 2%. It would take an inordinately long time to run this many histories for each bixel in a sequence of 20 gantry angles. However, at each gantry angle, the voxel will be struck, so the number of histories required for each bixel is only about 250,000. The calculations will be carried out using a network of 20 dedicated Pentium PC computers at Stanford. The calculation will be run

in parallel on this cluster of computers such that the total calculation time will be further reduced by another order of magnitude. However, if a given bixel is struck only a few times, this line of reasoning does not apply and the accuracy may be compromised. It is difficult to predict without a systematic investigation of the process how difficult it will be to compute sufficiently accurate H -matrix elements.

Cost computation acceleration using limited spatial domain techniques.

We propose to accelerate the *dose* computation by using bixel-to-voxel pointers. As described in the Preliminary Studies section, bixel-to-voxel pointers are look-up tables that point from a given bixel within the aperture of the MLC at a given gantry angle to the voxels that lie on the ray line passing from the target, through the bixel, and on through the calculation array. The bixel-to-voxel pointer allows the effect of opening or closing a voxel to be propagated rapidly through the dose distribution. The time required to compute the *cost* can be reduced further with additional applications of the bixel-to-voxel pointers. The procedure is applied during the recalculation of the dose in the optimization iterations. This allows one to consider only those voxels in the dose array, D_c , that change because of a test modification of one segment of the window sequence. Using the bixel-to-voxel pointers, changes in a set of bixels in the sweeping window sequence will be related to a set of voxels $(i, j, k) \in \delta$. The cost function before making the change in window sequence will be calculated by

$$\text{cost}_{old} = \sum_{i,j,k \notin \delta} (D_p - D_c)^2 + \Delta_{old}(\delta)$$

where $\Delta_{old}(\delta) = \sum_{\delta} (D_p - D_{c-old})^2$. The second term can be separated from the summation as a consequence of the cost function being a simple linear summation of terms of cost, each term arising from an individual voxel. The cost after the trial change in the window sequence will be computed by

$$\text{cost}_{new} = \sum_{i,j,k \notin \delta} (D_p - D_c)^2 + \Delta_{new}(\delta)$$

where $\Delta_{new}(\delta) = \sum_{\delta} (D_p - D_{c-new})^2$. The majority of the terms in the overall cost are common to both calculations and need not be recomputed for each trial. The change in cost function can be computed directly as

$$\Delta \text{cost} = \text{cost}_{new} - \text{cost}_{old} = \Delta_{new}(\delta) - \Delta_{old}(\delta)$$

using only the computation of dose on those voxels in the set δ identified by the bixel-to-voxel pointer. In those iterations in which a change is accepted, the dose calculation array, D_c , will also need to be up-dated with the changes in dose due to the bixels in the set δ . This strategy will result in a considerable time-savings. However, the addition of scatter to the H-matrix may reduce this time-savings to an extent that is hard to predict without carrying out a thorough investigation. More importantly, the use of pointer arrays uses a considerable amount of memory. Unless the pointer arrays as well as the two dose arrays, D_p and D_c , are held in directly accessible memory, the calculation will not be as fast as possible. For example, if the operating system is allowed to start disk swapping the arrays during the calculation, the acceleration will be lost. These and other details of the implementation will need to be tested during the course of the investigation.

Develop and verify computation of dose using analytic functions in the frequency domain.

Another approach to increasing the speed of the dose calculation of arced fields is to use mathematical tools borrowed in part from imaging theory. This theory allows the representation of the dose distribution in the Fourier frequency domain. The representation of dose in the frequency domain is intimately related to the theory of image formation developed for CT, PET, and SPECT reconstruction algorithms. In what follows we outline the theory.

Theory of dose calculation using central slice theory.

Dose is related to incident fluence by the relation $D = (\mu_{en}/\rho) \Psi$ where (μ_{en}/ρ) is the energy absorption coefficient and $\Psi = (h\nu)\Phi$ is the energy fluence due to a photon particle fluence Φ carrying energy $(h\nu)$. The dose distribution can be calculated by attenuating an incident energy fluence Ψ_0 to a depth d and calculating the dose at that depth with the energy absorption coefficient, $D(x',d) = (\mu_{en}/\rho) \Psi_0(x')e^{-\mu d}$ where μ is the linear attenuation coefficient (Boyer and Mok, 1985). $P(x',\theta)$ is the dose profile at the axis of rotation along the x' axis rotated through an angle θ at $y' = 0$ in Figure 10. It can be shown (Bortfeld and Boyer, 1995) that the total dose delivered by a complete rotation of a beam can be calculated using

$$D(\vec{r}) = \int_{\theta=0}^{2\pi} D_{\theta}(\vec{r}') d\theta = \int_{\theta=0}^{2\pi} P(x',\theta) e^{-\mu' d} d\theta$$

where

$$P(x', \theta) = \frac{\mu_{en}}{\rho} \Psi_0(x', \theta) e^{+\mu_{e0} x'}$$

is the beam profile associated with beam angle θ . Here we have written dose as if it were all deposited at the interaction point. This approximation neglects transport of dose in all directions by photons and electrons produced by the primary interaction. As this investigation continues, we will refine this approximation using rotation dose kernels (Desobry, 1991). The inverse treatment planning problem can be considered to be the inversion of this integral to calculate $P(x', \theta)$ for any dose distribution $D(\vec{r})$. The circular integral is formally an exponential back-projection followed by integration over the rotation angle θ . This process is used in image reconstruction in the context of the Radon transform. To apply image reconstruction theory to the dose calculation problem, consider the Fourier transform of the dose distribution

$$F(u, v) = \int_{-\infty}^{+\infty} \int_{-\infty}^{+\infty} D(x, y) e^{-2\pi i(xu + yv)} dx dy = \mathbf{F}_2 \{D(x, y)\}$$

The Fourier slice theorem provides a relationship between the two-dimensional Fourier transform of the dose distribution and the one-dimensional Fourier transform of a single profile,

$$S_\theta(u') = \int_{-\infty}^{+\infty} P(x', \theta) e^{-2\pi i u' x'} dx' = \mathbf{F}_1 \{P(x', \theta)\}$$

This is a single "slice" through the frequency domain distribution. The relationship can be expressed as

$$S_\theta(u') = F(\delta[u - u' \cos \theta], \delta[v - v' \sin \theta])$$

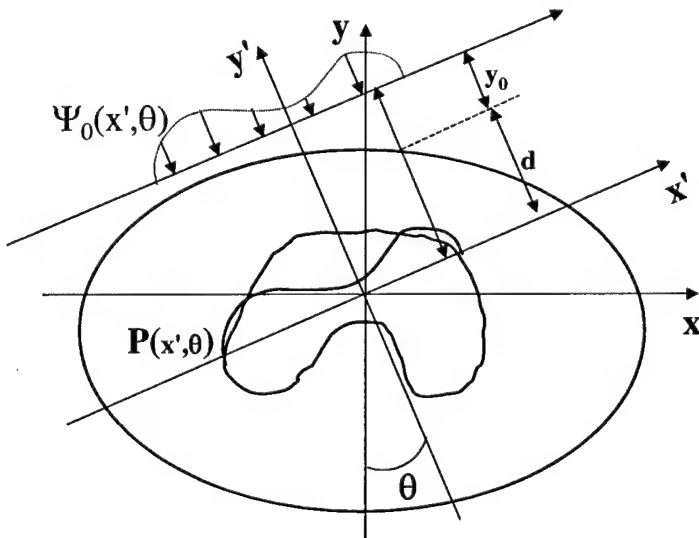


Figure 10. Geometry showing the calculation of dose using the exponential Radon transform.

One can formally construct the entire dose distribution from the one-dimensional Fourier transforms of the beam profiles. In diagnostic imaging, the Fourier slice theorem cannot be applied to image reconstruction because it is not feasible to interpolate from the polar coordinate system in which the single slices are computed to the rectilinear coordinate system in which the two-dimensional image is computed. However, we can compute the Fourier transform of the projection of the dose from a leaf gap using closed analytic functions.

Inverse transformation of analytic functions with the FFT. The proposed investigations will employ use of the inverse fast Fourier transform (IFFT) on data that has been calculated analytically. It is easy to transform real data

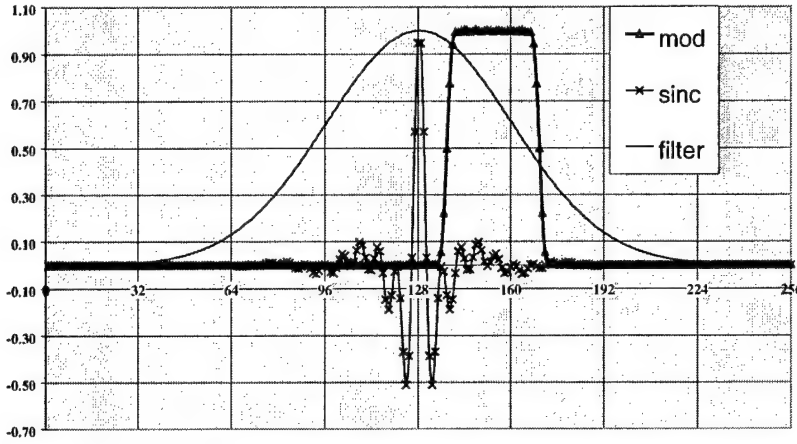


Figure 11. Demonstration of the formation of a square wave from an analytically calculated sinc function in the frequency domain.

from the spatial domain to the frequency domain and back again using a fast Fourier transform (FFT) algorithm followed by application of the complementary IFFT. In what is proposed here, the data will be computed analytically in the frequency domain *de novo*. It is essential that application of the IFFT to this computed data will yield the correct functional forms in the spatial domain. This section reports the demonstration of this capability by the investigators. The function of primary interest here is the rect function,

$$\Pi(x) = \frac{1+2x}{2|1+2x|} + \frac{1-2x}{2|1-2x|}$$

The function is a square-wave pulse of unit height and unit width. It has the property that $\Pi(x)=1$ when $|x| \leq 1/2$ and zero otherwise. Its Fourier transform is $\text{sinc}(x) = \sin(\pi x)/\pi x$. We are interested in using the rect function to represent the fluence produced by the gap between two MLC leaves. Consider a MLC leaf that projects to a width W_0 in the plane at isocenter. The m^{th} pair of leaves travel on a line offset from the field center a distance M_m^v . The fluence in this plane due to a gap between the m^{th} pair of leaves set to a width $W_m(\theta)$ can be expressed as

$$\Phi(x, y) = \int_{x'} \int_{y'} \Pi\left(\frac{x' - M_l(\theta) - x}{W_l(\theta)}\right) e^{-\frac{\pi}{2}\left(\frac{x'}{\sigma_x}\right)^2} \Pi\left(\frac{y' - M_l^y - y}{W_0}\right) e^{-\frac{\pi}{2}\left(\frac{y'}{\sigma_y}\right)^2} dx' dy'$$

where the Gaussian functions produce the penumbra due to a finite x-ray target size and leakage through the ends and sides of the leaves. This expression for $\Phi(x, y)$ is a convolution. It is composed of functions with known analytic Fourier transforms. Using the Fourier convolution theorem, the Fourier transform of the fluence can be written directly as

$$P(u, v) = W_l(\theta) \text{sinc}(W_l(\theta)) W_0(\theta) \text{sinc}(W_0(\theta)) e^{-2\pi i (u M_l(\theta) + v M_l^y)} e^{-2\pi (\sigma_x u^2 + \sigma_y v^2)}$$

Figure 11 is a demonstration of the proof of the principle that calculation of the sinc function analytically in the frequency domain yields, upon discrete Fourier transformation, the numerical values for the rect function in the spatial domain. The curve labeled sinc was calculated analytically for a pulse of width 32 using the expression for $P(u, v)$ given above. The offset was calculated as a complex exponential phase factor for a shift of 25 units. The real part of the frequency domain labeled sinc in Figure 11 demonstrates the modulation of the sinc function by the cosine term in the phase factor. The values were multiplied by a Gaussian (labeled filter in Figure xx) to produce the convolution accounting for edge blurring. The resulting numerical values were processed using the discrete Cooley-Tukey IFFT. The results are plotted in Figure 11. The resulting square pulse (labeled mod in Figure 11) demonstrates clearly that a rect function with the intended width and offset

was generated. Usually the frequency domain must be padded with zeros when transforming both with an FFT and an IFT. We found that the zero padding was unnecessary if the frequency domain was calculated purely analytically. The exercise demonstrated that we could carry out the steps properly to compute analytically in the frequency domain, and then transform to the spatial domain with the IFFT.

Since we know the closed analytic form of the Fourier transform of the profile at any desired gantry angle, we can calculate the transform values exactly at every rectilinear grid point in the frequency domain. We have shown above that we can inverse transform an analytically calculated frequency domain distribution back into the spatial domain using the discrete fast Fourier transform. Therefore, we can compute dose distributions by calculating the frequency domain representation analytically and inverse transforming the resulting array to obtain the dose distribution. We can calculate the frequency domain for a fluence distribution produced by a multileaf collimator as a sum of sinc functions for the gaps and offsets produce by the leaves.

We return to the problem of direct computation of the solution to the inversion of the rotation integral for the dose distribution. It is possible to compute this inversion analytically. Formally the process can be described as follows. One computes the projection profiles as the exponential Radon transform of the dose distribution at all projection angles,

$$P^*(x', \theta) = \int_{-\infty}^{+\infty} D_\theta(x') e^{i\mu y'} dy' = R_\mu \{D(x, y)\}$$

One then computes the one-dimensional Fourier transforms of the projection profiles

$$P(u', \theta) = F_1 \{P^*(x', \theta)\}$$

One then filters the transformed profiles

$$P(u', \theta) = K(u') P^*(u', \theta)$$

where $K = \frac{1}{2} |u'| \cdot H(|u'| - \mu/2\pi)$ is a filter function that is related to the conversion to polar coordinates.

The resulting frequency domain array is then inverse transformed to obtain the incident beam profile that will result in the desired dose distribution.

$$P(x', \theta) = F_1^{-1} \{P(u', \theta)\}$$

This process has been applied to the example given in Figure 12. The results are not the same as the intuitive solution. In the center of the field, for $|x| < W/2$, the optimal profile is $D_0/(2\pi) \cdot \cos(\mu r)$. For typical therapy beam energies, $\mu = 0.02/\text{cm}$ and this factor is essentially constant as anticipated. However, beyond the edge of the target volume, the optimal solution is

$$P(r) = \frac{D_0}{2\pi} \left[\cos(\mu r) - \frac{|r|}{\sqrt{r^2 + (W/2)^2}} \cos\left(\mu \sqrt{r^2 + (W/2)^2}\right) \right]$$

This solution takes on negative values and is therefore not feasible to deliver in practice. In the work we propose, we will not try to obtain the profiles by direct inversion of the Radon transforms of the prescribed dose distribution. Instead a search procedure will be investigated that seeks deliverable solutions based on the projections of MLC leaf gaps.

For a gap between two leaves, the fluence distribution is simply the product of rect functions. Consider the beam's-eye-view of a gap between two MLC leaves as in Figure 4.

$$\Phi_l(x', z', \theta) = \Phi_o \Pi\left(\frac{x' - M_l(\theta)}{W_l(\theta)}\right) \Pi\left(\frac{z' - M_l^z}{W_o}\right)$$

where M_l^z is the offset of leaf pair l (a constant for each leaf pair) and M_o is the width of the leaf (in the plane of projection) and is a constant across all leaves of the same width. The function $M_l(\theta) = \frac{1}{2}(x_i^A(\theta) + x_i^B(\theta))$ is the trajectory of the middle of the gap as a function of gantry angle θ . The function $W_l(\theta) = (x_i^B(\theta) - x_i^A(\theta))$ is the width of the gap between the leaves. These two functions constitute the solution sought by the inverse planning process for SWAT. The incident fluence within the cone beam formed by the MLC at a given gantry angle is

$$\Phi(x', z', \theta) = \sum_l \Phi_l(x', z', \theta)$$

The Fourier transform of this function, $F\{\Phi(x', z', \theta)\}$, is well known and is

$$S_\theta(u', v') = \sum_l W_l(\theta) \sin c(W_l(\theta)u') \cdot W_o \sin c(W_o v') e^{-2\pi i(u'M_l(\theta) + v'M_l^z)}$$

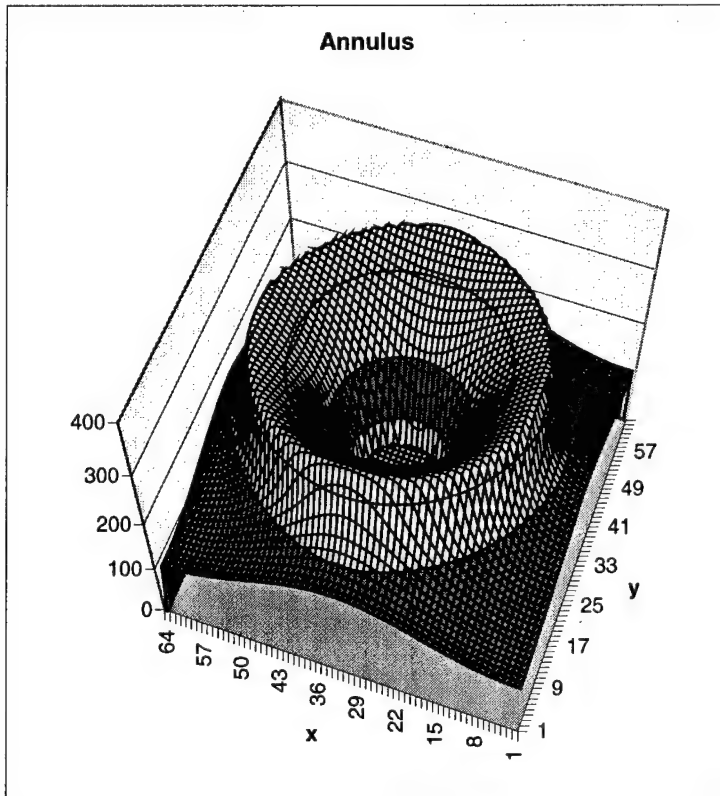


Figure 12. Dose in axial plane in the spatial domain due to a rotated gap. The gap was specified in the frequency domain and then inverse transformed to obtain the results in the figure.

The Fourier frequency domain representation of the MLC leaf trajectory can be calculated using analytic functions directly in the frequency domain without having to transform from the spatial domain. As a consequence, the frequency domain representation of the fluence (and dose) in the spatial domain can be calculated exactly for any point in the frequency domain. This is achieved by calculating the frequency domain profile $P(u', \theta)$ at angles $\theta_{i,j}$ corresponding to profile radii that pass through the rectilinear coordinate points at indices i,j . This allows one to fill the rectilinear space with analytically calculated Fourier transforms. Then one may use the Fourier slice theorem to use a three-dimensional discrete fast Fourier transform to directly calculate the spatial domain fluence (and dose) distribution.

A full three-dimensional calculation model was coded incorporating a three-dimensional IFFT. The parallel beam model was retained for the purposes of preliminary investigations. Sinc functions were generated for gaps

corresponding the MLC leaves where the direction of the leaf motion was parallel to the axis of rotation. Thus each gap between a leaf pair used a sinc function in the direction of the rotation axis and another sinc function computed in profiles corresponding to the rotation about the axis. The results for an offset gap is shown in Figure 12. The central region out to a radius R_1 is blocked, and the dose rises to a rim at a radius R_2 before falling off as a skirt of dose as expected. This demonstrates that we can calculate the frequency domain representation of a dose distribution for a given MLC leaf configuration during a complete arc rotation.

Optimization in the frequency domain.

Using Fourier transforms is a strategy that has been described in standard texts on optimization theory (Pierre1969). The technique was used by Bortfeld to investigate optimization of beam orientations in the frequency domain (Bortfeld, 1993). The basic approach is the same here. Let the cost function to be optimized be

$$G = \sum_x \sum_y \sum_z [D_p(x, y, z) - D_c(x, y, z)]^2$$

where $D_p(x, y, z)$ is the prescribed dose distribution and $D_c(x, y, z)$ is the calculated dose distribution. Define the Fourier transforms of these dose distributions to be $D_p(u, v, w) = F \{D_p(x, y, z)\}$ and $D_c(u, v, w) = F \{D_c(x, y, z)\}$. Using these functions one can define a cost function in the frequency domain,

$$G = \sum_u \sum_v \sum_w [D_p - D_c]^2$$

The advantage of calculating the cost function in the frequency domain is that one may cut off the sum used to calculate G at some low frequencies, $u_{cut}, v_{cut}, w_{cut}$, e.g.

$$G \cong \sum_{u=1}^{u-cut} \sum_{v=1}^{v-cut} \sum_{w=1}^{w-cut} [D_p - D_c]^2$$

Demonstration that optimization in the frequency domain is equivalent to optimization in the spatial domain.

We now demonstrated the proof of the principle that optimization in the frequency domain yields the same results as optimization in the spatial domain for a simple example. In the example in Figure xx, we sought the width of a rect function that would minimize the least square difference between itself and a Gaussian with a

fixed σ . The cost function in the frequency domain was constructed from the analytic forms of the Fourier transforms of the rect function and the Gaussian function. Functions were chosen with known analytic Fourier transforms. The frequency domain cost function was

$$G = \sum_s \left[\frac{\sin(\pi \cdot W u)}{\pi u} - \sqrt{2} \sigma e^{-(2\pi\sigma^2 u^2)} \right]^2$$

The corresponding cost function in the spatial domain cost function was

$$G = \sum_x \left[\Pi\left(\frac{x}{W}\right) - e^{-\frac{\pi(x/\sigma)^2}{2}} \right]^2$$

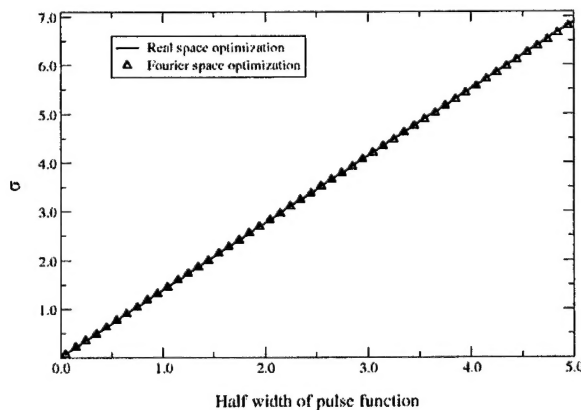


Figure 13. Precisely the same rect function width W was obtained in both the spatial and frequency domains.

A parabolic search algorithm was used to find the value of

W that minimized the cost functions in each domain for a range of values of the variance of the Gaussian function. The results are given in Figure 13. Precisely same values of the rect function widths were obtained by independent optimizations in both domains, as Parsaval's theorem predicts.

Demonstration that optimization need only be carried out for low frequencies.

This principal can be demonstrated using the same simple example as above. The Gaussian and rect functions are to be made as similar as possible as measured by the least squares cost function. In this second example, both the width and the height of the rect function were taken as variable parameters. This provided a two-dimensional search space with a minimum as shown in Figure 14. The optimal widths and amplitudes of the rect function were determined in both the frequency and spatial domains and were found to be the same consistent with the previous section. The calculation was then repeated in the frequency domain restricting the summation to ever decreasing cut-off limits.

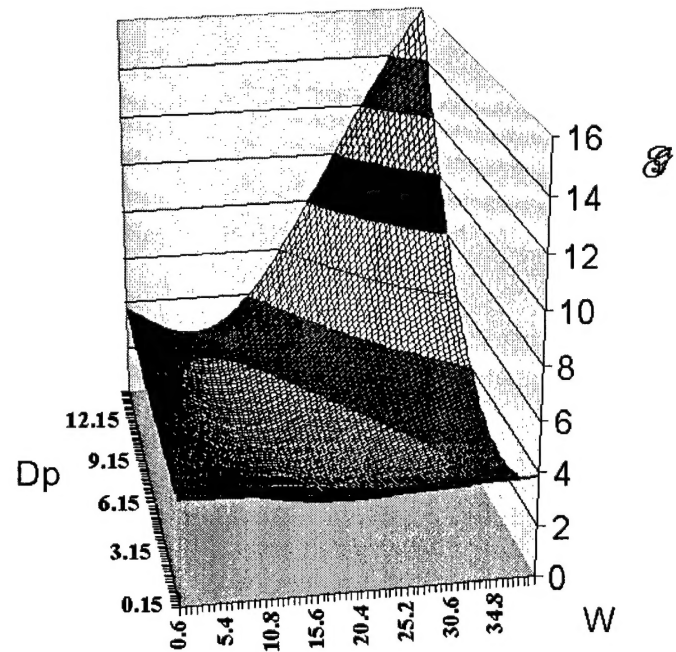


Figure 14. Cost function computed in the frequency domain as function of rect function amplitude (D_p) and width (W).

$$G = \sum_s^{s-cut} \left[\frac{\sin(\pi \cdot W s)}{\pi s} - \sqrt{2} \sigma e^{-(2\pi \sigma^2 s^2)} \right]^2$$

The results are plotted in Figure 15. Figure 15 demonstrates that as the upper limit of the summation over the frequency domain, s -cut, was lowered from 128 (the size of the frequency domain array used in this case) to about 32, the results of the search for the optimum values of W and D_p (the minimum in Figure 13) remained fairly stable. This suggests a search strategy that begins iteratively optimizing the treatment parameters with very low cutoff frequency.

If one starts with $1/4$ of each frequency domain axis or about 1.5% of the frequency domain volume, the search time will be reduced by a factor of approximately 100. As one approaches a final optimal value, the cut off frequency can be gradually raised to refine the precision of the final optimization parameters. By eliminating summation over a substantial volume of the frequency domain each time G is recomputed in the iterative search for its minimal value, a

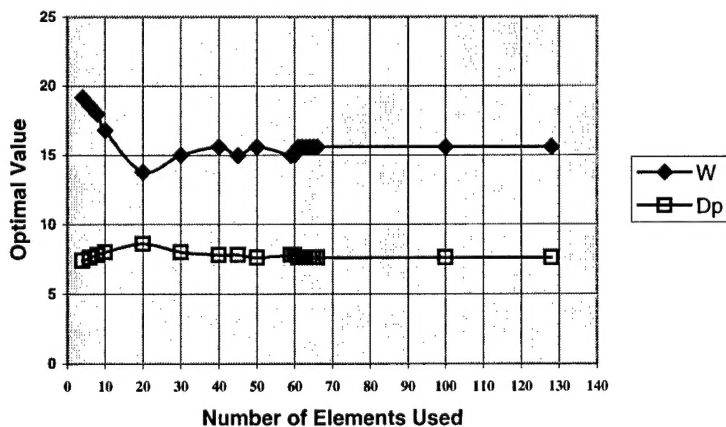


Figure 15. Demonstration of the stability of the optimization with an increasingly lower cutoff frequency, s_{cut}

substantial savings in computation time can be realized. Once the final values of the leaf trajectories are computed, a final dose calculation will be carried out in the spatial domain using a Monte Carlo calculation.

Conclusions

A line of investigation is described here that offers a strategy to seek means to plan and deliver IMRT more rapidly and efficiently than current methods using a continuous arc. The sweeping window produces a dose distribution within an unmodulated volume that is nearly the same as that produced by a Takahashi arc. However, the sweeping window offers opportunities to modulate the dose distribution at many angles to either shield structures or add dose to improve homogeneity within the target. Optimization of the gaps used in the arcs can be carried out by standard optimization methods. Optimization in the frequency domain may offer an opportunity to increase the computation speed. The efficacy of the ideas must be tested by developing the methodology and comparing the results with techniques presently in use. A definitive comparison cannot be made without first developing the SWAT technique to approximately the same level of sophistication as the fixed gantry and tomotherapy methods currently in use.

References

- Bortfeld T, Schlegel W (1993). Optimization of beam orientations in radiation therapy: some theoretical considerations. *Phys. Med. Biol.* 38:291-304.
- Bortfeld T, Boyer AL (1995). The exponential radon transform and projection filtering in radiotherapy planning. *Intl. J. of Imaging Systems & Tech.*, Vol. 6, 62-70.
- Brahme A, Roos JE, Lax I (1982). Solution of an integral equation in rotation therapy. *Phys. Med. Biol.* 27:1221-1229.
- Cormack AM. (1987) A problem in rotation therapy with x-rays. *Int. J. Radiat. Oncol. Biol. Phys.* 13:623-630.
- Cormack AM, Cormack RA (1987). A problem in rotation therapy with x-rays: Dose distributions with an axis of symmetry. *Int. J. Radiat. Oncol. Biol. Phys.* 13:1921-1925.
- Desobry GE, Wells NH, Boyer AL (1991). Rotational kernels for conformal therapy. *Medical Physics* 18(3):481-487.
- Oelfke U, Bortfeld T (1999). Inverse planning for x-ray rotation therapy: a general solution of the inverse problem. *Phys. Med. Biol.* 44: 1089-1104.
- Pierre D (1969). *Optimization Theory with Applications* (New York: Dover Publications, Inc).
- Takahashi S. Conformation radiotherapy (1965). rotation techniques as applied to radiography and radiotherapy of cancer. *Acta Radiol. Suppl.*;242:1-4.
- Webb S (2001). *Intensity-Modulated Radiation Therapy* (Bristol and Philadelphia: Institute of Physics Publishing).
- Yu CX (1995). Intensity modulated arc therapy with dynamic multileaf collimation : an alternative to tomotherapy. *Phys. Med. Biol.* 40:1435-1449.
- Xia P, Geis P, Xing L, Ma C, Findley D, Forster K, Boyer AL (1999). Physical characteristics of a miniature multileaf collimator. *Med. Phys.* 26(1):65-70.